UNIVERSITY OF MODENA AND REGGIO EMILIA

"Enzo Ferrari" Engineering Department

PhD Course in Industrial and Environmental Engineering
XXXV Cycle

Modelling, simulation and experimental characterization of hydraulic systems and components for off-highway vehicles

Supervisor:

Prof. Ing. Barbara Zardin

Candidate:

Andrea Fornaciari

Co-supervisors:

Ing. Luca Riccò

Prof. Ing. Massimo Borghi

Course coordinator:

Prof. Ing. Alberto Muscio

Academic year 2021/2022

Contents

Abstract

The presented thesis work summarizes the activities carried out during the Ph.D. in Industrial and Environmental Engineering performed in collaboration between the Fluid Power for Mobile Application Lab of the Enzo Ferrari Department of Engineering and Dana Incorporated. As the title suggests, the main topic was the modelling, simulation and experimental characterization of hydraulic systems and components for off-highway vehicles. The usage of fluid power in both agricultural and mining applications is indeed widespread. A thorough understanding of these systems and components allows their correct and potentially innovative design, considering both the improvement in performance and the energy savings achievable by implementing these innovative solutions. In collaboration with Dana Incorporated which has funded the Ph.D. scholarship, we selected two main research activities in which the company was interested.

The first regarded the design and prototyping process of a hydro-pneumatic independent suspension for agricultural tractors.
This is a multi-disciplinary activity where the hydraulics, the mechanical design and the control logics affect the vehicle dynamics and so its global performances. In parallel to this, several numerical models of both the system and the vehicle were developed in different simulation environments. These models were then used to study the system itself.
After these preliminary steps, it was possible to develop an optimization workflow for the whole suspension system, in which both the hydraulic hardware and the suspension architecture were optimized to improve the kinematic and dynamic performances of the vehicle. A prototype for the suspension was created starting from the optimized solution, and it was then subjected to experimental activities on a test rig. This prototype is also going to be installed on the reference tractor to perform the vehicle final tests.

The second main activity carried out during the Ph.D. was the study and detailed modelling of a bent axis unit (pump or motor). These machines are very common for example in hydrostatic transmissions, which are widely used in off-highway vehicles. Besides this aspect, we decided to investigate this topic also because there are not a lot of studies and methods concerning the design optimization of this kind of machine in the literature.
In particular, we focused the attention on the mechanical analysis of the unit to evaluate the reaction forces and moments between the main components and therefore the torque delivered to or absorbed by the shaft taking into account all the internal losses. The outcome of this activity was the development of a vectorial and parametric numerical model, which can be used both in the design phase and as virtual characterization for this kind of positive displacement machine.

During these Ph.D. years, I also spent a research period abroad at the Maha Fluid Power Lab of Purdue University, in West Lafayette, Indiana, US. In this period, I carried out the study of a hydraulic hybrid power-split transmission, performing the testing setup and the first experimental tests on the system installed on a pick-up truck.

So, the main research activities performed in these years are reported in the chapters of this thesis. These activities give an overview of what is the research approach in the field of hydraulic systems and components for mobile applications, from the modelling to the experimental tests.

Introduction

This work of thesis shows the main activities carried out by the candidate during the three years of PhD "Enzo Ferrari" course in Industrial and Environmental Engineering of the University of Modena and Reggio Emilia. These activities have been accomplished in collaboration with the Fluid Power for Mobile Application Lab of the "Enzo Ferrari" Engineering department and with Dana Incorporated, which funded the PhD scholarship.

In particular, the candidate has carried out two main activities, each of which is presented in a dedicated chapter. These two different topics were defined with the Dana Incorporated Engineering department, basing primarily on the research field of interest for the company. However, both activities rely on fluid power modelling, regarding hydraulic systems (the first one) and components (the second one).

The first activity concerned the analysis and modelling of an independent hydro-pneumatic suspension for agricultural tractors to create a validate a methodology for the complete optimization of this type of system. The activity objective was to create a tool capable of assisting the design of an axle with independent hydro-pneumatic suspension, optimizing its architecture, hydraulic system and control starting from the functional requests. In fact, these are multidisciplinary systems, where the mechanics, hydraulics and control logics must interact to ensure the optimization of the global performance of the vehicle.

The second main activity regarded the detailed modelling of bent axis positive displacement units. Despite being widely used in fixed and mobile applications, this type of machines is the subject of a limited number of research studies. The activity objective was the creation of a numerical model capable of simulating both the fluid dynamics and the mechanical aspect not only of the reference machine, but also of a whole family of machines with similar geometry and characteristics. Once validated, this tool turns out to be very useful in the design phase of this type of machine, thanks to the capability of evaluating the overall behaviour and efficiency of the unit, and the internal reactions exchanged between the components.

However, these activities are introduced in detail in the dedicated chapters. We indeed preferred to create two different introductions at the beginning of each chapter.

Similarly, the conclusions relating to these activities are reported at the end of each chapter, while some brief final conclusions are reported at the end of the thesis.

At the very end of this work of thesis there is also a brief appendix relating to the research abroad carried out at the Maha Fluid Power Research Center of Purdue University at West Lafayette (Indiana, USA) from February to September 2022.

Chapter 1: Advanced Front Suspension System

Introduction

The activity carried out in collaboration with Dana Incorporated concerning the realization of a design methodology for an independent hydro-pneumatic suspension for off-highway vehicles is presented in this first chapter.

The multibody analysis of vehicles turns out to be the state of the art for the study of the dynamic behaviour of these vehicles and the interactions between the different subsystems, such as the primary suspensions, the steering system or braking one. However, the multibody approach presents some difficulties, such as the modelling and parameterization of the tire-soil contact or the parameterization of some unknown information, such as frictions. Another important aspect to consider is the computational time required for multibody simulations, which is usually in the order of tens of minutes.

In this chapter, we applied the multibody modelling approach to a medium-sized agricultural tractor, with the aim of creating a virtual tool where it is possible to integrate the detailed model of different hydro-pneumatic suspension systems and architectures. In this way, it will be possible to compare different solutions and optimize different designs.

Suspension systems are essential for ensuring good comfort performance and effectiveness in terms of manoeuvrability and traction capacity of the vehicle, both in automotive and off-road field. Among all the types of existing suspensions, the focus here is on independent hydro-pneumatic suspensions, which appear to be the state of the art for off-highway vehicles. This type of suspensions is capable to achieve decidedly improved performance compared to the others in terms of comfort, handling and traction. Having a better traction capacity means also achieving a reduction of both fuel consumption and tire wear. Furthermore, this type of suspension manages to exploit the hydraulic system already integrated on the vehicle to manage the various requests of the tractor. Hydro-pneumatic suspensions are therefore the best choice for this type of vehicle [1].

Obviously, these benefits mean that more engineering effort is required to design these systems than non-independent suspensions or non-sprung axles. Indeed, this is a multidisciplinary activity where the mechanical design of the suspension architecture, the behaviour of the hydro-pneumatic circuit and its management through the control software must interface with each other to improve the overall performance of the complete vehicle.

The choice of the best solution and its calibration is essential because of the freedom to choose between both different possible architectures and stiffness and damping characteristics of the system. The optimal solution must be a compromise between performances and safety. This choice often turns out to be a complex activity that requires long and tiring experimental tests, on the test bench and on the ISO field/tracks, to test different dynamic conditions [2].

Despite the extensive knowledge regarding different layouts of these systems and their calibration, it is also recognised in the literature that there are aspects that can be investigated further. An example might be the comparison of different architectures, or the 'calibration' of a given suspension geometry. The guidelines for a correct calibration strategy for the chosen architecture have not been widely studied and developed [3]. In this context, a virtual tool capable of simulating the system would be very useful. Thank to this, indeed, it would be possible not only to compare different architectures or determine a calibration methodology for these, but also to achieve greater knowledge of the overall behaviour of the vehicle.

To obtain such a virtual tool, it is necessary for this model to be able to reliably replicate both the behaviour of the suspension, hydro-pneumatic in the case in question, and of the entire vehicle. The integration of the model relating to the hydraulic system with the multibody, kinematic and dynamic model of the tractor, although it may be challenging, seems to be the correct choice to address this problem.

In order to obtain such a virtual tool, it is necessary for this model to be able to reliably replicate both the behaviour of the hydro-pneumatic suspension and of the entire vehicle. Although it may be challenging, the integration of the hydraulic system model with the multibody model (kinematic and dynamic) of the tractor appears to be the correct choice to address this issue.

An example of a detailed multibody model of a tractor can be found in [4] and [5], where great attention was paid to the description of the tire-soil contact and the alignment with experimental results. In other publications by Biral et al., such as [6] or [7], the analysis focused on a semi-active hydro-pneumatic suspension system for a tractor and the optimization of its control logic. This study highlighted some limitations of the different control strategies for this type of suspension, given for example by the damping dynamics and non-linear behaviour of the hydraulic suspension. In other studies, the importance of considering the tractor's pitching motion for the suspension analysis was recognised, and a half-car model of the vehicle coupled with detailed thermo-hydraulic modelling of the hydro-pneumatic suspension was therefore proposed [8].

Moreover, several authors have focused their studies on the suspension system optimization in the last decades, both for light and heavy-duty vehicle. The identification of key parameters both for vehicle [9] and heavy-duty suspensions [10] is crucial to define an optimization methodology. This latter, in fact, translates into the optimization of these key parameters and must consider whether it is referring to road vehicles [11] [12] [13] or other types of vehicles (e.g. high speed railway vehicle [14]). Obviously, the optimization approach varies as the suspension type changes, for example for passive and semi-active suspensions [15], regenerative suspension [16], or independent suspension [17] as MacPherson type [18] [19] or double wishbone one [20]. Other authors have also focused the attention on particular aspects of these multi-domain systems, as the kinematics and compliance [21] or hydraulic circuits [22] [23], which commonly manage off-highway suspensions. Some publications have also highlighted the potential of different optimization algorithms for these applications, from genetic algorithms [24] to less common cascading methods [25] [26].

However, all these studies are based on the realization of numerical models or virtual tools capable of replicating the suspension behaviour. Obtaining a virtual tool capable of supporting the design and optimization of this type of system is therefore very advantageous and crucial but at the same time challenging from an engineering point of view.

Dana Incorporated therefore decided to start this activity of analysing and optimising hydro-pneumatic suspensions to design and build the prototype of an axle with independent suspension, with the aim to enter the market with the production of this solution. The company, in fact, is a manufacturer of axles, for light and off-highway vehicles, but not with independent suspension. It therefore lacked all the necessary know-how for the design of this type of system, which is what we sought to build with this activity.

During the PhD years, this project was one of the main activities pursued; in particular, the focus was on the development of the design methodology starting from the functional requirements of the system, and on the realisation of numerical models to support the design itself.

In this chapter, therefore, an account of the work carried out is reported. First, an overview on suspension systems and the theoretical studies from which we started are shown, and then the first draft of the Dana solution is presented. The various numerical models developed to support this activity will then be described. These models will be used within a logical flow of optimization of the entire suspension system, which is the central part of the activity. From the results of this optimization, it was possible to define the various aspects of the system under investigation, from the geometry of the suspension architecture to the dimensioning of the hydro-pneumatic system, which enabled the creation of the axle prototype. This prototype was then subjected to experimental tests to validate its performance and it will soon be installed on a farm tractor to assess the behaviour of the entire vehicle system. Parallel to the experimental work, an investigation was carried out into the development of a numerical model of the complete system capable of real time simulations. The successful outcome of this parallel activity would lead to the possibility of replacing complex multibody models within the optimization workflow, making the entire process faster, and thus more efficient and effective.

1.1 Suspension system: an overview

The suspension of a vehicle is the set of components by means of which the chassis is connected to the wheels of the vehicle, or more generally it refers to the connection between the suspended masses of the vehicle and the unsprung masses.
As with road vehicles, suspension for off-highway vehicles can be different and can be classified in many ways. In this paper, the classification according to the mechanism is presented to then focus on independent hydro-pneumatic suspensions.

1.1.1 Classification based on mechanism

As mentioned, there are numerous suspension types with different mechanical configurations in the vehicle industry. Each of these types has a specific kinematic behaviour, dependent on the architecture itself, which directly affects the stability and comfort conditions of the vehicle.

Depending on the mechanism, we can distinguish between steerable and non-steerable wheel suspension, driven or driving wheel suspension, or even independent or rigid axle suspension.

The latter differentiation is the one of most interest in this context. An independent suspension is any type of suspension system that allows each wheel on the same axle to move vertically independently of the other, for example in response to a bump in the road. This is not the case with rigid axles where the movement of one wheel also affects the other. Independent suspension usually offers better comfort and driveability characteristics both on and off road. At the same time, of course, these more complex systems require more engineering effort and higher development costs.

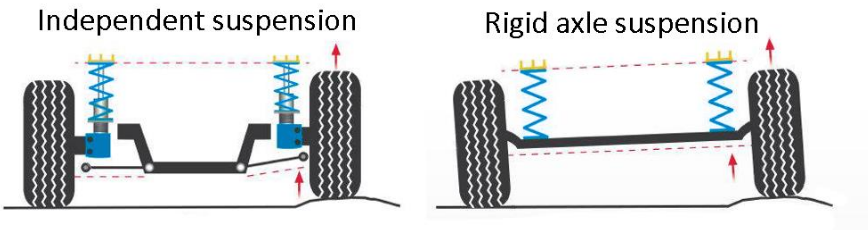

Figure 1.1: Comparison between independent suspension behaviour and rigid axle one

Among the independent-wheel suspension geometries are Chapman-type, MacPherson-type, and those known as multilink or double wishbone. The latter two are of particular interest in the off-highway sphere.

On the other hand, rigid axle suspensions are subdivided into rigid axle suspension without traction, rigid axle with traction and differential and De Dion axle (if they have traction without differential).

Agricultural tractors generally have a suspended front axle, while the rear axle is directly connected to the transmission and thus to the vehicle's sprung mass. Because of this, the rear axle almost completely transfers stresses from the ground to the cab, which is positioned on it. Therefore, the cab tends to be positioned between the rear and front axles in order to reduce stresses.

Small-size tractors generally have the front axle with rigid suspension, as a matter of cost and simplicity. The movement of the chassis, therefore, is greatly influenced by the unevenness of the ground. In these vehicles, the driver comfort is often improved by introducing secondary suspension, such as seat suspension (typically mechanical or pneumatic).

In cab tractors, another type of secondary suspension may also be used, such as the one under the cab itself.

However, it is easy to encounter the use of more complex suspension for the front axle in medium or large size agricultural tractors, while the rear axle remains almost always rigid. Only JCB Fastrac tractors have both axles suspended.

Axle with non-independent suspension still remain the most common solutions for these vehicles. Some examples are the CNH Terraglide II, with a suspended swing arm and hydraulic cylinder, or the Fendt 200 Vario. Another example is the John Deere TLS (Triple Link Suspension), which will be better explained later.

Solutions with independent suspension are obviously more complex than the ones mentioned above. Some examples of the multilink suspension type are John Deere's ILS (Independent Link Suspension), which uses articulated wishbones and two oblique hydraulic cylinders, or the Carraro SI series suspended axle with articulated wishbones and a centrally positioned hydraulic cylinder.

As said, multilink suspensions are characterised by greater mechanical complexity, but also by more effective elasto-kinematic behaviour, which allows both wheels to be kept perpendicular to the ground in almost every working condition. This means that the tyres always work with high efficiency, maximum stability and optimum traction for the vehicle in all ground conditions.

Figure 1.2: Two example of independent suspension architecture: MacPherson type (left) and double wishbone type (right)

1.1.2 Classification based on spring-damper nature

Suspension systems can also be classified according to the physical nature of the spring and damping elements. There are in fact mechanical, pneumatic, hydro-pneumatic or magneto-rheological suspensions.

In off-highway, the most common primary suspension systems are of hydro-pneumatic type, so called because it exploits a system with hydraulic actuators, gas accumulators, which act as the elastic element, and orifices or proportional valves for damping.

These suspensions are obviously more complex than the mechanical suspensions used in light vehicles, while magneto-rheological suspensions are not considered in off-highway for economic reasons.

The decision to use hydro-pneumatic suspensions obviously has several reasons. First of all, the masses involved are significantly greater than standard passenger cars (i.e. up to 10 tonnes difference). In addition, the height of the centre of mass above the ground is much greater than in a road vehicle: this results in a massive load transfer, for example during braking. This requires a robust suspension that can withstand high loads, both static and dynamic.

Another aspect to consider is the fact that the loading conditions of the tractor can vary considerably depending on the application and equipment used. For this reason, a suspension system such as hydro-pneumatic ones are perfect for this type of application because they allow both levelling and height control of the vehicle.

Moreover, particular applications may require the suspension to be locked, for example when lifting or unloading a load with a bucket or fork, or the total unlocking of the suspension once a certain threshold of forward speed has been exceeded. All this can be easily implemented using a hydraulic system, where the operator's direct control of one or more solenoid valves can easily manage these functions.

Another important feature that can be integrated with more complex hydraulic circuits is the possibility of varying the suspension's stiffness and damping characteristics depending on the working conditions. In fact, a stiffer suspension is generally preferred when the vehicle is on the road to improve driveability, while a softer one is more suitable when manoeuvring on field over uneven terrain.

1.1.3 Suspension requirements

Regardless of the type of vehicle, a suspension system must fulfil certain main functional requirements.

The first one is obviously to reduce as much as possible the accelerations and movements of the suspended mass coming from the uneven ground or results of special manoeuvres, in order to prevent mechanical damage and ensure the health and comfort of passengers.

Trying to minimize the normal force variation that is discharged in the tyre-ground contact is another functional requirement. In fact, each wheel is loaded with a fixed force component, which depends on the vehicle mass and balance, and a variable force component, which depends on the vehicle dynamics. By keeping this force as constant as possible, the tyre-soil contact surface will also be less variable and high longitudinal and lateral forces transmitted to the ground will always be guaranteed. This consequently implies a reduction in sliding and thus good traction and

braking capacity, which is also crucial in off-highway vehicles that are often equipped with trailers or other equipment to be towed.
Increasing grip without sliding means being able to reach higher speeds safely. In an off-highway vehicle such as a tractor, this aspect translates into increased productivity.

In addition to these functional requirements, a suspension system must also fulfil non-functional requirements in order to be integrated into the vehicle and be commercially attractive.
The first one may be the space required for the suspension to be mounted on the vehicle axle, which is obviously influenced by the suspension architecture and the geometry, and by the size of the various components.

This particular aspect can explain why a hydro-pneumatic suspension is generally preferred over a pneumatic one in off-highway. In fact, the possibility of obtaining pressures within the system that are an order of magnitude higher guarantees the potential reduction in the components number and their overall dimensions.
Furthermore, as mentioned in the previous paragraph, the capability of some hydro-pneumatic systems to vary their stiffness and damping characteristics is very attractive on the market. By stiffening or softening the suspension depending on the manoeuvre performed and the terrain on which it is made, it is possible to guarantee better comfort or driveability performance depending on the driver's requirements.
At the same time, a good suspension system must be reliable and robust. In off-highway, it is very important to have a reliable and low-maintenance suspension system, as failures or maintenance operations would directly affect the vehicle's productivity.
Another aspect to consider may be the cost of the suspension system compared to the vehicle on which it is installed and the demands of the various applications. Although it is purely not a requirement, this aspect limits, for example, the spread of suspensions such as magneto-rheological suspensions or active suspensions only in specific sectors such as luxury cars or military vehicles.

1.1.4 ISO 2631-1 and ISO 5008

The limiting factor regarding the requirement to minimise the accelerations of the suspended mass, mentioned in the previous paragraph, is the human being. In fact, mechanical parts can be designed to withstand even high levels of vibration, while the operator or passengers must be exposed to vibrations contained within certain frequency ranges.
On tractors, as on other vehicles, primary and secondary suspensions (such as those in the cab or under the seat) are used to minimize the vibrations to which the operator is exposed.
The comfort situation is subjectively perceived by the human being, but it is important to reduce lateral vibrations in the 1-2 Hz frequency range and vertical vibrations in the 4-8 Hz range.

The ISO (*International Organisation for Standardisation*) 2631-1/1997 [27] defines methods for calculating the total vibration value at a given point in a vehicle and the degree of acceptable vibration that ensures health and comfort.
This standard also states that accelerations in the frequency range of 0.1 to 0.5 Hz are responsible for musculoskeletal disorders in a human being. Depending on the amplitudes of these vibrations and the time of exposure to them, both fatigue and more or less serious health problems, such as spinal damage or heart problems, can occur.
This standard is widely used, also in the off-highway sector, to calculate the value of the overall acceleration to which a human being is subjected when driving a vehicle. In particular, accelerations can be measured at different points, such as at the seat back, the seating surface and at the feet. Since vibrations affect humans differently depending on their frequency, the same standard defines frequency weighting curves (W_i) to filter out these accelerations.
Six W_i curves are introduced in the standard, which are used according to the direction of the accelerations and where they are measured.
In order to measure driver (or passenger) comfort, The accelerations over time along the three axes of the reference frame used and the angular accelerations are first measured. Each of these is then filtered with the respective frequency curve W as shown in **Eq. (1.1)**.

$$a_w(t) = a(t) \cdot W(x, y, z) \tag{1.1}$$

For each of these accelerations, the RMS (*root mean square*) is calculated, i.e. the root mean square value of the accelerations over time, averaged over the duration T of the measurement.

$$a_w = \sqrt{\frac{1}{T}\int_0^T a_w^2(t)\,dt} \tag{1.2}$$

The accelerations along x, y and z as well as the angular accelerations are then combined to derive one all-inclusive term for the translational contributions, $a_{V,t}$, and one for the rotational ones, $a_{V,r}$, as given in **Eq. (1.3)-(1.4)**. The same standard, in fact, also defines the k coefficients, which are the multiplicative factors used to take into account the different sensitivity of the body to vibrations along or around the different axes.

$$a_{V,t} = \sqrt{\left(k_x \cdot a_{w,x}\right)^2 + \left(k_y \cdot a_{w,y}\right)^2 + \left(k_z \cdot a_{w,z}\right)^2} \tag{1.3}$$

$$a_{V,r} = \sqrt{\left(k_{r,x} \cdot a_{w,r,x}\right)^2 + \left(k_{r,y} \cdot a_{w,r,y}\right)^2 + \left(k_{r,z} \cdot a_{w,r,z}\right)^2} \tag{1.4}$$

Eq. (1.5) then shows how the total vibration value at the point under consideration is calculated.

$$a_V = \sqrt{{a_{V,t}}^2 + {a_{V,r}}^2} \tag{1.5}$$

To assess the total vibration value at the driver's seat, the square root of the sum of the squares of the accelerations a_V at the backrest, seat and feet is used. The lower this value, the better the comfort of the vehicle and thus the quality of the suspension system.

On the other hand, the ISO 5008/2002 [28] defines the methodology for assessing the total vibration value to which the operator of an agricultural tractor is subjected when the vehicle travels along a standard test track. The same standard also specifies the measurement procedure and instruments, the operating conditions and the profile of the test track.
It should be noted that this standard only considers vibrations that reach the driver through the seat or the base of the cab, while those passed through the steering wheel are not taken into account.
Two standard test tracks are defined in the ISO 5008, each with its own specific operating conditions for the test, such as the vehicle's forward speed. One track is 35 metres long, the other one is 100 meters long, and both consist of two parallel lanes formed by a succession of wooden beams of defined height and position on which the vehicle must advance.

Figure 1.3: ISO 5008 track at CREA research centre

In 2019, using the ISO 2631-1 and 5008 standards presented, CREA centre (research centre for agri-food engineering and transformations) in Treviglio (Italy) published an article [29] in which it illustrates an approach for assessing the comfort of a tractor driven by a 75 kg operator on the standard 100 metre test track.

Only seat vibrations are considered, and only accelerations along the three axes are measured. These are then filtered with frequency weighting curves, W_i, from which RMS root mean square values are derived according to ISO 2631-1.

In particular, the same W_d curve is used to filter the accelerations along the longitudinal axis (x axis) and along the transverse axis (y axis), and the W_k curve for those along the vertical axis (z axis) of the seat.

The total value of seat vibration is then evaluated according to **Eq. (1.6)**.

$$a_V = \sqrt{\left(k_x \cdot a_{W,x}\right)^2 + \left(k_y \cdot a_{W,y}\right)^2 + \left(k_z \cdot a_{W,z}\right)^2} \tag{1.6}$$

The coefficients k_x, k_y e k_z are tabulated in the article, as a function of the vehicle's forward speed during the test (10,12 and 14 km/h).

Finally, a comfort index Rn (Ride number) is defined, which is the arithmetic mean of the a_V values obtained after running the test on the same ISO track at the three considered forward speeds, i.e. 10,12 and 14 km/h.

$$Rn = \frac{a_{V,10} + a_{V,12} + a_{V,14}}{3} \tag{1.7}$$

This Rn index is therefore an indicative parameter of tractor comfort: the lower its value, the better the comfort level for the driving operator.

1.1.5 Hydro-pneumatic suspensions

As mentioned above, hydro-pneumatic suspensions find great use in the off-highway sector. In fact, this type of suspension system is particularly suitable for applications where:

a) levelling manoeuvres (levelling) are required, i.e. raising or lowering the suspension, after particular load changes,
b) these levelling manoeuvres may be frequent and must have short reaction times,
c) the possibility of control over the suspension by the operator is desired,
d) there is little space for the suspension elements,
e) robust components are needed due to the harsh working conditions,
f) total locking of the suspension is required in certain situations,
g) a suspension with stiffness adaptable to various working conditions is desired,
h) hydraulic power supply units are already installed.

The simplest possible hydro-pneumatic spring element, shown in **Figure 1.4**, consists of only three components: a hydraulic cylinder, a hydro-pneumatic accumulator (such as a gas diaphragm accumulator) directly connected to the cylinder and, of course, the hydraulic fluid. The general displacement of the piston is called cylinder deformation: the term 'compression' is used when the piston moves inside the cylinder compression, while 'extension' if the piston tends to move out and away from the cylinder.

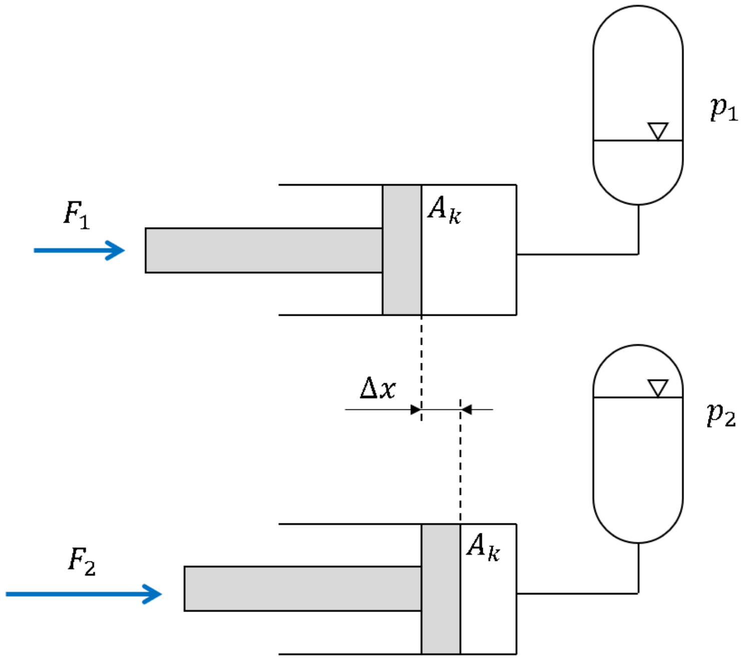

Figure 1.4: Hydraulic cylinder connected to a hydro-pneumatic accumulator

After adjusting the initial hydraulic pressure value by adding or releasing fluid, the system is ready to provide the suspension function. When a displacement of the piston Δx occurs, the volume of fluid in the accumulator changes, compressing the gas inside it changing its pressure from p_1 to p_2. This generates an increase in the force on the piston rod, from $A_k \cdot p_1$ to $A_k \cdot p_2$. The force increases due to the position variation Δx defines the stiffness k of the system.

Neglecting inertial and friction effects, the external force F acting on the rod is always in equilibrium with the force resulting from the pressure acting on the surface of the piston. When, therefore, the external force changes from F_1 to F_2, part of the hydraulic fluid flows into the accumulator until the balancing pressure level is reached. The expression of the stiffness of the system is given in **Eq. (1.8)**.

$$k = \frac{A_k \cdot p_2 - A_k \cdot p_1}{\Delta x} \tag{1.8}$$

A hydraulic resistor (such as a fixed orifice or proportional valve) can be inserted between the cylinder and the accumulator to consider an additional damping element. This converts part of the fluid kinetic energy into heat and pressure energy. The pressure increase, as before, generates an increase in force on the piston rod which is function of the fluid velocity. The pressure increase Δp given by the damping element can be derived using the law of hydraulic resistance, as given in **Eq. (1.9)-(1.10)**, where C_d is the discharge coefficient (or efflux coefficient), A the efflux area of the hydraulic resistance, Q the flow rate and ρ the fluid density.

$$Q = C_d \cdot A \cdot \sqrt{\frac{2\Delta p}{\rho}} \tag{1.9}$$

$$\Delta p = \frac{\rho \cdot Q^2}{2 \cdot (C_d \cdot A)^2} \tag{1.10}$$

Stiffness characteristics

As briefly seen for the simplest case of hydro-pneumatic suspension, the stiffness of these systems can be determined by the elastic force-displacement curve measured on the piston rod when all elastic resistances are removed. An increase in the force acting on the piston leads to an increase in hydraulic pressure and thus to a change in the position of the piston. This is caused by:

- the compression of the gas inside the accumulators,

- the deformation of pipes and fittings due to their elastic behaviour,
- the hydraulic fluid compressibility.

These effects can be seen as three springs in series, each of which with a characteristic stiffness. The total equivalent stiffness for a system of three springs in series is defined by **Eq. (1.11)**.

$$k_{susp} = \frac{k_{gas} \cdot k_{pipes} \cdot k_{fluid}}{k_{gas} \cdot k_{pipes} + k_{gas} \cdot k_{fluid} + k_{pipes} \cdot k_{pipes}} \tag{1.11}$$

However, the stiffness of the pipes, as well as the compressibility modulus of the hydraulic fluid, is generally very high, so their impact on the total stiffness is low. For this reason, the stiffness characteristics of these types of systems are practically only characterised by the behaviour of the gas contained in the accumulators.

First, it is necessary to place the gas inside the accumulator; this gas ideally behaves according to the equation of state of perfect gases, given in **Eq. (1.12)**, where p is the gas pressure, V the gas volume, n the amount of substance, T the temperature and R the universal gas constant.

$$pV = nRT \tag{1.12}$$

This process, however, can be traced back to an isochoric transformation since the volume of the accumulator remains constant.

Once the accumulator has been precharged (and thus reached state *0* of the gas), it can be integrated into the hydraulic system by pressurising the system. The volume of gas in the accumulator does not change as long as the hydraulic pressure is less than or equal to the gas precharge pressure. When this threshold is exceeded, however, the gas, separated from the fluid by a membrane, is compressed until it reaches the pressure that balances the system. This increase in hydraulic pressure that leads to gas compression can be explained, for example, by the loading of the suspended mass onto the suspension. This operation usually takes place quite slowly, and the new pressure level is maintained for a long period, which makes it possible to assume an isothermal transformation from state *0* to state *1*, defined by the Boyle-Mariotte law given in **Eq. (1.13)**.

$$p_1 V_1 = p_0 V_0 \tag{1.12}$$

This is usually referred as static (or quasi-static) loading of the suspension.

The dynamic loadings of the suspension are the normal operations of the suspension itself, absorbing ground inputs starting from state *1* to state *2*. These ground inputs are much more rapid oscillations than the loading seen previously. For this reason, it is not possible to model the compressions and expansions of the gas as isotherms in this case. Assuming zero heat exchange, this transformation could be modelled as adiabatic, defined by **Eq. (1.13)** where $\kappa \approx 1.4$ for diatomic gases (such as nitrogen, which is the gas generally used for these applications).

$$p_1 V_1^{\kappa} = p_2 V_2^{\kappa} \tag{1.13}$$

However, not having heat exchange is unrealistic. For this reason, the transformation that better model the behaviour of the gas during this dynamic loading is the polytropic transformation of **Eq. (1.14)**, where $1 < n < \kappa$.

$$p_1 V_1^{n} = p_2 V_2^{n} \tag{1.14}$$

The real conditions for heat transfer are unknown and very difficult to identify, so it is quite complex to find the exact value of n value to choose. Assuming $n = 1.3$, however, turns out to be a good compromise for preliminary calculations, while the adjustment of this value can be realised from the real force-displacement curves obtained with experimental tests.

There are many possible configurations of hydro-pneumatic springs, each of which has different stiffness characteristics. Some of these configurations are shown in **Figure 1.5**, such as single-acting cylinders with an accumulator (case *a*), double-acting cylinders with a regenerative connection and an accumulator (case *b*), a pair of single-acting cylinders each connected with an accumulator (case *c*) and double-acting cylinders with two accumulators (case *d*). Among these, a distinction can be made between hydro-pneumatic springs with (*c* and *d*) and without (*a* and *b*) hydraulic preload.

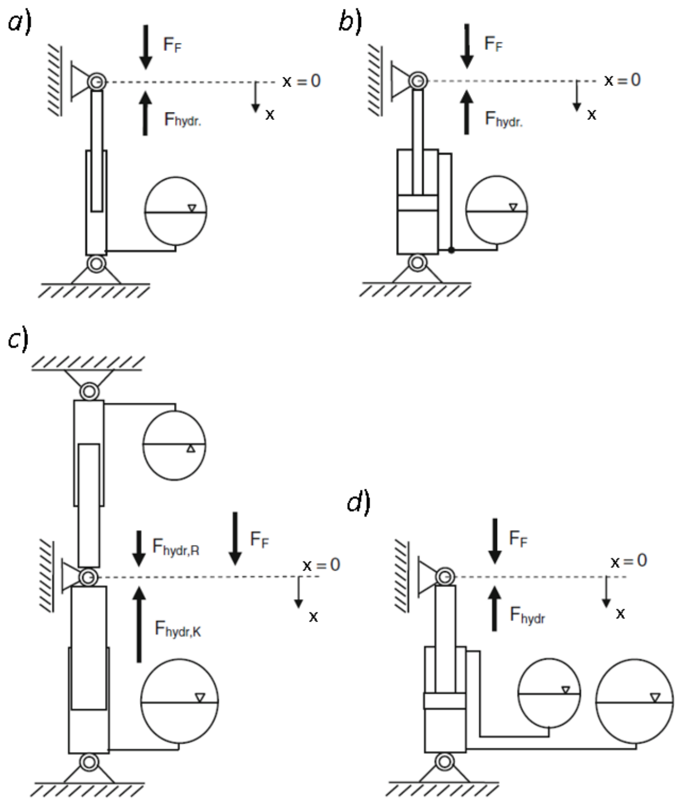

Figure 1.5: Some examples of hydro-pneumatic spring configurations [1]

It is easy to notice that cases *c* and *d* are more complex configurations than the previous two. At the same time, however, these configurations with hydraulic preload allow an extra degree of freedom in the stiffness characteristics, given precisely by the presence of the second accumulator.

In particular, in this work of thesis we focus our interest on the case of the double-acting hydraulic cylinder with two accumulators (case *c*), since it is the most commonly used solution for independent hydro-pneumatic suspensions. For an in-depth analysis of the other configurations, please refer to the reference texts [1].

Finally, it should be noted that the effect of temperature on the stiffness of the system has not been considered in this discussion, although it does exist, as it can easily be seen from the presence of T in **Eq. (1.12)**. In general, the lower the operating temperature, the higher the stiffness of the system (with all other conditions being equal).

Damping characteristics

As mentioned above, a hydraulic resistor can be inserted between the cylinder and the accumulator in order to introduce a further damping characteristic (in addition to the distributed pressure losses along the pipes) (**Figure 1.6**). In this way, the fluid kinetic energy (resulting from the dynamic oscillations to which the suspension is subjected) is converted into pressure energy and heat. Hydraulic resistance therefore creates a pressure drop, which generates a force opposing the piston motion acting on the effective areas in the cylinder. This force tends to subtract energy from the oscillation and is therefore a damping force.

In hydro-pneumatic suspension systems specifically, these hydraulic resistances will either be fixed orifices, proportional damping valves or a combination of these depending on the complexity of the system.

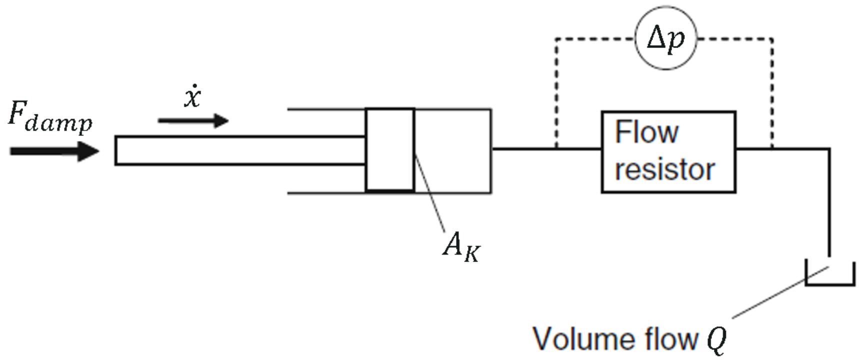

Figure 1.6: Hydraulic cylinder and resistance [1]

We assumed to always work with turbulent flow using **Eq. (1.9)-(1.10)** with constant efflux coefficient C_d equal to 0.7 for the preliminary dimensioning of the damping orifices and valves (and therefore of the damping forces). This turns out to be an assumption that tends to be well accepted for hydraulic systems, although, of course, it may be subject to slight modifications once the experimental results have been evaluated.

In the case **of Figure 1.6**, the damping force will simply be the one shown in **Eq. (1.15)**, given by the pressure drop generated by the resistance Δp multiplied by the effective area A_K.

$$F_{damp} = \Delta p \cdot A_K \tag{1.15}$$

The pressure drop generated on the piston and the rod side depend on the configuration of hydraulic resistances chosen. In fact, in the simplest case of a single hydraulic orifice with a fixed section mounted between the cylinder chamber and the accumulator, Δp will be as defined by **Eq. (1.10)**, where the flow rate Q is given by the deformation velocity $\dot{x}$ of the cylinder itself multiplied by the effective area of the side considered. The pressure drop Δp will therefore be proportional to the square of the flow rate Q through the fixed orifice, and therefore directly proportional to the square of the deformation velocity $\dot{x}$.

$$\Delta p \propto Q^2 \propto \dot{x}^2 \tag{1.16}$$

Recalling the expression of the damping force from **Eq. (1.17)**, it is easy to deduce that this damping force is also proportional to the square of the deformation velocity of the hydraulic cylinder.

$$F \propto \Delta p \propto \dot{x}^2 \tag{1.17}$$

In the ideal theoretical case, the damping force curve as function of the deformation speed of the hydraulic cylinder is a parabola through the origin.

In the case where the hydraulic resistance is a proportional damping valve instead of a fixed orifice, the approach does not change. In this case, however, it is possible to have an infinite number of force parabolas instead of one, depending on the opening of the valve itself. The expression of the damping force will be that given in **Eq. (1.18)**, where I is the supply current of the generic damping valve controlled by the vehicle ECU.

$$F_{damp} = \Delta p \cdot A_K = \frac{\rho \cdot Q^2}{2 \cdot \left(C_d \cdot A(I)\right)^2} \cdot A_K \tag{1.18}$$

The outflow area, in this case, is not constant but depends precisely on the opening of the proportional valve. The latter is uniquely defined by the supply current according to the characteristic of the valve itself.

In the more complex, but also more generic case in which the hydraulic resistance is a combination of orifices, proportional valves and check valves (assembled in series and parallel to obtain the desired damping characteristics), it is always possible to go back to the cases already seen. It is only necessary to proceed with the evaluation of the equivalent hydraulic resistance. **Eq. (1.19)** shows the generic hydraulic resistance characteristic, where R_{eq} is precisely the equivalent resistance.

$$Q = R_{eq} \cdot \sqrt{\Delta p} \tag{1.19}$$

Even in the most complex cases, therefore, the quadratic dependence between pressure drop Δp and cylinder deformation velocity $\dot{x}$ is maintained.

In the more complex and generic case of a double-acting cylinder (such as cases *b* and *d* in **Figure 1.5**) it is necessary to consider the increase or decrease in pressure in both chambers of the cylinder, which can be evaluated individually by means of the relations presented. The expression of the generic damping force is therefore the one given in **Eq. (1.20)**, where the subscript P is always used to define the quantities relative to the piston side and the subscript R is relative to the rod side.

$$F_{damp} = \Delta p_P \cdot A_P - \Delta p_R \cdot A_R \tag{1.20}$$

In the case of real suspensions, in addition to these elements, there is also the so-called anti-shock valves, which are relief valves designed to limit the maximum pressure level that can be reached in the system for safety reasons. If the pressure level in a chamber of the system reaches the setting of these limiting valves due to stiffness or damping effects, these valves will open, preventing the pressure from rising any higher (unless the gradient Δp-Q characteristic of the valve). A schematic of the case with a double-acting cylinder with two accumulators with variable orifices and anti-shock valves is shown in **Figure 1.7**.

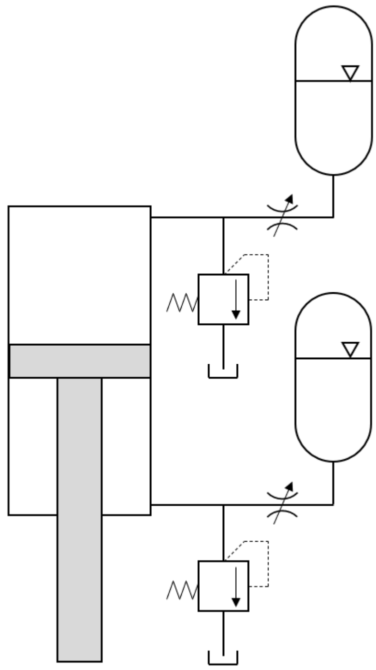

Figure 1.7: Double-acting cylinder with two accumulators, two variable orifices and two relief valves

There is then a cylinder compression velocity $\dot{x}$ that causes an opening of the anti-shock valve on the branch connected to the piston-side chamber. Similarly, there is a cylinder extension velocity that causes an opening of the anti-shock valve on the chamber branch on the piston side. Note that these velocities are usually not equal in modulus, due to the different effective areas in the two chambers of the cylinder. Once these velocities are reached, the saturation of the damping force curve is obtained, which does no longer follow the parabola branch, but rather a rectilinear course defined by the gradient $\Delta p - Q$ characteristic of the pressure limiting valve itself.

The generic curve of the damping force is therefore something similar to what is shown in **Figure 1.8**.

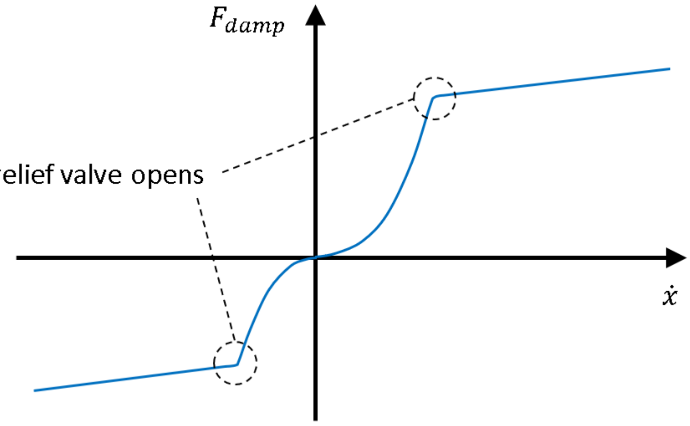

Figure 1.8: Generic curve of damping force as function of cylinder deformation velocity

Note that only one damping force curve is shown in **Figure 1.8**. As mentioned, an infinite number of parabolas can be obtained in the case of proportional valves. This means that the speed at which the restrictor valves open will also vary.

Minimum damping values (and so more open parabolas) can be obtained with fully open valve, while almost closed valves lead to maximum damping values (and so very steep parabolas).

The damping coefficient can be calculated by deriving the damping force with respect to the cylinder deformation velocity, similarly to the calculation of stiffness from the elastic force as a function of cylinder displacement.

The operating temperature also affects the damping of the system. In fact, the hydraulic fluid density ρ, which is greatly influenced by the temperature in the case of industrial oils used for these applications, is present in the equations. In general, density increases as temperature decreases, so the damping contribution will be greater for low temperatures (with all other conditions being constant).

Double-acting cylinder with hydro-pneumatic accumulators

The aim of this sub-section is to analyse in detail the behaviour of the hydro-pneumatic spring formed by a double-acting cylinder connected to two accumulators. This is indeed the basic element for the independent hydro-pneumatic suspension considered by Dana Incorporated on which the entire work presented in this chapter is based.

Figure 1.9 shows the double-acting cylinder with an accumulator connected to the chamber on the rod side and a second one connected to the chamber on the piston side.

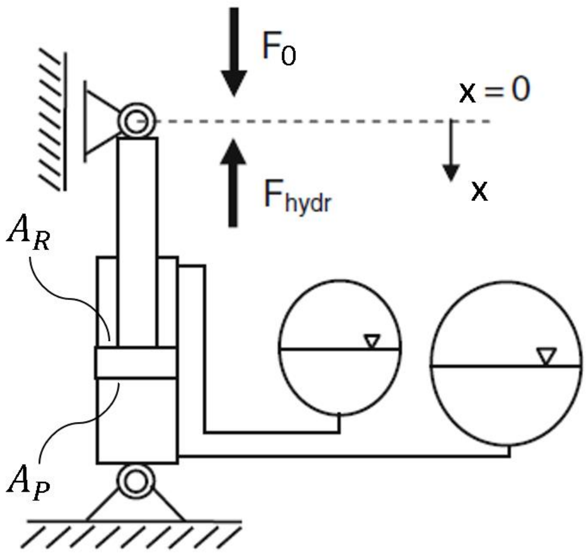

Figure 1.9: Double-acting cylinder with an accumulator on piston and rod side [1]

As reported for the generic case in the previous sub-section, we can define the three different states to which the suspension system is subjected as follows:

- **State *0***: precharge of the gas inside the accumulator, going from zero pressure to pressure p_0. The gas occupies the entire volume V_0 of the accumulator.
- **Stato *1***: quasi-static loading of the suspension until an external force F_1 acting on the rod is reached. This force is sufficient to isothermally compress the gas in the accumulator to a volume V_1 and pressure p_1.
- **Stato *2***: dynamic loading with force F_2 oscillating around F_1. The gas is compressed and expanded through polytropic transformations to volume V_2 and pressure p_2.

These state transitions can be applied to both accumulators in the system. Obviously, in state *2*, a compression of the gas in the rod-side accumulator results in an expansion of the gas in the piston-side accumulator.

Assuming this, it is possible to derive the analytical expression of the stiffness k_{susp} of the system as the ratio of the change in elastic force dF following a change in piston position dx.

The transition from state 0 to state 1, as mentioned, is modelled with an isothermal transformation. Using the subscript P for quantities referred to the piston side and the subscript R for those referred to the rod side, and applying the Boyle-Mariotte law of **Eq. (1.13)**, the following relations can be obtained in **Eq. (1.21)-(1.22)**.

$$p_{0_P}V_{0_P} = p_{1_P}V_{1_P} \tag{1.21}$$

$$p_{0_R}V_{0_R} = p_{1_R}V_{1_R} \tag{1.22}$$

From these equations, it is easy to find the volumes occupied by the gas in the two accumulators at the end of static loading.

$$V_{1_P} = \frac{p_{0_P}V_{0_P}}{p_{1_P}} \tag{1.23}$$

$$V_{1_R} = \frac{p_{0_R}V_{0_R}}{p_{1_R}} \tag{1.24}$$

A polytropic transformation defined by the relations of **Eq. (1.25)-(1.26)** is instead considered for the transition from state 1 to state 2.

$$p_{1_P}V_{1_P}^n = p_{2_P}{V^n}_{2_P} \tag{1.25}$$

$$p_{1_R}V_{1_R}^n = p_{2_R}{V^n}_{2_R} \tag{1.26}$$

The gas volumes within the accumulators are defined by the cylinder geometry and the piston displacement x during dynamic oscillations. By convention, this displacement x is considered positive if it tends to compress the hydraulic cylinder, as also shown in **Figure 1.9**. The expressions of these gas volumes is given in **Eq. (1.27)-(1.28)**. In **Eq. (1.29)-(1.30)**, on the other hand, the expressions of the effective areas on the piston and rod side of the hydraulic cylinder are reported, where D_P and D_R are the piston and rod diameters.

$$V_{2_P} = V_{1_P} - x \cdot A_P \tag{1.27}$$

$$V_{2_R} = V_{1_R} + x \cdot A_R \tag{1.28}$$

$$A_P = \frac{\pi}{4} \cdot D_P^2 \tag{1.29}$$

$$A_R = \frac{\pi}{4} \cdot (D_P^2 - D_R^2) \tag{1.30}$$

The pressure levels p_{2_P} and p_{2_R} achieved as a result of dynamic loading and can be made explicit by combining the relationships given in **Eq. (1.23)-(1.24)**, **Eq. (1.25)-(1.26)** and **Eq. (1.27)-(1.28)**.

$$p_{2_P} = p_{1_P}\left(\frac{V_{1_P}}{V_{2_P}}\right)^n = p_{1_P}\left(\frac{V_{1_P}}{V_{1_P} - x\cdot A_P}\right)^n = p_{1_P}\left(\frac{\dfrac{p_{0_P}V_{0_P}}{p_{1_P}}}{\dfrac{p_{0_P}V_{0_P}}{p_{1_P}} - x\cdot A_P}\right)^n \tag{1.31}$$

$$p_{2_R} = p_{1_R}\left(\frac{V_{1_R}}{V_{2_R}}\right)^n = p_{1_R}\left(\frac{V_{1_R}}{V_{1_R} + x\cdot A_R}\right)^n = p_{1_R}\left(\frac{\dfrac{p_{0_R}V_{0_R}}{p_{1_R}}}{\dfrac{p_{0_R}V_{0_R}}{p_{1_R}} + x\cdot A_R}\right)^n \tag{1.32}$$

In addition to these relationships, it is also possible to consider the static equilibrium of the forces acting on the piston when the system is in state *1* (i.e. before dynamic loading). In fact, the values of p_{1_P} and p_{1_R} are not independent of each other but are linked precisely by this static equilibrium of the piston. Excluding the contribution of weight force and frictions, the force balance equation is reported in **Eq. (1.33)**.

$$p_{1_P}\cdot A_P = F_0 + p_{1_R}\cdot A_R \tag{1.33}$$

This equation can be used to replace the value of p_{1_P} within **Eq. (1.31)** with an expression as a function of p_{1_R}. In this way, it is possible to consider p_{1_R} as the system's only degree of freedom (once the geometry has been defined).

$$p_{2_P} = \frac{F_0 + p_{1_R}\cdot A_R}{A_P}\left(\frac{\dfrac{p_{0_P}V_{0_P}}{\dfrac{F_0 + p_{1_R}\cdot A_R}{A_P}}}{\dfrac{p_{0_P}V_{0_P}}{\dfrac{F_0 + p_{1_R}\cdot A_R}{A_P}} - x\cdot A_P}\right)^n = \frac{F_0 + p_{1_R}\cdot A_R}{A_P}\left(\frac{\dfrac{p_{0_P}V_{0_P}}{F_0 + p_{1_R}\cdot A_R}}{\dfrac{p_{0_P}V_{0_P}}{F_0 + p_{1_R}\cdot A_R} - x}\right)^n \tag{1.34}$$

The force variation due to the system stiffness caused by a generic dynamic displacement x can be evaluated by considering the pressure variation in the two hydro-pneumatic accumulators connected to the cylinder chambers. For simplicity of calculation, two force variations are considered: one in the piston-side chamber, ΔF_P, and one in the rod-side chamber, ΔF_R. The expressions of these force variations are obtained in **Eq. (1.35)-(1.36)**.

$$\Delta F_P = A_P\cdot\left(p_{2_P} - p_{1_P}\right) = A_P\cdot\left[\frac{F_0 + p_{1_R}\cdot A_R}{A_P}\left(\frac{\dfrac{p_{0_P}V_{0_P}}{F_0 + p_{1_R}\cdot A_R}}{\dfrac{p_{0_P}V_{0_P}}{F_0 + p_{1_R}\cdot A_R} - x}\right)^n - p_{1_P}\right] \tag{1.35}$$

$$\Delta F_R = A_R\cdot\left(p_{2_R} - p_{1_R}\right) = A_R\cdot\left[p_{1_R}\left(\frac{\dfrac{A_R}{A_R}\cdot\dfrac{p_{0_R}V_{0_R}}{p_{1_R}}}{A_R\cdot\left(\dfrac{p_{0_R}V_{0_R}}{A_R\cdot p_{1_R}} + x\right)}\right)^n - p_{1_R}\right] \tag{1.36}$$

From here, the piston-side and rod-side stiffnesses can be found by deriving these expressions with respect to the displacement x.

$$k_P = \frac{d(\Delta F_P)}{dx} = A_P\cdot\frac{F_0 + p_{1_R}\cdot A_R}{A_P}\cdot\left(\frac{p_{0_P}V_{0_P}}{F_0 + p_{1_R}\cdot A_R}\right)^n\cdot(-n)\cdot\left(\frac{p_{0_P}V_{0_P}}{F_0 + p_{1_R}\cdot A_R} - x\right)^{-n-1}\cdot(-1) \tag{1.37}$$

$$k_R = \frac{d(\Delta F_R)}{dx} = A_R\cdot p_{1_R}\cdot\left(\frac{p_{0_R}V_{0_R}}{A_R\cdot p_{1_R}}\right)^n\cdot(-n)\cdot\left(\frac{p_{0_R}V_{0_R}}{A_R\cdot p_{1_R}} + x\right)^{-n-1}\cdot(1) \tag{1.38}$$

We then obtain the expressions given in **Eq. (1.39)-(1.40)** by reordering and simplifying the various terms.

$$k_P = n\frac{\left(F_0 + p_{1_R}\cdot A_R\right)\cdot\left(\dfrac{p_{0_P}V_{0_P}}{F_0 + p_{1_R}\cdot A_R}\right)^n}{\left(\dfrac{p_{0_P}V_{0_P}}{F_0 + p_{1_R}\cdot A_R} - x\right)^{n+1}} \tag{1.39}$$

$$k_R = -n \frac{(p_{1_R} \cdot A_R) \cdot \left(\frac{p_{0_R} V_{0_R}}{A_R \cdot p_{1_R}} \right)^n}{\left(\frac{p_{0_R} V_{0_R}}{A_R \cdot p_{1_R}} + x \right)^{n+1}} \tag{1.40}$$

Note that the minus sign in front of the expression of k_R is due to the convention chosen for the sign of x. With a positive displacement x, in fact, there is an increase in piston-side pressure and a decrease in rod-side pressure. Both these contributions tend to increase the force F on the piston rod. We then obtain the expression of the system stiffness (**Eq. (1.41)**) adding up these contributions (without considering the minus sign).

$$k_{susp}(x) = n \frac{(F_0 + p_{1_R} \cdot A_R) \cdot \left(\frac{p_{0_P} V_{0_P}}{F_0 + p_{1_R} \cdot A_R} \right)^n}{\left(\frac{p_{0_P} V_{0_P}}{F_0 + p_{1_R} \cdot A_R} - x \right)^{n+1}} + n \frac{(p_{1_R} \cdot A_R) \cdot \left(\frac{p_{0_R} V_{0_R}}{A_R \cdot p_{1_R}} \right)^n}{\left(\frac{p_{0_R} V_{0_R}}{A_R \cdot p_{1_R}} + x \right)^{n+1}} \tag{1.41}$$

We also can obtain the system stiffness in the neutral position for the hydraulic cylinder by evaluating this expression for $x = 0$. This represents the stiffness once the static loading is complete (and levelling manoeuvres have been carried out if necessary).

$$k_{susp}\Big|_{x=0} = n \frac{(F_0 + p_{1_R} \cdot A_R)^2}{p_{0_P} V_{0_P}} + n \frac{(p_{1_R} \cdot A_R)^2}{p_{0_R} V_{0_R}} \tag{1.42}$$

As can easily be seen from **Eq. (1.41)**, the stiffness of a hydro-pneumatic spring is not linear as it varies with the stroke x. A generic hydraulic spring has therefore has a different behaviour with respect to a mechanical spring, as highlighted in **Figure 1.10**.

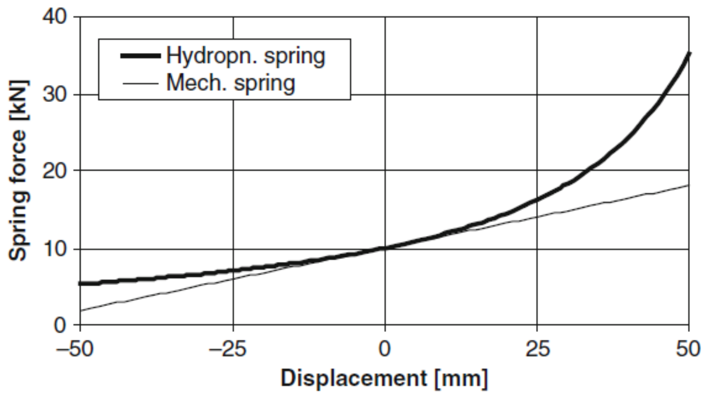

Figure 1.10: Comparison between the elastic force of a hydro-pneumatic spring and a mechanical spring one as function of the spring deformation [1]

At the same time, this hydro-pneumatic stiffness varies as the static load F_0 acting on the suspension varies.

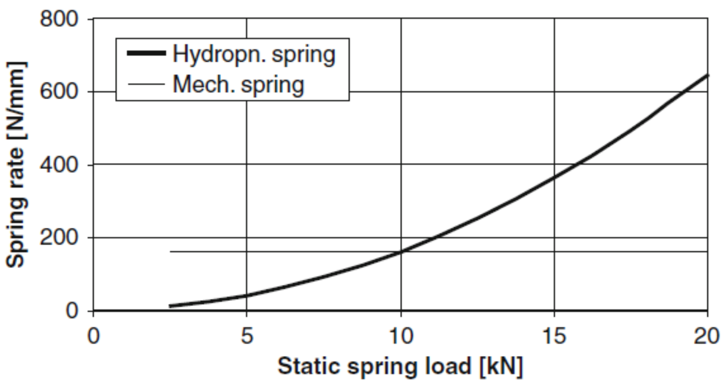

Figure 1.11: Comparison between hydro-pneumatic stiffness and mechanical one as function of the spring preload [1]

Once the geometry of the hydraulic cylinder (A_P and A_R), the geometry and preloading of the accumulators (p_{0_P}, V_{0_P}, p_{0_R} and V_{0_R}) and the static loading of the system (F_0) has been defined, the rod-side levelling pressure p_{1_R} can be varied to change the system stiffness.

This is very useful, especially in off-highway applications where the static load can vary greatly. In fact, by exploiting this degree of freedom, it is possible to adjust the stiffness of the system to always obtain good suspension performance, even when the static load F_0 varies. An example of this is shown in **Figure 1.12**, where the transition from one stiffness curve to another is highlighted.

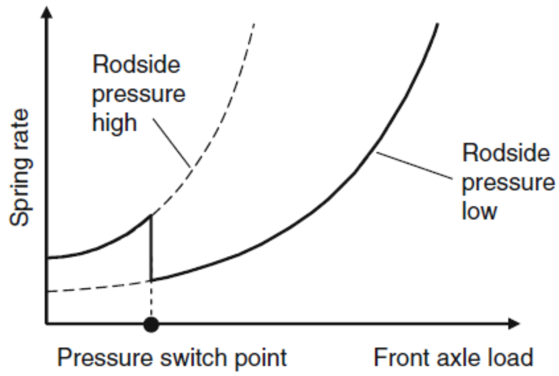

Figure 1.12: Hydro-pneumatic stiffness change varying the rod side pressure [1]

Note that piston side pressure also varies as p_{1_R} varies, always ensuring the force balance on the piston of **Eq. (1.33)**.

A further step which can be implemented can be the closed-chain control of the piston-side pressure p_{1_R} in order to adapt the stiffness over a wider range of load conditions, instead of just switching from one stiffness curve to another. All other parameters being equal, there is a minimum stiffness and a maximum stiffness that the system can guarantee for a given static load F_0. By analysing **Eq. (1.42)**, these minimum and maximum values can be respectively obtained for the minimum and maximum rod side pressure.

The first is defined by the safe working conditions of the hydraulic accumulators. It is indeed a good rule not to empty the accumulator in order not to ruin the diaphragm which separates the gas from the hydraulic fluid. To do so, it is necessary to maintain the fluid pressure above the gas pre-charge pressure (with fluid pressure equal to the pre-charge the accumulator is completely empty of fluid). This can prevent the membrane from coming into contact with the accumulator shell and risking damage.

Accumulator manufacturers usually recommend a fluid pressure level at least 10% higher than the gas precharge for safety reason, as shown in **Eq. (1.43)**.

$$p \geq \frac{p_0}{0.9} \tag{1.43}$$

This value limits the rod side pressure that can be imposed on the suspension. The minimum pressure p_{1_R} that can be imposed is thus exactly equal to the pressure that leads to having $p_{2_R} = p_{0_R}/0.9$ in the most critical working conditions. Considering the neutral position of the cylinder with p_{1_R} on the rod side, the most critical condition for the rod side accumulator is obtained by imposing the total compression of the cylinder itself, as also shown in **Figure 1.13**.

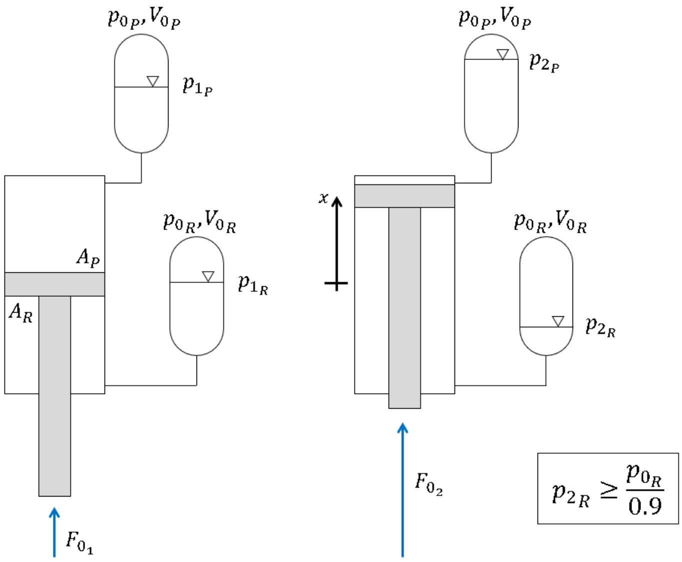

Figure 1.13: Minimum rod side pressure value evaluation

This check must also be carried out for the piston side accumulator, where $p_{2_P} = p_{0_P}/0.9$ must be applied.

On the other hand, the maximum levelling pressure of the system is always found to prevent degradation of the membrane contained in the accumulators. As the minimum pressure has been found by imposing the gas not to occupy more than 90% of the accumulator volume, the maximum pressure can be obtained by imposing the fluid not to occupy more than 90% of the accumulator.

Figure 14 shows these pressure limits imposed by membrane accumulators.

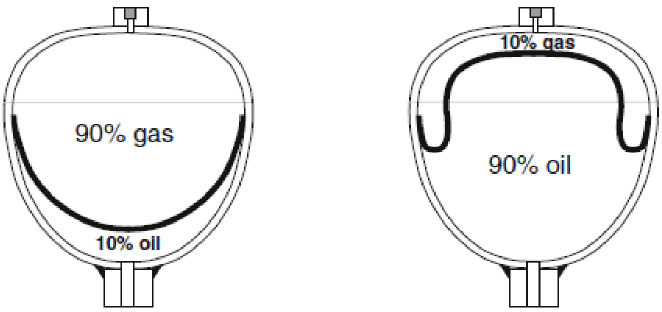

Figure 1.14: Limit conditions for diaphragm hydro-pneumatic accumulators

This maximum pressure value usually turns out to be very high. In these cases, therefore, the maximum pressure level that can be reached is defined by the pressure relief valve of the supply unit. This valve is generally installed on the delivery branch of the pump and is precisely used to limit the maximum pressure level for safety reasons.

Therefore, for each value of the static load F_0 it is possible to impose the desired stiffness on the system by varying the levelling pressure p_{1_R} within the described limits. A range of attainable stiffnesses can thus be obtained, just like the one shown in grey in **Figure 1.15**.

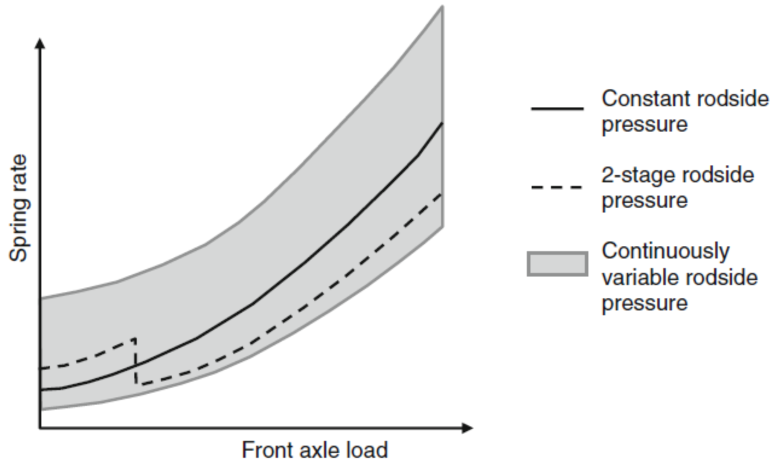

Figure 1.15: Comparison between stiffness with constant rod side pressure, 2-stage rod side pressure and a continuously variable rod side pressure [1]

Hydro-pneumatic suspension with 3 or 4 accumulators

Two independent hydro-pneumatic suspension solutions are presented in the following sub-section. These two solutions are similar to each other, but with some differences that impact their behaviour and the stiffness and damping characteristics. Both solutions have two double-acting cylinders, which act as shock absorbers for the left and right wheel of the vehicle. These types of suspension systems are very common in the off-highway sector.

The first of these solutions has three hydro-pneumatic accumulators: two are installed on the piston side, one per cylinder, while the third accumulator on the rod side is common to the two hydraulic actuators. There is a tendency to use two accumulators on the piston side and one on the rod side (and not vice versa) because the flow rates in and out of the cylinders are considerably greater on the piston side branches with the same oscillation. To manage these flow rates using only one accumulator on this branch would require the use of a very large volume. At the inlet port of each accumulator there is a hydraulic resistance, which can be represented by a generic orifice. A simplified schematic of the three-accumulator suspension is shown in **Figure 1.16**.

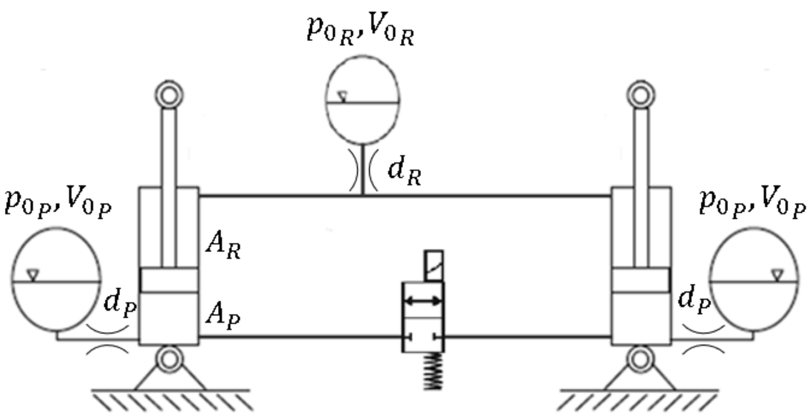

Figure 1.16: Simplified scheme of the three-accumulator hydro-pneumatic suspension [1]

Note that this suspension system can easily be traced back to the hydro-pneumatic spring case (double-acting cylinder with two accumulators) analysed in the previous subsection. In this case, the relationships are not exactly the same as it is necessary to consider the doubling of the flow in and out of the accumulator on the rod side.

Repeating the steps already seen, the pitch stiffness of the two-cylinder suspension with three-accumulator around its neutral position is reported in **Eq. (1.44)**.

$$k_{susp}\big|_{x=0} = n\frac{\left(F_0 + p_{1_R}\cdot A_R\right)^2}{p_{0_P}V_{0_P}} + n\frac{2\cdot\left(p_{1_R}\cdot A_R\right)^2}{p_{0_R}V_{0_R}} \tag{1.44}$$

Note how this expression differs from the hydro-pneumatic spring one in E**q. (1.42)** only by a factor of 2 in the contribution given by the rod side, which represents precisely the doubling of the flow in and out of the accumulator on that branch.

What is shown in **Eq. (1.44)** is, as mentioned, the pitch stiffness of the system. In fact, having introduced a second cylinder, it is now possible to differentiate the cases of pitching (i.e. when the deformation of the cylinders is symmetrical, so equal and concordant) and rolling (i.e. when the deformation of the cylinders is anti-symmetrical, so equal but discordant). These two cases are shown in **Figure 1.17** and **1.18**, where the flow rates on the different branches are also highlighted.

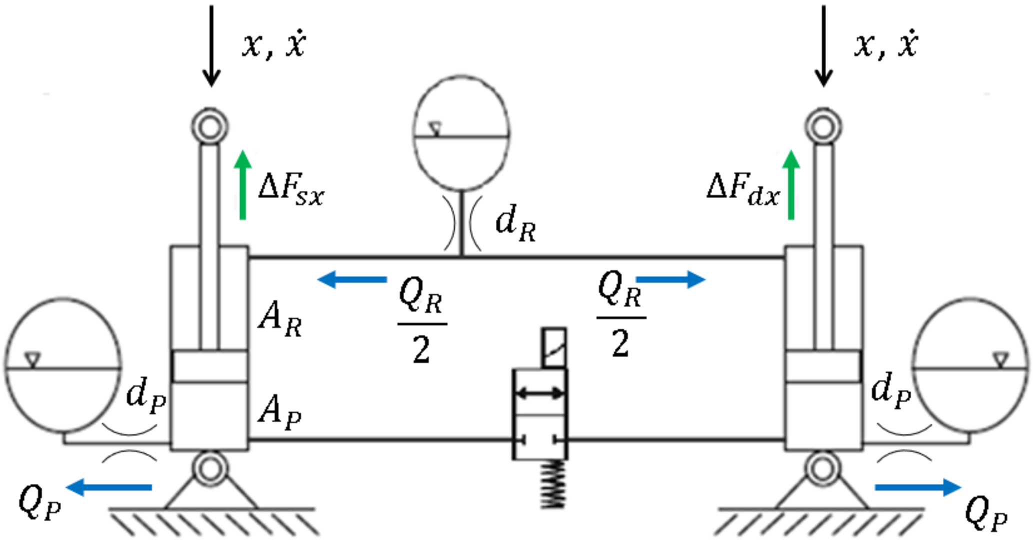

Figure 1.17: Pitch motion with three-accumulator and two cylinders suspension

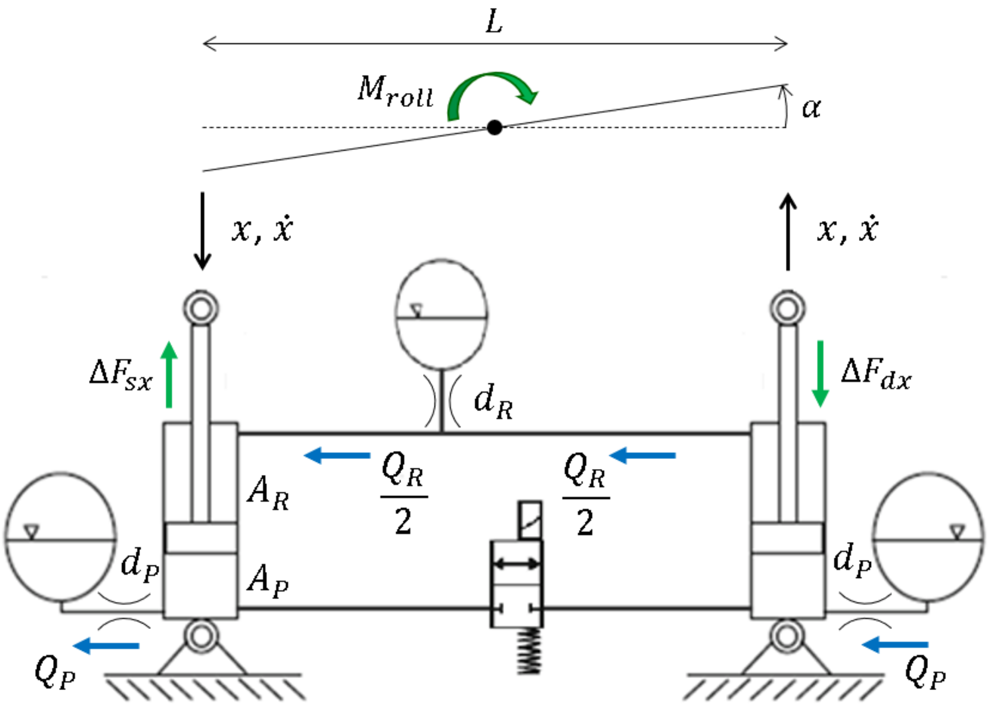

Figure 1.18: Roll motion (locked) with three-accumulator and two cylinders suspension

The roll stiffness can be assessed by considering a rotation α of the suspension. This rotation generates an anti-symmetrical deformation of the two cylinders, which causes a change in force on the rod of the two pistons. It can be easily seen that the contribution of the rod side to this force is zero, as the flow exiting the right cylinder flows directly into the left one. The roll stiffness is therefore given by the decrease in pressure in the right piston-side chamber and the increase in pressure in the left piston-side chamber. This creates a pair of forces on the cylinder rods that generate a resistant moment M_{roll} that opposes rotation α.

Following the approach already seen and used for pitch stiffness, the expression of the moment M_{roll} can be derived, as shown in **Eq. (1.45)**.

$$M_{roll} = \frac{L}{2} \cdot (F_0 + p_{1_R} \cdot A_R) \cdot \left[\left(\frac{\frac{p_{0_P} V_{0_P}}{p_{1_P}}}{\frac{p_{0_P} V_{0_P}}{p_{1_P}} - x \cdot A} \right)^n - \left(\frac{\frac{p_{0_P} V_{0_P}}{p_{1_P}}}{\frac{p_{0_P} V_{0_P}}{p_{1_P}} + x \cdot A} \right)^n \right] \tag{1.45}$$

Similarly to the pitch stiffness, the roll stiffness can be derived by considering the relationship between this resistant moment M_{roll} and a small rotation α. For small angles α the following relationship can be written.

$$\alpha \approx \tan \alpha = \frac{x}{\frac{L}{2}} = \frac{2x}{L} \tag{1.46}$$

With this relationship, the expression of roll stiffness w can then be derived, as given in **Eq. (1.47)**.

$$w = \frac{L^2}{4x} \cdot (F_0 + p_{1_R} \cdot A_R) \cdot \left[\left(\frac{\frac{p_{0_P} V_{0_P}}{p_{1_P}}}{\frac{p_{0_P} V_{0_P}}{p_{1_P}} - x \cdot A_P} \right)^n - \left(\frac{\frac{p_{0_P} V_{0_P}}{p_{1_P}}}{\frac{p_{0_P} V_{0_P}}{p_{1_P}} + x \cdot A_P} \right)^n \right] \tag{1.47}$$

Note that this expression represents the roll stiffness at 'locked' roll, i.e. with the valve on the rod side of **Figure 1.18** closed.

With the valve open, in fact, the roll is 'unlocked' and the roll stiffness is zero. As happens on the rod-side branch, in this case the flow coming out of one cylinder goes directly into the other without causing an increase in the pressure level in the accumulators also on the piston side (**Figure 1.19**).

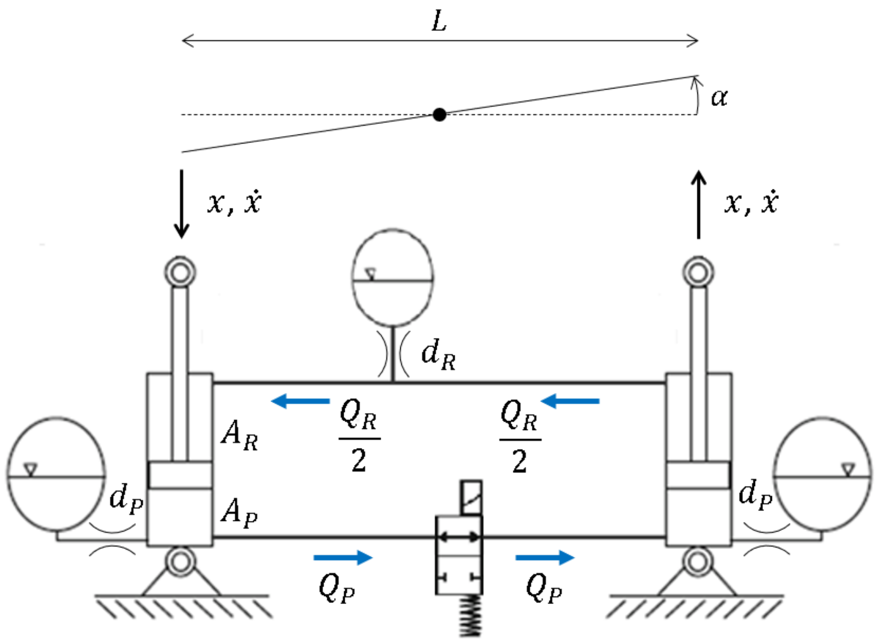

Figure 1.19: Unlocked roll with three-accumulator and two cylinders suspension

Obviously, the damping characteristics are also different considering pure pitch, pure locked roll and pure unlocked roll. This is again because the input and output flow rates in the accumulators are different, and so the flow rates passing through the hydraulic resistors. The expressions of the force variation on the single rod in the cases of pure pitch and pure locked roll are derived following the same approach and reported in **Eq. (1.48)-(1.49)**.

$$\Delta F_{damp\ pitch_3\ acc} = \Delta p_P \cdot A_P + \Delta p_P \cdot A_R = \frac{\rho(\dot{x} \cdot A_P)^2}{2C_d^2 \cdot \left(\frac{\pi d_P^2}{4}\right)^2} \cdot A_P + \frac{\rho(2\dot{x} \cdot A_R)^2}{2C_d^2 \cdot \left(\frac{\pi d_R^2}{4}\right)^2} \cdot A_R \tag{1.48}$$

$$\Delta F_{damp\ roll_3\ acc} = \Delta p_P \cdot A_P = \frac{\rho(\dot{x} \cdot A_P)^2}{2C_d^2 \cdot \left(\frac{\pi d_P^2}{4}\right)^2} \cdot A_P \tag{1.49}$$

Note that the damping contribution in the case of unlocked roll is zero (neglecting the contribution given by the concentrated and distributed pressure losses of the pipes).

These relationships are representative of pure pitch motion and pure roll motion. During the actual manoeuvres carried out by the operator driving the vehicle, the suspension is often subject to a combination of these motions, so the real stiffness and damping characteristics is consequently a combination of these relationships.

This three-accumulator system can be slightly complicated by adding a second accumulator (with the usual hydraulic resistance) on the rod side branch. **Figure 1.20** shows the simplified schematic of this suspension with two double-acting cylinders and four hydro-pneumatic accumulators.

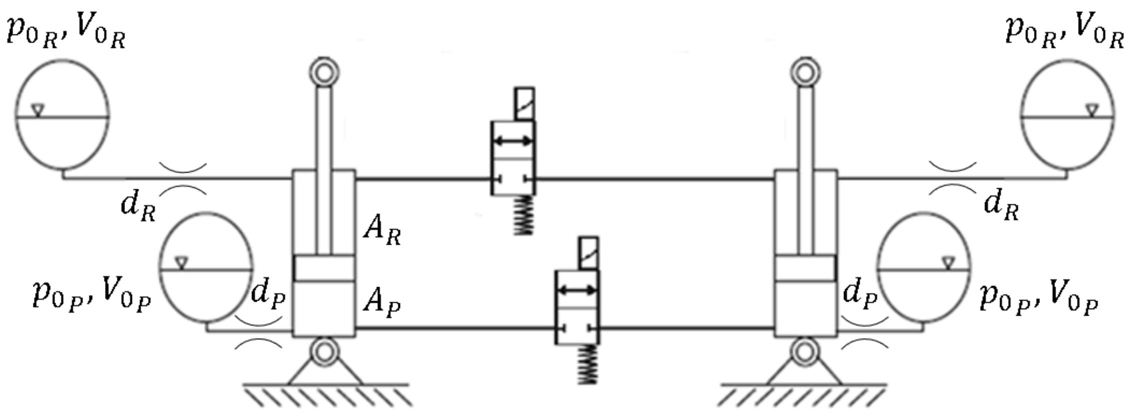

Figure 1.20: Simplified scheme of the three-accumulator hydro-pneumatic suspension

In addition to the second accumulator, an on/off valve was also inserted on the rod side branch in order to lock and unlock the roll, as was already done on the piston side branch.

The addition of these components obviously affects the stiffness and damping characteristics of the system, both for pitch and roll motion. **Figure 1.21-1.22** show the pure pitch and pure roll (locked) cases for the solution with four accumulators.

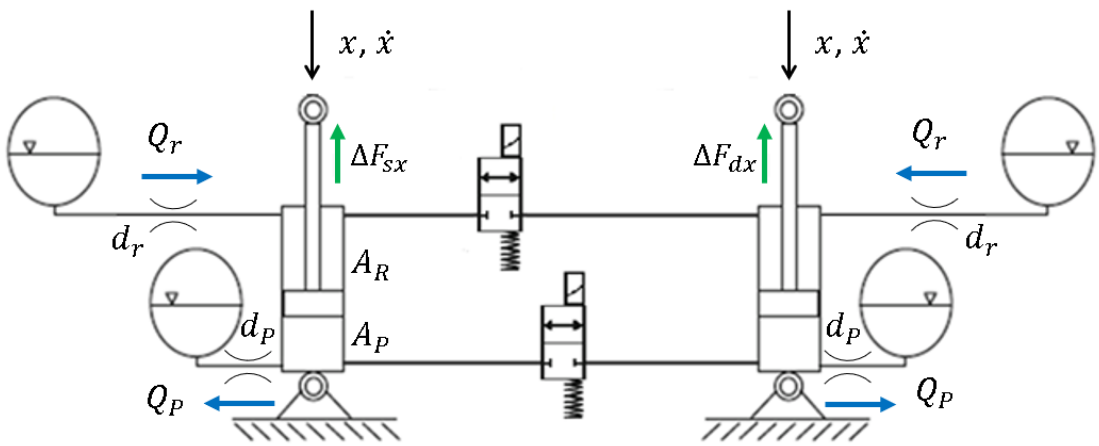

Figure 1.21: Pitch motion with four-accumulator and two cylinders suspension

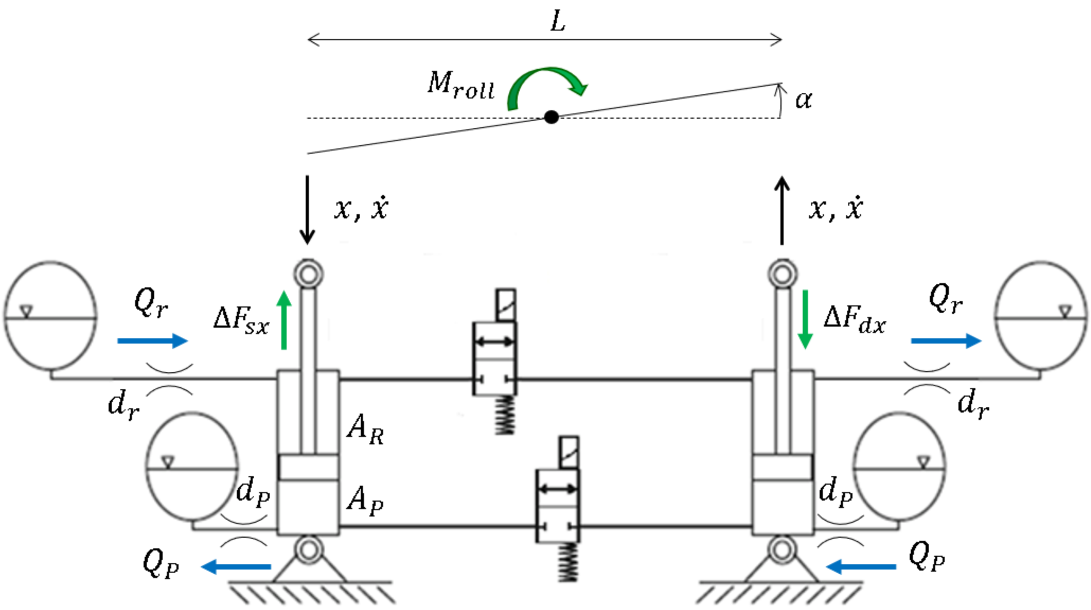

Figure 1.22: Roll motion (locked) with four-accumulator and two cylinders suspension

This two-cylinder and four-accumulator system consists of exactly two hydro-pneumatic springs with one cylinder and two accumulators, one for the right wheel and one for the left wheel. For each cylinder the pitch stiffness is defined by the relationships found in the previous sub-section, i.e. **Eq. (1.41)-(1.42)**. With everything else being equal, the pitch stiffness is greater in the three-accumulator layout, thanks to the factor 2 highlighted before.

Similarly to what was done before, it is possible to derive the roll stiffness of this solution. In this case both branches contribute to the generation of a resistant moment. The expression of the roll stiffness for the four-accumulator case is given in **Eq. (1.50)**.

$$w = \frac{L^2}{4x} \cdot \left\{ \left(F_0 + p_{1_R} \cdot A_R\right) \cdot \left[\left(\frac{\frac{p_{0_P} V_{0_P}}{p_{1_P}}}{\frac{p_{0_P} V_{0_P}}{p_{1_P}} - x \cdot A_P} \right)^n - \left(\frac{\frac{p_{0_P} V_{0_P}}{p_{1_P}}}{\frac{p_{0_P} V_{0_P}}{p_{1_P}} + x \cdot A_P} \right)^n \right] + \left(p_{1_R} \cdot A_R\right) \right.$$
$$\left. \cdot \left[\left(\frac{\frac{p_{0_R} V_{0_R}}{p_R}}{\frac{p_{0_R} V_{0_R}}{p_R} - x \cdot A_R} \right)^n - \left(\frac{\frac{p_{0_R} V_{0_R}}{p_R}}{\frac{p_{0_R} V_{0_R}}{p_R} + x \cdot A_R} \right)^n \right] \right\} \tag{1.50}$$

Both intuitively and by comparing this expression with **Eq. (1.47)**, it is easy to see that the roll stiffness is greater in the case with four accumulators. This is due precisely to the additional contribution of the rod side, which was zero in the previous layout.

Using the same approach, it is possible to evaluate the expressions of the damping force variation on the piston rod in the pure pitch and pure roll (locked) cases, which are reported in **Eq. (1.51)-(1.52)**.

$$\Delta F_{damp\ pitch_{4\ acc}} = \Delta p_P \cdot A_P + \Delta p_P \cdot A_R = \frac{\rho(\dot{x} \cdot A_P)^2}{2C_d^2 \cdot \left(\frac{\pi d_P^2}{4}\right)^2} \cdot A_P + \frac{\rho(\dot{x} \cdot A_R)^2}{2C_d^2 \cdot \left(\frac{\pi d_R^2}{4}\right)^2} \cdot A_R \tag{1.51}$$

$$\Delta F_{damp\ roll_{4\ acc}} = \Delta p_P \cdot A_P + \Delta p_P \cdot A_R = \frac{\rho(\dot{x} \cdot A_P)^2}{2C_d^2 \left(\frac{\pi d_P^2}{4}\right)^2} \cdot A_P + \frac{\rho(\dot{x} \cdot A_R)^2}{2C_d^2 \left(\frac{\pi d_R^2}{4}\right)^2} \cdot a_R \tag{1.52}$$

Comparing these expressions with the ones found for the three-accumulator layout, it can be seen that the four-accumulator case has greater roll damping but less pitch damping (with all other conditions being equal).

A non-negligible difference between the two layouts considered is the ability of four-accumulator systems to have less variable stiffness with piston travel. Thanks to the presence of the second accumulator on the rod side, two accumulators (instead of one) are available to manage the volumes of fluid entering and exiting the cylinder. This allows to have lower variations in the pressure level.

In this section, therefore, two different layouts for an independent hydro-pneumatic suspension have been presented, i.e. with three or four accumulators. The next section presents the suspension designed by Dana Incorporated, which is the main subject of this chapter. The introduction made so far has served precisely to introduce the subject and to present the theoretical basis behind the design of these systems. The company actually started by considering the two layouts seen in this sub-section for its solution, which were then modified according to internal requirements.

1.2 Adavanced Front Suspension System by Dana

The following section introduces the project regarding the independent hydro-pneumatic suspension for medium-sized agricultural tractors that Dana Incorporated decided to investigate. This activity turned out to be a novelty for the company, which is a manufacturer of rigid and suspended axles, but had no previous experience with independent suspension.

The company's desire was therefore not only to design and manufacture an independent suspension for tractors with certain characteristics, but also to expand its know-how and create a design methodology to follow for this type of axle.

The vehicle taken as the target reference for the suspension under consideration is the 116 kW John Deere JD 6130 tractor, shown in **Figure 1.23**. This is a medium-sized tractor on which it makes sense to install an independent suspension. These types of suspensions are indeed rarely installed on small tractors, where it is preferred to use rigid axles or simpler suspensions because the cost-benefit ratio is not sufficient to justify the use of independent ones.

Figure 1.23: John Deere JD 6130 tractor taken as reference for the Dana independent suspension

The standard axle installed on the vehicle taken as a reference is a suspended axle, but not an independent one. The suspension used, called TLS (Triple Link Suspension), is a hydro-pneumatic suspension with three suspension links. The first, called vertical linkage, consists of two hydraulic cylinders that manage the vertical oscillations coming from the ground. The second, called longitudinal linkage, is a ball joint connection positioned below the vehicle centre of gravity, thanks to which tractor traction is improved. The third, called lateral linkage, is nothing more than a Panhard rod, which stiffens the suspension transversely. A picture of the TLS suspension is shown in **Figure 1.24**.

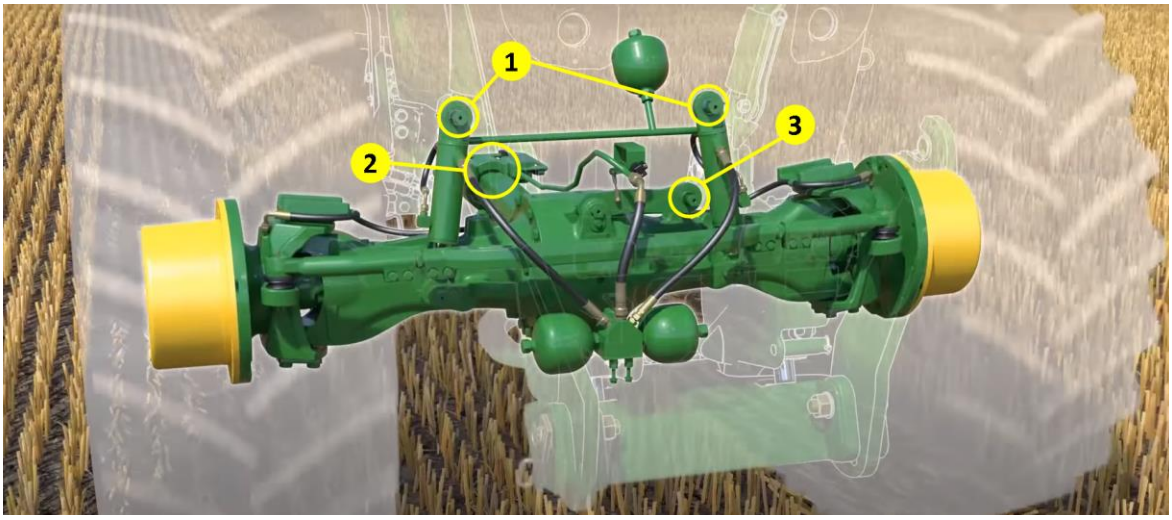

Figure 1.24: Standard TLS suspension installed on JD 6130 tractors with the three connections highlighted: hydraulic cylinders (1), longitudinal ball joint (2) and Panhard rod (3)

From **Figure 1.24** it is also easy to see the presence of three hydraulic accumulators. Two of these accumulators are installed on the piston side, while the third is on the rod side.

The objective of the presented activity is therefore the design and realisation of an independent hydro-pneumatic suspension with high performance to be placed on the market by the company. The reference vehicle was selected to ensure the suspension performance improvement using the Dana axle prototype instead of a standard suspension.

The company chose AFS, i.e. Advanced Front Suspension, as the name of the suspension. This name emphasises the objective of creating an advanced hydro-pneumatic suspension capable of being adjusted in terms of stiffness and damping according to operating conditions, either manually by the user or automatically by the control unit.

As mentioned in the introduction, independent suspensions are capable to offer better performance in terms of ride quality and traction capability. On the other hand, however, they also require more engineering effort for their design, as they are significantly more complex than non-independent suspensions. Moreover, the suspension cannot be considered as a stand-alone system, but its integration on the vehicle must be taken into account. This is therefore a multidisciplinary activity, in which the mechanical architecture, the hydraulic system and the control logic must be designed together to guarantee the best performance for the complete vehicle.

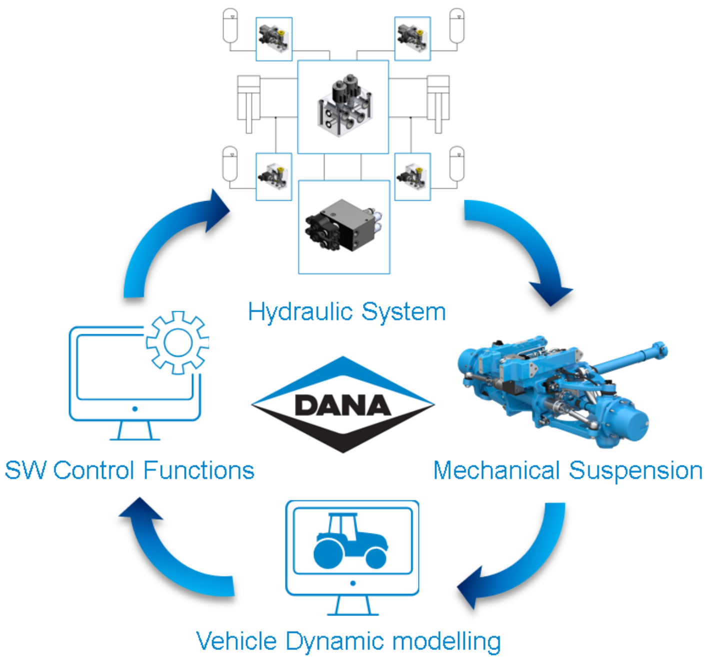

Figure 1.25: Multidisciplinary nature of the AFS project

After conducting a market analysis and consulting with Dana Incorporated's engineering department, the company selected the double wishbone suspension architecture (**Figure 1.2**) for its independent suspension. This is the most used architecture for off-highway independent suspension, such as those installed on Fendt 900 Vario and 1000 Vario tractors (**Figure 1.26**). These latter have been taken as a reference since Dana Incorporated is the axle body supplier. What is missing, however, is all the know-how behind this type of axle.

Figure 1.26: Axle with *double wishbone* suspension for Fendt 900 Vario and 1000 Vario

In addition to the mechanical design of the suspension architecture, the choice and sizing of the hydro-pneumatic system is also of the utmost importance.

Two different possible solutions were considered in the project initial phase: a layout with three accumulators, two on the piston side and one on the rod side, and one with four accumulators, two on the piston side and two on the rod side. In this way, it was possible to investigate the potential of both, to highlight the differences in performance and only then select the one most suitable for AFS suspension. Note that the layouts considered are precisely those analysed in the previous paragraph.

The hydraulic diagrams of these two different solutions were then sketched out in the Dana engineering department with a first parameterisation attempt but without actually dimensioning the circuits. The final dimensioning was carried out later according to the system requirements using the numerical models developed for the project, which are presented in **Section 1.3**.

Some of these numerical models were also used to evaluate the differences in performance between the three-accumulators layout and four-accumulators one. This comparison is reported in detail in the following section, and it was the basis for the choice of which solution to consider for the prototype.

1.2.1 Vehicle reference frame

Before proceeding with the presentation of the analyses performed on the system using numerical modelling, it is important to unambiguously define what the vehicle reference system is.

The term vehicle reference frame generally refers the reference system centred in the centre of gravity of the vehicle with the axes oriented as follows:

- longitudinal axis x: axis parallel to the ground directed in the same direction as the longitudinal axis of the vehicle, with direction concord with the vehicle forward direction.
- transversal axis y: axis parallel to the ground, obviously perpendicular to the x-axis and directed to the driver's left.
- vertical axis z: axis perpendicular to the ground and consequently directed upwards.

The vehicle reference system is shown in **Figure 1.27**.

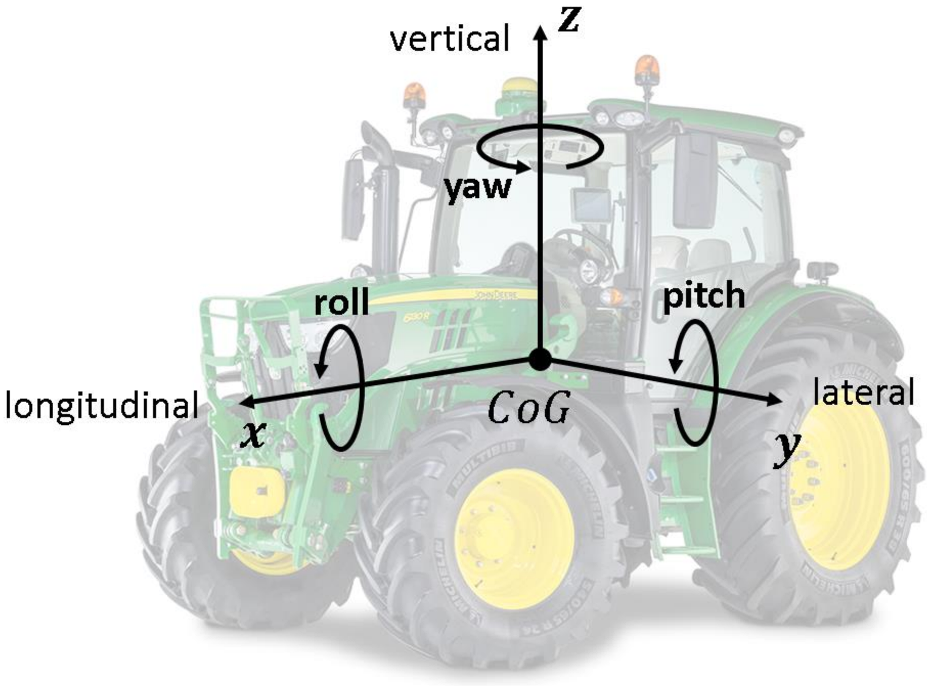

Figure 1.27: Vehicle reference frame and Euler angles for the vehicle orientation

However, it is not sufficient to consider the position of that reference frame (in relation to the ground reference frame) to unambiguously identify the vehicle in space. This vehicle reference frame does not give information regarding the orientation of the vehicle itself. It is thus also necessary to consider the three Euler angles used precisely to define the orientation of a reference system in space. As known [30], there are 12 possible ways to choose the triplet of angles that parameterize the orientation of a mobile reference system with respect to a fixed one. The vehicle Euler angles are precisely one of these triads and are the angles of rotation around the x, y and z axes of the vehicle reference system.

These three Euler angles are also called roll (φ), pitch (θ) and yaw (ψ) angles as they define the following vehicle motions:

- roll, i.e. the vehicle's oscillating motion around the longitudinal axis of its own reference system,
- Pitch, i.e. the vehicle's oscillating motion around the transverse axis of its own reference system,
- yaw, i.e. the vehicle's oscillating motion around the vertical axis of its own reference system.

These three motions, and consequently the Euler angles of the vehicle, are always shown in **Figure 1.27**.

The unambiguous definition of this reference system is fundamental since graphs relating to quantities in the x, y or z directions (such as accelerations) or graphs relating to the vehicle Euler angles will be shown in the following paragraphs.

1.2.1 Hydro-pneumatic system requests

As mentioned above, a tractor is a vehicle used to work in a variety of operating conditions. It can be used on its own, e.g. for travelling, or with working implements, such as buckets, ploughs or planters, attached at the front and/or rear.

This multitude of operating conditions may even more justify the choice of using a hydro-pneumatic suspension with hydraulic preload that can change its stiffness and damping characteristics. Each operating condition is usually characterised by a particular vehicle balance and static load on the suspension, leading to different dynamic responses of the vehicle. Each of these operating conditions should have certain stiffness k and damping c values that are optimal for the suspension and vehicle behaviour.

These characteristics can be adapted to better match the demands of vehicle dynamics only using an adjustable suspended axle. On the other hand, it is obviously impossible to do so with a rigid axle or with a non-adjustable suspension, where the only option is trying to design the suspension in order to have trade-off values of stiffness and damping.

The following example is given to show the approach used when dimensioning the hydraulic system.

Three different load configurations are considered: one with an empty vehicle (EVW, empty vehicle weight), one with a medium vehicle weight (MVW, medium vehicle weight) and one with a fully loaded vehicle (GVW, gross vehicle weight). For each loading configuration, there is a certain optimum stiffness value, which is usually defined by the modal analysis of the vehicle in that configuration. There are thus two vectors that uniquely identify the requirements to dimension the stiffness part of the hydro-pneumatic system. The first the vector of the static load F_0 acting on the suspension cylinders in the different configurations, while the second contains the corresponding optimum stiffness values.

These two vectors uniquely define three (because three load configurations were considered: EVW, MVW and GVW) points on the $F_0 - k$ graph, as shown in **Figure 1.28** using the following example values:

- EVW configuration: $F_0 = 25000\ \mathrm{N}$ and $k_{target} = 150\ \mathrm{N/mm}$;
- MVW configuration: $F_0 = 35000\ \mathrm{N}$ and $k_{target} = 250\ \mathrm{N/mm}$;
- GVW configuration: $F_0 = 50000\ \mathrm{N}$ and $k_{target} = 500\ \mathrm{N/mm}$;

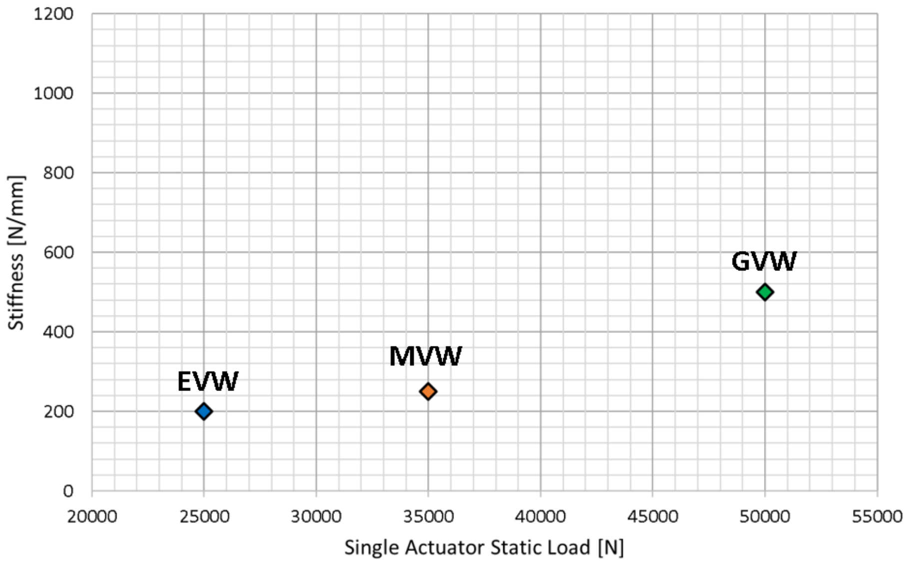

Figure 1.28: Example of optimal stiffnesses as function of the suspesnion static load

These requirements are to be compared with the range of stiffnesses obtainable from the hydro-pneumatic system under consideration, which is something similar to what is shown in **Figure 1.15**.

Considering therefore all the terms in the stiffness expression (given in **Eq. (1.42)** and **(1.44)** for the four and three-accumulator layouts respectively), it is possible to search for the optimal combination of parameters (geometric and non-geometric) to obtain a range of stiffnesses which contains all the required target stiffnesses. Once these parameters are fixed, it is then possible to achieve these target stiffnesses by varying the levelling pressure p_{R_1}, which is precisely the degree of freedom of the system thanks to which it is possible to adjust the stiffness.

Figure 1.29 shows the graph $F_0 - k$ with the range of available stiffnesses obtained with the following dimensioning for the four-accumulator layout.

- Hydraulic cylinder: $D_P = 72\ \mathrm{mm}$, $D_R = 60\ \mathrm{mm}$, $L_{stroke} = 120\ \mathrm{mm}$ ($x \in [-60\ \mathrm{mm}, 60\ \mathrm{mm}]$)
- Piston side accumulator: $V_{0_P} = 2\ \mathrm{L}$, $p_{0_P} = 30\ \mathrm{bar}$
- Rod side accumulator: $V_{0_R} = 0.75\ \mathrm{L}$, $p_{0_P} = 60\ \mathrm{bar}$
- Levelling maximum pressure: $p_{lev\ max} = 210\ \mathrm{bar}$

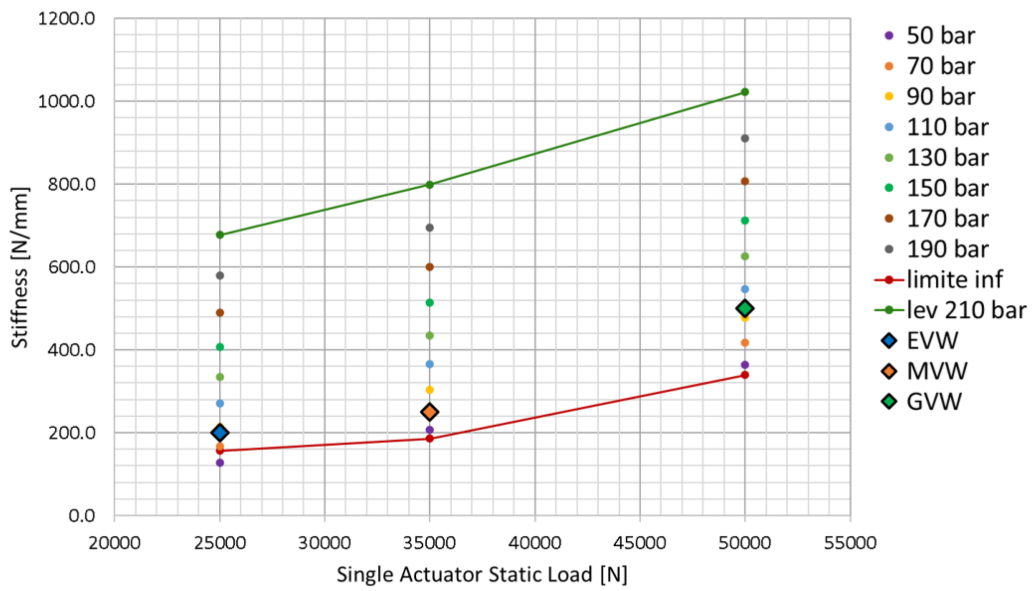

Figure 1.29: Example of the available stiffness range for a given dimensioning

As said, it is possible to vary the stiffness of the system within the range by varying the rod side levelling pressure p_{R_1}. There is a pressure p_{R_1} that exactly match the required target stiffness in the neutral position of the cylinder for all three load configurations considered.

The upper and lower limits of this range will be explained in detail later, when the actual methodology used for this dimensioning is presented.

The one reported is indeed only one of the possible combinations of parameters to obtain a satisfactory range of stiffnesses. This example, however, is illustrative of the approach chosen to utilize the requests derived from the modal analysis of the vehicle for the hydraulic layout dimensioning.

The creation of system numerical models to support the design of Dana Incorporated's AFS suspension is reported in the following section.

1.3 Numerical models

Together with the company we decided to develop different numerical models using software with different logics and purposes to assist the study of the system and its design. These models can allow the evaluation of the system characteristics, from constructive feasibility to hydraulic behaviour, up to the dynamic performance of the entire vehicle. They therefore turn out to be fundamental tools in the realization of complex system like the one under consideration where, as mentioned, the hydraulic behaviour, the geometry of the architecture and the various control logics influence the overall performance of the vehicle.

The first models that have been developed were the 3D CAD ones related to the suspended axle. These models have been developed in a parametric way in order to be able to vary the characteristic quantities of the individual components without needing to recreate the models themself. This is especially important in the early stages of the project, when the geometry of the architecture is not yet defined and even small changes can be frequent. Precisely because these CAD models are designed to support even the initial stages of the project, it was necessary for the assembly models to also consider any static or dynamic interferences that may occur between the various mechanical components once they are installed or when they are in relative motion with each other. Because of this, in addition to the detailed model of the parts and the suspension assembly, a simplified 3D CAD model was also created to immediately exclude unfeasible solutions without changing all the parameters of the detailed model.

Creo® CAD software was used for these models.

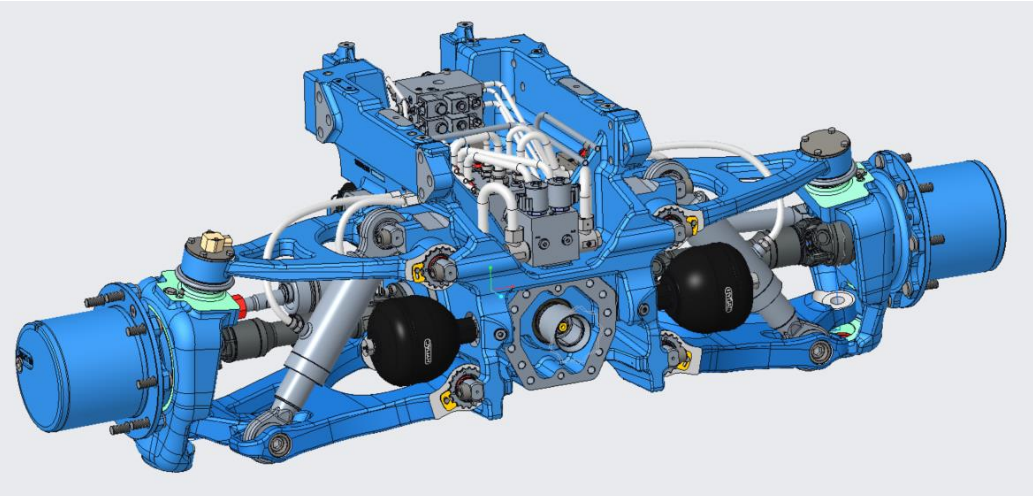

Figure 1.30: 3D CAD detailed model for the AFS suspension

Various FEM (Finite Element Method) models have been also realised, which are necessary for the structural analysis of both individual elements and the complete architecture. This analysis is fundamental for the evaluation of stresses and deformations of the suspension when the working loads are applied, which must be appropriately inserted into the model. The results of the FEM simulations can give indications of which points are most at risk of structural cracks or failure, which can then be reinforced by modifying their geometry or adding material. This analysis was only carried out for the final geometry before prototyping it. It would be unfeasible to carry out a FEM analysis for each intermediate design considered.

This structural analysis was carried out using the commercial software Tosca Structure®.

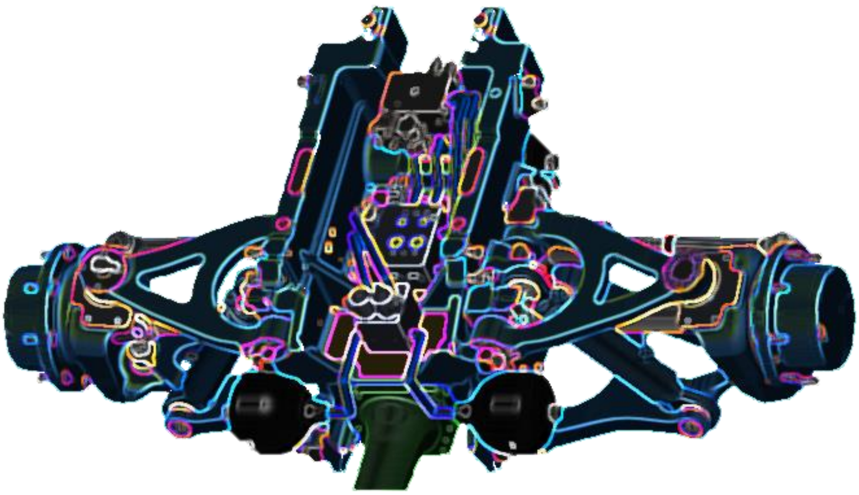

Figure 1.31: Example of FEM analysis for the considered solution

The so-called multibody models, i.e. systems consisting of rigid and/or deformable bodies, were also developed. These models were used to study the kinematic and dynamic behaviour of both the individual suspension and the entire vehicle once the latter has been installed. Multibody modelling is the state of the art for vehicle dynamics simulations.

Some of the models were developed to assess the kinematic characteristics of the chosen suspension architecture and geometry. These models were indeed exploited to define the suspension geometry itself. During the design phase, solutions that did not obtain certain values of these characteristics were directly excluded.

In addition to this, once the suspension geometry had been defined, a modal analysis of the entire vehicle was carried out to assess its own eigenmodes and calculate the target values of suspension stiffness and damping useful for dimensioning the hydraulic system.

Finally, multibody models were also exploited to evaluate the dynamic performance of the entire suspended vehicle in terms of comfort, handing and traction. Simulations of various standard tests such as ISO 5008, moose test (or double line change) or 4-poster tests were carried out extrapolating the results of interest. These final simulations were then used to define the optimal damping to be implemented with the hydraulic circuit. All of this will be presented in more detail in dedicated paragraphs.

The commercial software used for the realisation and simulation of these multibody models was MSC Adams®.

MSC Adams® is the most widely used software for the multibody modelling of 3D systems with rigid or deformable bodies subjected to forces or movements. External forces or torques can be applied to these systems to solve direct dynamics problems, or movements can be imposed to solve inverse dynamics problems. A graphical interface allows for simplification during model construction. This software is also widely used for modelling vehicles and their dynamic analysis.

The tractor multibody models with the standard front axle had been experimentally validated by the Dana engineering department and so these models can be considered a reliable reference.

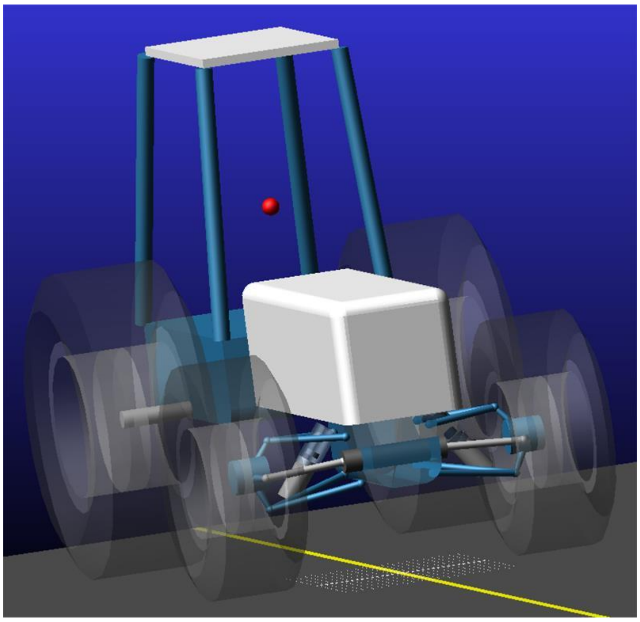

Figure 1.32: Example of dynamic multibody model of the complete vehicle

The models presented so far have mainly been developed before and during the activity reported in this work of thesis by the engineering department of the Arco (TN) site of Dana Italia, which is specialized in the design of axles, suspended and rigid. However, the candidate has supported the modification of the reference multibody models to adapt them to our study case by replacing the standard front axle with the Advanced Front Suspension one. As it will be shown in more detail later, in fact, Adams® cannot model a hydraulic system, so it was necessary to collaborate with the vehicle dynamics engineers of Dana Incorporated to integrate the hydraulic behaviour within the multibody model.

In addition to these already presented, we developed several lumped parameter models to simulate the hydraulic circuit and the complete suspension system. The lumped parameter approach allows to virtually study and optimize the performance of multi-physical systems, even complex ones, simplifying their mathematical description by attributing the various properties to distinct components (i.e. lumped parameters). The commercial software Simcenter Amesim® was used to model these models.

An introduction to the software followed by a more in-depth description of the various models realised is given in the following paragraphs, as this is precisely part of the work carried out during the PhD years.

1.3.1 Lumped parameter modelling: Simcenter Amesim®

As anticipated, the software used for modelling the hydro-pneumatic system of the suspension considered is the commercial software Simcenter Amesim® (acronym for *Advance Modeling Environment for performing Simulation of engineering systems*).

Simcenter Amesim® is a lumped parameter simulation software developed by Siemens, where a symbolic representation is used to identify each component of the system under analysis. The various symbols can either be compatible with a recognised engineering symbology, such as the UNI-ISO symbols for hydraulic and pneumatic components, or an intuitive representation of the element or its function in the system.

Each individual element in the software has ports through which it interfaces with the other components, defining the overall scheme of the system. With a few exceptions, the software manages the connection between the various elements by exchanging power at the interface ports ('Power-port principle') via input and output. To be connected, of course, two elements must be compatible (i.e. the same variable must be input for one element and output for the other).

With this assembly logic, the software allows the rapid construction and development of models of even complex dynamic systems. Thanks to the lumped parameter study, it is also possible to manage the parameterization, increasing the model flexibility.

The main steps for the realization and subsequent simulation of the model for the analysed engineering system are briefly outlined below.

1. System Sketch (*Sketch Mode*): the system reference diagram is created by connecting the ports of the individual elements.
2. Models Definition (*Submodel Mode*): We associate each element with a certain 'submodel', choosing from those available. In this way, it is possible to define the mathematical equations describing the components behaviour.
3. Model characterization (*Parameter Mode*): All geometric and operational data are assigned to the elements within the general scheme, in order to unambiguously parameterize the model.
4. Simulation Area (*Run Mode*): fourth and final phase, where it is possible to impose the simulation characteristics (simulation time, sampling rate, numerical integration method, etc.). Once the simulation has completed, the post-processing phase is available by processing and displaying the results.

For more detailed information, please refer to the internal help tool of the software [31].

The Simcenter Amesim® software is composed of a predefined number of libraries into which the various elements are subdivided. Other libraries created directly by the user can be added to these by means of the Amesim Submodel Editor® software, which will be discussed in more detail in **Chapter 2**.

Selecting one of the available libraries during the "Sketch Mode" phase opens a window containing all the icons representative of the models belonging to that library to drag and drop into the sketch.

The main standard libraries used for Amesim® numerical models relating to the considered hydro-pneumatic suspension are presented below.

- *1D Mechanical* Library: this library contains numerous elements representing basic mechanical components, such as masses, inertias, springs, joints, ropes and sensors for mechanical quantities. These elements allow the user to model a wide range of applications, from the simplest to more complex phenomena.

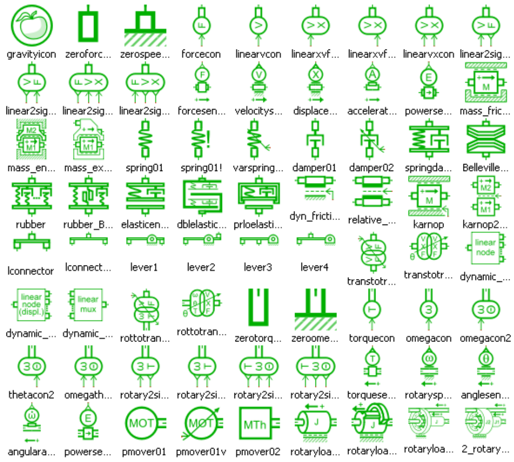

Figure 1.33: Example of the elements contained in the *1D Mechanical* Library of Simcenter Amesim®

- *Hydraulic* Library: this library contains models dedicated to the simulation of hydraulic systems, from industrial applications to those installed on road and off-highway vehicles. Components such as pumps, motors, valves, hydraulic volumes, etc. are present in this library. There are therefore elements that model real subsystems, but they obviously do so in a simplified manner, not considering certain detailed phenomena. However, they are still used for modelling complex systems, in which these detailed phenomena can be neglected.

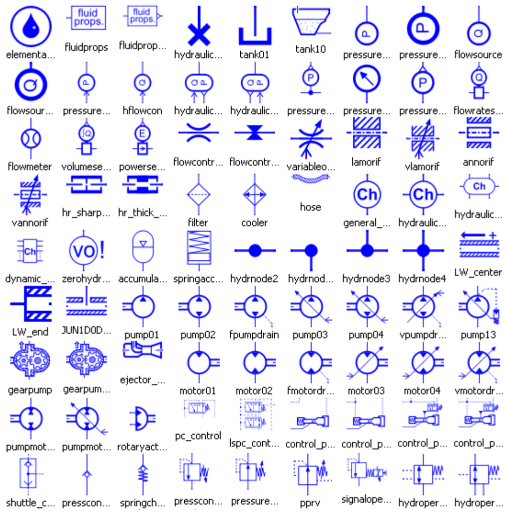

Figure 1.34: Example of the elements contained in the *Hydraulic* Library of Simcenter Amesim®

- *Hydraulic Component Design* Library: this library contains elements that allow the realization of a large number of hydromechanical systems. These elements allow for example the main valve geometries with spool-seat couplings, leakage, single or double-acting hydraulic cylinders, seal friction, etc.

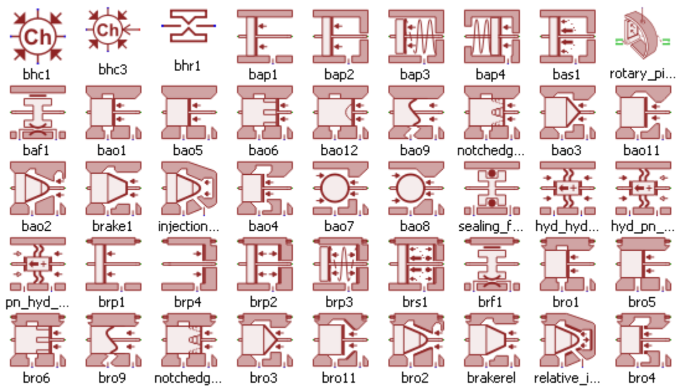

Figure 1.35: Example of the elements contained in the *Hydraulic Component Design* Library of Simcenter Amesim®

- *Signal, Control* Library: this library is dedicated to the realization of block diagrams for signals or controls. With this library, it is possible to model not only simple input signals, but also more complex control logics, such as PID controllers.

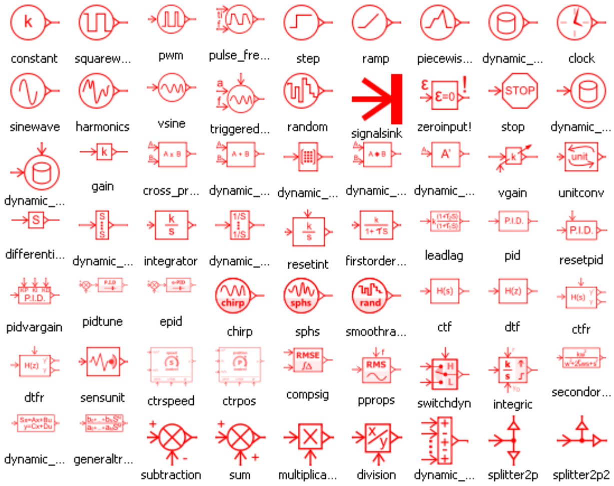

Figure 1.36 Example of the elements contained in the *Signal, Control* Library of Simcenter Amesim®

- *3D Mechanical* Library: this library is used for modelling the kinematic and dynamic behaviour of multibody systems in the 3D space. The main elements are therefore rigid or flexible bodies and connection joints. Inside this library there is also a 3D animation tool that is updated automatically as the system is parameterized. This tool is very useful as it allows to observe the system behaviour.

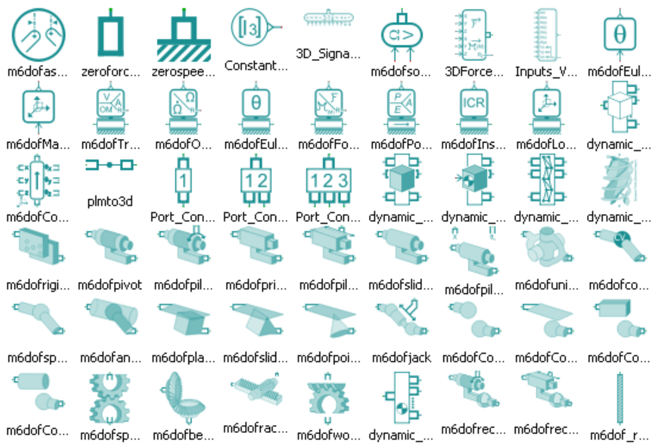

Figure 1.37: Example of the elements contained in the 3*D Mechanical* Library of Simcenter Amesim®

- *Vehicle Dynamics* Library: this library contains various elements useful for analysing vehicle dynamics, such as wheel and tyre models, road model, or simplified models for the entire vehicle with several degrees of freedom. It is possible to connect this library directly with the others presented in order to build a model of the entire vehicle.

Figure 1.38: Example of the elements contained in the *Vehicle Dynamics* Library of Simcenter Amesim®

Please refer to the Simcenter Amesim® Help tool for further details.

As anticipated, the elements of these libraries were used to develop various lumped parameter models of the system under investigation. In particular, we developed the following ones:

- model of the hydro-pneumatic suspension system
- complete model of the vehicle with the suspended front axle
- simplified vehicle model for Real Time simulations

The first two models are presented in detail in the following subsections, while the real-time model and the methodology used to realise it will be explained in **Section 1.5**.

1.3.2 Lumped parameter model of the hydro-pneumatic system

The first lumped parameter model developed in Simcenter Amesim® is the hydro-pneumatic suspension circuit one. In this thesis, only the model for the four-accumulator solution will be reported. In fact, the one for the three-accumulator circuit was also developed in a completely similar manner. The comparison between these two models allowed to select the four-accumulator solution, since it is more performing both in terms of stiffness and damping characteristics and in terms of comfort for the total vehicle, as will be shown in the following paragraph.

A first attempt solution for the hydraulic circuit was developed basing on the experience of the Fluid Control department of Dana Incorporated's Off-Highway division and taking inspiration from some solutions already present on the market. Starting from the ISO scheme of this solution, it was then possible to develop the hydro-pneumatic numerical model using the various libraries present in the software.

This turns out to be a fundamental step in a design phase, where the hydraulic hardware is not yet fixed and it can be interesting to evaluate the behaviour of the system as a function of it. It would be unthinkable to create a prototype for each small modification to the circuit and assess its behaviour by means of tests characterization. On the other hand, developing a reliable and parametric numerical model allows any design to be examined very easily by changing the values of the geometric and non-geometric parameters of the model. This is undoubtedly one of the advantages of numerical modelling and simulation. For these reasons, the reliability of numerical models is obviously crucial to make decisions based on their results.

Figure 1.39 shows the simplified schematic of the suspension hydro-pneumatic system, where the different hydraulic valve blocks are highlighted.

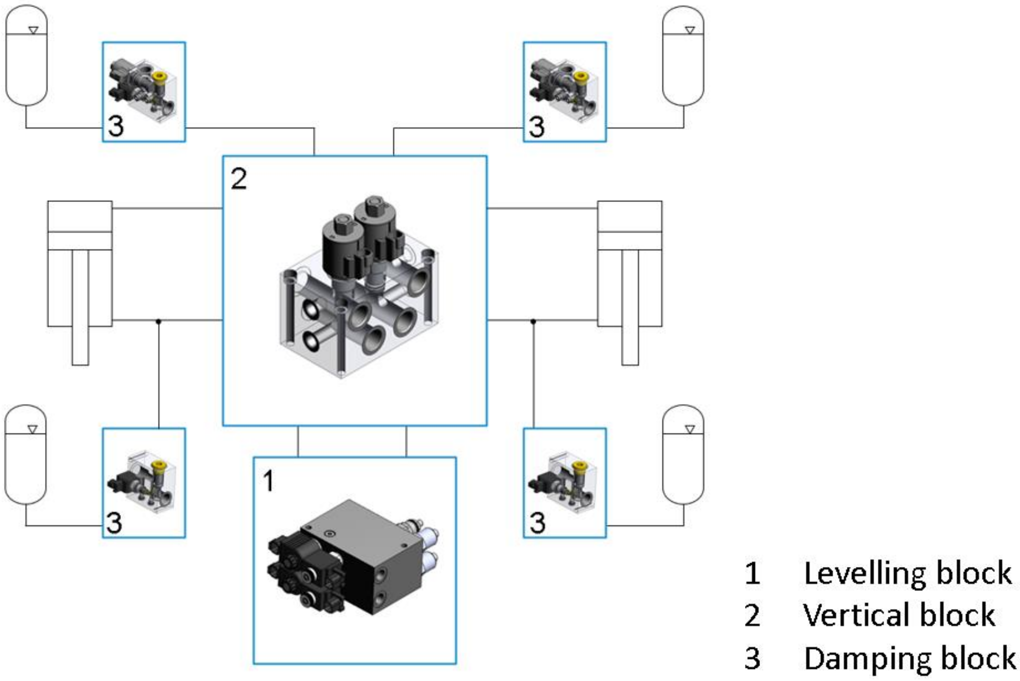

Figure 1.39: Simplified scheme of the hydro-pneumatic suspension system

In particular, the system is designed to have a levelling valve block, which has to manage the levelling phase of the vehicle (i.e. the raising or lowering of the suspension) or the increase or decrease of its stiffness. This levelling block directs the flow to the so-called vertical hydraulic block, which manages the connection between the suspension cylinders and the four accumulators through on-off valves, check valves and orifices.

Finally, there are as many hydraulic damping blocks as accumulators. These blocks, mounted upstream of the accumulators, must guarantee the correct system damping by introducing an appropriate hydraulic resistance into the flow conveyed towards the accumulator.

Figure 1.40 shows the complete ISO scheme of the hydro-pneumatic system, where the main hydraulic components that may be subject to modification are highlighted, such as valves (identified by the generic letter *V*, or *R* if they are relief valves), orifices (identified by the letters *O* or *GR*).

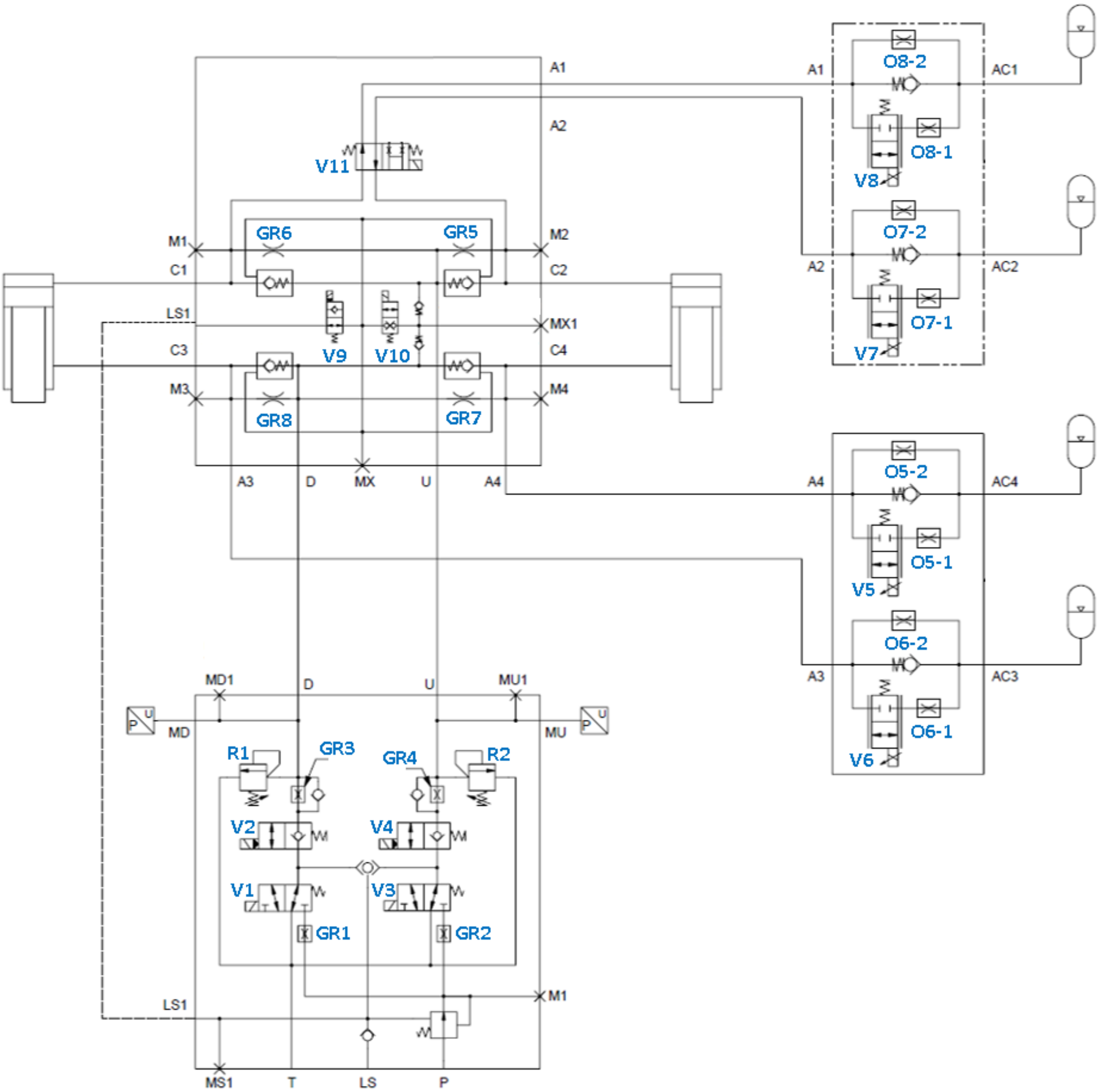

Figure 1.40: Detailed ISO scheme of the hydro-pneumatic suspension system

In addition to the highlighted components, there are both piloted and non-piloted check valves, which have been calibrated based on the company's hydraulics experience.

Finally, hydraulic cylinders and accumulators are also present. These cylinders are characterised by the piston and rod diameters, and by the stroke. The accumulators have as characteristic parameters the total volume and the gas pre-charge pressure.

As seen in the section relating to the analysis of the hydro-pneumatic system, these last parameters are those which affect the stiffness of the system and are therefore to be modified according to the demands deriving from the modal analysis of the vehicle. The vehicle modal analysis provides the target stiffness and damping value that the system should have to minimise the vehicle's natural frequency for each load configuration.

Obviously, however, these parameters also influence the hydraulic behaviour. For example, the rod and piston diameters of the suspension cylinders also define the flow rates passing through the various blocks, and so the system damping. Moreover, many parameters affect each other. It is thus complicated to modify them manually in an iterative process (trial and error) while taking everything into account without the risk of missing information. For this reason, the final dimensioning of these parameters was done using a suspension optimization process, including both this hydraulic model and the entire vehicle, which will be described in detail in **Section 1.4**.

On the other hand, other parameters of the system are less complex to dimension, and this operation can be done using only the model of the hydro-pneumatic system presented in this paragraph.

The first step for the construction of the numerical model in the Simcenter Amesim® environment, as seen, is the reproduction of the system in the sketch environment using the elements of the various libraries. This step is straightforward as the elements of the *Hydraulics* library use precisely the symbolism of the ISO standard, also used in **Figure 1.40**. It is therefore a matter of replicating the starting sketch component by component. In the same library, elements for modelling gas accumulators, tanks and flow sources can also be selected. Since we had no information on the tractor power unit, we decided to simply replace the pump with an ideal flow source.

It is also essential to include the element to specify the type of fluid used and its properties in the sketch. In particular, the hydraulic oil ISO VG 46 - Mobil DTE Medium was selected. In addition to the choice of fluid, the software also allows the setting of other parameters such as the operating temperature and the percentage of air/gas contained in it.

Using elements from the *Hydraulic Component Design* and *1D Mechanical* libraries, it was possible to carry out more detailed modelling of the two suspension cylinders. In fact, elements for modelling linear actuators do exist in the *Hydraulics* library, but they are simplified and do not allow certain aspects to be taken into account.

Finally, it is necessary to consider the elements in the *Signal, Control* library to manage the load signals or the control of the hydraulic valves. In this way, it is possible to simply replicate the vehicle ECU.

When creating the sketch, it is important to remember that the hydraulic elements cannot be connected freely, but rather a resistive element must be connected to each capacitive element and vice versa. Resistive elements are those in which the flow rate is evaluated while capacitive elements are those in which the pressure is calculated. Examples of the former are orifices and generic valves, in which the flow rate is a function of the equivalent outflow area and the pressure drop at the ends of these. On the other hand, capacitive elements are hydraulic chambers and volumes (based on the capacity equation) or the gas accumulators themselves.

It is therefore good practice to insert equivalent hydraulic capacitances between two resistive elements, so that the sub-models of direct pipe connections can then be used. In fact, there are more complex sub-models for pipes that can calculate pressure internally without using equivalent hydraulic chambers, but they require very accurate parameterization with usually unknown data. In addition, the use of these submodels slows down the simulation considerably. It is much more efficient to use equivalent chambers and concentrated pressure drops.

After building the model sketch, the next step is the submodel selection for each element within the sketch. The choice of one submodel over another implies a difference in the equations that the software uses to model that element. An example may be the submodels available for the flow source element. It is thus possible to select flow source for isothermal modelling, or a thermo-hydraulic flow source to also consider heat exchange between the elements. Obviously, such a submodel must be connected to other thermo-hydraulic elements.

Each submodel has certain variables exchanged at its ports, as shown for the mass element for one-dimensional motion with friction and limit end stroke in **Figure 1.41**.

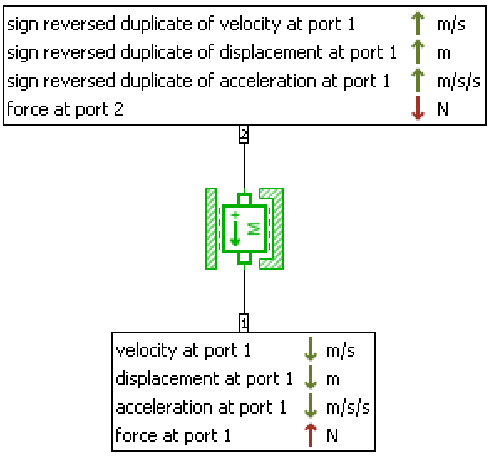

Figure 1.41: Inputs/outputs exchanged through the ports of the *MECMAS21* element of the *1D Mechanical* Library

The variables identified by red arrows are inputs to the element (forces in this case) while the outputs are represented by green arrows, which are the variables calculated internally within the element and passed to adjacent elements. Obviously, this element must be connected with two elements that provide a force as output and require displacement, velocity and acceleration as input in order to 'close the system loop'.

Once the submodel has been assigned to each element of the system, it is possible to move on to the third step, which is the introduction of the parameters required for the system unique characterisation. Each element requires the input of a certain number of parameters. Some of these parameters can however be left with default values as they are not particularly impactful or unknown.

For example, still considering the *MECMAS21* element in **Figure 1.41**, some of the parameters required from the user are:

- mass [kg]
- stiction (or static friction) force [N]
- kinetic friction force [N]
- viscous friction coefficient [N/m/s]
- initial position [m]
- initial velocity [m/s]
- upper end stroke [m]
- lower end stroke [m]

These values are used by the model for the model parameterization and initialization. Similarly, all other parameters are required for the remaining elements.

Some of the parameters are geometric, such as the end stops of the mass element for one-dimensional motion, which depend on the hydraulic cylinder. Other parameters are not geometric, such as the forces and friction coefficients, which can be obtained, for example, from the seal catalogues in hydraulic pistons or from literature values.

Another good rule is the use of so-called global parameters. Simcenter Amesim® allows a list of all parameters to be entered in the model, defining the name, description, unit of measurement and value. When parameterising individual elements, it is then possible to simply call up the various parameters entered in the list of global parameters. Changing a global parameter, therefore, implies the parameter change each time it is called up in an element. This method is very useful, especially in the design phase where changes are frequent. Moreover, it is also much more convenient to keep track of all the parameters in one place instead of having them in the various model elements.

Once all the characterising parameters for each element of the system have been entered, it is possible to move on to the simulation environment after performing the model compilation (i.e. the translation of the entire constructed model into machine language). Certain setting parameters should be defined before launching the simulation, such as the duration of the simulation, the result sampling frequency, or the choice between variable or fixed step integrator.

Once the simulation has been completed, it is possible to access the results directly from the model elements. These results can be displayed as graphed in the simulation section, or exported as vectors to be analysed, processed or displayed outside the software. Using the *MECMAS21* element from the *1D Mechanical* library as an example, this element allows to display the results regarding the displacement, velocity and acceleration of the mass in question, the input forces and the various friction contributions.

Figure 1.42 shows the schematic of the lumped parameter model of the hydro-pneumatic system realised in Simcenter Amesim®.

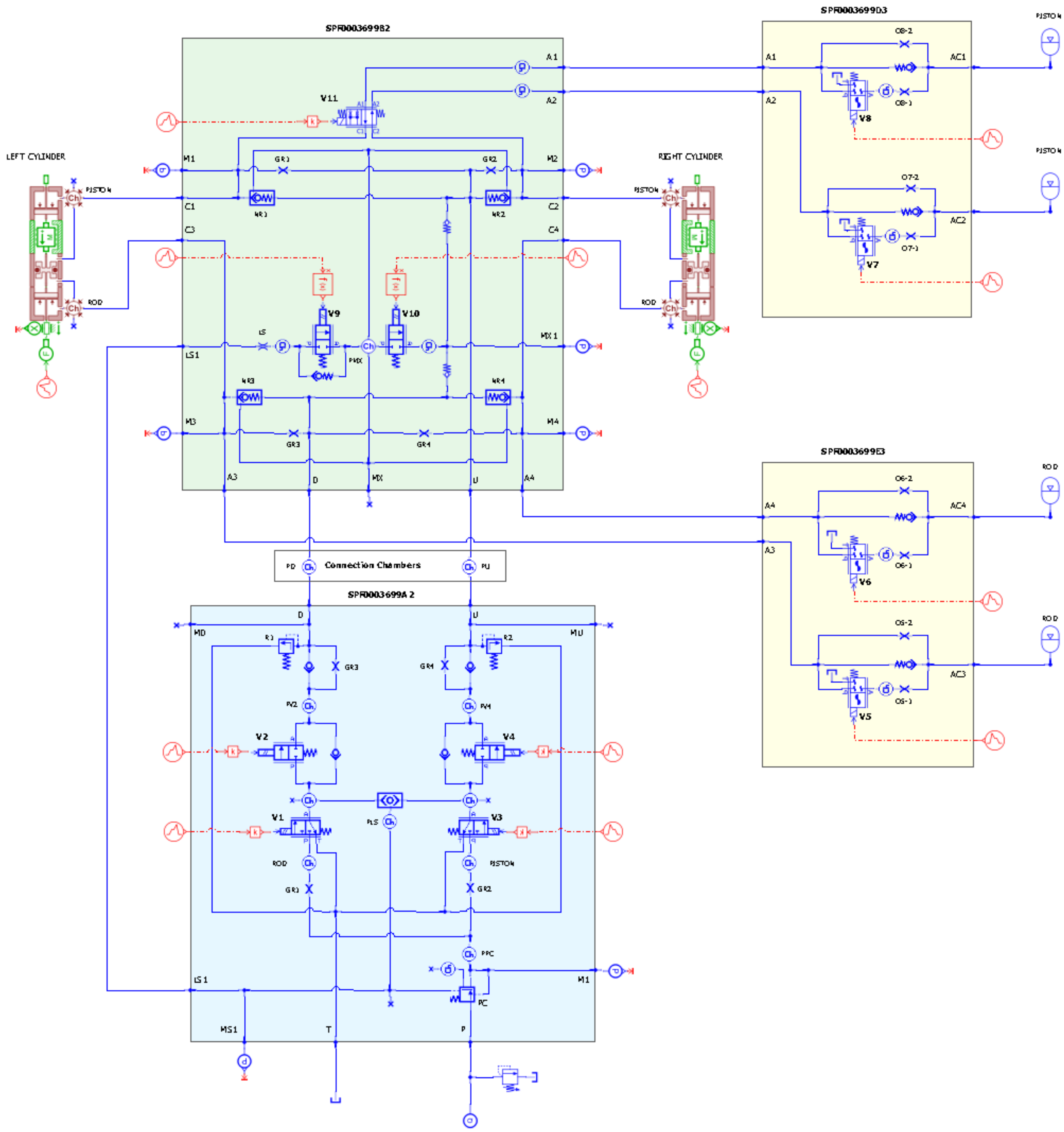

Figure 1.42: Complete lumped parameter model of the hydro-pneumatic suspension

Note that the division of the various hydraulic blocks has been maintained in order to make the diagram as comprehensible as possible.

1.3.3 Lumped parameter and multibody model of the complete vehicle

In addition to the model of the hydro-pneumatic system presented in the previous paragraph, we decided to develop a 3D multibody model of the complete vehicle with suspension to be integrated with the previous one. It is indeed possible to build the vehicle model connecting the jacks of the suspended axle with the hydraulic actuators of the hydro-pneumatic model thanks to the modularity that characterises Simcenter Amesim®. In this way, it is also possible to assess the impact of potential changes on the performance of the entire tractor, or study levelling manoeuvres in more detail, taking into account the raising or lowering of the vehicle and thus the resulting changes to the balance.

The development of a further multibody model in Simcenter Amesim® is motivated by the impossibility of integrating the hydraulic system within the Adams® one, (unless using a co-simulation, which is expensive in terms of realisation and generally quite onerous regarding simulation times). Adams® models indeed involve the use of simple spring-damper systems instead of the actual hydro-pneumatic system. It is so necessary to characterize these springs and dampers with correct functions and/or tables to replicate the real behaviour.

However, it would be inefficient to re-characterize these spring-damper systems every time a change is made to the hydraulic circuit, especially in the initial phase. On the other hand, having a complete vehicle model capable of considering the detailed modelling of the hydro-pneumatic system within it allows to make any change and immediately assess its impact on the overall system. In addition, in this model it would also be possible to assess the impact of any hydraulic failure on the vehicle. This is obviously impossible to realize in Adams® where the entire hydro-pneumatic system is described within ideal springs and dampers.

However, the tractor model realised in MSC Adams® can be used as benchmark for the Simcenter Amesim® one.

Tire-soil modelling

In this sub-section, the modelling of the tire-soil interaction realised in Simcenter Amesim® is reported. As anticipated, we exploited the modularity approach of the software using different elements to model different aspects. Each of these elements, in fact, takes as input a certain number of characteristic parameters of the wheel, the ground or the tyre, and calculates certain variables. **Figure 1.43** shows the set of elements required to model the tire-soil assembly and their brief description.

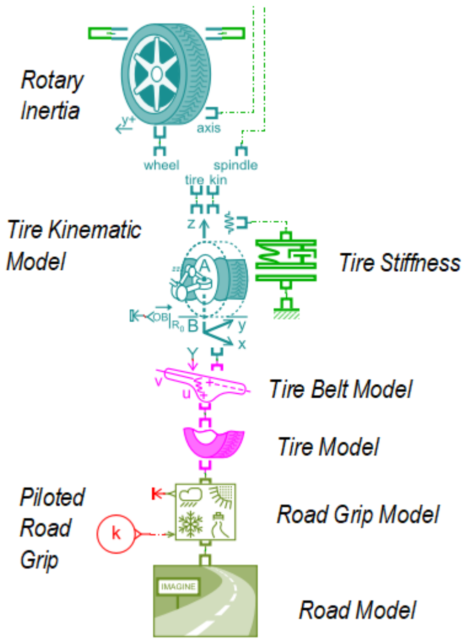

Figure 1.43: Modular tire-contact model in Simcenter Amesim®

Starting from the bottom of **Figure 1.43**, it is possible to identify the *Road Model* element with which the road profile under each wheel is modelled. Depending on the selected submodel, different profiles can be implemented, such as flat profiles, sinusoidal profiles or generic profiles defined through a **.data* file.

With this type of modelling, it is possible to run each wheel on a different road profile.

The element immediately above is the so-called *Road Grip Model*, which can be used to simulate non-standard grip conditions between tyre and ground, for example when considering a wet or icy road.

The next element is the *Tire Model*, where it is possible to choose the tire-soil contact model to calculate the reaction forces and moments between them. The Pacejka 2002 model was selected. As anticipated, the Pacejka 2002 Magic-Formula [32] is the state of the art for modelling tire-soil interaction in vehicle dynamics applications. Starting from inputs entered by the user such as tyre and road parameters, and wheel position/ orientation and speed passed by adjacent elements, this element calculates the vertical load and the longitudinal and lateral forces between tires and ground.

On the other hand, the *Tire Belt Model* element is used to evaluate some characteristic variables regarding the wheel kinematics, such as the lateral slip angle α, the longitudinal slip coefficients or the camber angle (or camber) ε_V. **Figure 1.44** shows an image of the Amesim® Help tool in which α and ε_V are highlighted.

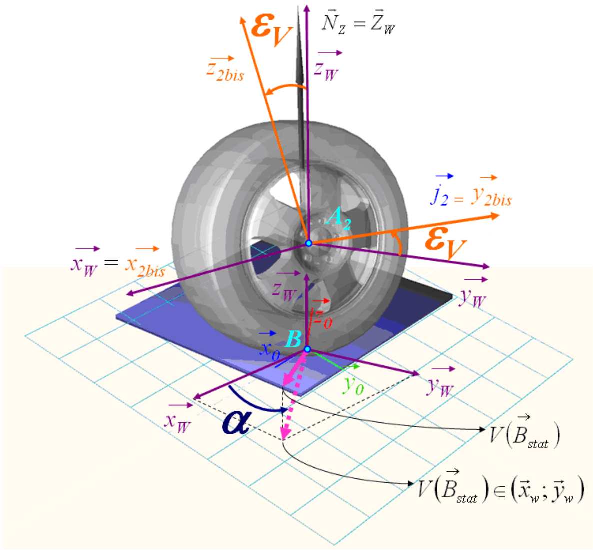

Figure 1.44: Wheel characteristic angles [31]

The *Tire Model* and *Tire Belt Model* elements require the input of several characteristic tire parameters necessary for the selected Pacejka formulation. All these parameters are usually collected in a single **.tir* file that characterize the tire itself. It is thus possible to enter all required parameters manually or use an internal tool within the software to import these parameters directly from the **.tir* file.

The following element in **Figure 1.43** is the **Tire Kinematic Model**, whose function is the calculation of the kinematic quantities regarding the contact point between the tire and the ground (identified by the letter B) exploiting the wheel centre (A_2) kinematics calculated above. Another important function is the passage of the contact forces from B to A_2.

This element is also connected to a spring-damper system used to define the tire vertical stiffness and damping coefficients, also shown in **Figure 1.45**. These parameters allow the *Tire Kinematic Model* to calculate the deformation and deformation rate of the tire along the z_{2bis} axis, i.e. the vertical axis of a reference frame connected to the wheel which takes into account the camber and steering angles.

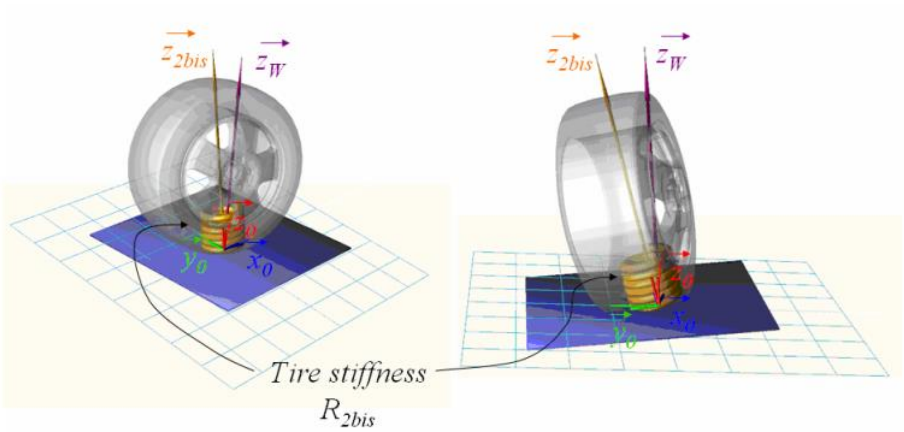

Figure 1.45: Vertical stiffness and damping characteristics of the tire

The different submodels allow the user to select between modelling with a constant effective rolling radius (or dynamic rolling radius [33]) or modelling with a variable rolling radius as the simulation progresses. The latter, of course, requires longer computation times. The effective rolling radius is then used by the element to calculate the speed of contact point B during longitudinal wheel slip.

Finally, the last element is the so-called *Rotary Inertia*, in which information regarding the moments of inertia of the wheel assembly is entered.

It is possible to connect drive and resistance torque signals directly to this element, either from other subsystems (such as transmission or braking system) or using signal inputs. The combination between these torques and the tire-soil interface reactions determine the acceleration and angular velocity of the wheel, and thus the kinematics of wheel centre A_2.

The whole assembly shown in **Figure 1.43** can be connected to the wheel upright element.

Mechanical modelling

As anticipated, each of the four sets of elements for modelling the tire-soil contact must be connected to the so-called wheel upright assembly elements. These elements and all the other mechanical components of the vehicle (in particular the suspended axle) were modelled using the *3D Mechanical* library. This library, in fact, allows the multibody modelling of rigid bodies and interconnecting joints between them in the 3D space.

We then proceeded to develop component by component the suspended axle first and then the rest of the vehicle. Like any other modelling in Simcenter Amesim®, the steps to follow are always the creation of the sketch, the submodels selection, and parameterization.

The sketch realization started with the introduction of the rigid body representing the vehicle's sprung mass and with four additional rigid bodies representing the front and rear wheel upright assemblies. Since the rear wheel assemblies are directly connected to the vehicle drive train, we used four fixed joints to connect these elements. On the other hand, the front wheel units are connected to the sprung mass through the various suspension components, which must therefore be modelled using rigid bodies and joints in order to replicate the suspension architecture.

Figure 1.46 shows the suspension architecture with the components to be modelled and connected.

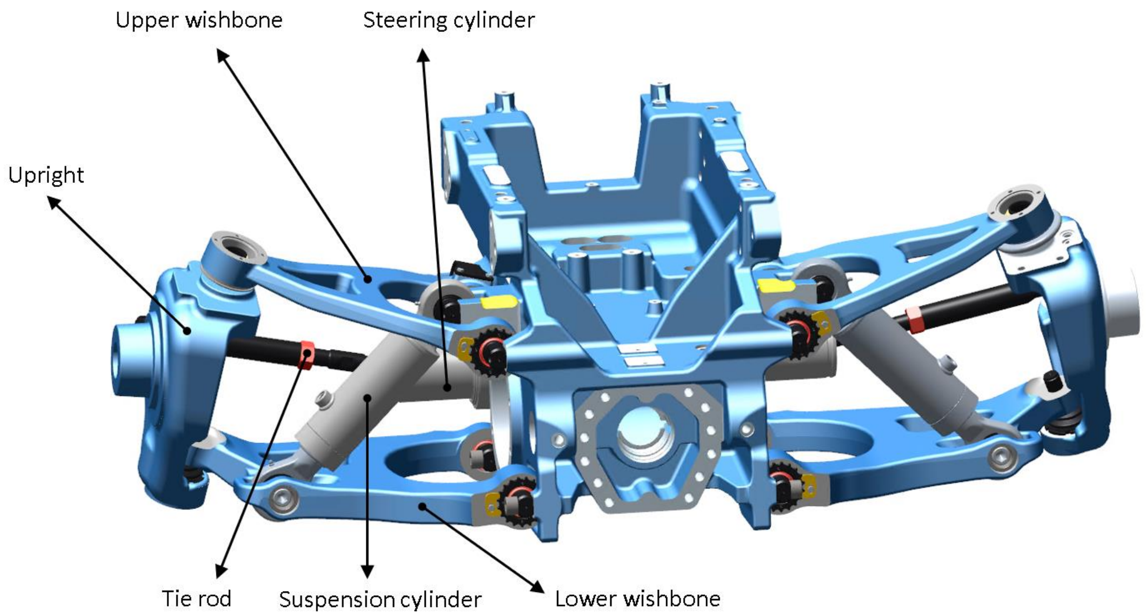

Figure 1.46: Double wishbone suspension architecture and its main components

Other rigid bodies representing the lower and upper suspension wishbones and the steering links were then introduced and connected to the wheel upright assembly through the appropriate joints. The lower and upper wishbone have been also connected to the suspension mass with two further ball joints. The steering links must be connected via two universal joints to the rod of the double-acting steering cylinder, which is modelled using another rigid body connected to the suspended mass via a prismatic joint. Finally, the suspension hydraulic cylinders have been added using two *M6DOFJACK00* elements from the *3D Mechanical* library, which can model jacks or linear actuators.

In addition to these, a further rigid body was introduced and attached to the suspended mass to model the mass of the axle and the hydraulic blocks.

An example of the followed approach is shown for the lower left suspension wishbone. **Figure 1.47** shows this component and the various ball joints connecting it to the rest of the suspension architecture.

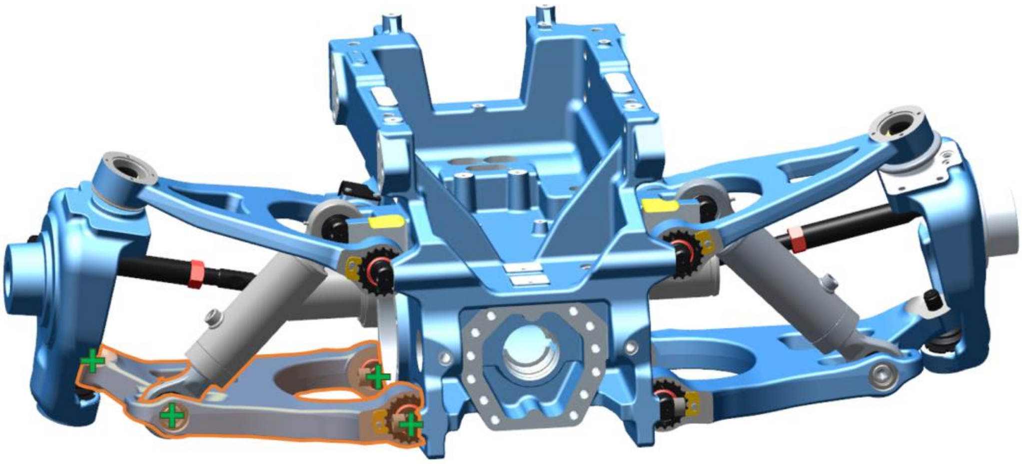

Figure 1.47: Lower left wishbone and its connections with the suspension architecture

It is necessary to consider a connection port for each joint of the considered rigid body. In this case there are four connection ports: one port for the joint with the wheel assembly, one for the joint with the suspension cylinder rod, and two for the joints with the suspended axle body. A rigid body with a total of four ports was then introduced into the sketch. The process is repeated for each suspension component. After that, it was possible to introduce the correct joints to connect the various ports together.

Figure 1.48 shows the model sketch of the mechanical part just described.

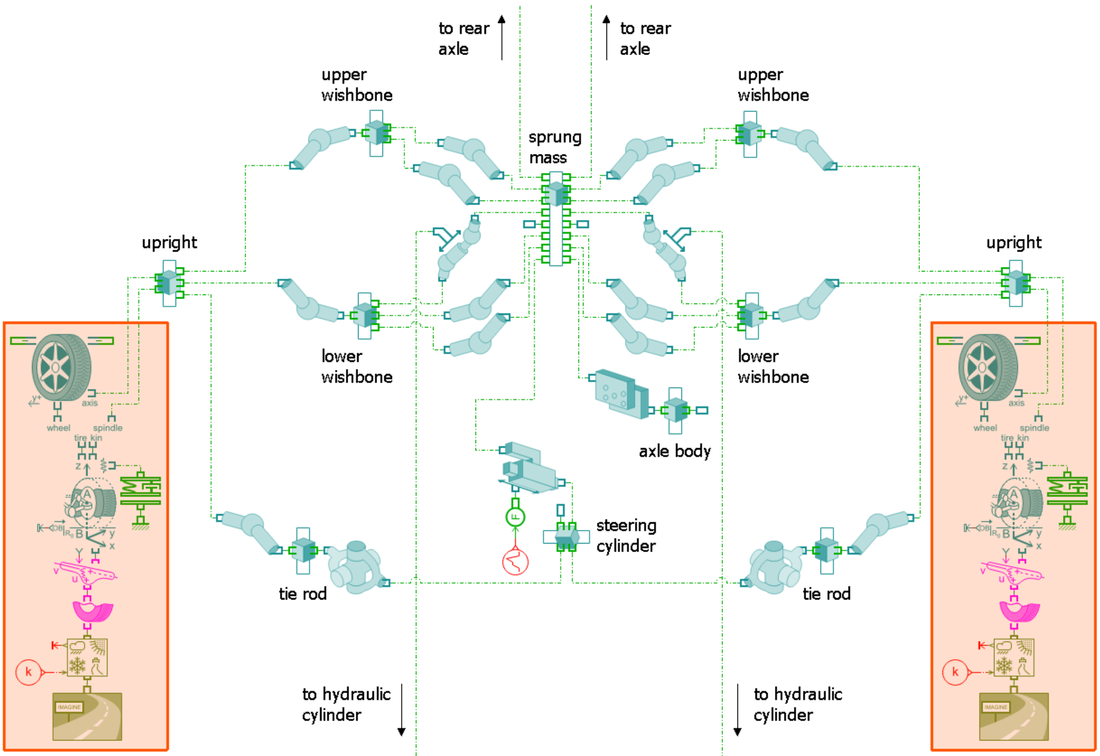

Figure 1.48: Simcenter Amesim® model sketch for the vehicle mechanical part

Once the sketch had been completed and the submodels for rigid bodies and joints had been selected, each element was then parameterised. Joint elements require the introduction of the stiffness and damping characteristics of the joint itself, which are usually left at their default values. On the other hand, rigid bodies require the introduction of all information regarding mass and inertia, the position of the centre of gravity, but also the position of all the varios ports used for connection with other rigid bodies. These positions can be expressed with respect to an absolute or relative reference frame. In order to connect two ports of different bodies through a generic joint, it is necessary to parameterize these ports so that they are located in the same point in the 3D space.

In the *3D Mechanical* library of Simcenter Amesim® there is also a tool that allows a 3D view of the system. This tool is very useful both when constructing the model and when analysing the simulation results. It is in fact possible to watch directly how the system behaves by means of an animation.

Figure 1.49 shows the 3D model of the vehicle with the detailed suspended axle.

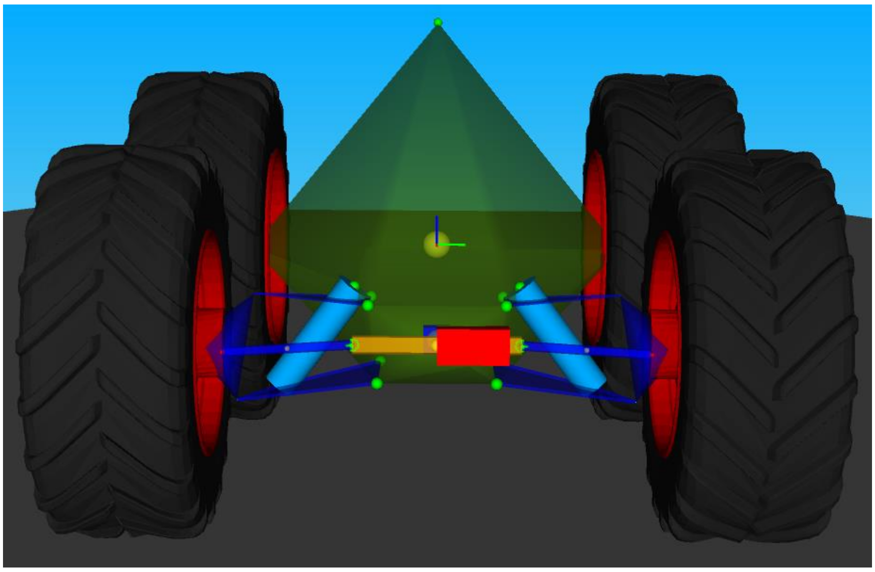

Figure 1.49: Simcenter Amesim® 3D model of the vehicle with the detailed suspended axle

The apex of the sprung mass in **Figure 1.49** represents the point under the driver seat, whose accelerations are of particular interest. It is indeed possible to parameterize one of the unused ports to locate a point of interest (if it is not a connection one). When analysing the results, in fact, it is possible to access all the variables concerning the parameterized points.

It is also possible to introduce **.stl* files into the graphic visualization tool in order to make the aesthetics of the model more realistic. The **Figure 1.50** shows the 3D visualization of the vehicle once these files have been introduced.

Figure 1.50: Simcenter Amesim® 3D model of the vehicle **.stl* files

The fundamental equations underlying the modelling of the mechanical part of the vehicle can be traced back to the Newton's second law of motion. The linear and angular positions, velocities and accelerations of rigid bodies can be found basing on the forces and torques applied to them, as reported in **Eq. (1.53)-(1.54)**.

$$\sum_{i=0}^{n} \vec{F_i} = m\vec{a} \tag{1.53}$$

$$\sum_{i=0}^{n} \overrightarrow{M(G)_i} = J\vec{\alpha} \tag{1.54}$$

After completing the modelling of the mechanical part of the vehicle, several virtual position, velocity and acceleration sensors (both linear and angular) were added. These elements can be used to have the results of interest readily available, without having to search through long lists of rigid body results. In addition to these sensors, some external signals relating to the drive and braking torque and the steering signal (and their own PID controllers) have been added to simulate the operator action. Obviously, these signals must vary as the considered manoeuvre varies.

Before proceeding to use the Simcenter Amesim® vehicle model just created, it is necessary to validate the model itself. The multibody model of the tractor developed in MSC Adams® was therefore taken as a reference, as it had been previously had validated with experimental test.

Benchmark with MSC Adams®

This section shows a virtual comparison between the vehicle multibody models realised in MSC Adams® and Simcenter Amesim® to validate the latter.

This benchmark is carried out, firstly, by exploiting the test described in the ISO 5008 standard with the 100 meters track. According to this standard already described in the introduction section, the vehicle must travel along the two straight tracks at constant speed.

Both simulations (in Adams® and Amesim®) were set up so that the vehicle starts from a standstill to stabilize the model. Then the vehicle can start the acceleration phase until it reaches the desired speed and thus it drives up the track maintaining this constant speed.

It is the operator who has to adjust the pedals and steering wheel to maintain a straight line at a constant speed in the real test. On the other hand, in the models, these aspects must be handled by two controllers, in which the difference between the reference signal (speed and yaw angle of the vehicle) and the actual simulated variable is the input to a

PID controller, which provides the appropriate output (drive torque and steering cylinder position) to cancel out the error. The calibration of the coefficients of these PID controllers was carried out, under the advice of the Siemens developers of the Simcenter Amesim® *Vehicle Dynamics* library, to come as close as possible to the Adams® simulations. Since the element modelling the steering cylinder requires a force as input and not a position, it was then necessary to add a spring-damper element from the *1D Mechanical* library between the output of the PID and the steering cylinder itself. This element was calibrated with a very high stiffness so that the output signal from the controller and the input signal to the steering cylinder is practically identical. This detail is also shown **in Figure 1.51**.

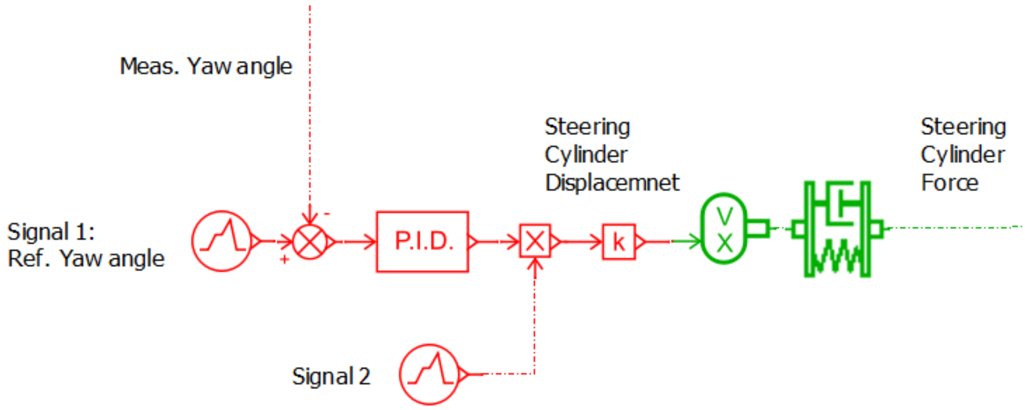

Figure 1.51: Detail of the PID controller for the steering cylinder position

A third signal called Signal 2 in addition to the yaw angle reference signal and the measurement of the vehicle's actual yaw is highlighted in **Figure 1.51**. This is a dimensionless and normalised signal with the purpose of cancelling the force at the steering cylinder when the reference yaw is zero. In fact, in the first seconds of simulation, when the vehicle has to settle and find its equilibrium condition, small variations in yaw or speed are possible. It is therefore important to introduce these signals so that the PID controllers do not intervene before the vehicle has settled. A similar signal was therefore also introduced in the vehicle speed controller.

Unlike the Adams® model in which equivalent springs and dampers were used to model the suspension behaviour, in Simcenter Amesim® it was possible to connect the jack elements directly with the hydro-pneumatic circuit model. In this comparison, the four-accumulator system was used. This solution was preloaded to obtain the optimum stiffness derived from the vehicle modal analysis for the considered configuration. However, note that this dimensioning of the hydro-pneumatic system was carried out manually using an iterative method starting from certain first attempt parameters found in the literature (such as suspension cylinder dimensions, accumulator volumes, etc.). Obviously, the Adams® model was parameterised with the respective equivalent stiffness and damping coefficients.

Below the comparison of the results obtained by the two models for the ISO 5008 test conducted at 10 km/h is reported. The same magnitude of interest assessed in the two different software are compared in the same graph.

Figure 1.52 depicts the comparison between the displacements of the wheel centres, where only the data for the front and rear left wheels are shown. The results for the right wheels are, in fact, entirely similar. It is easy to see that these results are well aligned.

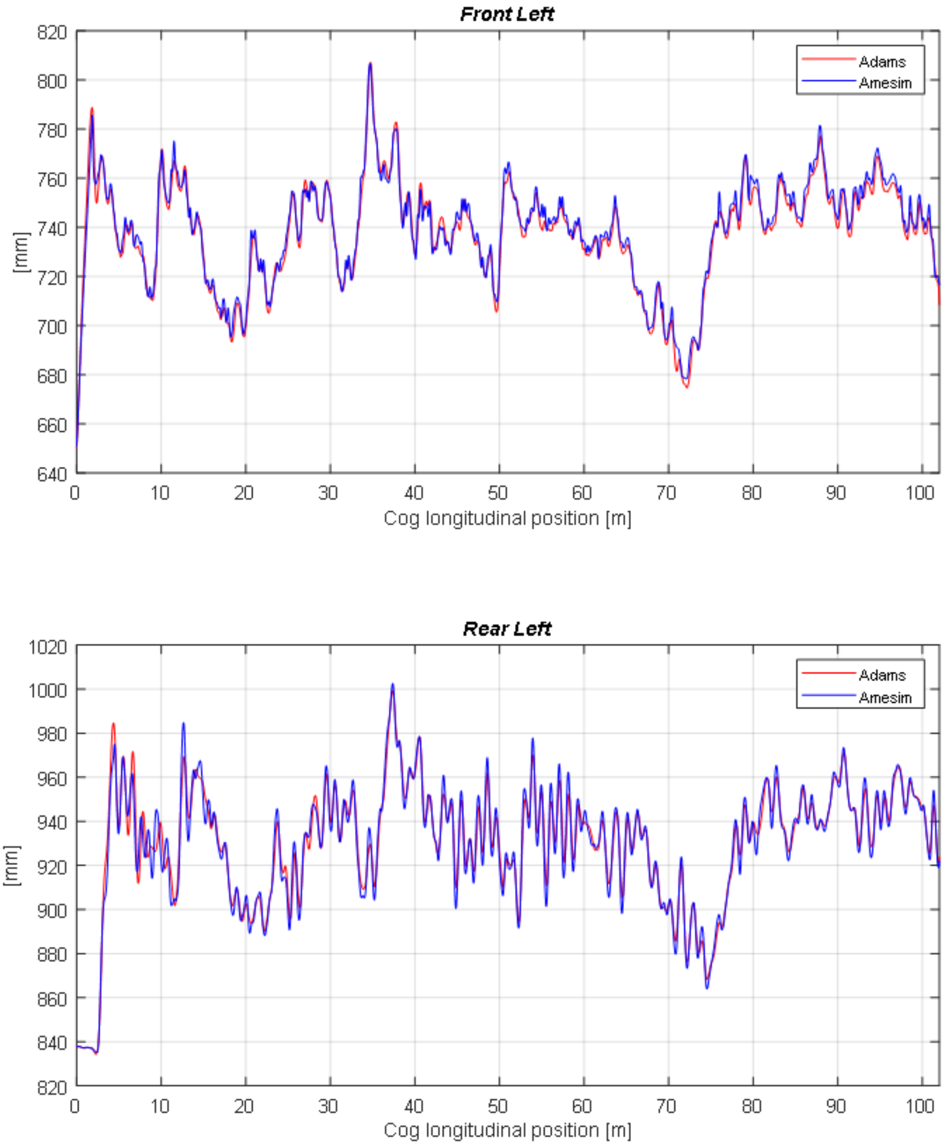

Figure 1.52: Front left and rear left wheel centre comparison with the ISO 5008 test: Adams® (in red) vs Amesim® (in blue)

Figure 1.53 shows the displacements of the pistons in the suspension cylinders evaluated in Amesim® and Adams® as a function of the longitudinal position of the vehicle's centre of gravity. The total cylinder stroke was used to make the graph dimensionless. The same figure also shows the profiles of the two tracks (right and left), which are obviously the same in the two models.

Again, the suspension deformation is very similar in the two models.

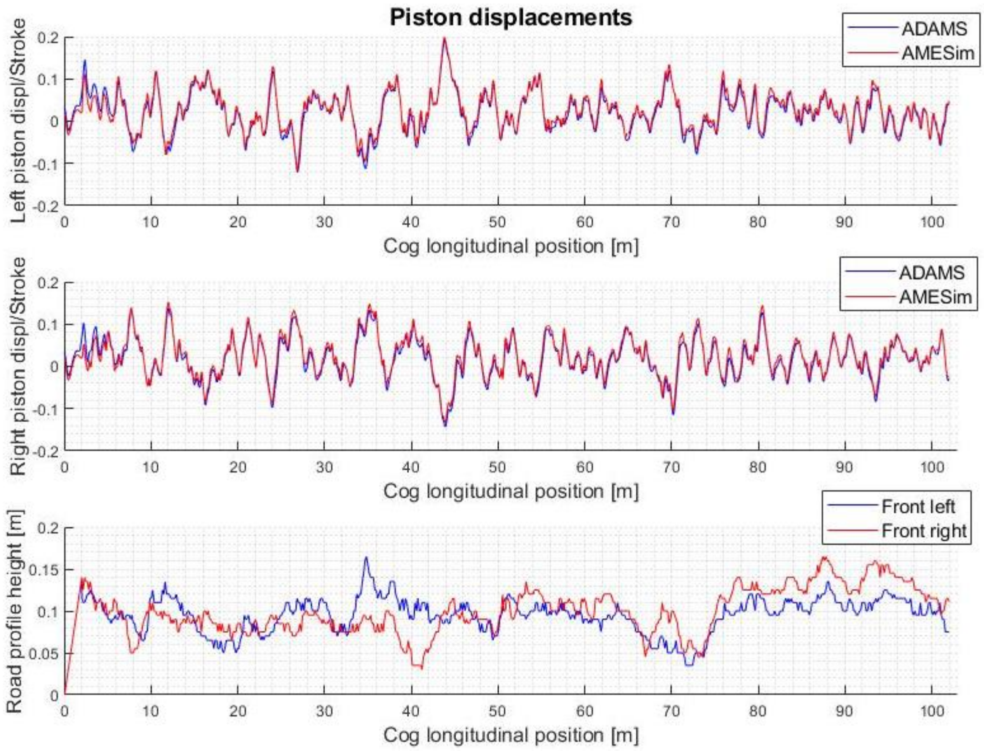

Figure 1.53: Adams® (in blue) vs Amesim® (in red) regarding the dimensionless displacement of the left and right suspension pistons and ISO 5008 track profiles

Figure 1.54 depicts the corresponding forces acting on the suspension piston rod as a function of the position of the vehicle's centre of gravity. We used the suspension static load to make the graph dimensionless. Note that only the initial part of the track is shown to make the results more readable.

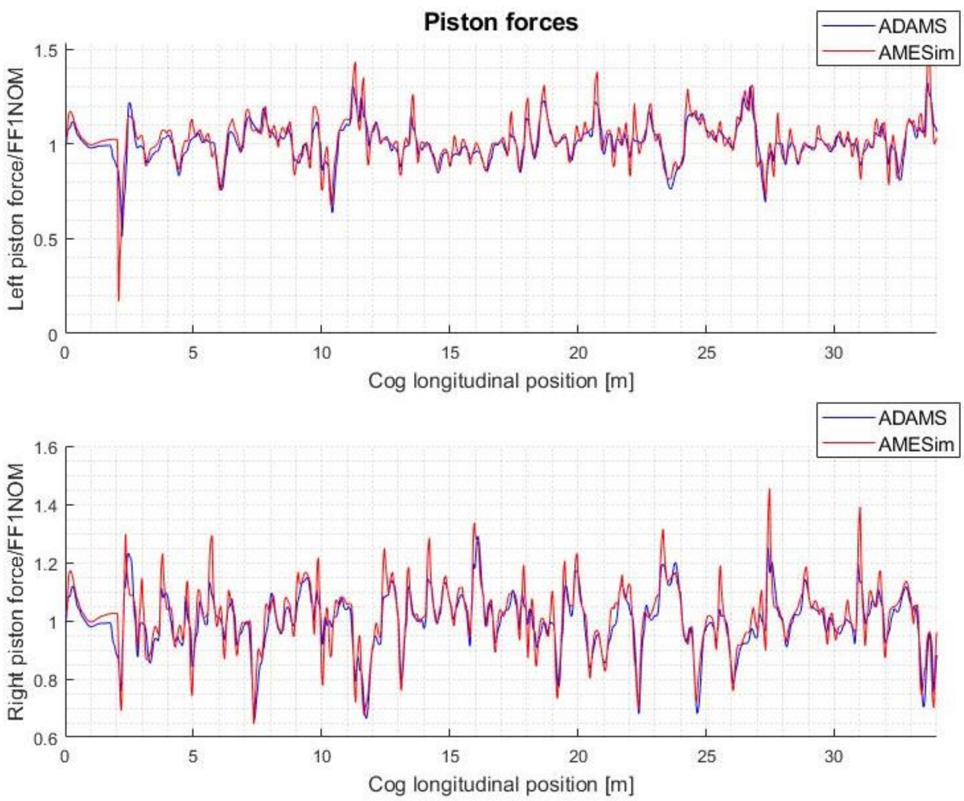

Figure 1.54: Dimensionless forces on suspension cylinders with the ISO 5008 test: Adams® (in blue) vs Amesim® (in red)

The trend is generally aligned between the two models. However, the forces evaluated using the Amesim® model show greater peaks than the Adams® counterpart.

After performing a sensitivity analysis and consulting with the Siemens developers of the Simcenter Amesim® *Vehicle Dynamics* library, we have concluded that this difference can be explained by the different modelling of the tire-soil contact. In fact, while MSC Adams® models this using a contact surface, Amesim® limits the modelling choice between a single contact point and two contact points (using a model called *tandem-egg* [31]).

This difference leads to different ground contact forces, which are smoother and with smaller peaks in Adams® and more abrupt in Amesim®. These contact forces are then transmitted to the wheel centre and then to the pistons of the suspension cylinders, as can be seen in the graph in **Figure 1.54**.

This aspect also gives rise to some differences in the vehicle accelerations, for example in those measured at the operator seat, which are shown in **Figures 1.55-1.56-1.57**. Again, the results of the Amesim® model are less damped and with more pronounced peaks and valleys. These accelerations measured at the seat seem to be more affected by the difference in the modelling of tire-soil contact. This is because the operator seat is positioned very close to the rear axle, which, as mentioned, is not suspended. The road force input is only filtered by the tyres and therefore has a high impact on these vibrations.

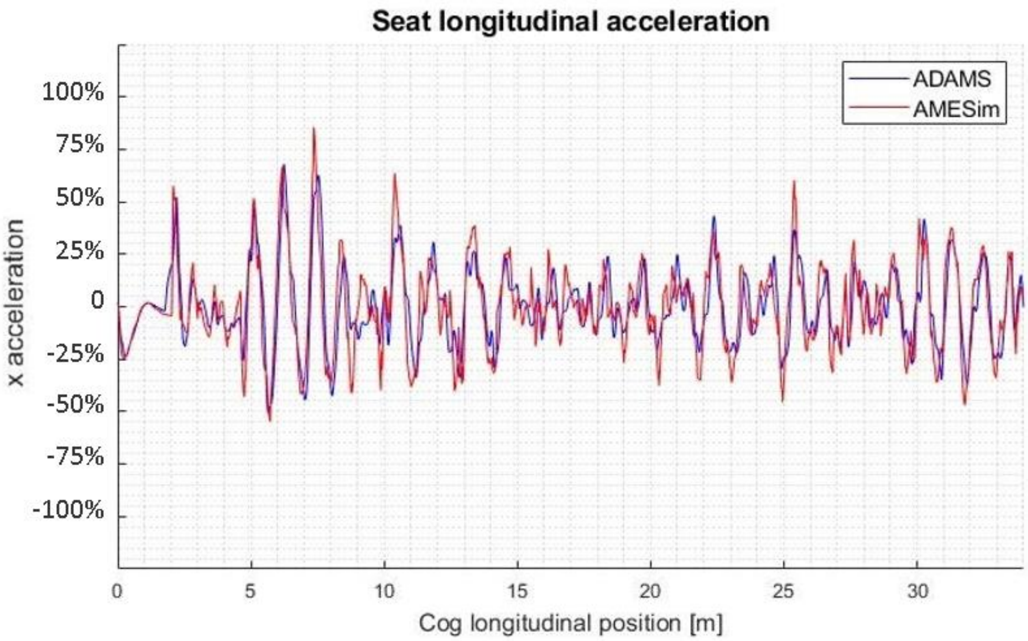

Figure 1.55: x-axis acceleration under the operator seat with the ISO 5008 test: Adams® (in blue) vs Amesim® (in red)

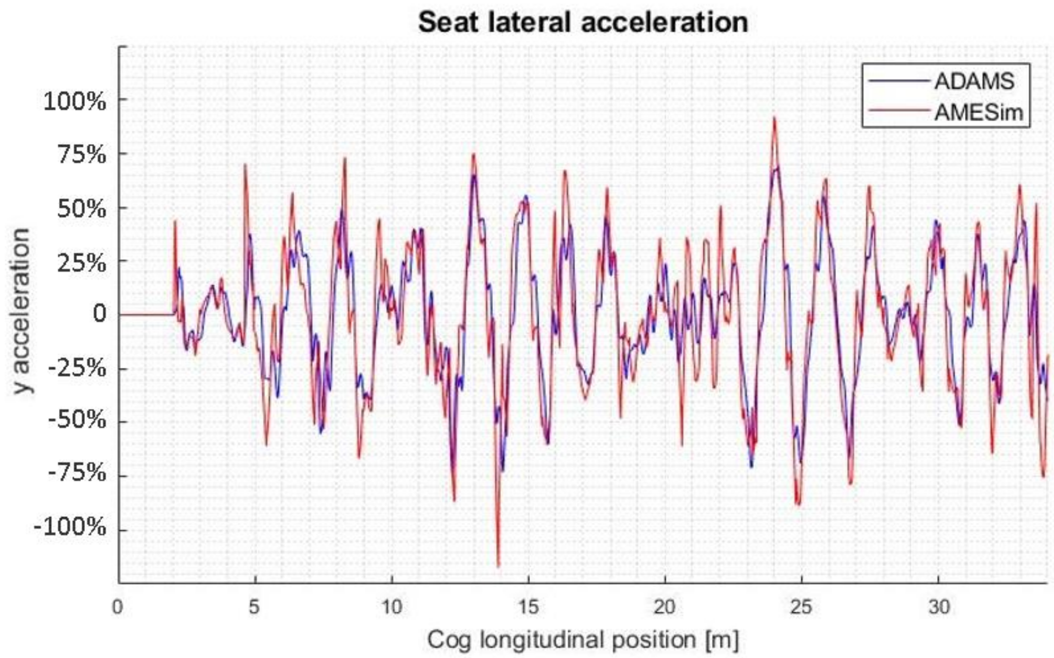

Figure 1.56: y-axis acceleration under the operator seat with the ISO 5008 test: Adams® (in blue) vs Amesim® (in red)

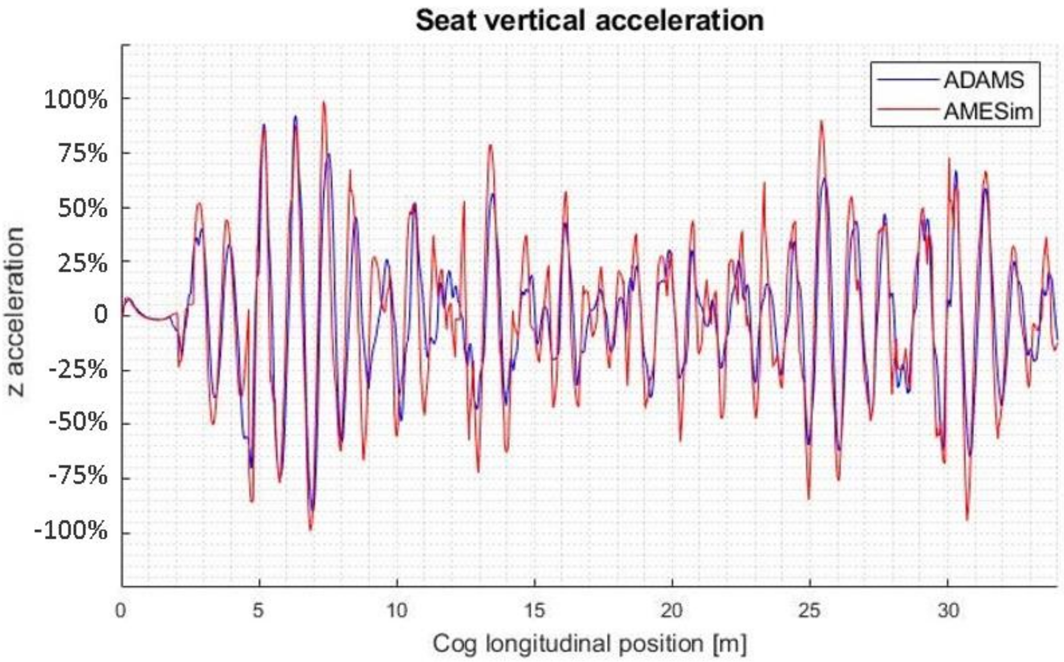

Figure 1.57: z-axis acceleration under the operator seat with the ISO 5008 test: Adams® (in blue) vs Amesim® (in red)

Finally, **Figure 1.58-1.59** show the comparison between the trends of the steering cylinder deformation and the vehicle speed, which are the quantities controlled via the PID introduced.

The calibration of the PID controllers was also carried out to minimize the differences between these results. Indeed, they turned out to be well aligned, although not perfectly. The two models thus have some slightly different inputs regarding the vehicle steering and its forward speed. This turns out to be a further difference between the two models in addition to the different modelling of the tire-soil contact: these two aspects, obviously, do not allow for a better alignment of the results, which is still good.

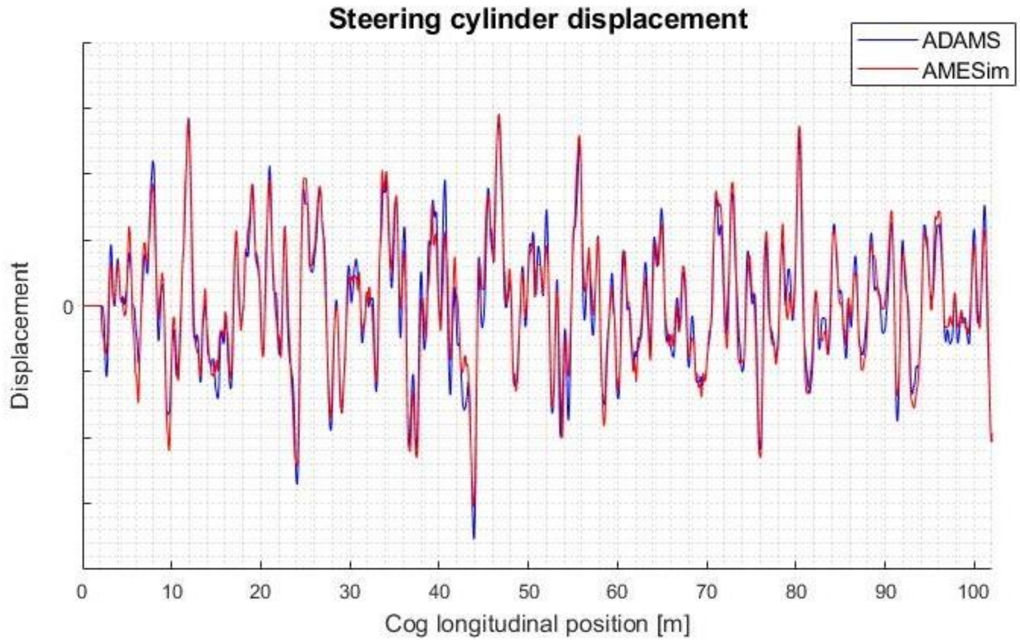

Figure 1.58: Steering cylinder deformation with the ISO 5008 test: Adams® (in blue) vs Amesim® (in red)

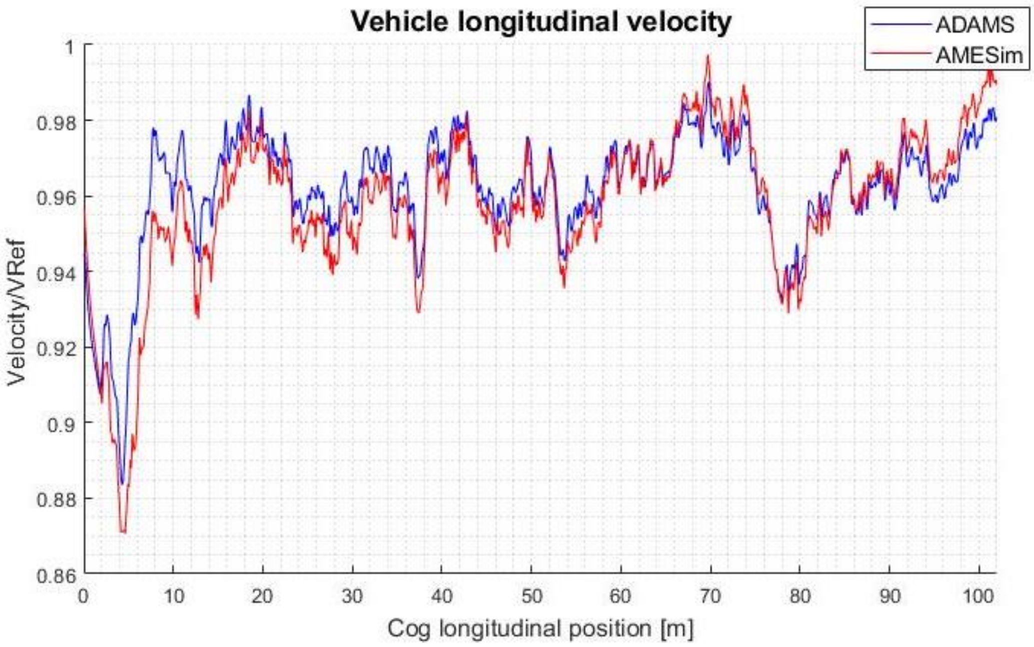

Figure 1.58: Vehicle longitudinal speed with the ISO 5008 test: Adams® (in blue) vs Amesim® (in red)

We decided to consider a further simulation test to obtain a complete picture regarding the benchmark between the two software. Such a comparison could be useful to confirm the impact of the main difference between the models, i.e. the modelling of the tire-soil contact. The considered test was the asymmetric bump test.

In this particular test, the tractor is driven by the operator over four bumps, with fixed geometry, positioned two for the right and two for the left wheels. These bumps are not aligned with each other, in order to stimulate the tractor's free roll response once the last two bumps have been overcome. This test was also recommended by the specialised research centre CREA.

Figure 1.60 illustrates a schematic representation of this test, where the side and top views of the tractor are shown and the bumps for the right wheels are highlighted in blue and those for the left wheels in green.

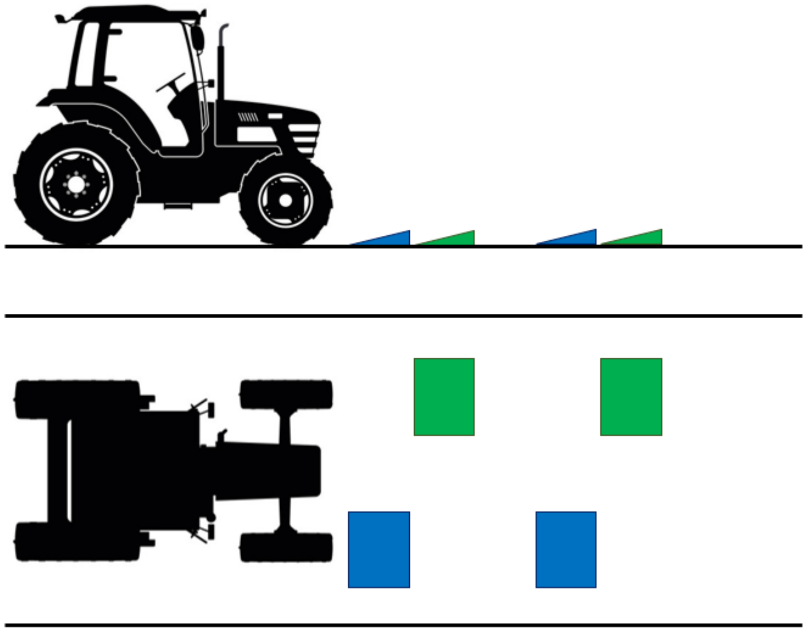

Figure 1.60: Schematic representation of the asymmetric bump test

The comparison of the numerical results obtained in Adams® and Amesim® for this test underlined how much the difference in tire-soil modelling impacts on the vehicle behaviour. While in the ISO 5008 test the differences were "limited" to an effect on the forces course (at the wheels and then consequently at the suspension cylinders), in this test macroscopic differences can also be seen in the displacements of the wheel centres themselves. This can be explained by the fact that the ISO 5008 test subjects the system to a high frequency forcing road input due to the geometry of the track. On the other hand, the asymmetric bump test stimulates the system free response in roll, without other road inputs.

Figure 1.61 shows the comparison of the wheel centre positions for the left front and rear. This comparison already shows a decidedly different behaviour of the tractor in the two models for these variables, which can be attributed practically completely to the use of a different tire-soil contact model (because it is the only element present between the ground input and the wheels).

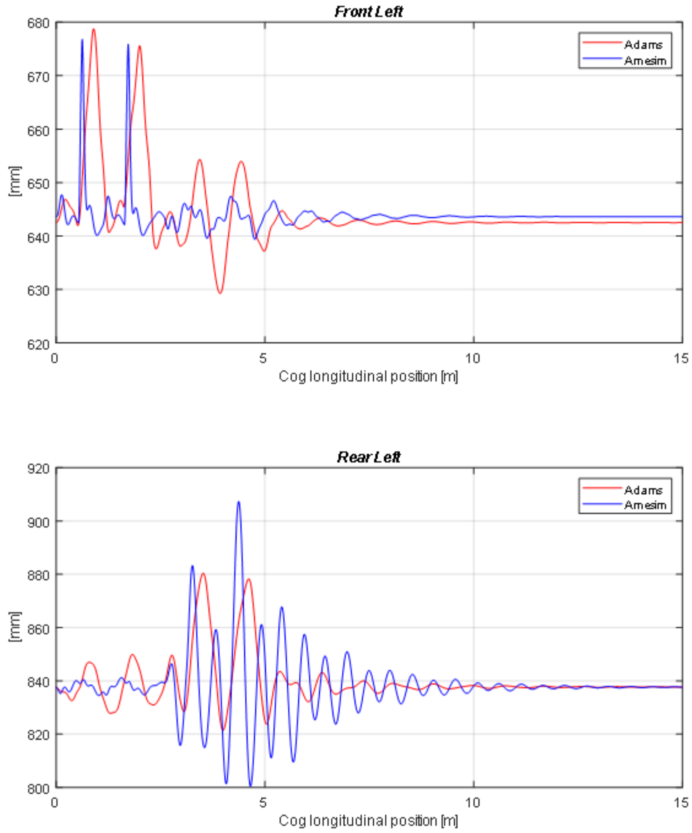

Figure 1.61: Front left and rear left wheel centre comparison with the asymmetric bump test: Adams® (in red) vs Amesim® (in blue)

As usual, **Figure 1.61** reports only the data for the left front and rear wheels, as those for the right wheels are quite similar. As anticipated, it is easy to see how the wheel behaviour is substantially different, both in the displacement peaks when the vehicle hits the bumps and during the vehicle free response.

This macroscopic difference makes the complete validation of the Simcenter Amesim® model complex.

Having pointed out this difference in behaviour and having also reported it to the developers of the Simcenter Amesim® software, we started an investigation into the implementation of the *tandem-egg* model (two contact point) as a replacement for the single contact point model, trying to make the numerical results closer to the Adams® ones. Unfortunately, we found some bugs within the code of this *tandem-egg* model in the software version used (which was also the most recent at the time of this activity, i.e. v2020.2). A direct intervention by the Siemens developers was therefore necessary, who used the data we provided to modify certain equations and calibrate various parameters of the new model version precisely to minimize the differences with the reference results.

This analysis will lead to an effective modification of the software code in the new versions of Simcenter Amesim® to allow the user to use this two-contact point model. This latter is obviously not yet exactly analogous to the Adams® contact surface, but it is decidedly closer in behaviour than a single contact point.

In conclusion, the Simcenter Amesim® model of the complete vehicle with a suspended axle is not perfectly correlated with its counterpart realised in MSC Adams®. In particular, non-negligible differences have been observed for the asymmetric bump test, where the free response of the system to a 'low frequency' input was analysed. These differences, as mentioned, can be attributed to the use of a different tire-soil contact model, which leads to a different vehicle behaviour. On the contrary, vehicle behaviour is very similar in simulations where the road inputs are at a fairly high frequency, as observed for the standard ISO 5008 test. In that test, there are indeed some differences in the analysed variables, but the general behaviour of the vehicle is much more aligned to the reference one.

For this reason, it was accepted to use the Simcenter Amesim® model with the standard ISO 5008 manoeuvre to compare the qualitative performance in terms of comfort of the two hydro-pneumatic solutions considered, i.e. with three or four accumulators. In fact, although this model is not perfectly aligned with the Adams® model, it can still give an indication of which solution is better for vehicle comfort, and indicatively by how much. In fact, although it is not possible to take values in absolute terms, it is still possible to consider the relative difference between the comfort levels obtained for the two considered solutions.

Having the possibility of using this model in the Amesim® environment is certainly a great advantage because, as seen, it allows the mechanical part to be directly interfaced with the hydro-pneumatic system. It is therefore very easy to switch from the solution with four accumulators to the three accumulator one. If we could not do so, the equivalent stiffness and damping would have had to be derived for both solutions and implement them in Adams®. Any changes, whether in levelling pressure or supply current to the damping valves, would have meant re-evaluating these equivalent values. It would therefore certainly have been a less immediate and less efficient process.

1.3.4 ISO 5008 comparison: 3-accumulators vs 4-accumulators

The model of the complete vehicle with suspended axle realised in Simcenter Amesim® was then used to evaluate the comfort performances of the hydro-pneumatic systems with three or four accumulators. In addition to the differences highlighted when the two solutions were presented, in fact, decided to consider the dynamics of the entire vehicle to have a complete picture and to be able to choose which solution was more suitable for the prototype.

Obviously, the more complex four-accumulator solution is also expected to be the better one in terms of vehicle comfort, but we wanted to assess by how much. Only substantially better performance, in fact, can justify the selection of this solutions and thus a higher total cost.

Two simulations of the standard ISO 5008 test on the 100 meters track have been carried out to compare the results obtained considering the use of three or four gas accumulators. In these simulations, the proportional valves of the damping blocks have been supplied by the same constant current (not optimized for either solution) in order to maintain the same opening and thus the same damping characteristic. The PID controllers were also kept identical in the two simulations.

Some graphs show below the comparison of some variables of interest relating to the vehicle comfort performance for a limited section of the manoeuvre. In particular, **Figure 1.62** depicts the trend of the deformations of the right and left suspension cylinders, **Figure 1.63** the trend of the vehicle Euler angles and **Figure 1.64** the deformation of the steering cylinder.

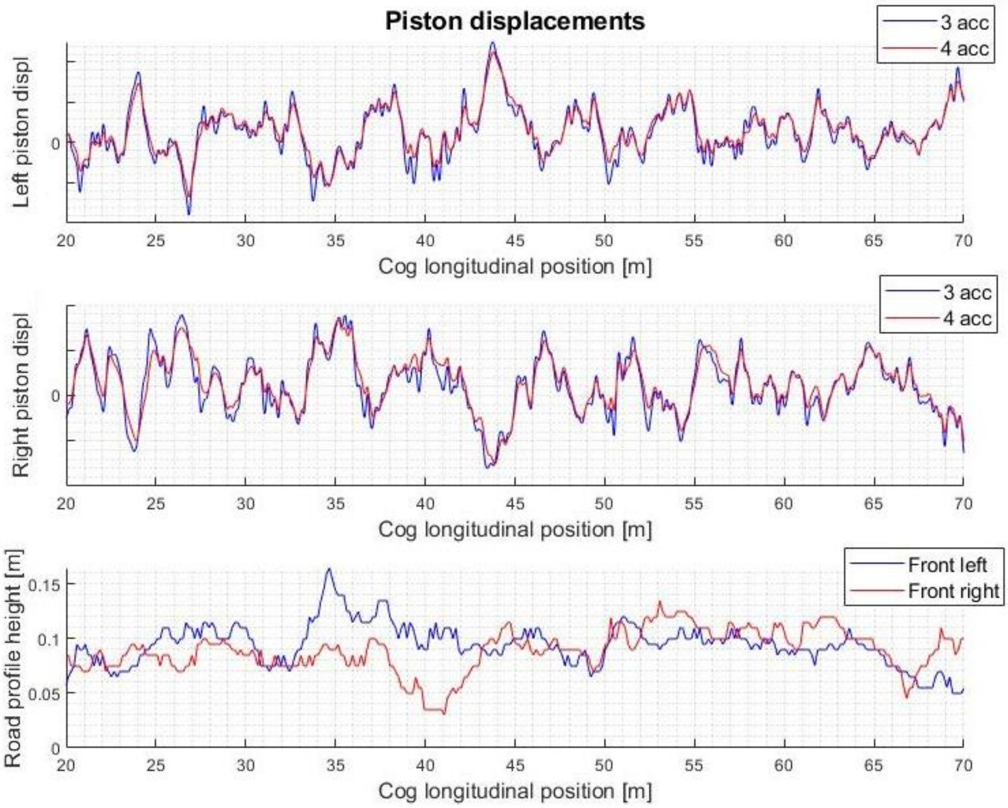

Figure 1.62: Suspension piston displacements with the ISO 5008 test: 3-accumulators (in blue) vs 4-accumulators (in red)

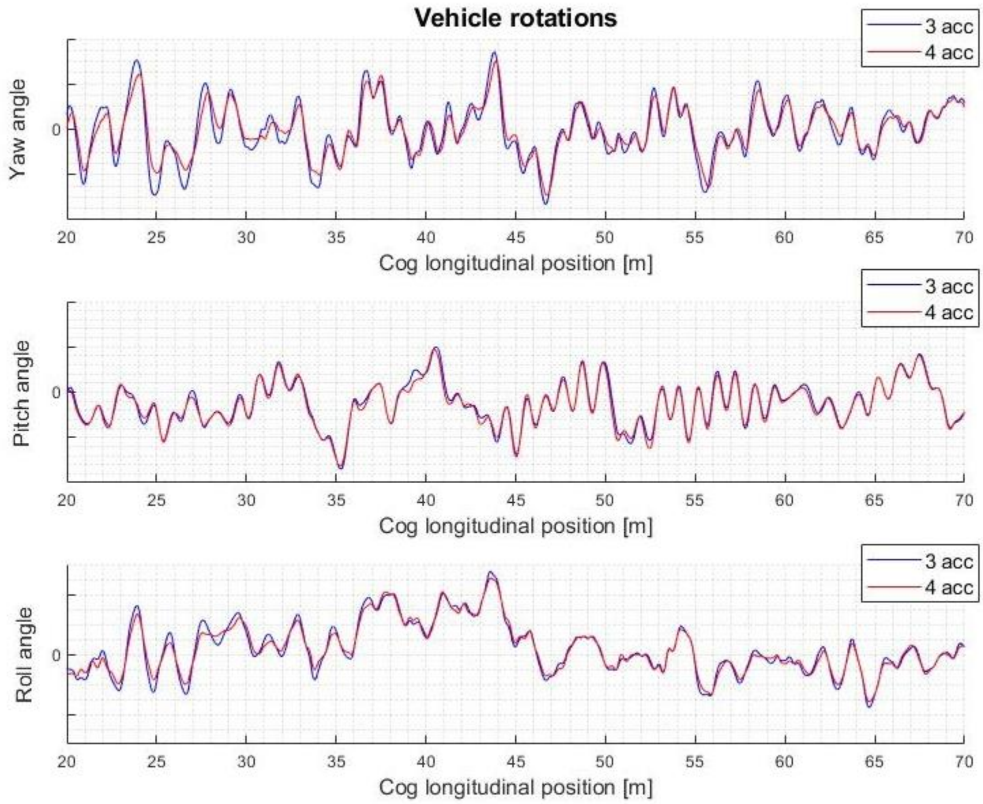

Figure 1.63: Euler angles with the ISO 5008 test: 3-accumulators (in blue) vs 4-accumulators (in red)

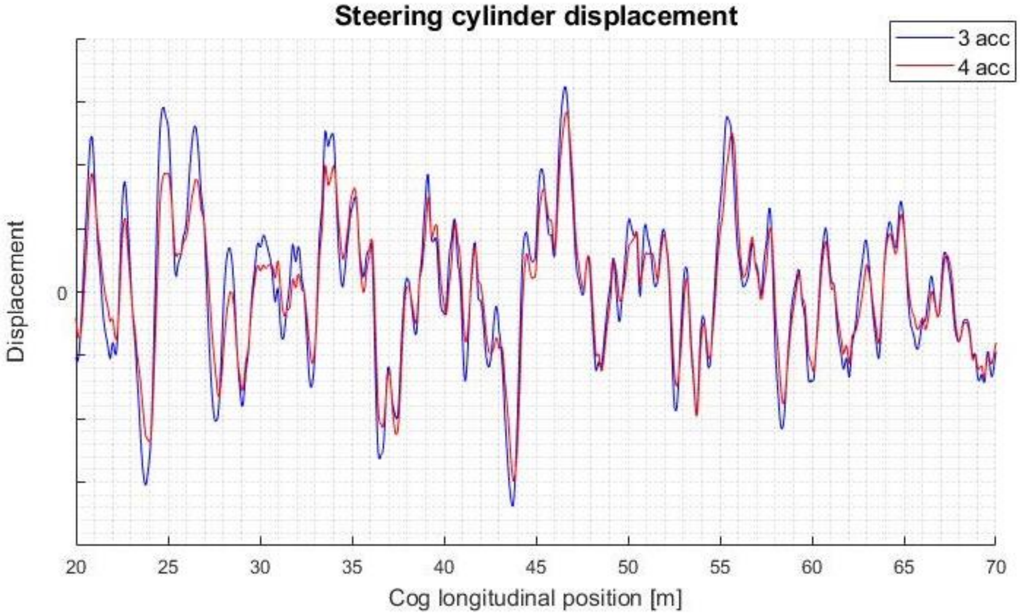

Figura 1.64: Steering cylinder displacement with the ISO 5008 test: 3-accumulators (in blue) vs 4-accumulators (in red)

Note that the behaviour of the four-accumulator solution is everywhere better than the three-accumulator solution. In fact, the deformation of the suspension cylinders is less with the same road input, meaning better stiffness and damping characteristics. Variations in Euler angles are also smaller, especially roll and yaw. The vehicle is therefore less affected by the roughness of the terrain. Lastly, it is interesting to note that the steering cylinder also deforms less with the four-accumulator solution. Since the steering PID controller is the same for the two simulations, this can be translated as greater simplicity for the operator in maintaining a straight trajectory using the four-accumulator solution.

Figures 1.65-1.66-1.67 then show the accelerations along the three axes of the vehicle's centre of gravity (longitudinal x, lateral y and vertical z). In addition, the comparison of the *FFT* (Fast Fourier Transform [34]) is also shown, i.e. the result of an optimized algorithm to obtain the discrete Fourier transform, which allows a spectral analysis of these accelerations.

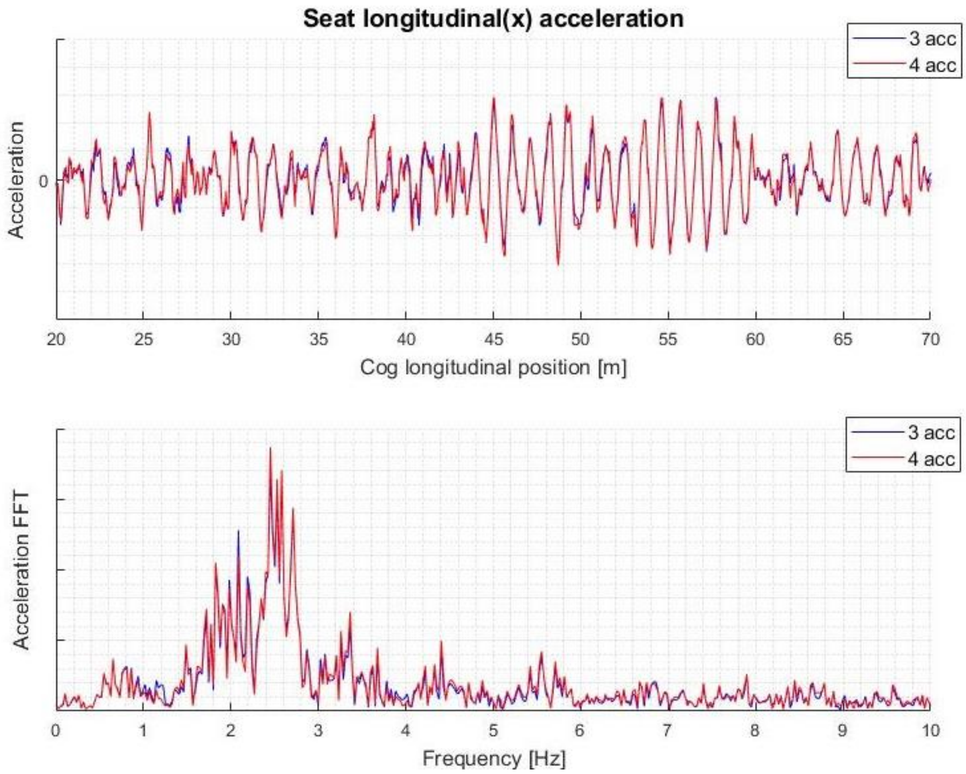

Figure 1.65: Comparison of the x-axis acceleration of the vehicle's CoG with the ISO 5008 test and *FFT*

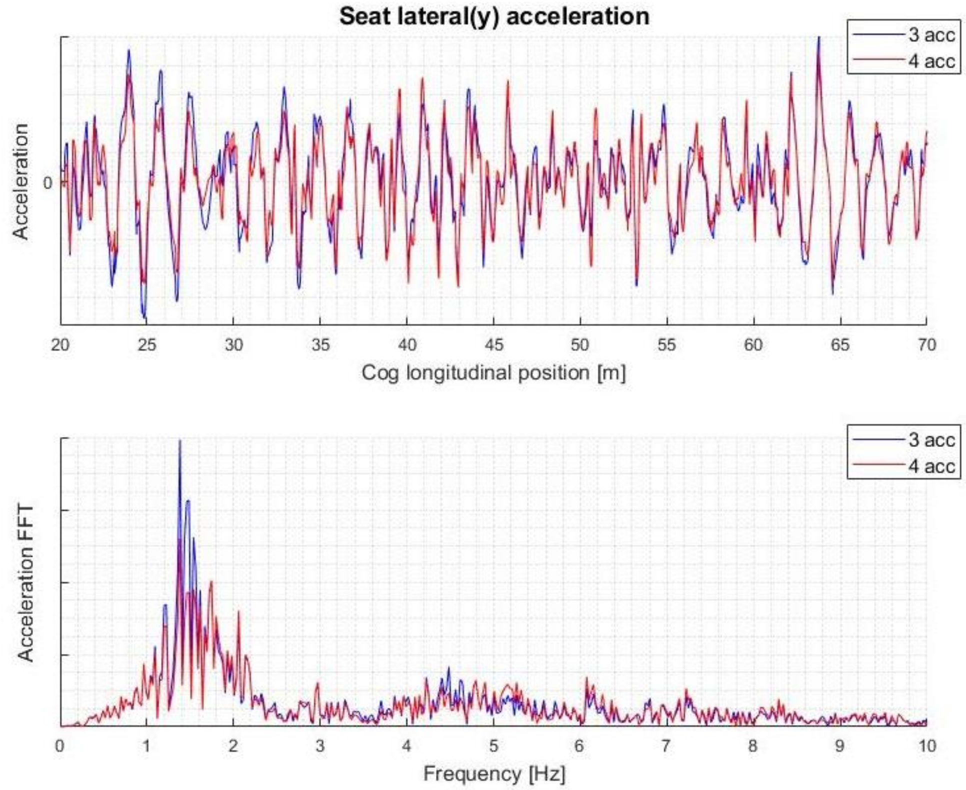

Figure 1.66: Comparison of the y-axis acceleration of the vehicle's CoG with the ISO 5008 test and *FFT*

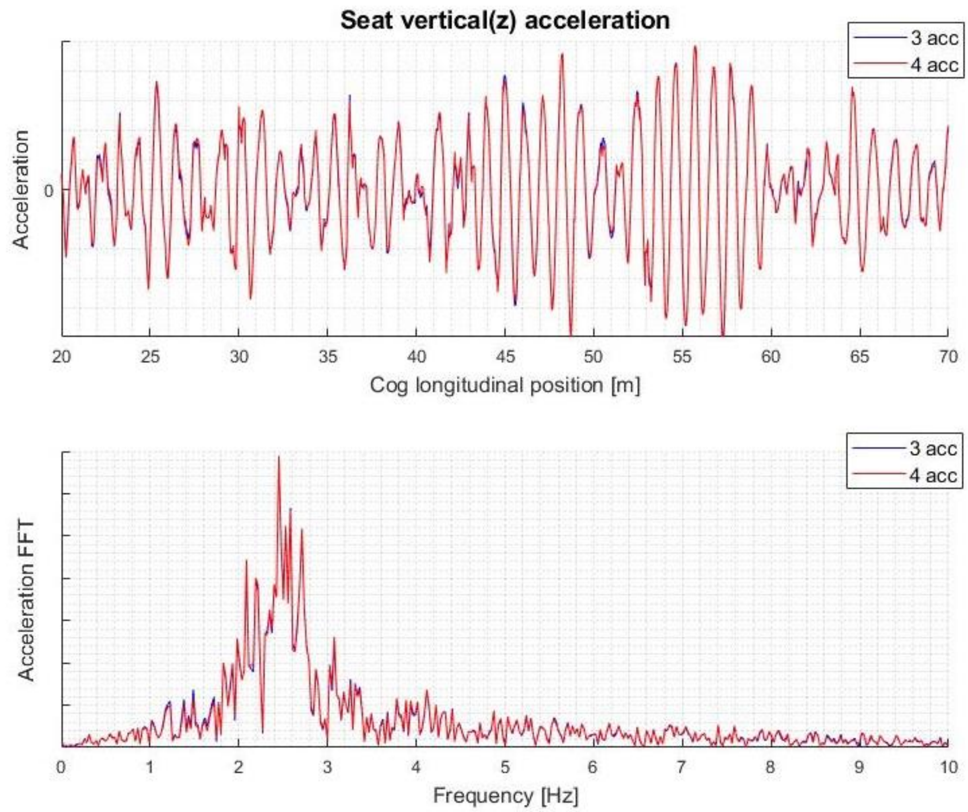

Figure 1.67: Comparison of the z-axis acceleration of the vehicle's CoG with the ISO 5008 test and *FFT*

The four-accumulator solution brings a visible improvement in terms of acceleration only along the lateral y-axis, while the longitudinal and vertical accelerations are similar to the three-accumulator ones. Looking at the lateral acceleration trend in the frequency domain, however, it is easy to note that the greatest deviation of the two curves occurs in the range between 1 and 2 Hz. Lateral vibrations in this frequency range are precisely those that have the greatest impact on operator's comfort, as stated in ISO 2631-1 [27], and therefore their reduction should not be neglected.

The average variations of the variables of interest using the four-accumulator system versus the three-accumulator one have been evaluated using **Eq. 1.55** to make a quantitative and not just a graphical comparison. This percentage variation of the generic variable x is obtained by dividing the average value of the deviation between the four-accumulators and the three-accumulators by the average value of the variable evaluated with the three-accumulator system (which is thus taken as a reference). The result is the averaged value of how much the four-accumulator solution is better (or worse) than the three-accumulator one.

$$\Delta x_{4/3}\% = \frac{\frac{\sum_{i=1}^{n}\left(|x_{4,i}| - |x_{3,i}|\right)}{n}}{\frac{\sum_{i=1}^{n}|x_{3,i}|}{n}} \cdot 100 \tag{1.55}$$

Figure 1.68 shows a histogram with the average deviations evaluated in this way for the main variables of interest. This graph thus gives an indication of which aspects are improved by using the four-accumulator system and by how much.

The numerical results emphasise what has already been said in the quantitative graphical comparison. Significant improvements can be achieved in suspension cylinder deformation (≈ 7-8%) and steering cylinder deflection (≈ 18%), in roll (≈ 5.5%) and yaw (≈ 17%), and in lateral acceleration at the operator's seat (≈ 17%). These values are not negligible and could justify the decision to use four accumulators instead of three.

However, the value of total vibrations at the operator's seat can also be calculated to have a single index of performance in terms of comfort of the two hydraulic solutions considered. Following the procedure already presented in **Section 1.1**, after filtering the accelerations along the three axes using the frequency weighting curves, we proceeded to calculate the *RMS* value for the vehicle with the two hydro-pneumatic solutions.

This calculation shows that the *RMS* value for the solution with four accumulators is 12% lower than the three-accumulators solution. This value is also far from negligible, as it is a direct index of vehicle comfort.

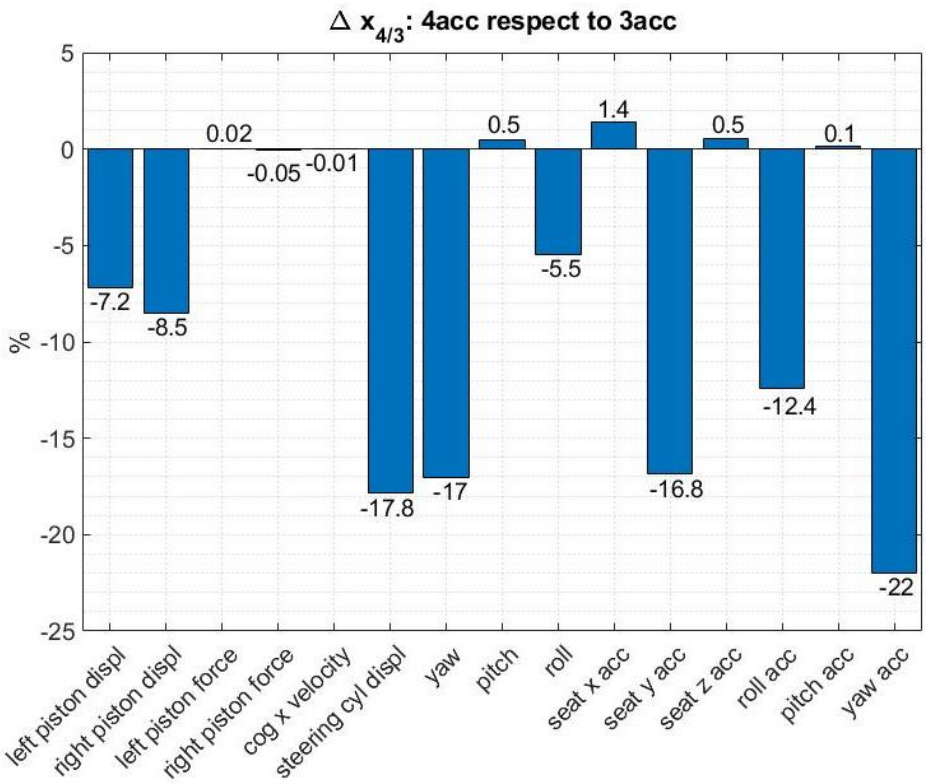

Figure 1.68: Averaged differences of the variables of interest using the 4-accumulators solution

We decided to consider the four-accumulators solution for the prototype because of the various reasons outlined in this paragraph. This solution is undoubtedly the more expensive and complex of the two, as there is simply one more accumulator and one more hydraulic damping block, but it allows for better performance both in terms of the range of stiffnesses and damping that can be obtained, and in terms of vehicle overall performances. This choice can be justify also by the fact that Dana wanted to develop a top-of-the-range independent suspension and the four accumulator solution has clearly better characteristics.

1.4 Optimization workflow

As anticipated, we decided to proceed with the four-accumulator hydro-pneumatic system thanks to the analyses reported in the previous paragraph. The four-accumulator solution has indeed decidedly better performances than the three-accumulators one. However, this choice is not sufficient to guarantee optimal suspension performances. It is in fact a complex and multidisciplinary system, where the hydro-pneumatic circuit and the chosen suspension architecture (double wishbone in this case) must interact to guarantee the best possible kinematic and dynamic behaviour for the entire vehicle. Another important aspect to consider are the various constraints of the system, such as construction constraints and overall dimensions ones.

The complete independent suspension design is therefore a multi-disciplinary and multi-objective activity for which a non-automated approach is strongly based on experience and on iterative processes. For this reason, together with the company, we decided to start a research activity to:

- define a multi-objective optimization methodology for the entire independent suspension,
- carry out a sensitivity analysis for the suspension (i.e. identify the independent parameters influencing the vehicle behaviour),
- identify the optimal solution based on the chosen *KPI*s (Key Performance Indicators),
- define a fully automated process for such optimization.

The first step of this activity was therefore the definition of the main objectives of the entire process. Together with the engineering department of Dana Incorporated, in particular with the vehicle dynamics department, we decided to define some objectives purely relating to the suspension kinematics and some others relating to the dynamic behaviour of the entire vehicle. We managed to reduce the number of the former after performing a sensitivity analysis. The kinematic objectives were indeed numerous at the beginning, nut the sensitivity analysis allowed us to identify only two independent objectives among these. In fact, an improvement of these two independent objectives would also lead to the improvement of the others. These two kinematic objectives are:

- the maximization of the *Roll Stability Factor*
- the minimization of the *Camber Loss*

The *Roll Stability Factor* RSF is a vehicle parameter that indicates the stability of the vehicle. In particular, it indicates the vehicle "resistance" to lateral roll-over. The higher this RSF value is, the lower the probability that the vehicle rolls over. In other words, the roll-over will occur due to more critical conditions for the vehicle. This RSF is, in fact, derived from the *Contact Factor* CF (**Eq. (1.56)**) for the front and rear wheels. The *Contact Factor* is defined as the smaller value of the vertical force F_z of the tire-soil contact between the right and left wheel, during a manoeuvre, and divided by the mean value of these forces.

$$CF = \frac{\min\left[F_{z_{dx}}, F_{z_{sx}}\right]}{\frac{F_{z_{dx}} + F_{z_{sx}}}{2}} \tag{1.56}$$

This *Contact Factor* CF is thus a curve evaluated moment by moment throughout the selected manoeuvre. CF gives an indication of how close the vehicle is to tipping. A null CF implies that one of the two wheels has zero vertical contact force, and therefore that the detachment of that wheel has occurred. Two curves will then be created, one for the front wheels, $CF_{front} = CF_{front}(t)$, and one for the rear wheels, $CF_{rear} = CF_{rear}(t)$. From these vectors, the *Roll Stability Factor* RSF is defined as the absolute minimum of these two curves (**Eq. (1.57)**).

$$RSF = \min\left[CF_{front}, CF_{rear}\right] \tag{1.57}$$

As anticipated, it is necessary to define a manoeuvre to calculate the CFs for the front and rear wheels. In this case, we wanted to consider an RSF that is an index of kinematic performance, i.e. assessing how much the suspension geometry impacts the moment when the vehicle tips over. It is therefore necessary to select a stationary manoeuvre in which the damping of the system does not intervene. We then selected a Ramp Steering manoeuvre, i.e. at a constant speed, a ramp is provided to the vehicle as a steering input that starts from zero and ends at the moment when such steering causes the vehicle to tip over. Obviously, this manoeuvre was considered as a simulation within the optimization workflow, like all the others considered.

The *Camber Loss* minimization is the second kinematic objective function. In automotive, the camber angle, is the angle between the vertical axis and the wheel centre plane, when looking at the front of the vehicle and with the wheels not steered. If the wheels have their tops tilted towards the outside of the car, the camber is positive, if inwards it is negative, while the absence of camber indicates neutral camber. Note that changing this angle changes the position of the wheel relative to the contact surface. Ideally, this angle should be modified as the vehicle roll varies. It should, in fact, be ensured that the vehicle's camber always leads the wheel to be as parallel as possible to the road, and therefore to have the maximum contact surface and grip. The correct wear of the tyres also depends on the camber angle.

In-road vehicles are designed to work mainly on flat roads with limited suspension travel due to unevenness of the ground, but where correct tire-to-ground contact during cornering must be ensured. For these vehicles there is a tendency to consider the concept of "*Camber Recovery*", i.e. the ability of a suspension to compensate for the roll angle of the suspended mass, while keeping the tyre orthogonal to the ground. **Figure 1.69** shows the schematization of this concept.

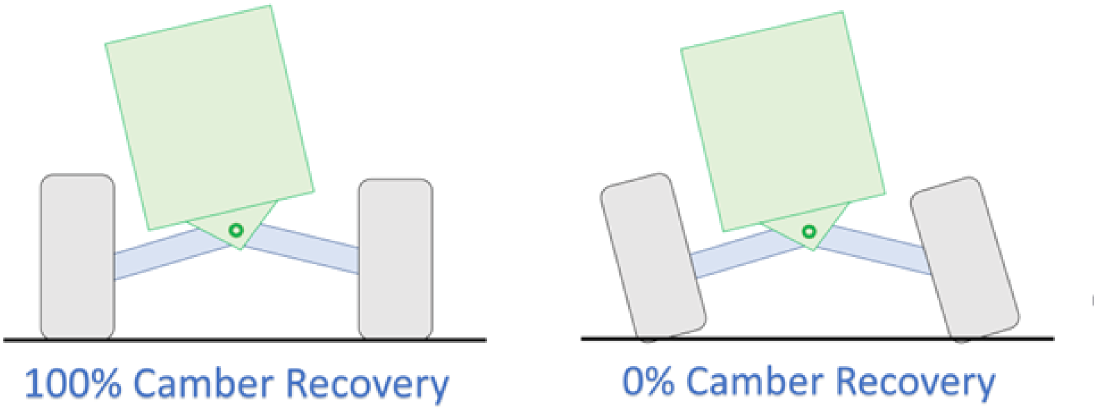

Figure 1.69: *Camber Recovery*

However, the working conditions of the suspension change dramatically in off-highway vehicles. In these applications, in fact, the suspension travel due to roll is reduced (due to the high position of the vehicle's centre of gravity), while the suspension travel generated by irregularities in the terrain increases considerably (due to the on-field applications). For these reasons, the camber variation associated with suspension travel should be considered primarily related to the ability to maintain maximum grip and thus traction in the field. Instead of camber recovery, therefore, it makes sense to consider the camber loss, i.e. how much change in camber is achieved as a result of vertical wheel travel. A diagram of the *Camber Loss* concept is shown in **Figure 1.70**.

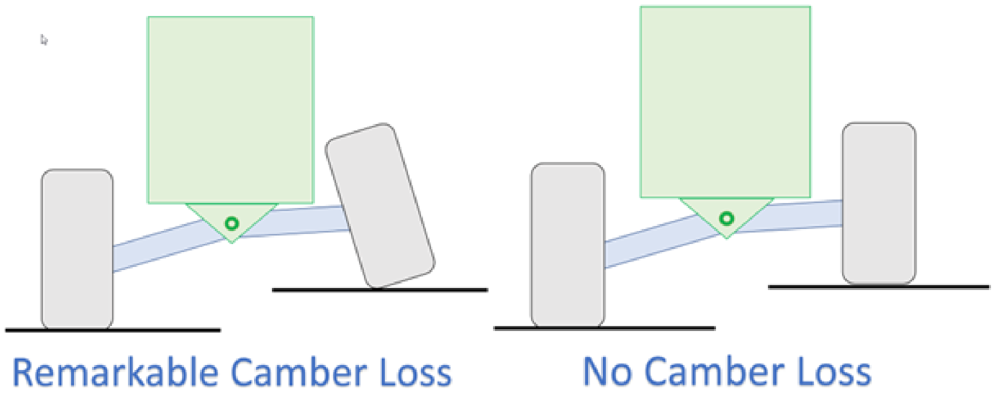

Figura 1.70: *Camber Loss*

The *Camber Loss* minimization ensures a high contact surface between the tires and the ground and thus the maintenance of optimum traction characteristics of the vehicle even in the case of unevenness. This parameter also depends, of course, on the geometry of the suspension architecture.

On the other hand, the objective functions related to vehicle dynamics are the improvement of the main KPIs linked to the vehicle's behaviour. The main characteristics that can describe the vehicle's behaviour are comfort, handling (i.e. manoeuvrability, driveability of the vehicle) and traction (which assesses the effective grip of the vehicle on the ground). The improvement of these indicators translates into:

- the minimization of the Rn (*Ride number*) value,
- the maximization of the dynamic RSF (*Roll Stability Factor*) value,
- the maximization of the total CF (*Contact Factor*) value.

The Ride number Rn has already been described in **Section 1.1.4** and defined in **Eq. (1.7)**, relating to ISO 2631-1 [27] and 5008 [28].

The definition of the dynamic *Roll Stability Factor* RSF is identical to the one previously presented in **Eq. (1.56)-(1.57)** for kinematic objectives. The difference between the two is simply in the manoeuvre considered for the calculation of the RSF. In this case, in fact, we must consider a manoeuvre designed to highlight the vehicle transient behaviour. The manoeuvre to do so is the Double Line Change test, also known as Moose Test. This is a particular manoeuvre also used in the automotive sector to assess vehicle manoeuvrability (or handling).

Finally, the *Total Contact Factor* CF is a vehicle parameter representative of the vehicle's traction capability. This parameter is again defined from the vectors CF_{front} and CF_{rear} of **Eq. (1.56)** for the front and rear axles respectively. It is indeed impossible to have a direct measurement of the tire contact surface and thus the vehicle's grip and traction capability. However, the greater the vertical contact forces between the wheel and the soles, the greater the tire deformation and thus its footprint. The total CF is defined as the weighted sum of the average values of these vectors, where the weights are equal to the load distribution of the vehicle under consideration (**Eq. (1.58)**).

$$CF = \%_{load_{front}} \cdot \mathrm{mean}\left[CF_{front}\right] + \%_{load_{rear}} \cdot \mathrm{mean}[CF_{rear}] \tag{1.58}$$

Eq. (1.58) shows the expression of the *Contact Factor*, where $\%_{load_{front}}$ and $\%_{load_{rear}}$ represent the load distribution of the vehicle, while $\mathrm{mean}[CF]$ is used to consider the average of the CF_{front} and CF_{rear} curves. Considering a load distribution so that the 60% is at the rear and 40% is at the front (i.e. 60% of the vehicle's weight is on the rear axle and the remaining 40% on the front axle), **Eq. (1.59)** would become the following.

$$CF = 0.40 \cdot \mathrm{mean}\left[CF_{front}\right] + 0.60 \cdot \mathrm{mean}[CF_{rear}] \tag{1.59}$$

As in previous cases, it is necessary to select a manoeuvre suitable for highlighting the tractor's traction characteristics, especially in the most critical working conditions, i.e. when it is in the field. In collaboration with the CREA research centre, we selected a maize sowing cycle on a ploughed field, which turns out to be a very heavy cycle for the suspension and the vehicle itself. This cycle was carried out experimentally by CREA itself. Wheel displacement data was then exported from the experimental measurements to be used as input to the multibody numerical model. Creating a 3D mapping of the actual ploughed field and simulate the tractor's passage over it would have been much more complex. Instead, it is much more convenient to exploit the model of a 4-poster test rig (an example of which is also shown in **Figure 1.71**), which basically consists of a seismic isolator acting as a base and four hydraulic actuators on which the vehicle's wheels rest. The wheel displacements can be applied directly to these actuators to replicate the maize cycle.

Figure 1.71: 4-poster test rig for an agricultural tractor

The total CF value can be derived from the results of this simulation using **Eq. (1.58)**. The higher this CF value is, the greater the tractor contact with the ground and thus the greater the grip with it.

As briefly mentioned earlier, we have reported only the objectives of the final version of the optimization process. In fact, initially, we defined many more kinematic and dynamic objective functions. Having so many objective functions, however, slows down the optimization process considerably. It is therefore necessary to reduce them as much as possible. Some of those objectives initially defined were removed, as mentioned, because they turned out to be dependent on others after a sensitivity analysis, i.e. the improvement of the five presented above also implies the improvement of these others.

Other objective functions have been transformed into constraints for the optimization process. The step following the objectives definition, in fact, is precisely the constraints specification. These constraints are not values that the optimizer tries to maximize or minimize, but minimum (or maximum) values of acceptability. If a considered design does not respect all these limits, it will be considered as unfeasible solution.

Even the 'transformation' of an objective function into a constraint is not an immediate process. The risk, in fact, is setting acceptability values that are too demanding, which makes any design as unfeasible. It is indeed necessary for the optimizer to find some feasible solutions to "recognize" a direction to follow even in the initial phase.

For this reason, we used the following procedure. Initially, we kept all the objective functions. We then used the optimizer to evaluate a fairly large number of designs, either defined randomly or using more advanced and intelligent methods (which will be presented later) but without activating the optimization process. The optimizer just had to evaluate the performance of these designs. We then performed a sensitivity analysis from the results, which made it possible to identify (and thus exclude) objective functions that are dependent on others. Afterwards, the results obtained for the remaining objective functions have been analysed. When we realised an acceptable value has often been reached for a given objective function, this objective function could be transformed into a constraint. This value will then be set as the threshold of acceptability. Only solutions capable of exceeding this threshold will be considered feasible in subsequent optimizations.

Two examples of constraints which were defined in this way are reported below.

The first is the constraint related to the bump steer. From vehicle dynamics point of view, the presence of the smallest possible steering angle induced by the suspension travel is a very important characteristic that the suspension must guarantee. Due to the suspension geometry, in fact, a given vertical wheel travel corresponds to a slight rotation of the wheel, which induces precisely unwanted steering. It is so necessary to minimize this parameter as much as possible to reduce the consequent correction operation that the operator has to make by acting on the steering wheel when driving over uneven ground. The reduction of the operator action also means the reduction of the energy demand of the steering system.

Initially, the minimization of bump steer was set as objective function. We then realised that it might be possible to transform this objective into a constraint with the process described above. In this way, once the acceptability value had been set, the optimizer could ensure that each solution satisfied this limited bump steer requirement.

A second example is the constraint on the maximum steering angle value. This parameter is also strongly linked to the geometry of the suspension architecture. For manoeuvrability reasons, we wanted to maximize the value of this maximum steering angle at the wheels, and an appropriate objective function was thus defined. However, we realised it was possible to transform this requirement to an optimization constraint. In this way, each feasible design satisfied that minimum requirement for maximum steering angle at the wheels.

Other constraints have been defined 'directly', without being an objective function first. The absence of static and dynamic interference between the various suspension components is an example of these. Lastly, we added some other constraints during the construction of the optimization workflow, such as those that will be presented in the following paragraphs.

In addition to the objective functions and constraints, it was necessary to define all the variable inputs of the optimization process, i.e. all those characteristic parameters of the independent hydro-pneumatic suspension that can be subject to variation to find the optimal solution(s). An optimization workflow works as follows. The user defines the variable inputs and their range of variation. The optimizer then starts the design evaluation by varying these inputs in order to explore the spectrum of possible solutions, using the chosen method. The optimizer runs the controls or simulations included in the workflow checking the acceptability of the constraints and values of the various objective functions. The optimizer then identifies the direction to follow and thus finally the combination of inputs that provides the optimal solution.

If there is only one objective function defined in the optimization process, there will only be an absolute maximum or minimum value for this function. Note that different sets of variable inputs can realize this maximum or minimum value for the objective function. However, as said, more than one objective function has been defined in this case. We are then considering a multi-objective optimization. In such cases, there is usually no solution that optimizes all the objective functions, but rather a set of solutions, called the Pareto frontier (or Pareto front), that are non-dominated by other solutions, i.e. a solution is non-dominated when it is not possible to improve the condition of one objective without worsening another.

Figure 1.72 shows a graphic example of a Pareto frontier. In the example, f1 and f2 are the objective functions to be minimized. Considering points A and B (but the same would be true for any other pair of points on the Pareto frontier), it is easy to see how solution A is better than B with respect to the function f2, but worse with respect to f1. There is no solution that 'dominates' the ones on the Pareto frontier.

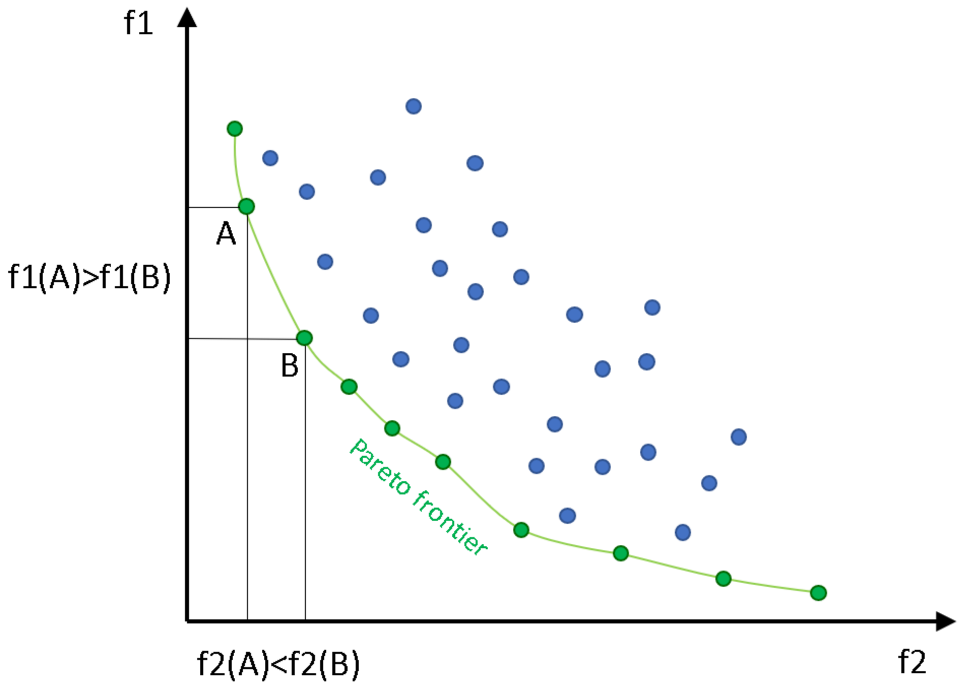

Figure 1.72: Example of a Pareto frontier

Once the optimizer have found the Pareto, it is then up to the user to decide which solution to consider. It is therefore a trade-off situation.

The different cycles (called *loops*) of realised optimization are presented below. Initially, we considered a single optimization workflow with all the presented objective functions and constraints. However, we realised that the number of the workflow variable inputs was decidedly high. These variable inputs, in fact, include the spatial coordinates (i.e. x, y, z) of each hardpoint of the suspension architecture, the various parameters (geometric and non-geometric) that characterize the hydraulic circuit such as volumes and preloads of the accumulators or the dimensions of cylinders and orifices. The large number of variable inputs and objective functions would have led to the need to evaluate a very large number of designs to ensure the effectiveness of the optimization process. Furthermore, for each of these designs, it would have been necessary to perform all the numerical simulations, some of which have computational times of minutes or tens of minutes. This would therefore have led to an inefficient and ineffective process.

For this reason, we decided to divide this workflow into three different *loops*. In this way, it was possible to have fewer variable inputs per loop, fewer objective functions per loop, and thus fewer designs needed by the optimizer to converge to solutions of interest. Each of these loops is thus specialized in optimizing only certain aspects of the complete system. As shown in the diagram of **Figure 1.73**, Loop 1 deals with the definition of the suspension kinematics, Loop 2 deals with the definition of the suspension cylinder geometry and the main hydraulic parameters, while Loop 3 deals with the definition of the damping requirements of the system.

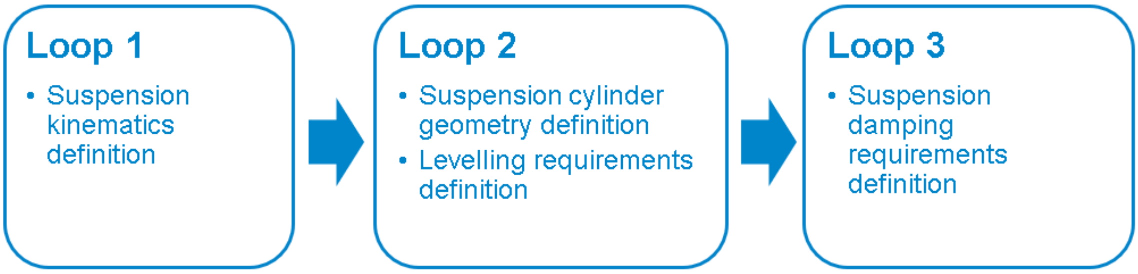

Figure 1.73: Scheme of the various workflow *loops* for the independent suspension optimization

However, these loops are not independent of each other. It is necessary to execute them in order as some of the parameters taken as constant inputs in a loop derive directly from the optimum results of the previous one.

These three loops, as anticipated, are described in detail in the following paragraphs.

1.4.1 Loop 1

We designed the first of the three optimization loops to define the geometry of the suspension architecture, i.e. the positions of the various hardpoints affecting the kinematic behaviour of the suspension itself. It is, in fact, obviously not sufficient to define the type of architecture (double wishbone in this case). There is indeed a precise number of characteristic points of connection between the rigid bodies, which uniquely define the suspension. These points are called *hardpoints* and must be specifically defined in space. Depending on their location, the kinematic behaviour of the suspension obviously changes.

Figure 1.74 shows a simplified diagram of the main elements of the suspension, which have been reduced to the simplest possible shapes, in which the hardpoints considered are also highlighted. Note that these hardpoints have been named according to a nomenclature chosen by the company. The objective of this **Loop 1** is thus the definition of the suspension "skeleton" to optimize its kinematic behaviour. Once the optimizer has defined so, it will be up to the Dana Incorporated designers to design the final solution starting from this skeleton.

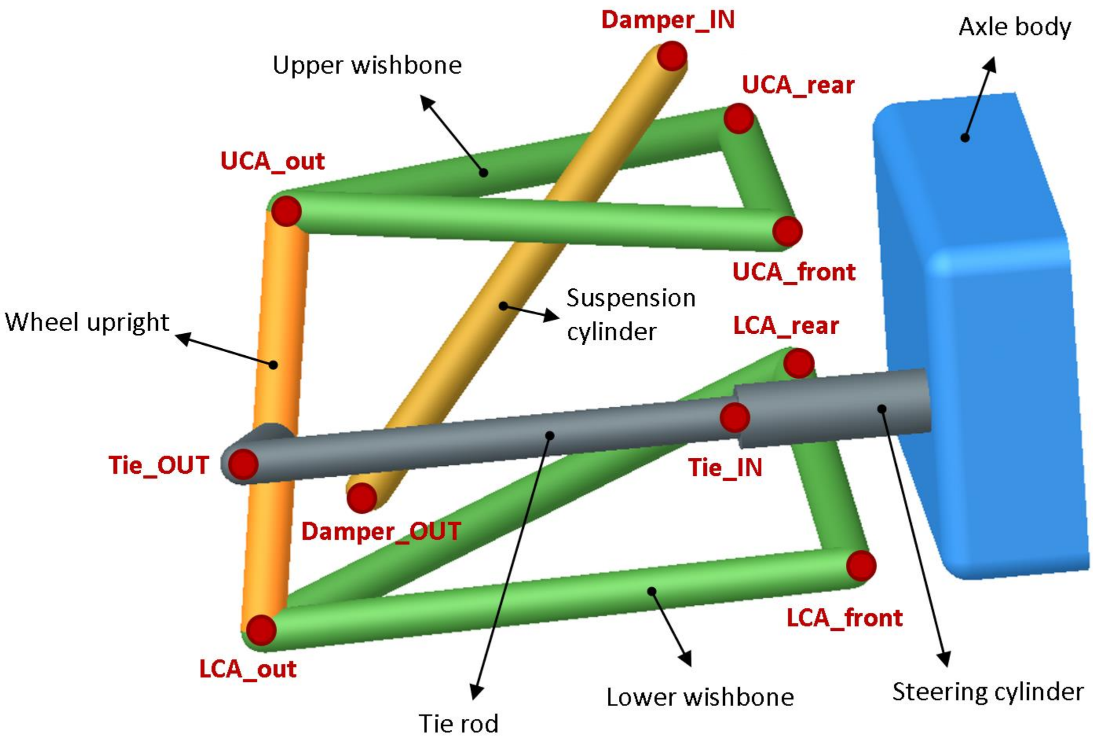

Figure 1.74: Simplified scheme of the double wishbone suspension with main components and hardpoints

While defining the variable inputs for the Loop 1 optimization, we realised how considering only the coordinates of the hardpoints as independent inputs would have led to lots of unfeasible solutions, even defining the ranges of variation of these coordinates. This because there would have been no control over several characteristic parameters of the suspension which have a huge impact on its kinematic behaviour. These parameters must be monitored in order to achieve a sensible design.

Figure 1.75 depicts some of these parameters as the roll centre height, the front view swing arm, the scrub radius and the kingpin angle. More detailed information on these parameters can be found in the vehicle dynamics academic texts [35].

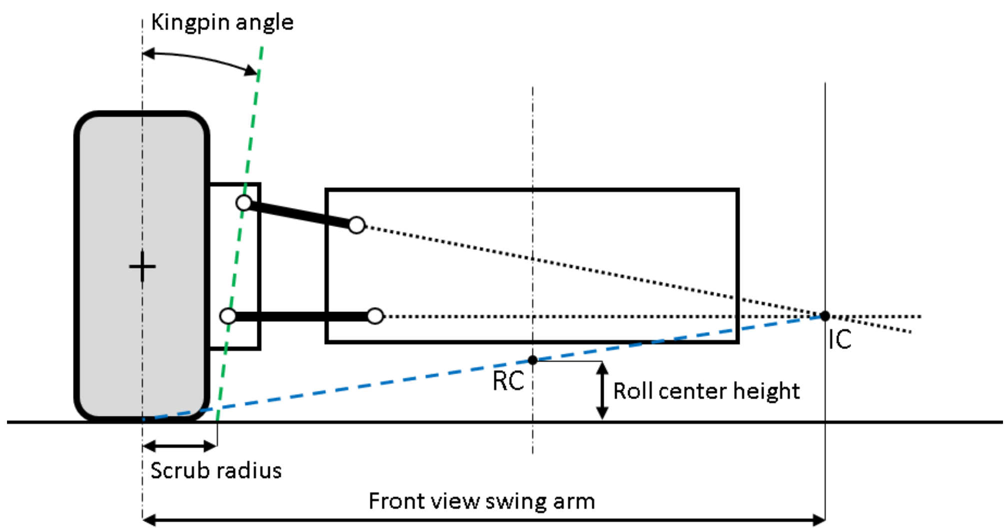

Figure 1.75: Simplified scheme of the double wishbone suspension with some kinematic characteristic parameters

For this reason, we decided to remove some dependent coordinates of the hardpoints from the variable inputs and consider instead these characteristic parameters. This allowed us not to introduce a large number of constraints to check these characteristic parameter values. It was then sufficient to set the correct range for these new input variables. The dependent coordinates just excluded are then evaluated basing on the remaining (independent) coordinates and these characteristic parameters.

An example is given to better show what was done. Consider **Figure 1.76**.

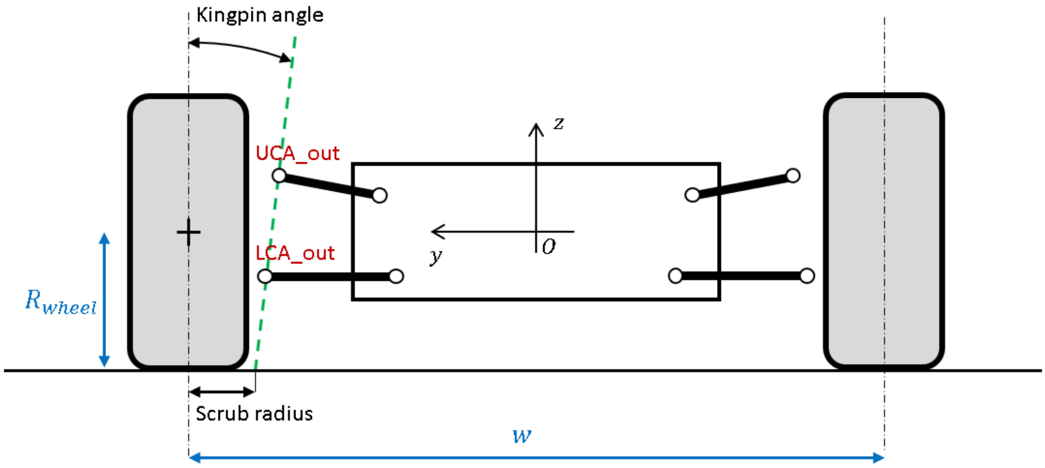

Figure 1.76: Simplified scheme of the double wishbone suspension to show the reduction of independent hardpoint positions

Knowing the geometry of the vehicle and thus the wheel radius R_{wheel} and the vehicle track width w, it is easy to note that the y and z coordinates of the hardpoints UCA_out and LCA_out uniquely defines the vehicle scrub radius and kingpin angle. Similarly, knowing the values of kingpin angle $\vartheta_{kingpin}$, the scrub radius R_{scrub}, and two of the four coordinates in the yz plane of hardpoints UCA_out and LCA_out, it would be possible to derive the other two dependent coordinates using **Eq. (1.60)-(1.61)**.

$$UCA_{out_y} = \frac{w}{2} - R_{scrub} - \left(R_{wheel} + UCA_{out_z}\right) \cdot \tan\left(\vartheta_{kingpin}\right) \tag{1.60}$$

$$LCA_{out_y} = \frac{w}{2} - R_{scrub} - \left(R_{wheel} + LCA_{out_z}\right) \cdot \tan\left(\vartheta_{kingpin}\right) \tag{1.61}$$

And this is precisely what we have done with the variable inputs of Loop 1. The characteristic parameters of the suspension (kingpin angle and scrub radius in the example) and some independent coordinates (UCA_{out_z} and LCA_{out_z} in the example) were taken into account and from these the remaining dependent coordinates (UCA_{out_y} and LCA_{out_y} in the example) were then evaluated.

Note that we left some coordinates of the suspension hardpoints as constant in this loop. These coordinates, in fact, have very little influence on the kinematic characteristics of the system, whereas they have a great impact in the modal analysis of the system. We thus decided to 'optimize' these coordinates at a later stage, i.e. in Loop 2.

Loop 1 thus aims to define the part of the suspension geometry that affects its kinematic behaviour. Therefore, the two objective functions, presented earlier, related precisely to the kinematics of the suspension are considered in this loop, which are the minimization of bump steer and the maximization of steady state RSF.

It is necessary to perform various steps to proceed to the evaluation of these functions, which may be calculations, checks or simulations. All these steps can ensure the evaluation of all the necessary outputs for this analysis.

The conceptual workflow of Loop 1 is shown in **Figure 1.77**, where we have also highlighted which third-party software we used. The processes without a specified software exploited spreadsheets or calculator nodes to complete their task.

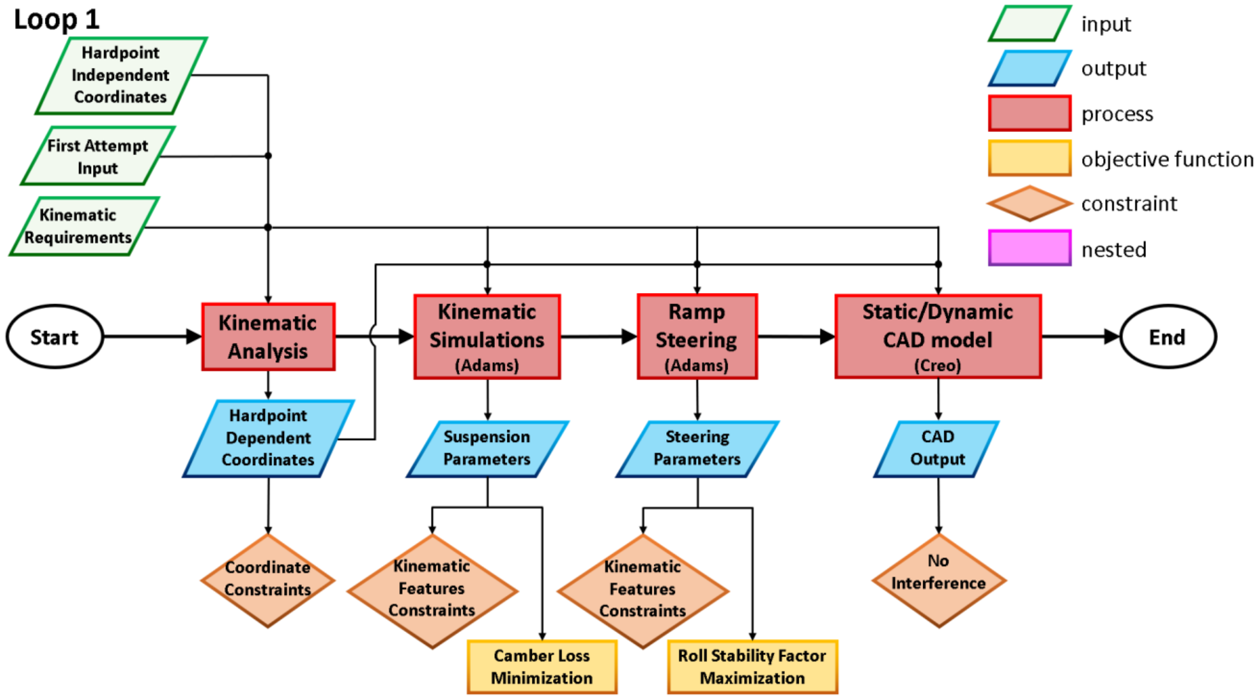

Figure 1.77: Loop 1 scheme for the independent suspension optimization

The Loop 1 optimization thus consists of the succession of different processes, performed for each design (defined by a vector of input values). These processes then provide outputs that can be used as inputs in subsequent processes, or subject to objective functions or constraints.

Starting from the vector of input values that univocally defines the design, the first step is the kinematic analysis to obtain all the remaining coordinates or dependent parameters, exactly as done in the example reported with **Eq. (1.60)-(1.61)**. The results of this analysis complete the definition of the suspension geometry. Some of these dependent coordinates are also subject to constraints to exclude unfeasible designs.

The next process relates to the execution of certain kinematic simulations of the suspension, which are designed to fully study the kinematic behaviour of the solution under consideration. In particular, these multibody simulations are:

- parallel vertical displacement of the two wheels: while keeping the axle body fixed, an identical vertical displacement is applied to the two wheels to complete the entire suspension travel,
- opposite vertical displacement of the two wheels: keeping the axle body fixed, a displacement of opposite sign is applied to the two wheels to complete the entire suspension travel, emulating a pure roll manoeuvre,
- complete displacement of the steering cylinder piston: keeping the axle body fixed, a complete left and right steering of the wheels is performed.

It is thus possible to know the kinematic behaviour in each working configuration of the suspension by combining these three simulations. The output of these simulations, therefore, are the characteristic parameters of the suspension, which can then be subjected to acceptability constraints. One of these parameters is the camber loss presented above, which can then be the subject of an objective function relating to its minimization to guarantee a high degree of vehicle grip on uneven terrain.

We decided to exploit the Adams® multibody models to evaluate the system kinematic (Loop 1) and dynamic (Loop 2 and 3) behaviour because they had been already developed and validated at the time. However, it can be possible to replace these Adams® models with correspondent Amesim® ones.

It is also possible to add some appropriately defined constraints to these outputs to better control their minimum or maximum values.

The process related to the simulation of the ramp steering manoeuvre follows the kinematic simulations just described. As anticipated, this quasi-static simulation is used to evaluate the influence of suspension kinematics on the vehicle RSF.

Note that it was necessary to consider some first attempt inputs (particularly regarding preload, stiffness, damping and the suspension's transmission ratio) to allow the virtual simulations included in the optimization loop. We derived these first attempt values for a given solution before the optimization process. It is the possible to adjust these attempt values basing on the kinematic simulation results, upstream of the ramp steering simulation. The results obtained in this way are not exactly the correct and optimal values (which will be found in the next loop through modal analysis), but they are sufficient to guarantee the correct execution of the multibody simulations of the entire vehicle.

From the ramp steering simulation, it is possible to obtain as output the characteristics related to the steering of the vehicle and above all the quasi-static RSF value, which is the object of the second objective function in the loop.

In addition to these processes, we also decided to consider the evaluation of possible interference between the various bodies constituting the suspension once the positions of the hardpoints had been defined. It is indeed necessary to ensure the total absence of interference, both static and dynamic, to guarantee the feasibility of the solution considered. A 3D CAD model was therefore introduced within the loop. This 3D model represented a simplified geometry of the suspension under consideration starting from the vector of variable inputs and the outputs of the previous processes, as shown in **Figure 1.78**. As said, this is a simplified suspension, but it is suitable for evaluating the presence or absence of interference between the bodies. From this then, a second model was inserted to also consider the movement of the suspension and verify any contacts and dynamic interferences between the bodies.

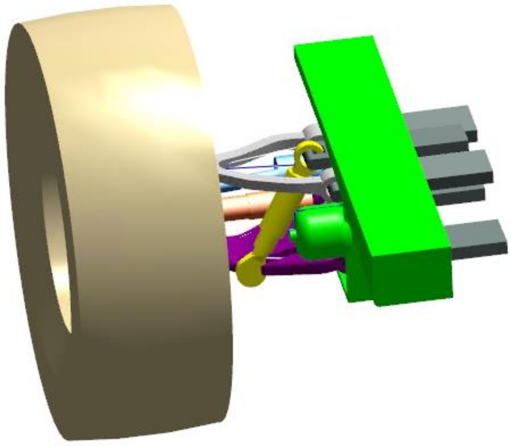

Figure 1.78: Simplified 3D CAD model of the suspension

Note that the 3D model in **Figure 1.78** consists of very simplified geometries of the various parts but is only used to consider their overall dimensions. The detailed modelling of the suspension will only be carried out once the results of the optimization workflow have been obtained.

In this paragraph we thus presented the Loop 1 relating to the suspension kinematics optimization. Having considered two objective functions, the result is a Pareto frontier similar to the one shown in **Figure 1.79**, which shows that the set of optimum results are those which minimize the camber loss and/or maximize the roll stability factor.

The results of this and the other loops will be shown in more detail in a later section.

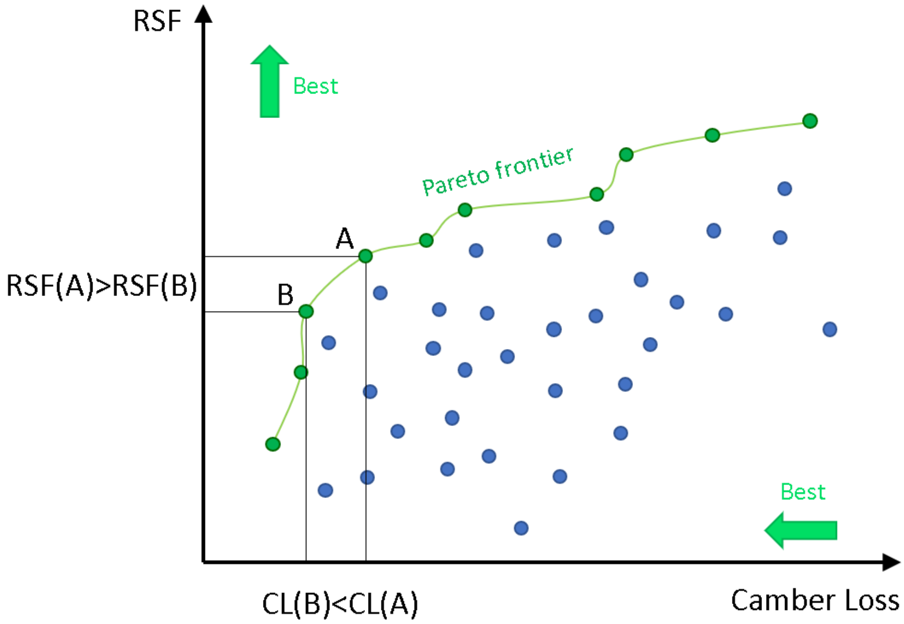

Figure 1.79: Example of the Loop 1 Pareto frontier

1.4.2 Loop 2

As mentioned in the previous paragraph, only the suspension hardpoint coordinates that most influence the system kinematic behaviour were defined in Loop 1. On the other hand, other coordinates have a great impact on the dynamic behaviour of the system and the vehicle eigenmodes (i.e. on the results of the vehicle modal analysis).

We decided then to optimize the remaining positions of these hardpoints by considering the results of the vehicle modal analysis, while keeping the positions already defined in the previous loop as constant. However, we have seen how the tractor can operate in different working configurations during its life, i.e. at nominal load (empty vehicle weight or EVW), full load (gross vehicle weight or GVW, defined by catalogue) or intermediate load and with different weight balances between front and rear. However, it would be difficult to define these remaining coordinates trying to optimize the modal results of all these *n* working configurations, as it would imply defining *n* objective functions that would slow down the optimization process.

We thus decided to divide the Loop 2 into two parts. The first part defines the remaining coordinates basing only on the results of the modal analysis for the nominal vehicle working configuration, simply called empty vehicle weight (EVW). This nominal working condition is defined by the mass of the tractor and its weight balance without front or rear implements or ballast weights. Once the definition of the suspension geometry has been complete, in the second part of Loop 2 it is possible to carry out the modal analyses of the other working configurations to obtain the optimum values of stiffness and equivalent damping for the system. It is then possible to optimize the dimensioning of the hydro-pneumatic system to achieve the requirements defined by these modal analyses.

Figure 1.80 shows the diagram for the first part of Loop 2 relating, as mentioned, to the definition of the remaining hardpoint coordinates according to the results of the EVW modal analysis. As before, we have also highlighted which third-party software we used.

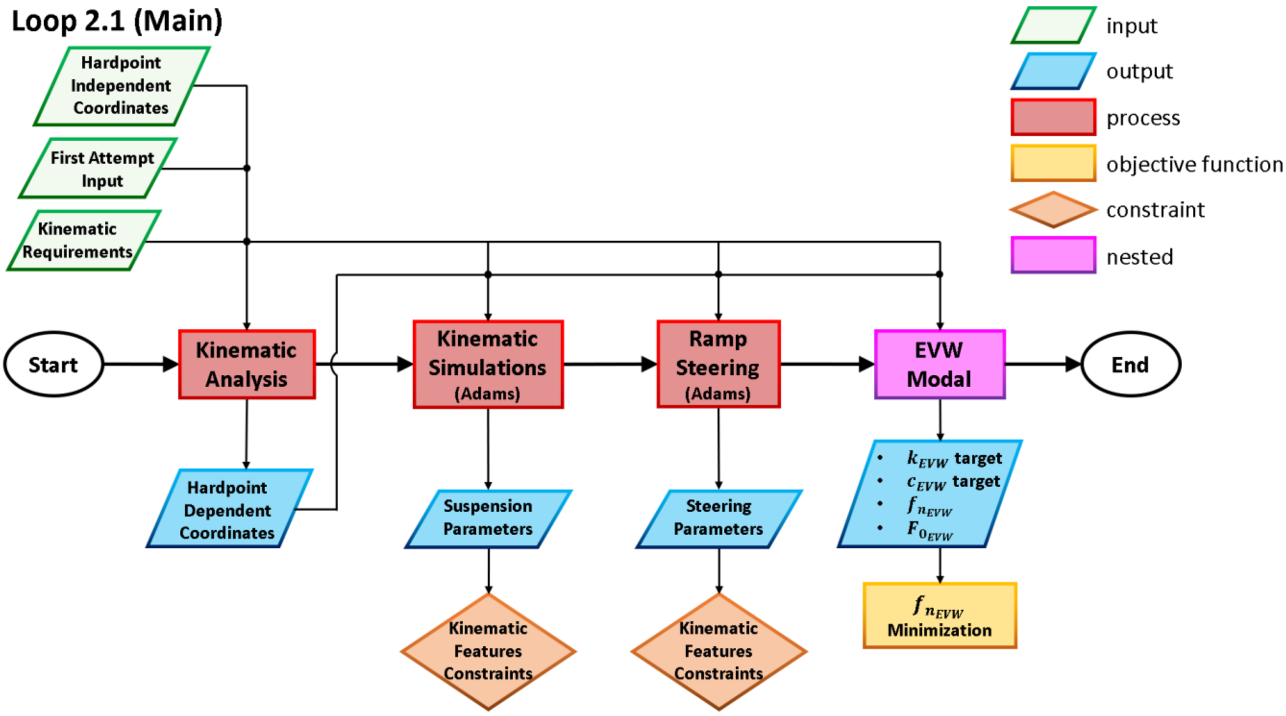

Figure 1.80: Scheme of the first part of Loop 2 for the independent suspension optimization

This loop is identical to Loop 1 in its first part, with the execution of the kinematic analysis and ramp steering simulation. It is, in fact, necessary to consider these processes again to ensure that the considered design always fulfils the requirements defined by the kinematic constraints also used in the previous loop. This loop keeps the coordinates defined in Loop 1 as constant inputs. On the other hand, all coordinates that most influence the modal analysis, held constant in the previous loop, are now variable inputs.

We then inserted a nested optimization relating precisely to the modal analysis of the vehicle in EVW configuration after the repetition of the processes already seen in Loop 1. It is necessary to consider this nested optimization since it must optimize the equivalent stiffness k and damping c values to minimise the first natural frequency of the system. This operation must be repeated for each design considered, so for each suspension geometry. That is why it was necessary to insert a nested optimization. Among all these different geometric designs with relative k and c then, the optimization at a higher level must converge to the solution that always minimizes the first natural frequency of the system.

MSC Adams® allows to identify the main vehicle eigenmodes and provides, for each of them, information on the natural frequency, damping ratio and an animation of the proper mode. Before defining this optimization workflow, some sensitivity analyses had been carried out in relation to this process. Regardless of the suspension configuration, the following eigenmodes are the most interesting ones for the vehicle itself:

1. 1st pitch mode around the rear axle, which involves the front suspension
2. 1st roll mode, which involves the front suspension
3. 2nd pitch mode around the front axle, which does not involve the front suspension
4. 2nd roll mode, caused only by the tire deformations, which does not involve the front suspension

We then observed that mode 3 is totally independent of the suspension geometry, depending only on the vertical stiffness and damping characteristics of the rear wheels and the weight distribution of the sprung mass. Similarly, a change in the suspension has no impact on mode 4.

The characteristics of the front suspension influence the remaining modes 1 and 2 and their natural frequency. We also noted that mode 1 is the one with the lowest natural frequency of the two, regardless of the suspension. Through various sensitivity analyses carried out by Dana Incorporated's Engineering Department, we assessed that the amplitude of the vehicle frequency response was lower (and therefore better) as the natural frequencies of the system decreased, as shown in the dimensionless graph of **Figure 1.81**.

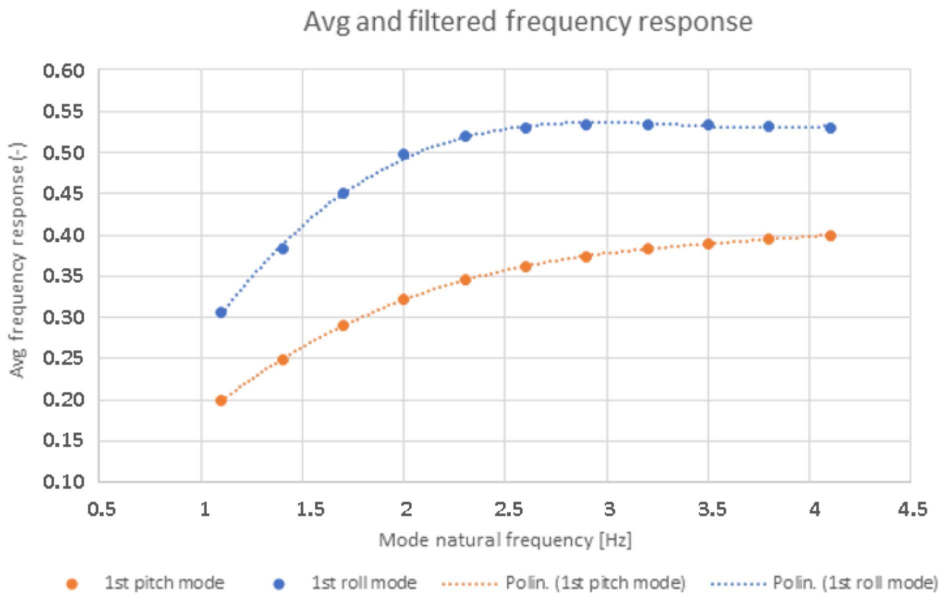

Figure 1.81: Dimensionless frequency response as function of the vehicle natural frequency

We then decided to use this information to precisely define the objective function of this loop, which is the minimization of the first natural frequency. We considered only the natural frequency of mode 1, as it is intrinsically linked to the second. An improvement in the impact of the suspension on the first pitch mode leads to an improvement on the first rolling mode as well, since the front suspension affects them both.

We considered only the first natural frequency also to control the lower limit of this frequency. Nota that this would not have been possible if we had minimized the second natural frequency. It is, in fact, also necessary to consider a constraint relating to motion sickness on the vehicle to ensure that it remains above the 1 Hz threshold. Having the first natural frequency equal to 1 Hz would implies the amplification of 1 Hz excitation and so the generation of the motion sickness effect on the operator as the vehicle passes over uneven ground. If we had considered the second natural frequency as the object of minimization, it would have been impossible to control the decrease of the first natural frequency, which could have reached 1 Hz.

We thus added a constraint (**Eq. (1.62)**) to avoid this result, where 1.1 Hz threshold was used for safety reasons.

$$f_{n_{1st\,mode\,pitch}} \geq 1.1 \text{ Hz} \tag{1.62}$$

Note that there is also an upper limit for the natural frequency of the first pitching mode due to the effect known as *power hop*, which is the bouncing of the vehicle on all four wheels. It is necessary to keep this natural frequency below 2.5 Hz to avoid this effect.

The outputs of this nested optimization are all the main results of interest from the modal analysis. In particular, the most interesting results are the natural frequency, which will be the subject of the objective function, the static preload values of the suspension and the corresponding optimal equivalent stiffness and damping values for each design. The preload, stiffness, and damping values (together with the results of the other modal analyses in the next part of the loop) will be used for the dimensioning of the hydro-pneumatic system, which precisely provides the real stiffness and damping values of the suspension.

A nested optimization is an optimization to be performed for each design considered in the main optimization. It is therefore, obviously, something that slows down the process, but (here and also in the following loop) it turns out to be necessary to ensure the effectiveness of the process.

Figure 1.82 therefore shows the logical scheme of this nested process. The variable inputs of this optimization are only the equivalent stiffness and damping values, while all other inputs are taken as constants from the main optimization in order to precisely analyse the design under consideration.

Some constraints have been inserted before the modal analysis to exclude unfeasible solutions. One of these constraints relates to the value of the ratio between k and c, which must be within a certain range to ensure the stability of the simulations. On the other hand, the other constraint is defined downstream of a panic stop simulation (i.e. sudden tractor braking) to ensure that the suspension cylinders do not reach the end stop during the manoeuvre. If this contact happens, it means that the values of k and c are not acceptable and, therefore, it does not make sense to consider this solution further.

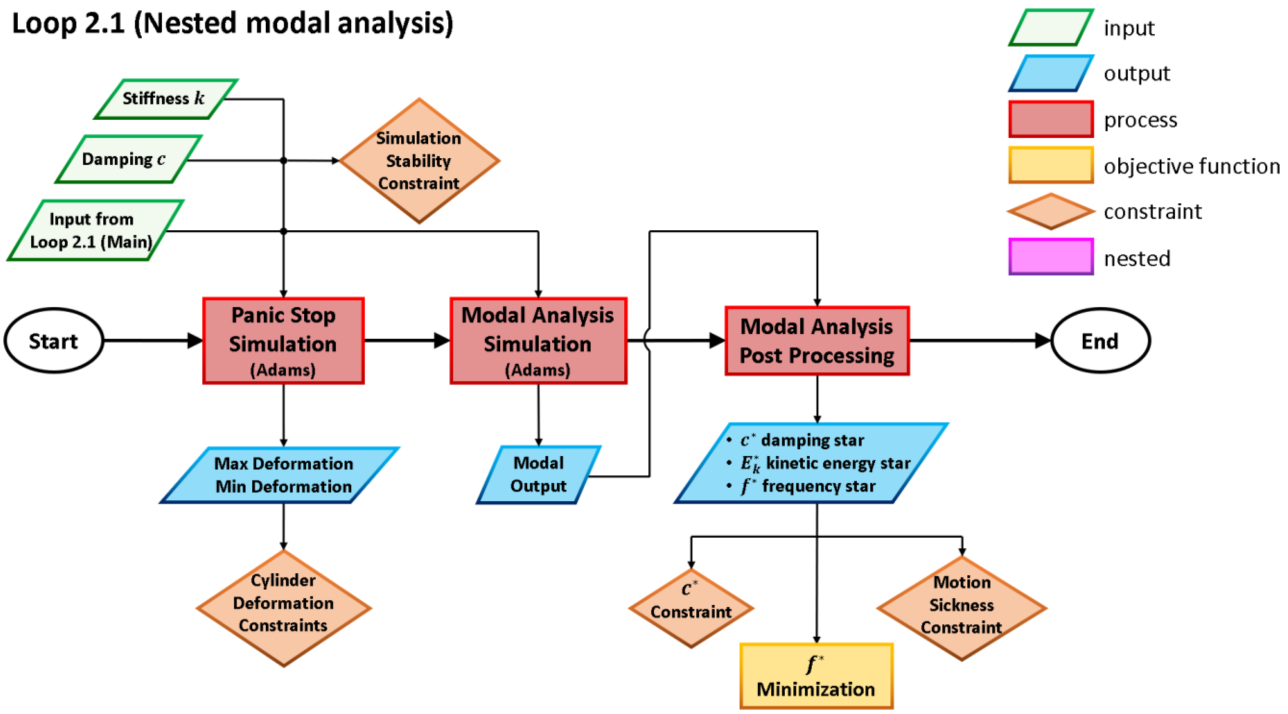

Figure 1.82: Scheme of the nested optimization regarding the EVW modal analysis

Once the design has passed all these constraints, it can be subjected to the modal analysis simulation.

The outputs of this simulation are then subjected to a post-processing process to derive all the information of interest. The optimizer then applies the constraints (such as the one on motion sickness) and the objective function (the minimization of the first natural frequency) to these results of interest.

Each main loop design, therefore, enters the nested process and is subject to the optimization of k and c values. Once this nested optimization is complete, the main loop is also concluded, which is then restarted by examining another design until the results converge or the maximum number of designs is reached.

Once this first part of Loop 2 has been concluded, the optimizer guarantees the fully and unambiguously definition of the suspension geometry. We can thus proceed with the subsequent analyses, starting from the second part of Loop 2, in which the modal analyses of all the other vehicle configurations will be considered. **Figure 1.83** shows the logic diagram relating to the second part of Loop 2.

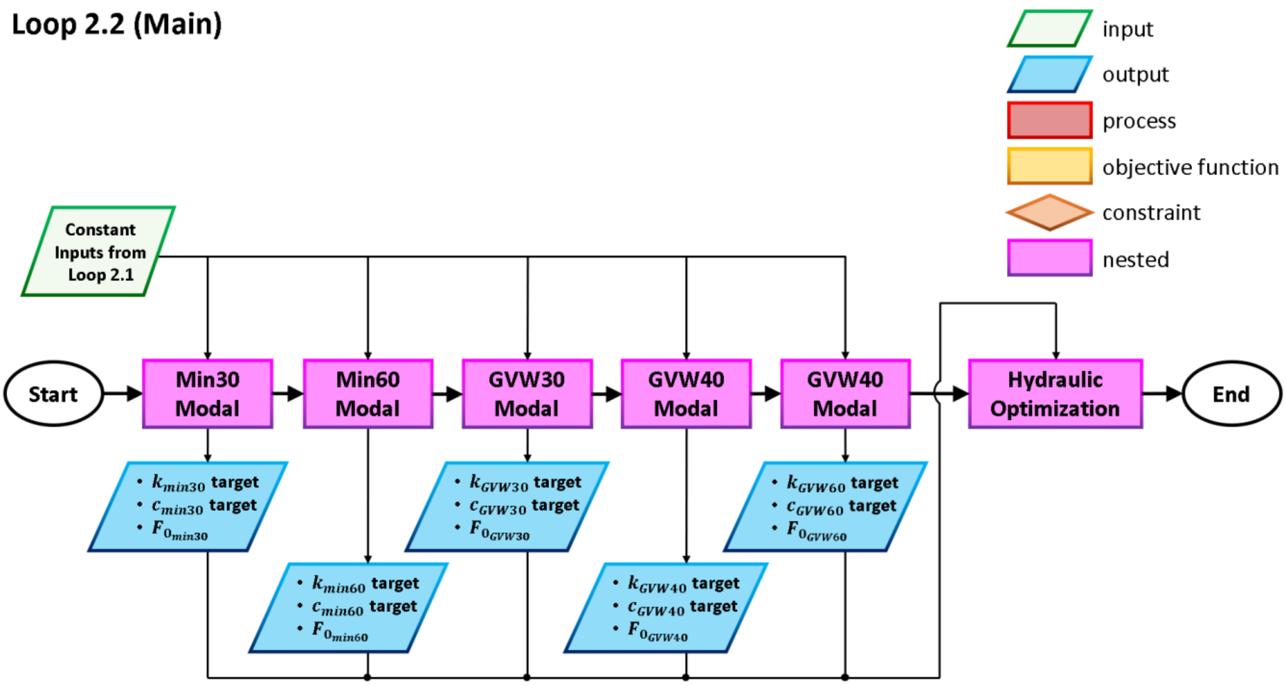

Figure 1.83: Scheme of the second part of Loop 2 for the independent suspension optimization

All the nested processes relating to the various modal analyses shown in **Figure 1.83** are entirely analogous to what has already been done for the nominal EVW vehicle configuration (**Figure 1.82**). Once, therefore, the optimum target stiffness and damping values and the corresponding suspension preloads for each vehicle configuration have been defined, it is possible to proceed with the dimensioning of the hydro-pneumatic system.

We identified the different tractor working configurations, for simplicity's sake, with a correspondent name as follow:

- Min30: configuration with 30% balance at the front and 70% at the rear realised with the lowest possible load
- Min60: configuration with 60% balance at the front and 40% at the rear realised with the lowest possible load
- GVW30: configuration with 30% balance at the front and 70% at the rear realised with full load
- GVW40: configuration with 40% balance at the front and 60% at the rear realised with full load
- GVW60: configuration with 60% balance at the front and 40% at the rear realised with full load

The process immediately following these modal optimizations is a nested optimization relating to the sizing of the hydro-pneumatic hardware that defines the stiffness of the suspension. Various hydraulic parameters, in fact, affect the system stiffness. It is therefore necessary to size them correctly to optimize the overall impact on the vehicle. This translates into the search for the design that would allow the achievement of all the target stiffness requirements (found with the various modal analyses considered), as the suspension preload varies. In addition to this objective, we also considered the minimization of system costs. Note that we only considered the hydraulic accumulators, so the objective on costs minimization translates into the minimization of the accumulator volumes.

We will use the modal damping requirements in Loop 3 for the selection of the correct damping valves.

Figure 1.84 shows the nested optimization workflow related to the hydro-pneumatic system. This workflow has as input the suspension stiffness requirements as a function of preload, as defined by the modal analyses. These are also constant parameters, not to be varied within the workflow. On the other hand, the variable inputs are all the characteristic parameters of the hydro-pneumatic system that influence its stiffness. **Eq (1.63)** shows the expression of the equivalent stiffness of the suspension cylinder its neutral position (i.e. for $x = 0$), already shown in **Section 1.2**. Note that the stroke of the piston x is positive for a cylinder compression and negative for a cylinder extension.

$$k_{susp} = n\frac{\left(F_0 + p_{1_R}A_R\right)^2}{p_{0_P}V_{0_P}} + n\frac{\left(p_{1_R}A_R\right)^2}{p_{0_R}V_{0_R}} \tag{1.63}$$

The hydraulic parameters considered as variable inputs are:

- V_{0_R} rod side accumulator volume
- p_{0_R} gas precharge in the rod side accumulator
- V_{0_p} piston side accumulator volume
- p_{0_R} gas precharge in the piston side accumulator
- A_R cylinder differential area, i.e. the effective area of the rod side
- p_{1_R} initial (levelling) rod side pressure

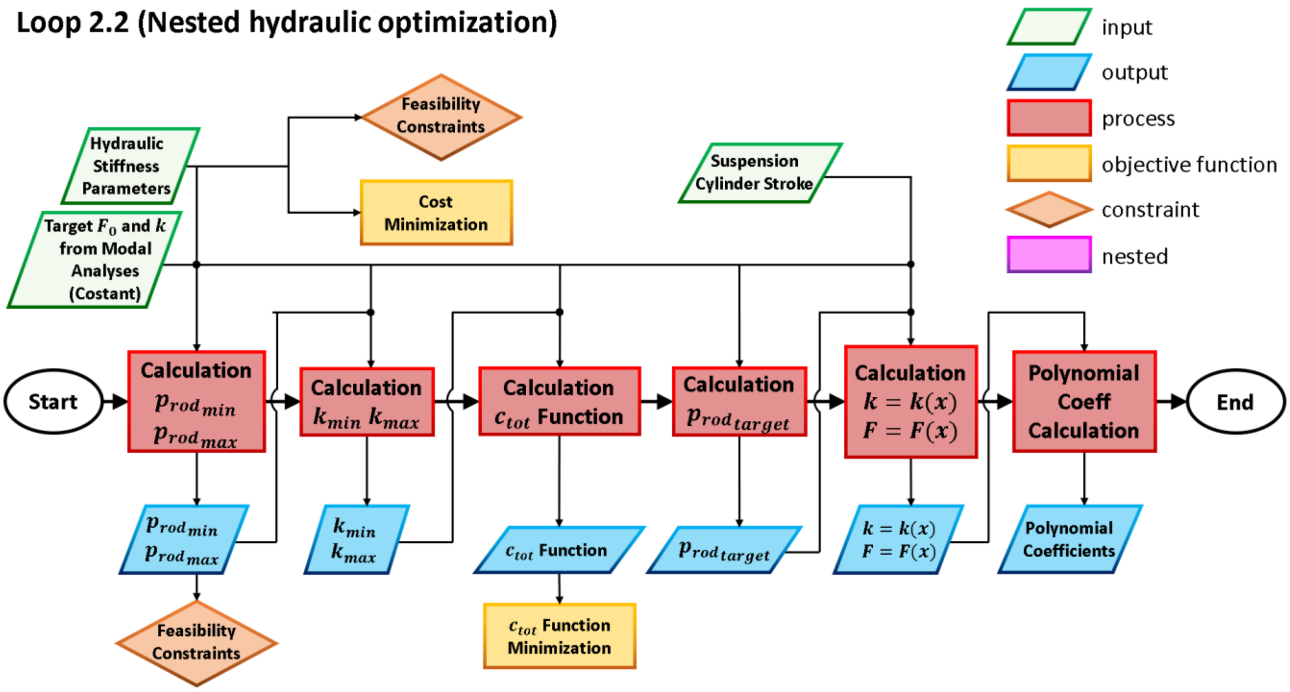

Figure 1.84: Scheme of the hydro-pneumatic system optimization

Note that we did not let the accumulator volumes 'free' to vary in continuous, but we considered only certain discrete values taken from the manufacturers' catalogues. We then associated each volume with its corresponding price to be considered in the cost minimization function.

The first process of this workflow is the calculation of the minimum and maximum levelling pressure for the considered design, which are necessary for the evaluation of the minimum k_{min} and maximum k_{max} available stiffness. Considering all the other parameters as constant, **Eq. (1.63)** highlights how the maximum stiffness can be obtained for the maximum $p_{1_R}$and the minimum stiffness is obtained with the minimum p_{1_R}.

As previously said, the minimum rod side levelling pressure is defined by the minimum pressure that can occur in the system, which is limited by the hydraulic accumulators. The working pressure of the accumulator, in fact, must not fall below a certain threshold, so as not to empty the accumulator itself and risk damaging the diaphragm. This threshold depends on the precharge pressure of the gas in the accumulator. Naming p_0 the gas precharge pressure and p_1 the working pressure of the accumulator, **Eq. (1.64)** repots the condition to be verified.

$$p_1 \geq \frac{p_0}{0.9} \tag{1.64}$$

For this reason, the minimum levelling pressure is the starting pressure for which exactly $p_1 = p_0/0.9$ is obtained when the cylinder is fully compressed or extended. Obviously, it is necessary to carry out this check for both the piston side and rod side accumulators, and then select the lowest value obtained.

On the other hand, the maximum rod side levelling pressures is defined by the maximum pressure obtainable from the supply unit (defined by its pressure relief valve). This maximum rod side levelling pressure is thus equal to the same maximum supply pressure, or to pressure for which the maximum piston side pressure is obtained. We exploited the piston equilibrium (**Eq. (1.65)**) to verify this aspect.

$$F_0 + p_{1_R} \cdot A_R = p_{1_P} \cdot A_P \tag{1.65}$$

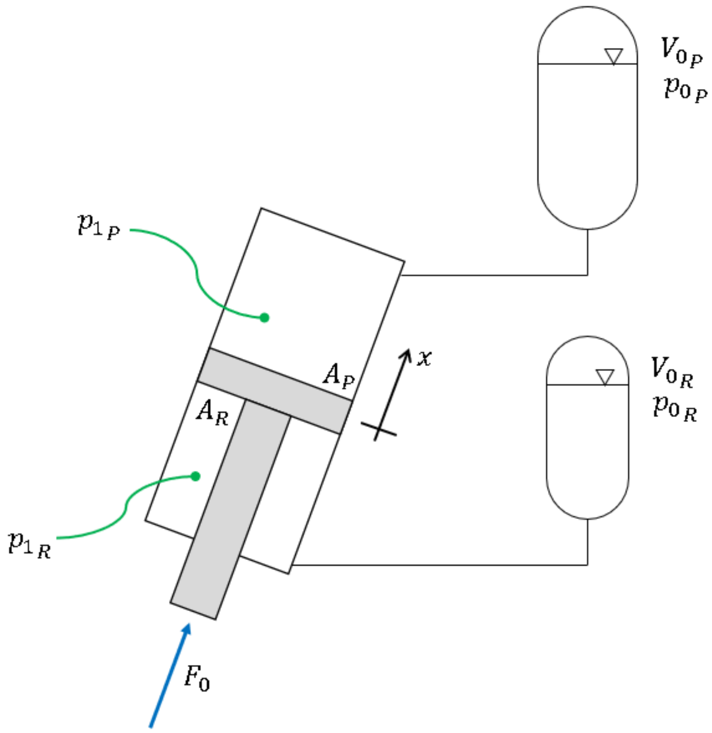

Figure 1.85: Piston equilibrium in the suspension cylinder

Once the minimum and maximum levelling pressures of the considered design have been found for all the working configurations, the minimum and maximum stiffnesses obtainable in the neutral position can be assessed. The optimizer then compares these values the target stiffnesses defined by the modal analyses. If the target stiffness for a given working configuration is within the range defined by the minimum and maximum stiffness, then this target stiffness can be attained.

As mentioned, finding the design that realises, if possible, all the target stiffness requirements defined by the various modal analyses is the main objective function of this workflow. We thus introduced so-called *penalty function* c_{tot} to do so. This penalty function was defined to be equal to zero only if all target stiffnesses can be achieved. Otherwise, the higher the value of c_{tot}, the greater the distance to the target stiffness values.

Furthermore, we also introduced a “weight” for each working configuration. In fact, the achievement of the target stiffnesses is more important for low-load configurations, while this achievement is less impactful with the vehicle and the front suspension heavily loaded.

Eq. (1.66) shows the expression of this penalty function.

$$
\begin{aligned}
c_{tot} = w_{EVW} \cdot \frac{1}{2} \cdot \left(1 + sign\left(k_{EVW_{min}} - k_{EVW_{target}}\right)\right) \cdot \frac{\left|k_{EVW_{min}} - k_{EVW_{target}}\right|}{k_{EVW_{target}}} + w_{EVW} \cdot \frac{1}{2} \\
\cdot \left(1 + sign\left(k_{EVW_{target}} - k_{EVW_{max}}\right)\right) \cdot \frac{\left|k_{EVW_{target}} - k_{EVW_{max}}\right|}{k_{EVW_{target}}} + \cdots + w_{GVW60} \cdot \frac{1}{2} \\
\cdot \left(1 + sign\left(k_{GVW60_{min}} - k_{GVW60}\right)\right) \cdot \frac{\left|k_{GVW60_{min}} - k_{GVW60}\right|}{k_{GVW60_{target}}} + w_{GVW60} \cdot \frac{1}{2} \\
\cdot \left(1 + sign\left(k_{GVW60_{target}} - k_{GVW60_{max}}\right)\right) \cdot \frac{\left|k_{GVW60_{target}} - k_{GVW60_{max}}\right|}{k_{GVW60_{target}}}
\end{aligned} \tag{1.66}
$$

Each term of the c_{tot} function relates to a specific control. For example, the first term in **Eq. (1.66)** checks that the EMW k_{min} is less than the k_{target} of that configuration. If this is true, the entire term is zero. If not, its value is defined by both the "distance" between the obtainable k_{min} and the k_{target}, and the weight (w_{EVW}) of that specific configuration. The second term is constructed in a similar manner but relates to the control that the obtainable EVW k_{max} is greater than the k_{target} of that configuration, and so on for all other working configurations.

Having defined the penalty function in this way, it is then possible to translate the search for the design that best satisfies the requirements on the k_{target} precisely with the minimization of this c_{tot} function. This is precisely the second objective function of the hydro-pneumatic nested optimization.

Once the penalty function has been evaluated, we moved on to the next processes, which is the calculation of the rod side levelling pressures that realise (if possible) the target stiffnesses.

Finally, it is also necessary to derive the entire suspension stiffness curve as a function of piston travel, $k = k(x)$. The stiffness of a hydro-pneumatic suspension system, in fact, is not constant like an ideal mechanical spring, but is variable with the compression or extension of the suspension itself [1].

Eq. (1.63) reports the system stiffness with the suspension cylinders in neutral position, i.e. for $x = 0$. **Eq. (1.67)** shows the expression of the system generic stiffness, evaluated as a function of the piston position x.

$$
k(x) = n \frac{\left(F_0 + p_{1_R} A_R\right)\left(\frac{p_{0_P} V_{0_P}}{F_0 + p_{1_R} A_R}\right)^n}{\left(\frac{p_{0_P} V_{0_P}}{F_0 + p_{1_R} A_R} - x\right)^{n+1}} + n \frac{\left(p_{1_R} A_R\right)\left(\frac{p_{0_R} V_{0_R}}{p_{1_R} A_R}\right)^n}{\left(\frac{p_{0_R} V_{0_R}}{p_{1_R} A_R} + x\right)^{n+1}} \tag{1.67}
$$

Note that **Eq. (1.63)** can be derived from **Eq. (1.67)** by imposing $k(x)|_{x=0}$.

It is thus necessary to consider how this stiffness varies over the entire stroke of the suspension cylinder. This process allowed to derive the polynomial coefficients of this curve, which can then be inserted into the MSC Adams® numerical models of the next loop. As anticipated, it is not possible to consider the hydro-pneumatic system in Adams®, but it is necessary to properly calibrate springs and equivalent dampers, using these coefficients. The curve described by **Eq. (1.67)** have been therefore approximated to a fourth-degree polynomial, whose coefficients are also outputs of the nested workflow.

Having defined two objective functions, the results of this nested optimization allowed us to find a Pareto frontier. We indeed considered both the penalty function minimization and the cost minimization, i.e. the accumulator volumes. The selection of the most suitable solution is then up to the user, considering the trade-off between cost and performances.

At this point, therefore, thanks to Loop 1 and 2, we could define both the geometry of the suspension architecture and the stiffness of the hydro-pneumatic system. What is still missing is the information regarding the damping part of the hydraulic circuit, which will be the main subject of Loop 3.

1.4.3 Loop 3

As anticipated, we defined the Loop 3 to complete the optimization of the entire independent suspension. In particular, the damping aspects of the hydro-pneumatic system are the subjects of this last part. These features should be dimensioned to meet the requirements of the modal analyses and, at the same time, consider the overall performances of the vehicle. The optimal damping values found with modal analyses, in fact, may not be exactly those suitable for improving the vehicle dynamic performance, especially considering different dynamic aspects, i.e. comfort, handling and traction.

Considering the hydraulic damping blocks also shown in **Figure 1.86**, we exploited the minimum and maximum values of optimum damping (obtained from the various modal analyses for different working configurations) to realize the general dimensioning of the block.

Always considering the nomenclature used in **Figure 1.86**, the minimum damping condition is realised when the proportional valve *V5* (and *V6*) is fully open. We thus decided to size this valve *V5* (and *V6*) to match the minimum target damping value in its fully open position.

On the other hand, the maximum damping achievable with such a block occurs when the proportional valve *V5* (and *V6*) is totally closed, and all the flow passes through orifice *O5-2* (and *O6-2*). In a similar way, we thus exploit the maximum target damping value to define the dimensioning of orifice *O5-2* (and *O6-2*).

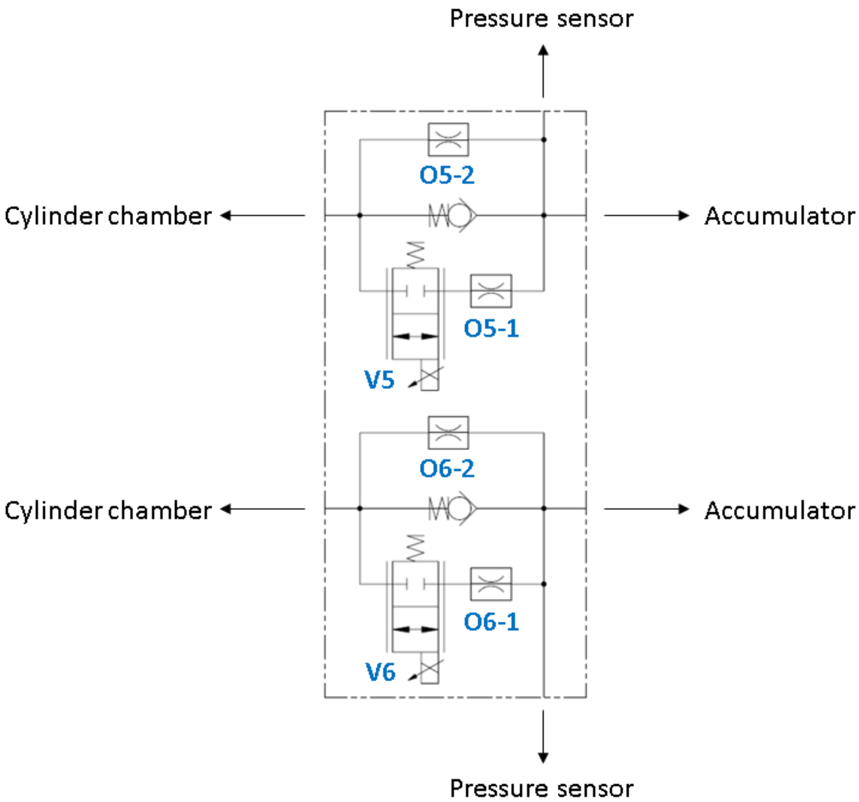

Figure 1.86: ISO diagram of the AFS damping block

In this way, we could ensure to reach all the intermediate damping values between the minimum and maximum values by simply varying the opening of the proportional valve *V5* (and *V6*).

Note that the target damping values found with the modal analyses are constant values, which generate a linear contribution of the damping force with the suspension deformation velocity ($F = c \cdot \dot{x}$). However, as already seen, the actual damping given by a hydraulic system is not a constant value.

As already said, the hydraulic damping contribution can be described by the hydraulic resistance equation (**Eq. (1.68)**), which has been derived from the Bernoulli's principle.

$$Q = C_d \cdot A \cdot \sqrt{\frac{2\Delta p}{\rho}} \tag{1.68}$$

It is precisely the crossing flow rate that generates the pressure difference between upstream and downstream of the orifice. The differential pressure Δp is then proportional to the square of the flow rate Q that pass through the hydraulic resistance.

$$\Delta p \propto Q^2 \tag{1.69}$$

Figure 1.87 depicts the hydraulic cylinder connected to two accumulators. In this case, the flow rate through the equivalent orifice defining the damping of the system is linearly proportional to the suspension piston velocity $\dot{x}$. The flow rate exiting (or entering) the cylinder piston side is equal to $A_P \cdot \dot{x}$, while the flow rate entering (or exiting) the rod side is equal to $A_R \cdot \dot{x}$. It is then easy to see how the damping force is proportional to the square of the suspension deformation rate $\dot{x}$.

$$F \propto \Delta p \propto \dot{x}^2 \tag{1.70}$$

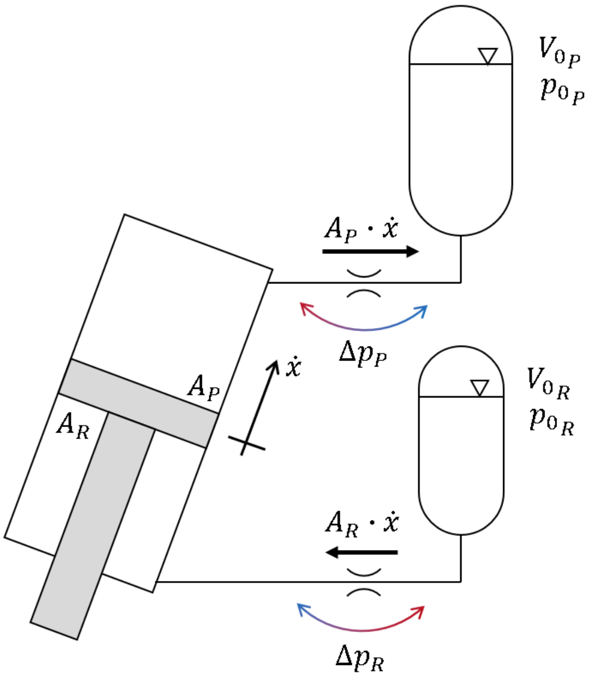

Figure 1.87: Damping effects in a hydraulic cylinder connected with two accumulators

For this reason, it was necessary to translate the constant damping requirements obtained from the modal analyses into a quadratic damping force curve, which can be exploited to size the hydraulic circuit.

It is important to note that we carried out the dimensioning of the hydraulic components in the continuous and not in the discrete. This aspect is not a particular problem concerning the orifices for maximum damping thanks to the existence numerous different orifices on the market. The same cannot be said for the sizing of proportional valves. There are not proportional valves of any size, but only with well-defined characteristics. It is thus necessary to consider this aspect, comparing the continuous sizing with the availability of the actual valves. The valve, or valves, which comes closest to the size that achieves the minimum target damping value will then be chosen.

Figure 1.88 shows the first part of Loop 3 relating, precisely, to the sizing and choice of orifices and valves. Again, the loop has been divided into two parts for convenience. The second part will be inherent to the evaluation of optimal damping for the improvement of the vehicle dynamic performance.

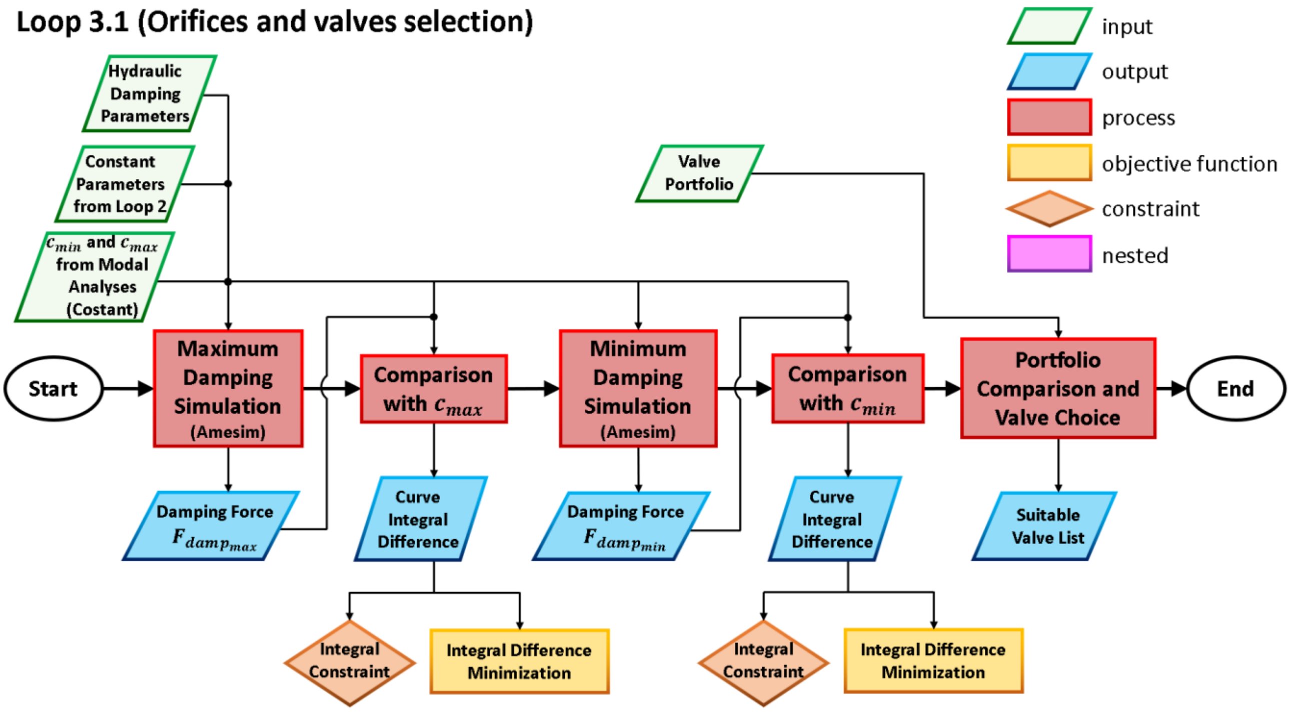

Figure 1.88: Scheme of the first part of Loop 3 for the independent suspension optimization

This first part of Loop 3 has as constant inputs all the hydraulic parameters relating to the stiffness of the system, already defined in Loop 2. This ensures the consideration of all the already optimized aspects of the hydro-pneumatic system. The minimum and maximum damping values found thanks to the modal analyses are other constant inputs. In addition, a portfolio of real valves must also be considered in order to search, within this list, for the valves that come closest to the ideal solution found.

The hydraulic parameters that characterize the damping of the system are instead variable inputs for this workflow, i.e. the diameter of equivalent orifices. This equivalent diameter is the actual diameter of the orifice itself in the case of *OX-2* orifices. On the other hand, this equivalent dimension can be used to trace back to the typical characteristics of the valves in the case of *VX* valves. It is, in fact, very convenient to compare this equivalent diameter with the information usually provided in valve catalogues. This information concerns the flow rate Q and differential pressure Δp at maximum opening of the valve, from which it is easy to trace back to the equivalent outflow area (and therefore the diameter) using **Eq. (1.68)**.

The first process of the **Figure 1.88** workflow is the simulation to provide all the information relating to the maximum damping force curve of the considered design. As mentioned, we considered the valves totally closed in this simulation to force the flow rates to pass through the parallel *OX-2* orifices of **Figure 1.86**. We could then obtain the maximum damping force curve as function of the suspension deformation velocity imposing a ramp as deformation velocity input. The accumulators had been replaced by constant pressure sources not to consider the system stiffness effects in these simulations. Keeping the hydraulic accumulators, in fact, would not have made it possible to separate the contribution of pure damping from the pressure variations caused by fluid volumes entering and exiting these accumulators.

The maximum damping force curve obtained with this simulation can then be compared with the maximum target damping curve. The search for the equivalent diameter that allows precisely such a maximum damping value translates in the minimization of the difference between these two curves, which can be achieved by minimising the difference of the curve integrals. We also introduced a special constraint to ensure that the actual damping force is always greater than or equal to the target one.

Similarly, the following processes concern the numerical simulation to obtain the minimum damping force curve and its comparison with the reference target curve defined by the constant inputs. We then inserted an objective function to minimize of the difference between the integrals of these curves and a constraint to ensure that the actual force curve of minimum damping is always less than or equal to the minimum damping target.

Once these processes had been realised, we could proceed with the selection of the real valve that comes closest to the equivalent orifice diameter found for minimum damping.

Note that the two objective functions, i.e. the minimization of the differences between the integrals for the maximum and minimum damping force curves, are independent of each other. In fact, only the dimensions of the *OX-2* orifices in **Figure 1.86** impact on the former, while the latter depends only on the equivalent diameter of the *VX* valves. For this reason, although we have two objective functions, we will not obtain a Pareto frontier, but only a single optimum solution.

For the sake of symmetry, even considering the complete hydro-pneumatic circuit in **Figure 1.40**, the right and left *VX* valves and *OX-2* orifices on the piston side must be equal. Similarly, *VX* valves and *OX-2* orifices must be equal on the right and left branches of the rod side. Between piston side and rod side, however, it is possible to have differences in terms of equivalent dimensions (considering the different fluid flow rates involved).

Once the optimization defined in this first part of Loop 3 has been realised, the mechanical and hydro-pneumatic dimensioning of the independent suspension is almost completely concluded. The mechanical part relating to the geometry of the suspension architecture was defined in Loops 1 and 2, while Loop 2 and this first part of Loop 3 defined all the hydraulic parameters.

The only missing aspect to be defined is the actual damping values that maximise the different vehicle dynamic performances. The minimum and maximum target damping values used so far, in fact, are not sufficient to ensure the improvement of all dynamic performances.

It is therefore necessary to set a further optimization to define the different optimum damping values to improve the comfort, handling and traction characteristics of the vehicle. In this way, it is possible to identify the optimum *VX* valves opening (**Figure 1.86**). These optimum openings can then be entered into the vehicle's ECU and used in the various working conditions of the tractor. For example, the operator could select the valve opening (and thus the damping) which optimize the comfort or traction characteristics for on field operation. On the other hand, it is better to set the optimum damping for the handling characteristic for manoeuvring on road.

This is precisely the aim behind the second part of Loop 3. **Figure 1.89** depicts the scheme of this optimization.

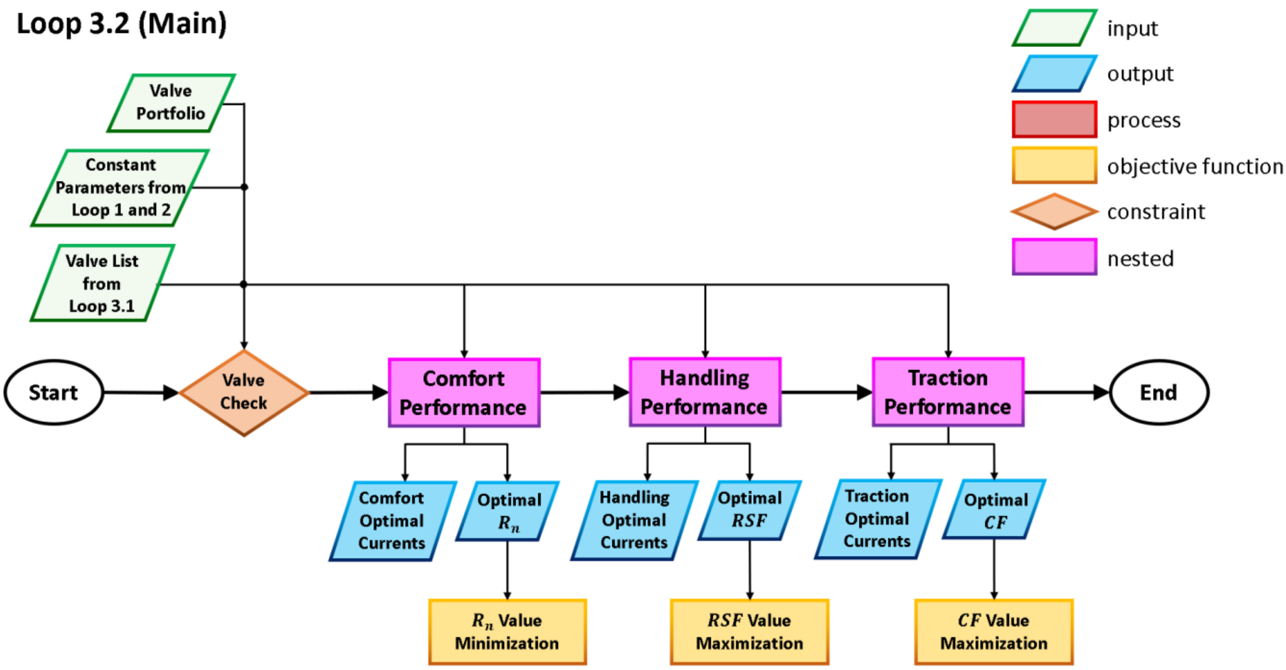

Figure 1.89: Scheme of the first part of Loop 3 for the independent suspension optimization

The constant inputs of this workflow are all the inputs required for the unambiguous definition of the independent hydro-pneumatic suspension, which have been optimized in the previous loops.

We decided not to manually enter the characteristics of the chosen valves in the first part of Loop 3, but rather to write these valves and their characteristics into a special **.txt* file to automate the process. In this second part, the optimizer considers all the possible combinations of piston and rod side valves. However, only the combinations within the list of chosen valves pass the control positioned as first process in **Figure 1.89**. This is, as said, a simply way of automating the process. If the valve portfolio consists of n valves with their corresponding characteristics, the total number of combinations will be $n \cdot n$ (i.e. n possibilities on the rod side and n on the piston side). Among these, only the optimal combinations pass the control.

The optimizer then proceeds to the nested optimizations of the dynamic performances (i.e. comfort, handling and traction) with the designs that have passed the valve check.

The information regarding the valve supply currents are outputs of these three nested processes. These supply currents define the valve openings that optimize the various dynamic aspects of the tractor. The optimizer has thus defined three pairs of currents, one for the rod side valves and one for the piston side valves, which respectively improve comfort, handling and traction. The corresponding vehicle dynamic performance parameter is the other output of each nested optimization. As mentioned in the introduction of the objective functions, these dynamic performance parameters are:

- the Rn (ride number) value concerning comfort
- the RSF (roll stability factor) value concerning handling aspects
- the CF (contact factor) value concerning traction

These parameters are the subject of the objective functions within the three nested optimizations. The aim is indeed to define the supply currents to improve these performance KPIs. However, we also considered three similar objective functions in the main optimization to search for the best possible valve combination among those available. The optimizer, in fact, defines the optimum currents for dynamic performances for each combination that passes the valve control. Among these, the optimizer must select the best combination of valves and supply currents. Note that there can be one best solution for one reason or another (e.g. the particular opening-current characteristic) but there also cannot if the various combinations are all similar to each other in terms of performance.

Figures 1.90-1.91-1.92 show the logic diagrams of the three nested optimizations relating to the tractor dynamic behaviour where we have also highlighted the different third-party software. Note how these three are all similar in structure. All these three nested optimizations start from the parameters that define the suspension geometry and the hydro-pneumatic system as constant inputs, and from the damping valve supply currents as variable ones. The evaluation of the damping characteristics obtained with precisely the currents considered in the design under consideration is the first process in all three nested optimizations. Once the damping force at these currents has been calculated, the workflow approximates the damping force to a third-degree polynomial to enter in the Adams® multibody model for dynamic performances. As already mentioned, Adams® does not allow to model a hydro-pneumatic system, so we had to replace it with equivalent springs and dampers.

These Adams® models for dynamic simulations, as already mentioned, relate to the ISO 5008 test (carried out at three different speeds according to the ISO standard) concerning comfort, the moose test concerning handling, and the maize cycle on 4-poster test rig concerning traction.

The optimizer then processes the results of these multibody simulations to evaluate the characteristic parameter of interest (Rn, RSF or CF), which is subject to a dedicated objective function. Thanks to this, the optimizer looks for the valve supply currents that optimize each dynamic performance.

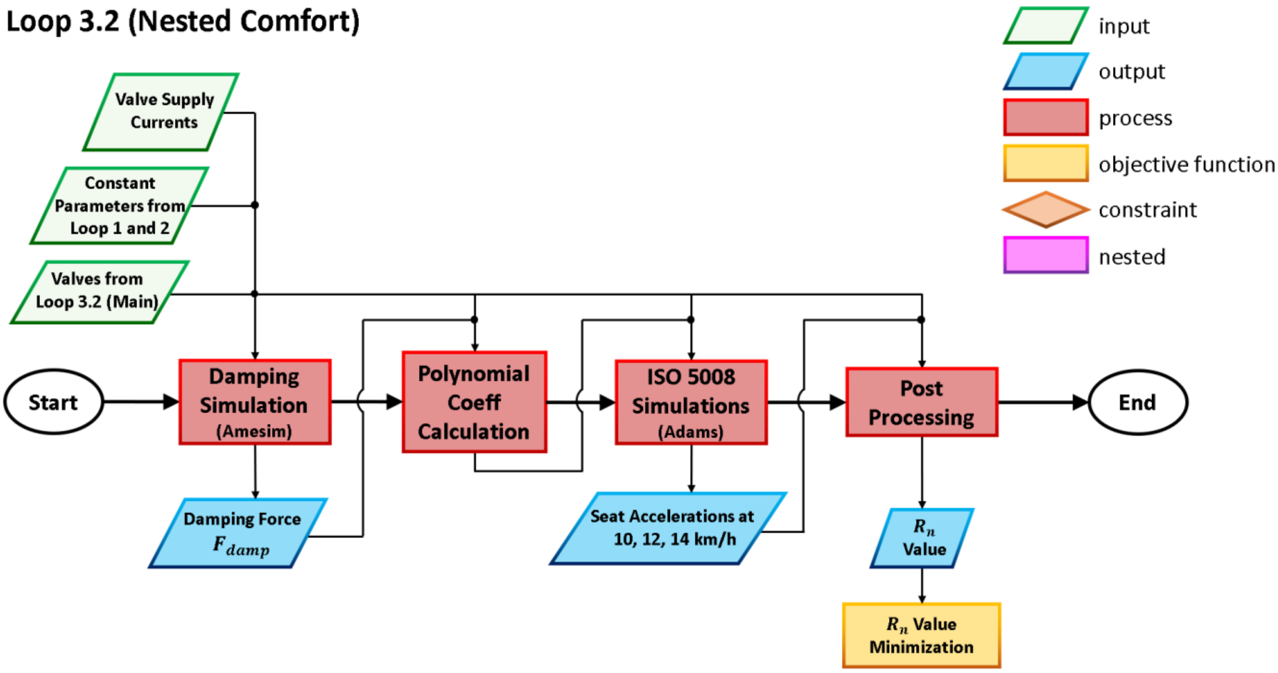

Figure 1.90: Scheme of the comfort nested optimization of the second part of Loop 3

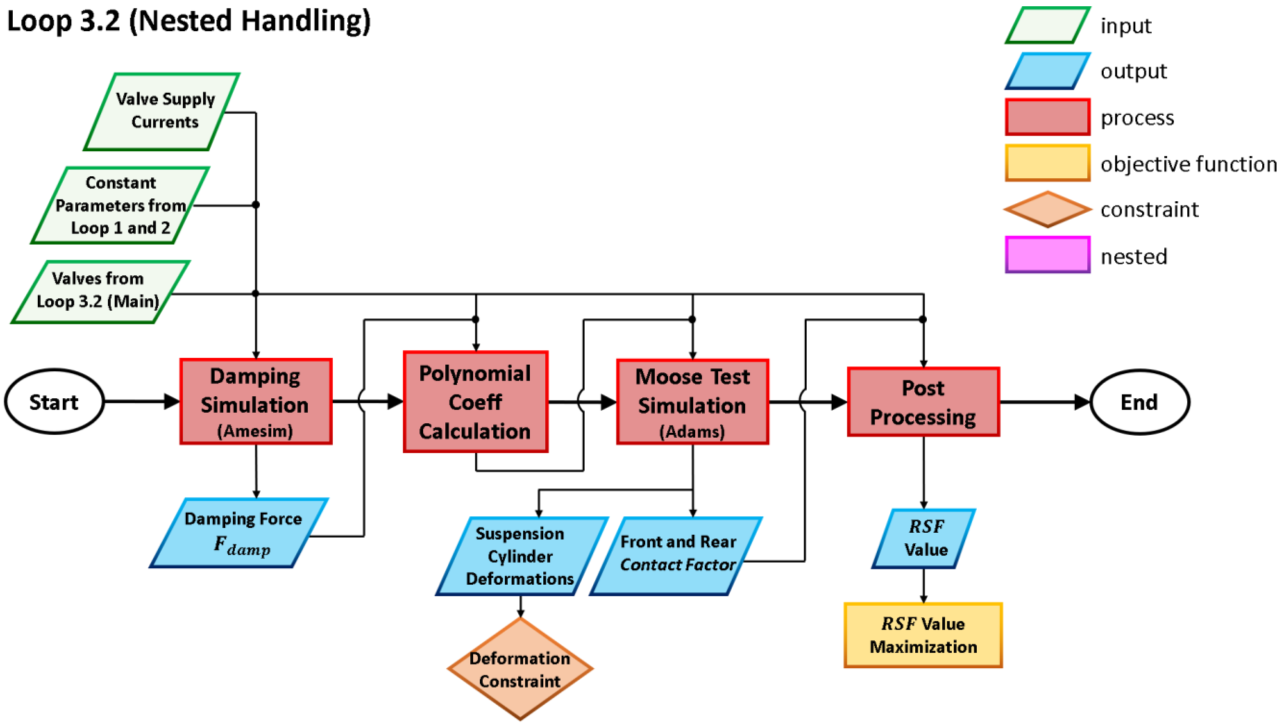

Figure 1.91: Scheme of the handling nested optimization of the second part of Loop 3

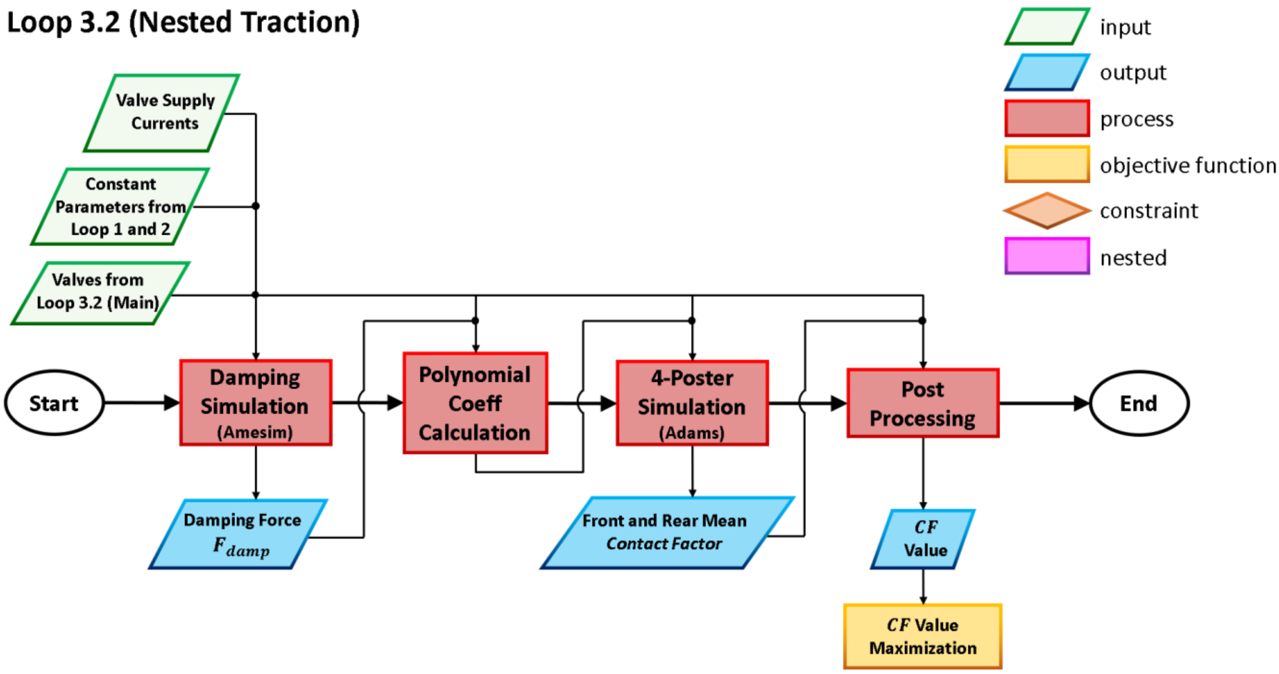

Figure 1.92: Scheme of the traction nested optimization of the second part of Loop 3

It is thus possible to look for the complete optimum solution regarding the hydro-pneumatic independent suspension thanks to the three loops presented in these last paragraphs. In this way, we could define the mechanical and hydraulic aspects to improve the kinematic and dynamic performance of the tractor complete system.

1.4.4 ModeFrontier®

We decided to exploit the capabilities of the commercial software modeFrontier® developed by Esteco S.p.A. to realise the three optimization loops. This software, in fact, allows to manage multi-disciplinary optimization (MDO), like the ones just presented.

ModeFrontier® allows the graphical realization of the optimization workflow(s) through the selection of different icons, which can represent inputs, outputs, processes, constraints or other. These icons are generically called “nodes”. Once selected and inserted into the sketch environment, the user must link together these nodes according to the logical scheme of the optimization, such as those shown in the previous paragraphs.

The user must also appropriately parametrize these nodes. Considering for example an input node, the user must specify the name of the input, the type of input (variable, constant, function of another input, but also scalar or vectorial), the default value, the minimum and maximum, i.e. the minimum value by which it can vary during optimization, and so on.

ModeFrontier® also allows the direct integration of commercial or open-source third-party software via dedicated nodes. It was therefore possible to integrate MSC Adams® or Simcenter Amesim® or Creo® nodes into the workflow without any particular difficulty. In this way we could insert the various numerical simulations to be performed.

We could also insert other processes of any nature, such as inserting parts of code (e.g. to post-process certain results), simple *if* nodes, etc.

The user must then connect each output node to the corresponding process node, always defining its name and type. These outputs, along with the inputs, can then be the subject of various workflow constraints, which must also be entered and defined using a dedicated node. It is, in fact, possible to combine the inputs and outputs connected to a constraint to realize the equation or inequality that characterises the constraint itself.

Finally, the user must introduce the objective function nodes. It is necessary to specify the type of the objective (minimization, maximization or target, i.e. pointing to a specific value to be defined) within these nodes.

Figure 1.93 shows, as an example case, the optimization workflow realised in modeFrontier® starting from the logical scheme of the nested optimization concerning the Loop 3 traction performance (**Figure 1.92**). We have added boxes and corresponding names to highlight the similarity of the structure with **Figure 1.92**.

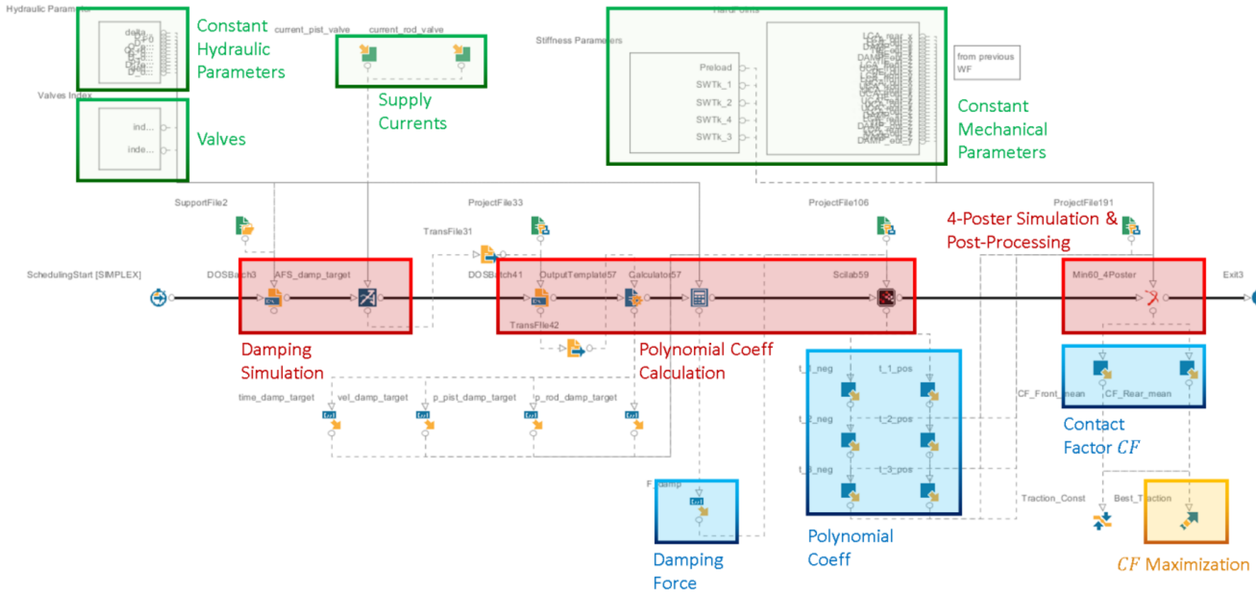

Figure 1.93: ModeFrontier® workflow concerning the traction nested optimization of Loop 3

Note how we decided to merge or divide some processes depending on the node availability and for the sake of simplicity of implementation. The logical structure of the workflow remained completely unchanged.

We thus realized in the same way all the optimization workflows presented above.

Once we had realized the sketch of a workflow, we defined the optimization algorithm to be used in the appropriate node. Some optimization algorithms may be more effective or efficient than others depending on the number of inputs, the number of objective functions or other characteristics of the workflow under consideration.

Some examples of optimization algorithms used are:

- Genetic algorithms (such as MOGA or NSGA-II): these algorithms allow different starting solutions to be evaluated and produce new solutions by recombining them and introducing elements of disorder. The algorithm the evaluate these new solutions choosing the best ones to converge towards 'optimal' solutions. There is no certainty of the effectiveness of this kind of algorithm due to their inherently random nature. However, these algorithms suit multi-objective optimizations very well.
- Gradient algorithms (such as BFGS): these algorithms use an iterative method to look for the optimum by proceeding in the direction indicated by the gradient of the solution, i.e. where the objective function grows (or falls) the most. Obviously, these algorithms require the presence of only one objective function and work well if the starting solution is sufficiently close to the zone of absolute optimum. They are therefore very useful in a second optimization phase, when the first roughing out of the results has already been carried out.
- SIMPLEX algorithm (or simplex algorithm): this is an algorithm that looks for the optimal solution by moving over the so-called response surface of the objective function. This algorithm starts from the polyhedron formed by n evaluations of the function to optimize. Exploiting the value of this function on the n vertices of this polyhedron, the algorithm proceeds by trial and error and step by step to look for a new vertex of the starting polyhedron which replaces the worst vertex at the previous step, i.e. the one where the value of the function is furthest from the objective (e.g. the lowest value if we are looking for a maximization). The process is then repeated until the results converge. **Figure 1.94** shows a graphic example of a SIMPLEX application for a two-dimensional function F(x1,x2). The starting polyhedron is a triangle in this simple case, but the concept can be extended to any n-dimensional function.

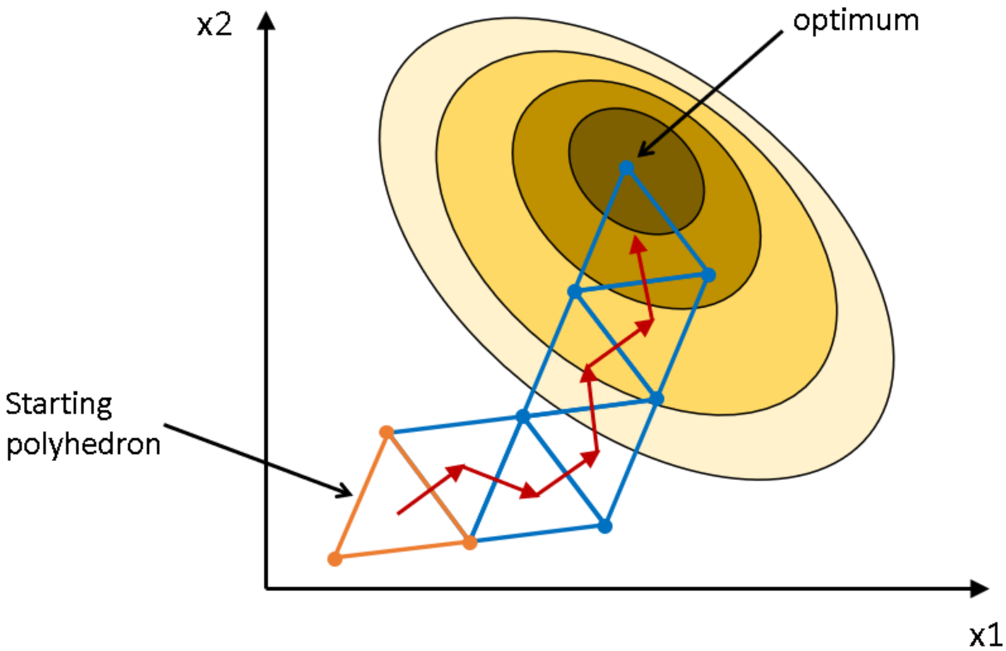

Figure 1.94: Graphical application of the SIMPLEX algorithm

As mentioned, some optimization algorithms require a set of designs to start from, called Design of Experiments (DoE). The number of designs to include in this starting set usually depends on the chosen algorithm, the number of inputs and the number of objective functions. In fact, the size of the DoE should allow the optimizer to "understand" the relationships between input, output, constraints and objective functions. Proper sizing and filling of the DoE allows for more robust and more accurate optimization. **Eq. (1.71)** shows a generally well accepted rule for defining the number of elements of the DoE, where n is the number of variable inputs and o is the number of objective functions.

$$DoE\ size = 2 \cdot n \cdot o \tag{1.71}$$

There are many different algorithms for filling the DoE, and some examples of the most used ones are the following:

- Random Algorithm: this algorithm, as the name suggests, randomly fills the DoE with a user-selected number of designs. Obviously, with both this algorithm and the following ones, the designs created have inputs that respect the defined existence intervals.
- Sobol Algorithm: this is an algorithm known as quasi-random. It indeed imitates the behaviour of Random Algorithm but avoids the possible formation of clusters, i.e. groupings of designs close to each other.
- Uniform Latin Hypercube algorithm: this algorithm also generates random designs but conforms to a uniform distribution. The design space is divided into n intervals having the same probability and a random value is selected for each interval. In this way, a uniform distribution of points in the input space can be generated, minimizing the correlation between them and maximizing the distance between the generated designs.
- Space Filler Algorithm: this is an algorithm used to fill the space of designs, introducing new ones where the minimum distance between the designs already present is maximized. This aspect allows this algorithm to be very useful to generate a distribution to cover the entire design space.

The DoE realization is not only useful as an initial step for certain optimization algorithms. It is also possible, in fact, to exploit a specially generated DoE to study the possible relationships between the inputs and the introduced objective functions by selecting a *DoE Sequence* process. Note that this process is not an optimization but only an evaluation and analysis of the DoE. This allows to perform a sensitivity analysis and find correlations, if any, between two different objective functions, i.e. the improvement of an objective inevitably also leads to the improvement of a second one. Knowing this, it would be possible to consider only one of these objective functions, greatly simplifying the subsequent optimization process. Higher the number of objective functions, in fact, more difficult the optimization. Obviously, the DoE created for this analysis must be quite extensive to be representative of the entire design space.

Once the DoE has been defined, it is necessary to set the characteristic parameters of the chosen optimization process, such as the total number of evaluations to be performed or the number of generations.

In the optimization options, however, it is also possible to select the Self-Initialising or Autonomous modes, which are self-adjusting concerning these characteristic parameters. Using these modes allows not to define all parameters and the starting DoE, but, on the other hand, risks of achieving a less accurate and precise optimization than a manually defined one.

The optimization duration is obviously influenced by the number of designs evaluated and the duration of the single workflow processes. Once the optimization process has been completed, modeFrontier® allows the post-processing of the results in a fairly intuitive way. Starting from the matrix of analysed designs (where the values of inputs, outputs, constraints, and objective functions are entered) it is possible to realise any type of graph that can be useful to highlight the information of interest.

ModeFrontier® is thus the ideal tool for this independent hydro-pneumatic suspension optimization task. The optimization workflows, moreover, can also be used for future activities on axles of similar geometry but installed on different vehicles with different performance requirements thanks to its parametric nature. Obviously, we have designed the workflows for the optimization of a hydro-pneumatic double wishbone suspension with four accumulators, but it is still possible to make a few modifications to the various loops to consider a different suspension system without starting from scratch.

For more details on the optimization algorithms, please refer to the reference texts [36].

Process automatization

As anticipated, the automation of the independent suspension design and optimization was one of the main goals of this activity. We have, in fact, developed the presented methodology in modeFrontier® properly to ensure a high level of process automation. However, it is impossible to fully automate the suspension optimization as it requires some choices from the user.

The user can, in fact, act at the beginning of each loop, for example to adjust some input variation ranges or set different objective/constraint values or introduce info from previous loops or modify the optimization algorithm.

Once this preparatory phase has been completed, modeFrontier® can manage the loop optimization following the defined workflow until it reaches the result convergence or the maximum number of designs.

The user must then act again once the loop has been completed for the result analysis and the consequent selection of the optimal design (or designs). This design (or designs) must then be entered as starting point for the next loop. In many cases, as anticipated and as it will be shown in the next paragraph, the optimization process output is a Pareto frontier that is a set of optimal solutions without a dominating optimal one. For this reason, modeFrontier® cannot automate the optimal solution selection. The user must select the appropriate design (or designs) basing on its suitability concerning the Pareto frontier’s trade-off and the design performances.

1.4.4 Optimization results

This section compares the performances of some designs of particular interest found in the various optimizations with a reference design developed before this activity exploiting the experience of Dana Incorporated's engineering department in the manufacture of suspended axles. Following the company's request, we ran several optimization cycles characterised by different objectives. We initially consider an optimization process keeping the geometry of the suspension architecture as constant. The company, in fact, had already started the prototyping procedures of the solution found by hand exploiting the designers' know-how before the start of this activity. The company thus required us to start from this geometry and optimize only the part concerning the hydro-pneumatic system to improve the vehicle dynamic performances. We then carried out the complete optimization of the entire independent suspension exploiting all the loops presented previously only in a second phase.

We are thus presenting the comparison between:

- the starting solution, defined “by hand” via iteration processes,
- the intermediate solution, with the starting geometry but an optimised hydro-pneumatic system,

- the final optimum solution.

The first graphical comparison shows the Loop 2 results concerning the optimization of the suspension stiffness aspects. As described in detail in the dedicated section, the optimizer defined the optimization of the hydraulic dimensioning starting from the modal analysis requirements in the different working configurations. We decided to consider two optimal solutions since, as mentioned, a Pareto frontier had been found. Considering the two objective functions introduced in the hydraulic optimization of Loop 2, i.e. the minimization of the penalty function c_{tot} and the costs (or accumulator volumes) minimization, we selected the two solutions highlighted in **Figure 1.95**. Note that solution 1 (design 9818) has the same cost (and so the same accumulator volumes) as the starting solution, but with much better performance, while solution 2 (design 4677) has lower cost than 1 but slightly worse performance (neither dominates the other).

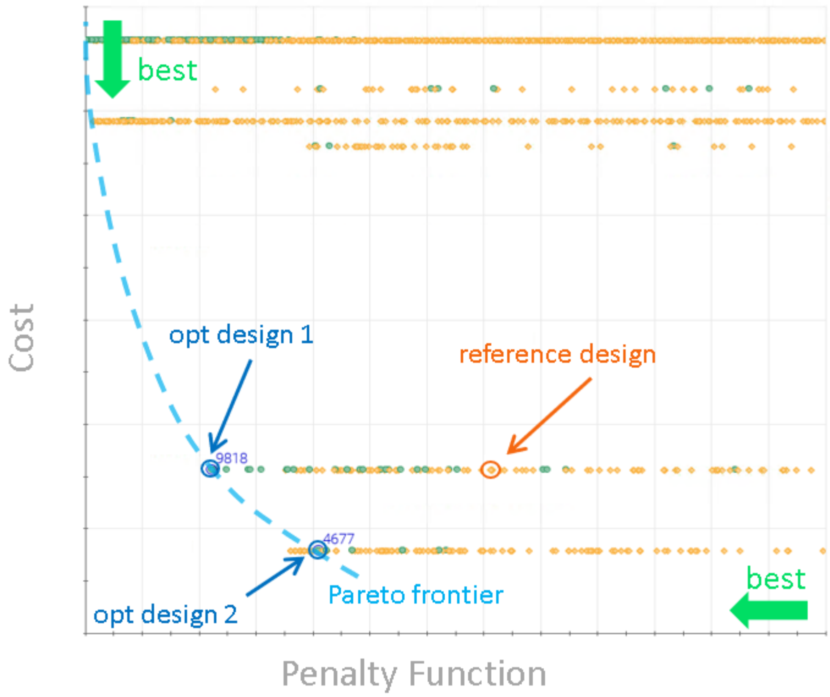

Figure 1.95: Results of the Loop 2 hydro-pneumatic optimization: optimal solutions

It is easy to note how both optimal solutions are way better than the starting reference one concerning the stiffness performances. The penalty function values are, in fact, lower than the reference one.

To show even better the improvement obtained by using the optimization workflow developed with respect to the starting solution,

Figure 1.96 shows the graphical comparison of the stiffnesses range obtainable from the suspension as function of the preload (i.e. all the stiffnesses that the system is capable of guaranteeing simply by varying the levelling pressure on the rod side) to highlight the solution improvement. This stiffness range is, in fact, quite narrow for the 'manual' solution, while it is much wider for the one with optimised hydraulics. Furthermore, the optimized solution includes almost all of the target stiffnesses required from the modal analyses, while some of them are quite far from the starting solution.

Figure 1.96 depicts only the comparison between the starting solution and the optimised design #9818. However, the comparison with the design #4677 and the conclusions that can be drawn from it are totally similar.

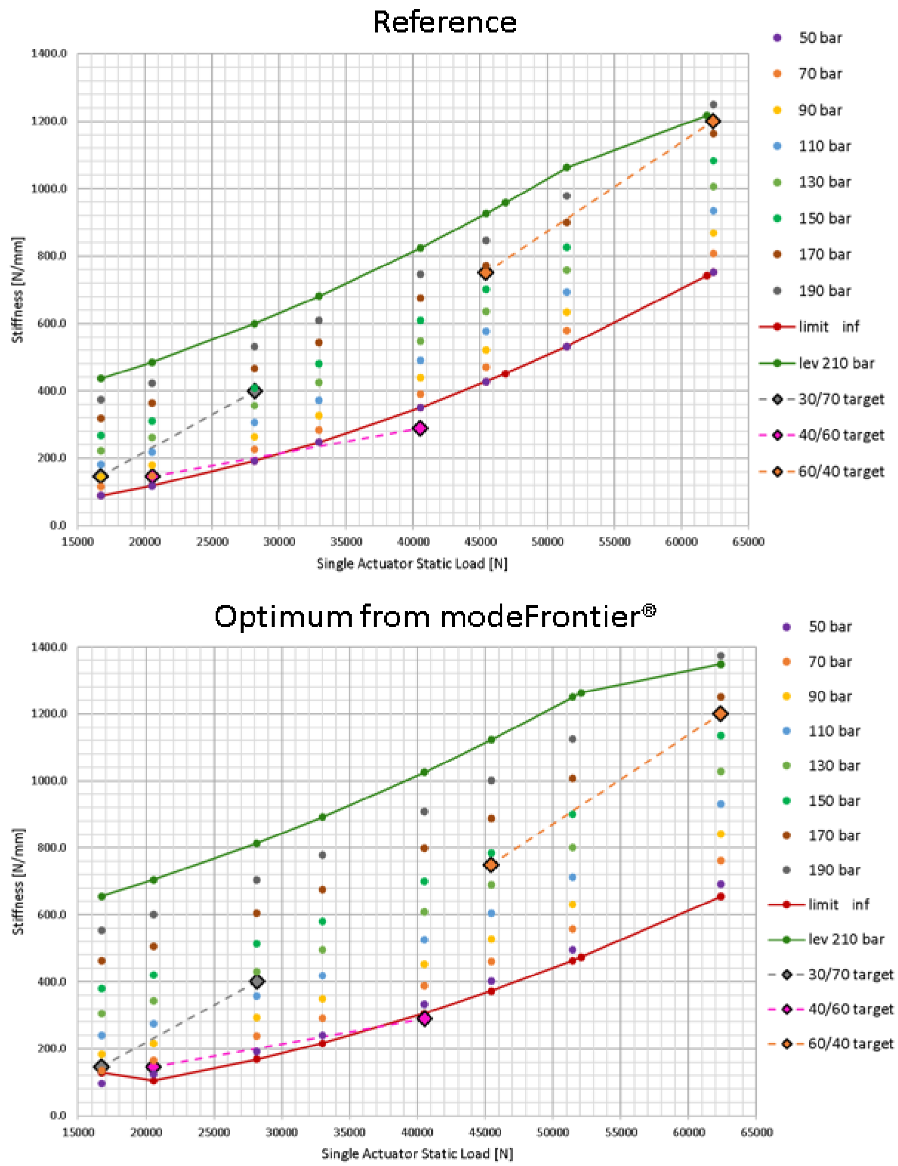

Figure 1.96: Results of the Loop 2 hydro-pneumatic optimization: stiffness obtainable range

The penalty function numerical values highlight the solution improvement. Considering the starting solution as reference, design #9818 allows to reduce the penalty function by 68%, while design #4677 allows to reduce it by 42%. However, design #9818 has the same cost as the reference, while design #4677 leads to a cost reduction of 2.2%.

The company decided to exploit these results for its prototype, modifying the hydro-pneumatic hardware to match design #9818. This design is thus characterised by certain parameters that differ from the starting reference design. In this way, although the company did not vary the starting geometry, it was possible to create a partially optimized prototype. We then subjected this solution to Loop 3 to optimize the damping characteristics and dynamic performances of the entire vehicle.

We then carried out a second optimization including all aspects after completing the first partial one. This allowed us to find a final optimum solution to compare with the prototype. We expected the best improvements concerning the suspension kinematics as it was the only non-optimized aspect for the prototype.

Table 1.1 shows a comparison of the kinematic performance parameters between the final optimum solution and the partially optimized prototype. We used the percentage differences from the latter's reference values to highlight the improvement of the final optimal solution.

Table 1.1: Percentage differences concerning the kinematic performances between the optimal solution and the reference prototype

RSF	Max Bump Steering	Camber Loss	
+7.7%	-29.4%	-4.7%	-11.2%

As expected, it is easy to note how the kinematic characteristics of the fully optimised solution are significantly better than the prototype with fixed geometry. This is precisely because the kinematic aspects of the reference solution had not been optimised, but only found thanks to the experience of the Dana Incorporated engineering department. These results highlight the effectiveness of this approach.

Once the geometry of the final optimum solution had been fixed through Loop 1 and the first part of Loop 2, it was possible to optimize the hydro-pneumatic system (according to the requirements of the modal analyses) and the dynamic performances of the complete vehicle. This step is necessary precisely because the optimizer modified the suspension geometry, and so the suspension loads, and so the vehicle eigenmodes. The accordingly modification of the stiffness and damping requirements from the modal analyses implied a new optimal dimensioning of the entire hydro-pneumatic system.

After concluding all the loops with this final optimum solution, we can report the percentage comparison of the dynamic results with the reference prototype (**Table 1.2**).

Table 1.2: Percentage differences concerning the dynamic performances between the optimal solution and the reference prototype

Rn (Comfort)	RSF (Handling)	CF (Traction)
+2.7	+1.8	+0.5

The dynamic performances of the optimized solution are not unequivocally better than the prototype ones. In particular, vehicle comfort is slightly worse than in the prototype, while handling and traction are slightly better. We can explain this result noting that we used the workflows to optimize both hydraulics and vehicle dynamic behaviour for the prototype too. It would therefore have been optimistic to expect improvements such as those obtained on the kinematic aspects.

Furthermore, note that we made this comparison with the final optimum solution mainly for reasons of analysis completeness. There were, in fact, no real interest from the company, since the partially optimised prototype had already been defined and realised. For this reason, it was not possible to carry out the second round of optimizations in a particularly thorough manner, mainly due to time issues. For these reasons, we could have further improved the final optimum design with more detailed optimizations.

Anyway, it was possible to find a solution that was significantly better than the prototype in terms of kinematic characteristics and still comparable in terms of dynamic performance even with a non-detailed optimization. Furthermore, note that the prototype had been partially optimised. If we had considered a totally "manual" solution, the optimization workflow would have led to even greater improvements even in the dynamic aspects, comparable to those obtained on the kinematics.

The results presented once again underline the effectiveness of the optimization process presented. Obviously, the development of the various loops presented was not immediate and we spent time to complete it, but we now have a tool capable of optimizing an entire hydro-pneumatic independent suspension system from the requirements imposed by the user. Parallel to this, the methodology and concepts behind this workflow have been also studied, so that, through small modifications and adaptations, it can easily be adapted to different suspension types, both in terms of architecture and in terms of stiffness and damping characteristics.

1.5 Vehicle Real Time modelling

Analysing the optimization workflow presented in the previous paragraph, we realised how the length of certain numerical simulations could affect the efficiency and effectiveness of the optimization process itself. In particular, the longest simulations are clearly the multibody ones used in Loop 3 to evaluate the dynamic performances of the vehicle in terms of comfort, handling and traction. These simulations may last minutes or tens of minutes for each design. It is thus easy to imagine how the total time required to complete the entire process can be decidedly high. It was, in fact, necessary to reduce the total number of designs to a fixed number to realize the optimization in a non-prohibitive time. However, this design reduction could have led to a less effective process if the optimization had stopped before converging to the optimum solution.

Within this context, we started an activity in collaboration with Siemens, to investigate the capabilities of Simcenter Amesim® in developing a complete vehicle model capable of real time simulations to replace the slower multibody simulations in the optimization process.

The starting point was the lumped parameter and multibody model of the vehicle developed in Amesim® presented in a previous paragraph. As said, the hydro-pneumatic suspension system connected directly to the 3D axle mechanics is also present in this model. However, hydraulic circuits are not perfectly suitable for real-time modelling due to their high frequencies characteristic of these systems. Hydraulic real time modelling is possible but requires either a considerable simplification of the system (which can lead to differences in behaviour) or the usage of neural networks (which must be programmed and trained).

The modelling of the hydro-pneumatic system was therefore replaced with an equivalent spring-damper system appropriately calibrated using lookup tables. In this way, it was possible to both faithfully reproduce the shock-absorbing behaviour of the hydraulic circuit and facilitate the transformation process into a real time model. This substitution allowed also to align this model to the Adams® ones, where there are equivalent springs and dampers. Similarly to what we had done for the Adams® models in the Loop 3 optimization, we inserted the $F_k = F_k(x)$ and $F_c = F_c(\dot{x})$ relations within the equivalent Amesim® spring and damper.

As already highlighted, a comparison with the Adams® multibody model for numerical alignment revealed a difference in the modelling of the tire-soil contact. The discussion presented in this chapter, however, turns out to be valid regardless of this difference in modelling which, obviously, remains even if we obtain a real time model developed in Simcenter Amesim®.

The following paragraphs then present the steps of the methodology followed to simplify the complete vehicle model until obtaining a model capable of Real Time simulations with fixed integration step. Finally, we are reporting a numerical comparison for the validation of the model and the methodology itself.

1.5.1 Kinematics tables generation and validation

The first logical step of the proposed methodology is the creation of several kinematics lookup tables of the suspension and their subsequent numerical validation. These lookup tables are necessary to replace the 3D suspension kinematics model, while ensuring the correct response to pure bounce, pure roll, or pure steer input.

A Simcenter Amesim® tool named *K&C* (*Kinematics and Compliance*) *Data Generator* was used for these lookup tables creation. This tool works as a virtual test bench for the examined suspended axle. The inputs for the K&C Data Generator are thus the suspension type and the hardpoints coordinates. This tool already provides a hardpoints template for McPherson and Double Wishbone suspensions, as the examined one, but it is also possible to create a template for other types.

The hardpoints coordinates must refer to the left wheel and must be expressed in the chassis reference frame. With reference to **Fig. 1.97**, the hardpoints to be defined for a double wishbone suspension are the following*:*

- A: wheel center
- B: center of tire contact patch
- C1: upper wishbone link with chassis (external)
- C2: upper wishbone link with chassis (internal)
- D: spindle link with lower wishbone
- E1: lower wishbone link with chassis (external)
- E2: lower wishbone link with chassis (internal)
- M: spindle link with tie rod of steering system
- N: tie rod link with steering rack body or cylinder
- K: spindle link with upper wishbone

- R1: damper lower link with spindle
- R2: dumper upper link with chassis
- W: external point defining the wheel rotation axis

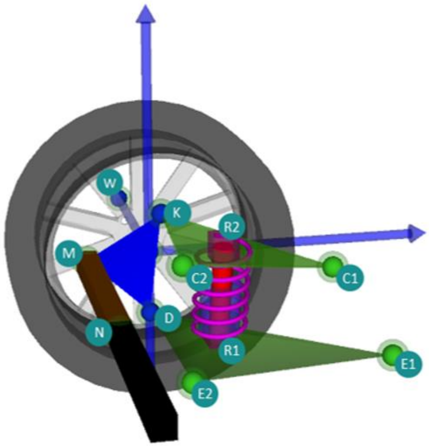

Figure 1.97: K&C template for double wishbone suspension

Note that these points are the same as those highlighted in **Figure 1.74**. The only difference is the use of a different nomenclature. In this case, in fact, we kept the nomenclature used in Simcenter Amesim®, whereas previously we used the Dana Incorporated nomenclature.

Once the information regarding the suspension geometry is entered, it is necessary to set the variation range for vertical wheel displacement and steering rack displacement and the intermediate steps to analyze the suspension behaviour. This step defines the total number of combinations of vertical displacement and steering displacement to consider, so that is the total number of batch runs for the virtual bench. The total number of runs is thus $n \cdot m$ where m is the dimension of the vertical displacement vector and n is the dimension of the steering rack displacement vector.

The outputs of this tool are the 3D lookup table for the suspension kinematics parameters as a function of the vertical wheel displacement and the steering rack displacement. These kinematics parameters are the toe angle, the camber angle, the dive angle, X and Y displacement, the damper length, and the damper length variation. There are 14 lookup tables, 7 for the left wheel and 7 for the right one. As anticipated, the subsequent step is the numerical validation of the newly created kinematic lookup tables.

Both the starting multibody model of the vehicle and the so-called functional model where the kinematics lookup tables are entered were considered in the same Simcenter Amesim® sketch to facilitate the comparison. This functional model is based on a specific sub-model (VDCAR15DOF1 [31]) available in the Vehicle Dynamics library of the software. This element represents the vehicle chassis with several connection ports for the vehicle subsystems (wheels, transmission, brakes, etc). The input elements and sensors of the K&C demo are replicated for both models. This allows considering the same combination of pure bounce, pure roll, and pure steer for both of them. Furthermore, both the models are clamped.

Figure 1.98 depicts the comparison of some suspension kinematics parameters of the two models with a pure bounce input, where toe, camber, and caster angles are reported for the left wheel. The results for the right wheel are obviously similar, so they were not reported in figure. It is easy to note that the graphs are almost perfectly aligned. Similar results were obtained with a pure roll input, a pure steer, and with a combined input.

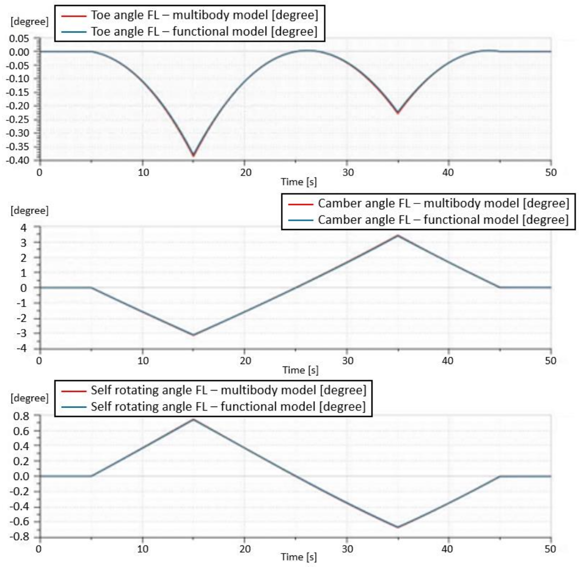

Figura 1.98: Confronto del comportamento cinematico della sospensione tra modello 3D (in rosso) e *functional model* (in blu)

The kinematics lookup tables are thus validated, and the kinematics behaviour of the functional model is aligned with the multibody model one.

1.5.2 Vehicle dynamics integration

The following steps regard the introduction of the dynamic aspects in the functional model, like gravity, masses, inertias, and the tire model.

Firstly, all the information related to masses and inertias was introduced into the simplified functional model. This passage was repeated for the following main system components:

- sprung mass m_{sp}
- tire and wheel structure m_{wheel_f}, m_{wheel_r}, m_{strut_f}, m_{strut_r}
- front axle m_{axle}
- suspension wishbones $m_{wishbone_{low}}$, $m_{wishbone_{up}}$
- steering cylinder and links $m_{steer_{cyl}}$, $m_{steer_{link}}$

The first model considered for the vehicle dynamics validation was a Comfort Bench Model, which was used only for the analysis of the vertical dynamics. Both the multibody model and the functional one were subjected to a frequency sweep displacement of the front wheels to evaluate the frequency response.

In addition to the entering of masses and inertias into the VDCAR15DOF1 element of the functional model, it was necessary to also include the tire vertical stiffness, the tire lateral and longitudinal stiffness, the road vertical excitation and its connection to the vehicle. The tire parameters were entered in the model from the datasheet or the correspondent *.tir file.

Moreover, the equilibrium for the functional model was calculated to evaluate the vertical loads on the front and rear axle. This information allows to estimate the loaded wheel radius.

While this aspect is self-adjusted in the 3D model, the equilibrium guestimate at the start of the simulation turns out to be a fundamental step for the functional model to ensure the system stability and avoid settling motions.

However, this is a complex system with many components. It is thus impossible not to make certain simplifications, especially concerning the moments of inertia and the positions of the centres of mass of the suspension elements. Moreover, some elements of the suspension geometry do not uniquely belong to the sprung or unsprung mass. These are, in fact, intermediate elements between these, such as the suspension wishbones or steering links, which on the one hand are connected to the wheel upright assembly and on the other to the sprung axle body. We thus introduced the term $perc_{sprung}$ to represent the mass percentage of these elements that should be considered as sprung mass. The remaining percentage $\left(1 - perc_{sprung}\right)$ belongs to the unsprung mass.

The first logical step is the identification of the system centre of gravity, which can be estimated as the centre of gravity of a two particles system (**Figure 1.99**), representing the sprung mass of the tractor without the front axle and the group formed by the axle body and all the other suspended components. For simplicity's sake, as anticipated, we did not consider the positions of the individual components (also because they were not precisely known at the design stage), but we considered them have as concentrated in the centre of gravity of the axle body. Note that this assumption is not particularly impactful, since the masses are relatively small compared to the others (tractor and axle). Moreover, all these masses are symmetric with respect to the longitudinal axis of the vehicle.

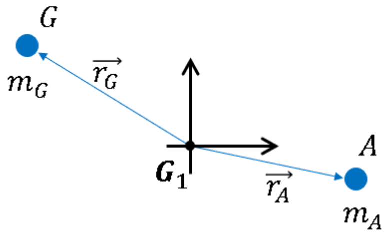

Figure 1.99: Two particles system, used to estimate the system CoG

Eq. (1.72) defines the system centre of gravity.

$$\begin{pmatrix} x_{G_1} \\ y_{G_1} \\ z_{G_1} \end{pmatrix} = \begin{pmatrix} 0 \\ 0 \\ 0 \end{pmatrix} = \frac{\sum m_i \vec{r_i}}{\sum m_i} = \frac{m_G \overrightarrow{r_G} + m_A \overrightarrow{r_A}}{m_G + m_A} \tag{1.72}$$

The terms $\overrightarrow{r_G}$ and $\overrightarrow{r_A}$ concerning the positions of the centre of mass of the tractor and axle are known from the vehicle geometry, while the masses **Eq. (1.73)-(1.74)** define the masses. We set $perc_{sprung} = 50\%$ after completing a sensitivity analysis.

$$m_G = m_{sp} \tag{1.73}$$

$$m_A = m_{axle} + 2 \cdot perc_{sprung} \cdot (m_{wishbone_{up}} + m_{wishbone_{low}} + m_{steer_{link}}) \tag{1.74}$$

Knowing the position of the system centre of mass, we could evaluate values of the moments of inertia referring to the barycentric reference frame (centred in G_1) exploiting the Huygens-Steiner theorem [37].

Eq. (1.75)-(1.76) reports the calculation of the tractor balancing, i.e. the proportion of load discharged on the front and rear axles, where the subscript f means "front" and r means "rear".

$$F_{z_{susp_f}} = \left(\left(w - w_f\right) \cdot m_{sp} + \left(w - x_{axle_{CoG}}\right) \cdot m_A\right) \cdot \frac{g}{w} \tag{1.75}$$

$$F_{z_{susp_r}} = \left(w_f \cdot m_{sp} + x_{axle_{CoG}} \cdot m_A\right) \cdot \frac{g}{w} \tag{1.76}$$

It is then necessary to consider the weight of the unsprung components to evaluate the total forces acting on the individual wheels (**Eq. (1.77)-(1.78)**). Note that we used the term $\left(1 - perc_{sprung}\right)$ to consider the unsprung part of the intermediate components.

$$F_{z_{tire_f}} = \frac{F_{z_{susp_f}}}{2} + \left(m_{wheel_f} + m_{strut_f} + (1 - perc_{sprung}) \cdot \left(m_{wishbone_{up}} + m_{wishbone_{low}} + m_{steer_{link}}\right)\right) \cdot g \tag{1.77}$$

$$F_{z_{tire_r}} = \frac{F_{z_{susp_r}}}{2} + \left(m_{wheel_r} + m_{strut_r}\right) \cdot g \tag{1.78}$$

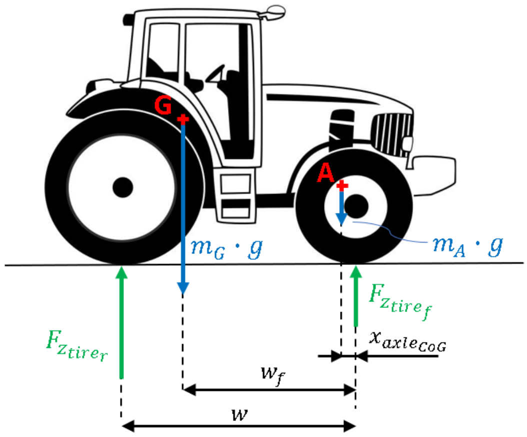

Figura 1.100: Schema del trattore usato per la stima dell'equilibrio iniziale

Eq. (1.79)-(1.80) show the calculation for the loaded radius of front and rear wheels, considering the tires as elastic components with defined vertical stiffnesses. Tire catalogues should provide for this information concerning $k_{z_{tire_f}}$ and $k_{z_{tire_r}}$.

$$R_{w_{load_f}} = R_{w_f} - \frac{F_{z_{tire_f}}}{k_{z_{tire_f}}} \tag{1.79}$$

$$R_{w_{load_r}} = R_{w_r} - \frac{F_{z_{tire_r}}}{k_{z_{tire_r}}} \tag{1.80}$$

After entering all the information concerning the system equilibrium within the functional model, we could evaluate the system frequency response and compare it with the 3D model one.

We exploited an excitation signal recommended by Siemens to do so. Siemens (i.e. the developer of Simcenter Amesim®), in fact, had already carried out similar analyses in collaboration with PSA Peugeot Citroen. This excitation signal is a sinusoidal signal of 2.5 mm amplitude and increasing frequency, from 0 to 15 Hz.

Figure 1.101 shows the graphical comparison of the vertical acceleration frequency responses of the centre of gravity and wheel centre for the 3D model, in red, and for the functional model, in blue. On the other hand, **Figure 1.102** shows the enlargement of a generic section of the graphs (the interval between 6 and 8 Hz) to make the result alignment easier to see.

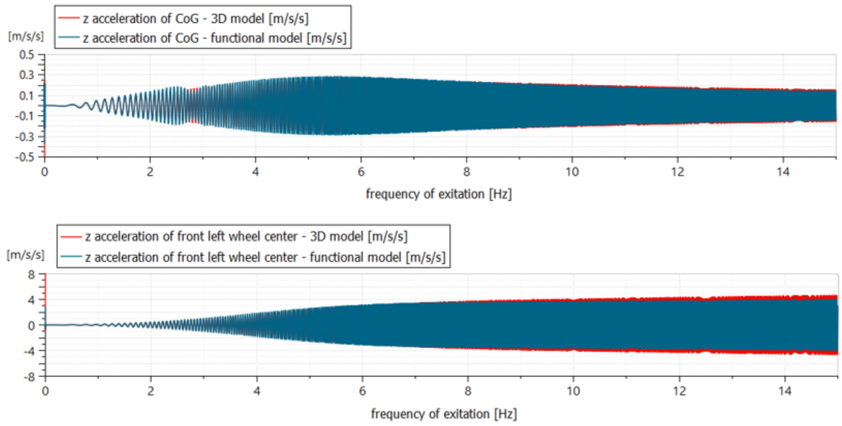

Figure 1.101: Vertical frequency response comparison: 3D multibody model (red) vs functional model (blue)

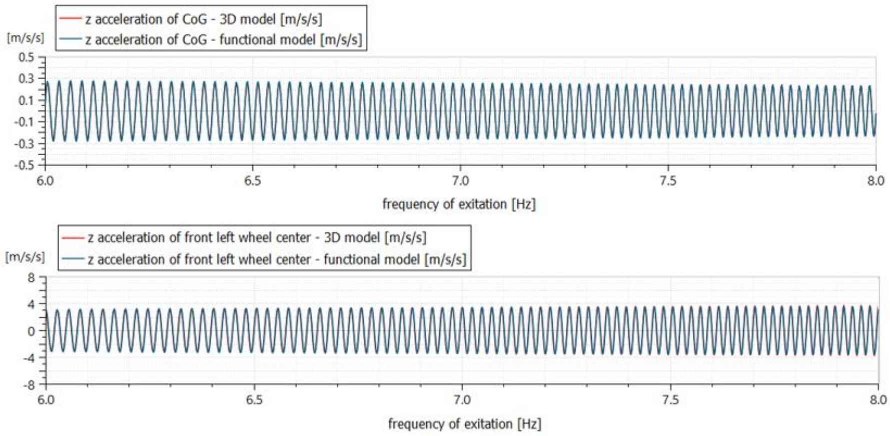

Figure 1.102: Enlargement between 6 and 8 Hz of Fig. 1.101

The result trends are generally aligned. Some differences remain in some specific frequencies, which can be explained by the simplifications made in the introduction of the moments of inertia and centre of gravity positions for the individual components. Nevertheless, after consulting Siemens, the alignment of these results was deemed more than satisfactory to continue the discussion. Note, in fact, that the functional model is and must be a simplified model, so it cannot require absolute precision.

The next step involves the replacement of the tire longitudinal and lateral stiffness with the Pacejka 2002 model [32], both for the rear and front axle. As mentioned in the section on the Amesim® 3D model, the Pacejka 2002 model is a version of the so-called 'Magic Formula' models with extended validity for low speeds. Like the previous Pacejka models, this version provides the forces and moments generated in the tire-soil contact from drift parameters. We chose this version of the model because it is the same that we used in both the Amesim® 3D model and the Adams® multibody reference one.

In addition, we also replaced the vertical sinusoidal excitation with 3D modelling of the road surface. We then integrate a suitably calibrated PID controller to regulate the vehicle speed.

We could compare the 3D model and functional model results considering a manoeuvre on the road after these modifications. In particular, we selected the asymmetric bump test as reference manoeuvre, in which the tractor drives over four misaligned bumps, two for the right and two for the left wheels. As already said, this test stimulates the free roll of the vehicle. We selected this particular manoeuvre as it is short but at the same time suitable for stimulating the longitudinal and lateral dynamics of the vehicle.

Figure 1.103 shows the comparison between 3D model and functional model regarding the trend of some variables of interest. In particular, it reports the position coordinates of the left wheel centre and the Euler angles of the vehicle (i.e. roll, pitch and yaw).

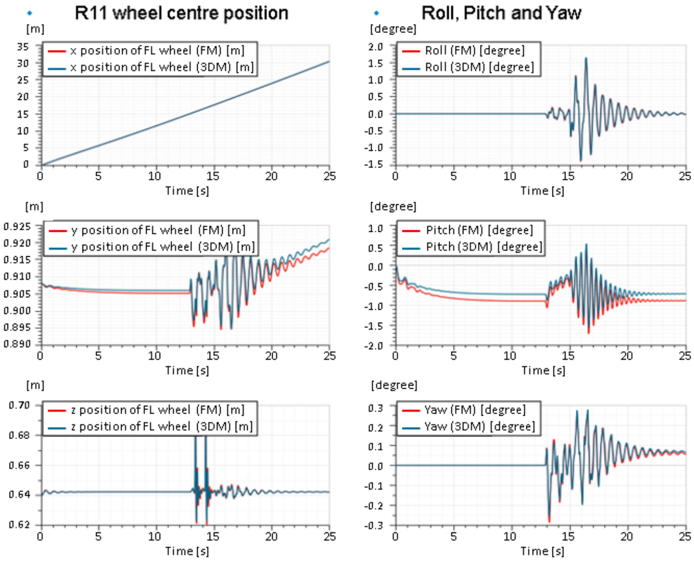

Figure 1.103: Result comparison concerning the asymmetric bump test: 3D multibody model (blue) vs functional model (red)

The qualitative trends of these quantities of interest are generally aligned. We can explain the offset difference present in the pitch trend as an imperfect introduction of masses and barycentres into the functional model. However, these differences are in the order of tenths of a degree, and therefore negligible. anyway, note that this is just a qualitative comparison, while a quantitative one will be made between the 3D model and the final Real Time model.

We then considered dynamic aspects of the functional model validated thanks to the good result alignment, both for the vertical Comfort Test Bench and for the asymmetric bump test concerning longitudinal and lateral dynamics.

1.5.3 Real Time final model

The last step regards the modification necessary to make the functional model able to run in real time. Switching from a variable time step solver for the differential equations (the default one for Amesim® simulations) to a fixed time step solver is a pre-requisite for using a model for Real-Time study. However, this is not an immediate step as it may lead to divergent results if not well calibrated.

To ensure numerical stability and real-time target limitation, in fact, the value of the fixed time step must be in a dedicated range that depends on the model. Moreover, it is necessary to adjust certain parameters to match the frequency range of interest for the solver. We exploited the Simcenter Amesim® tool called Performance Analyzer to make these adjustments. This tool, in fact, allows to identify the information concerning the numerical stability region of the system and the critical eigenmodes for the selected integration method with simple steps. This information relates precisely to the eigenmodes contributions that cause the greatest problems (i.e. the requests to decrease the integration step) and the time instants at which these problems appear. Noting this information, it is possible to modify these contributions and thus choose a suitable fixed step for the model simulation, which is again recommended by the Performance Analyzer tool.

Once these changes have been made, we could test the functional model in real time.

We thus considered three different simulations of three different standard manoeuvres to compare the Real Time model results and the 3D model ones and thus validate the presented methodology. The three standard manoeuvres are:

- the asymmetric bump test, already presented in the previous section
- the ISO5008 test [28] for the evaluation of vehicle comfort
- the so-called moose test [38] (or double line change) for the evaluation of vehicle handling

Figure 1.104 shows the graphical comparison between the real time model and the 3D model concerning the trend of some quantities of interest during the asymmetric bumps test. In particular, we reported the x, y and z positions of the left front wheel centre and the trends of vehicle's Euler angles (roll, pitch and yaw).

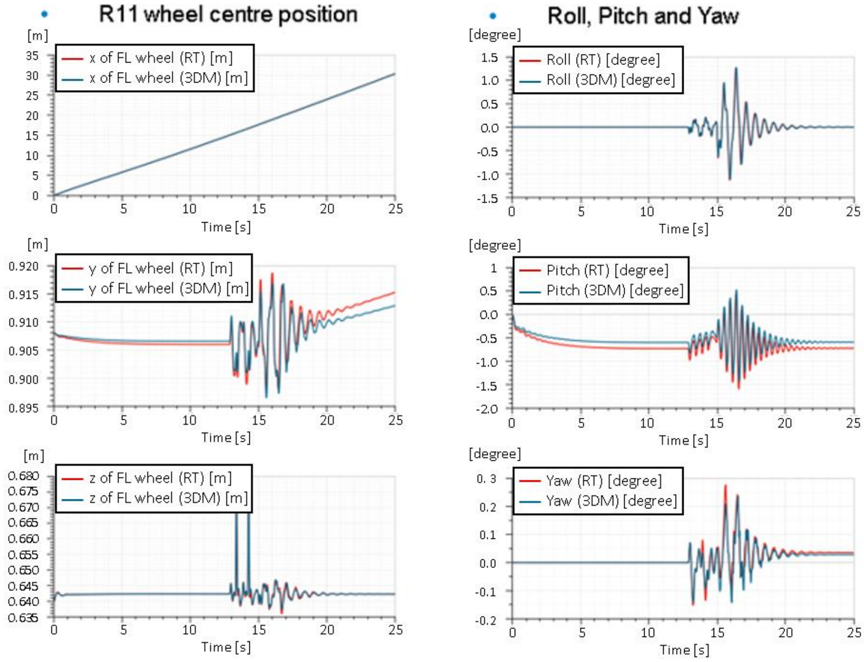

Figure 1.104: Result comparison concerning the asymmetric bump test: 3D multibody model (blue) vs Real Time model (red)

The results turned out to be very similar to those obtained in the previous section before the latest modifications for simulations with a fixed step integrator (**Figure 1.103**). Small differences are thus still present, which can be justified with the model simplification. As anticipated, however, we are reporting a quantitative comparison obtained considering the relative errors between the Real Time simulation and the reference 3D model. **Figure 1.105** depicts a histogram with the error values for some variables of interest. In particular, we are reporting the relative error values for suspension piston displacements (left and right), suspension piston forces (left and right), longitudinal vehicle speed and steering piston displacement.

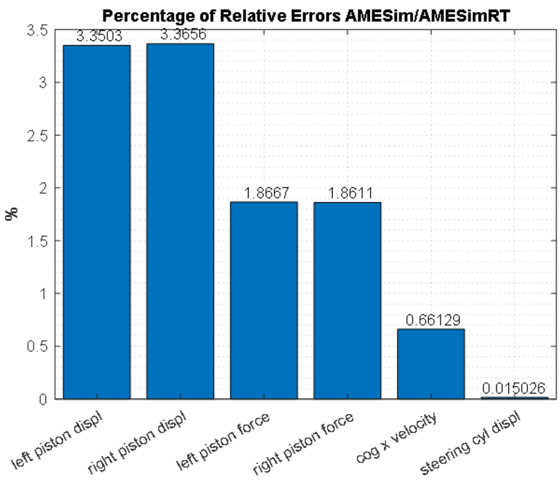

Figure 1.105: Histogram of the errors between the Real Time model and the 3D reference one concerning the asymmetric bump test

Note that we used **Eq. (1.81)** to evaluate these relative error values, where x_{RT} is the value of the generic quantity x resulting from the Real Time simulation and x_{3D} is the x value in the 3D model.

$$err_x = \frac{|x_{RT} - x_{3D}|}{|x_{3D}|} \cdot 100 \tag{1.81}$$

The error values in **Figure 1.105** histogram are all below the 4% threshold. We obtained similar values also comparing the other quantities of interest.

Similarly, **Figure 1.106** shows a graphic comparison of the numerical results concerning the ISO 5008 test. As anticipated in previous chapters, this standard test consists of the vehicle passage on a track formed by two parallel lanes univocally defined in the standard and created by a succession of wooden beams of different heights and inclination to replicate the passage on uneven ground. This test is used to assess the comfort of a generic off-highway vehicle.

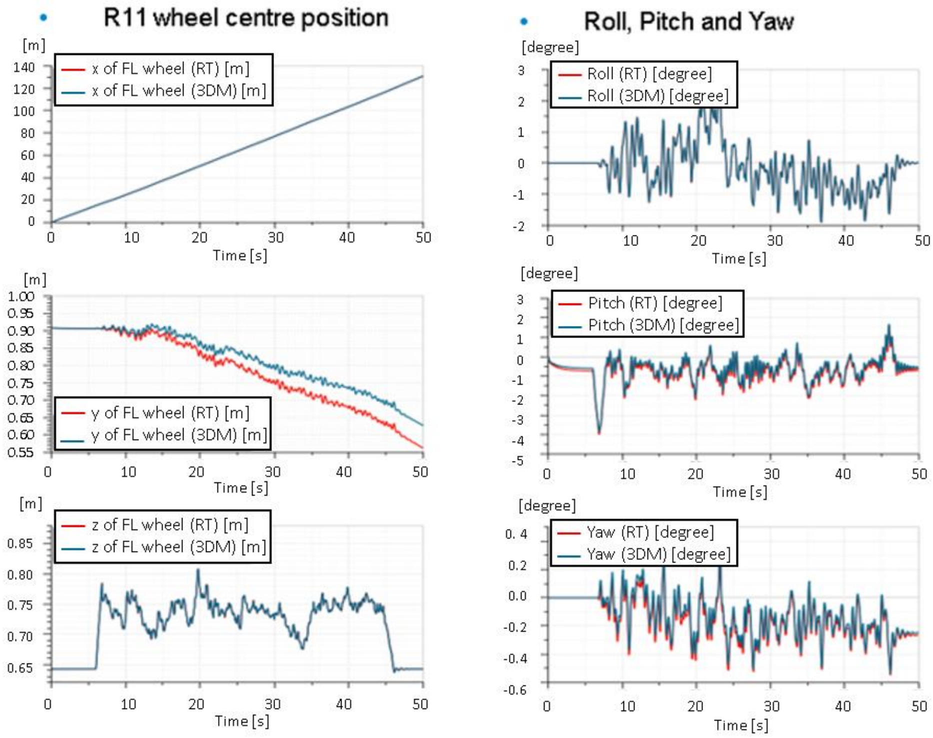

Figure 1.106: Result comparison concerning the ISO 5008 test: 3D multibody model (blue) vs Real Time model (red)

The result alignment is again very good. Almost each Real Time graph is indeed identical to its 3D model counterpart. Note that the deviation in the y position of the front left wheel is negligible since it is in the order of 10 cm after 100 m of vehicle longitudinal travel.

As done before, **Figure 1.107** shows the error histogram concerning the ISO 5008 test for the two models.

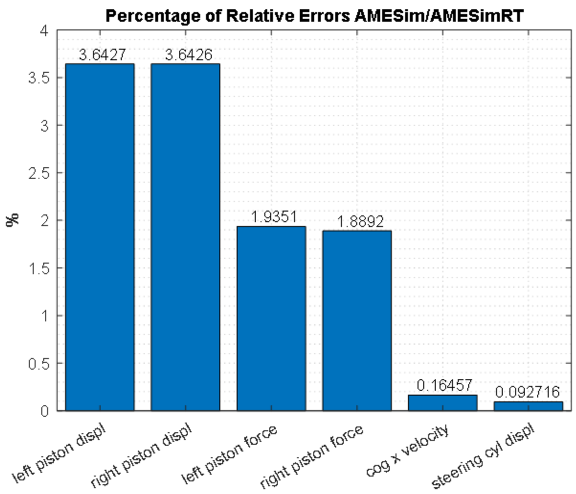

Figure 1.107: Histogram of the errors between the Real Time model and the 3D reference one concerning the ISO 5008 test

Again, all errors are below the 4% threshold.

Finally, **Figure 1.108** reports the results concerning the moose test simulations. This test [38] involves a sudden double change of trajectory, as to avoid an obstacle that suddenly appears in front of the vehicle. It is a fundamental test for assessing the road holding of automotive vehicles, but we have exploited and adapted to a tractor to give an assessment of its manoeuvrability and handling characteristic.

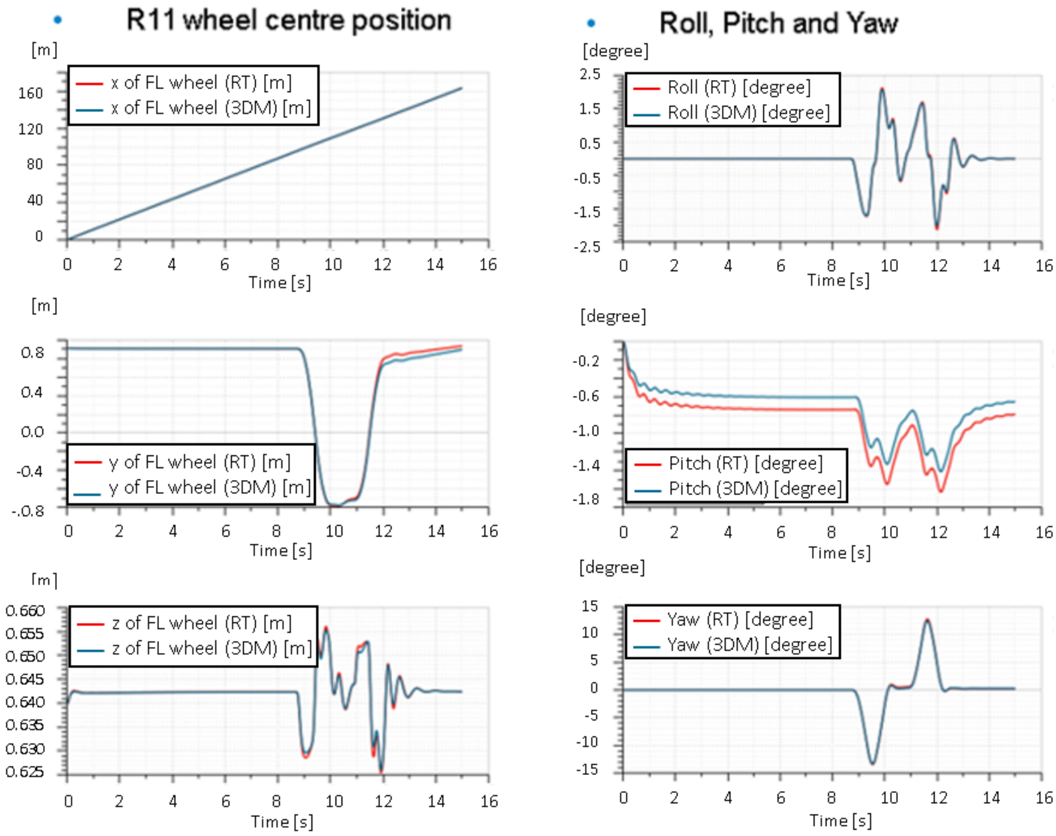

Figure 1.108: Result comparison concerning the moose test: 3D multibody model (blue) vs Real Time model (red)

The result alignment is satisfactory. Note that the difference offset in the vehicle pitch graph can again be traced back to the imperfect introduction of masses, inertias and centre of gravity positions into the simplified model. Anyway, we could neglect this error as it is in the order of tenths of a degree.

Finally, **Figure 1.109** shows the error histogram concerning this third test.

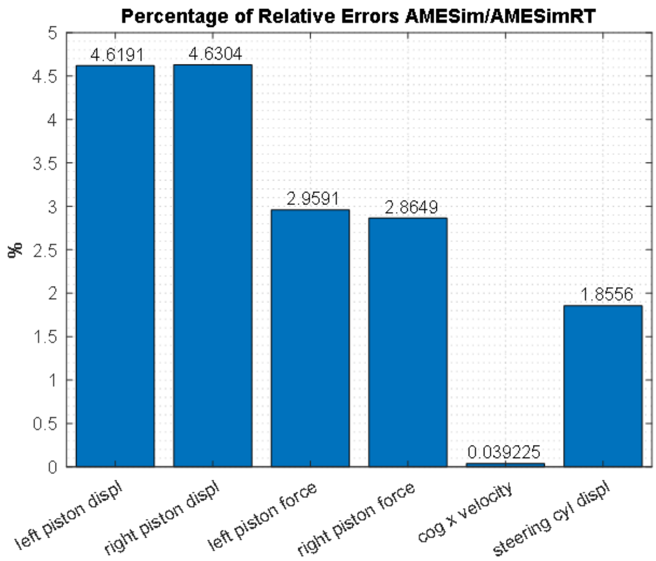

Figura 1.109: Histogram of the errors between the Real Time model and the 3D reference one concerning the moose test

In this case, the relative errors between the results of the real-time model and the reference 3D model are all below 5%.

The results are satisfactory for all three manoeuvres, also considering the simplifications made and what has been achieved in terms of time savings concerning the simulation times. The latter is, in fact, the fundamental aspect to consider for this study, which had been started to reduce the long simulation times of multibody models while maintaining results consistency. **Table 1.3** shows the simulated times for realising the three considered manoeuvres and the indicative simulation times for the Adams® multibody model, the 3D Simcenter Amesim® model and the Real Time model realised with the steps just described.

Table 1.3: Comparison between the various simulation times using the different models to simulate the three considered manoeuvres

	Simulated time	Multibody Adams®	Amesim® 3D	Amesim® Real Time
Asymmetric bump	25 s	≈ 10 min	≈ 70 s	≈ 7 s
ISO 5008	50 s	≈ 20 min	≈ 45 min	≈ 20 s
Moose Test	15 s	≈ 2 min	≈ 5 min	≈ 5 s

The improvement in simulation time is considerable. The possibility to have a vehicle model that can run in Real Time and provide reliable results is already a benefit. However, this aspect is highlighted if this model can be used within an optimization workflow for the whole independent suspension system where it is necessary to evaluate the performances of a high number of consecutive designs. Passing from minutes to seconds of computational time for a single simulation, it is easy to imagine that the total time-saving during the entire optimization can easily be tens of hours. If we instead consider the same amount of time, this model ensures to evaluate more designs and so a more robust and accurate optimization.

The development of the presented methodology in Simcenter Amesim® enabled the creation of a tractor simplified model with independent suspension which can run in Real Time. The followed steps allowed us to consider both the kinematics and dynamics aspects of the starting multibody model. Thanks to this, the results of the RT model turned out to be well aligned with the multibody reference ones. The key aspect of this work is the improvements in terms of computational time to run the simulations. In fact, while both the Amesim® multibody model and the Adams® reference one has computational times in the range of minutes (depending on the simulated manoeuvre), the RT model can simulate all the tested manoeuvres in just a few seconds.

Note that this Real Time model can only replace the multibody simulations of Loop 3 optimization, i.e. when the axle geometry is already fixed and the optimizer exploit dynamic simulations to evaluate the vehicle performances. In fact, it would be impossible to develop a Real Time model for each design of Loop 1 and 2 with different geometries using the methodology presented.

1.6 Experimental tests

Exploiting the optimization workflow implemented and all the numerical model developed, it was possible to define the suspension architecture geometry and the dimensioning of the hydro-pneumatic system. After doing this, Dana Incorporated could proceed with the actual realization of the AFS independent suspension prototype.

The realization of this prototype involved several departments of the company, as it required the integration of the suspension mechanical design, the experimental validation and assembly of all the hydraulic components of the hydro-pneumatic system, and the realization of a control software to insert into the vehicle ECU.

The correct software development for the system control functions is fundamental for the suspension correct use. This tool, in fact, must allow the implementation of all the control logics for the system as well as all the information concerning the various maps to exploit, like the suspension stiffness maps as function of the vehicle weight, or the damping maps for the different dynamic performances.

It was, in fact, possible to create all the lookup tables necessary for defining the rod side levelling pressure p_{R_1} (which remains the only degree of freedom once the prototype has been defined) as a function of the required stiffness and vice versa, as the suspension static load varies. Exploiting these tables, the software can manage the various requests from the user adjusting the suspension system as defined thanks to the optimization workflow.

Similarly, the optimization process allowed the realization of the tables for the damping valve supply currents $I_{P_{damp}}$ (piston side) and $I_{R_{damp}}$ (rod side) to obtain the optimum damping required, depending on the dynamic aspect to improve (comfort, handling or traction). As the operator calls for improving a particular dynamic aspect, the ECU must adjust the system damping as defined within these tables.

Once the Dana engineering department had completed all the experimental tests on the individual components, in particular those on the hydraulic blocks, and the assembling of the prototype, it was possible to carry out various tests for the entire axle with the AFS independent suspension. These experimental tests are obviously necessary both to verify the performance of the AFS prototype and to further validate the methodology followed for its design.

Figure 1.110 shows the test rig used for testing the AFS suspension, installed at the Dana Incorporated's location in Arco (TN), Italy. This is a 2-poster test rig, consisting of a pair of hydraulic jacks (1) on which the wheels rest, a beam (2) on which the axle is hooked, and a third central hydraulic cylinder (3) connected to the beam via a tie rod and used to manage the load on the axle itself and raise/lower the beam (simulating levelling manoeuvres). Once the suspension height and the load on it have been defined, it is possible to impose the desired movements on the hydraulic cylinders under the two wheels to simulate the desired manoeuvres.

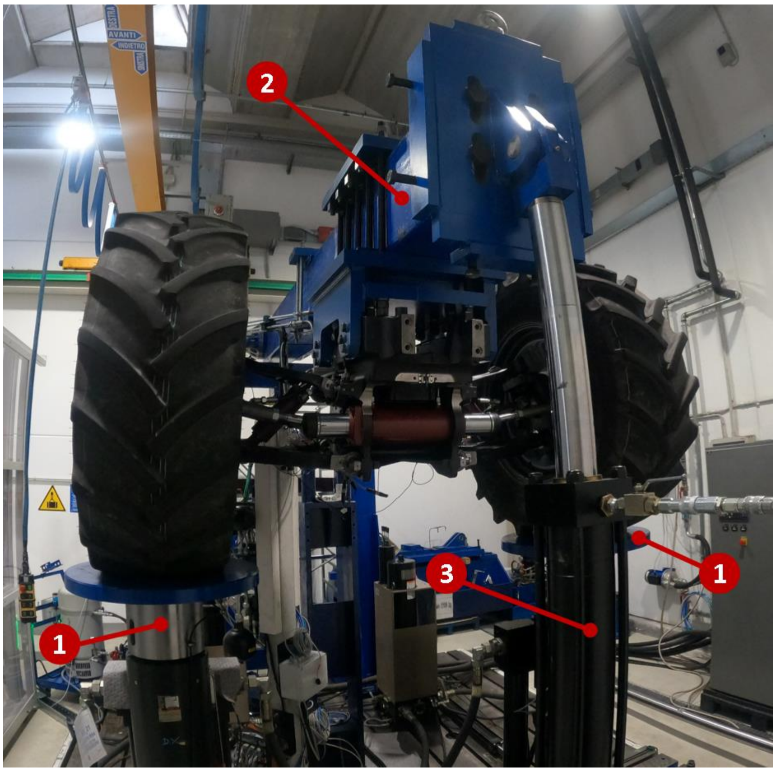

Figure 1.110: 2-poster test rig used for the experimental tests on the AFS suspension

The company provided for the installation of all the sensors required to acquire the data of interest, from pressure sensors in the hydro-pneumatic system to load cells and cylinder position sensors.

Using the test rig shown in **Figure 1.110**, it was possible to perform all the experimental tests necessary for the final validation of the prototype, from the simplest ones (such as levelling manoeuvres to raise/lower the suspension by pumping/draining oil from the suspension cylinders) to more complex tests (such as the replication of the ISO 5008 test, obtained by imposing wheel displacements on the test rig jacks to simulate the passage on the ISO track).

The main experimental tests performed were the following:

- test to verify the levelling speed under different operating conditions,
- test to verify the pitch and roll stiffness of the suspension by varying p_{R_1} under different operating conditions,
- test to evaluate the suspension cylinder hysteresis in the suspension cylinders under different operating conditions (to estimate internal friction),
- test to verify the internal leakage in the suspension cylinders under different operating conditions,
- test to verify the system's response after applying a step load variation to the suspension: verification of the software capability to return the suspension to its nominal starting position by adjusting the pressures in the circuit,
- test to verify the system's pitch response,
- test to verify the system's free roll response,
- test to verify the system's controlled roll response,
- test to replicate the ISO 5008 test.

Other tests were also carried out to evaluate the various safety functions introduced into the software. In fact, the company had to consider a series of additional functions to guarantee the functional requirements for an off-highway vehicle suspension.

Each test was repeated several times to guarantee the results accurancy.

The following sub-section shows some of the results obtained from the experimental tests. Unfortunately, it was not possible to show more results due to the sign of NDA agreements for reasons related to the data sensitivity.

1.6.1 Test results

As anticipated, this sub-section presents some of the results obtained from the experimental tests carried out on the 2-poster test rig. We decided to report the ISO 5008 test results to show the behaviour of the entire system without considering many tests to evaluate individual aspects. Starting from the experimental results, it was possible to report the comparison between these and the numerical results obtained through the models developed for this activity to provide the validation of the prototype itself.

As mentioned above, we carried out the test by imposing the displacements required to replicate the passage over the ISO 5008 track [28] on the hydraulic jacks under the wheels of the axle. The graphs in **Figure 1.111** shows the bench jack strokes.

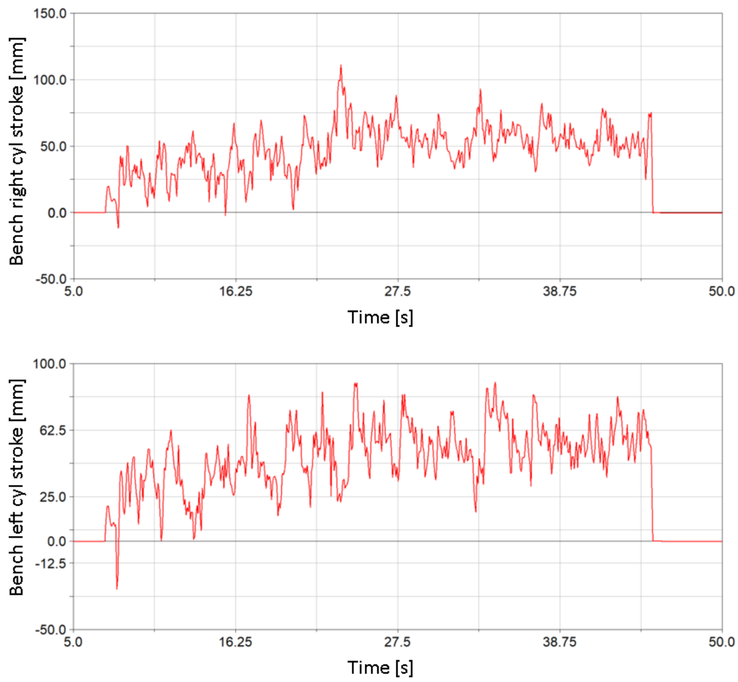

Figure 1.111: Bench jack strokes to replicate the ISO 5008 test

We repeated this test several times to evaluate the behaviour of the suspension under different operating conditions. However, we decided to report in this thesis only some of the results obtained for the nominal EVW operating condition. Regarding the stiffness, we set the rod side levelling pressure p_{R_1} to match the optimum stiffness required for the EVW configuration. Regarding the system damping, on the other hand, we considered the optimal supply currents of the damping valves to improve the systems dynamic aspects, as found with the optimization workflow.

In particular, the following graphs show the comparison between experimental and numerical data relating only to the most interesting results, i.e. the piston displacements in the suspension cylinders and the forces discharged on the piston rods of the same pistons. We obtained the numerical results the multibody model developed in MSC Adams® and calibrated using the stiffness and damping characteristics obtained from the modelling of the hydro-pneumatic system (in Amesim®).

Figures 1.112-1.113 show the comparisons of the results obtained for the EVW configuration with optimal damping for handling performance. For the sake of compactness, we reported only the results obtained for the right cylinder. The result comparison for the lest cylinder was completely similar.

We reported in each graph an enlargement concerning a time interval of 20 s to make the comparison between the experimental results (in blue) and the numerical results (in red) more comprehensible.

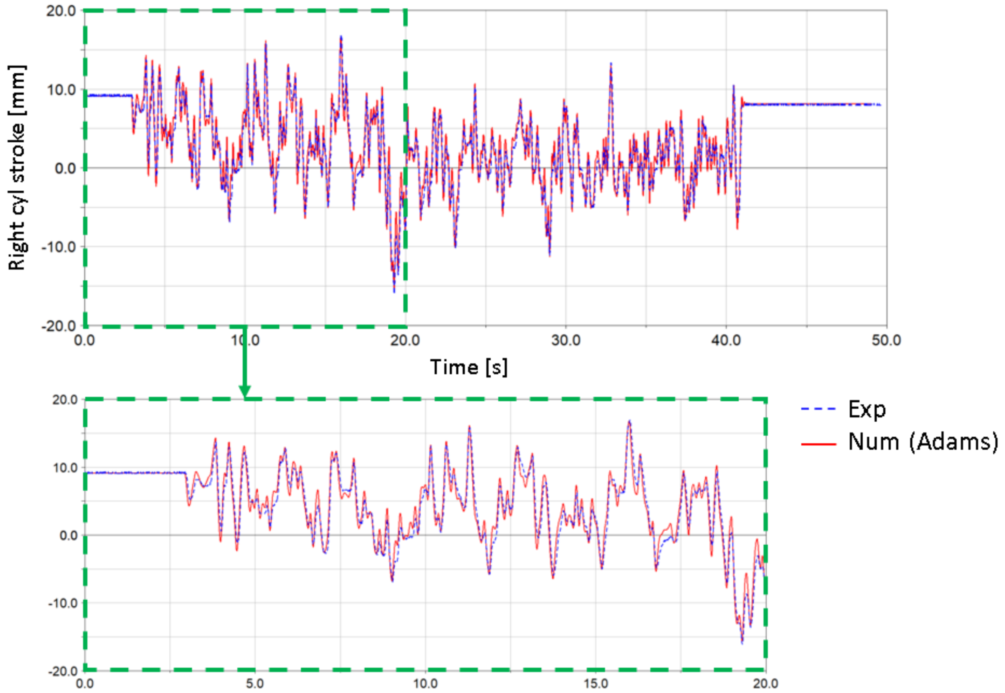

Figure 1.112: Comparison of the suspension right piston stroke concerning the ISO 5008 test for EVW with optimized handling: experimental results (blue) vs Adams® numerical results (red)

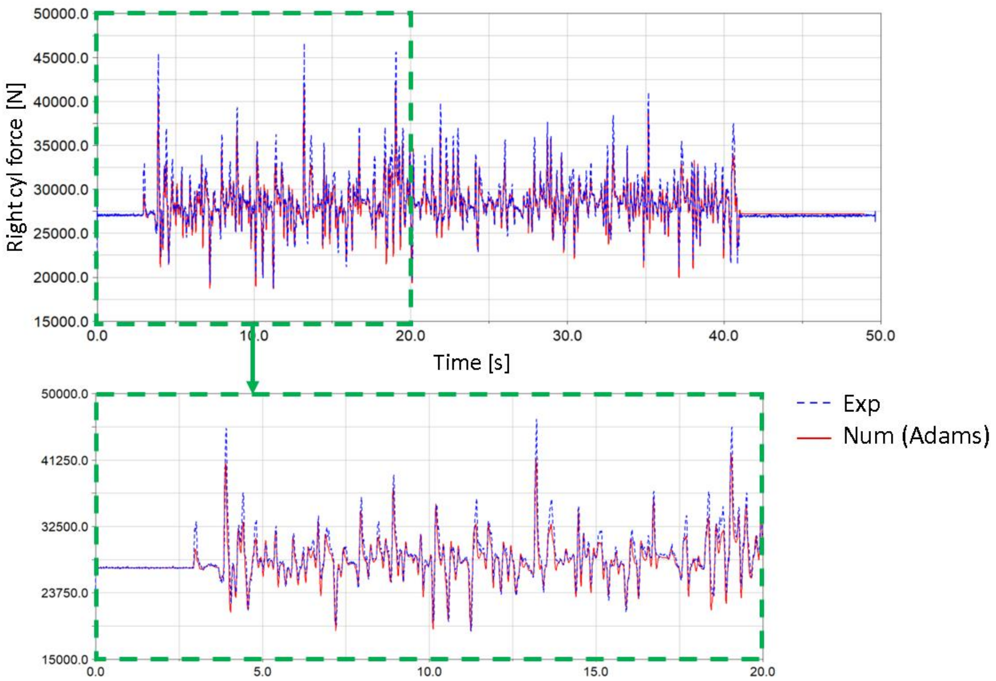

Figure 1.113: Comparison of the suspension right piston force concerning the ISO 5008 test for EVW with optimized handling: experimental results (blue) vs Adams® numerical results (red)

It is easy to note good alignment between of the experimental results with the expected numerical ones both in the general trend and in the various peaks. Some differences are still present, especially in the force peaks of the **Figure 1.113** graph. We could justify this aspect with a possible slight difference in the damping level of the real system compared to the modelled one. However, note how the use of real sensors can justify some of these differences too. It is obviously more difficult to evaluate very fast transients in experimental tests with respect to numerical simulations.

Note also that we made some simplifications in the hydraulic numerical model, as we neglected thermal effects, or we simplified suspension frictions (within both the cylinders and all the joints). Obviously, these simplifications could lead to some result differences.

Lastly, note also that the test rig behaviour could influence the experimental results. We did not consider, indeed, the stiffness, damping and friction effects concerning all the test rig components within the numerical simulations. However, all of these may slightly influence the tests.

Figures 1.114-1.115, on the other hand, show the comparisons of the results obtained for the EVW configuration with optimal damping for traction performance. Always for the sake of compactness, we reported only the results obtained for the right cylinder.

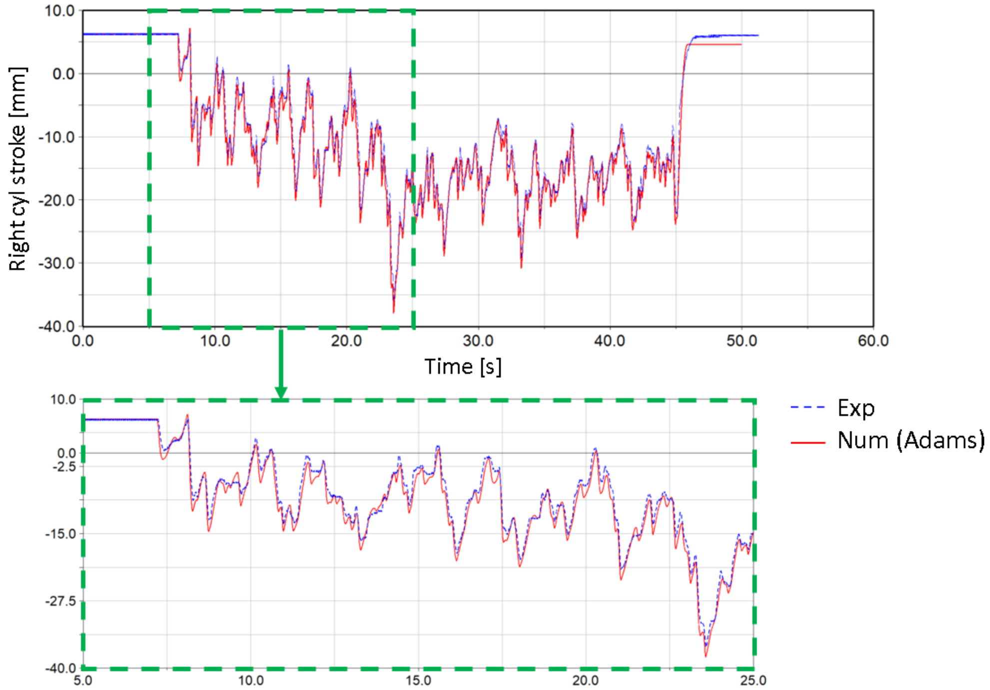

Figure 1.114: Comparison of the suspension right piston stroke concerning the ISO 5008 test for EVW with optimized traction: experimental results (blue) vs Adams® numerical results (red)

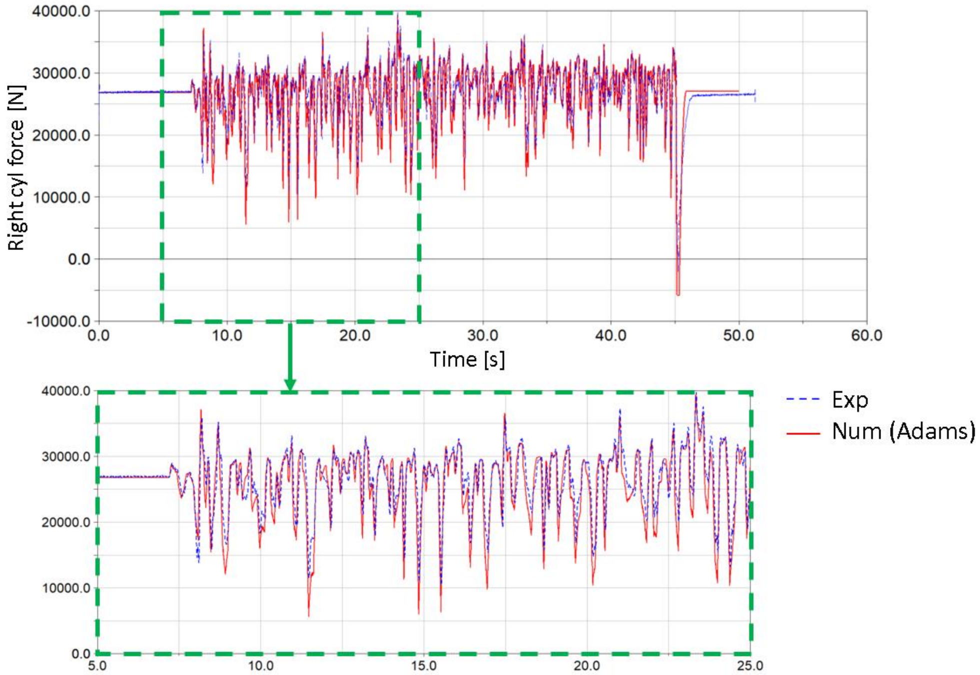

Figure 1.115: Comparison of the suspension right piston force concerning the ISO 5008 test for EVW with optimized traction: experimental results (blue) vs Adams® numerical results (red)

We obtained a good result alignment for this comparison between experimental and numerical data too. The reasons already mentioned could justify the minor differences that are present also here.

Since these experimental tests are not intended to validate the numerical models, we are not evaluating the percentage differences between these examined quantities.

However, we exploited this result comparison to confirm the expected performance of the prototype built for Dana Incorporated's AFS hydro-pneumatic suspension. Once these tests have been done, it is possible to move on to the next phase, which is the realization of experimental tests on the entire tractor with the AFS axle installed. As it has already been emphasised several times, this is a complex system that aims to optimize the dynamic behaviour of the entire vehicle. For this reason, we must evaluate it experimentally to complete the validation of the prototype before starting a possible production.

1.6.2 Future tests

We have already planned a long experimental test session on the entire vehicle at the CREA research centre in Treviglio (BG), Italy. This research centre is, in fact, an expert in carrying out experimental tests on tractors using both test rig (e.g. 4-poster with seismic isolator) and several standard tracks (e.g. ISO 5008, moose test, symmetric and asymmetric bumps, etc).

The AFS prototype will then be installed on the JD 6130 reference tractor, which will be shipped to the CREA centre. Here we will proceed with the installation of all the sensors required to acquire the data of interest, whether hydraulic sensors for the hydro-pneumatic system, load cells, linear or angular sensors for the suspension mechanics, or accelerometers to assess vehicle oscillations.

We are thus planning to carry out various tests on the entire vehicle, such as those mentioned in this chapter (ISO 5008 test, moose test, maize test, etc.), to complete the evaluation of the tractor dynamic behaviour. Starting from these tests, we will perform the required post-processing to obtain the characteristic parameters of interest. After doing this, we will have the complete picture of the tractor with the AFS suspension.

1.7 Conclusions

We presented in this chapter the entire design and optimization methodology for an independent hydro-pneumatic suspension system realized for and in collaboration with Dana Incorporated. We developed this methodology to consider the main functional requirements of the system and then optimize the various aspects of the suspension in order to improve its overall performance once installed on a vehicle.

It was also necessary to develop numerical models using different software to consider the various aspects of the multi-disciplinary system and aim to the process automation. It would be impossible to assess the system behaviour as function of all the parameters involved (geometric and non-geometric) without these numerical models.

We thus exploited the optimization process precisely to make decisions concerning the prototype design, which has been (and will still be) subjected to experimental tests. This experimental activity is necessary to confirm the prototype expected performance and consequently validate the optimization methodology we developed.

The entire methodology allows also to consider the optimization of other types of suspension, with different architecture and/or hydraulic layout, or designed to be used on a different vehicle with different functional requirements.

Chapter 2: Bent axis unit modelling

Introduction

The academic literature is full of studies focused on the analyses and mathematical modelling of the fluid-dynamic and mechanical aspects of swash plate positive displacement machines or gear machines. However, the same cannot be said concerning bent axis positive displacement units, which are rarely considered despite their wide use in both industrial and mobile applications.

Similarly, to swash plate units, these bent axis piston machines (with fixed or variable displacement) are complex machines, whose correct functioning is also based on friction coefficients between the components in relative motion and leakage/lubricant films between them. On one hand, oil films must guarantee the lubrication of the parts keeping them in mediated contact to exchange reaction forces and moments. On the other hand, the leakage created by these films must not affect the volumetric efficiency of the machine too much.

It is thus possible to consider two main aspects of the machine: the fluid-dynamic aspect and the mechanical one. These two main parts connected together define the general behaviour and efficiencies, of these machines. An in-depth analysis of these two aspects is fundamental to understand this type of positive displacement machine and realize numerical models capable of simulating its behaviour.

As mentioned above, several studies concerning the detailed modelling of both external and internal gear positive displacement machines have been published in the last decades.
Mancò and Nervegna carried out some of the first publications concerning the detailed simulation of external gear pump and its consequent experimental validation [39]. This publication was the starting point of further modification and improvements realized by the same authors or others, for example [40] where the implementation of these models using lumped parameter software have been reported. Starting from these numerical models then, the research activities could focus on more specific aspects, as the development of dedicated software (e.g. [41]), particular phenomena (i.e. [42]) or alternative approaches (e.g. [43]).
We must cite again Mancò et al. even concerning the detailed modelling of internal gear machines [44] [45] [46]. In these studies, the author reported both the mechanical and fluid-dynamic analysis of this type of positive displacement units to properly model their behaviour. Starting from these reference publications, Rundo and Altare published some reviews [47] and integration [48] to improve them defining the state of the art concerning the lumped parameter modelling of internal gear machines.

Similarly, there are many publications concerning the detailed analysis of swash plate units, both regarding fluid-dynamic aspects and mechanical (kinematic and dynamic) ones. In addition to reference texts, such as [49] or [50], the study carried out by Zeiger et al. [51] is an example of a publication concerning the dynamic analysis of swash plate main components, where the authors analysed this aspect to develop a high-performance controller for the swash plate. Both published text [52] concerning the most common machine geometries and more recent publications for particular designs of interest [53] have studied the kinematic aspects of the main components of these machines. Regarding the fluid-dynamics part, Bing et al. [54] investigated viscous friction losses of rotating components in oil, which affect the hydro-mechanical performance of the unit. The in-depth analysis of these aspects has therefore also allowed the realisation of increasingly reliable numerical models in the simulations of these machines, as also shown by Mancò et al. [55] in their publication. Other publications focused on the detail integration of fluid properties within the numerical models of this kind of positive displacement machines [56]. The study carried out by Roccatello et al [57] is another important publication we want to cite. In this study, the authors reported a numerical model for swash plate units realized through a co-simulation of a lumped parameter model for the fluid-dynamic part, and a multibody model for the mechanical one.

Note that similar approaches have been used to study also other type of positive displacement machines, as vane pumps (e.g. [58]) or radial piston pump (e.g. [59]).

However, as anticipated, fewer publications have studied something similar concerning bent axis positive displacement machines. Abuhaiba et al. [60], for example, carried out a kinematic and geometric analysis for a particular bent axis pump where a double universal joint guarantees the transmission of motion between the shaft and cylinder block. As anticipated, one of the fundamental aspects for understanding the volumetric and hydro-mechanical efficiencies of these machines is the study of friction and leakage flow rates. In addition to the reference texts concerning tribology [61] and lubrication [62], several publications have focused on precisely these aspects, as done by Hong et al. [63] and Kumar et al. [64]. Concerning the detailed mechanical modelling of the main components of bent axis units, the state of the art is the study carried out by Roccatello et al. [65], where the authors propose the analysis and resolution of the equilibrium equations systems of the individual components to obtain all the unknown reactions of the system and, therefore, the overall view of the machine global behaviour.

Always in collaboration with Dana Incorporated, we started the activity presented in this chapter to study and model in detail the fluid-dynamic and, above all, mechanical part of bent axis positive displacement units. The activity objective was the creation of a numerical tool capable of replicating in detail the operation not only of the units taken as reference for modelling, but also of many machines of similar geometry and characteristics. We thus decided to consider pump/motor units to make the analysis as general as possible and not to limit the model to a single operation mode. Such a tool can support the design of these machines, which is why it was strongly desired by the company.

We considered two different reference geometries, from which we realized the model parameterisation. Once we had achieved this, it was possible to identify the main mechanical components and fluid-dynamic aspects to focus on, which were modelled in detail. Concerning mechanical components, we decided to indicatively follow the approach also used by Roccatello et al. [65], with the definition of all contributions acting on the individual components and the subsequent resolution of the equilibrium equations.

Once we had completed the modelling of the fluid-dynamic and mechanical part of the machine, it was possible to develop a parametric, vectorial and modular model exploiting Simcenter Amesim® and, in particular, the Submodel Editor tool. This tool, in fact, allows the creation of a library of customized elements that can be used in Amesim®, which can be linked together or with other standard software elements.

The final result of the activity was this virtual tool, which is able to simulate the general and detailed behaviour of a family of bent axis units with similar geometry.

2.1 Bent axis piston units: modelling introduction

This section introduces the basic concepts for the modelling of positive displacement machines and, in particular, of bent axis piston units. We are presenting two examples of bent axis unit, which have been used as a reference for the analysis presented in the entire chapter. Obviously, this is a brief introduction to some concepts, while a more complete treatment of generic volumetric machines can be found in reference texts [49] [50]. We will also briefly present the tool used to implement all the analyses performed to obtain the actual numerical model capable of simulating the behaviour of this type of machine in detail, i.e. the Simcenter Amesim Submodel Editor® tool.

The distinctive aspect that distinguishes and characterizes the size of a hydraulic machine is the displacement V. The theoretical displacement is the volume of fluid transferred per revolution of the drive shaft, under ideal conditions, between the suction and delivery ports, for a pump, and between inlet and outlet for a motor.

The theoretical flow rate of a hydraulic machine is thus given by the product of displacement and the angular speed of the machine, expressed in number of revolutions in the unit of time.

$$Q = V \cdot n \tag{2.1}$$

The ideal conditions mentioned above, for positive displacement machine, such as a pump or a piston motor, are:

- the absence of leakage flow rates, i.e. losses through the gaps between the various parts of the machine are zero,

- the absence of viscous and dry friction on and between the various machine components,
- the presence of infinitely rigid components to pressure and temperature,
- the presence of a direct and instantaneous connection between the piston chambers and suction/delivery (or inlet/outlet).

It is appropriate to make an important distinction between positive displacement pumps and motors. These two types of positive displacement machines have in common that they both exchange energy with a fluid (i.e. mineral oil with specific physical characteristics in this case). What distinguishes them is the 'direction' that this transfer of energy has. Pumps absorb mechanical energy from a prime mover (typically an internal combustion engine or electric motor) which is then transferred to the working fluid as hydraulic energy. on the other hand, hydraulic motors receive hydraulic energy from the fluid and transform it into mechanical energy available to the user connected to the motor shaft.

Figure 2.1 shows the graphic symbols defined in ISO 1219-1 [66] used to facilitate the understanding and qualitative description of how pumps and motors operate. The black arrowhead indicates both the fluid direction and the energy flow. As mentioned, hydraulic energy 'enters' the motor to be transformed into mechanical energy, while the mechanical energy supplied by the prime mover is transformed into hydraulic energy 'exiting' from pumps.

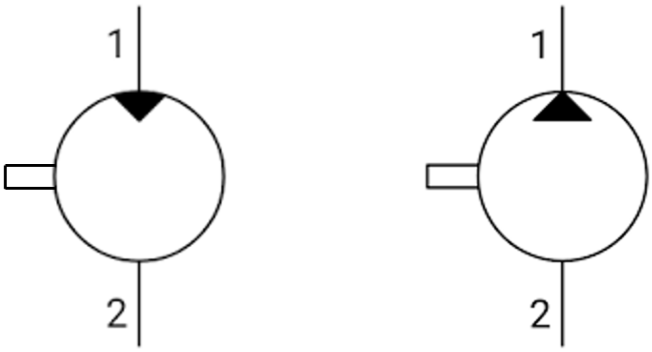

Figure 2.1: ISO symbols of hydraulic motor (left) and pump (right) with the correspondent inlet/delivery (1) and outlet/suction (2) ports

Some appropriately designed positive displacement machines can be capable not only of reversing the direction of flow, but also of working both as a pump and motor depending on their use in the system. The capability of vary the displacement is another feature that can be found in hydraulic machines, going from a minimum displacement, usually zero, to a maximum V_{max}. **Figure 2.2** shows the ISO symbols for a bidirectional hydraulic motor and a bidirectional pump/motor unit with variable displacement.

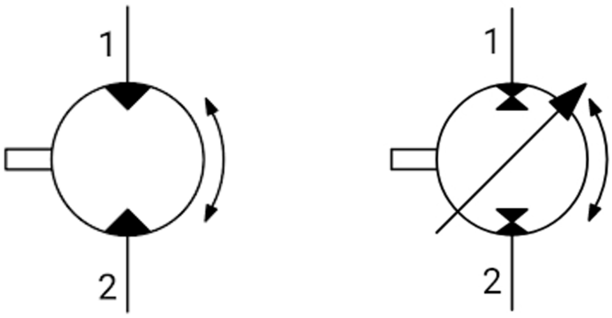

Figure 2.2: ISO symbols of bidirectional hydraulic motor (left) and bidirectional pump/motor unit with variable displacement (right)

Bidirectional pump/motor units are thus capable of working in the so-called four quadrants, i.e. both as a pump in both directions and as a motor in both directions.

It is possible to graphically visualise these four quadrants of use (**Figure 2.3**) by defining a sign convention [67] for the main quantities of interest for volumetric machines, i.e. the pressure difference Δp across the machine, the rotational speed ω of the machine shaft and the torque M (absorbed or delivered) at the machine shaft.

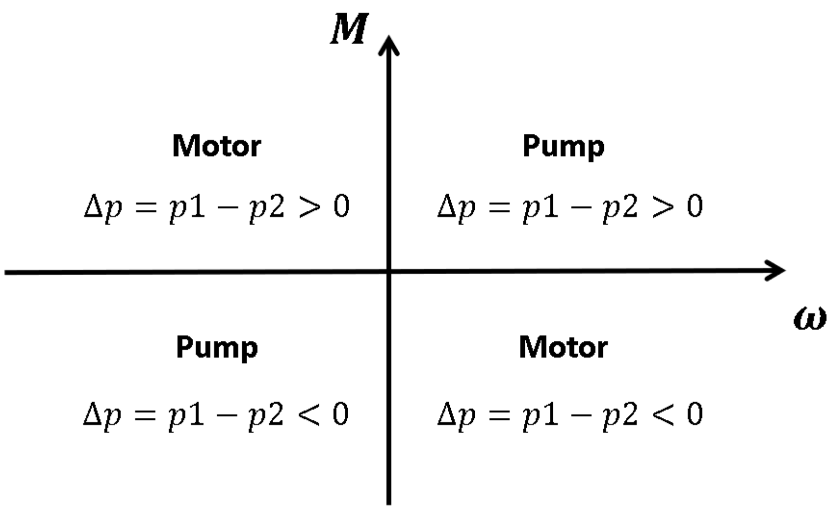

Figure 2.3: Four quadrants of use for a bidirectional pump/motor unit

Efficiency of positive displacement machines

Before the evaluation of efficiencies in hydraulic positive displacement machines, it is necessary to highlight the working cycles of these type of machines. Considering a generic positive displacement pump, the variables that describe and characterize the fluid physical state at the pump suction are pressure p_1, temperature T_1, internal energy u_1, density ρ_1 and velocity v_1. Similarly, we have the characteristic variables p_2, T_2, u_2, ρ_2, v_2 for the pump delivery.

Neglecting the variation of the fluid gravitational potential energy (since it is very small compared to the other forms of energy in the applications of this type of hydraulic machine), **Eq. (2.2)-(2.3)** define the specific energy (i.e. the energy per unit mass [J/kg]) at the suction and delivery of the pump.

$$u_1 + \frac{p_1}{\rho_1} + \frac{v_1^2}{2} \tag{2.2}$$

$$u_2 + \frac{p_2}{\rho_2} + \frac{v_2^2}{2} \tag{2.3}$$

The fluid density, temperature and velocity between inlet and outlet remains constant throughout the working cycle assuming to use an ideal fluid. Therefore, since $\rho_1 = \rho_2$, $u_1 = u_2$ and $v_1 = v_2$, **Eq. (2.4)** reports the variation of specific energy passing from state 1 (suction) to state 2 (delivery).

$$\Delta e = e_2 - e_1 = \frac{p_2 - p_1}{\rho} = \frac{\Delta p}{\rho} \tag{2.4}$$

The fluid mass can be written as the product of the fluid density ρ and the fluid volume V (**Eq. (2.5)**). From here, considering the assumptions of using an ideal fluid, and thus incompressible ($\rho = cost$), the mass flow rate can be evaluated as given in **Eq. (2.6)**.

$$m = \rho \cdot V \tag{2.5}$$

$$\dot{m} = \frac{dm}{dt} = \frac{d(\rho \cdot V)}{dt} = \rho \cdot \frac{dV}{dt} = \rho \cdot Q \tag{2.6}$$

The mass flow rate $\dot{m}$ ($\left[\frac{kg}{s}\right]$) is thus the product of the density ($\left[\frac{kg}{m^3}\right]$) and the volume flow rate Q ($\left[\frac{m^3}{s}\right]$). Note that this relationship, although it has been obtained considering an ideal fluid, applies well considering hydraulic components and systems where the fluid density is almost constant as the pressure varies.

The hydraulic power supplied by the pump can therefore be written as the product of in specific energy variation Δe and the mass flow rate $\dot{m}$.

$$P_h = \dot{m} \cdot \Delta e = \rho \cdot Q \cdot \frac{\Delta p}{\rho} = Q \cdot \Delta p \tag{2.7}$$

It is possible to describe the duty cycle of a hydraulic motor by simply reverse the inlet and outlet ports. The subscript *2* now refers to the motor inlet while the subscript *1* refers to the motor outlet.

The expression of ideal mechanical power at the hydraulic machine shaft. This represents the power absorbed by the machine directly from the prime mover considering a pump, and power available to the user considering a motor. In both cases, this mechanical (rotational) power can be written as the product of the angular speed ω of the machine shaft and the torque M at the same shaft.

$$P_m = M \cdot \omega \tag{2.8}$$

These hydraulic and mechanical powers are equal in the ideal case, as the input power to the machine (mechanical considering pump, hydraulic considering a motor) is equal to the output power from the machine (hydraulic considering a pump, mechanical considering a motor).

$$Q \cdot \Delta p = M \cdot \omega \tag{2.9}$$

Figure 2.4 shows a simplified diagram of a generic ideal hydraulic positive displacement machine and highlights the terms involved within the power balance of **Eq. (2.9)**.

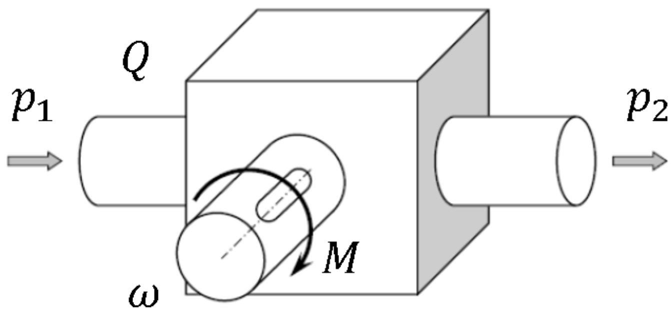

Figure 2.4: Schematic representation of the power balance of a positive displacement machine

We could have obtained the power balance found in **Eq. (2.9)** also considering an infinitesimal rotation $d\varphi$ of the machine shaft. Neglecting the variations in fluid gravitational potential energy and kinetic energy, the generalized equation of motion can be applied, as given in **Eq. (2.10)**.

$$dV_2 p_2 - dV_1 p_1 = -dL = M d\varphi \tag{2.10}$$

The integration of **Eq. (2.10)** over a complete revolution leads to **Eq. (2.11)**, from which **Eq. (2.12)** can be obtained.

$$\int_0^{2\pi} M d\varphi = \int_0^{2\pi} p_2 dV_2 - \int_0^{2\pi} p_1 dV_1 \tag{2.11}$$

$$M = V \cdot \frac{\Delta p}{2\pi} \tag{2.12}$$

Replacing M within **Eq. (2.8)** leads back to the ideal power balance of hydraulic positive displacement machines.

$$P_m = M \cdot \omega = V \cdot \frac{\Delta p}{2\pi} \cdot \omega = V \cdot n \cdot \Delta p = Q \cdot \Delta p = P_h \tag{2.13}$$

In real machines, of course, the input power to the machine is not equal to the output power. There are in fact losses, both mechanical and hydraulic, that define a certain efficiency of the machine, which is less than 1.

Concerning the hydraulic losses, these lead to a flow rate delivered by a pump which is lower than the ideal flow rate due to several factors. The most relevant one is the leakage that occurs in the gaps between the components in relative motion. A proportion of oil must be used to lubricate the mechanisms and thus allow this relative motion without restrictions and problems (excessive wear, seizure and/or sticking) through lubricated interfaces (i.e. gaps between the parts in which an oil film is present). Here, leakage flows occur due to several factors like:

- the pressure difference between the suction and delivery of the machine
- the pressure difference between the suction and the case of the machine
- the viscous effect on the fluid between two surfaces in relative motion
- the relative speed between the moving parts
- the temperature variation that varies the fluid characteristics

All these effects lead to a portion of fluid that is not available to transfer energy.

It is thus possible to define the volumetric efficiency for pump and motor as the ratio between ideal machine flow rate and real flow rate. Referring to **Figure 2.5** where the cases of a pump and motor with leakage are shown schematically, **Eq. (2.14)-(2.15)** report the two expressions of the volumetric efficiencies for the two cases.

$$\text{pump:} \quad \eta_v = \frac{Q}{Q_{id}} = \frac{V \cdot n - Q_f}{V \cdot n} \tag{2.14}$$

$$\text{motor:} \quad \eta_v = \frac{Q_{id}}{Q} = \frac{V \cdot n}{V \cdot n + Q_f} \tag{2.15}$$

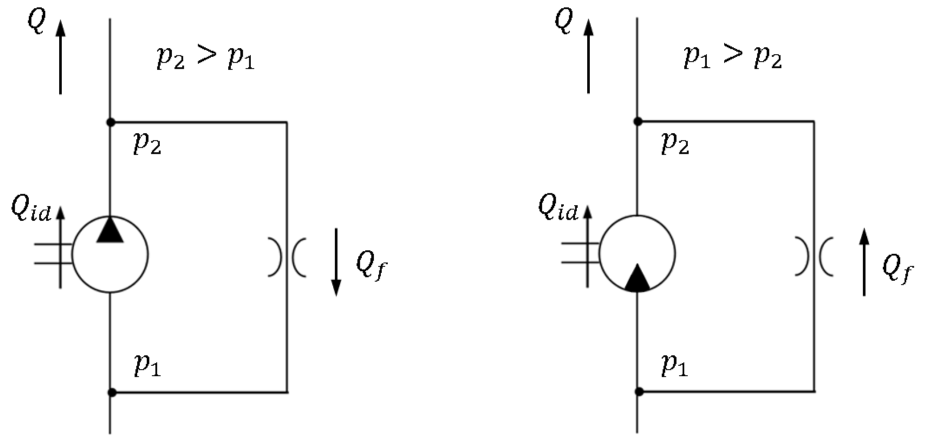

Figure 2.5: Simplified scheme of a pump (left) and motor (right) with leakage

Figure 2.5 represents the leakage as a flow rate crossing a hydraulic resistance interposed between the high-pressure zone and the low-pressure zone. However, in reality there are two types of leakage: an internal one from the high-pressure zone towards the low-pressure zone, and an external one from the high-pressure zone towards the machine case and, therefore, towards the tank.

In both cases, these leakages can be written as proportional to the pressure difference $\Delta p = |p_2 - p_1|$. **Eq. (2.16)-(2.17)** show the relationships obtained combining this assessment with **Eq. (2.14)-(2.15)**.

$$\text{pump:} \;\; \eta_v = \frac{Q}{Q_{id}} = \frac{V \cdot n - Q_f}{V \cdot n} = 1 - \frac{k \cdot \Delta p}{V \cdot n} = \eta_v(\Delta p, n) \tag{2.16}$$

$$\text{motor:} \;\; \eta_v = \frac{Q_{id}}{Q} = \frac{V \cdot n}{V \cdot n + Q_f} = \frac{1}{1 + \frac{k \cdot \Delta p}{V \cdot n}} = \eta_v(\Delta p, n) \tag{2.17}$$

The coefficient k is function of the film geometric characteristics, as well as the fluid dynamic viscosity μ.

On the other hand, it is possible to define the hydro-mechanical efficiency of the positive displacement machine considering the real and ideal torque at the shaft. This efficiency is thus the ratio between these torques, always differentiating the cases of pump and motor. In the former case, the torque required by the machine to the prime mover is greater than the ideal torque due to internal friction. In the latter case the torque available to the user is less than the ideal torque.

$$\text{pump:} \;\; \eta_{hm} = \frac{M_{id}}{M} = \frac{\frac{V \cdot \Delta p}{2\pi}}{\frac{V \cdot \Delta p}{2\pi} + M_a} \tag{2.18}$$

$$\text{motor:} \;\; \eta_{hm} = \frac{M}{M_{id}} = \frac{\frac{V \cdot \Delta p}{2\pi} - M_a}{\frac{V \cdot \Delta p}{2\pi}} \tag{2.19}$$

Bent axis piston machines

This sub-section presents bent axis piston units in more detail, as these are precisely the machines considered for this activity.

As the name implies, these units (pumps and/or motors) are positive displacement machines with axial pistons, which can be used within open or closed hydraulic circuits. The main difference with swash plate piston units is the inclination of the cylinder block and pistons defined by a certain angle with respect to the shaft axis. It is exactly this inclination angle that determines the piston strokes and so the volume of each piston chamber, and consequently the machine displacement.

The piston geometry cannot be cylindrical like in swash plate units since the pistons are not aligned with the machine shaft. A cylindrical geometry, in fact, would not allow a block inclination different from zero. This inclination requires a truncated cone geometry for the pistons to allow the coupling between them and the corresponding chambers in the cylinder block. These pistons must be coupled to the shaft with ball joints to allow rotations in all the three directions.

Figure 2.6 shows the main components of this type of positive displacement machine (without considering the casing).

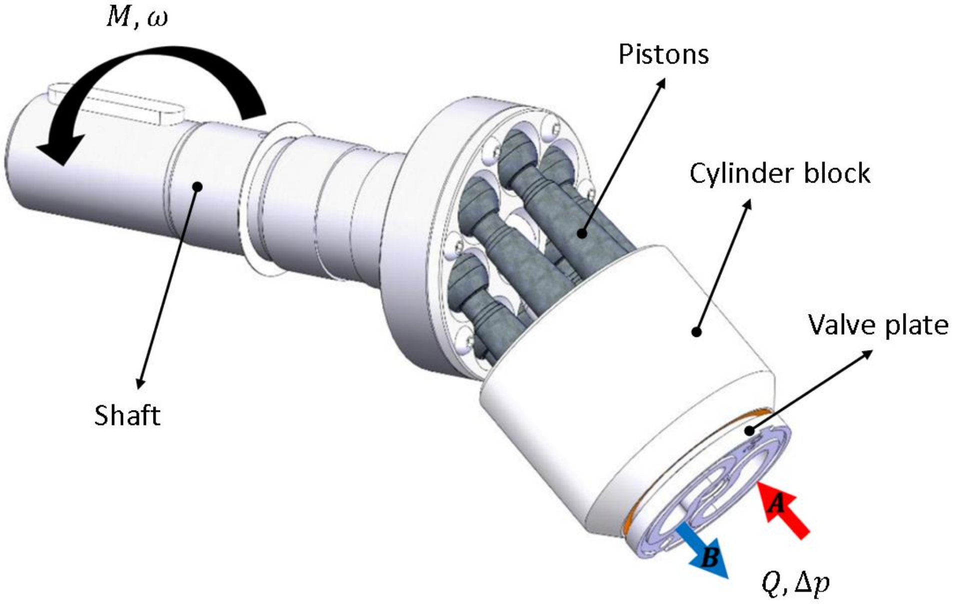

Figure 2.6: Main components of a bent axis piston unit (working as a motor)

Consider **Figure 2.6** where the machine operates as a hydraulic motor. The valve plate directs the fluid in and out of the piston chambers of the cylinder block. During the fluid inlet phase, each piston travels within the chambers on the cylinder block, moving from the inner dead centre (*IDC*) to the outer dead centre (*ODC*). The fluid high pressure within the chambers in communication with port A generates pushing forces on the pistons, which create a rotation moment at the shaft through the ball joint connections. The shaft rotation then leads to the rotation of the cylinder block and pistons. When a piston chamber is connected with the discharge outlet port B through the rotation of the system, the fluid is conveyed out of the cylinder block by the piston stroke, which goes from the *ODC* to the *IDC*. Once the chamber has been emptied, it is ready to start a new revolution.

Obviously, this type of machine can also be designed to work as a pump, where the output torque from the prime mover connected to the shaft drives the system, generating a flow from the low-pressure suction to the high-pressure delivery.

As seen in the introduction of the ISO symbolism for hydraulic components, some positive displacement units can work in the four quadrants, i.e. either as bidirectional pumps or bidirectional motors.

Bent axis piston units suit well to this application with four quadrants operating mode. It is “sufficient” to realize an appropriate symmetrical design of the machine to ensure its correct operation in these four quadrants.

The design of these machines can be of various types. The balancing and centring of the cylinder block and its connection with the shaft for the motion transmission is the aspect on which it is possible to find the greatest design differences. The cylinder block, in fact, can be coupled with the valve plate via a planar interface, and then kept centred by means of bearings and/or pins. Another possible solution is the design of a spherical cap interface between cylinder block and valve plate, capable therefore of supporting the block radially. Concerning the cylinder block-shaft transmission of motion, we can find designs that use a universal joint, or a bevel gear. In other cases, the transmission of motion takes place by exploiting the contact between the piston side and the cylinder block itself.

For a more in-depth analysis of the different designs of bent axis units, please refer to the reference texts [49].

We are presenting two reference geometries of bent axis unit in the following sub-section, which are produced by Dana Incorporated. We exploited these two units as the basis for the modelling of bent axis piston units presented in this chapter.

2.1.1 Reference positive displacement units

As anticipated, we considered two reference designs (both produced by Dana Incorporated) to realize the generic modelling of bent axis piston machines.

These two reference machines are the *SH11C* unit and the *SH7V55* unit. Both are bent axis units capable of working in the four quadrants, i.e. as bidirectional pump or motor. The main difference between them is that the former is a fixed-displacement unit, i.e. with a fixed valve plate, while the latter has a movable valve plate controlled by a servo actuator, which allows for the displacement variation.

We decided to both these units to extend the modelling to a larger 'family' of machines with similar geometry. We followed, in fact, a modular approach, thanks to which it is possible to choose whether to use the model relating to a fixed valve plate (and thus simulate the behaviour of a fixed displacement machine) or variable valve plate (and thus simulate a variable displacement machine).

Figures 2.7-2.8 show sections of the SH11C and SH7V55, with their main components.

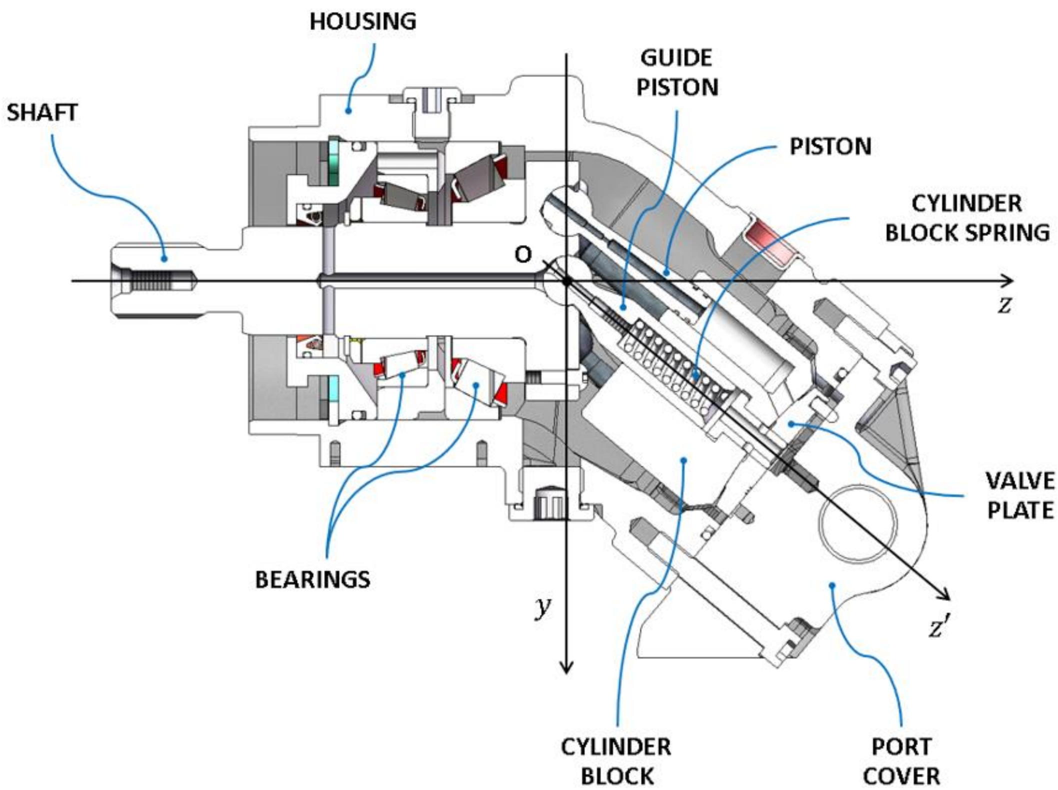

Figure 2.7: Section of the bidirectional bent axis unit with fixed displacement SH11C produced by Dana Incorporated

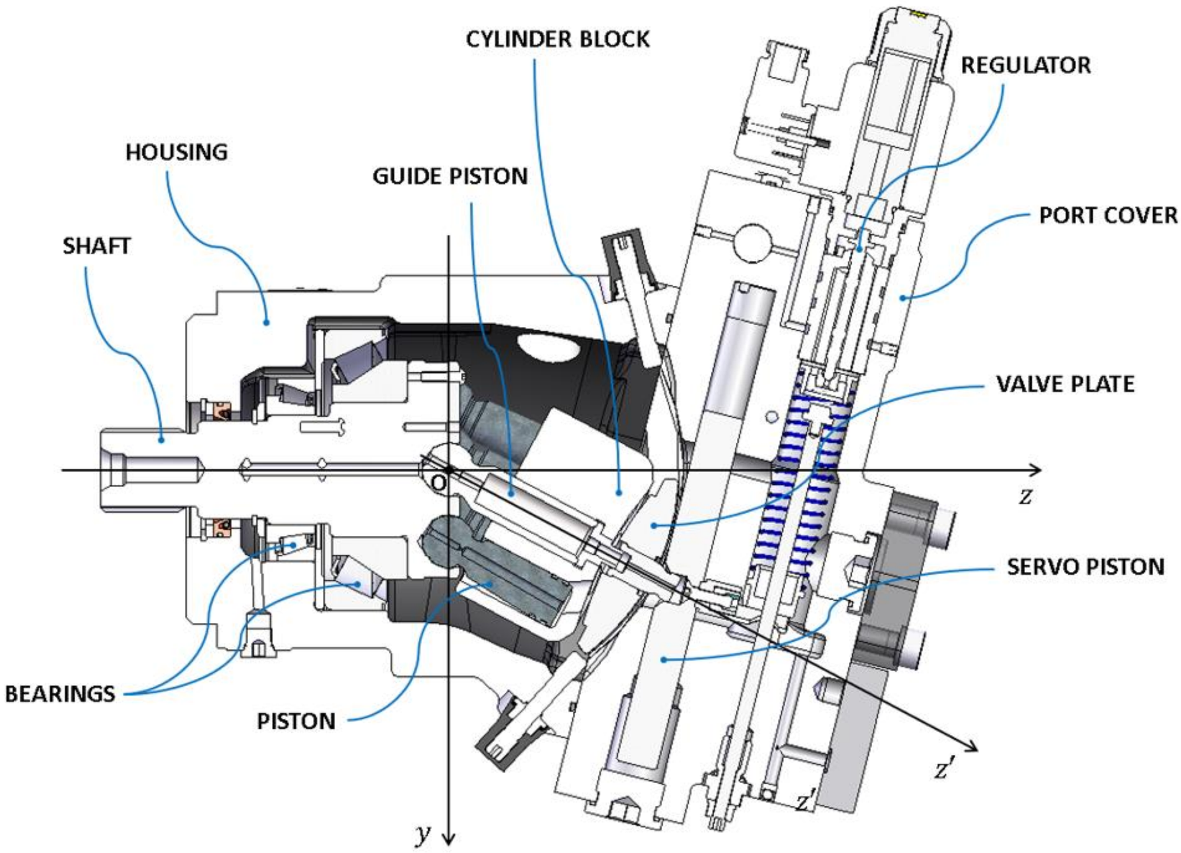

Figure 2.8: Section of the bidirectional bent axis unit with variable displacement SH7V55 produced by Dana Incorporated

Except for the valve plate and the corresponding machine cover, the other components of the two designs are quite similar. Obviously, the machine cover must provide for the regulator and servo piston in the variable displacement SH755 geometry, and that explains why it is so different from the SH11C one.

In both cases, the pistons have an internal channel that allows the fluid to flow through it conveying to the piston spherical coupling with the shaft. This oil leakage is used both for lubricating the coupling and for balancing the axial forces acting on the piston. The pressure force acting in the pump chamber tends to push the piston against the shaft. This would cause premature wear of pistons and ball joints without an adequate balancing force, which is generated exploiting this oil film pressure.

Figure 2.9 shows a 3D isometric view of an example of piston and its section highlighting its internal channel.

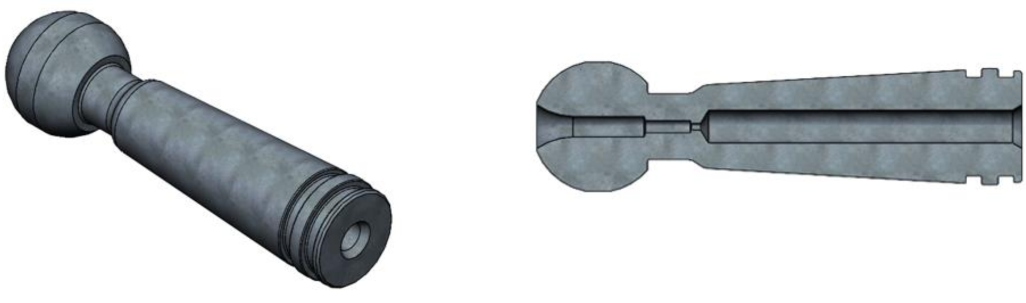

Figure 2.9: Piston example

Note the presence of two circumferential grooves in the conical area near the piston head. These are the housings for two sealing gaskets, inserted to minimize the amount of leakage between the side of the piston and its seat in the cylinder block.

The inclination of the cylinder block and its rotation causes the sealing zones to vary with the angular position, as shown in **Figure 2.10**.

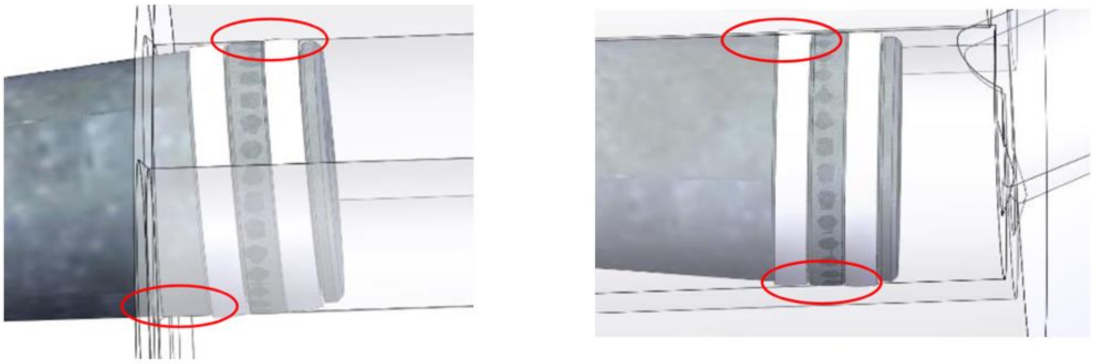

Figure 2.10: Variation of the sealing zone at the ODC (left) e IDC (right)

The rear part of the cylinder block has a concave geometry suitable for interfacing with the spherical cap of the valve plate in the two machines taken as a reference (and therefore in the family of similar machines to model with this study). Both units, in fact, realize the support of the cylinder block mainly via a spherical interface. **Figure 2.11** shows some isometric views of the cylinder block and the two examples of possible valve plates (i.e fixed or variable).

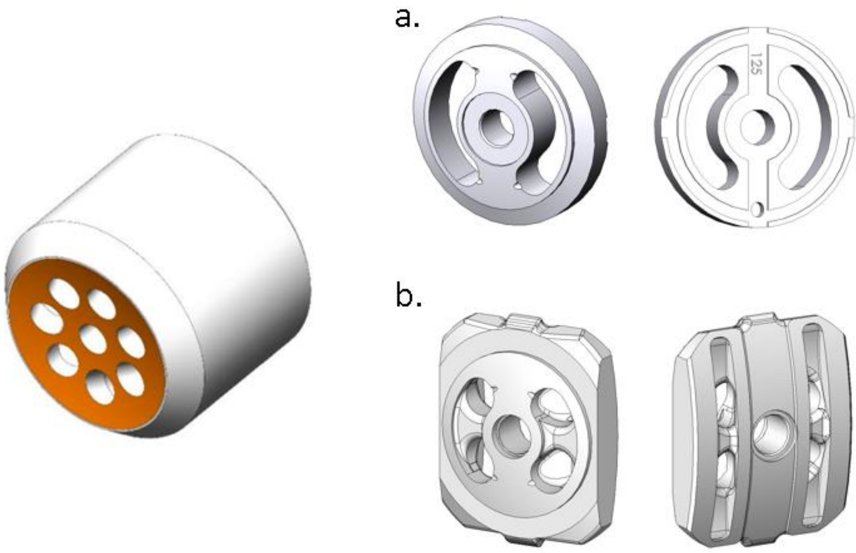

Figure 2.11: Examples of the cylinder block and the two possible valve plate: fixed (a) and variable (b)

The central hole in the cylinder block is the seat for a central pivot (**Figure 2.12**) used as connection between the shaft and the block itself to further ensure synchronism between the two components. Within this pivot there is a slot for the insertion of a pre-loaded spring, which pushes the block against the valve plate and the pivot against the shaft. Like the pistons, there is also an internal channel that ensures the lubrication of the ball joint coupling with the shaft.

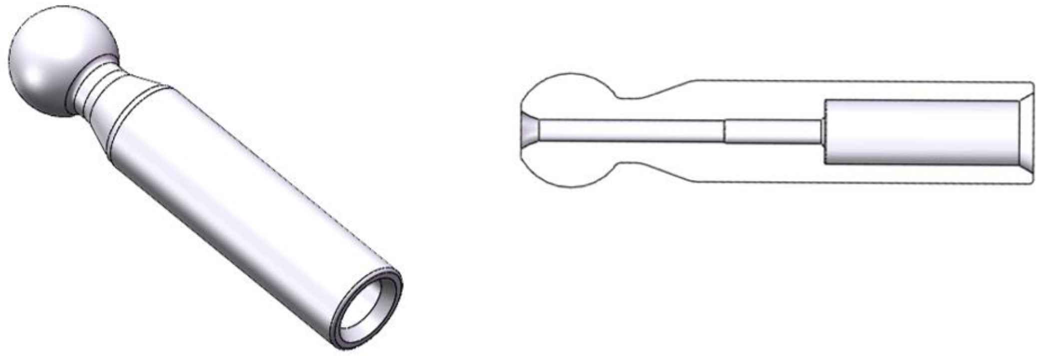

Figure 2.12: Central pivot for the connection between shaft and cylinder block

The hydrodynamic counter-pressure within the oil film between the cylinder block and the valve plate should ensure the cylinder block balancing. This hydrodynamic function is necessary to prevent the cylinder block seizing against the distributor plate. On the other hand, this oil film must absorb the tilting moments of the cylinder block to avoid excessive detachment of the components with consequent increase in leakage and losses of the hydraulic connection.

We used a coefficient or balancing factor B to assess the degree of balancing of the cylinder block. This balancing factor is defined by the ratio between the forces F_{pull} that push the block towards the valve plate and the hydrodynamic counter-pressure forces F_{push} generated within the oil film.

$$B = \frac{F_{pull}}{F_{push}} \cdot 100\% \tag{2.20}$$

Typical values of this balancing factor range between 92% and 98%. The dependence of many forces on shaft speed and operating conditions can justify this relatively large feasible range.

As mentioned above, the presence of a spherical interface between cylinder block and valve plate facilitates the support of the block itself in radial directions. With a planar interface, the oil film could only generate axial forces, while a force with generally non-zero components (in the three directions) is generated using a spherical interface.

Figure 2.11 shows the two possible types of valve plate for fixed and variable displacement. These two components are quite different in shape, geometry and characteristics. On both, however, it is possible to recognize the typical kidney-shaped holes used to connect the cylinder block chambers with the high and low pressure areas of the machine. The symmetry of these components with respect to the vertical axis is another easily recognizable aspect. This feature is crucial for machines used in the four quadrants, where the high and low-pressure environments can 'swap' during the life of the unit.

It is also possible to note the opening/closing grooves at the beginning/end of these kidney holes, which are special grooves exploited to make the transition from the high-pressure to the low-pressure more gradual and less abrupt.

Finally, **Figure 2.13** shows some views of shaft example for the reference machines.

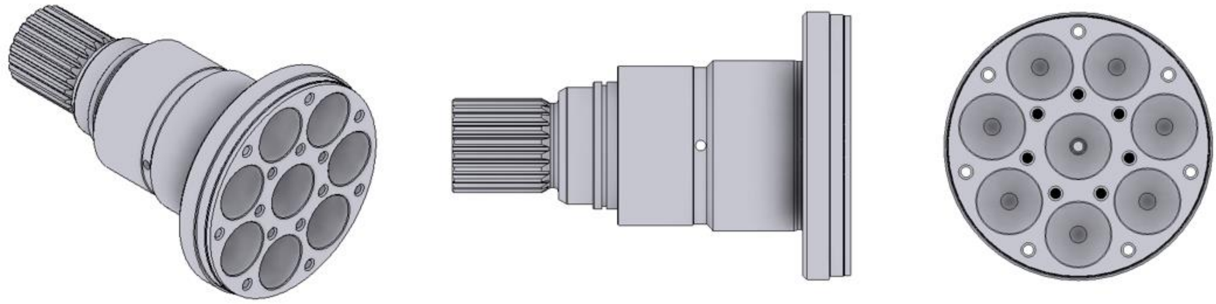

Figure 2.13: Shaft example

It is easy to note the various housings for the spherical joints connecting the pistons and the central pivot. A pair of tapered roller bearings (also shown in **Figures 2.7-2.8**) is installed in *X* or *O* arrangement to support the shaft in the radial and axial directions in this type of machines.

Further details of the machines will be shown in the following paragraphs, where we are presenting the modelling of the various aspects of the units.

Note again that the units presented have been only used as a reference for modelling. The objective of this activity is, in fact, not to create a numerical model that can be used for only one or two specific bent axis units, but for an entire family of machines with similar geometry and characteristics.

2.1.2 Introduction to the mechanical modelling

This sub-section introduces the approach we have followed to model the mechanical part of bent axis piston units.

One of the fundamental aspects was the realization of a parametric model of the reference machines. We indeed considered the various geometric and non-geometric feature that characterize the two reference units as pure parameters. In this way, we obtained a model capable of be adapted to all the machines with similar geometry and characteristics by simply introducing different parameter values.

Another fundamental aspect of the mechanical model is the vector format feature we have considered in its development. Using this approach, we could focus the attention on the *i*-th piston of the unit instead of considering all the pistons together. This method allows the model to consider machines with a different number of pistons n_P, which became one of the many parameters characterizing the model and identifying the machine under analysis. Obviously, it was possible to consider all the other pistons by simply shifting the *i*-th piston by the correct angular offset ($k \cdot \frac{2\pi}{n_P}$, with $k = 1, 2, \dots, n_P - 1$).

We also developed the mechanical model in a modular manner, identifying and modelling the various main components of the unit individually. Referring to **Figure 2.14**, these components are:

- the machine shaft and bearings,
- the pistons,
- the cylinder block and central pivot,
- the valve plate.

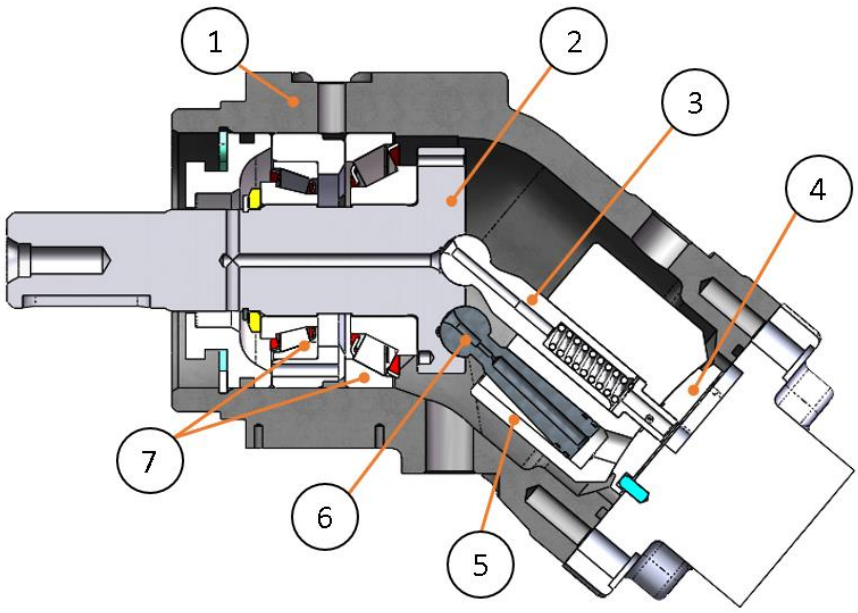

1) Casing
2) Shaft
3) Central pivot
4) Valve plate
5) Cylinder block
6) Pistons
7) Bearings

Figure 2.14: Main components considered in the mechanical model of the bent axis unit

Note that we considered some components as linked together, as it will be explained in more detail in the dedicated paragraphs.

As mentioned, we have analysed these components individually and then connected together to realize the complete mechanical model of the unit. It was thus necessary to define all the inputs and outputs for the modelling of the individual components to interface each of them with the adjacent components.

We considered both the kinematic and dynamic aspects of each component.

However, we analysed the kinematic part only for certain components of major interest as some other do not have a relevant kinematics. We thus wrote the equations of motion in space for these elements of interest. Starting from these equations, it was then possible to derive the velocities and accelerations that characterize the various points of interest of the component.

On the other hand, the dynamic analysis is necessary to find the value of the reactions (forces and moments) exchanged between the various components. We have used these following steps to do so:

1. identification of all forces and moments (known or unknown) acting on the component under examination
2. realization of the free body diagrams of the component under examination
3. writing of the equilibrium equations (static or dynamic) in space for the component under examination
4. possible introduction of simplifying hypotheses
5. solving the determined system formed by the equilibrium equations to derive the unknown terms.

Note that step 4 was necessary for several components. In fact, it is impossible to carry out a modelling of this type without using an in-depth CFD or multibody analysis for certain specific aspects (such as contacts between bodies, or hydrodynamic forces of oil film) and without the introduction of certain simplifying hypotheses.

Once the modelling of the individual components has been defined, it is then possible to 'connect' them together to obtain the complete model of the bent axis piston unit.

We then exploited the mathematical modelling as the basis for the realization of a numerical model developed in Simcenter Amesim®. This Amesim® model is thus parametric, vector-based, modular, and it is capable of simulating the behaviour of generic bent axis unit after the values of all the parameters necessary for the unambiguous identification of the machine have been entered.

2.1.3 Simcenter Amesim Submodel Editor®

The Submodel Editor tool of the Simcenter Amesim® software (a lumped parameter commercial software, as already seen) is the tool we used to create the numerical models of the various components after their detailed analysis. This tool, in fact, allows the creation of elements that can be used in Simcenter Amesim®, which was already introduced in **Section 1.3.1**.

As said, the user can select elements from several multi-physical libraries available within this software to replicate the system under examination. However, of course, there is no specific library capable of modelling these bent axis piston units in detail. It is therefore necessary to develop these elements from scratch, using precisely the Submodel Editor tool.

The basic steps for creating a Simcenter Amesim® element using this tool are as follows:

1. definition of both the connection ports with adjacent elements and input and output variables exchanged via these ports.
2. definition of all the parameters, geometric and non-geometric, required for parameterization of the component under examination (name, unit of measurement, default value and extreme values, etc.).
3. declaration and definition of all other internal variables required by the element to complete its modelling.
4. writing of the code (in C++ language) for the implementation of all the kinematic and dynamic analyses for the calculation of the outputs and quantities of interest of the model.
5. definition of the variables that the user can visualize in the post-processing phase of the simulation results.

Note that point 1 is crucial for the interconnection of different elements. Connecting two generic elements *A* and *B*, it is necessary for the connection port of *A* to have 'opposite' inputs and outputs with respect to the *B* connection port. The inputs of A are the output of B and vice versa. The consistency of the inputs/outputs in terms of type (scalar or vector) and size (unit of measurement) is also crucial to ensure a correct connection.

Defining the element ports in a correct way allows not only the connection with the other adjacent user-defined elements, but also with elements already present within the software's 'standard' libraries.

This tool, moreover, allows to create an identifying icon of the user-defined element to make it immediately recognizable within the Simcenter Amesim® sketch.

We are then presenting in the following paragraphs the analyses made on the various components and the corresponding Simcenter Amesim® element created using the Submodel Editor, highlighting the icon used, the connection ports and the variables exchanged through these.

Having completed this introductory section, it is now possible to proceed to the actual modelling of the bent axis piston machines.

2.2 Fluid-dynamic model

We are briefly reporting the main analyses done for the fluid-dynamic modelling of the bent axis piston in this section. In fact, this activity concerning the fluid-dynamic aspects had already been partly carried out previously by the Dana Incorporated virtual engineering department. In particular, we are not reporting in this thesis the analysis made for the evaluation of the equivalent flow areas between the valve plate and the cylinder block inlet/outlet which was realized by the company. This study allowed the writing of C++ code for the analytic evaluation of these areas as function of the cylinder block angular position, which was then exploited to calculate the fluid flow rate within the piston chambers. However, we could integrate this part of code within the valve plate submodel, which will be presented later.

In addition to this study already carried out before this work of this thesis, we are presenting the approach used for modelling the fluid-dynamic part of the bent axis unit and the main submodels created. This general approach had been already used by the company to model a swash plate unit and it was modified and adapted to our study case.

These fluid-dynamic submodels are fundamental for the completeness of the total model as they exchange information (input/output) with the mechanical elements. For example, the fluid-dynamic part of the model calculates the pressure acting inside the piston chambers generating forces and moments. On the other hand, the mechanical elements provide for the information concerning the piston strokes, chamber volumes and volume variations. We must consider the model in its entirety, where the fluid-dynamic part is complementary to the mechanical part and vice versa.

We selected the Eulerian specification of the flow field to mathematically describe the fluid-dynamic part of the unit. This is a way of looking at fluid motion that focuses on specific locations in the space through which the fluid flows as time passes. It thus consists of the study of a control volume (of time-varying mass) with the possibility of exchanging energy, mass and momentum through its surfaces.

We neglected thermal effects within the activity reported in this thesis. However, we also started an activity to transform this fluid-dynamic modelling into thermofluidic-dynamics, still maintaining the lumped parameter approach.

Neglecting wave propagation effects, the main equations required for the problem solution are the continuity equation (**Eq. (2.21)**), which links the pressure in the control volume to the mass flow rate, and the fluid equation of state (**Eq. (2.22)**), which describes the fluid's properties.

$$\frac{dp}{dt} = \frac{B}{V} \cdot \left(Q_{in} - Q_{out} - \frac{dV}{dt} \right) \tag{2.21}$$

$$\frac{d\rho}{dt} = \frac{\rho}{B} \cdot \frac{dp}{dt} \tag{2.22}$$

Figure 2.15 shows a schematic of the fluid-dynamic model of the unit, where we consider a bent axis motor with port B of the valve plate (on the left in **Figure 2.15**) as the input port and port A (on the right) as the output port. Note that a lumped parameter modelling approach requires to always connect a capacitive element to a resistive one and vice versa. In fact, it is not possible to directly connect two capacitive or two resistive elements to guarantee the necessary inputs/outputs to the various elements.

Following this approach, we considered a hydraulic resistance defined by the fluid inlet channel into the hydraulic machine (A_B) and then a capacitive element representing the constant volume of this inlet port (Ch_B) downstream of the input port pressure signal (p_{IN}). We inserted a first hydraulic node downstream of Ch_B. Most of the total flow rate Q_B, in fact, flows into the piston chambers of the cylinder block (Q_{BC}) through variable orifices ($A_{BC,i}$) defined by the kidney holes and by the block rotation, i.e. the inlet ports. However, part of the total flow rate is a leakage flow (Q_{L-B}) that is conveyed into the casing through the oil film between the valve plate and the cylinder block. The flow rate entering the variable piston chambers (Ch_i) then defines the fluid pressure. Here, the flow rate becomes a vector ($Q_{BC,i}$) to consider the different chambers it enters. We then considered two other leakages to the casing. The first one occurs between the piston side and its seat ($Q_{L-PC,i}$), while the second happens in the ball joint connecting the piston with the shaft ($Q_{L-SC,i}$). The piston chambers are then connected to a constant volume representing the machine outlet port (Ch_A) through another variable orifice ($A_{AC,i}$), which represents the outlet ports. Here, the flow rate changes back to scalar (Q_{BC}). We also consider another leakage between cylinder block and valve plate (Q_{L-A}). Finally, there is a last resistive element representing the machine outlet channel, which is connected to the pressure signal of port A.

Note that all the leakage flows considered flow into a capacitive element representative of the unit casing, which is then connected to the tank.

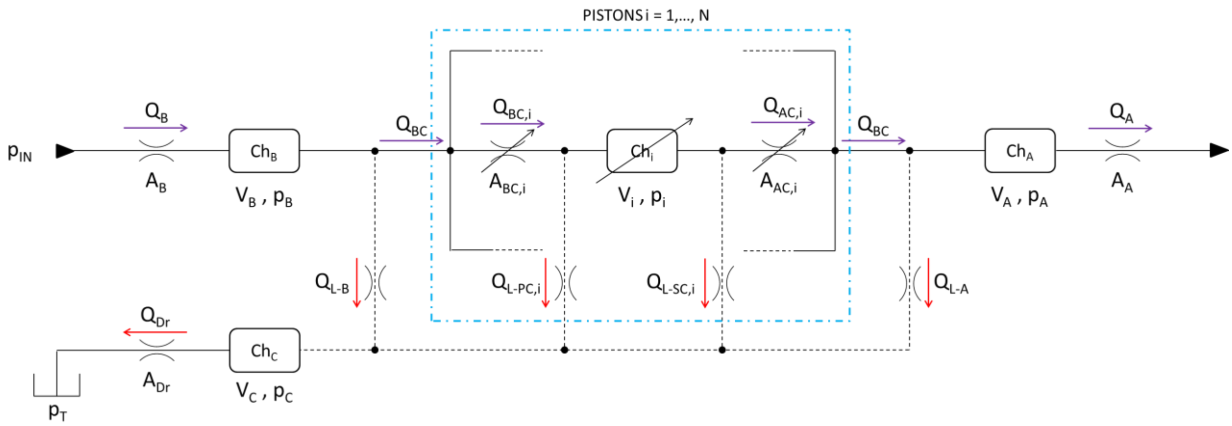

Figure 2.15: Fluid-dynamic model schematic for the bent axis unit

The evaluation of all these leakages is necessary to assess the total drain flow rate (Q_{Dr}) and thus the volumetric efficiency of the bent axis piston unit.

We are thus reporting below the main elements of the lumped parameter model of the fluid-dynamic part of the machine:

- variable volume chambers, which represent the piston chambers within the cylinder block (Ch_i in **Figure 2.15**),
- variable orifices, which represents the inlet and outlet ports of the unit (A_{BC_i} and A_{AC_i} in **Figure 2.15**),
- oil film and leakage of the unit (Q_{L-B}, $Q_{L-PC,i}$, $Q_{L-SC,i}$ and Q_{L-A} in **Figure 2.15**).

We are not presenting the other elements as they can be modelled through simple fixed orifices or constant volumes, which can be found within the Amesim® standard libraries.

2.2.1 Variable volume chambers

Figure 2.16 shows in detail the central part of the **Figure 2.15** diagram representing the unit pistons.

As anticipated, for each pumping unit there is:

- a variable-section orifices A_{BC_i} that connects port B with the *i*-th piston chamber,
- a variable volume V_i, which constitutes the *i*-th piston chamber,
- a variable-section orifices A_{AC_i} that connects the *i*-th piston chamber with port A.

The inlet and outlet flow rates are divided and summed at nodes B and A respectively.

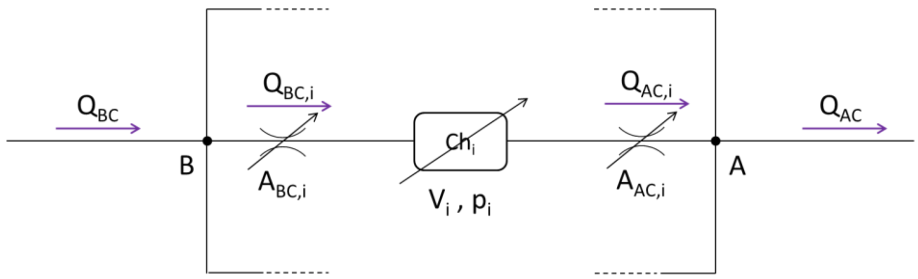

Figure 2.16: Pistons fluid-dynamic schematic

We can obtain **Eq. (2.23)** by applying **Eq. (2.21)** to the *i*-th piston chamber Ch_i and referring to its angular position ϑ_i, which is directly related to time in the case of a rotational positive displacement machine working at speed ω.

$$\frac{dp_i}{d\vartheta_i} = \frac{B_i}{V_i \cdot \omega} \cdot \left(Q_{BC,i} - Q_{AC,i} - \omega \frac{dV_i}{d\omega_i} \right) \tag{2.23}$$

This relationship (as indicated by subscript i) must be applied to each chamber to make this model vector based.

Exploiting these equations, it was possible to realize the submodel concerning the variable volume chambers of the cylinder block using the Simcenter Amesim Submodel Editor® to define the connection ports with the other elements and write the C++ code.

Figure 2.17 shows the Simcenter Amesim® icon associated with the variable volume chamber submodel described by **Eq. (2.23)**, while **Table 2.1** describes the variables at each submodel port.

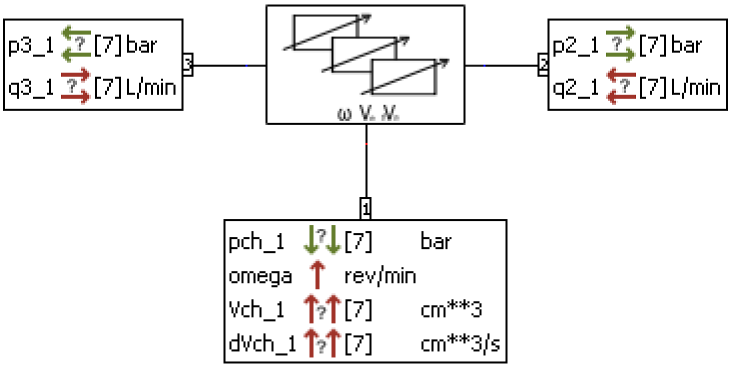

Figure 2.17: Icon of the variable volume chambers submodel developed in Simcenter Amesim®

Table 2.1: Inputs/outputs at each port of the variable volume chambers submodel developed in Simcenter Amesim®

PORT	VARIABLE	DESCRIPTION	SYMBOL	TYPE
1	Input	Angular speed	ω	Scalar
		Volume	V	Vector
		Volume variation	dV/dt	
	Output	Chamber pressure	p	Vector
2	Input	Flow rate	Q	Vector
	Output	Pressure	p	
3	Input	Flow rate	Q	Vector
	Output	Pressure	p	

The parameters required to characterize the variable volume chambers within the cylinder block are:

- the pressure initial values of each chamber, used at time $t = 0$ of the simulation,
- the hydraulic fluid detection index, which is then characterized in a special element of the Simcenter Amesim® *Hydraulics* library,
- the piston number n_p of the unit.

The model calculates the instantaneous value of the pressure within the *i*-th chamber using the parameters introduced by the user and the inputs received from adjacent elements.

Note that an element representing a vectorial variable volume chamber is already present within the standard Amesim® *Hydraulic Component Design* library. However, we had to replicate it anyway to insert an additional connection port with the mechanical part of the model. This connection port, in fact, is necessary to pass the info concerning the chamber volumes and volume derivatives from the mechanical part to this element, and the info concerning the chamber pressure from this element to the mechanical part for the pressure force evaluations. The same applies to other elements, like the orifice elements.

2.2.2 Flow inlet and outlet port

We are presenting the modelling for the variable-section orifices ($A_{BC,i}$ and $A_{AC,i}$) in this subsection, which were used to model the inlet and outlet ports between the valve plate and the cylinder block chambers.

Eq. (2.24) defines the flow rate through an orifice with cross-section A_0 for a turbulent flow.

$$Q = c_q \cdot A_0 \cdot \sqrt{\frac{2 \cdot \Delta p}{\rho} \cdot \frac{\rho}{\rho(0)}} \cdot \text{sgn}(\Delta p) \tag{2.24}$$

On the other hand, **Eq. (2.25)** defines the laminar flow rate crossing a circular cross-section A_0 with radius r.

$$Q = 48 \cdot \pi \cdot r \cdot \mu \cdot L \cdot \Delta p \cdot \text{sgn}(\Delta p) \tag{2.25}$$

The Reynolds number given in **Eq. (2.26)** is used to discriminate the flow regime of the fluid, where ρ is the fluid density, v is the fluid velocity, μ the fluid dynamic viscosity and d_H is the hydraulic diameter of the considered section.

$$Re = \frac{\rho \cdot v \cdot d_H}{\mu} \tag{2.26}$$

The turbulent flow regime typically arises for Reynolds values above the critical Reynolds number.

In Simcenter Amesim® the flow regime is discriminated using the flow number λ defined by **Eq. (2.27)**, which is function of the Reynolds number.

$$\lambda = \frac{d_h}{v} \sqrt{\frac{2 \cdot \Delta p}{\rho}} = \frac{Re}{c_q} \tag{2.27}$$

Eq. (2.28) defines the correlation between the flow coefficient c_q and the flow number value λ, while **Figure 2.18** shows this correlation.

$$c_q = c_{q-MAX} \cdot \tanh\left(\frac{2 \cdot \lambda}{\lambda_{cr}}\right) \tag{2.28}$$

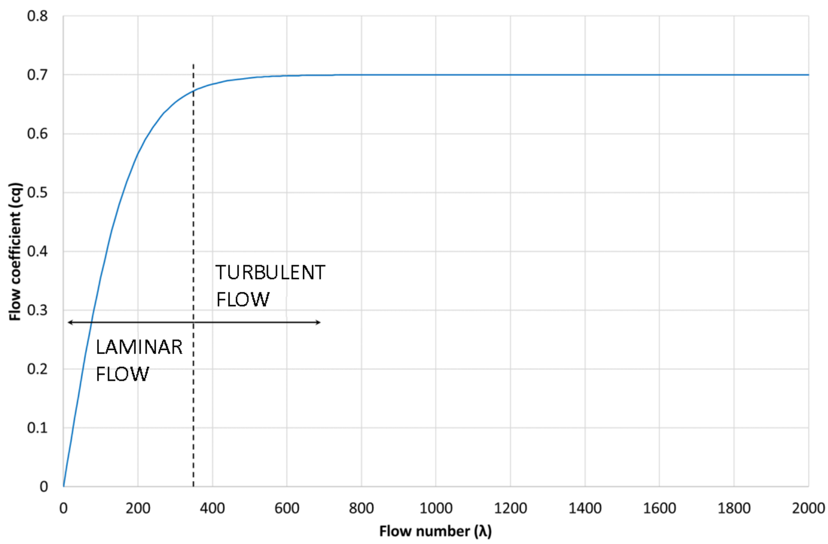

Figure 2.18: Flow coefficient c_q as function of the flow number λ

Eq. (2.29) then evaluate the flow rate through an orifice with a relationship that is valid for both laminar and turbulent flows.

$$Q = c_{q-MAX} \cdot \tanh\left(\frac{2 \cdot \lambda}{\lambda_{cr}}\right) \cdot A_0 \cdot \sqrt{\frac{2 \cdot \Delta p}{\rho} \cdot \frac{\rho}{\rho(0)}} \cdot sgn(\Delta p) \tag{2.29}$$

Eq. (2.29) can therefore be used for modelling the n_P variable-section orifices of the n_P cylinder block chambers, where inlet $A_{BC,i}$ and outlet $A_{AC,i}$ areas are used instead of A_0.

We thus realized the submodel of these variable-section orifices in Simcenter Amesim® starting from these equations.

Figure 2.19 shows the representation of the Simcenter Amesim® icon concerning the inlet and outlet variable orifices, while **Table 2.2** describes the variables associated with the different ports of the submodel.

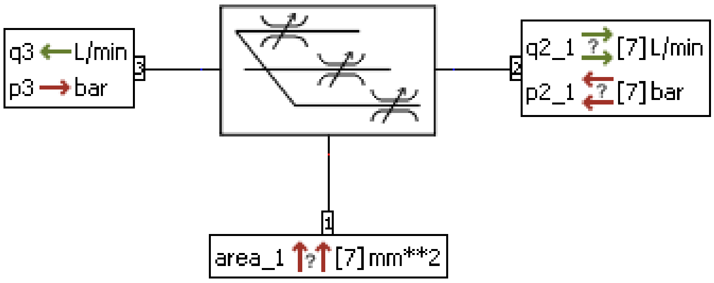

Figure 2.19: Icon of the variable-section orifices submodel developed in Simcenter Amesim®

Table 2.2: Inputs/outputs at each port of the variable-section orifices submodel developed in Simcenter Amesim®

PORT	VARIABLE	DESCRIPTION	SYMBOL	TYPE
1	Input	Pressure	p	Vector
	Output	Flow rate	Q	
2	Input	Variable section areas	A	Vector
3	Input	Pressure	p	Scalar
	Output	Flow rate	Q	

Port 3 represents a summing hydraulic node. Here, the model realizes the sum of the flow rates characterizing the connected branches while keeping the same pressure for all of them.

The parameterization of the inlet and outlet ports requires the definition of the following parameters:

- the hydraulic fluid detection index, which is then characterized in a special element of the Simcenter Amesim® *Hydraulics* library,
- the piston number n_P,
- the values of the maximum flow coefficient c_{q-MAX} usually set equal to 0.7 and the critical Reynolds number Re_{cr}.

Note that **Figure 2.19**, considering the convention of **Figure 2.15**, is oriented to represent the input spans, with the summing node on the left. The element for modelling the outlet lights, with the summing node on the right, will be obtained by simply mirroring the element in **Figure 2.19**.

2.2.3 Leakage

As mentioned, it is necessary to consider all the leakages between the various interface surfaces between the components in relative motion within the bent axis unit to evaluate its volumetric efficiency η_V. These leakages must guarantee both lubrication and counter-pressure forces to balance the various components, keeping them in equilibrium. Despite part of the flow rate theoretically processable by the machine is lost through these leakages, affecting the unit volumetric efficiency, these losses are accepted as necessary for the proper functioning of the machine itself. However, these leakages must be 'sized' correctly.

As anticipated, we considered the following leakages:

- leakage in the spherical interface between the cylinder block and the valve plate (Q_{L-A} and Q_{L-B}),
- leakage between each piston and its seat in the cylinder block ($Q_{L-PC,i}$),
- leakage between the ball joint of each piston and its seat in the shaft ($Q_{L-SC,i}$).

Figure 2.20 shows a picture taken from the 3D CAD of some machine components where we highlighted the leakage flow rates we are considering.

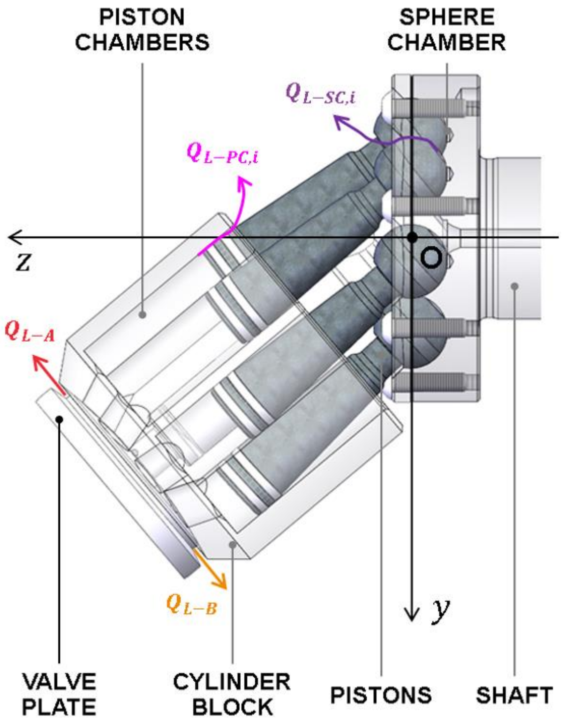

Figure 2.20: Main leakage flow rates of the unit

We considered oil film with constant height to simplify the study and allow the lumped parameter modelling without the need of CFD analysis.

The user must thus enter the height value of the oil film of interest. This value, of course, is generally unknown, especially without carrying out a CFD analysis. We thus used standard values taken from literature in the first instance.

Once we had completed the model, we decided to proceed as follow in agreement with the company. We performed an 'optimization' of these unknown values for each machine of interest replicated through the final model. In this way, we were able to carry out the height values by imposing the minimization of the error between the simulated volumetric efficiency and the experimental one. In this way, it was possible to experimentally 'calibrate' these unknown values.

Note that this approach may lead to errors on the evaluation of the individual gap height as it is impossible to evaluate the individual contribution without CFD analysis. However, the proposed methodology allowed to find a combination of gap heights that minimizes the error on the volumetric efficiency of the machine.

This approach will be described in more detail in the result section (**Section 2.5**).

We are reporting an analysis of the three leakages in the following sub-sections.

Leakage between cylinder block and valve plate

Figure 2.21 shows the schematic for the geometric parameterization of the oil film between cylinder block and valve plate. Note that this parameterization is valid both for valve plates with and without ribs.

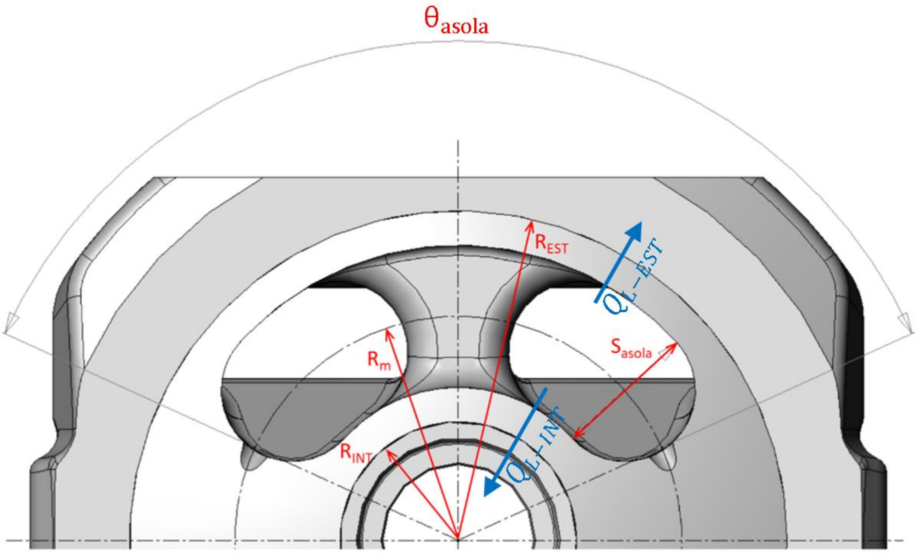

Figure 2.21: Parametrization for the leakage gap between cylinder block and valve plate

Table 2.3 shows the quantities required to parameterize the leakage gap between the cylinder block and the valve plate.

Table 2.3: Parameters required for the cylinder block-valve plate leakage

Symbol	Description
R_m	Kidney central radius
R_{INT}	Internal radius of the valve plate seals
R_{EST}	External radius of the valve plate seals
s_{asola}	Kidney width
θ_{asola}	Kidney angular extension
h_{CV}	Leakage gap height

Figure 2.21 also shows the two contributions of flow rate, Q_{L-INT} and Q_{L-EST}. These leakages can be assimilated to annulus sectors, which can be reduced to an equivalent rectangle by linearly developing the two gaps for simplicity. We could thus obtain two rectangular gaps with constant height h_{CV}, width defined by **Eq. (2.30)-(2.31)** and length defined by **Eq. (2.32)-(2.33)**.

$$l_{INT} = R_m - \frac{s_{asola}}{2} - R_{INT} \tag{2.30}$$

$$l_{EST} = R_{EST} - R_m - \frac{s_{asola}}{2} \tag{2.31}$$

$$L_{INT} = \left(R_m - \frac{s_{asola}}{2}\right) \cdot \theta_2 \tag{2.32}$$

$$L_{EST} = \left(R_m + \frac{s_{asola}}{2}\right) \cdot \theta_2 \tag{2.33}$$

Assuming laminar flow, the total leakage flow rate (**Eq. (2.36)**) can be evaluated as the sum of the inner (**Eq. (2.24)**) and outer (**Eq. (2.25)**) gap leakages.

$$Q_{L-INT} = \frac{(p - p_{Dr}) \cdot l_{INT} \cdot {h_{CV}}^3}{12 \cdot \mu(p_{mid}) \cdot L_{INT}} \tag{2.34}$$

$$Q_{L-EST} = \frac{(p - p_{Dr}) \cdot l_{EST} \cdot {h_{CV}}^3}{12 \cdot \mu(p_{mid}) \cdot L_{EST}} \quad (2.35)$$

$$Q_L = (Q_{L-INT} + Q_{L-EST}) \cdot \frac{\rho(p_{mid})}{\rho(0)} \quad (2.36)$$

Note that these relationships include the fluid density ρ, which varies with pressure. We thus considered an average pressure between the involved areas and the casing drain to define the correct density.

$$p_{mid} = \frac{(p + p_{case})}{2} \quad (2.37)$$

Obviously, we doubled these relationships to consider both kidney holes.

It was thus possible to realize the submodel concerning the leakage gap between cylinder block and valve plate in the Simcenter Amesim Submodel Editor® by implementing these relationships in C++ code.

As usual, it was necessary to define the connection ports with the other elements of the model and the corresponding inputs/outputs considering the diagram in **Figure 2.15**. **Figure 2.22** shows the Simcenter Amesim® icon associated with the element concerning the calculation of the leakage flow rates between cylinder block and valve plate.

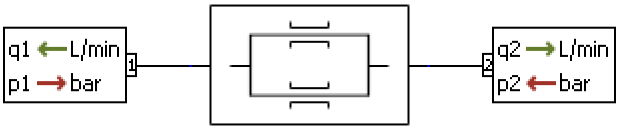

Figure 2.22: Icon of the submodel concerning the leakage flow rates between cylinder block and valve plate developed in Simcenter Amesim®

Table 2.4 describes the variables associated with the ports of this submodel.

Table 2.4: Inputs/outputs at each port of the submodel concerning the leakage flow rates between cylinder block and valve plate developed in Simcenter Amesim®

PORT	VARIABLE	DESCRIPTION	SYMBOL	TYPE
1	Input	Pressure	p	Scalar
	Output	Flow rate	Q	
2	Input	Pressure	p	Scalar
	Output	Flow rate	Q	

The parameterization of this element requires the following parameters:

- the hydraulic fluid detection index, which is then characterized in a special element of the Simcenter Amesim® *Hydraulics* library,
- the kidney central radius R_m,
- the kidney width s_{asole},
- the seals inner radius R_{INT} and outer radius R_{EST},
- the kidney angular extension θ_{asola},
- the gap height h_{CV}.

Leakage between piston and seat

We are now proceeding with the modelling of the leakage between the piston side and its seat in the cylinder block.

As said, the pistons have a truncated cone geometry which does not allow for a perfect coupling with the cylindrical seats. For this reason, these pistons have two seals positioned within dedicated grooves near the piston head to minimize the leakage flow from the pressure chambers to the casing. However, these seals cannot ensure zero leakage. We thus considered a leakage annular gap with length equal to the distance between the seal centres.

Figure 2.23 shows the schematic view concerning the geometric parameterization of the leakage gap between the piston and its seat in the cylinder block. On the other hand, **Table 2.5** lists and describes the geometric quantities for the parameterization of this leakage gap.

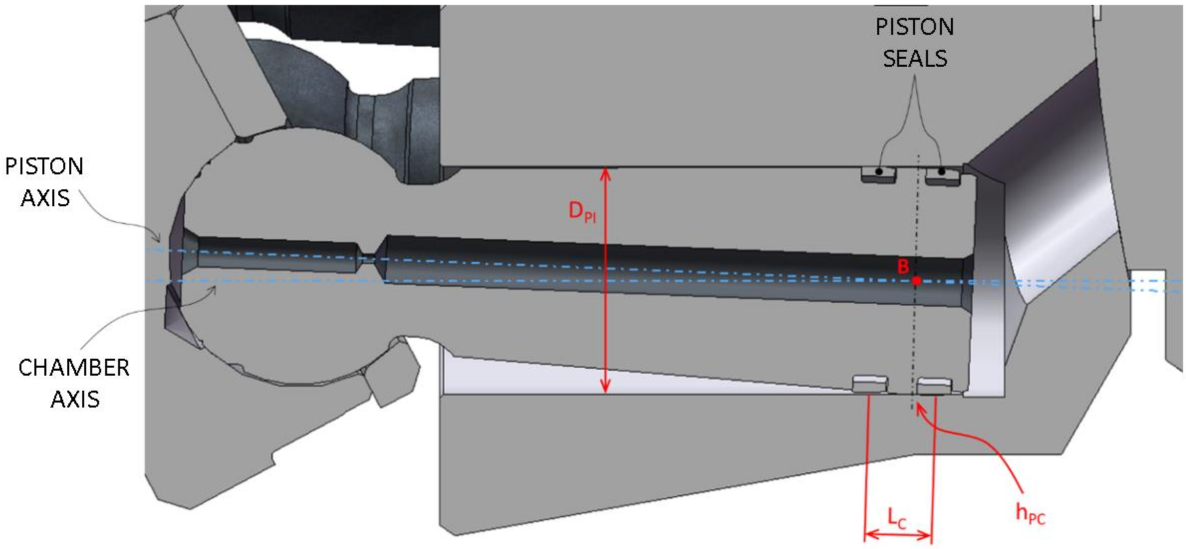

Figure 2.23: Parametrization for the leakage gap between piston side and its seat

Table 2.5: Parameters required for the leakage between piston side and its seat

Symbol	Description
D_{PI}	Nominal piston diameter
L_C	Leakage gap length (distance between the seal centres)
h_{PC}	Leakage gap height

Eq. (2.38) expresses the leakage flow rate between the piston side and its seat. We have considered the sum of the leakage flow rate through an annular gap of diameter D_{PI} and height h_{PC} and the drag flow contribution due to the relative velocity between the piston and its seat.

$$Q_{L-PC} = \frac{\pi \cdot (p - p_{Dr}) \cdot D_{PI} \cdot {h_{PC}}^3}{12 \cdot \mu(p_{mid}) \cdot L_C} \cdot \frac{\rho(p_{mid})}{\rho(0)} - \frac{\pi \cdot D_{PI} \cdot h_{PC} \cdot v_{PI}}{2} \tag{2.38}$$

Similarly to what we have done before, we considered an average pressure between the chamber pressure and the drain pressure to assess the fluid density in the gap.

$$p_{mid} = \frac{(p + p_{case})}{2} \tag{2.39}$$

Obviously, **Eq. (2.38)** must be applied for each piston to evaluate all the leakage flows through the gaps between pistons and seats.

As usual, it was then possible to proceed with the realization of the element for this leakage gap in the Simcenter Amesim Submodel Editor® environment. **Figure 2.24** shows the Simcenter Amesim® icon associated with the submodel for calculating the leakage flow rates between cylinder block and piston.

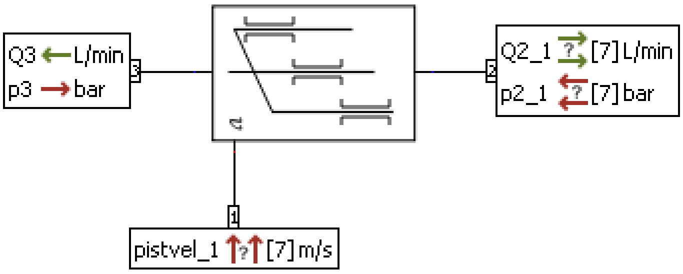

Figure 2.24: Icon of the submodel concerning the leakage flow rates between piston side and cylinder block developed in Simcenter Amesim®

Table 2.6 describes the variables associated with the ports of the submodel.

Table 2.6: Inputs/outputs at each port of the submodel concerning the leakage flow rates between piston side and cylinder block developed in Simcenter Amesim®

PORT	VARIABLE	DESCRIPTION	SYMBOL	TYPE
1	Input	Piston velocities	v	Vector
2	Input	Pressure	p	Vector
	Output	Flow rate	Q	
3	Input	Pressure	p	Scalar
	Output	Flow rate	Q	

The parameterization of the element relating to the leakage gap between the piston side and its seat in the cylinder block requires the following parameters:

- the hydraulic fluid detection index, which is then characterized in a special element of the Simcenter Amesim® *Hydraulics* library,
- the piston number n_P,
- the nominal piston diameter D_{PI},
- the leakage gap length L_C, i.e. the distance between the seal centres,
- the leakage gap height h_{CP}.

Leakage between piston and spherical joint

The third contribution we considered is the leakage between the spherical part of the pistons and the ball joint seats in the shaft. Observing the section of the piston in its ball joint seat (**Figure 2.25**), it is possible to note the inner channel within the piston connecting the piston chamber with the ball joint recess, which can be considered as a hydraulic chamber. The internal channel and its fixed orifice must ensure oil flow into the hydrostatic ball joint recess to compensate the leakage occurring through the spherical gap towards the unit casing.

Figure 2.25 also shows the parameters necessary for the leakage gap characterization.

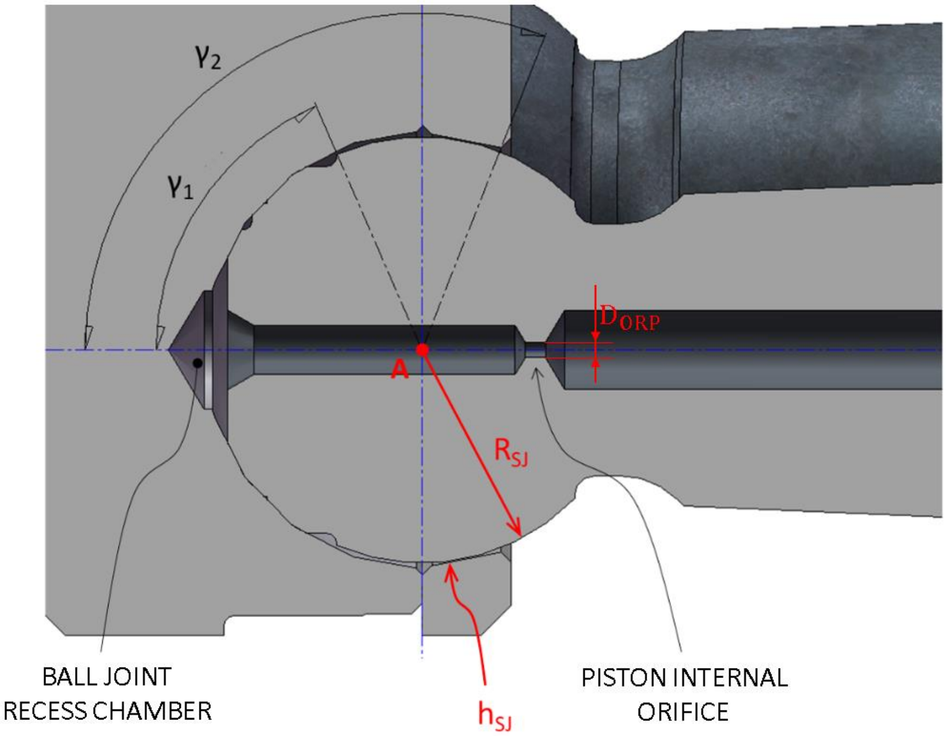

Figure 2.25: Parametrization for the spherical leakage gap between piston and ball joint seat

Table 2.7 lists and describes the geometric quantities for the parameterisation of this leakage gap.

Table 2.7: Parameters required for the spherical leakage gap between piston and ball joint seat

Symbol	Description
R_{SJ}	Nominal radius of the piston spherical end
h_{SJ}	Leakage gap height
d_{ORP}	Piston internal orifice diameter
γ_1	Starting angle for the spherical leakage gap (defined by the sealing groove on the piston spherical end)
γ_2	Ending angle for the spherical leakage gap (defined by the ball joint seat)

We decided to separate the contribution of the fixed orifice to simplify the analysis. Since this orifice and the leakage gap are two resistive elements, it is necessary to introduce a capacitive element representing the recess hydraulic chamber between these two.

We modelled the piston internal orifices using the analysis previously made for the variable diameter orifices (**Eq. (2.29)**). **Eq. (2.40)** implements the same relationship using a circular flow area with diameter d_{ORP}.

$$Q = c_{q-MAX} \cdot \tanh\left(\frac{2 \cdot \lambda}{\lambda_{cr}}\right) \cdot \frac{\pi \cdot d_{ORP}{}^2}{4} \cdot \sqrt{\frac{2 \cdot \Delta p}{\rho} \cdot \frac{\rho}{\rho(0)}} \cdot \mathrm{sgn}(\Delta p) \tag{2.40}$$

Starting from this relationship, we realized the 140ength140ondent element for the fixed internal piston orifice**. Figure 2.26** depicts the Simcenter Amesim® icon, ports and inputs/outputs.

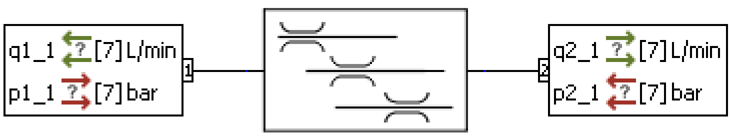

Figure 2.26: Icon of the piston internal orifice submodel developed in Simcenter Amesim®

Table 2.8, as usual, lists the variables associated with the ports of this element.

Table 2.8: Inputs/outputs at each port of the piston internal orifice submodel developed in Simcenter Amesim®

PORT	VARIABLE	DESCRIPTION	SYMBOL	TYPE
1	Input	Pressure	p	Vector
	Output	Flow rate	Q	
2	Input	Pressure	p	Vector
	Output	Flow rate	Q	

The parameterization of the piston internal orifice element requires the following parameters:

- the hydraulic fluid detection index, which is then characterized in a special element of the Simcenter Amesim® *Hydraulics* library,
- the piston number n_P,
- the internal orifice diameter d_{ORP},
- the maximum flow coefficient c_{q-MAX}, usually set at 0.7 for turbulent flows,
- the critical Reynolds number Re_{cr}.

The leakage flow rate of the ball joint spherical gap can be obtained integrating the differential equation of **Eq. (2.41)** [68], valid for $\gamma_1 < \gamma < \gamma_2$.

$$\frac{\partial}{\partial \gamma} h^3 \cdot \sin \gamma \cdot \frac{\partial p}{\partial \gamma} = 0 \tag{2.41}$$

The boundary conditions required to solve the differential equation are given in **Eq. (2.42)**.

$$\begin{aligned} \gamma = \gamma_1 \quad &\rightarrow \quad p = p_{pozz} \\ \gamma = \gamma_2 \quad &\rightarrow \quad p = p_{case} \end{aligned} \tag{2.42}$$

Eq. (2.43) shows the result of this integration which represents the leakage flow rate through the spherical gap of the ball joint connecting a piston with the shaft.

$$Q = \frac{(p_{pozz} - p_{case}) \cdot \pi \cdot \left(R_{SJ} \frac{{h_{SJ}}^3}{6} + \frac{{h_{SJ}}^4}{12} \right)}{\mu \left(\frac{p_{pozz} + p_{case}}{2} \right) \cdot \left(R_{SJ} + \frac{h_{SJ}}{2} \right) \cdot \log \frac{\tan \frac{\gamma_2}{2}}{\tan \frac{\gamma_1}{2}}} \cdot \frac{\rho \left(\frac{p_{pozz} + p_{case}}{2} \right)}{\rho(0)} \tag{2.43}$$

Note that this flow rate must be evaluated for each piston.

We then realized the Simcenter Amesim® element concerning the model of this leakage.

Figure 2.27 shows the representation of the Simcenter Amesim® icon with its ports and the exchanged variables. **Table 2.9** reports these input/output variables.

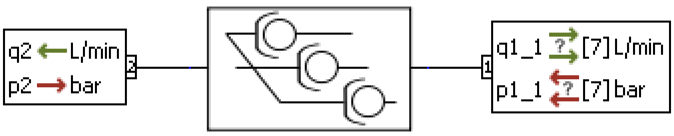

Figure 2.24: Icon of the submodel concerning the leakage flow rates between piston and the ball joint seat developed in Simcenter Amesim®

Table 2.9: Inputs/outputs at each port of the submodel concerning the leakage flow rates between piston and the ball joint seat developed in Simcenter Amesim®

PORT	VARIABLE	DESCRIPTION	SYMBOL	TYPE
1	Input	Pressure	p	Vector
	Output	Flow rate	Q	
2	Input	Pressure	p	Scalar
	Output	Flow rate	Q	

The parameterization of leakage gap between the piston and the ball joint seat requires the following parameters:

- the hydraulic fluid detection index, which is then characterized in a special element of the Simcenter Amesim® *Hydraulics* library,
- the piston number n_P,
- the radius of the piston spherical end R_{SJ},
- the starting angle γ_1 and ending angle γ_2 for the spherical gap,
- the spherical gap height h_{SJ}.

We can now move on to the mechanical part modelling, which was the core of this activity.

2.3 Mechanical model

This section describes the mathematical modelling of the main mechanical components of the machine, which has then been implemented in C++ code to create the various submodels in the Simcenter Amesim Submodel Editor® tool. As already mentioned, this mathematical modelling was defined in a parametric way considering the possibility of varying the model parameters (geometric and non-geometric) to assess their effects on the machine performance. Moreover, this approach allows to simulate not only the behaviour of the machines taken as a reference, but also all the units with similar geometry and features.

Firstly, we identified the main components guaranteeing the correct operation of the machine (**Figure 2.28**). We analysed in detail the following components:

- pistons,
- cylinder block and central pivot,
- valve plate for fixed or variable displacement,
- unit shaft.

We followed the reported approach for each main component:

1. choice of the appropriate reference frame for the analysis.
2. parametrization of the component identifying all the independent parameters the user has to insert.
3. kinematic analysis of the component (when necessary), i.e. position, velocity and acceleration analysis.
4. dynamic analysis of the component identifying all the forces and moments acting on the component.
5. writing and solving of the equilibrium equation.

The realization of the free body diagrams allows the writing of the translational equilibrium equations ($\sum F = 0$) and rotational equilibrium equations ($\sum M = 0$) for each mechanical component by applying the second law of motion. These equations have been exploited to individuate the unknown terms, in particular the reaction forces and moments between the different components.

It was thus possible to carry out a detailed analysis of the entire bent axis machine by combining the analyses of all the mechanical components. This allowed to assess the torque delivered/absorbed by the unit, and thus the mechanical efficiency considering all the mechanical losses within the machine.

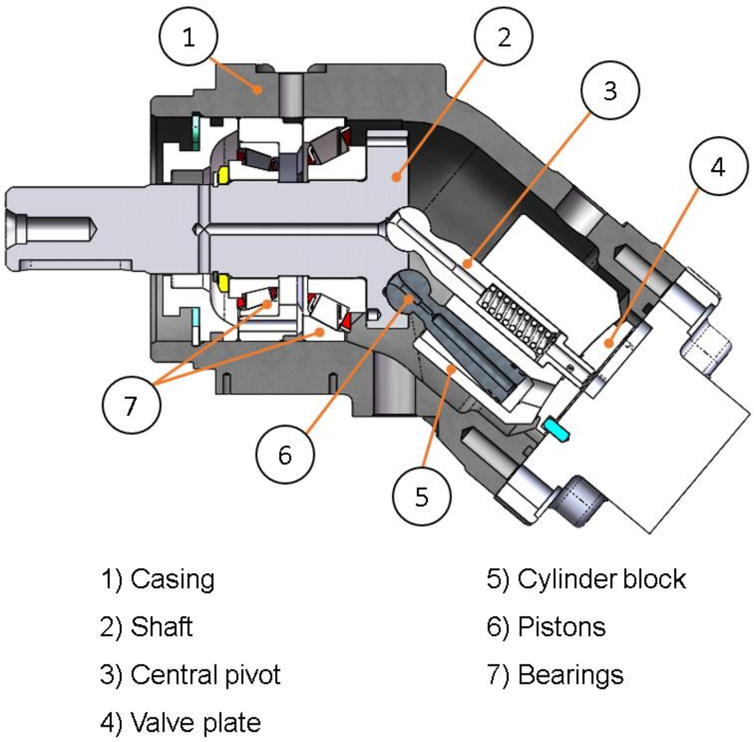

Figure 2.28: Main components of the bent axis piston unit considered for the mechanical analysis

Nomenclature

We are now presenting a compact and unambiguous nomenclature used to define the various terms and facilitate the writing and understanding of both the equations and the code. **Tables 2.10-2.11-2.12** show this nomenclature.

Table 2.10: Nomenclature concerning the component names

Element	**Abbreviation**
Piston	pi
Cylinder block	cb
Shaft	sh
Valve plate	vp
Casing	$case$

Table 2.11: Nomenclature concerning the force types

Element	**Abbreviation**
Weight	g
Pressure	pr
Viscous friction	$visc$
Dry friction	fr

Table 2.12: Nomenclature concerning the moment types

Element	**Abbreviation**
Viscous friction between two components	$visc$
Churning losses	cl

If the force or moment type is not specified, the term refers to a mutual reaction between two components. In this case, we used $(A - B)$ as subscripts to indicate that component A exerts this force (or moment) on component B.

We are reporting below some useful examples for a better understanding of the nomenclature used.

$$F_{(A-B)_{force\,type_{reference\,axis}}}$$

$$F_{(pi-cb)fr_z}$$

Friction force exerted by the pistons on the cylinder block along the *z*-axis

$$F_{(A)_{force\,type_{reference\,axis}}}$$

$$F_{pi_{press_z}}$$

Pressure force exerted on the pistons along the *z*-axis

$$M_{(A-B)_{moment\,type_{reference\,axis}}}$$

$$M_{(cb-vp)_{visc_z}}$$

Viscous friction moment exerted by the cylinder block on the valve plate around the *z*-axis

$$M_{(A)_{moment\,type_{areference\,axis}}}$$

$$M_{cb_{cl_z}}$$

Churning losses moment acting on the cylinder block around the *z*-axis

Convention for force and moment signs

We are also defining the convention on the signs of forces and moments.

We considered any force to have the same direction of the chosen reference frame axis. If the force acts with an opposite direction to the axis one, it will present a minus sign within its analytical expression (**Figure 2.29**). In this way, the generic translational equilibrium will thus be a sum of all the contributions, where the minus signs may only be present in the analytical expression of the various contributions.

We considered both forces and distances as positive in the realization of the rotational equilibrium equations with respect to a generic point. If the cross product between the force and distance results in a negative moment considering the right-hand rule, a minus sign will be inserted in the equation. Always consider **Figure 2.29** as example.

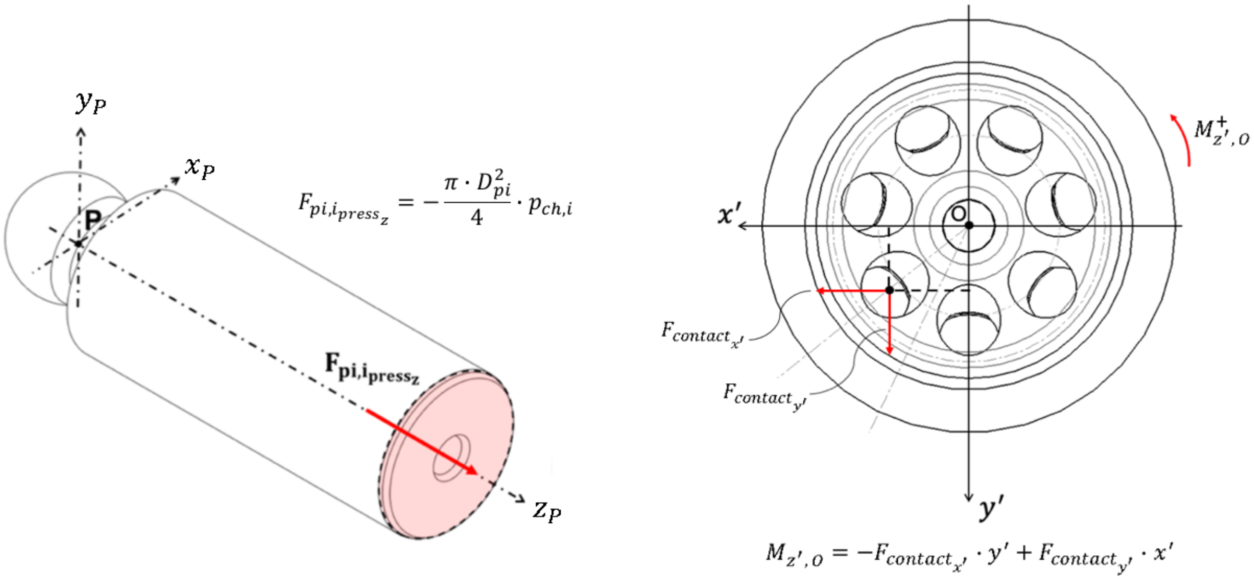

Figure 2.29: Sign convention for forces (left) and moments (right)

Space orientation

It is necessary to introduce one or more reference frames to carry out the kinematic and dynamic analysis of the machine's components. We considered a fixed reference frame $Oxyz$ and a rotating one $Ox'y'z'$ (**Figure 2.30**) obtained from the former by means of a rotation β around the *x*-axis (which is the bent axis inclination). Note that rotation β in **Figure 2.30** is negative as it is discordant from the positive direction defined by the right-hand rule.

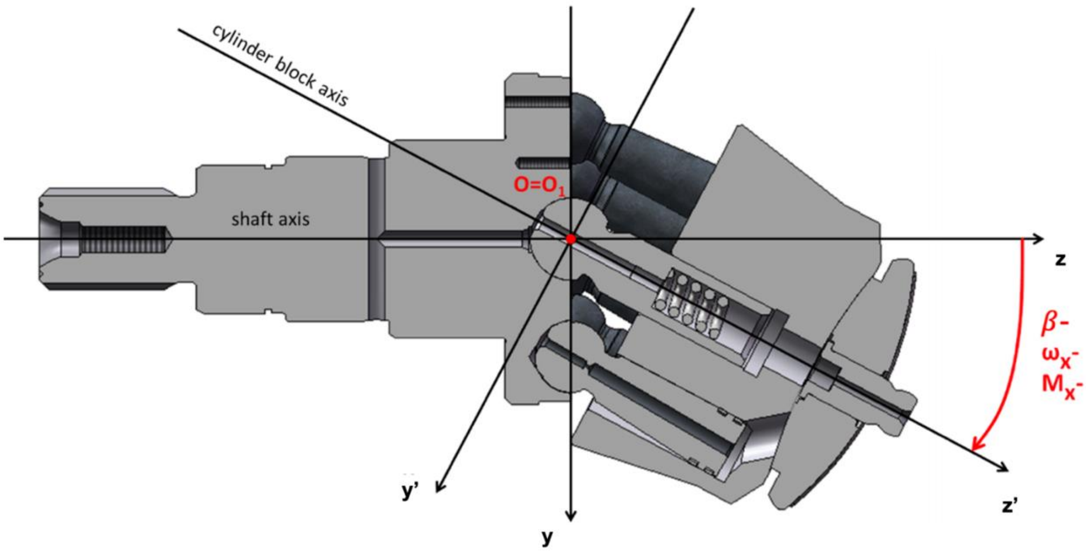

Figure 2.30: Fixed reference frame $Oxyz$ and mobile one $Ox'y'z'$

In this way, we could analyse the behaviour exploiting the more suitable frame of reference, switching from the fixed to the rotating one without losing validity in the expressions. The reference frame switch relies on two rotation matrices. We must specify which is the starting frame and which is the ending one to properly choose the correct matrix to use. Naming O the fixed frame $Oxyz$ and O' the rotating frame $Ox'y'z'$, **Eq. (2.44)-(2.45)** define the rotation matrices. These matrices must be multiplied to the generic vector to pass from one reference frame to the other.

$$R_{O\rightarrow O'} = \begin{bmatrix} 1 & 0 & 0 \\ 0 & \cos\beta & \sin\beta \\ 0 & -\sin\beta & \cos\beta \end{bmatrix} \tag{2.44}$$

$$R_{O'\rightarrow O} = \begin{bmatrix} 1 & 0 & 0 \\ 0 & \cos\beta & -\sin\beta \\ 0 & \sin\beta & \cos\beta \end{bmatrix} \tag{2.45}$$

Once we have defined the machine reference frames, we can move on to the convention definition concerning the directions of the reference quantities for the kinematic and dynamic analysis, as well as the directions of the angular position and angular velocity of the shaft (**Figure 2.31**).

Rotations that agree with the right-hand rule are considered positive, as shown in **Figure 2.31**. The generic angular position of the shaft ϑ is measured from the reference position also shown in **Figure 2.31**.

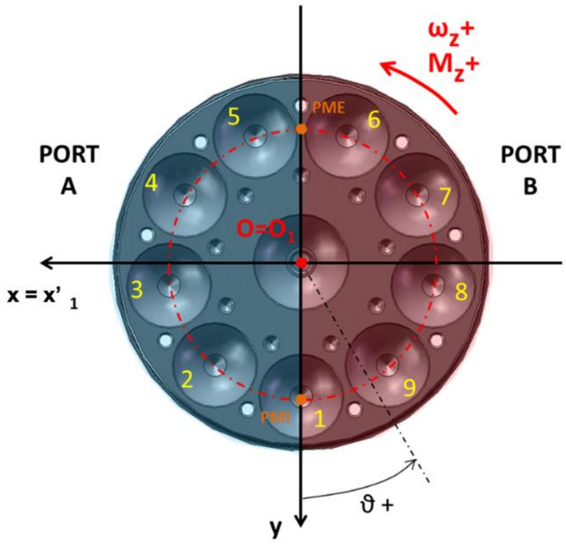

Figure 2.31: Convention on the angular position and speed

We also included the possibility of orienting the unit in space to consider the effects caused by the weight force of the different components. We thus defined a ground reference frame $O_{ground}x_{ground}y_{ground}z_{ground}$ thanks to which it is possible to orientate the unit at will and simulate its behaviour in different spatial orientations by varying the Euler angles α_e, β_e , γ_e (also highlighted in **Figure 2.32**).

These three angles uniquely define the orientation of the generic $O_{BAU}x_{BAU}y_{BAU}z_{BAU}$ machine reference frame with respect to the ground one. Specifically, α_e is the relative rotation around the z_{BAU} axis, β_e the relative rotation around the x_{BAU} axis, and γ_e the relative rotation around the y_{BAU} axis.

Starting from the ground reference frame, we must consider a triplet of Euler angles equal to $[\alpha_e, \beta_e, \gamma_e] = [\pi, 0, 0]$ to obtain the orientation of the $O_{BAU}x_{BAU}y_{BAU}z_{BAU}$ frame in **Figure 2.32**.

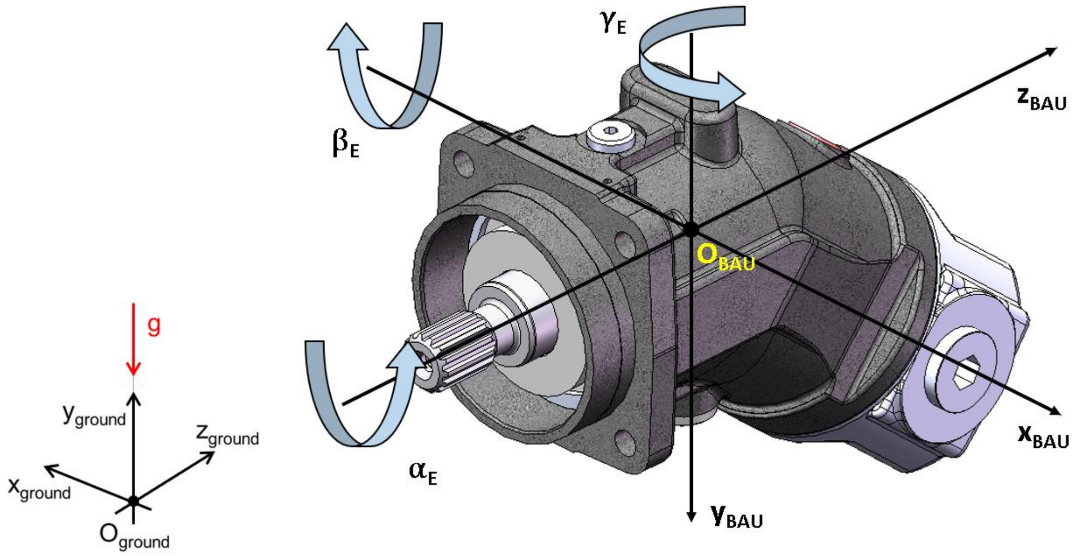

Figure 2.32: Ground reference frame $O_{ground}x_{ground}y_{ground}z_{ground}$, machine reference frame $O_{BAU}x_{BAU}y_{BAU}z_{BAU}$ and Euler angles

The weight force has different components within the machine's reference frame depending on the orientation of the unit. The determination of these components can be obtained by multiplying the weight force vector expressed in the ground reference frame by the three rotation matrices derived from the three Euler angles (**Eq. (2.46)**).

$$[F_{g_{BAU}}] = R_{\beta_e} R_{\gamma_e} R_{\alpha_e} \, [F_{g_{ground}}] \tag{2.46}$$

The orientation of the ground reference frame $O_{ground}x_{ground}y_{ground}z_{ground}$ causes the weight force vector to have only a negative y_{ground} component.

$$[F_{g_{ground}}] = \begin{bmatrix} 0 \\ -m \cdot g \\ 0 \end{bmatrix} \tag{2.47}$$

The rotation matrices used in **Eq. (2.46)** can be fully expressed as reported in **Eq. (2.48)-(2.49)-(2.50)**, also considering **Figure 2.33**.

$$R_{\beta_e} = \begin{bmatrix} 1 & 0 & 0 \\ 0 & \cos\beta_e & -\sin\beta_e \\ 0 & \sin\beta_e & \cos\beta_e \end{bmatrix} \tag{2.48}$$

$$R_{\gamma_e} = \begin{bmatrix} \cos\gamma_e & 0 & -\sin\gamma_e \\ 0 & 1 & 0 \\ \sin\gamma_e & 0 & \cos\gamma_e \end{bmatrix} \tag{2.49}$$

$$R_{\alpha_e} = \begin{bmatrix} \cos\alpha_e & -\sin\alpha_e & 0 \\ \sin\alpha_e & \cos\alpha_e & 0 \\ 0 & 0 & 1 \end{bmatrix} \tag{2.50}$$

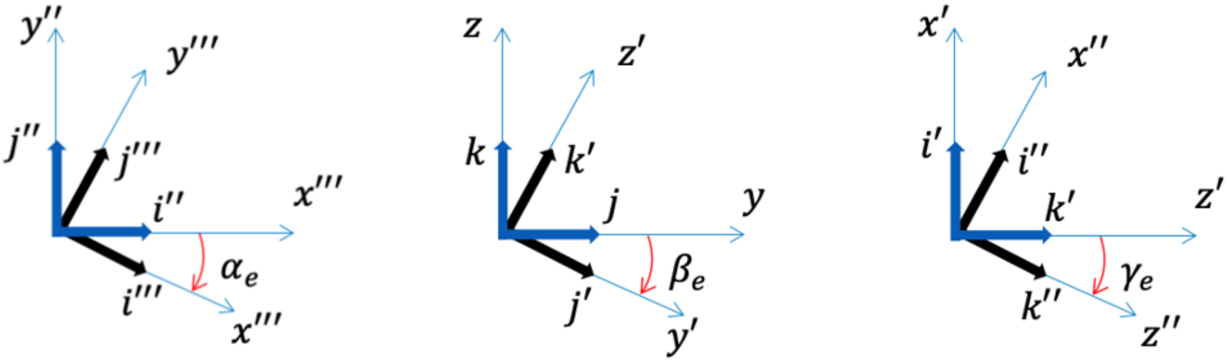

Figure 2.33: Rotation matrices defined by the three Euler angles

The rotation matrix for moving from the ground reference frame to the unit's own one is the product $R_{\beta_e} R_{\gamma_e} R_{\alpha_e}$. **Eq. (2.51)** reports the expanded form of this total rotation matrix.

$$\begin{bmatrix} \cos\gamma_e \cdot \cos\alpha_e & -\cos\gamma_e \cdot \sin\alpha_e & \sin\gamma_e \\ \sin\beta_e \cdot \sin\gamma_e \cdot \cos\alpha_e + \sin\alpha_e \cdot \cos\beta_e & -\sin\beta_e \cdot \sin\gamma_e \cdot \sin\alpha_e + \cos\beta_e \cdot \cos\alpha_e & -\sin\beta_e \cdot \cos\gamma_e \\ -\cos\beta_e \cdot \sin\gamma_e \cdot \cos\alpha_e + \sin\beta_e \cdot \sin\alpha_e & \cos\beta_e \cdot \sin\gamma_e \cdot \sin\alpha_e + \sin\beta_e \cdot \cos\alpha_e & \cos\beta_e \cdot \cos\gamma_e \end{bmatrix} \tag{2.51}$$

The weight force does not change in absolute terms considering these Euler angles. However, the weight components in the three Cartesian directions change, as reported in **Eq. (2.52)-(2.53)-(2.54)** for the oriented reference frame of the unit.

$$F_{g_{x_{BAU}}} = (-\cos\gamma_e \cdot \sin\alpha_e) \cdot (-m \cdot g) \tag{2.52}$$

$$F_{g_{y_{BAU}}} = (-\sin\beta_e \cdot \sin\gamma_e \cdot \sin\alpha_e + \cos\beta_e \cdot \cos\alpha_e) \cdot (-m \cdot g) \tag{2.53}$$

$$F_{g_{z_{BAU}}} = (\cos\beta_e \cdot \sin\gamma_e \cdot \sin\alpha_e + \sin\beta_e \cdot \cos\alpha_e) \cdot (-m \cdot g) \tag{2.54}$$

Vector format model

As anticipated, the modelling of the mechanical part includes the identification and analysis of the main components of the machine. These components must interface with each other by exchanging forces and reaction moments. It is necessary to consider the union of the individual components for the complete modelling of the bent axis piston unit under consideration, as shown in the block diagram of **Figure 2.34**. We used this diagram as the basis of the machine mechanical model.

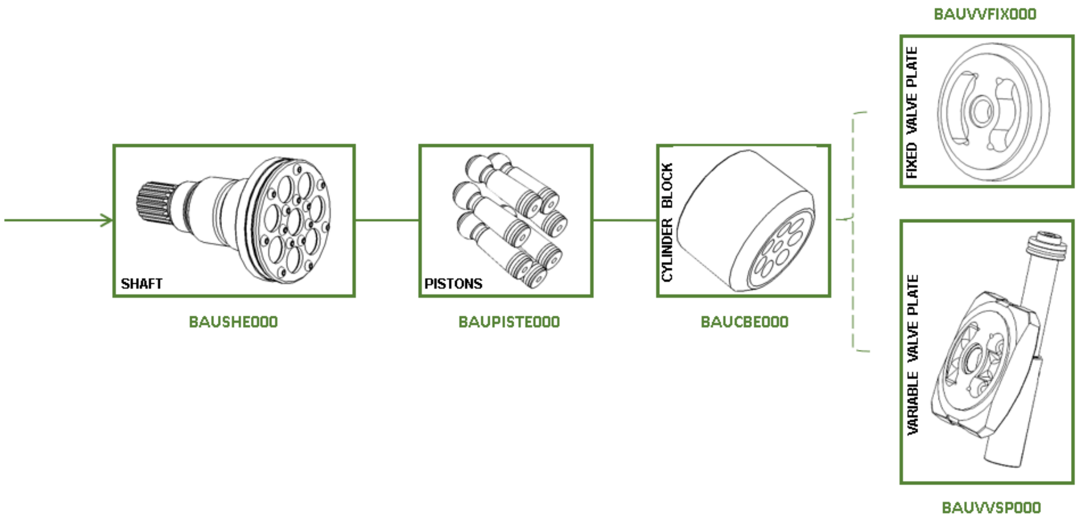

Figure 2.34: Mechanical model schematic for the bent axis unit

Note how the BAUPISTE000 includes all the pistons in the unit, each of which exchanges different reactions with the shaft and cylinder block. It was therefore necessary to develop this model and consequently also the others that interface with it in a vectorial manner. This allowed to carry out the kinematic and dynamic analysis referring only to the generic *i*-th piston. It was then possible to consider all the other pistons by shifting the *i*-th piston results with the appropriate angular steps. This model feature is also very useful for expanding the model validity to other machines. The piston number, in fact, will be a parameter like any other, and the model can be used to model positive displacement machines with a different number of pistons.

Note that we have reported two different valve plate elements in the model diagram of **Figure 2.34**. We indeed developed two different submodels, one for fixed displacement units and one for variable displacement units, which will be presented individually in the dedicated section.

2.3.1 Piston model

We are presenting in this sub-section the kinematic and dynamic analysis relating to the pistons of the machine. The kinematics of the bent axis piston units turned out to be more complex than the swash plate units one. The piston motions in the latter case, in fact, can be factored in a rotation around the shaft axis and an axial translation determined by the inclination of the swash plate. On the other hand, the ball joints connecting the bent axis pistons with the shaft flange generate an inclination variation during the shaft rotation. This aspect thus does not allow the pistons to be parallel to each other, leading to a more complex motion.

Figure 2.35 shows a section of the reference machine where we have highlighted the *i*-th piston (with centre of gravity G_{pi_i}).

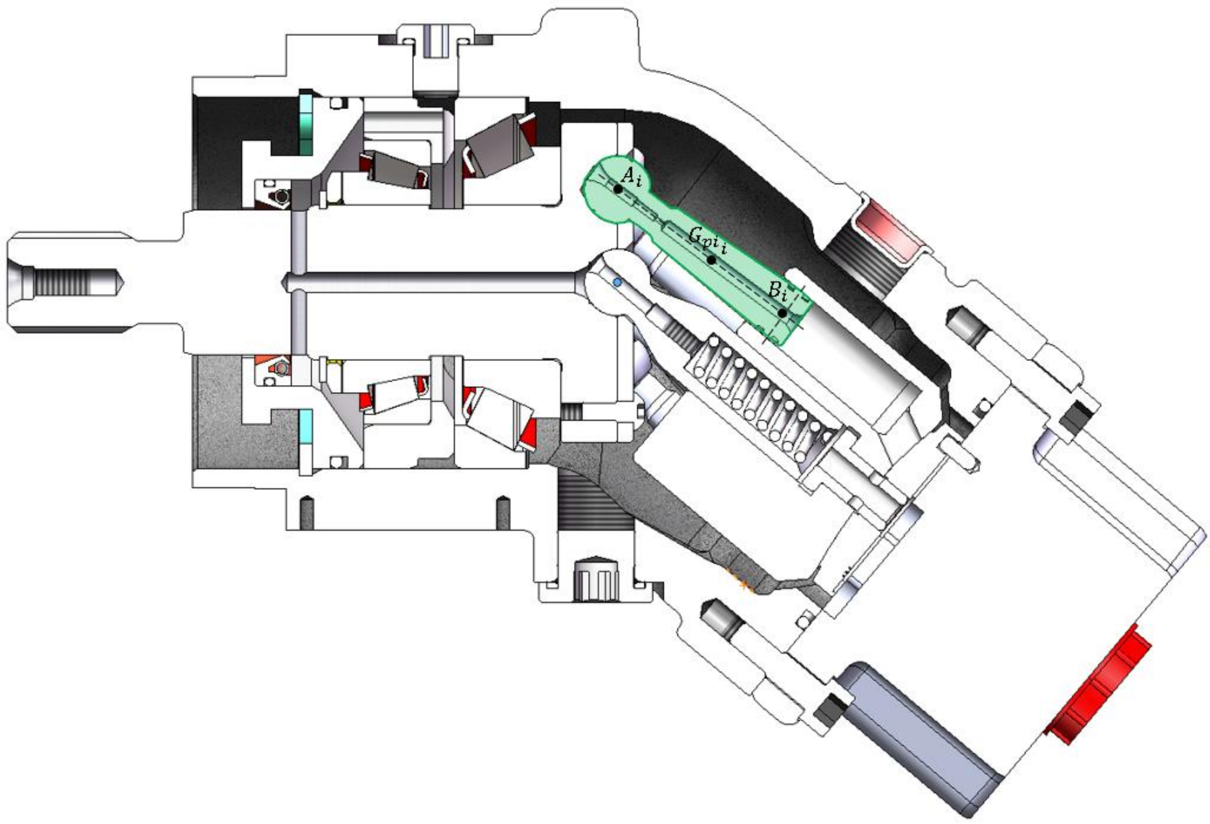

Figure 2.35: Section of the reference machine and *i*-th piston (in green)

We must introduce the assumptions and hypotheses we considered before proceeding with the analysis:

- the piston stiffness is considered infinite, i.e. no piston deformations,
- the contact between a piston and the cylinder block is considered centred in a point, which can be transported to point B_i of **Figure 2.35**,

- the contact between piston and shaft is considered centred in the spherical joint centre A_i of **Figure 2.35**,
- we neglected the relative rotation of the *i*-th piston around its own axis,
- points A_i and B_i are not out of phase, i.e. we neglected a possible phase shift between shaft and cylinder block,
- point B_i travels along the piston chamber axis and its position depends only on the cylinder block rotation,
- the heights of the leakage gaps in ball joints and piston chambers are constant,
- the pressure trend within the leakage gaps is considered linear and not logarithmic.

We carried out the piston kinematic analysis considering the two reference frames $Oxyz$ and $Ox'y'z'$ already introduced (**Figure 2.30**), and a third rotating reference system $B_i x_P y_P z_P$ connected to the piston (**Figure 2.36**). Note that z_P axis is not parallel to z and z' due to the variable piston inclination.

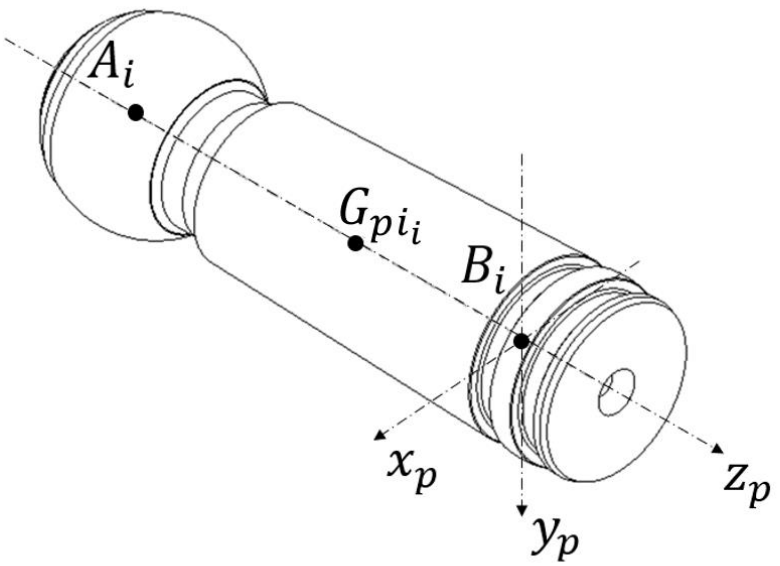

Figure 2.36: Reference frame $B_i x_P y_P z_P$ rotating with the piston

The main outputs of the piston analysis are:

- the piston kinematics,
- the piston chamber volume,
- the reaction forces exchanged with cylinder block,
- the reaction forces and moments exchanged with shaft flange,
- the friction forces exchanged with cylinder block and shaft.

As anticipated, we carried out the mechanical modelling in a parametric manner, i.e. identifying all the independent parameters necessary for the unambiguous definition of the system to allow the model use with all the similar units.

Figure 2.37-2.38 shows the parameterisation scheme of a single piston. Note the $-\beta$ angle of inclination of the cylinder block. The minus sign indicates that the rotation has the opposite direction to the positive rotation defined by the right-hand rule. However, we are using β in the following analytic relationships, as we considered the possible minus sign within β expression.

We have reported two different views with $\vartheta = 0$ and $\vartheta = 45°$ as angular position of the *i*-th piston to highlight the change in piston inclination during its rotation. The first view highlights the rotation δ_i around the x_P axis, while the second view highlights the rotation λ_i around the y_P axis. The alignment constraint between points A_i and B_i leads to these variable angles with one shaft rotation.

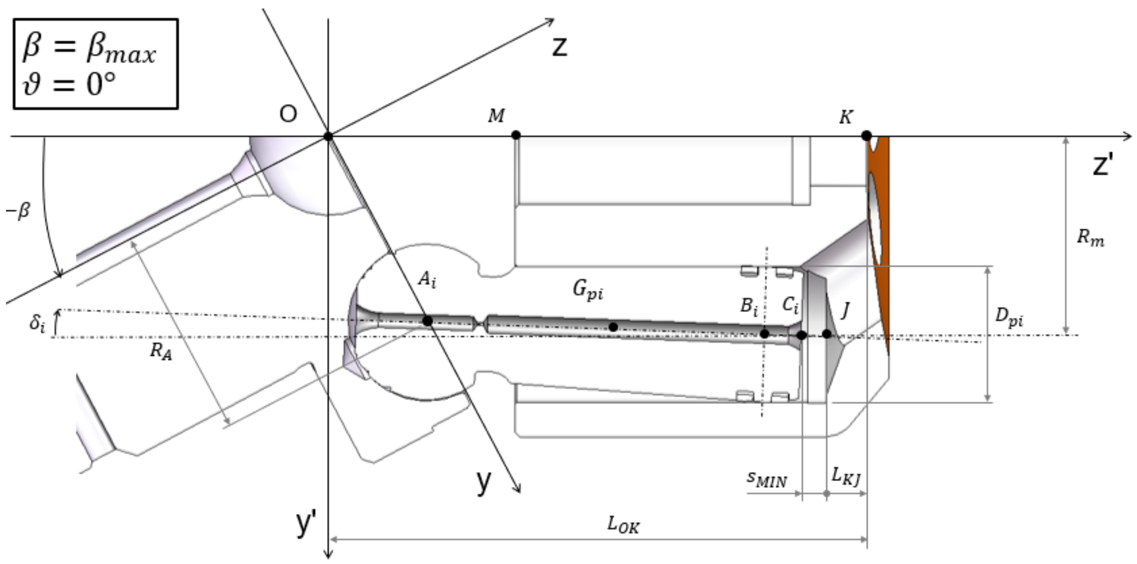

Figure 2.37: Piston parametrization ($y'z'$ plane)

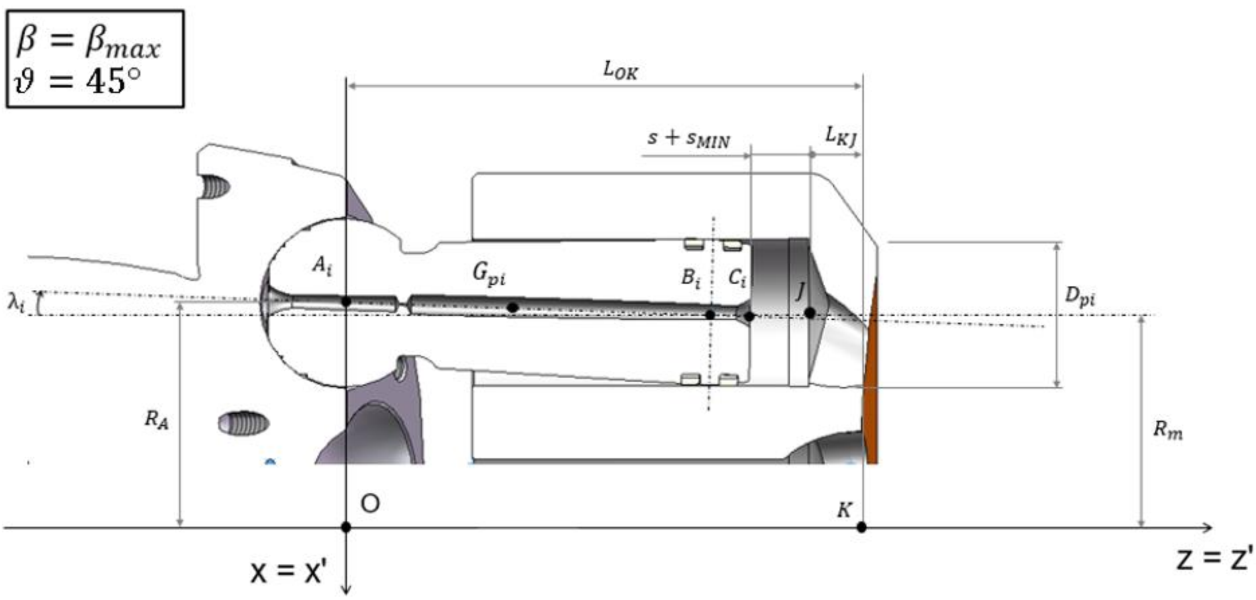

Figure 2.38: Piston parametrization ($x'z'$ plane)

Table 2.13 lists and describes the geometrical and non-geometrical parameters required for the piston parameterization and modelling.

Table 2.13: Parameters required for the piston model

Symbol	Description
D_{pi}	Piston diameter
m_{pi}	Piston mass
R_A	Radius of the ball joint centres
R_m	Radius of the piston chamber centres
α_E	Euler angle α
β_E	Euler angle β
γ_E	Euler angle γ
D_{sphere}	Diameter of the piston spherical end
$\overline{OM}$	Distance between O (reference frame centre) and M (cylinder block front surface)
$\overline{OK}$	Distance between O (reference frame centre) and K (spherical cap)
$\overline{KJ}$	Distance between points K and J
$\overline{AC}$	Distance between points A and C
$\overline{AB}$	Distance between points A and B

$\overline{AG}$	Distance between points A and G
h_{pi-cb}	Leakage gap height between piston and cylinder block
h_{pi-sh}	Leakage gap height between piston and ball joint seat
$l_{c,pi}$	Distance between piston seal groove centres
f_{pi-cb}	Friction coefficient between piston and cylinder block
$\varphi_{pist,2}$	Angle between z_P axis and spherical grooves
$I_{pi,x'x'}$	Piston $x'x'$ moment of inertia
$I_{pi,y'y'}$	Piston $y'y'$ moment of inertia

Kinematic analysis

We are reporting below the piston kinematic analysis. As anticipated, we have shifted the results of the *i*-th piston by the opportune angular step to assess the kinematics of all the other pistons. We are thus investigating the positions, velocities, and accelerations of the points of interest.

The subscript i used in the relationships refers to the *i*-th piston.

Point A_i must move on a circular trajectory in the xy plane of the fixed reference frame $Oxyz$. **Eq. (2.55)** shows the coordinates of point A_i expressed in this fixed reference frame.

$$A_i = \begin{cases} x_{A,i} = -R_A \cdot \sin(\vartheta_i + \vartheta_{i0}) \\ y_{A,i} = R_A \cdot \cos(\vartheta_i + \vartheta_{i0}) \\ z_{A,i} = 0 \end{cases} \tag{2.55}$$

We have introduced the term ϑ_{i0} to consider the possible non-zero initial position of the *i*-th pump.

We can obtain the position of A_i expressed in the rotating reference frame $Ox'y'z'$ by exploiting the rotation matrix $R_{O\to O'}$ of **Eq. (2.44)**.

$$A_i' = \begin{cases} x'_{A,i} = x_{A,i} \\ y'_{A,i} = y_{A,i} \cdot \cos\beta + z_{A,i} \cdot \sin\beta \\ z'_{A,i} = -y_{A,i} \cdot \sin\beta + z_{A,i} \cdot \cos\beta \end{cases} \tag{2.56}$$

On the other hand, point B_i must move on a circular trajectory in the $x'y'$ plane of the rotating reference frame $Ox'y'z'$. The coordinate z' can be defined by the sum of the distance $z'_{A,i}$ and the term $|\overline{AB}| \cdot \cos\delta_i$.

$$B_i' = \begin{cases} x'_{B,i} = -R_m \cdot \sin(\vartheta_i + \vartheta_{i0}) \\ y'_{B,i} = R_m \cdot \cos(\vartheta_i + \vartheta_{i0}) \\ z'_{B,i} = z'_{A,i} + |\overline{AB}| \cdot \cos\delta_i \end{cases} \tag{2.57}$$

It is possible to derive the B_i position expressed in the fixed reference frame $Oxyz$ using the inverse rotation matrix $R_{O'\to O}$ of **Eq (2.45)**.

$$B_i = \begin{cases} x_{B,i} = x'_{B,i} \\ y_{B,i} = y'_{B,i} \cdot \cos\beta - z'_{B,i} \cdot \sin\beta \\ z_{B,i} = y'_{B,i} \cdot \sin\beta + z'_{B,i} \cdot \cos\beta \end{cases} \tag{2.58}$$

As illustrated in **Figure 2.37-2.38**, it is necessary to introduce the piston inclination angles to obtain the $z'_{B,i}$ coordinate and the positions of the piston centre of gravity G_{pi_i}. **Eq. (2.59)-(2.60)** thus define angles δ_i and λ_i referring to **Figure 2.37-2.38**.

$$\delta_i = \arcsin\left(\frac{y'_{A,i} - y'_{B,i}}{|\overline{AB}|}\right) \tag{2.59}$$

$$\lambda_i = -\arcsin\left(\frac{x'_{A,i} - x'_{B,i}}{|\overline{AB}|}\right) \tag{2.60}$$

In this way, **Eq. (2.61)** can report the coordinates of G_{pi_i}.

$$G_{pi_i}{}' = \begin{cases} x'_{G_{pi,i}} = x'_{A,i} + |\overline{AG}| \cdot \sin\lambda_i \\ y'_{G_{pi,i}} = y'_{A,i} - |\overline{AG}| \cdot \sin\delta_i \\ z'_{G_{pi,i}} = z'_{A,i} + |\overline{AG}| \cdot \cos\delta_i \end{cases} \tag{2.61}$$

We can then obtain the transition in absolute coordinates expressed in the fixed reference frame of **Eq. (2.62)** by using the inverse rotation matrix $R_{O'\to O}$ of **Eq. (2.45)**.

$$G_{pi_i} = \begin{cases} x_{G_{pi,i}} = x'_{G_{pi,i}} \\ y_{G_{pi,i}} = y'_{G_{pi,i}} \cdot \cos\beta - z'_{G_{pi,i}} \cdot \sin\beta \\ z_{G_{pi,i}} = y'_{G_{pi,i}} \cdot \sin\beta + z'_{G_{pi,i}} \cdot \cos\beta \end{cases} \tag{2.62}$$

It is then possible to consider the velocities analysis by deriving these expressions of the positions. Note that these velocities must take into account the variation of δ_i and λ_i during the rotation. We decided to isolate the arcsine arguments to derive the expressions of δ_i and λ_i in a simpler way. **Eq. (2.63) — (2.68)** show the derivatives of interest after defining K_i and J_i as the arguments of δ_i and λ_i.

$$K_i = \frac{y'_{A,i} - y'_{B,i}}{|\overline{AB}|} = \frac{R_A \cdot \cos(\vartheta_\mathrm{i} + \vartheta_{i0}) \cdot \cos\beta - R_m \cdot \cos(\vartheta_\mathrm{i} + \vartheta_{i0})}{|\overline{AB}|} \tag{2.63}$$

$$\dot{K_i} = \frac{-R_A \cdot \omega \cdot \sin(\vartheta_\mathrm{i} + \vartheta_{i0}) \cdot \cos\beta - R_A \cdot \dot{\beta} \cdot \cos(\vartheta_\mathrm{i} + \vartheta_{i0}) \cdot \sin\beta + R_m \cdot \omega \cdot \sin(\vartheta_\mathrm{i} + \vartheta_{i0})}{|\overline{AB}|} \tag{2.64}$$

$$\begin{aligned} \ddot{K_\iota} = {} & \frac{-R_A \cdot \omega^2 \cdot \cos(\vartheta_\mathrm{i} + \vartheta_{i0}) \cdot \cos\beta + 2 \cdot R_A \cdot \omega \cdot \dot{\beta} \cdot \sin(\vartheta_\mathrm{i} + \vartheta_{i0}) \cdot \sin\beta}{|\overline{AB}|} + \frac{-R_A \cdot \dot{\omega} \cdot \sin(\vartheta_\mathrm{i} + \vartheta_{i0}) \cdot \cos\beta}{|\overline{AB}|} \\ & + \frac{-R_A \cdot \dot{\beta}^2 \cdot \cos(\vartheta_\mathrm{i} + \vartheta_{i0}) \cdot \cos\beta - R_A \cdot \ddot{\beta} \cdot \cos(\vartheta_\mathrm{i} + \vartheta_{i0}) \cdot \sin\beta}{|\overline{AB}|} \\ & + \frac{R_m \cdot \omega^2 \cdot \cos(\vartheta_\mathrm{i} + \vartheta_{i0}) + R_m \cdot \dot{\omega} \cdot \sin(\vartheta_\mathrm{i} + \vartheta_{i0})}{|\overline{AB}|} \end{aligned} \tag{2.65}$$

$$J_i = \frac{x'_{A,i} - x'_{B,i}}{|\overline{AB}|} = \frac{-\mathrm{R_A} \cdot \sin(\vartheta_\mathrm{i} + \vartheta_{i0}) + R_m \cdot \sin(\vartheta_\mathrm{i} + \vartheta_{i0})}{|\overline{AB}|} \tag{2.66}$$

$$\dot{J_\iota} = \frac{-\omega \cdot (\mathrm{R_A} - R_m) \cdot \cos(\vartheta_\mathrm{i} + \vartheta_{i0})}{|\overline{AB}|} \tag{2.67}$$

$$\ddot{J_\iota} = \frac{\omega^2 \cdot (\mathrm{R_A} - R_m) \cdot \sin(\vartheta_\mathrm{i} + \vartheta_{i0}) - \dot{\omega} \cdot (\mathrm{R_A} - R_m) \cdot \cos(\vartheta_\mathrm{i} + \vartheta_{i0})]}{|\overline{AB}|} \tag{2.68}$$

Eq. (2.69)-(2.72) then report the derivatives of δ_i and λ_i.

$$\dot{\delta}_i = \frac{1}{\sqrt{1-K_i^2}} \cdot \dot{K}_i \tag{2.69}$$

$$\ddot{\delta}_i = -\frac{1}{2}(1-K_i^2)^{-\frac{3}{2}} \cdot (-2K_i) \cdot \dot{K}_i \cdot \dot{K}_i + \frac{1}{\sqrt{1-K_i^2}} \cdot \ddot{K}_i \tag{2.70}$$

$$\dot{\lambda}_i = -\frac{1}{\sqrt{1-J_i^2}} \cdot \dot{J}_i \tag{2.71}$$

$$\ddot{\lambda}_i = +\frac{1}{2}(1-J_i^2)^{-\frac{3}{2}} \cdot (-2J_i) \cdot \dot{J}_i \cdot \dot{J}_i - \frac{1}{\sqrt{1-J_i^2}} \cdot \ddot{J}_i \tag{2.72}$$

It is now possible to derive the positions to obtain the velocity expressions of the points of interest.

$$v_{y'_{A,i}} = D\left[y'_{A,i}\right] = D[R_A \cdot \cos\beta \cdot cos\ (\vartheta_\mathrm{i} + \vartheta_{i0}) = = \omega\ [-R_A \cdot \sin(\vartheta_\mathrm{i} + \vartheta_{i0}) \cdot \cos\beta] + \dot{\beta}\ [-R_A \cdot \cos(\vartheta_\mathrm{i} + \vartheta_{i0}) \cdot \sin\beta] \tag{2.73}$$

$$v_{z'_{A,i}} = D\left[z'_{A,i}\right] = D[-R_A \cdot \sin\beta \cdot \cos(\vartheta_\mathrm{i} + \vartheta_{i0})] = \omega\ [R_A \cdot \sin(\vartheta_\mathrm{i} + \vartheta_{i0}) \cdot \sin\beta] + \dot{\beta}\ [-R_A \cdot \cos(\vartheta_\mathrm{i} + \vartheta_{i0}) \cdot \cos\beta] \tag{2.74}$$

$$v_{z'_{B,i}} = D\left[z'_{B,i}\right] = D[-R_A \cdot \sin\beta \cdot \cos(\vartheta_i + \vartheta_{i0}) + |\overline{AB}| \cdot \cos\delta_i] = \omega\ [R_A \cdot \sin\beta \cdot \sin(\vartheta_i + \vartheta_{i0})] + \dot{\beta}\ [-R_A \cdot \cos(\vartheta_i + \vartheta_{i0}) \cdot \cos\beta] + \dot{K}_i\ [-\ |\overline{AB}| \cdot \sin\delta_i \cdot \frac{1}{\sqrt{1-K_i^2}}\ ] \tag{2.75}$$

$$v_{x'_{Gpi,i}} = D\left[x'_{Gpi,i}\right] = D[-R_A \cdot \sin(\vartheta_\mathrm{i} + \vartheta_{i0}) + |\overline{AG}| \cdot \sin\lambda_i] = \omega\ [-R_A \cdot \cos(\vartheta_\mathrm{i} + \vartheta_{i0})] + \dot{J}_i\ [-|\overline{AG}| \cdot \cos\lambda_i \cdot \frac{1}{\sqrt{1-J_i^2}}] \tag{2.76}$$

$$v_{y'_{Gpi,i}} = D\left[y'_{Gpi,i}\right] = D[R_A \cdot \cos\beta \cdot \cos(\vartheta_\mathrm{i} + \vartheta_{i0}) - |\overline{AG}| \cdot \sin\delta_i\ ] = \omega\ [-R_A \cdot \cos(\beta) \cdot \sin(\vartheta_\mathrm{i} + \vartheta_{i0})] + \dot{\beta}\ [-R_A \cdot \sin\beta \cdot \cos(\vartheta_\mathrm{i} + \vartheta_{i0})] + \dot{K}_i\ [-|\overline{AG}| \cdot \cos\delta_i \cdot \frac{1}{\sqrt{1-K_i^2}}] \tag{2.77}$$

$$v_{z'_{Gpi,i}} = D\left[z'_{Gpi,i}\right] = D[-R_A \cdot \sin\beta \cdot \cos(\vartheta_\mathrm{i} + \vartheta_{i0}) + |\overline{AG}| \cdot \cos\delta_i\ ] = \omega\ [R_A \cdot \sin\beta \cdot \sin(\vartheta_\mathrm{i} + \vartheta_{i0})] + \dot{\beta}\ [-R_A \cdot \cos\beta \cdot \cos(\vartheta_\mathrm{i} + \vartheta_{i0})] + \dot{K}_i\ [-|\overline{AG}| \cdot \sin\delta_i \cdot \frac{1}{\sqrt{1-K_i^2}}] \tag{2.78}$$

Similarly, the accelerations can be obtained by deriving these velocities. The accelerations of the centre of mass G_{pi_i} are of particular interest for calculating the inertial contributions.

$$a_{y'_{A,i}} = D\left[v_{y'_{A,i}}\right] = \ \omega^2[-R_A \cdot \cos(\vartheta_i + \vartheta_{i0}) \cdot \cos\beta] + 2 \cdot \omega \cdot \dot{\beta}\ [R_A \cdot \sin(\vartheta_i + \vartheta_{i0}) \cdot \sin\beta] + \dot{\omega}\ [-R_A \cdot \sin(\vartheta_i + \vartheta_{i0}) \cdot \cos\beta] + \dot{\beta}^2\ [-R_A \cdot \cos(\vartheta_i + \vartheta_{i0}) \cdot \cos\beta] + \ddot{\beta}\ [-R_A \cdot \cos(\vartheta_i + \vartheta_{i0}) \cdot \sin\beta] \tag{2.79}$$

$$a_{z'_{A,i}} = D\left[v_{z'_{A,i}}\right] = \omega^2[\ R_A \cdot \cos(\vartheta_i + \vartheta_{i0}) \cdot \sin\beta] + 2 \cdot \omega \cdot \dot{\beta}\ [R_A \cdot \sin(\vartheta_i + \vartheta_{i0}) \cdot \cos\beta] + \dot{\omega}[\ R_A \cdot \sin(\vartheta_i + \vartheta_{i0}) \cdot \sin\beta] + \dot{\beta}^2\ [R_A \cdot \cos(\vartheta_i + \vartheta_{i0}) \cdot \sin\beta] + \ddot{\beta}\ [\ -R_A \cdot \cos(\vartheta_i + \vartheta_{i0}) \cdot \cos\beta] \tag{2.80}$$

$$a_{z'_{B,i}} = D\left[v_{z'_{B,i}}\right] = \omega^2 \left[R_A \cdot \cos(\vartheta_i + \vartheta_{i0}) \cdot \sin\beta\right] + 2 \cdot \omega \cdot \dot{\beta} \left[R_A \cdot \sin(\vartheta_i + \vartheta_{i0}) \cdot \cos\beta\right] + \dot{\omega} \left[R_A \cdot \sin(\vartheta_i + \vartheta_{i0}) \cdot \sin\beta\right] + \dot{\beta}^{\,2}\left[R_A \cdot \cos(\vartheta_i + \vartheta_{i0}) \cdot \sin\beta\right] + \ddot{\beta} \left[-R_A \cdot \cos(\vartheta_i + \vartheta_{i0}) \cdot \cos\beta\right] - \dot{K_i}^2 \left[|\overline{AB}| \cdot \cos\delta_i \cdot \frac{1}{1-K^2} + |\overline{AB}| \cdot \sin\delta_i \cdot \frac{K_i}{(1-{K_i}^2)^{\frac{3}{2}}}\right] - \ddot{K_i} \tag{2.81}$$

$$a_{x'_{Gpi,i}} = D\left[v_{x'_{Gpi,i}}\right] = \omega^2 \left[R_A \cdot \sin(\vartheta_i + \vartheta_{i0})\right] + \dot{\omega}\left[-R_A \cdot \cos(\vartheta_i + \vartheta_{i0})\right] + \dot{J_i}^2 \left[|\overline{AG}| \cdot \sin\lambda_i \cdot \frac{1}{1-J_i^2} - |\overline{AG}| \cdot \cos\lambda_i \cdot \frac{J_i}{(1-J_i^2)^{\frac{3}{2}}}\right] + \ddot{J_i} \left[-|\overline{AG}| \cdot \cos\lambda_i \cdot \frac{1}{\sqrt{1-J_i^2}}\right] \tag{2.82}$$

$$a_{y'_{Gpi,i}} = D\left[v'_{y_{Gpi,i}}\right] = \omega^2\left[-R_A \cdot \cos\beta \cdot \cos(\vartheta_i + \vartheta_{i0})\right] + 2 \cdot \omega \cdot \dot{\beta} \left[R_A \cdot \sin\beta \cdot \sin(\vartheta_i + \vartheta_{i0})\right] + \dot{\omega}\left[-R_A \cdot \cos\beta \cdot \sin(\vartheta_i + \vartheta_{i0})\right] + \dot{\beta}^2\left[-R_A \cdot \cos\beta \cdot \cos(\vartheta_i + \vartheta_{i0})\right] + \ddot{\beta}\left[-R_A \cdot \sin\beta \cdot \cos(\vartheta_i + \vartheta_{i0})\right] + \dot{K_i}^2 \left[|\overline{AG}| \cdot \sin\delta_i \cdot \frac{1}{1-K_i^2} - |\overline{AG}| \cdot \cos\delta_i \cdot \frac{K_i}{(1-K_i^2)^{\frac{3}{2}}}\right] + \ddot{K_i} \left[-|\overline{AG}| \cdot \cos\delta_i \cdot \frac{1}{\sqrt{1-K_i^2}}\right] \tag{2.83}$$

$$a_{z'_{Gpi,i}} = D\left[v'_{z_{Gpi,i}}\right] = \omega^2\left[R_A \cdot \sin\beta \cdot \cos(\vartheta_i + \vartheta_{i0})\right] + 2 \cdot \omega \cdot \dot{\beta} + \left[R_A \cdot \cos\beta \cdot \sin(\vartheta_i + \vartheta_{i0})\right] + \dot{\omega} \left[R_A \cdot \sin\beta \cdot \sin(\vartheta_i + \vartheta_{i0})\right] + \dot{\beta}^2\left[R_A \cdot \sin\beta \cdot \cos(\vartheta_i + \vartheta_{i0})\right] + \ddot{\beta}\left[-R_A \cdot \cos\beta \cdot \cos(\vartheta_i + \vartheta_{i0})\right] - \dot{K_i^2} \left[|\overline{AG}| \cdot \cos\delta_i \cdot \frac{1}{1-K_i^2} + |\overline{AG}| \cdot \sin\delta_i \cdot \frac{K_i}{(1-K_i^2)^{\frac{3}{2}}}\right] + \ddot{K_i} \left[-|\overline{AG}| \cdot \sin\delta_i \cdot \frac{1}{\sqrt{1-K_i^2}}\right] \tag{2.84}$$

Once we had completed the kinematic analysis of the main points of interest, we could proceed to the piston dynamic analysis identifying all the forces/moments acting on the piston and writing the equilibrium equations.

Before doing this, however, we decided to exploit this kinematic analysis to evaluate the variable piston chamber volumes, as shown in the following sub-section.

Chamber volumes

Eq. (2.85) reports the volume of the piston chamber, which consist of two constant terms V_{ch_0} and V_{pist_0} and a variable term that is function of both the cylinder block inclination β and the angular position ϑ_i (**Figure 2.39**).

V_{ch_0} represents the dead volume given by the inclined inlet/outlet channels of the cylinder block, while V_{pist_0} is the dead volume given by the inner bore of the piston.

On the other hand, the variable term is the sum of the chamber length when the piston is at inner dead centre (IDC), i.e. s_{mim} (which is function of β), and the generic piston stroke, i.e. s_i (which is function of β and ϑ_i). This sum must be multiplied by the circular area of the piston chamber to obtain a volume. **Eq. (2.85)** reports the expression of the generic *i*-th chamber volume.

$$V_{ch_i}(\vartheta_i,\beta) = \frac{\pi}{4} D_{pi}^2 \cdot (-R_a \cdot (1-\cos\vartheta_i)\cdot \sin\beta + s_{min}) + V_{ch_0} + V_{pist_0} \tag{2.85}$$

We could identify the value of s_{min} considering **Figure 2.39**.

$$s_{min} = s_{min}(\beta) = L_{OK} - L_{KJ} + (R_a \cdot \sin\beta) - \overline{AC} \cdot \cos\delta|_{\vartheta_i=0} \tag{2.86}$$

$\delta|_{\vartheta_i=0}$ in **Eq. (2.86)** is the piston inclination angle with respect to its seat for a zero angular position $\vartheta_i = 0$. We can obtain **Eq. (2.87)** by substituting δ with its analytical expression (**Eq. (2.59)**).

$$s_{min}(\beta) = L_{OK} - L_{KJ} + (R_a \cdot \sin\beta) - \overline{AC} \cdot \cos\left(\arcsin\left(\frac{R_a \cos\beta - R_c}{L_{AB}}\right)\right) \tag{2.87}$$

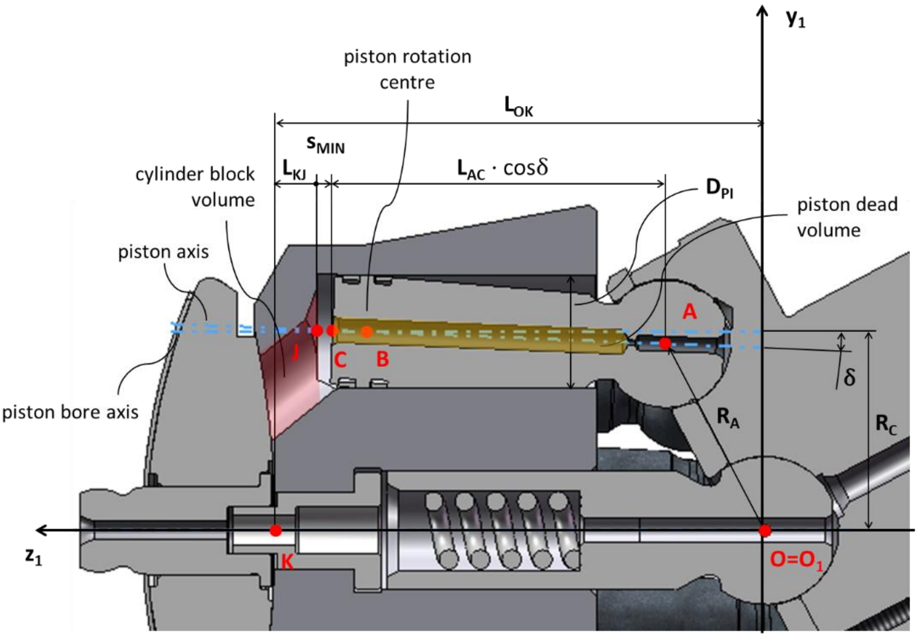

Figure 2.39: Parametrization of the piston chamber volume

Eq. (2.88) reports the analytical expression of the *i*-th piston chamber volume derivative.

$$\frac{d}{dt} V_{ch_i}(\vartheta_i,\beta) = \frac{\pi}{4} D_{pi}^2 \cdot (-R_a \cdot \cos\beta \cdot \dot{\beta} - R_a \cdot \omega \cdot \sin\vartheta_i \cdot \sin\beta + R_a \cdot \cos\vartheta_i \cdot \cos\beta \cdot \dot{\beta}) \tag{2.88}$$

The calculation of the volume and the volume variation for the *i*-th piston chamber is necessary to evaluate the pressures (and pressure variations) within the chambers.

Figure 2.40 shows the trend of the 1st piston chamber volume and its derivative as a function of angular position for a defined reference design and β inclination angle.

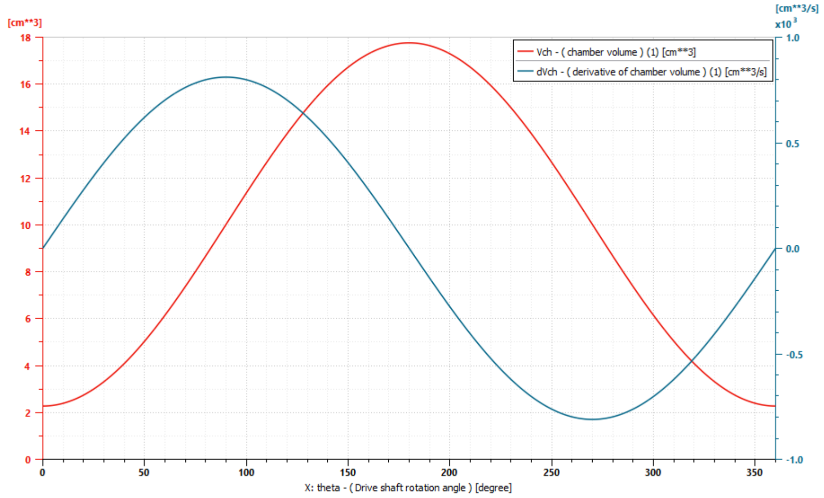

Figure 2.40: Volume (red) and volume variation (blue) concerning the *i*-th piston chamber as function of the angular position

Dynamic analysis

We are presenting in this sub-section the dynamic analysis starting with the identification of all forces and moments, known and unknown, acting on the *i*-th piston. Once we have introduced all the terms, it will be possible to move on to the realization of the free body diagrams and, therefore, to the writing and solving of the equilibrium equations.

We decided to use the rotating reference frame $Ox'y'z'$ to express the equilibrium equations.

Weight force. The weight force expressed in the $Ox'y'z'$ reference frame can be obtained by rotating the components of the weight force vector expressed in the fixed reference frame of the machine (assumed known) using the rotation matrix $R_{O\to O'}$ (**Eq. 2.44**).

$$F_{pi,i_{gx'}} = F_{pi,i_{gx}} \tag{2.89}$$

$$F_{pi,i_{gy'}} = F_{pi,i_{gy}} \cdot \cos\beta - F_{pi,i_{gz}} \cdot \sin\beta \tag{2.90}$$

$$F_{pi,i_{gz'}} = F_{pi,i_{gy}} \cdot \sin\beta + F_{pi,i_{gz}} \cdot \cos\beta \tag{2.91}$$

This weight force is applied in the piston centre of mass G_{pi_i}.

Pressure forces. The pressure forces acting on the piston can be located on three different zones, which are:

- Pressure force on the piston head
- Pressure force on the piston spherical end
- Pressure force on the areas exposed to the oil in the casing

Eq. (2.92) reports the force exerted on the piston head by the oil within the chamber. We considered a single force component along the piston z_p axis, which can be applied in B_i.

$$F_{pi,i_{presszp}} = -p_{ch,i} \cdot \frac{\pi \cdot D_{pi}^2}{4} \tag{2.92}$$

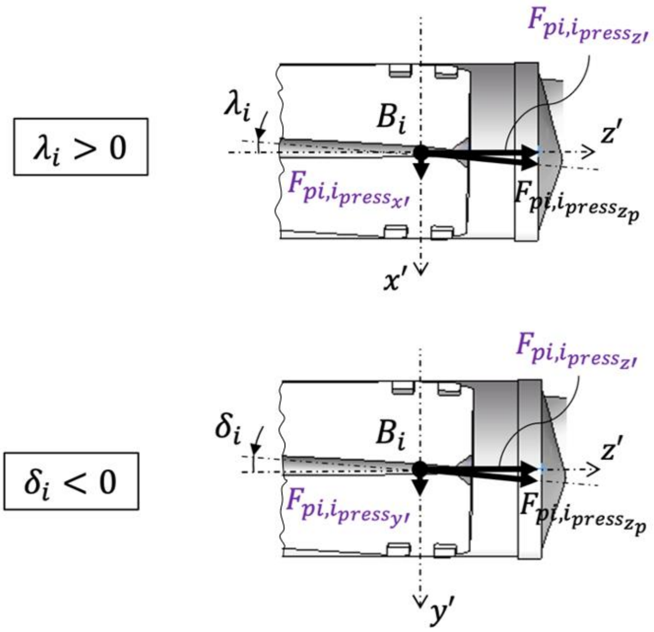

Figure 2.41: Schematic for the decomposition of pressure forces

This force can be decomposed on the $Ox'y'z'$ reference frame using angles δ_i and λ_i (**Figure 2.41**). **Eq. (2.93)-(2.94)-(2.95)** reports the components in the $Ox'y'z'$ rotating frame.

$$F_{pi,i_{press_{x'}}} = +F_{pi,i_{press_{zp}}} \cdot \sin(\lambda_i) \tag{2.93}$$

$$F_{pi,i_{press_{y'}}} = -F_{pi,i_{press_{zp}}} \cdot \sin(\delta_i) \tag{2.94}$$

$$F_{pi,i_{press_{z'}}} = F_{pi,i_{press_{zp}}} \cdot (\cos(\lambda_i) \cdot \cos(\delta_i)) \tag{2.95}$$

We repeated this process to identify the pressure force exerted by the oil in the casing. We assumed this force as applied in the ball joint centre A_i

We considered the difference between the projection on the $x'y'$ plane of the piston spherical end and the piston head as thrusting area.

$$F_{pi,i_{press-case_{zp}}} = p_{case} \cdot \frac{\pi}{4} \left(D_{pi}^2 - D_{sphere,i}^2\right) \tag{2.96}$$

$$F_{pi,i_{press-case_{x'}}} = +F_{pi,i_{press-case_{zp}}} \cdot \sin(\lambda_i) \tag{2.97}$$

$$F_{pi,i_{press-case_{y'}}} = -F_{pi,i_{press-case_{zp}}} \cdot \sin(\delta_i) \tag{2.98}$$

$$F_{pi,i_{press-case_{z'}}} = F_{pi,i_{press-case_{zp}}} \cdot (\cos(\lambda_i) \cdot \cos(\delta_i)) \tag{2.99}$$

The evaluation of the pressure force acting on the piston spherical end is a bit more complex due to the geometry and the presence of different pressure zones. For simplicity of treatment, we did not consider the usual logarithmic trend of pressure within the gap, but we instead identified a full pressure zone and a medium pressure one (where a mean pressure between full pressure and casing pressure is acting). The area considered at full pressure, i.e. the same pressure present in the chamber, is the area directly connected with the chamber through the ball joint recess. We considered the area between the recess chamber and the unit casing at medium pressure, which can be identified as the difference between the total thrust area (defined by the projection on the x_P y_P plane of the circumferential groove on the sphere) and the full pressure area.

As said, we considered the full pressure acting in the recess generated by the milling of diameter D_{fr} on the piston spherical end. If this zone is connected to the recess obtained in the ball joint seat of the shaft flange, the full pressure will act on this area too. The projection of this ball joint seat recess on the x_P y_P plane is a circle only when the inclination angle of the cylinder block is zero. In all other cases this projection is an ellipse. On the other hand, the other areas of interest (defined by the milling and by the circumferential grooves) remain circular since they 'lie' on the piston spherical end. Please refer to **Figure 2.42** for a graphic illustration of these areas.

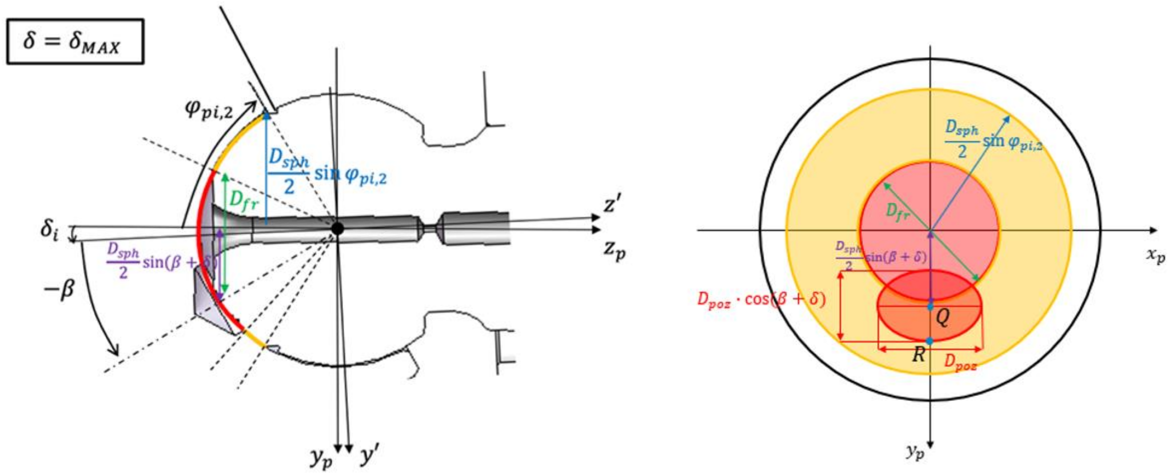

Figure 2.42: Full pressure area and medium pressure area on the piston spherical end

Note that we are neglecting the pressure forces in the y_P direction which would arise from the non-symmetry of the areas of interest with respect to the x_P axis. We are considering only the pressure forces along the z_P axis.

Eq. (2.100) reports this pressure force expression, where $A_{fullpress}$ is the full pressure area and $A_{midpress}$ is the medium pressure area.

$$F_{pi,i_{press-bal_{z_p}}} = p_{sphere,i} \cdot A_{fullpress} + \frac{p_{sphere,i} - p_{case}}{2} \cdot A_{midpress} \tag{2.100}$$

It is therefore necessary to proceed with the analytical evaluation of these areas of interest.

We distinguished these following cases the following cases to consider the different situations that may occur:

1. The projection of the ball joint seat recess is totally inside the circle of diameter D_{fr}
2. The projection of the ball joint seat recess is partially inside the circle of diameter D_{fr}
3. The projection of the ball joint seat recess is totally outside the diameter circle D_{fr}

The full pressure areas relating to these cases are:

1. $A_{fullpress} = \frac{\pi}{4} D_{fr}^2$
2. $A_{fullpress} = \frac{\pi}{4} D_{fr}^2 + A_{ellipse} - A_{intersection}$
3. $A_{fullpress} = \frac{\pi}{4} D_{fr}^2$

The ellipse area can be easily found referring to **Figure 2.42** by means of **Eq. (2.101)**.

$$A_{ellipse} = \pi \frac{D_{poz}}{2} \cdot \frac{D_{poz} \cdot \cos(\beta + \delta)}{2} \tag{2.101}$$

We considered **Figure 2.43** to evaluate the intersection area $A_{intersection}$ between the circle and the ellipse, identifying:

- elliptic sector area QNM $A_{sett\ ell_{QNM}}$,
- triangle area QNM $A_{tri_{QNM}}$,
- circular sector area ONM $A_{sett\ circ_{ONM}}$,
- triangle area ONM $A_{tri_{ONM}}$,
- circular segment area $A_{seg\ circ_{NM}}$ with arc NM, calculated as difference between $A_{sett\ circ_{ONM}}$ and $A_{tri_{ONM}}$.

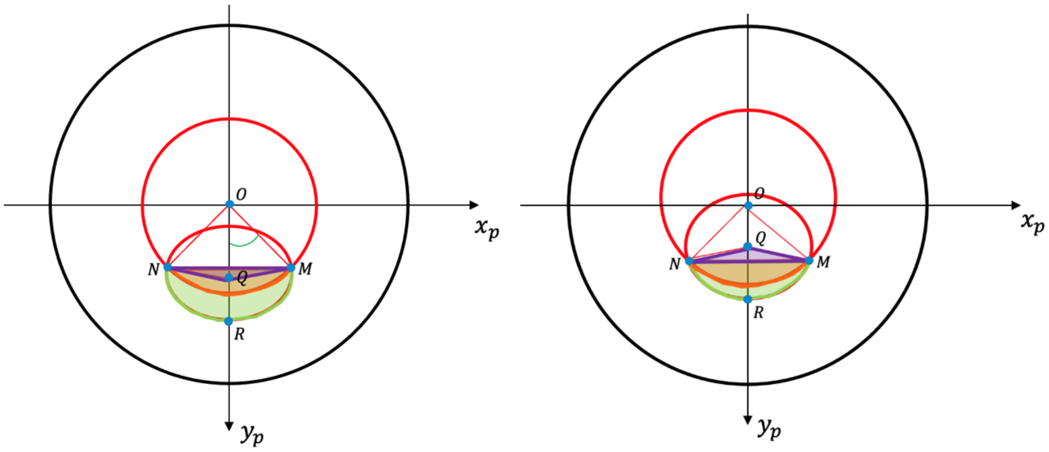

Figure 2.43: Schematic for the spherical pressure area calculation with $y_Q > y_M$ (left) and $y_Q < y_M$ (right)

It is, in fact, necessary to consider two distinct cases depending on the position of the following points:

- point Q: centre of the ellipse
- point R: lower extremity of the ellipse calculated by adding the length of the minor semi-axis to the ordinate y_p of the ellipse centre Q
- point M: point of intersection between the circle of diameter D_{fr} and the ellipse

The calculation of the intersection between the circle and the ellipse changes depending on the position of these points. **Eq. (2.102)** expresses the full pressure area calculation for $y_Q > y_M$, while **Eq. (2.103)** does the same for $y_Q < y_M$ it will be that in.

$$A_{fullpress} = \frac{\pi}{4} D_{fr}^2 + A_{sett\ ell_{QNM}} + A_{tri_{QNM}} - A_{seg\ circ_{NM}} \tag{2.102}$$

$$A_{fullpress} = \frac{\pi}{4} D_{fr}^2 + A_{sett\ ell_{QNM}} - A_{tri_{QNM}} - A_{seg\ circ_{NM}} \tag{2.103}$$

Once we have estimated the areas of full and medium pressure, it is possible to express this contribution in the $Ox'y'z'$ reference frame.

$$F_{pi,i_{press-bal_{x'}}} = +F_{pi,i_{press-bal_{zp}}} \cdot \sin(\lambda_i) \tag{2.104}$$

$$F_{pi,i_{press-bal_{y'}}} = -F_{pi,i_{press-bal_{zp}}} \cdot \sin(\delta_i) \tag{2.105}$$

$$F_{pi,i_{press-bal_{z'}}} = F_{pi,i_{press-bal_{zp}}} \cdot (\cos(\lambda_i) \cdot \cos(\delta_i)) \tag{2.106}$$

<u>Friction force</u>. We considered in this contribution the effects of friction between the piston and chamber surfaces which are in relative motion. Both the viscous friction in the seal leakage gap and the static pressure force have been considered.

$$F_{pi,i_{visc_{z'}}} = -\frac{\pi\left(\left(D_{pi}+h_{pi-cb}\right)^2-D_{pi}^2\right)}{4}\cdot p_{ch,i} - \frac{\pi\cdot\mu_{pi,i}\cdot D_{pi}\cdot v_{z'}{}_{B,i}\cdot l_{c,pi,i}}{h_{pi-cb}} \quad (2.107)$$

<u>Churning losses moment</u>. Among the viscous effects, the rotation of the pistons in the casing oil causes a churning loss moment (**Figure 2.44**) [54].

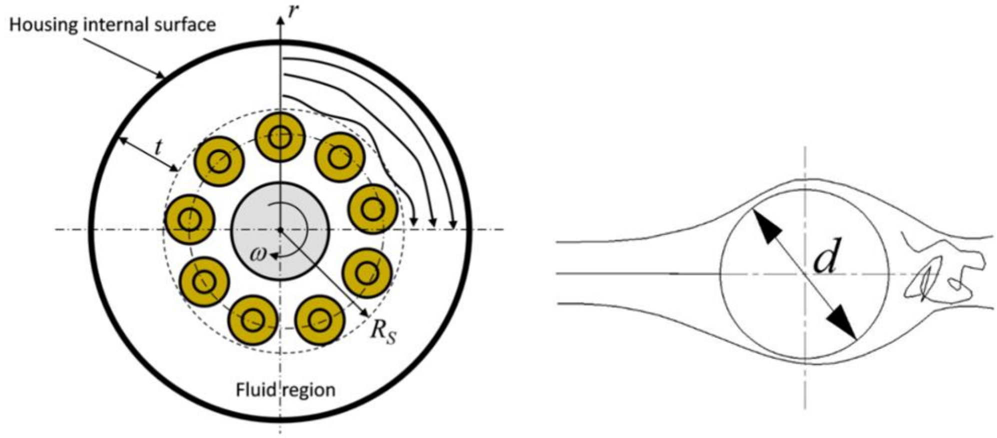

Figure 2.44: Piston churning losses due to the rotation in the casing oil [54]

The expression of this moment can be written as given in **Eq. (2.108)**.

$$M_{pi,i_{cl_{z'}}} = -F_i \cdot R_m \quad (2.108)$$

Eq. (2.109)-(2.110)-(2.111) define the various terms of **Eq. (2.108)**.

$$F_i = \frac{1}{2} C_d\, \rho\, v_p^2\, dl_i \quad (2.109)$$

$$v_p = \omega R_m \quad (2.110)$$

$$l_i = l_0 + R(1-\cos\theta_i)\tan\beta \quad (2.111)$$

The term l_i is the length of the piston out of the chamber, l_0 the length of the piston out of the chamber at $\theta_i = 0$ and C_d can be calculated basing on the operating conditions, i.e. basing on the Reynolds number defined in **Eq. (2.112)**.

$$Re = \frac{\rho\, v_p\, d}{\mu} \quad (2.112)$$

Note that we are not including the torque calculated in **Eq. (2.108)** within the piston equilibrium of the piston. This churning losses, in fact, will be directly reported to the $Oxyz$ system and considered in the shaft equilibrium. This friction moment, in fact, subtracts torque from the torque delivered by the machine considering a motor, or increase the torque absorbed by the machine considering a pump.

<u>Mixed friction moments in the piston-shaft contact</u>. Another non-negligible friction component is located on the mixed (metal to metal and mediated through oil film) contact between piston and shaft. We chose to include this effect by defining a friction torque for each plane ($y'z'$ and $x'z'$), i.e. a friction torque for each relative rotation ($\dot{\delta}_i$ and $\dot{\lambda}_i$), to simplify the analysis.

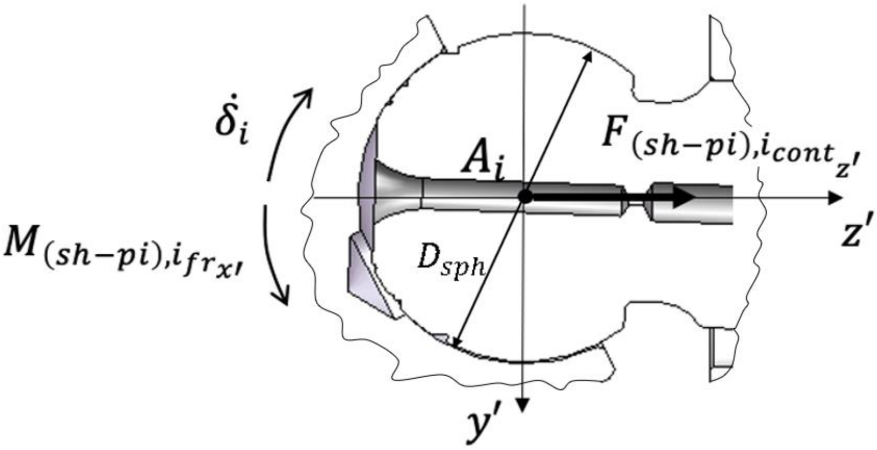

Figure 2.45: Friction moment in the piston-shaft contact ($y'z'$ plane)

Eq. (2.113)-(2.114) report the expression used for the evaluation of these friction moments given by the product of the contact force $F_{(sh-pi),i_{cont_{z'}}}$ and the distance $\frac{D_{sph}}{2}$.

$$M_{(sh-pi),i_{fr_{x'}}} = -f_a \cdot F_{(sh-pi),i_{z'}} \cdot \frac{D_{sph}}{2} \cdot \tanh(\dot{\delta}_i) \tag{2.113}$$

$$M_{(sh-pi),i_{fr_{y'}}} = -f_a \cdot F_{(sh-pi),i_{z'}} \cdot \frac{D_{sph}}{2} \cdot \tanh(\dot{\lambda}_i) \tag{2.114}$$

We inserted the terms $\tanh(\dot{\delta}_i)$ and $\tanh(\dot{\lambda}_i)$ to simply integrate this contribution the C++ code. These terms, in fact, ensure the continuity of these contribution even across the zero for their argument. In this way, it is possible not to cause discontinuities in the integrator.

Shaft reaction forces. The reaction forces due to contact between pistons and shaft or cylinder block cannot be expressed through known expressions. These reactions are thus unknown terms which must be derived from the piston equilibrium. Once we have evaluated these terms, we will use these reactions as inputs for the shaft and cylinder block submodels, after adding a minus sign to consider the forces that the piston exerts on them.

Each piston is coupled to the shaft flange with a ball joint. There are therefore mutual reactions between the two components along the three axes of the $Ox'y'z'$ system. We have considered these reactions as located in the ball joint centre A_i.

$$F_{(sh-pi),i_{x'}} = -F_{(pi-sh),i_{x'}} \tag{2.115}$$

$$F_{(sh-pi),i_{y'}} = -F_{(pi-sh),i_{y'}} \tag{2.116}$$

$$F_{(sh-pi),i_{z'}} = -F_{(pi-sh),i_{z'}} \tag{2.117}$$

As said, these reaction forces that the shaft exerts on the *i*-th piston are some of the system unknowns.

Cylinder block reaction forces. As mentioned, we considered piston and cylinder block to be always in contact with each other, locating their contact point in B_i. We are introducing reaction forces along x' and y' as piston can travel along the chamber axis (which is parallel to z').

$$F_{(cb-pi),i_{x'}} = -F_{(pi-cb),i_{x'}} \tag{2.118}$$

$$F_{(cb-pi),i_{y'}} = -F_{(pi-cb),i_{y'}} \tag{2.119}$$

On the other hand, there must be a mutual friction force along the z' axis, which opposes the motion of the piston. **Eq. (2.120)** expresses this friction force exploiting the total contact normal force.

$$F_{(cb-pi),i_{frz'}} = -f_{pi-cb} \cdot \sqrt{F^2_{(cb-pi),i_{x'}} + F^2_{(cb-pi),i_{y'}}} \cdot \tanh\left(v_{z'_{B,i}}\right) = -F_{(pi-cb),i_{frz'}} \qquad (2.120)$$

We have inserted the hyperbolic tangent again 'safety' reason for the C++ code crossing $v_{z'_{B,i}} = 0$.

Free body diagrams

Once we have introduced all the contributions acting on the *i*-th piston, it is possible to proceed with the realization of the free body diagrams.

Figure 2.46-2.47 show the free body diagrams of the piston including the forces and moments acting on it in the three Cartesian directions of the rotating reference frame $Ox'y'z'$. We have also reported the z_p axis of the piston's reference frame.

We have decided not to consider a particular angular position as the inner dead centre IDC ($\vartheta_i = 0$), the outer dead centre ODC ($\vartheta_i = 180°$) or quadrature points to show the completeness of the possible cases. We have rather considered a generic intermediate point, such as the one obtained for $\vartheta_i = 45°$.

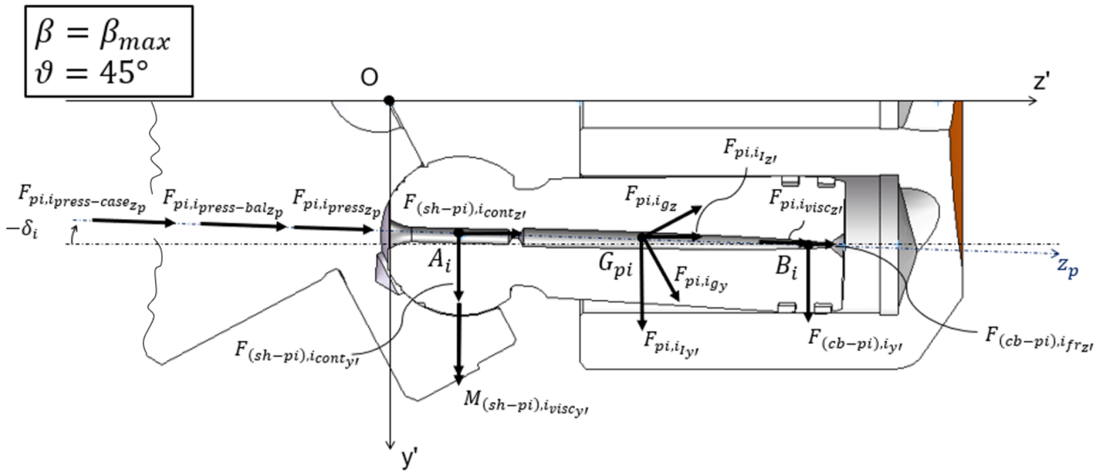

Figure 2.46: Piston free body diagram on $y'z'$ plane

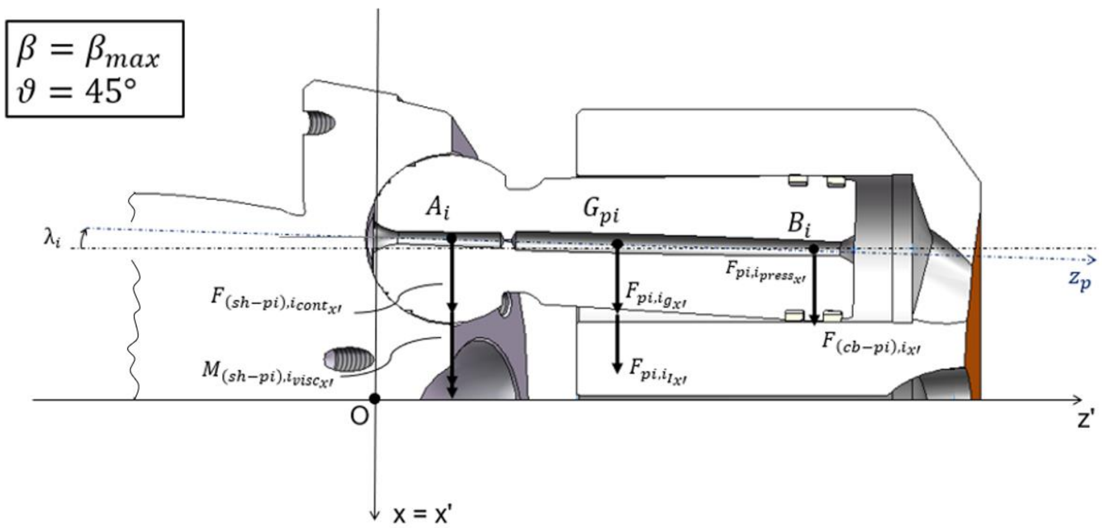

Figure 2.47: Piston free body diagram on $x'z'$ plane

We have exploited **Figure 2.48** to assign the correct sign to the contributions that enter the rotational equilibrium equations. Note that force F_z generates a negative moment around the x' axis, despite does not have a minus sign in the relationship. However, the one reported is the case for $\delta_i < 0$ so the minus sign will appear inside the expression of the distance b_y.

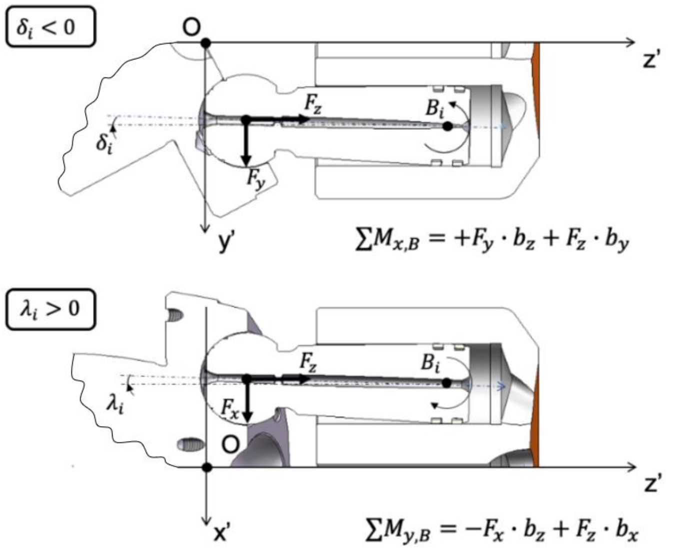

Figure 2.48: Convention for the piston moments around y' and x' axes

Table 2.14 shows the equilibrium equations developed for the *i*-th piston, written using the second law of motion ($\sum F = m \cdot a$ e $\sum M = I \cdot \alpha$).

Table 2.14: Equilibrium equations for the i-th piston

Translational equilibrium – x' axis	
$F_{(sh-pi),i_{x'}} + F_{pi,i_{g_{x'}}} + F_{(cb-pi),i_{x'}} + F_{pi,i_{press_{x'}}} + F_{pi,i_{press-bal_{x'}}} + F_{pi,i_{press-case_{x'}}} = m_{pi,i} \cdot a_{G_i,x'}$	(2.121)
Translational equilibrium – y' axis	
$F_{(sh-pi),i_{y'}} + F_{pi,i_{g_{y'}}} + F_{(cb-pi),i_{y'}} + F_{pi,i_{press_{y'}}} + F_{pi,i_{press-bal_{y'}}} + F_{pi,i_{press-case_{y'}}} = m_{pi,i} \cdot a_{G_i,y'}$	(2.122)
Translational equilibrium – z' axis	
$F_{pi,i_{press_{z'}}} + F_{pi,i_{visc_{z'}}} + F_{(sh-pi),i_{z'}} + F_{pi,i_{press-bal_{z'}}} + F_{pi,i_{press-case_{z'}}} + F_{pi,i_{g_{z'}}} + F_{(cb-pi),i_{fr_{z'}}} = m_{pi,i} \cdot a_{G_i,z'}$	(2.123)
Rotational equilibrium about $B_i - x'$ axis	
$M_{(sh-pi),i_{fr_{x'}}} + M_{(sh-pi),i_{visc_{x'}}} + F_{pi,i_{g_{y'}}} \cdot \overline{G_{pi,i}B_i} \cdot \cos(\delta_i) + F_{pi,i_{g_{z'}}} \cdot \overline{G_{pi,i}B_i} \cdot \sin(\delta_i) + \left(F_{pi,i_{press-bal_{y'}}} + F_{pi,i_{press-case_{y'}}} + F_{(sh-pi),i_{y'}}\right) \cdot \overline{A_iB_i} \cdot \cos(\delta_i) + \left(F_{pi,i_{press-bal_{z'}}} + F_{pi,i_{press-case_{z'}}} + F_{(sh-pi),i_{z'}}\right) \cdot \overline{A_iB_i} \cdot \sin(\delta_i) = I_{xx,B_i} \cdot \ddot{\delta}_i$	(2.124)
Rotational equilibrium about $B_i - y'$ axis	
$M_{(sh-pi),i_{fr_{y'}}} + M_{(sh-pi),i_{visc_{y'}}} - F_{pi,i_{g_{x'}}} \cdot \overline{G_{pi,i}B_i} \cdot \cos\lambda_i + F_{pi,i_{g_{z'}}} \cdot \overline{G_{pi,i}B_i} \cdot \sin\lambda_i - \left(F_{pi,i_{press-bal_{x'}}} + F_{pi,i_{press-case_{x'}}} + F_{(sh-pi),i_{x'}}\right) \cdot \overline{A_iB_i} \cdot \cos\lambda_i + \left(F_{pi,i_{press-bal_{z'}}} + F_{pi,i_{press-case_{z'}}} + F_{(sh-pi),i_{z'}}\right) \cdot \overline{A_iB_i} \cdot \sin(\lambda_i) = I_{xx,B_i} \cdot \ddot{\lambda}_i$	(2.125)

$\overline{G_{pi,i}B_i}$ and $\overline{A_iB_i}$ are positive terms.

Note that we have not considered the rotational equilibrium equation concerning the z' axis.

As anticipated, the reaction forces exchanged with the adjacent components are the system unknowns, i.e.:

- $F_{(sh-pi),i_{x'}}$
- $F_{(sh-pi),i_{y'}}$

- $F_{(sh-pi),i_{z'}}$
- $F_{(cb-pi),i_{x'}}$
- $F_{(cb-pi),i_{y'}}$

The terms $F_{(cb-pi),i_{fr_{z'}}}$, $M_{(sh-pi),i_{fr_{x'}}}$ and $M_{(sh-pi),i_{fr_{y'}}}$, in fact, can be written as a function of the five unknowns listed above. **Table 2.14** therefore reports a system of 5 equations in 5 unknowns.

However, $F_{(cb-pi),i_{fr_{z'}}}$ is a non-linear term, as shown in **Eq. (2.120)**. We decided to exploit an iterative process instead of using a known method for non-linear system resolution as it is less complex to implement within the C++ code.

The following steps summarize the iterative procedure to evaluate the unknowns:

1. We simplify the system imposing some unknow terms to be equal to zero:
   - $F_{(sh-pi),i_{z'}} = 0$
   - $F_{(cb-pi),i_{fr_{z'}}} = 0$
   - $M_{(sh-pi),i_{fr_{x'}}} = 0$
   - $M_{(sh-pi),i_{fr_{y'}}} = 0$
2. We evaluate the remaining four unknown terms (everyone except $F_{(cb-pi),i_{fr_{z'}}}$):
   - $F_{(sh-pi),i_{y'}}$ from the rotation around the x' axis
   - $F_{(cb-pi),i_{y'}}$ from the translation along the y' axis
   - $F_{(sh-pi),i_{x'}}$ from the rotation around the y' axis
   - $F_{(cb-pi),i_{x'}}$ from the translation along the x' axis
3. We evaluate the terms $M_{(sh-pi),i_{fr_{x'}}}$, $M_{(sh-pi),i_{fr_{y'}}}$, $F_{(cb-pi),i_{fr_{z'}}}$ exploiting **Eq. (2.113)-(2.114)-(2.120)**.
4. We then calculate the first value of the unknown $F_{(sh-pi),i_{z'}}$ from the translation along the z' axis.
5. We return to step 2 for the recalculation of the unknown terms.
6. We continue by deriving the remaining unknown until the result convergence.

We noted that three iterations were sufficient to obtain a very good result convergence.

Simcenter Amesim Submodel Editor® model

As anticipated, we also implemented this analysis in C++ code starting from the piston parameterization and equilibrium equations to develop the Simcenter Amesim® element relating to the piston. Exploiting the Simcenter Amesim Submodel Editor® tool, we managed to create the piston submodel by defining the characteristic parameters, the connection ports with the other components, the variables exchanged at these ports, the internal variables and, obviously, the code to solve the mechanical equilibrium equations as seen above.

Figure 2.49 shows the representation of the Simcenter Amesim® icon created using the Simcenter Amesim Submodel Editor®, concerning the piston submodel BAUPISTE000. **Table 2.15** describes the variables associated with the submodel connection ports.

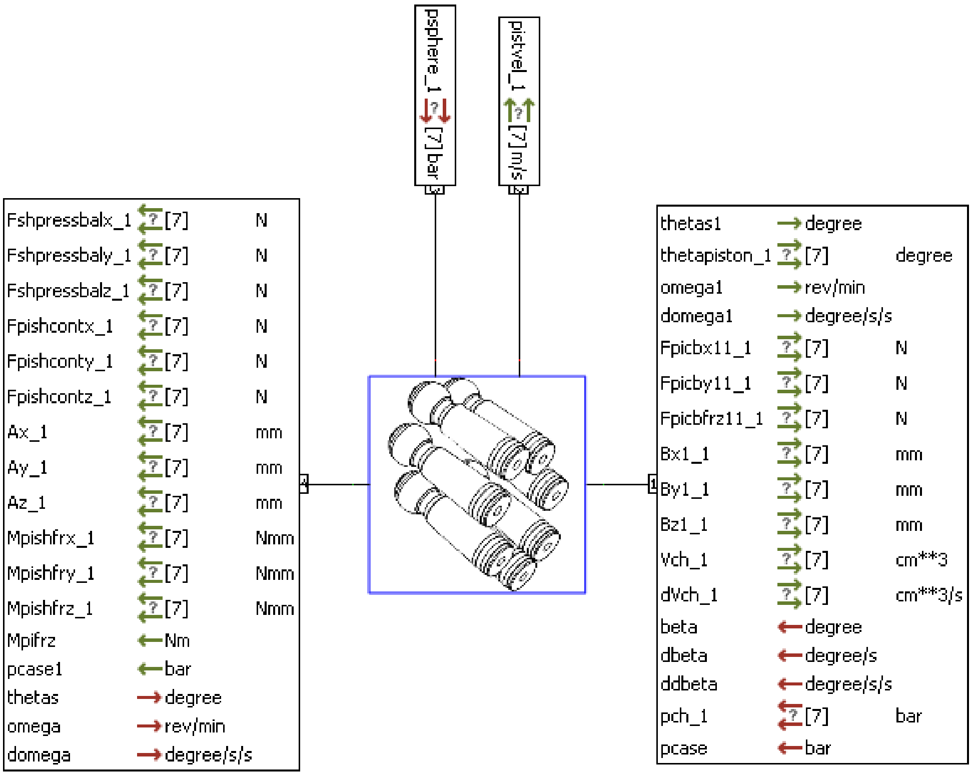

Figure 2.49: Icon of the pistons submodel developed in Simcenter Amesim®

Table 2.15: Inputs/outputs at each port of the pistons submodel developed in Simcenter Amesim®

PORT	VARIABLE	DESCRIPTION	SYMBOL	TYPE
1	Input	Cylinder block inclination angle	β	Scalar
		Derivative of the cylinder block inclination angle	$d\beta$	
		Second derivative of the cylinder block inclination angle	$dd\beta$	
		Piston chamber pressures	p_{ch}	Vector
		Casing pressure	p_{case}	Scalar
	Output	Duplicate of shaft angular position	ϑ_{s1}	Scalar
		Piston angular positions	ϑ_{pist}	Vector
		Duplicate of shaft angular velocity	ω_1	Scalar
		Duplicate of shaft angular acceleration	$d\omega_1$	
		Piston-cylinder block contact force – x' axis	$F_{(pi-cb)_{ix'}}$	Vector
		Piston-cylinder block contact force – y' axis	$F_{(pi-cb)_{iy'}}$	
		Piston-cylinder block contact force – z' axis	$F_{(pi-cb)_{ifrz'}}$	
		B_i position – x' axis	x'_{Bi}	
		B_i position – y' axis	y'_{Bi}	
		B_i position – z' axis	z'_{Bi}	
		Piston chamber volumes	V_{ch}	
		Derivative of piston chamber volumes	dV_{ch}	
2	Output	Piston velocities	v_{pist}	Vector
3	Input	Piston spherical end pressure	p_{sphere}	Vector
4	Input	Shaft angular position	ϑ_s	Scalar
		Shaft angular velocity	ω	

		Shaft angular acceleration	$d\omega$	
	Output	Ball joint pressure force on shaft – x' axis	$F_{p_{sphere_x}}$	Vector
		Ball joint pressure force on shaft – y' axis	$F_{p_{sphere_y}}$	
		Ball joint pressure force on shaft – z' axis	$F_{p_{sphere_z}}$	
		Piston-shaft contact force – x' axis	$F_{(pi-sh)_{i_x}}$	
		Piston-shaft contact force – y' axis	$F_{(pi-sh)_{i_y}}$	
		Piston-shaft contact force – z' axis	$F_{(pi-sh)_{i_z}}$	
		A_i position – x axis	x_{Ai}	
		A_i position – y axis	y_{Ai}	
		A_i position – z axis	z_{Ai}	
		Piston-shaft friction moment – x axis	$M_{(pi-sh)_{i_{fr_x}}}$	
		Piston-shaft friction moment – x axis	$M_{(pi-sh)_{i_{fr_y}}}$	
		Piston-shaft friction moment – x axis	$M_{(pi-sh)_{i_{fr_z}}}$	
		Piston churning losses moment – z' axis	$M_{pi,i_{cl_{z'}}}$	Scalar

2.3.2 Cylinder block model

In this section we are presenting the analysis of the machine's cylinder block and central pivot, which was considered rigidly connected to the block itself after an evaluation of the couplings and tolerances.

The reaction forces with the pistons are now known thanks to the analysis made in the previous section.

The cylinder block mechanical modelling focuses on the analysis of the pressure forces and their point of application, which push the block away from the valve plate, and the evaluation of the thrust forces that push the block against the valve plate. The spherical cap interface between cylinder block and valve plate must guarantee the component balancing adjusting the unbalanced contribution. The cylinder block balancing is essential to ensure the alignment with the valve plate and then the correct filling of the chambers.

We have simplified the analysis by considering only the axial contribution of the pressure thrust within the spherical cap gap.

Before proceeding with the analysis and the free body diagram of the cylinder block, we are reporting the assumptions we have considered:

- the cylinder block (and central pivot) stiffness is considered infinite, i.e. no cylinder bock deformations,
- the cylinder block angular position is considered equal to the shaft one, i.e. no angular shift,
- the heights of the leakage gaps are constant,
- the contact between central pivot and shaft is considered centred in the central ball joint centre O,
- the contact between cylinder block and valve plate is considered mixed (metal to metal and mediated through oil film) and the reaction forces exchanged (fluid-dynamic and contact forces) are concentrated in a single term applied at point H_2,
- the pressure trend within the leakage gaps is considered linear and not logarithmic.

The main outputs of the cylinder block analysis are:

- the hydrodynamic/contact force generated within the leakage spherical gap between cylinder block and valve plate,
- the equivalent point of application of this force,
- the mutual reaction forces between cylinder block and shaft.

Figure 2.50 shows the cylinder block and central pivot with their combined centre of mass G_{cb}.

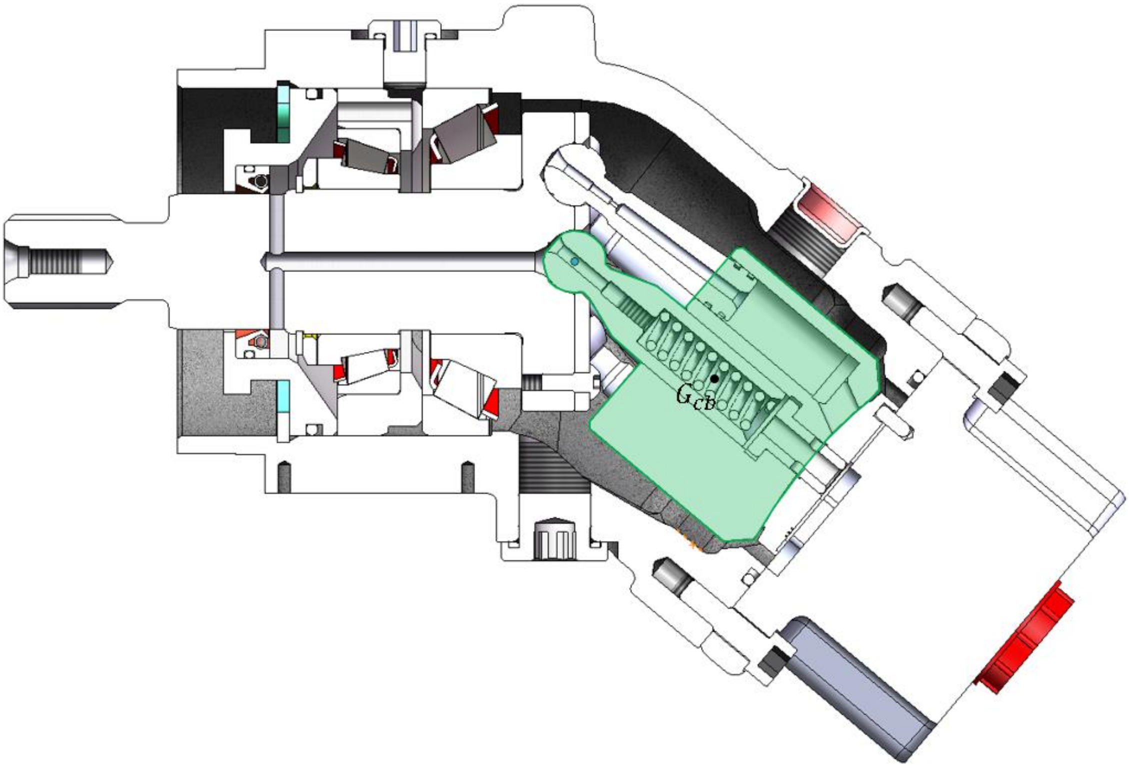

Figure 2.50: Section of the reference machine and cylinder block-central pivot system (in green)

The centre of mass G_{cb} of the system, of course, considers the distribution of both cylinder block and central pivot.

Figure 2.51-2.52 depicts the parameterization diagram of the cylinder block, considering the $y'z'$ and $x'y'$ planes.

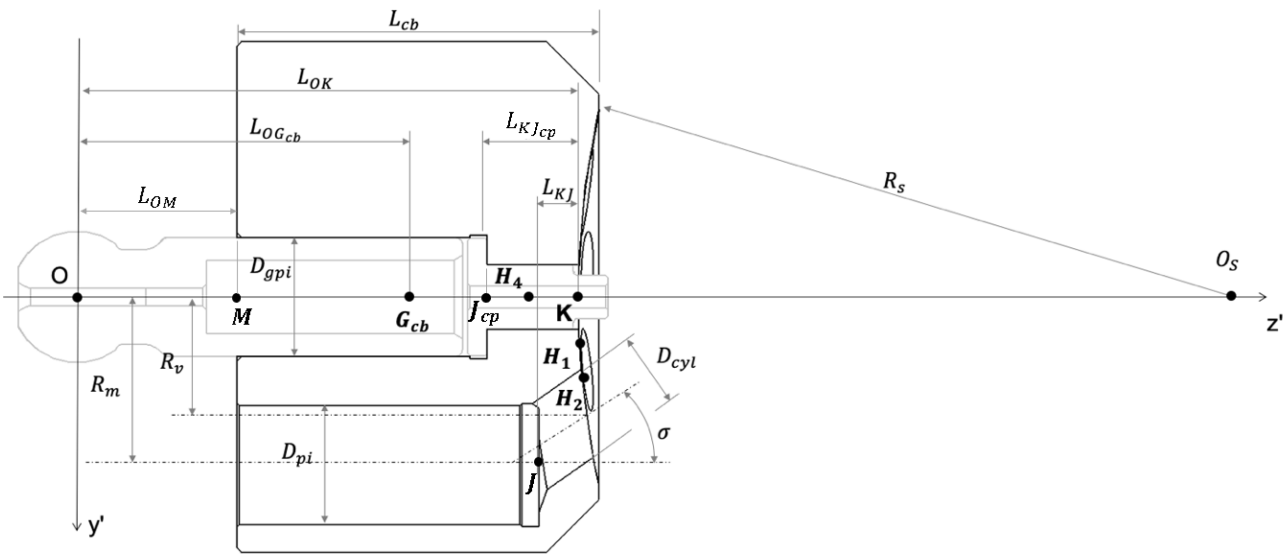

Figure 2.51: Cylinder block parametrization ($y'z'$ plane)

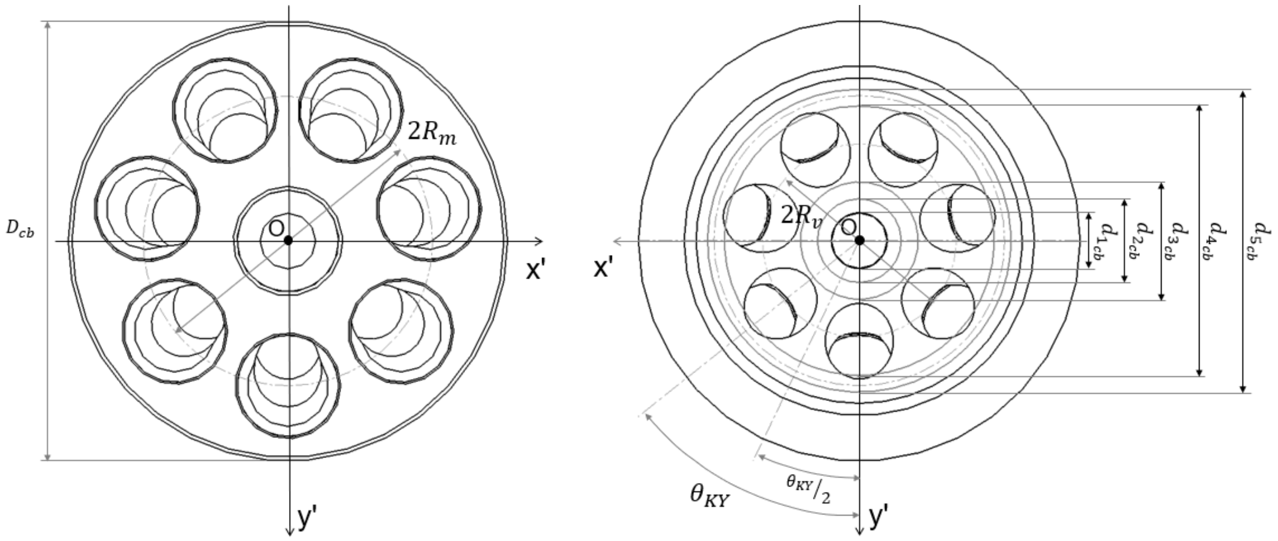

Figure 2.52: Cylinder block parametrization ($x'y'$ plane)

Table 2.16 lists and describes the geometric and non-geometric quantities used for the cylinder block parameterization and modelling.

Table 2.16: Parameters required for the cylinder block model

Symbol	**Description**
D_{pi}	Piston chamber diameter
m_{cb}	Cylinder block-central pivot mass
R_m	Radius of the piston chamber centres
R_v	Radius of the inlet/outlet bore centres
α_e	Euler angle α
β_e	Euler angle β
γ_e	Euler angle γ
D_{gpi}	Central pivot bore diameter
L_{cb}	Cylinder block axial length
D_{cb}	Cylinder block diameter
$L_{OG_{cb}}$	Distance between O (reference frame centre) and G_{cb} (cylinder block centre of mass)
L_{OK}	Distance between O (reference frame centre) and K (cylinder block rear surface centre)
L_{KJ}	Distance between K (cylinder block rear surface centre) and J (piston chamber end)
$L_{KJ_{cp}}$	Distance between K (cylinder block rear surface centre) and J_{cp} (central pivot bore end)
L_{OO_s}	Distance between O (reference frame centre) and O_s (sphere cap centre)
R_s	Radius of curvature of cylinder block sphere cap
D_{cyl}	Milling diameter of inlet/outlet bores
σ	Inclination angle of inlet/outlet bores
$d_{1_{cb}}$	Sealing diameter 1 between cylinder block and valve plate
$d_{2_{cb}}$	Sealing diameter 2 between cylinder block and valve plate
$d_{3_{cb}}$	Sealing diameter 3 between cylinder block and valve plate
$d_{4_{cb}}$	Sealing diameter 4 between cylinder block and valve plate
$d_{5_{cb}}$	Sealing diameter 5 between cylinder block and valve plate
$I_{cb,x'x'}$	Cylinder block $x'x'$ moment of inertia

We are now proceeding directly with the dynamic analysis. The kinematic analysis, in fact, is of no particular interest since it has been already included in piston one with the evaluation of the B_i motion. The rigid body formed by the cylinder block and central pivot simply rotates around its z' axis with angular speed ω.

Dynamic analysis

We are carrying out the cylinder block dynamic analysis in the same we have previously done for the pistons. As done with piston, we have considered the rotating reference frame $Ox'y'z'$ to express forces/moments and equilibrium equations.

Weight force. The weight force expressed in the $Ox'y'z'$ reference frame can be obtained by rotating the components of the weight force vector expressed in the fixed reference frame of the machine (assumed known) using the rotation matrix $R_{O \to O'}$ (**Eq. 2.44**). The point of application of this force is the centre of mass G_{cb} of the cylinder block-central pivot system.

$$[F_{cbg_{Ox'y'z'}}] = R_{O \to O'}[F_{cbg_{BAU}}] \tag{2.126}$$

which translates into:

$$F_{cbg_{x'}} = F_{cbg_x} \tag{2.127}$$

$$F_{cbg_{y'}} = F_{cbg_y} \cdot \cos\beta - F_{cbg_z} \cdot \sin\beta \tag{2.128}$$

$$F_{cbg_{z'}} = F_{cbg_y} \cdot \sin\beta + F_{cbg_z} \cdot \cos\beta \tag{2.129}$$

Pressure forces. It is necessary to evaluate the areas of interest on the front and rear serfaces of the cylinder block (**Figure 2.53**) to determine the hydrostatic axial thrusting forces acting on the component.

Figure 2.53 shows the front and rear views of the cylinder block, where we have highlighted the areas of interest. **Figure 2.54** shows the inner walls of the cylinder block on which the pressure acts, generating other axial thrusts.

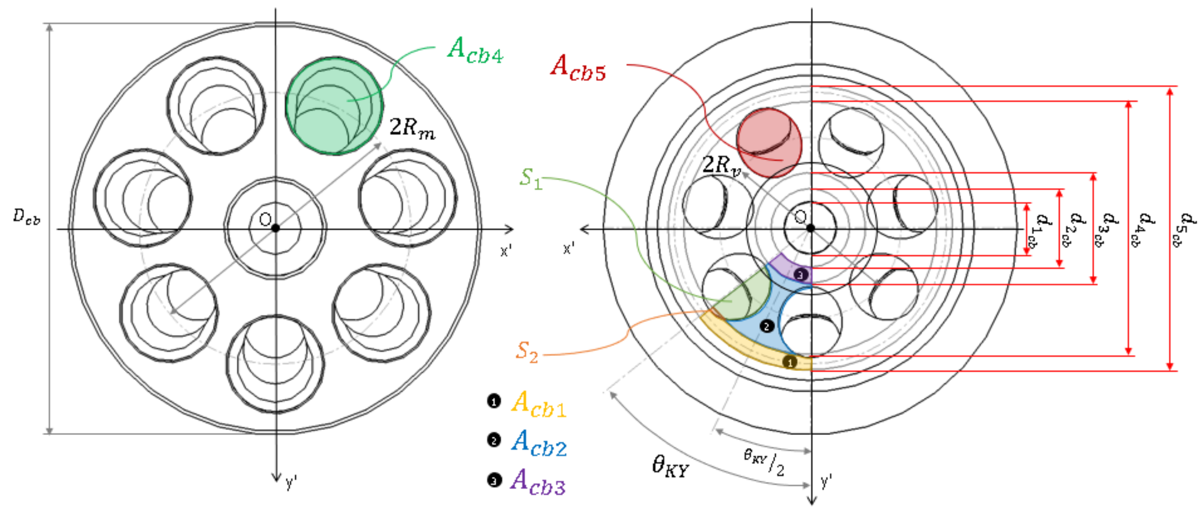

Figure 2.53: Pressure areas on the front and rear surfaces of the cylinder block

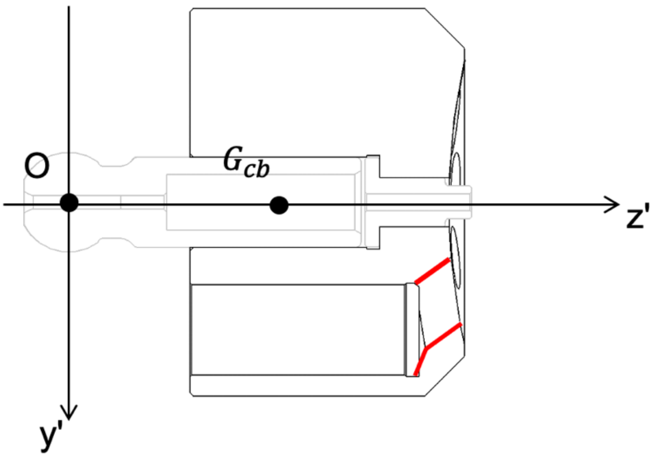

Figure 2.54: Inner pressure areas of the cylinder block inlet/outlet bores (y'z' plane)

We can identify the following areas considering the rear part of the cylinder block between two adjacent inlet/outlet bores (**Figure 2.53**):

- external area A_{cb1}: considering a linear pressure trend within the gap, we can assume a mean pressure between casing pressure and the average value of the two adjacent chambers as acting on this area.
- area A_{cb2}: considering a linear pressure trend within the gap, we can assume a mean pressure between the two adjacent chambers as acting on this area.
- internal area A_{cb3}: considering a linear pressure trend within the gap, we can assume a mean pressure between casing pressure and the average value of the two adjacent chambers as acting on this area.

Note that the sealing diameters $d_{1_{cb}}$, $d_{2_{cb}}$, $d_{3_{cb}}$, $d_{4_{cb}}$ and $d_{5_{cb}}$ of the valve plate define these areas of interest.

Figure 2.55 depicts the area concerning the calculation of the cylinder block inner thrust (**Figure 2.54**). The pressure acts on the red areas of **Figure 2.55**, while we considered the exceeding green areas just to simplify the area evaluation. It is, in fact, easier to consider the circle ($A_{cb,4}$) and ellipse ($A_{cb,5}$) areas instead of calculating the analytical expression of the red areas with complex geometries. The green area thrust contributions, in fact, will compensate each other when if consider their sum.

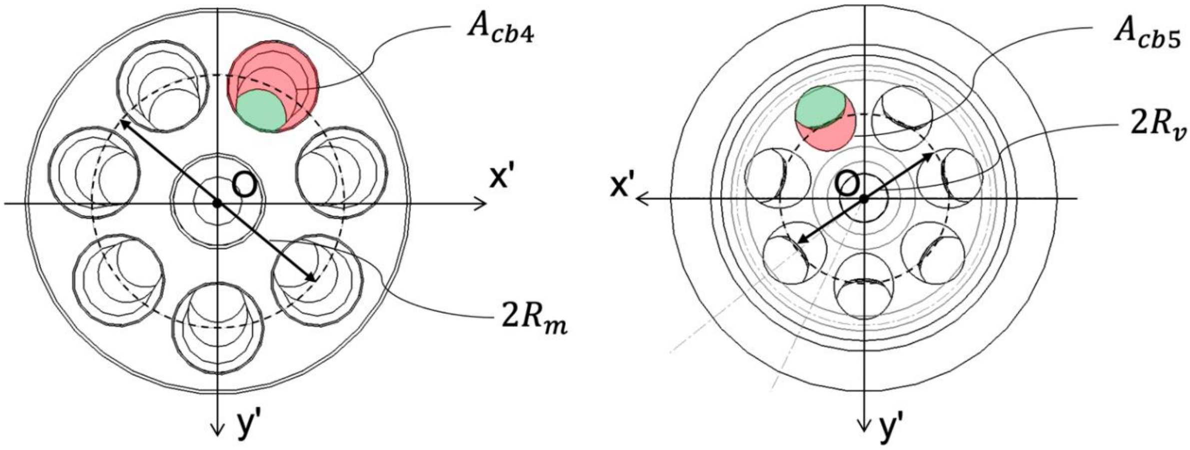

Figure 2.55: Inner thrusting areas within the i-th inlet/outlet bore (x'z' plane)

We are reporting below the analytic evaluation of these areas of interest.

- Area A_{cb4}

This is the circle area with diameter D_{pi} whose analytical expression is given in **Eq. (2.130)**.

$$A_{cb4} = \frac{\pi}{4} \cdot D_{pi}^2 \tag{2.130}$$

- Area A_{cb5}

This is an ellipse area given by $\pi \cdot (L_1/2) \cdot (L_2/2)$, where L_1 and L_2 are the two ellipse axes.

Figure 2.56 shows a side view of the $y'z'$ section of the cylinder block. We have highlighted a temporary reference frame $O_S x_S y_S$, showing also the diameter (D_{cyl}) of the cylindrical milling cutter used to realize the inclined inlet/outlet channels.

The ellipse minor axis is equal to the diameter D_{cyl}, regardless of the cutter inclination σ.

$$L_2 = D_{cyl} \tag{2.131}$$

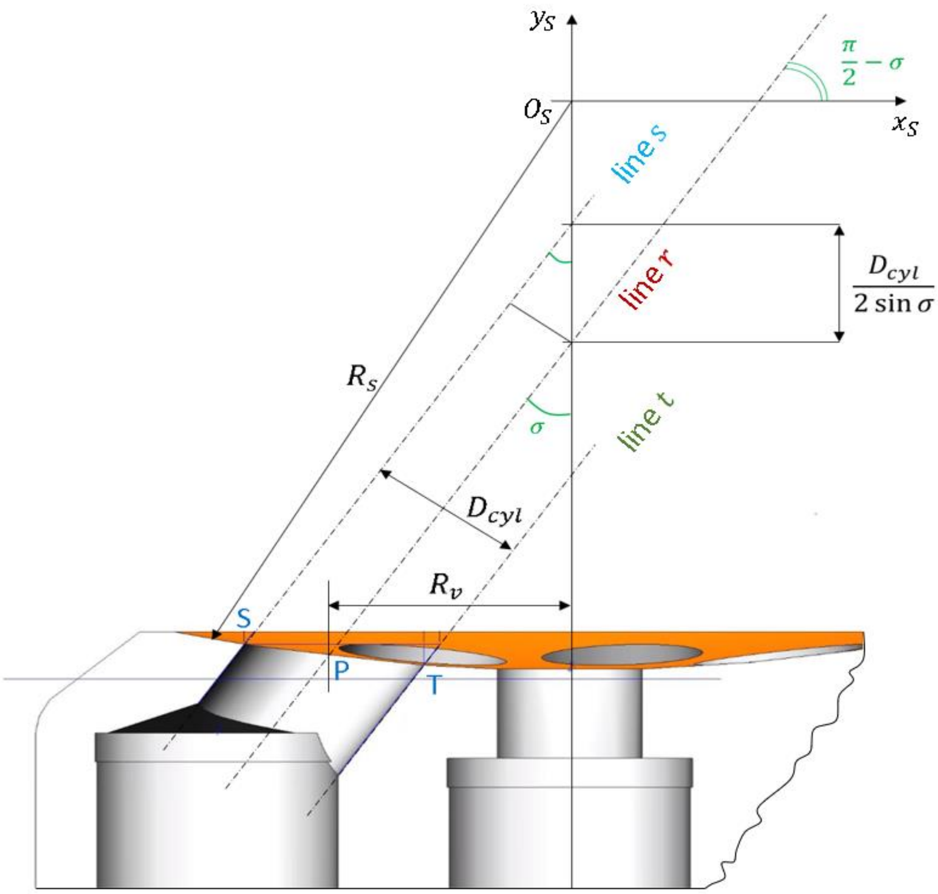

Figure 2.56: Schematic for the evaluation of A_{cb5} area

On the other hand, the ellipse major axis L_1 depends on the milling inclination σ. Always considering **Figure 2.56**, we are reporting below the steps necessary to evaluate L_1.

Equation of line r, i.e. line through point P with inclination $\left(\frac{\pi}{2} - \sigma\right)$:

$$y - y_P = \tan\left(\frac{\pi}{2} - \sigma\right) \cdot (x - x_P) \tag{2.132}$$

$$y = \tan\left(\frac{\pi}{2} - \sigma\right) \cdot x + R_v \cdot \tan\left(\frac{\pi}{2} - \sigma\right) - \sqrt{R_S^2 - R_v^2} \tag{2.133}$$

Equation of line s, parallel to r and through a known point, which has abscissa zero and ordinate that differs by $\frac{D_{cyl}}{2\, sin\sigma}$ from the line r correspondent point:

$$y = \tan\left(\frac{\pi}{2} - \sigma\right) \cdot x + R_v \cdot \tan\left(\frac{\pi}{2} - \sigma\right) - \sqrt{R_S^2 - R_v^2} + \frac{D_{cyl}}{2 \sin\sigma} \tag{2.134}$$

Equation of line t, parallel to r and through a known point, which has abscissa zero and ordinate that differs by $-\frac{D_{cyl}}{2\, sin\sigma}$ from the line r correspondent point:

$$y = \tan\left(\frac{\pi}{2} - \sigma\right) \cdot x + R_v \cdot \tan\left(\frac{\pi}{2} - \sigma\right) - \sqrt{R_S^2 - R_v^2} - \frac{D_{cyl}}{2 \sin\sigma} \tag{2.135}$$

Point S, i.e. the point of intersection between the circle of radius R_s and line s, obtained from the system given in **Eq. (2.136)**.

$$\begin{cases} y = \tan\left(\frac{\pi}{2} - \sigma\right) \cdot x + R_v \cdot \tan\left(\frac{\pi}{2} - \sigma\right) - \sqrt{R_S^2 - R_v^2} + \frac{D_{cyl}}{2 \sin\sigma} \\ x^2 + y^2 = R_S^2 \end{cases} \tag{2.136}$$

Eq. (2.137) reports the substitution of one equation into the other written as a second-degree equation $x^2 \cdot a_S + 2x \cdot b_S + c_S = 0$.

$$x^2\left(1 + \tan^2\left(\frac{\pi}{2} - \sigma\right)\right) + 2x\left(\tan\left(\frac{\pi}{2} - \sigma\right) \cdot \left(R_v \cdot \tan\left(\frac{\pi}{2} - \sigma\right) - \sqrt{R_S^2 - R_v^2} + \frac{D_{cyl}}{2 \sin\sigma}\right)\right) + \left(\left(R_v \cdot \tan\left(\frac{\pi}{2} - \sigma\right) - \sqrt{R_S^2 - R_v^2} + \frac{D_{cyl}}{2 \sin\sigma}\right)^2 - R_S^2\right) = 0 \tag{2.137}$$

Eq. (2.137) has two solutions, one negative and one positive. We must consider only the negative solution as the S abscissa is negative in the $O_S x_S y_S$ reference frame (**Figure 2.56**). **Eq. (2.138)** reports the equation solution.

$$x_S = \frac{-b_S - \sqrt{b_S^2 - a_S c_S}}{a_S} \tag{2.138}$$

where

$$a_S = \left(1 + \tan^2\left(\frac{\pi}{2} - \sigma\right)\right) \tag{2.139}$$

$$b_S = \left(\tan\left(\frac{\pi}{2} - \sigma\right) \cdot \left(R_v \cdot \tan\left(\frac{\pi}{2} - \sigma\right) - \sqrt{R_S^2 - R_v^2} + \frac{D_{cyl}}{2 \sin\sigma}\right)\right) \tag{2.140}$$

$$c_S = \left(\left(R_v \cdot \tan\left(\frac{\pi}{2} - \sigma\right) - \sqrt{R_S^2 - R_v^2} + \frac{D_{cyl}}{2 \sin\sigma}\right)^2 - R_S^2\right) \tag{2.141}$$

We used a similar procedure to evaluate the point of intersection T between the circle of radius R_s and line t (**Eq. (2.142)-(2.143)-(2.144)**).

$$\begin{cases} y = \tan\left(\frac{\pi}{2} - \sigma\right) \cdot x + R_v \cdot \tan\left(\frac{\pi}{2} - \sigma\right) - \sqrt{R_S^2 - R_v^2} - \frac{D_{cyl}}{2\sin\sigma} \\ x^2 + y^2 = R_S^2 \end{cases} \tag{2.142}$$

$$x^2\left(1 + \tan^2\left(\frac{\pi}{2} - \sigma\right)\right) + 2x\left(\tan\left(\frac{\pi}{2} - \sigma\right) \cdot \left(R_v \cdot \tan\left(\frac{\pi}{2} - \sigma\right) - \sqrt{R_S^2 - R_v^2} - \frac{D_{cyl}}{2\sin\sigma}\right)\right) + \left(\left(R_v \cdot \tan\left(\frac{\pi}{2} - \sigma\right) - \sqrt{R_S^2 - R_v^2} - \frac{D_{cyl}}{2\sin\sigma}\right)^2 - R_S^2\right) \tag{2.143}$$

$$x_T = \frac{-b_T - \sqrt{b_T^2 - a_T c_T}}{a_T} \tag{2.144}$$

The ellipse major axis of the ellipse can then be evaluated as the difference between the point T abscissa and the point S one, as shown in **Eq. (2.145)**.

$$L_1 = x_T - x_S \tag{2.145}$$

Eq. (2.146) therefore reports the evaluation of area A_{cb5}.

$$A_{cb5} = \pi \cdot \left(\frac{L_1}{2}\right) \cdot \left(\frac{L_2}{2}\right) \tag{2.146}$$

- Areas A_{cb1}, A_{cb2}, A_{cb3}

Figure 2.57 shows a front view of the cylinder block-valve plate interface where we have highlighted some areas of interest for the evaluation of A_{cb1}, A_{cb2} and A_{cb3}.

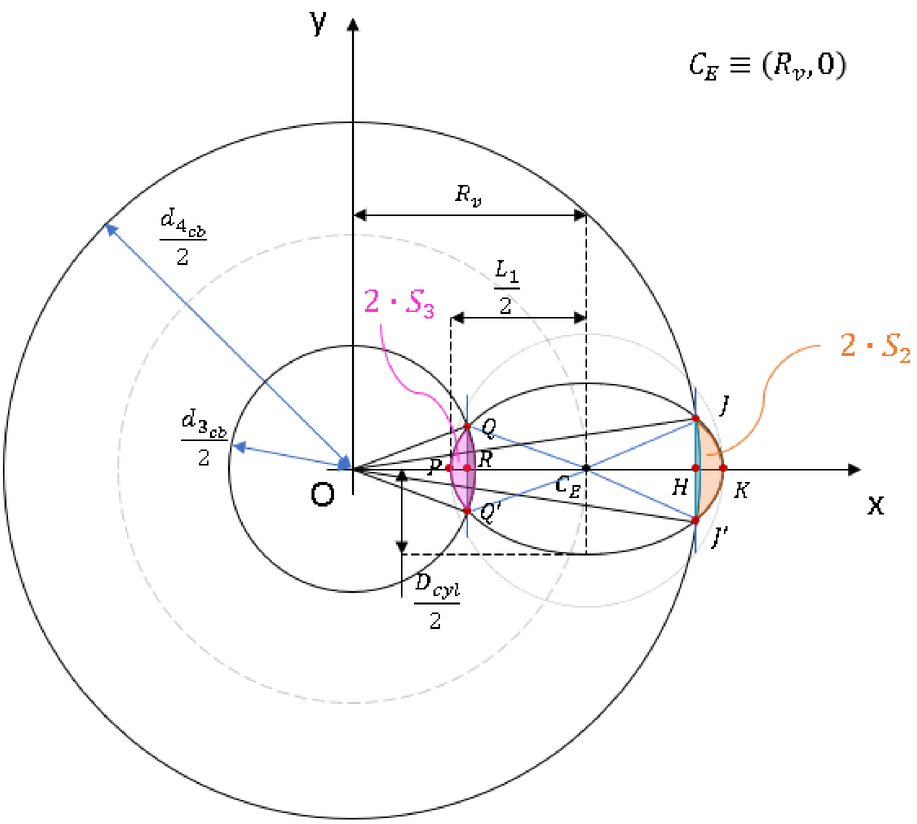

Figure 2.57: Schematic for the evaluation of areas S_2 and S_3

It is in fact necessary to first evaluate the areas S_2 and S_3 to proceed with the calculation of the areas A_{cb1}, A_{cb2}, A_{cb3}. Note that these areas are not always present (e.g. in **Figure 2.53** S_2 is present but S_3 is not). The presence of these areas, in fact, depends on the dimensions of the block inlet/outlet ports and valve plate sealing diameters. Considering **Figure 2.57**, area S_2 is present if the condition $\left(R_v + \left(\frac{L_1}{2}\right)\right) > \frac{D_{4cb}}{2}$ is verified, while area S_3 is present if the condition $\left(R_v - \left(\frac{L_1}{2}\right)\right) < \frac{D_{3cb}}{2}$ is verified.

We are now proceeding with the steps required to calculate S_2 and S_3, starting with S_2.

Eq. (2.147)-(2.148) report the equations of the circle of diameter $d_{4_{cb}}$ centred in O and the ellipse centred in $C_E \equiv (R_v,\ 0)$, obtained by considering the projection of the inclined inlet/outlet channel on the xy plane.

$$x^2 + y^2 = \left(\frac{d_{4cb}}{2}\right)^2 \tag{2.147}$$

$$\frac{(x-R_v)^2}{\left(\frac{L_1}{2}\right)^2} + \frac{y^2}{\left(\frac{D_{cyl}}{2}\right)^2} = 1 \tag{2.148}$$

We can consider only the upper semicircle (**Eq. (2.149)**) and the upper semi-ellipse (**Eq. (2.150)**).

$$y = +\sqrt{\frac{d_{4cb}^2}{4} - x^2} \tag{2.149}$$

$$y = +\frac{D_{cyl}}{2}\sqrt{1 - \frac{(x-R_v)^2}{\left(\frac{L_1}{2}\right)^2}} \tag{2.150}$$

Point J in **Figure 2.57** is the point of intersection between the upper semicircle and the upper semi-ellipse (**Eq. (2.151)-(2.152)-(2.153)**).

$$\begin{cases} y = +\sqrt{\frac{d_{4cb}^2}{4} - x^2} \\ y = +\frac{D_{cyl}}{2}\sqrt{1 - \frac{(x-R_v)^2}{\left(\frac{L_1}{2}\right)^2}} \end{cases} \tag{2.151}$$

$$\sqrt{\frac{d_{4cb}^2}{4} - x^2} = \frac{D_{cyl}}{2}\sqrt{1 - \frac{(x-R_v)^2}{\left(\frac{L_1}{2}\right)^2}} \tag{2.152}$$

$$x^2 \cdot \left(\frac{D_{cyl}^2}{L_1^2} - 1\right) + x \cdot \left(-2R_v \frac{D_{cyl}^2}{L_1^2}\right) + \left(\frac{d_{4cb}^2}{4} - \frac{D_{cyl}^2}{4} + R_v^2 \frac{D_{cyl}^2}{L_1^2}\right) = 0 \tag{2.153}$$

Note that we have written the second-degree equation in the unknown x in the form $x^2 \cdot a_J + 2x \cdot b_J + c_J = 0$. Considering only the feasible solution, **Eq. (2.154)-(2.155)** report the coordinates of point J.

$$x_J = \frac{-b_J - \sqrt{b_J^2 - a_J c_J}}{a_J} \tag{2.154}$$

$$y_J = +\sqrt{\frac{d_{4_{cb}}^2}{4} - x_J^2} \tag{2.155}$$

Once we have made these preliminary evaluations, it is possible to proceed with the calculation of S_2, reported in **Eq. (2.156)**, where $A_{segm\,ell\,JJ'H}$ is the area of the elliptical segment $JJ'H$ and $A_{segm\,circ\,JJ'H}$ is the area of the circular segment $JJ'H$.

$$S_2 = \frac{1}{2}\left(A_{segm\,ell\,JJ'H} - A_{segm\,circ\,JJ'H}\right) \tag{2.156}$$

Eq. (2.157)-(2.158) report the terms $A_{segm\,ell\,JJ'H}$ and $A_{segm\,circ\,JJ'H}$.

$$A_{segm\,ell\,JJ'H} = A_{sett\,ell\,C_EJJ'} - A_{tri\,C_EJJ'} \tag{2.157}$$

$$A_{segm\,circ\,JJ'H} = A_{sett\,circ\,OJJ'} - A_{tri\,OJJ'} \tag{2.158}$$

where

$$A_{sett\,ell\,C_EJJ'} = \frac{L_1}{L_2} \cdot acos\left(\frac{x_J - R_v}{\frac{L_1}{2}}\right) \cdot \frac{L_1^2}{4} \tag{2.159}$$

$$A_{triC_EJJ'} = y_J \cdot \left(x_J - R_v\right) \tag{2.160}$$

$$A_{sett\,circ\,OJJ'} = \frac{d_{4_{cb}}^2}{4} \cdot a\,tan\left(\frac{y_J}{x_J}\right) \tag{2.161}$$

$$A_{triOJJ'} = y_J \cdot x_J \tag{2.162}$$

Once we have evaluated these areas, it is possible to obtain the area S_2 using **Eq. (2.156)**.

The procedure for calculating the area S_3 is completely similar starting from the system formed by the equations of the upper semicircle of diameter $D_{3_{cb}}$ and the upper semi-ellipse to evaluate point Q.

Knowing the values of S_2 and S_3, **Eq. (2.163)-(2.164)-(2.165)** show the expressions of the areas of interest.

$$A_{cb1} = \frac{2\pi}{N_p} \cdot \frac{1}{2} \cdot \frac{1}{4}\left(d_{5_{cb}}^2 - d_{4_{cb}}^2\right) - 2 \cdot S_2 \tag{2.163}$$

$$A_{cb2} = \frac{2\pi}{N_p} \cdot \frac{1}{2} \cdot \frac{1}{4}\left(d_{4_{cb}}^2 - d_{3_{cb}}^2\right) - 2 \cdot S_1 = \frac{2\pi}{N_p} \cdot \frac{1}{2} \cdot \frac{1}{4}\left(d_{4_{cb}}^2 - d_{3_{cb}}^2\right) - \left(A_{cb5} - 2 \cdot S_2 - 2 \cdot S_3\right) \tag{2.164}$$

$$A_{cb3} = \frac{2\pi}{N_p} \cdot \frac{1}{2} \cdot \frac{1}{4}\left(d_{3_{cb}}^2 - d_{2_{cb}}^2\right) - 2 \cdot S_3 \tag{2.165}$$

- Area A_{cb6}

Considering **Figure 2.58**, we are now calculating area A_{cb6} (projection of the spherical cap on the $y'z'$ plane) to then evaluate the forces in the x' direction generated by the pressure distribution within the spherical gap. Note that we have assumed the forces in the y' direction to be zero for symmetry reasons.

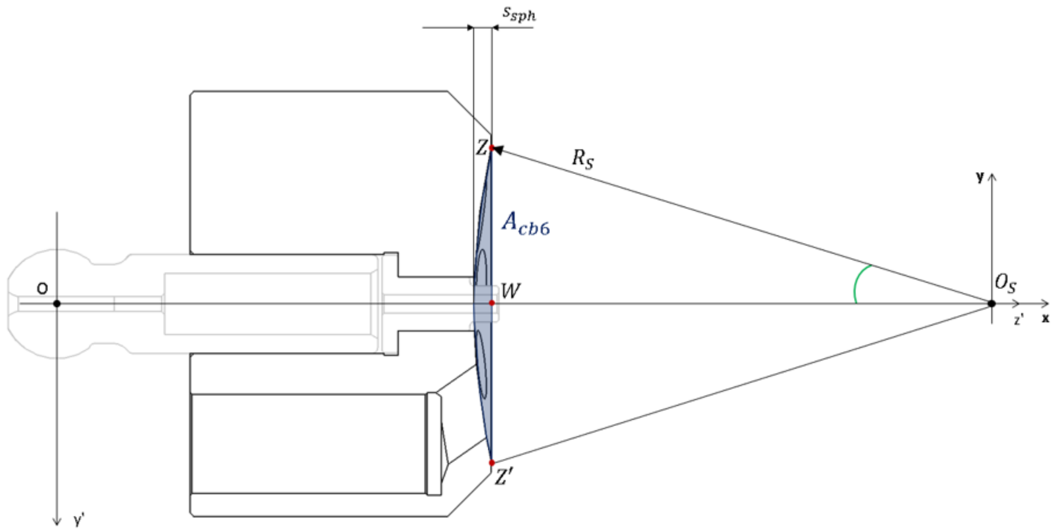

Figure 2.58: Projection on the the $y'z'$ plane of the spherical cap

Eq. (2.166) shows the calculation of the spherical cap thickness s_{sph} as a function of the quantities used for the cylinder block parameterization.

$$s_{sph} = L_{OM} + L_{cb} + R_S - O'O_S \tag{2.166}$$

Eq. (2.167) reports the equation of the circle of radius R_S centred in O_S.

$$x^2 + y^2 = R_S^2 \tag{2.167}$$

Eq. (2.168)-(2.169) then gives the coordinates of point Z, obtained from the system formed by this circle and the end surface line of the cylinder block.

$$x_Z = -R_S + s_{sph} \tag{2.168}$$

$$y_Z = \sqrt{R_S^2 — R_S + s_{sph} 2} \tag{2.169}$$

Area A_{cb6} is then the difference between the area of the circular sector $ZZ'O_S$ and the area of the triangle $ZZ'O_S$, as given in **Eq. (2.170)**.

$$A_{cb6} = A_{sett\ circ_{ZZ'O_S}} - A_{tri_{ZZ'O_S}} \tag{2.170}$$

where

$$A_{sett\ circ_{ZZ'O_S}} = \tan^{-1}\left(\left|\frac{y_Z}{x_Z}\right|\right) \cdot R_S^2 \tag{2.171}$$

$$A_{tri_{ZZ'O_S}} = y_Z \cdot |x_Z| \tag{2.172}$$

Having completed the evaluation of the reported areas, we can also identify the area contributions on which the casing pressure acts in the front and rear surface of the block as the difference between the total area and the areas already calculated (**Figure 2.59**).

$$A_{case\ rear} = \frac{\pi}{4}D_{cb}^2 - \frac{\pi}{4}{d_1}_{cb}^2 - N_p\frac{\pi}{4}D_{pi}^2 \tag{2.173}$$

$$A_{case\ front} = \frac{\pi}{4}\cdot\left[\left({D_{cb}}^2 - {d_{5cb}}^2\right) + \left({d_{2cb}}^2 - {d_{1cb}}^2\right)\right] \tag{2.174}$$

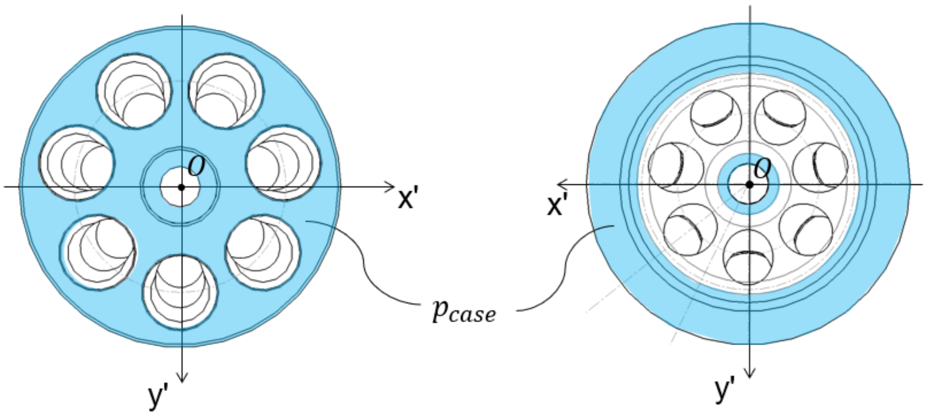

Figure 2.59: Front and rear surface areas where the casing pressure acts

It is now possible to proceed with the calculation of the hydrostatic pressure forces acting on these areas. As anticipated in the assumptions, the logarithmic pressure trend in the annular gap was not considered. We instead considered a mean pressure defined by the boundary conditions for the considered area.

We derived the pressure forces exploiting the following expressions.

$$F_{press_{Acb1,i_{z'}}} = -\frac{p_{case}+\frac{p_{ch,i}+p_{ch,i+1}}{2}}{2}\cdot A_{cb1} \tag{2.175}$$

$$F_{press_{Acb2,i_{z'}}} = -\frac{p_{ch,i}+p_{ch,i+1}}{2}\cdot A_{cb2} \tag{2.176}$$

$$F_{press_{Acb3,i_{z'}}} = -\frac{p_{case}+\frac{p_{ch,i}+p_{ch,i+1}}{2}}{2}\cdot A_{cb3} \tag{2.177}$$

$$F_{press_{Acb4,i_{z'}}} = p_{ch,i}\cdot A_{cb4} \tag{2.178}$$

$$F_{press_{Acb5,i_{z'}}} = -p_{ch,i}\cdot A_{cb5} \tag{2.179}$$

$$F_{press_{Acb6_{x'A}}} = \frac{p_{case}+p_A}{2}\cdot A_{cb6} \tag{2.180}$$

$$F_{press_{Acb6_{x'B}}} = -\frac{p_{case}+p_B}{2}\cdot A_{cb6} \tag{2.181}$$

$$F_{cb_{press_{casefront_{z'}}}} = -p_{case}\cdot A_{cb_{casefront}} \tag{2.182}$$

$$F_{cb_{press_{caserear_{z'}}}} = p_{case}\cdot A_{cb_{caserear}} \tag{2.183}$$

Subscripts A and B in **Eq. (2.180)-(2.181)** refer to the machine inlet and outlet ports. The thrust forces along x' are two, opposite to each other. We have considered an average pressure acting on the areas A_{cb6} for simplicity, instead of considering the projection of the different pressure areas on the $y'z'$ plane.

We decided to group some of these forces together in order to make the writing of the subsequent equations more compact. In particular, we considered the hydrostatic force $F_{cb_{hydro_{z'}}}$ as the contributions that tend to move the block away from the distributor plate shown in **Eq. (2.184)**.

$$F_{cb_{hydro_{z'}}} = F_{press_{Acb1_{z'}}} + F_{press_{Acb2_{z'}}} + F_{press_{Ac31_{z'}}} \tag{2.184}$$

The subscripts i are not present in **Eq. (2.184)** because we have considered all the forces relating to all the surface portions between two consecutive holes.

It is then necessary to know the position of all the *i*-forces to evaluate the position of the total hydrostatic force. For this purpose, we considered the angle $\frac{\theta_{ky}}{2}$ (θ_{ky} is the angular step between two consecutive inlet/outlet channels, i.e. $2\pi/n_P$) between the y' axis and the symmetry axis of areas A_{cb1}, A_{cb2} and A_{cb3} (**Figure 2.60**). **Eq. (2.185)-(2.186)-(2.187)** report the points of application of the forces $F_{press_{Acb1_{z'}}}$, $F_{press_{Acb2_{z'}}}$ and $F_{press_{Ac31_{z'}}}$.

$$F_{press_{Acb1,i_{z'}}}: \begin{cases} x'_{press_{Acb1,i}} = -\left(\frac{d_{cb4}}{2} + \frac{d_{cb5}-d_{cb4}}{4}\right)\sin\left(\vartheta_i - \frac{\theta_{ky}}{2}\right) \\ y'_{press_{Acb1,i}} = \left(\frac{d_{cb4}}{2} + \frac{d_{cb5}-d_{cb4}}{4}\right)\cos\left(\vartheta_i - \frac{\theta_{ky}}{2}\right) \end{cases} \tag{2.185}$$

$$F_{press_{Acb2,i_{z'}}}: \begin{cases} x'_{press_{Acb2,i}} = -R_V \cdot \sin\left(\vartheta_i - \frac{\theta_{ky}}{2}\right) \\ y'_{press_{Acb2,i}} = R_V \cdot \cos\left(\vartheta_i - \frac{\theta_{ky}}{2}\right) \end{cases} \tag{2.186}$$

$$F_{press_{Acb3,i_{z'}}}: \begin{cases} x'_{press_{Acb2,i}} = -\left(\frac{d_{cb2}}{2} + \frac{d_{cb3}-d_{cb2}}{4}\right)\sin\left(\vartheta_i - \frac{\theta_{ky}}{2}\right) \\ y'_{press_{Acb2,i}} = \left(\frac{d_{cb2}}{2} + \frac{d_{cb3}-d_{cb2}}{4}\right)\cos\left(\vartheta_i - \frac{\theta_{ky}}{2}\right) \end{cases} \tag{2.187}$$

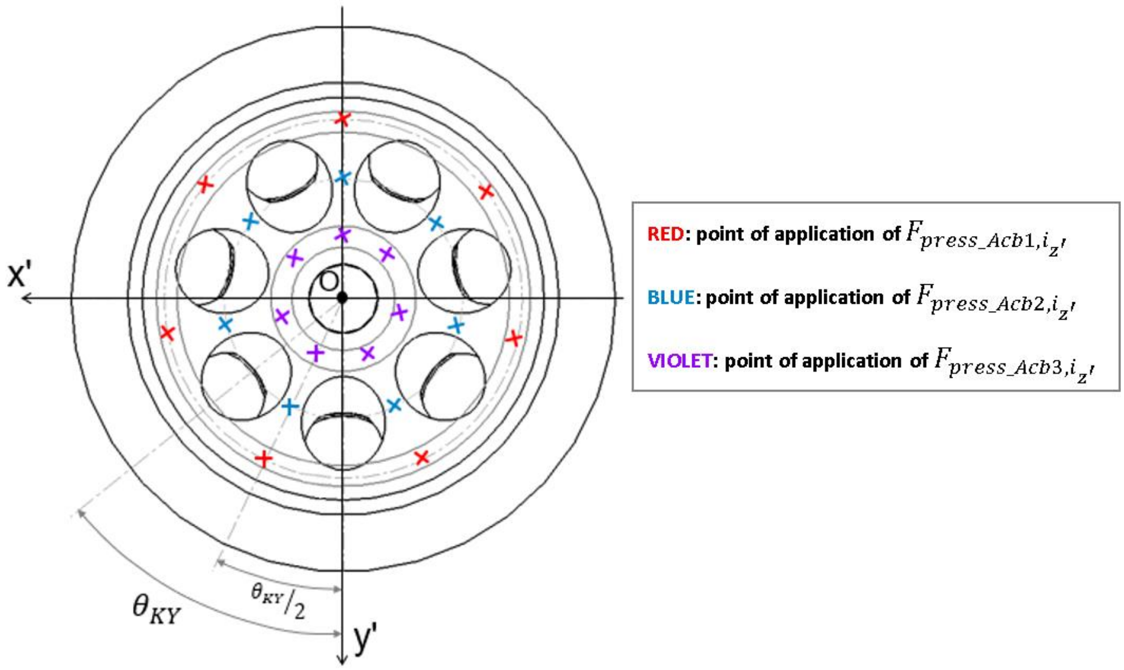

Figure 2.60: Points of application of $F_{press\_Acb1,i_{z'}}$, $F_{press\_Acb2,i_{z'}}$, $F_{press\_Acb3,i_{z'}}$

We considered the points of application of $F_{press_{Acb4,i_{z'}}}$ and $F_{press_{Acb5,i_{z'}}}$ as centred in the *i*-th chamber bore and inlet/outlet ellipse.

$$F_{press_{Acb4,i_{z'}}}:\begin{cases} x'_{press_{Acb4,i}} = -R_m \sin(\vartheta_i) \\ y'_{press_{Acb4,i}} = R_m \cos(\vartheta_i) \end{cases} \tag{2.188}$$

$$F_{press_{Acb5,i_{z'}}}:\begin{cases} x'_{press_{Acb5,i}} = -R_v \sin(\vartheta_i) \\ y'_{press_{Acb5,i}} = R_v \cos(\vartheta_i) \end{cases} \tag{2.189}$$

In addition to pushing the cylinder block towards or away from the valve plate, these pressure forces generate tilting moments for the block itself as the pressure distribution is not symmetrical. The cylinder block then tends to rotate around its x' and y' axes.

We have reported below the evaluation of these tilting contributions referring to the convention shown in **Figure 2.61**.

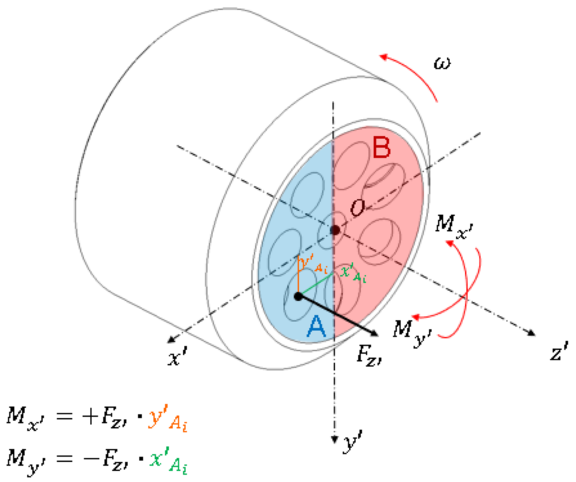

Figure 2.61: Cylinder block sectors A and B for the evaluation of tilting moments

Eq. (2.190)-(2.195) report these tilting moment contributions caused by the pressure acting on areas A_{cb1}, A_{cb2} and A_{cb3}.

$$M_{Acb1,i_{y'}} = -F_{press_{Acb1,i_{z'}}} \cdot x'_{press_{Acb1,i}} \tag{2.190}$$

$$M_{Acb2,i_{y'}} = -F_{press_{Acb2,i_{z'}}} \cdot x'_{press_{Acb2,i}} \tag{2.191}$$

$$M_{Acb3,i_{y'}} = -F_{press_{Acb3,i_{z'}}} \cdot x'_{press_{Acb3,i}} \tag{2.192}$$

$$M_{Acb1,i_{x'}} = F_{press_{Acb1,i_{z'}}} \cdot y'_{press_{Acb1,i}} \tag{2.193}$$

$$M_{Acb2,i_{x'}} = F_{press_{Acb2,i_{z'}}} \cdot y'_{press_{Acb2,i}} \tag{2.194}$$

$$M_{Acb3,i_{x'}} = F_{press_{Acb3,i_{z'}}} \cdot y'_{press_{Acb3,i}} \tag{2.195}$$

These contributions can be added together to find the total tilting moment given by the forces that tend to move the block away from the valve plate (or against it).

$$M_{press_{y'_{tot}}} = \sum_i \left(M_{Acb1,i_{y'}} + M_{Acb2,i_{y'}} + M_{Acb3,i_{y'}} \right) \tag{2.196}$$

$$M_{press_{x'tot}} = \sum_i \left(M_{Acb1,i_{x'}} + M_{Acb2,i_{x'}} + M_{Acb3,i_{x'}} \right) \tag{2.197}$$

Similarly, **Eq. (2.198)-(2.201)** give the tilting contributions given by the forces acting on A_{cb4} and A_{cb5}, which can be grouped as shown in **Eq. (2.202)-(2.203)**.

$$M_{Acb4,i_{y'}} = -F_{press_{Acb4,i_{z'}}} \cdot x'_{press_{Acb4,i}} \tag{2.198}$$

$$M_{Acb5,i_{y'}} = -F_{press_{Acb5,i_{z'}}} \cdot x'_{press_{Acb5,i}} \tag{2.199}$$

$$M_{Acb4,i_{x'}} = F_{press_{Acb4,i_{z'}}} \cdot y'_{press_{Acb4,i}} \tag{2.200}$$

$$M_{Acb5,i_{x'}} = F_{press_{Acb5,i_{z'}}} \cdot y'_{press_{Acb5,i}} \tag{2.201}$$

$$M_{push_{y'tot}} = \sum_i \left(M_{Acb4,i_{y'}} + M_{Acb5,i_{y'}} \right) \tag{2.202}$$

$$M_{push_{x'tot}} = \sum_i \left(M_{Acb4,i_{x'}} + M_{Acb5,i_{x'}} \right) \tag{2.203}$$

These moments tend to tilt the cylinder block around the x' and y' axes in one direction or the other depending on their sign.

Still considering **Figure 2.61**, we decided to separate the resultant of these pressure forces according to the position of the individual contributions. We, in fact, divided the resulting force into F_{press_A} and F_{press_B} depending on whether the considered contribution is in sector A or B of the cylinder block. We must introduce a check on the sign of the x' coordinate of the individual contributions to make this distinction. A contribution will be added to F_{press_A} if x' is greater than zero, otherwise it will be added to F_{press_B}.

Similarly, we divided the tilting moments into $M_{press_{A_x}}$, $M_{press_{B_x}}$, $M_{press_{A_y}}$ and $M_{press_{B_y}}$.

The position of the hydrostatic force $F_{cb_{hydro_{z'}}}$ (defined by **Eq. (2.184)**) can be evaluated exploiting the Varignon's theorem, which states that the torque of a resultant of two or more concurrent forces about any point is equal to the algebraic sum of the torques of its components about the same point.

$$M_{tot} = M_1 + \cdots + M_n \tag{2.204}$$

$$R \cdot b = F_1 \cdot b_1 + \cdots + F_n \cdot b_n \tag{2.205}$$

It is then possible to obtain the point of application of the resultant force knowing the magnitude and points of application of the single contributions. Using this approach, **Eq. (2.206)-(2.207)** give the coordinates of the point of application of $F_{cb_{hydro_{z'}}}$, called H_1.

$$\overline{OH_1}|_{x'} = -\frac{M_{press_{y'tot}}}{F_{cb_{hydro_{z'}}}} \tag{2.206}$$

$$\overline{OH_1}|_{y'} = \frac{M_{press_{x'tot}}}{F_{cb_{hydro_{z'}}}} \tag{2.207}$$

Note that we have inserted a minus sign in **Eq. (2.206)** to comply with the convention introduced in **Figure 2.61**.

The z′ coordinate of the point H_1,, $\overline{OH_1}|_{z'}$, can be obtained considering the equation of the sphere with centre $C(0,0,\overline{OO_S})$ and radius $\rho = \overline{O_S K}$ (**Figure 2.63**). This point H_1, in fact, necessarily lies on the spherical cap interface between the cylinder block and the valve plate.

$$\overline{OH_1}|_{x'}{}^2 + \overline{OH_1}|_{y'}{}^2 + \overline{OH_1}|_{z'}{}^2 - 2\cdot\overline{OO_S}\cdot\overline{OH_1}|_{z'} + \overline{OO_S}^2 = \overline{O_S K}^2 \tag{2.208}$$

Solving **Eq. (2.208)** as a second-degree equation in the single unknown $\overline{OH_1}|_{z'}$, we could obtain **Eq. (2.209)**. Note that we selected the only feasible solution of the second-degree equation.

$$\overline{OH_1}|_{z'} = \frac{-(-2\cdot\overline{OO_S}) - 2\cdot\overline{OO_S}}{} 2 - 4\cdot\left(\overline{OO_S}^2 + \overline{OH_1}|_{x'}{}^2 + \overline{OH_1}|_{y'}{}^2 - \overline{O_S K}^2\right)2 \tag{2.209}$$

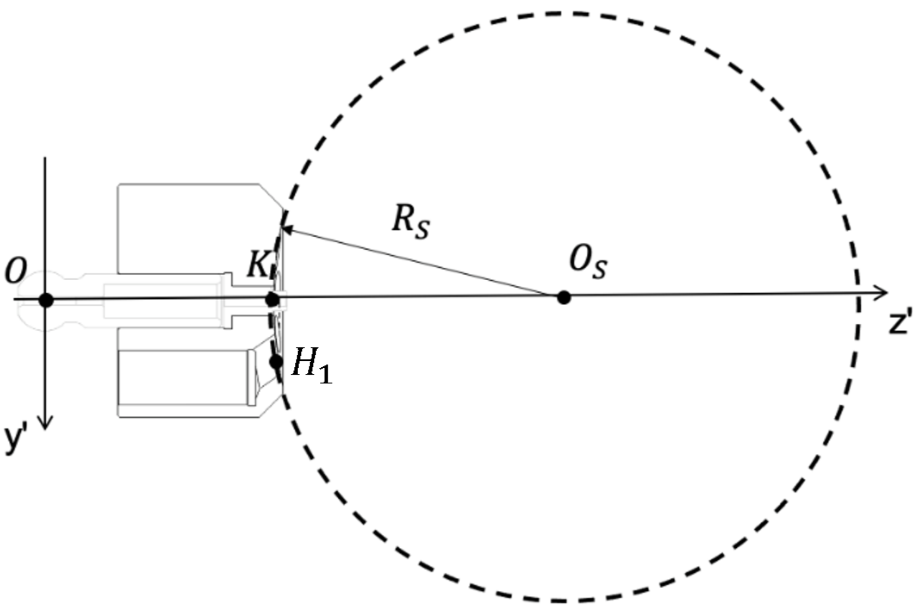

Figure 2.63: Planar ($y'z'$) representation of the sphere of radius R_s

Shaft reaction forces. The forces that the shaft exerts on the cylinder block-central pivot system are among the unknowns of the submodel.

$$F_{(sh-cb)_{x'}} = -F_{(cb-sh)_{x'}} \tag{2.210}$$

$$F_{(sh-cb)_{y'}} = -F_{(cb-sh)_{y'}} \tag{2.211}$$

However, the reaction along z' is known, as it is given by the elastic force of the spring inside the centre pivot itself. During the machine assembly, the central spring is compressed to pushe the cylinder block against the valve plate and, at the same time, the central pin against the shaft flange.

$$F_{(sh-cb)_{z'}} = -F_{(cb-sh)_{z'}} = -k_{spring}\left(l_{2_{spring}} - l_{0_{spring}}\right) \tag{2.212}$$

Piston reaction forces and moments. The forces that the cylinder block exerts on the pistons are known from the resolution of the pistons modelling. By inverting the sign of these reactions, it is therefore possible to derive the forces that the pistons exert on the cylinder block, as shown in **Eq. (2.213)-(2.215)**.

$$F_{(pi-cb),i_{x'}} = -F_{(cb-pi),i_{x'}} \tag{2.213}$$

$$F_{(pi-cb),i_{y'}} = -F_{(cb-pi,i),i_{y'}} \tag{2.214}$$

$$F_{(pi-cb),i_{fr_{z'}}} = -F_{(cb-pi),i_{fr_{z'}}} \tag{2.215}$$

These forces also generate moments on the cylinder block which can be evaluated as reported in the following relationships.

$$M_{F_{(pi-cb),i_{z'}}} = F_{(pi-cb),i_{y'}} \cdot x'_{Bi} - F_{(pi-cb),i_{x'}} \cdot y'_{Bi} \tag{2.216}$$

$$M_{F_{(pi-cb),i_{y'}}} = F_{(pi-cb),i_{x'}} \cdot z'_{Bi} \tag{2.217}$$

$$M_{F_{(pi-cb),i_{x'}}} = F_{(pi-cb),i_{y'}} \cdot z'_{Bi} \tag{2.218}$$

$$M_{F_{(pi-cb),i_{fr_{y'}}}} = F_{(pi-cb),i_{fr_{z'}}} \cdot x'_{Bi} \tag{2.219}$$

$$M_{F_{(pi-cb),i_{fr_{x'}}}} = F_{(pi-cb),i_{fr_{z'}}} \cdot y'_{Bi} \tag{2.220}$$

Guide pin reaction forces. The reaction forces exchanged between the cylinder block and the guide pin connected to the valve plate are unknowns of the system. We have then simply kept these contributions as unknown terms in the equilibrium equations.

$$F_{(gp-cb)_{x'}} = -F_{(cb-gp)_{x'}} \tag{2.221}$$

$$F_{(gp-cb)_{y'}} = -F_{(cb-gp)_{y'}} \tag{2.222}$$

Viscous friction moment between cylinder block and valve plate. The relative rotation between the cylinder block and the valve plate generates a viscous friction moment due to the presence of spherical leakage gap. For simplicity's sake, we divided this friction moment into different contributions, according to different zones of interest.

Eq. (2.223) reports the sum of the different contributions which can be individuated in **Figure 2.64**.

$$\begin{aligned} M_{visc_{(vp-cb)}} = {} & M_{(vp-cb)_{1pAB}} + M_{(vp-cb)_{2pAB}} + M_{(vp-cb)_{1pA}} + M_{(vp-cb)_{2pA}} + M_{(vp-cb)_{1pB}} \\ & + M_{(vp-cb)_{2pB}} \end{aligned} \tag{2.223}$$

In particular, we have identified the following interface zones:

- zone $1pAB$: zone between the end of the port B kidney and the beginning of the port A kidney,
- zone $2pAB$: zone between the end of the port A kidney and the beginning of the port B kidney,
- zone $1pA$: outer semi annulus of port A defined by $d_{4_{cb}}$ e $d_{5_{cb}}$,
- zone $2pA$: inner semi annulus of port A defined by $d_{1_{cb}}$ e $d_{2_{cb}}$,
- zone $1pB$: outer semi annulus of port A defined by $d_{4_{cb}}$ e $d_{5_{cb}}$,

- zone $2pB$: inner semi annulus of port A defined by $d_{1_{cb}}$ e $d_{2_{cb}}$.

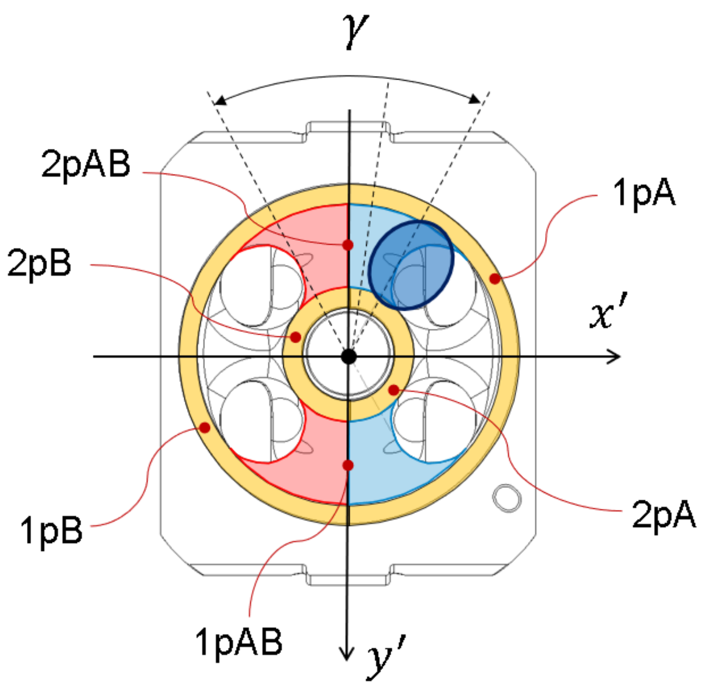

Figure 2.64: Areas of interest for the calculation of the viscous friction moment between cylinder block and valve plate

It is possible to start from the analytical expression of the friction moment generated in a circular recess pad, given in **Eq. (2.224)** [62], to evaluate the semi-annulus contributions.

$$M_{visc} = -\int_{R_1}^{R_2} (r\tau) \cdot 2\pi r \, dr \tag{2.224}$$

where

$$\tau = \frac{\mu \omega r}{h} \tag{2.225}$$

Eq. (2.226)-(2. 229) reports the expression of the individual semi-annulus contributions of interest, where we have considered π as angle and radius between $\frac{d_{4cb}}{2}$ and $\frac{d_{5cb}}{2}$ and between $\frac{d_{1cb}}{2}$ e $\frac{d_{2cb}}{2}$.

$$M_{(vp-cb)_{1pA}} = -\frac{\pi\mu\omega\cdot\left(d_{5_{cb}}^4 - d_{4_{cb}}^4\right)}{64 h_{cb-vp}} \tag{2.226}$$

$$M_{(vp-cb)_{2pA}} = -\frac{\pi\mu\omega\cdot\left(d_{3_{cb}}^4 - d_{2_{cb}}^4\right)}{64 h_{cb-vp}} \tag{2.227}$$

$$M_{(vp-cb)_{1pB}} = -\frac{\pi\mu\omega\cdot\left(d_{5_{cb}}^4 - d_{4_{cb}}^4\right)}{64 h_{cb-vp}} \tag{2.228}$$

$$M_{(vp-cb)_{2pB}} = -\frac{\pi\mu\omega\cdot\left(d_{3_{cb}}^4 - d_{2_{cb}}^4\right)}{64 h_{cb-vp}} \tag{2.229}$$

Note that the gap pressure does not appear directly in **Eq. (2.226)-(2.229)**. However, the viscosity μ for industrial oil is function of the fluid pressure. It is therefore necessary to consider the viscosity at the mean pressure between the boundary conditions in the various zones, i.e. between p_A and the casing pressure for $1pA$ and $2pA$ contributions, and the mean pressure between p_B and the casing pressure for $1pB$ and $2pB$ contributions.

On the other hand, $M_{(vp-cb)_{1pAB}}$ and $M_{(vp-cb)_{2pAB}}$ contributions are not constant since the relative sliding surface varies as the cylinder block angular position changes. We cannot consider the entire area between the two kidneys, as we must subtract the area of the inlet/outlet bores which are rotating with the cylinder block.

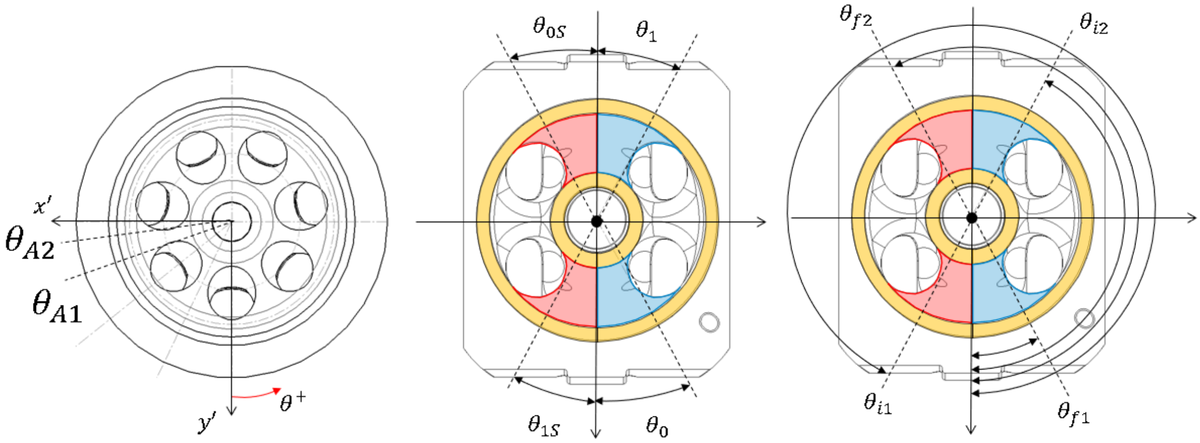

Figure 2.65: Schematic for the evaluation of the actual relative sliding surface between cylinder block and valve plate

We could divide the cases according to the angular position of the *i*-th inlet/outlet bore considering the angles introduced in **Figure 2.65**. In this way, it was possible to assess whether or not the space between two consecutive channels overlaps with the zone between kidneys. We could then calculate two equivalent angular sectors by summing each overlapping zone, one for the upper (σ_{2eff}) and one for the lower zone (σ_{1eff}) in **Figure 2.65**.

Eq. (2.230)-(2.32) reports these last contributions of friction moment once we have evaluated these equivalent angles.

$$M_{(vp-cb)_{1pAB}} = -\frac{\sigma_{1eff}\mu\omega \cdot \left(d_{4_{cb}}^4 - d_{3_{cb}}^4\right)}{64h_{cb-vp}} \tag{2.230}$$

$$M_{(vp-cb)_{1pAB}} = -\frac{\sigma_{1eff}\mu\omega \cdot \left(d_{4_{cb}}^4 - d_{3_{cb}}^4\right)}{64h_{cb-vp}} \tag{2.231}$$

<u>**Cylinder block churning losses.**</u> The rotation of the cylinder block in the casing oil generates a viscous friction moment which must be subtracted (or added considering a pump) from the moment available at the machine shaft. **Eq. (2.232)** express this churning losses torque obtained by integrating the velocity profile within the gap between the casing and the block itself, as illustrated in **Figure 2.66**.

$$M_{cbcase_{cl_{z'}}} = 2\pi \cdot L_{cb} \cdot \mu \cdot \omega \cdot \left(\frac{D_{cb}}{2}\right)^2 \cdot \left(\frac{\frac{D_{cb}}{2}+h_{cbcase}}{h_{cbcase}}\right)^2 \cdot \ln\left(1 - \frac{h_{cbcase}}{\frac{D_{cb}}{2}+h_{cbcase}}\right) \tag{2.232}$$

where we have considered a linear velocity profile $v = \omega R_B\left(\frac{R_B+t-r}{t}\right)$.

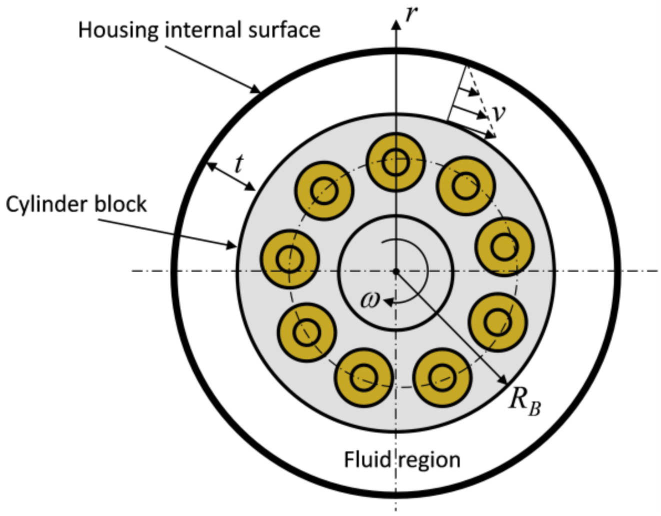

Figure 2.66: Churning losses moment on the cylinder block [54]

Hydrodynamic/contact forces between cylinder block and valve plate. As anticipated in the analysis assumptions, we have merged together the hydrodynamic contributions generated within the leakage gap and the metal to metal contact forces. In this way it was possible to consider a single unknown term. It is, in fact, complex to evaluate the individual portions of these contributions without carrying out CFD analyses to assess the pressures and heights of the oil gaps.

These terms are unknowns for the cylinder block model. This unknow term consist in three non-zero components along the axes of the $Ox'y'z'$ reference frame since the interface between cylinder block and valve plate is a spherical cap.

$$\begin{gathered} F_{cb_{contact_{x'}}} \\ F_{cb_{contact_{y'}}} \\ F_{cb_{contact_{z'}}} \end{gathered} \tag{2.233}$$

The point of application of this force, called $H_2 \equiv (x_{H_2}, y_{H_2}, z_{H_2})$, is unknown too. However, we decided to report this force on the z' axis and consider the equivalent transport moments (**Eq. (2.234)**) as unknowns for the sake of convenience, as done by Roccatello and Nervegna [65] in their discussion for similar machines.

$$\begin{gathered} M_{cb_{contact_{x'}}} \\ M_{cb_{contact_{y'}}} \end{gathered} \tag{2.234}$$

These moments are, of course, function of the H_2 position, as given in **Eq. (2.235.)-(2.236)**.

$$M_{cb_{contact_{x'}}} = +F_{cb_{contact_{z'}}} \cdot \overline{OH_2}|_{y'} - F_{cb_{contact_{y'}}} \cdot \overline{OH_2}|_{z'} \tag{2.235}$$

$$M_{cb_{contact_{y'}}} = -F_{cb_{contact_{z'}}} \cdot \overline{OH_2}|_{x'} + F_{cb_{contact_{x'}}} \cdot \overline{OH_2}|_{z'} \tag{2.236}$$

In addition to these terms just introduced, there must be a balancing moment which ensure the cylinder block rotation at constant speed ω around the z' axis (as assumed at the beginning of the analysis).

$$M_{cb_{equil_{z'}}} \tag{2.237}$$

Free body diagrams

Figures 2.67-2.68-2.69 show the free body diagrams of the cylinder block including all the forces/moments acting on it along the three Cartesian directions of the rotating reference frame $Ox'y'z'$.

As we have done for the pistons model, these images were obtained from the CAD model of particular bent axis unit, but the analysis remains valuable also for the others.

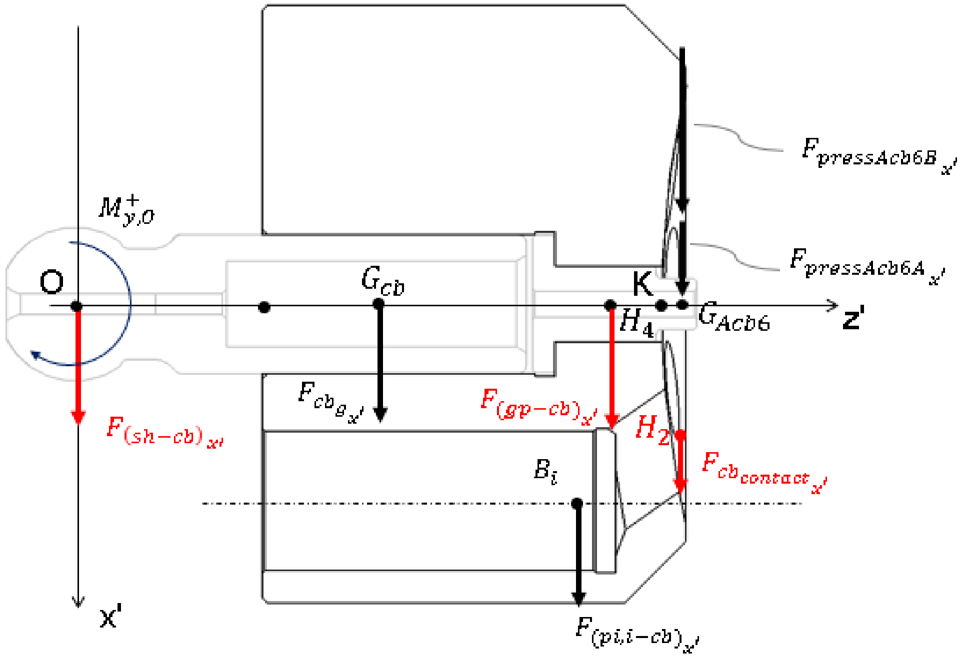

Figure 2.67: Free body diagram for the cylinder block forces along the x' axis

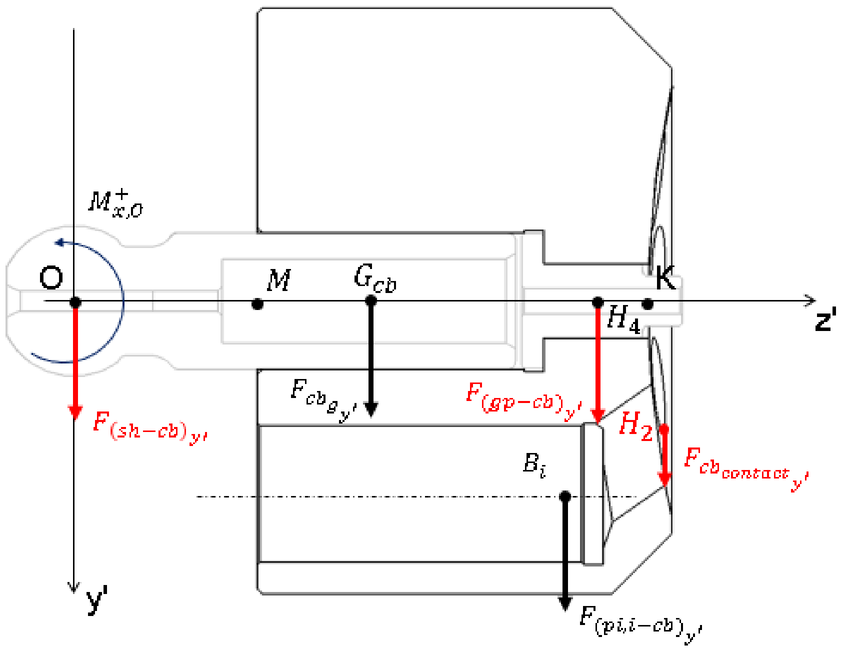

Figure 2.68: Free body diagram for the cylinder block forces along the y' axis

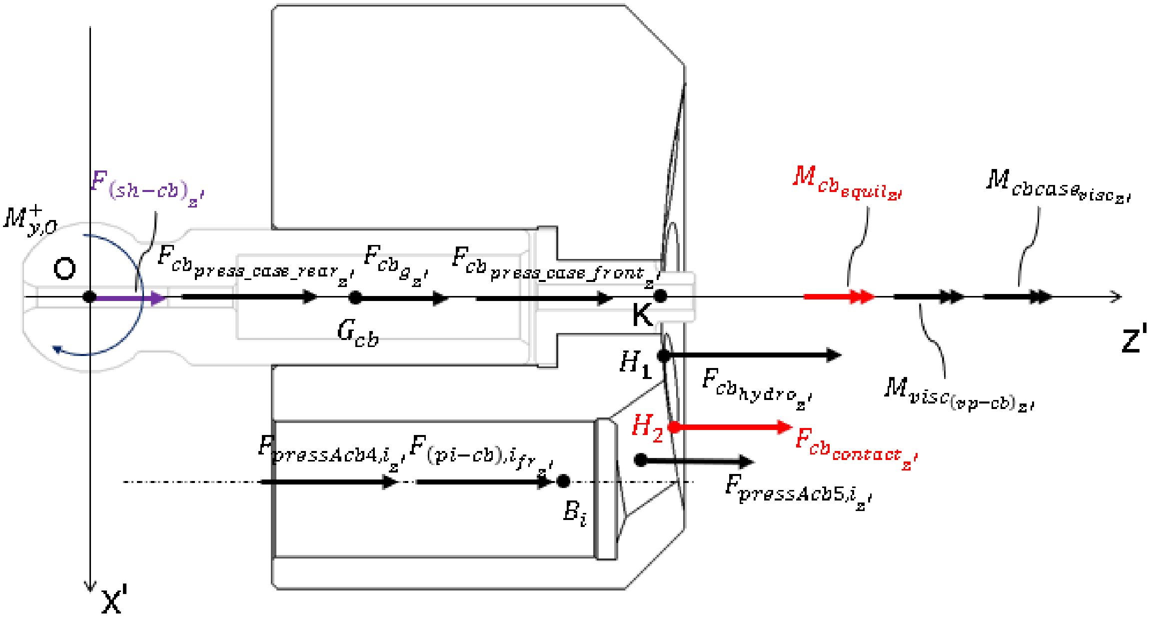

Figure 2.69: Free body diagram for the cylinder block forces along the z' axis

Table 2.17 shows the equilibrium equations developed for the cylinder block, written using the second law of motion ($\sum F = m \cdot a$ e $\sum M = I \cdot \alpha$).

Table 2.17: Equilibrium equations for the cylinder block

Translational equilibrium – x' axis	
$\sum_{i=1}^{N_p} F_{(pi-cb),i_{x'}} + F_{cb_{g_{x'}}} + F_{(gp-cb)_{x'}} + F_{cb_{contact_{x'}}} + F_{(sh-cb)_{x'}} + F_{pressAcb6A_{x'}} + F_{pressAcb6B_{x'}} = 0$	(2.238)
Translational equilibrium – y' axis	
$\sum_{i=1}^{N_p} F_{(pi-cb),i_{y'}} + F_{cb_{g_{y'}}} + F_{(gp-cb)_{y'}} + F_{cb_{contact_{y'}}} + F_{(sh-cb)_{y'}} = 0$	(2.239)
Translational equilibrium – z' axis	
$\sum_{i=1}^{N_p} F_{(pi-cb),i_{fr_{z'}}} + F_{cb_{g_{z'}}} + F_{pressAcb4_{z'}} + F_{pressAcb5_{z'}} + F_{(sh-cb)_{z'}} + F_{cb_{hydro_{z'}}} + F_{cb_{contact_{z'}}} + F_{cb_{press\_case\_rear_{z'}}} + F_{cb_{press\_case\_front_{z'}}} = 0$	(2.240)
Rotational equilibrium about $O - x'$ axis	
$-F_{cb_{g_{y'}}} \cdot \overline{OG_{cb}}\vert_{z'} - F_{(gp-cb)_{y'}} \cdot \overline{OH_4}\vert_{z'} - \sum_{i=1}^{N_p} F_{(pi-cb),i_{y'}} \cdot \overline{OB_\iota}\vert_{z'} + M_{press_{x'_{tot}}} + M_{push_{x'_{tot}}} + \sum_{i=1}^{N_p} F_{(pi-cb),i_{fr_{z'}}} \cdot \overline{OB_\iota}\vert_{y'} + M_{cb_{contact_{x'}}} = J_{cb,x'} \cdot \ddot{\beta} + c_{cb} \cdot \dot{\beta}$	(2.241)
Rotational equilibrium about $O - y'$ axis	
$F_{cb_x} \cdot \overline{OG_{cb}}\vert_{z'} + F_{(gp-cb)_{x'}} \cdot \overline{OH_4}\vert_{z'} + \sum_{i=1}^{N_p} F_{(pi-cb),i_{x'}} \cdot \overline{OB_\iota}\vert_{z'} + \left(F_{pressAcb6A_{x'}} + F_{pressAcb6B_{x'}}\right) \cdot \overline{OG_{Acb6}}\vert_{z'} + M_{press_{y'_{tot}}} + M_{push_{y'_{tot}}} - \sum_{i=1}^{N_p} F_{(pi-cb),i_{fr_{z'}}} \cdot \overline{OB_\iota}\vert_{x'} + M_{cb_{contact_{y'}}} = 0$	(2.242)
Rotational equilibrium about $O - z'$ axis	
$\sum_{i=1}^{N_p} F_{(pi-cb),i_{y'}} \cdot \overline{OB_\iota}\vert_{x'} - \sum_{i=1}^{N_p} F_{(pi-cb),i_{x'}} \cdot \overline{OB_\iota}\vert_{y'} + M_{cb_{equil_{z'}}} + M_{visc_{(vp-cb)}} + M_{cbcase_{cl_{z'}}} = 0$	(2.243)

Hypothesis for the system resolution

The system of equations reported in **Table 2.17** has 6 equations in 10 unknowns:

- $F_{(gp-cb)_{x'}}$
- $F_{cb_{contact_{x'}}}$
- $F_{(sh-cb)_{x'}}$
- $F_{(gp-cb)_{y'}}$
- $F_{cb_{contact_{y'}}}$
- $F_{cb_{contact_{z'}}}$
- $F_{(sh-cb)_{y'}}$
- $M_{cb_{contact_{x'}}}$ (which is function of $\overline{OH_2}|_{y'}$ and $\overline{OH_2}|_{z'}$)
- $M_{cb_{contact_{y'}}}$ (which is function of $\overline{OH_2}|_{x'}$ and $\overline{OH_2}|_{z'}$)
- $M_{cb_{equil_{z'}}}$

This is an underdetermined system with fewer equations than unknowns with thus ∞^4 solutions. It is therefore necessary to introduce some assumptions to obtain a determined system of n equations in n unknowns.

- **Hydrodynamic forces**

We assumed the contact point H_2 between cylinder block and valve plate not to lie to the spherical cap but to the plane shown in **Figure 2.70**.

This assumption is necessary not to include the equation of the sphere of radius R_s, which would introduce a nonlinearity in the system of equations. Note that the actual z' coordinate of point H_2 should not vary a lot since this point must lie on a spherical cap of huge radius. This leads to a reduced error by making the assumption mentioned above.

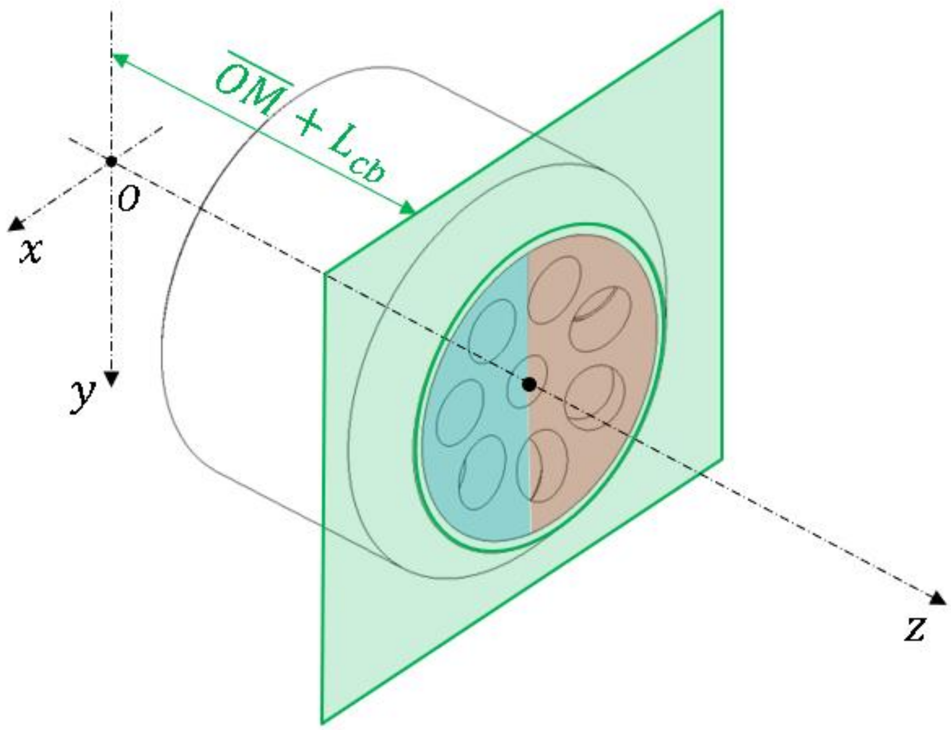

Figure 2.70: Plane on which the contact point between cylinder block and valve plate is assumed to lie

- **Guide pin reaction forces**

We assumed the reactions that the guide pin (connected to the valve plate) exerts on the cylinder block (and vice versa) to be zero. The reactions ensuring the equilibrium are therefore entirely attributed to the cylinder block-valve plate interface (hydrodynamic/contact forces).

We made this assumption based on an analysis concerning coupling tolerances between the components. Moreover, there are some unit designs that maintain the balancing even without including this guide pin.

- **Shaft reaction forces**

We assumed the reaction forces exerted by the shaft on the central pivot along the x' and y' axes to be zero (at first). However, we have left these reactions in the equilibrium equations as they could be reintroduced in specific cases we are describing in the following pages.

We have thus obtained a determined system of 6 equations in 6 unknows after considering these assumptions. The six remaining unknowns are:

- $F_{cb_{contact_{x'}}}$
- $F_{cb_{contact_{y'}}}$
- $F_{cb_{contact_{z'}}}$
- $M_{cb_{contact_{y'}}}$ (which is function of $\overline{OH_2}|_{x'}$)
- $M_{cb_{contact_{x'}}}$ (which is function of $\overline{OH_2}|_{y'}$)
- $M_{cb_{equil_{z'}}}$

Table 2.18 shows the simplified system of equations.

Table 2.18: Simplified equilibrium equations for the cylinder block

Translational equilibrium – x' axis	
$$\sum_{i=1}^{N_p} F_{(pi-cb),i_{x'}} + F_{cb_{g_{x'}}} + F_{cb_{contact_{x'}}} + F_{(sh-cb)_{x'}} + F_{pressAcb6A_{x'}} + F_{pressAcb6B_{x'}} = 0$$	(2.244)
Translational equilibrium – x' axis	
$$\sum_{i=1}^{N_p} F_{(pi-cb),i_{y'}} + F_{cb_{g_{y'}}} + F_{cb_{contact_{y'}}} + F_{(sh-cb)_{y'}} = 0$$	(2.245)
Translational equilibrium – x' axis	
$$\sum_{i=1}^{N_p} F_{(pi-cb),i_{fr_{z'}}} + F_{cb_{g_{z'}}} + F_{pressAcb4_{z'}} + F_{pressAcb5_{z'}} + F_{(sh-cb)_{z'}} + F_{cb_{hydro_{z'}}} + F_{cb_{contact_{z'}}} + F_{cb_{press\_case\_rear_{z'}}} + F_{cb_{press\_case\_front_{z'}}} = 0$$	(2.246)
Rotational equilibrium about $O - x'$ axis	
$$-F_{cb_{g_{y'}}} \cdot \overline{OG_{cb}}|_{z'} - \sum_{i=1}^{N_p} F_{(pi-cb),i_{y'}} \cdot \overline{OB_\iota}|_{z'} + M_{press_{x'_{tot}}} + M_{push_{x'_{tot}}} + \sum_{i=1}^{N_p} F_{(pi-cb),i_{fr_{z'}}} \cdot \overline{OB_\iota}|_{y'} + M_{cb_{contact_{x'}}} = J_{cb,x'} \cdot \ddot{\beta} + c_{cb} \cdot \dot{\beta}$$	(2.247)
Rotational equilibrium about $O - z'$ axis	
$$F_{cb_x} \cdot \overline{OG_{cb}}|_{z'} + \sum_{i=1}^{N_p} F_{(pi-cb),i_{x'}} \cdot \overline{OB_\iota}|_{z'} + \left(F_{pressAcb6A_{x'}} + F_{pressAcb6B_{x'}}\right) \cdot \overline{OG_{Acb6}}|_{z'} + M_{press_{y'_{tot}}} + M_{push_{y'_{tot}}} - \sum_{i=1}^{N_p} F_{(pi-cb),i_{fr_{z'}}} \cdot \overline{OB_\iota}|_{x'} + M_{cb_{contact_{y'}}} = 0$$	(2.248)

Rotational equilibrium about $O-z'$ axis	
$\sum_{i=1}^{N_p} F_{(pi-cb),i_{y'}} \cdot \overline{OB_i}\|_{x'} - \sum_{i=1}^{N_p} F_{(pi-cb),i_{x'}} \cdot \overline{OB_i}\|_{y'} + M_{cb_{equil_{z'}}} + M_{visc_{(vp-cb)}} + M_{cbcase_{cl_{z'}}} = 0$	(2.249)

We are reporting below the steps to solve this system of equation after making the simplifying assumptions.

After initially imposing the x' and y' shaft reactions equal to zero, we can evaluate the following unknowns from the three translational equilibrium and the rotational equilibrium around z':

- $F_{cb_{contact_{x'}}}$
- $F_{cb_{contact_{y'}}}$
- $F_{cb_{contact_{z'}}}$
- $M_{cb_{equil_{z'}}}$

It is thus possible to evaluate the remaining unknown by performing some substitutions in the fourth and fifth equations:

- $M_{cb_{contact_{x'}}}$
- $M_{cb_{contact_{y'}}}$

We can now derive the position of the point of application H_2 exploiting **Eq. (2.235)-(2.236)**. We can then obtain **Eq. (2.235)-(2.236)** considering the assumption $\overline{OH_2}|_{z'} = \text{const} = \overline{OM} + L_{cb}$.

$$\overline{OH_2}|_{y'} = \frac{1}{F_{cb_{contact_{z'}}}} \left(F_{cb_{contact_{y'}}} \cdot \overline{OH_2}|_{z'} + M_{cb_{contact_{x'}}} \right) \tag{2.250}$$

$$\overline{OH_2}|_{x'} = \frac{1}{F_{cb_{contact_{z'}}}} \left(F_{cb_{contact_{x'}}} \cdot \overline{OH_2}|_{z'} - M_{cb_{contact_{y'}}} \right) \tag{2.251}$$

However, the position of point H_2 calculated by the system may falls outside the real spherical interface cap between cylinder block and valve plate. Obviously, this contact point cannot be outside the real contact zone (spherical cap). We then decided to proceed as follows.

If the point H_2 is outside the boundary circumference of the spherical cap (also shown in **Figure 2.70**), this point will be brought back and saturated on the circumference itself to ensure a realistic contact. We can obtain the 'new' point of application $H_{2\,sat}$ by intersecting the circumference with the line through H_2 and the projection of O on the plane. **Figure 2.71** depicts the process just described.

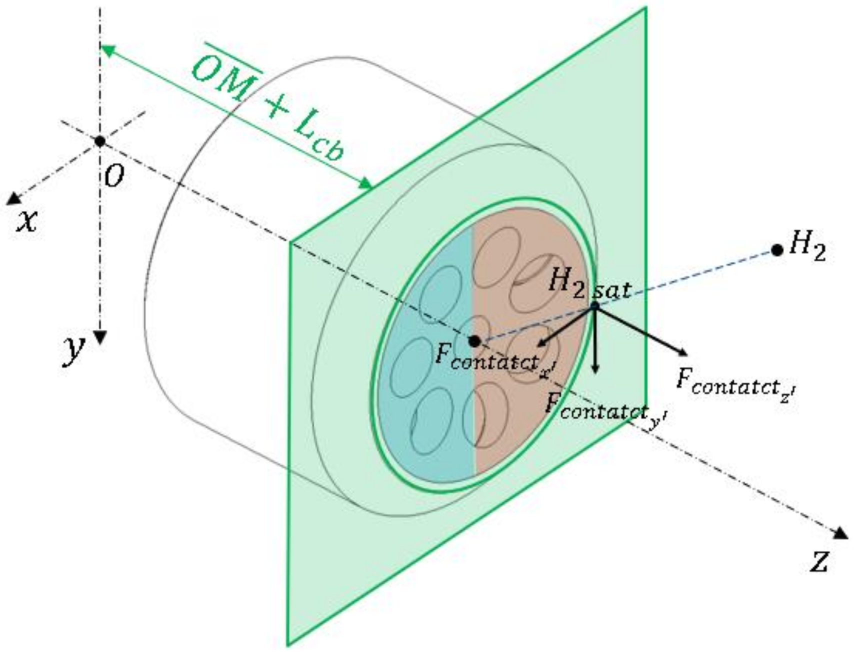

Figure 2.71: Saturation of point H_2 when out of the contact circle

If H_2 point is outside the contact boundary circumference ($\overline{OH_2}|_{x'}^2 + \overline{OH_2}|_{y'}^2 > R_{contact}^2$), we will then use the following system of equations to derive the saturated position at the edge of the contact zone.

$$\begin{cases} x'^2 + y'^2 = R_{contact}^2 \\ y' = \dfrac{\overline{OH_2}|_{y'}}{\overline{OH_2}|_{x'}} \cdot x \end{cases} \tag{2.252}$$

$$\begin{cases} x' = \operatorname{sign}(\overline{OH_2}|_{x'}) \cdot R_{contact} \cdot \sqrt{1 + \left(\dfrac{\overline{OH_2}|_{y'}}{\overline{OH_2}|_{x'}}\right)^2} = \overline{OH_2}|_{x'\,sat} \\ y' = \dfrac{\overline{OH_2}|_{y'}}{\overline{OH_2}|_{x'}} \cdot x' = \overline{OH_2}|_{y'\,sat} \end{cases} \tag{2.253}$$

Once we have derived the position of point $H_{2_{sat}}$ from **Eq. (2.253)**, we can recalculate the new contact forces along x' and y', which must change to balance the transport of the point of application from H_2 to $H_{2_{sat}}$ in order to maintain the rotational equilibrium.

$$F_{cb\,contact_{y'new}} = -\frac{1}{\overline{OH_2}|_{z'}}\left(M_{cb_{contact_{x'}}} - F_{cb_{contact_{z'}}} \cdot \overline{OH_2}|_{y'\,sat}\right) \tag{2.254}$$

$$F_{cb\,contact_{x'new}} = \frac{1}{\overline{OH_2}|_{z'}}\left(M_{cb_{contact_{y'}}} + F_{cb_{contact_{z'}}} \cdot \overline{OH_2}|_{x'\,sat}\right) \tag{2.255}$$

However, an imbalance has been introduced in the translational equilibrium equations having modified these terms with **Eq. (2.254)-(2.255)**. It is therefore necessary to reintroduce the shaft reactions on the central pivot-cylinder block system. These reactions are thus precisely the forces that realize the translational equilibrium along x' and y' when the point H_2 is outside the real contact zone.

Simcenter Amesim Submodel Editor® model

Once we have completed the mechanical analysis of the cylinder block, it is possible to proceed with the development of the corresponding Simcenter Amesim® submodel. We have thus defined the connection ports and the various inputs/outputs exchanged through these, the parameterization of the component, and the code to implement within it.

Figure 2.72 shows the representation of the Simcenter Amesim® icon concerning the cylinder block submodel BAUCBE000, while **Table 2.19** describes the variables associated with its ports.

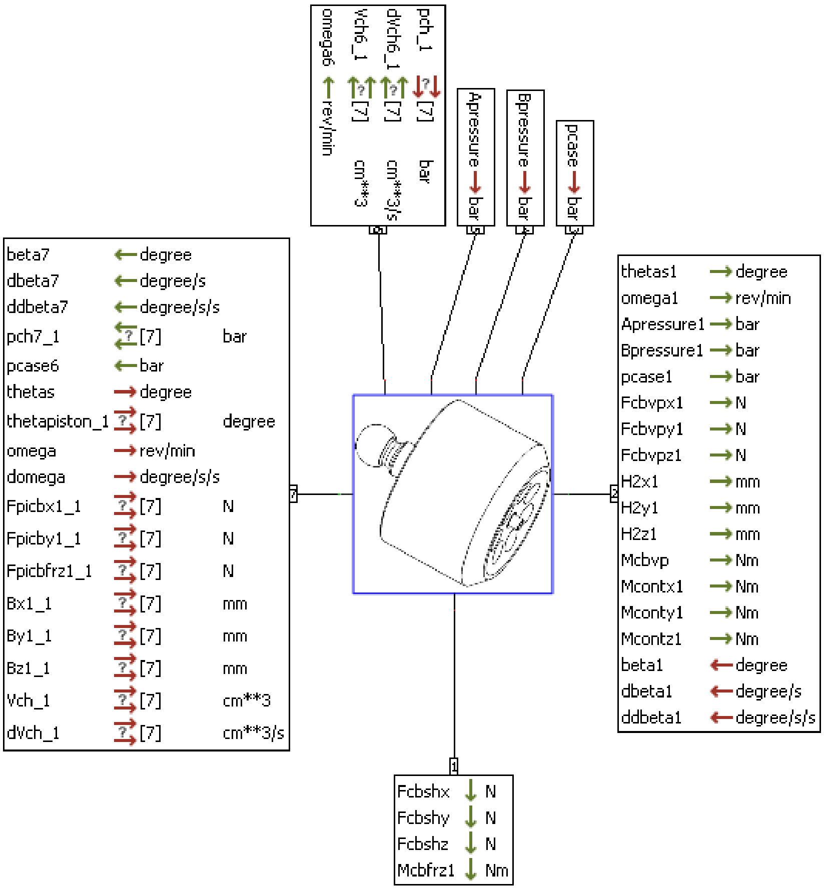

Figure 2.72: Icon of the pistons submodel developed in Simcenter Amesim®

Table 2.19: Inputs/outputs at each port of the cylinder block submodel developed in Simcenter Amesim®

PORT	VARIABLE	DESCRIPTION	SYMBOL	TYPE
1	Output	Cylinder block-shaft contact force – x axis	$F_{(cb-sh)_x}$	Scalar
		Cylinder block-shaft contact force – y axis	$F_{(cb-sh)_y}$	
		Cylinder block-shaft contact force – z axis	$F_{(cb-sh)_z}$	
		Cylinder block churning losses moment – z' axis	$M_{cb_{cl_{z'}}}$	
2	Input	Cylinder block inclination angle	β	Scalar
		Derivative of cylinder block inclination angle	$d\beta$	
		Second derivative of cylinder block inclination angle	$dd\beta$	
	Output	Duplicate of shaft angular position	ϑ_{as1}	Scalar
		Duplicate of shaft angular velocity	ω_1	
		Duplicate of port A pressure	p_{A1}	
		Duplicate of port B pressure	p_{B1}	
		Duplicate of casing pressure	p_{case1}	

		Cylinder block-valve plate mixed contact force – x' axis	$F_{cb_{cont_{x'}}}$	
		Cylinder block-valve plate mixed contact force – y' axis	$F_{cb_{cont_{y'}}}$	
		Cylinder block-valve plate mixed contact force – z' axis	$F_{cb_{cont_{z'}}}$	
		H_2 position – x' axis	x'_{H2}	
		H_2 position – y' axis	y'_{H2}	
		H_2 position – z' axis	z'_{H2}	
		Cylinder block-valve plate friction moment	M_{cbvp}	
		Moment of the mixed contact force between cylinder block and valve plate – x' axis	$M_{cb_{cont_{x'}}}$	
		Moment of the mixed contact force between cylinder block and valve plate – y' axis	$M_{cb_{cont_{y'}}}$	
		Moment of the mixed contact force between cylinder block and valve plate – z' axis	$M_{cb_{cont_{z'}}}$	
3	Input	Casing pressure	p_{case}	Scalar
4	Input	Port B pressure	p_A	Scalar
5	Input	Port A pressure	p_B	Scalar
6	Input	Piston chamber pressures	p_{ch}	Vector
	Output	Duplicate of shaft angular velocity	ω_6	Scalar
		Duplicate of piston chamber volumes	V_{ch6}	Vector
		Duplicate of derivative of piston chamber volumes	dV_{ch6}	
7	Input	Shaft angular position	ϑ_s	Scalar
		Piston angular positions	ϑ_{pist}	Vector
		Shaft angular velocity	ω	Scalar
		Shaft angular acceleration	$d\omega$	
		Piston-cylinder block contact force – x' axis	$F_{(pi,i-cb)_{x'}}$	Vector
		Piston-cylinder block contact force – y' axis	$F_{(pi,i-cb)_{y'}}$	
		Piston-cylinder block contact force – z' axis	$F_{(pi,i-cb),fr_{z'}}$	
		B_i position – x' axis	x'_{Bi}	
		B_i position – y' axis	y'_{Bi}	
		B_i position – z' axis	z'_{Bi}	
		Piston chamber volumes	V_{ch}	
		Derivative of piston chamber volumes	dV_{ch}	
	Output	Duplicate of cylinder block inclination angle	β	Scalar
		Duplicate of derivative of cylinder block inclination angle	$d\beta$	
		Duplicate of second derivative of cylinder block inclination angle	$dd\beta$	
		Duplicate of piston chamber pressures	p_{ch7}	Vector
		Duplicate of casing pressure	p_{case7}	Scalar

2.3.3 Valve plate model for fixed displacement

We are presenting in this sub-section the analysis relating to the valve plate for bent axis unit with fixed displacement. As mentioned, in fact, we have considered both a fixed-displacement and a variable-displacement valve plate to extend the model validity.

Figure 2.73 shows the valve plate for fixed displacement in the machine section.

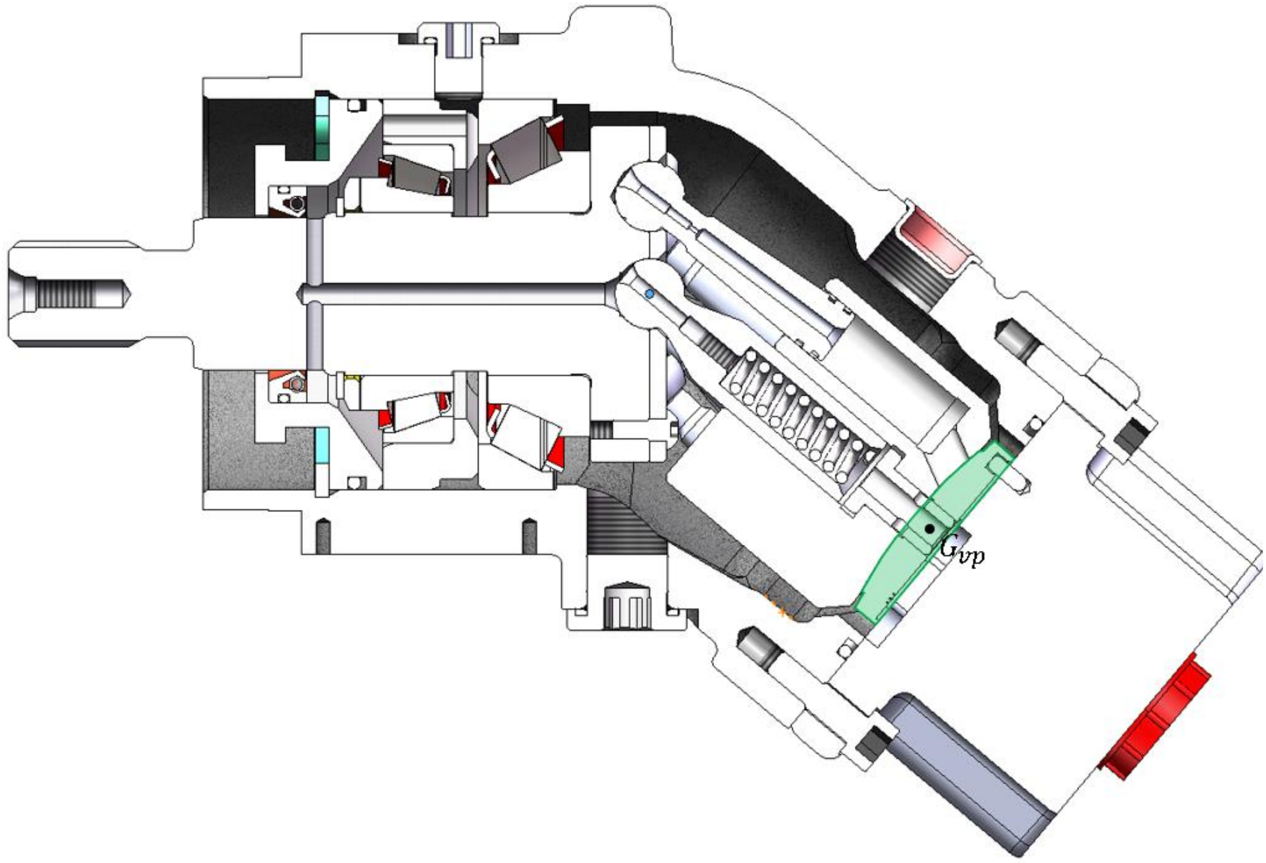

Figure 2.73: Valve plate for fixed displacement in the bent axis unit section

Before proceeding with the analysis and the free body diagram of the valve plate, we are reporting the assumptions we have considered in addition to those already introduced for the cylinder block-valve plate interface:

- the valve plate stiffness is considered infinite, i.e. no valve plate deformations,
- the pressure trend within the front and rear leakage gaps of the valve plate is considered linear and not logarithmic,
- the valve plate is considered fixed as the reactions with the machine cover must ensure its balancing.

The main outputs of the valve plate analysis are:

- the resultant reaction force exerted by the machine cover to maintain the valve plate static equilibrium, merging together the hydrodynamic and contact contributions,
- the position of the point of application of this reaction.

Considering the Dana Incorporated bent axis units, we identified two possible geometries for the fixed valve plate, which differ concerning the rear part. **Figure 2.74** shows the views of interest and the parametrization for the front part of the fixed valve plate and for the two different types of rear part.

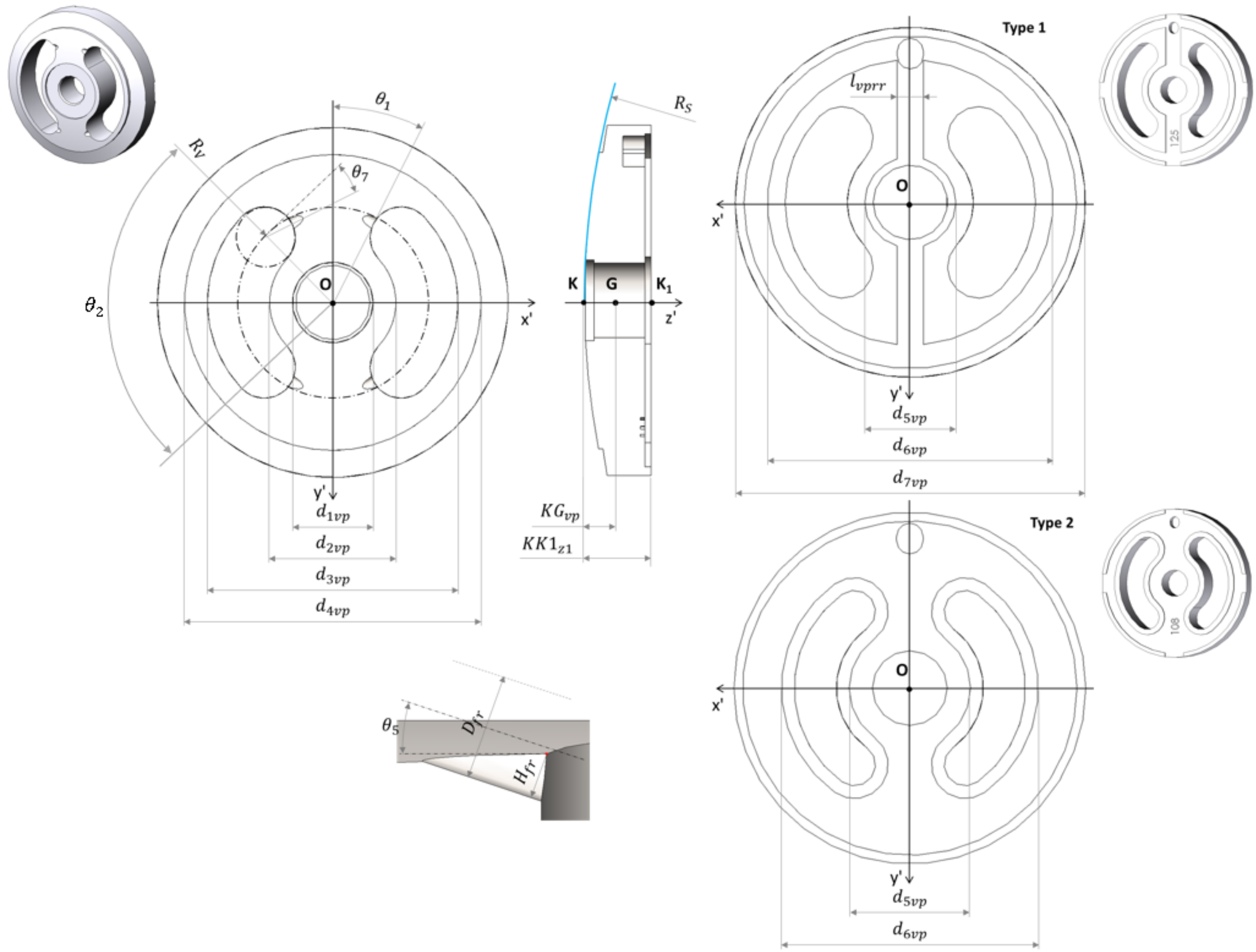

Figure 2.74: Parametrization for the two types of valve plate (Type 1 and Type 2) for fixed displacement

Figure 2.74 also shows a detail view for the parameterization of the opening and closing 'triangular' grooves at the kidney beginning and end. The model also allows the choice between grooves with triangular or parabolic geometry, which have a different parameterization.

Table 2.20 lists and describes the geometric and non-geometric quantities used for the valve plate parameterization and modelling.

Table 2.20: Parameters required for the fixed valve plate model

Symbol	Description
α_E	Euler angle α
β_E	Euler angle β
γ_E	Euler angle γ
R_s	Radius of curvature of valve plate sphere cap
R_v	Kidney mean radius
s_{asola}	Kidney width
θ_1	Kidney starting angular position
θ_2	Kidney angular extension
L_{OK}	Distance between O (reference frame centre) and K (valve plate front surface centre)
KK'_{z1}	Distance between K (valve plate front surface centre) and K' (valve plate rear surface centre)
$KG_{vp_{z1}}$	Distance between K (valve plate front surface centre) and G_{vp} (valve plate centre of mass)
m_{vp}	Valve plate mass
$d_{1_{vp}}$	Sealing diameter 1 between cylinder block and valve plate
$d_{2_{vp}}$	Sealing diameter 2 between cylinder block and valve plate

$d_{3_{vp}}$	Sealing diameter 3 between cylinder block and valve plate
$d_{4_{vp}}$	Sealing diameter 4 between cylinder block and valve plate
$d_{5_{vp}}$	Sealing diameter 5 between cylinder block and valve plate
$d_{6_{vp}}$	Sealing diameter 6 between cylinder block and valve plate
$d_{7_{vp}}$	Sealing diameter 7 between cylinder block and valve plate
θ_5	Groove angular inclination with respect to the horizontal plane
θ_7	Groove angular inclination with respect to R_v
D_{fr}	Diameter of the groove milling cutter
H_{fr}	Groove height
l_{vprr}	Distance between the two seals on the valve plate rear surface (Type 1)

As anticipated, we integrated within this submodel (and its variable displacement counterpart) the analysis for the analytic evaluation of the flow areas between valve plate and cylinder block carried out by the company before this activity. However, we are not reporting it because it was carried out before this activity and because it is merely a geometric analysis calculating the flow areas as function of the shaft angle.

We are now proceeding directly to the valve plate dynamic analysis as the the kinematic one is of no particular interest (the valve plate is considered fixed).

Dynamic analysis

Similarly to what we have done with the previous components, we can now move on with the introduction of all the known and unknown forces/moments acting on the valve plate.

Weight force. The weight force expressed in the $Ox'y'z'$ reference frame can be obtained by rotating the components of the weight force vector expressed in the fixed reference frame of the machine (assumed known) using the rotation matrix $R_{O\to O'}$ (**Eq. 2.44**). The point of application of this force is the centre of mass G_{vp} of the valve plate.

$$[F_{vpg_{Ox'y'z'}}] = R_{O\to O'}[F_{vpg_{BAU}}] \tag{2.256}$$

which translates into **Eq. (2.257)-(2.258)-(2.259)**.

$$F_{vpg_{x'}} = F_{vp\,g_x} \tag{2.257}$$

$$F_{vpg_{y'}} = F_{vpg_y} \cdot \cos\beta - F_{vp\,g_z} \cdot \sin\beta \tag{2.258}$$

$$F_{vpg_{z'}} = F_{vpg_y} \cdot \sin\beta + F_{vp\,g_z} \cdot \cos\beta \tag{2.259}$$

Pressure forces. It is first necessary to identify the different areas of interest on which a certain pressure acts to assess the different contributions of hydrostatic forces (analogous to the cylinder block). Again, we have made a distinction between the areas on which the full pressure acts (directly connected to ports A and B) and the areas on which an average pressure between the boundary conditions acts (since a linear pressure trend in the meatus has been assumed).

It is also necessary to identify the barycentres of these areas of interest to know the points of application of the pressure forces acting on these areas.

Figures 2.75-2.76 show the two types of fixed displacement valve plates, where we have highlighted the various areas of interest.

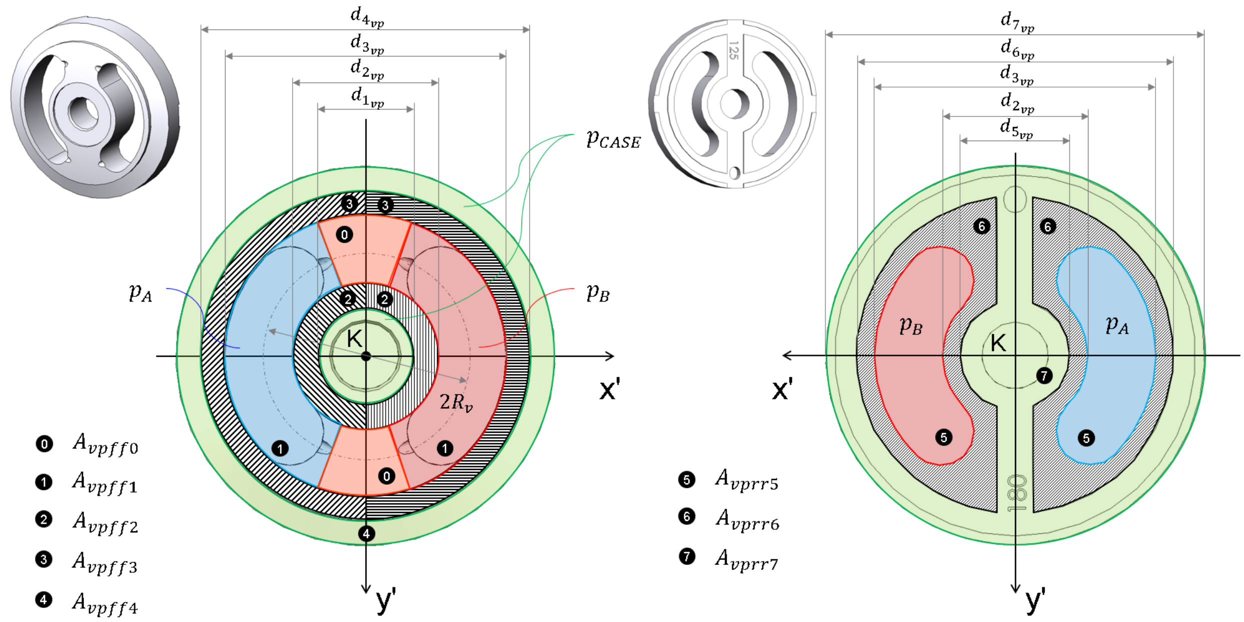

Figure 2.75: Areas of interest for the pressure forces calculation on fixed valve plate (Type 1)

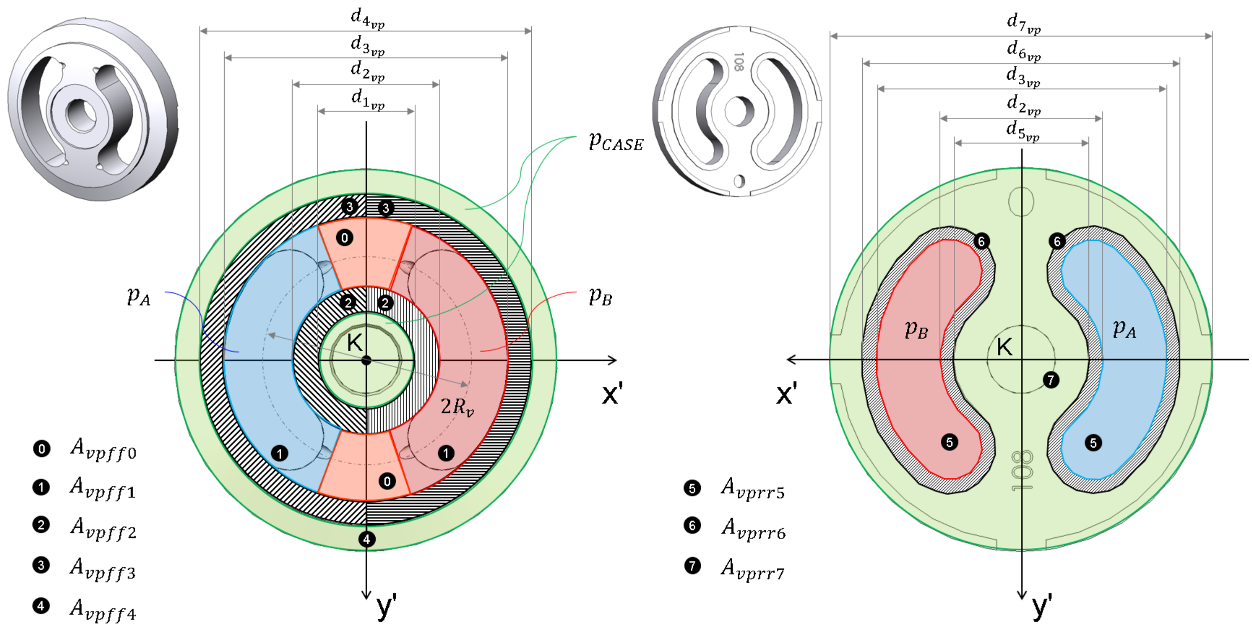

Figure 2.76: Areas of interest for the pressure forces calculation on fixed valve plate (Type 1)

Note that we are evaluating the kidney 'empty' surface (on which, of course, the pressure does not act) as the difference between A_{vpff_1} and A_{vpff_5}.

The following relationships express the various areas of interest for Type 1 fixed valve plate as a function of the parameters exploiting some known expressions for geometric area calculations.

$$A_{vpff0} = \frac{\pi}{180}\frac{\left(2\pi - \theta_{fbc_S} + \theta_{iba}\right)}{2}\frac{1}{4}\left(d_{3_{vp}}^2 - d_{2_{vp}}^2\right) \tag{2.260}$$

$$A_{vpff0_S} = \frac{\pi}{180}\frac{\left(\theta_{iba_S} - \theta_{fbc}\right)}{2}\frac{1}{4}\left(d_{3_{vp}}^2 - d_{2_{vp}}^2\right) \tag{2.261}$$

$$A_{vpff1} = \frac{\pi}{180}\frac{\left(\theta_{fbc} - \theta_{iba}\right)}{2}\frac{1}{4}\left({d_3}_{vp}^2 - {d_2}_{vp}^2\right) \tag{2.262}$$

$$A_{vpff1_S} = \frac{\pi}{180}\frac{\left(\theta_{fbc_S} - \theta_{iba_S}\right)}{2}\frac{1}{4}\left({d_3}_{vp}^2 - {d_2}_{vp}^2\right) \tag{2.263}$$

$$A_{vpff2} = \frac{1}{2}\cdot\frac{\pi}{4}\left(d_{2_{vp}}^2 - d_{1_{vp}}^2\right) \tag{2.264}$$

$$A_{vpff3} = \frac{1}{2}\cdot\frac{\pi}{4}\left(d_{4_{vp}}^2 - d_{3_{vp}}^2\right) \tag{2.265}$$

$$A_{vpff4} = \frac{\pi}{4}\cdot d_{7_{vp}}^2 - 2\left(A_{vpff2} + A_{vpff3}\right) - A_{vpff0} - A_{vpff0_S} - A_{vpff1} - A_{vpff1_S} \tag{2.266}$$

$$A_{vprr5} = \frac{\theta}{8}\left(d_{3_{vp}}^2 - d_{2_{vp}}^2\right) + \frac{\pi}{4}\left(\frac{d_{3_{vp}} - d_{2_{vp}}}{2}\right)^2 \tag{2.267}$$

$$A_{vprr6} = \frac{1}{2}\cdot\frac{1}{4}\left(d_{6_{vp}}^2 - d_{5_{vp}}^2\right) - \frac{1}{2}\left(d_{6_{vp}} - d_{5_{vp}}\right)\cdot l_{vp_{rr}} - A_{vprr5} \tag{2.268}$$

$$A_{vprr7} = \frac{\pi}{4}\cdot d_{7_{vp}}^2 - 2\left(A_{vpff5} + A_{vpff6}\right) \tag{2.269}$$

We are now reporting below the barycentre positions for all the pressure areas of interest.

Note that we have considered the two A_{vpff0} areas ('upper' and 'lower' in **Figure 2.75-2.76**) together so that their barycentre is positioned at the point K (since the pressure is the same on both A_{vpff0} areas). We have exploited the component symmetry and some geometric analytic expression to derive the following positions.

$$x_{ff0} = 0 \tag{2.270}$$

$$y_{ff0} = 0 \tag{2.271}$$

$$x_{ff1B} = \frac{2}{3}\cdot\frac{\sin\left(\theta_{fbc} - \theta_{iba}\right)}{\left(\theta_{fbc} - \theta_{iba}\right)}\cdot\frac{180}{\pi}\cdot\frac{\left(\frac{d_{3_{vp}}}{2}\right)^2 + \left(\frac{d_{2_{vp}}}{2}\right)^2 + \frac{d_{3_{vp}}}{2}\cdot\frac{d_{2_{vp}}}{2}}{\frac{d_{3_{vp}}}{2} + \frac{d_{2_{vp}}}{2}} \tag{2.272}$$

$$y_{ff1B} = 0 \tag{2.273}$$

$$x_{ff1A} = -\frac{2}{3}\cdot\frac{\sin\left(\theta_{fbc_S} - \theta_{iba_S}\right)}{\left(\theta_{fbc_S} - \theta_{iba_S}\right)}\cdot\frac{180}{\pi}\cdot\frac{\left(\frac{d_{3_{vp}}}{2}\right)^2 + \left(\frac{d_{2_{vp}}}{2}\right)^2 + \frac{d_{3_{vp}}}{2}\cdot\frac{d_{2_{vp}}}{2}}{\frac{d_{3_{vp}}}{2} + \frac{d_{2_{vp}}}{2}} \tag{2.274}$$

$$y_{ff1A} = 0 \tag{2.275}$$

$$x_{ff2B} = \frac{4}{3\pi}\frac{\left(\frac{d_{2_{vp}}}{2}\right)^2 + \left(\frac{d_{1_{vp}}}{2}\right)^2 + \frac{d_{2_{vp}}}{2}\cdot\frac{d_{1_{vp}}}{2}}{\frac{d_{2_{vp}}}{2} + \frac{d_{1_{vp}}}{2}} \tag{2.276}$$

$$y_{ff2B} = 0 \tag{2.277}$$

$$x_{ff2A} = -x_{A_{vpff2B}} \tag{2.278}$$

$$y_{ff2A} = 0 \tag{2.279}$$

$$x_{ff3B} = \frac{4}{3\pi}\frac{\left(\frac{d_{4_{vp}}}{2}\right)^2 + \left(\frac{d_{3_{vp}}}{2}\right)^2 + \frac{d_{4_{vp}}}{2}\cdot\frac{d_{3_{vp}}}{2}}{\frac{d_{4_{vp}}}{2} + \frac{d_{3_{vp}}}{2}} \tag{2.280}$$

$$y_{ff3B} = 0 \tag{2.281}$$

$$x_{ff3A} = -x_{A_{vpff3B}} \tag{2.282}$$

$$y_{ff3A} = 0 \tag{2.283}$$

$$x_{ff4} = 0 \tag{2.284}$$

$$y_{ff4} = 0 \tag{2.285}$$

$$x_{rr5B} = \frac{2}{3}\cdot\frac{\sin(\theta)}{(\theta)}\cdot\frac{180}{\pi}\cdot\frac{\left(\frac{d_{3_{vp}}}{2}\right)^2 + \left(\frac{d_{2_{vp}}}{2}\right)^2 + \frac{d_{3_{vp}}}{2}\cdot\frac{d_{2_{vp}}}{2}}{\frac{d_{3_{vp}}}{2} + \frac{d_{2_{vp}}}{2}} \tag{2.286}$$

$$y_{rr5B} = 0 \tag{2.287}$$

$$x_{rr5A} = -x_{rr5B} \tag{2.288}$$

$$y_{rr5A} = 0 \tag{2.289}$$

$$x_{rr6B} = 2\sin\left(\frac{\pi - 2\tan^{-1}\left(\frac{2\cdot l_{vp_{rr}}}{d_{6_{vp}} + d_{5_{vp}}}\right)}{2}\right) \cdot \frac{\left(d_{6_{vp}}^2 + d_{5_{vp}}^2 + d_{6_{vp}}\cdot d_{5_{vp}}\right)}{3\left(\pi - 2\tan^{-1}\left(\frac{2\cdot l_{vp_{rr}}}{d_{6_{vp}} + d_{5_{vp}}}\right)\right)\cdot\left(d_{6_{vp}} + d_{5_{vp}}\right)} \tag{2.290}$$

$$y_{rr6B} = 0 \tag{2.291}$$

$$x_{rr6A} = -x_{rr6B} \tag{2.292}$$

$$y_{rr6A} = 0 \tag{2.293}$$

$$x_{rr7} = 0 \tag{2.294}$$

$$y_{rr7} = 0 \tag{2.295}$$

Eq. (2.296)-(2.297)-(2.298) report the pressure area expressions concerning the rear surface of Type 2 fixed valve plate, which, as said, are different from Type 1.

$$A_{vpff5} = \frac{\theta}{8}\left(d_{3_{vp}}^2 - d_{2_{vp}}^2\right) + \frac{\pi}{4}\left(\frac{d_{3_{vp}} - d_{2_{vp}}}{2}\right)^2 \tag{2.296}$$

$$A_{vpff6} = \frac{\theta}{8}\left(d_{6_{vp}}^2 - d_{5_{vp}}^2\right) + \frac{\pi}{4}\left(\frac{d_{6_{vp}} - d_{5_{vp}}}{2}\right)^2 \tag{2.297}$$

$$A_{vpff7} = \frac{\pi}{4} \cdot d_{7_{vp}}^2 - 2\left(A_{vpff5} + A_{vpff6}\right) \tag{2.298}$$

Similarly, **Eq. (2.296)-(2.297)-(2.298)** show the expressions for the barycentres of the Type 2 rear areas. Note that we have only reported the position for A_{vpff6} as it is the only one that actually changes compared to Type 1.

$$x_{rr6B} = 2\sin\left(\frac{\theta_2 - \frac{d_{3_{vp}} - d_{2_{vp}}}{2R_v} + \frac{d_{6_{vp}} - d_{5_{vp}}}{2R_v}}{2}\right) \cdot \frac{\left(d_{6_{vp}}^2 + d_{5_{vp}}^2 + d_{6_{vp}} \cdot d_{5_{vp}}\right)}{3\left(\theta_2 - \frac{d_{3_{vp}} - d_{2_{vp}}}{2R_v} + \frac{d_{6_{vp}} - d_{5_{vp}}}{2R_v}\right) \cdot \left(d_{6_{vp}} + d_{5_{vp}}\right)} \tag{2.299}$$

$$y_{rr6B} = 0 \tag{2.300}$$

$$x_{rr6A} = -x_{rr6B} \tag{2.301}$$

$$y_{rr6A} = 0 \tag{2.302}$$

Once we have obtained all the areas of interest and their respective barycentres, it is possible to move on with the evaluation of the hydrostatic forces acting on the valve plate.

Eq. (2.303)-(2.311) report the hydrostatic force acting on the front surface of both the valve plate types (Type 1 and Type 2).

$$F_{ff0_A} = \frac{p_A + p_B}{2} \cdot A_{vpff0} \tag{2.303}$$

$$F_{ff0_B} = \frac{p_A + p_B}{2} \cdot A_{vpff0} \tag{2.304}$$

$$F_{ff1_A} = p_A \cdot A_{vpff1} \tag{2.305}$$

$$F_{ff1_B} = p_B \cdot A_{vpff1} \tag{2.306}$$

$$F_{ff2_A} = \frac{p_A + p_{case}}{2} \cdot A_{vpff2} \tag{2.307}$$

$$F_{ff2_B} = \frac{p_B + p_{case}}{2} \cdot A_{vpff2} \tag{2.308}$$

$$F_{ff3_A} = \frac{p_A + p_{case}}{2} \cdot A_{vpff3} \tag{2.309}$$

$$F_{ff3_B} = \frac{p_B + p_{case}}{2} \cdot A_{vpff3} \tag{2.310}$$

$$F_{ff4} = p_{case} \cdot A_{vpff4} \tag{2.311}$$

We decided to group these forces together in order to make the writing of the subsequent equations more compact. We then considered the hydrostatic force $F_{hydro_{ff_{z'}}}$ acting on the valve plate front surface and its point of application, which can be evaluated exploiting the Varignon's theorem. Note that the y' coordinate of the point of application of the resultant force is zero for symmetry reasons.

$$F_{hydro_{ff_{z'}}} = F_{ff0_A} + F_{ff0_B} + F_{ff1_A} + F_{ff1_B} + F_{ff2_A} + F_{ff2_B} + F_{ff3_A} + F_{ff3_B} + F_{ff4} \tag{2.312}$$

$$x_{F_{vp_{hydro-ff}}} = \frac{F_{ff0_A} \cdot x_{ff0_A} + F_{ff0_B} \cdot x_{ff0_B} + F_{ff1_A} \cdot x_{ff1_A} + \ \dots \ + F_{ff4} \cdot x_{ff4}}{F_{ff0_A} + F_{ff0_B} + F_{ff1_A} + F_{ff1_B} + F_{ff2_A} + \ \dots + F_{ff3_B} + F_{ff4}} \tag{2.313}$$

The point of application of $F_{hydro_{ff_{z'}}}$, called H_3, has the following coordinates.

$$\overline{OH_3}|_{x'} = x_{F_{vp_{hydro-ff}}} \tag{2.314}$$

$$\overline{OH_3}|_{y'} = 0 \tag{2.315}$$

$$\overline{OH_3}|_{z'} = \overline{OK}|_{z'} \tag{2.316}$$

Similarly, **Eq. (2.317)-(2.321)** report the hydrostatic force acting on the rear surface of the fixed valve plate. Note that these expressions are valuable for both the valve plate types, as the area terms are already including their differences.

$$F_{rr5_A} = p_A \cdot A_{vpff5} \tag{2.317}$$

$$F_{rr5_B} = p_B \cdot A_{vpff5} \tag{2.318}$$

$$F_{rr6_A} = \frac{p_A + p_{case}}{2} \cdot A_{vprr6} \tag{2.319}$$

$$F_{rr6_B} = \frac{p_B + p_{case}}{2} \cdot A_{vprr6} \tag{2.320}$$

$$F_{rr7} = \frac{p_A + p_{case}}{2} \cdot A_{vprr7} \tag{2.321}$$

Eq. (2.322)-(2.326) reports the total hydrostatic pressure force $F_{hydro_{rr_{z'}}}$ acting on the valve plate rear surface and its point of application, which can be obtained as done before.

$$F_{hydro_{rr_{z'}}} = F_{rr5_A} + F_{rr5_B} + F_{rr6_A} + F_{rr6_B} + F_{rr7} \tag{2.322}$$

$$x_{F_{vp_{hydro-rr}}} = \frac{F_{rr5_A} \cdot x_{rr5_A} + F_{rr5_B} \cdot x_{rr5_B} + F_{rr6_A} \cdot x_{rr6_A} + F_{rr6_B} \cdot x_{rr6_B} + F_{rr7} \cdot x_{rr7}}{F_{rr5_A} + F_{rr5_B} + F_{rr6_A} + F_{rr6_B} + F_{rr7}} \tag{2.323}$$

The point of application of $F_{hydro_{rr_{z'}}}$, called H_4, has the following coordinates.

$$\overline{OH_4}|_{x'} = x_{F_{vp_{hydro-rr}}} \tag{2.324}$$

$$\overline{OH_4}|_{y'} = 0 \tag{2.325}$$

$$\overline{OH_4}|_{z'} = \overline{OK}|_{z'} + \overline{KK'}\big|_{z'} \tag{2.326}$$

Cylinder block reaction forces. These are the contact/hydrodynamic forces generated at the spherical cap interface between cylinder block and valve plate, which are known from the cylinder block analysis.

$$\begin{gathered} F_{cb_{contact_{x'}}} \\ F_{cb_{contact_{y'}}} \\ F_{cb_{contact_{z'}}} \end{gathered} \tag{2.327}$$

The point of application of this force (H_2) has position $(x_{H_2}, y_{H_2}, z_{H_2})$ known from the cylinder block analysis.

<u>Unit cover reaction forces/moments</u>. The mixed contact between the fixed valve plate and the unit cover generates a mutual reaction force with three non-zero components along the three axes of the reference frame. These terms are unknowns of the equilibrium equations.

$$\begin{gathered} F_{pp-vp_{contact_{x'}}} \\ F_{pp-vp_{contact_{y'}}} \\ F_{pp-vp_{contact_{z'}}} \end{gathered} \tag{2.328}$$

This force has, of course, its own point of application, called H_5 with coordinates $(x'_{H_5}, y'_{H_5}, z'_{H_5})$, which are unknowns too. However, this contact point must lie on the valve plate rear surface, so its z' dimension is known.

$$\overline{OH_5}|_{z'} = \overline{OK}|_{z'} + \overline{KK'}\big|_{z'} \tag{2.329}$$

In addition to these forces, we have considered an unknown reaction moment between the plate and the unit cover around the z' axis, which is necessary to ensure the rotating equilibrium of the valve plate around the same axis.

$$M_{pp-vp} \tag{2.330}$$

Note that these reaction contributions are of no particular interest as they have been introduced only to ensure the valve plate static balancing.

Friction moment between cylinder block and valve plate. This contribution is already known from the cylinder block analysis.

$$M_{cb-vp} \tag{2.331}$$

Free body diagrams

Once we have introduced all the forces/moments acting on the valve plate, it is possible to proceed to the realization of the free body diagrams.

Figure 2.77 shows the free body diagrams for the fixed valve plate, where we have highlighted the unknown terms in red.

We are considering the equilibrium equations equal to zero since this is a fixed component. The bent axis inclination angle β is thus constant ($\beta = cost$), and its first and second derivative are zero ($\dot{\beta} = 0$, $\ddot{\beta} = 0$).

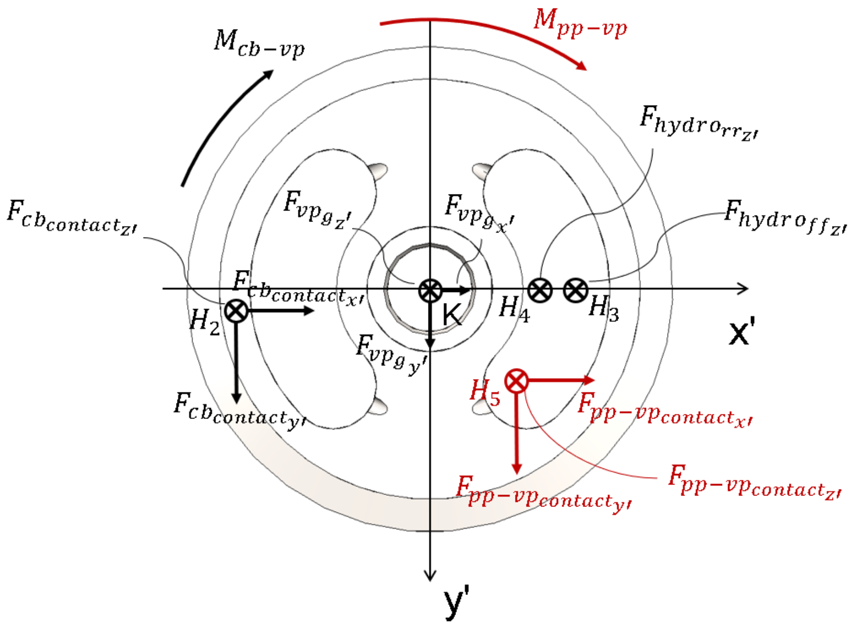

Figure 2.77: Free body diagram for the fixed displacement valve plate

Table 2.21 shows the equilibrium equations developed for the valve plate.

Table2.21: Equilibrium equations for the fixed displacement valve plate

Translational equilibrium – x' axis	
$F_{pp-vp_{contact_{x'}}} + F_{cb_{contact_{x'}}} + F_{vpg_{x'}} = 0$	(2.332)
Translational equilibrium – y' axis	
$F_{pp-vp_{contact_{y'}}} + F_{cb_{contact_{y'}}} + F_{vpg_{y'}} = 0$	(2.333)
Translational equilibrium – z' axis	
$F_{pp-vp_{contact_{z'}}} + F_{cb_{contact_{z'}}} + F_{vpg_{z'}} + F_{hydro_{ff_{z'}}} + F_{hydro_{rr_{z'}}} = 0$	(2.334)
Rotational equilibrium about $O - x'$ axis	
$F_{cb_{contact_{z'}}} \cdot \overline{OH_2}\|_{y'} + F_{pp-vp_{contact_{z'}}} \cdot \overline{OH_5}\|_{y'} + F_{hydro_{ff_{z'}}} \cdot \overline{OH_3}\|_{y'} + F_{hydro_{rr_{z'}}} \cdot \overline{OH_4}\|_{y'} - F_{cb_{contact_{y'}}} \cdot \overline{OH_2}\|_{z'} - F_{vpg_{y'}} \cdot \left(\overline{OK}\|_{z'} + \overline{OG_{vp}}\|_{z'}\right) - F_{pp-vp_{contact_{y'}}} \cdot \overline{OH_5}\|_{z'} = 0$	(2.335)
Rotational equilibrium about $O - y'$ axis	

$F_{cb_{contact_{x'}}} \cdot \overline{OH_2}\|_{z'} + F_{pp-vp_{contact_{x'}}} \cdot \overline{OH_5}\|_{z'} + F_{vpg_{x'}} \cdot \left(\overline{OK}\|_{z'} + \overline{OG_{vp}}\|_{z'}\right) - F_{cb_{contact_{z'}}} \cdot \overline{OH_2}\|_{x'} - F_{hydro_{ff_{z'}}} \cdot \overline{OH_3}\|_{x'} - F_{hydro_{rr_{z'}}} \cdot \overline{OH_4}\|_{x'} - F_{pp-vp_{contact_{z'}}} \cdot \overline{OH_5}\|_{x'} = 0$	(2.336)
Rotational equilibrium about $O - z'$ axis	
$F_{cb_{contact_{y'}}} \cdot \overline{OH_2}\|_{x'} + F_{pp-vp_{contact_{y'}}} \cdot \overline{OH_5}\|_{x'} - F_{cb_{contact_{x'}}} \cdot \overline{OH_2}\|_{y'} - F_{pp-vp_{contact_{x'}}} \cdot \overline{OH_5}\|_{y'} + M_{pp-vp} + M_{cb-vp} = 0$	(2.337)

This is a system of 6 equations in following 6 unknowns:

- $F_{pp-vp_{contact_{x'}}}$
- $F_{pp-vp_{contact_{y'}}}$
- $F_{pp-vp_{contact_{z'}}}$
- $\overline{OH_5}|_{y'}$
- $\overline{OH_5}|_{x'}$
- M_{pp-vp}

The system thus has only one solution, which can be obtained using known resolution methods.

Simcenter Amesim Submodel Editor® model

It was then possible to realize the Simcenter Amesim® submodel concerning the valve plate for fixed displacement units, from the definition of the connection ports with adjacent elements to the implementation of the C++ code.

Figure 2.78 shows the representation of the Simcenter Amesim® icon of the fixed valve plate submodel BAUVVFIX000, while **Table 2.22** describes the variables associated to the submodel ports.

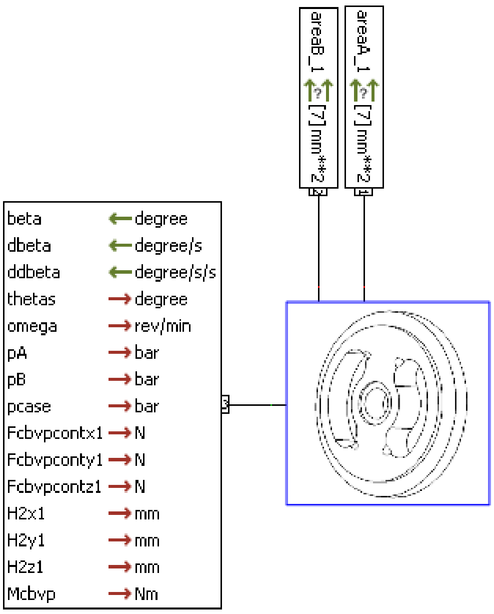

Figure 2.78: Icon of the submodel concerning the fixed displacement valve plate developed in Simcenter Amesim®

Table 2.22: Inputs/outputs at each port of the submodel concerning the fixed displacement valve plate developed in Simcenter Amesim®

PORT	VARIABLE	DESCRIPTION	SYMBOL	TYPE
1	Output	Flow areas between chambers and port A	$Area_A$	Vector
2	Output	Flow areas between chambers and port B	$Area_B$	Vector
3	Input	Cylinder block angular position	θ_S	Scalar
		Cylinder block angular velocity	ω	

		Port A pressure	p_A	
		Port B pressure	p_B	
		Casing pressure	p_{case}	
		Cylinder block-valve plate mixed contact force – x' axis	$F_{cb_{contact_{x'}}}$	
		Cylinder block-valve plate mixed contact force – y' axis	$F_{cb_{contact_{y'}}}$	
		Cylinder block-valve plate mixed contact force – z' axis	$F_{cb_{contact_{z'}}}$	
		H_2 position – x' axis	$H_{2_{x'}}$	
		H_2 position – y' axis	$H_{2_{y'}}$	
		H_2 position – z' axis	$H_{2_{z'}}$	
		Cylinder block-valve plate friction moment	M_{cbvp}	
	Output	Cylinder block inclination angle	β	Scalar
		Derivative of cylinder block inclination angle	$\dot{\beta}$	
		Second derivative of cylinder block inclination angle	$\ddot{\beta}$	

2.3.4 Valve plate model for variable displacement

The following subsection deals with the modelling of the valve plate for bent axis unit with variable displacement. We considered the machine guide pin as rigidly connected to the valve plate itself. This guide pin is also coupled with the machine's servo piston through a ball joint to control the bent axis inclination β.

Figure 2.79 depicts the valve plate for variable displacement in the machine section. Note that the reference unit used in this sub-section differs from the unit considered in the previous one precisely for analysing the valve plate for variable displacements. However, apart from the valve plate, all the other components are analogous to the fixed-displacement reference unit. Also considered integral with the cylinder plate is the pin coupled with a ball joint to the machine's servo actuator.

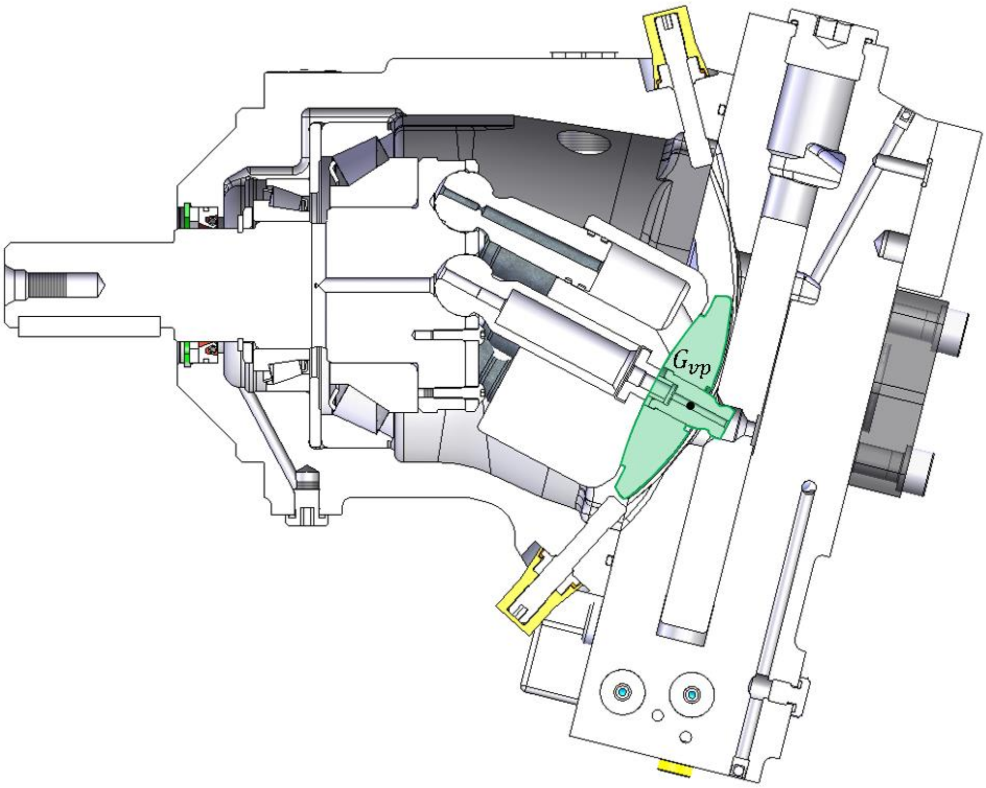

Figure 2.79: Valve plate for variable displacement in the bent axis unit section

The assumptions made for the modelling of this component are the same as those presented for the fixed displacement valve plate.

- the resultant reaction force exerted by the machine cover to maintain the valve plate static equilibrium, merging the hydrodynamic and contact contributions,
- the position of the point of application of this reaction.

The main outputs of the variable valve plate analysis can be summarized in the following points:

- the resultant reaction forces generated by mixed contact with the machine cover, merging the hydrodynamic and contact contributions,
- the position of the point of application of this reaction
- the servo piston force that must maintain the inclination angle fixed in steady-state analysis (i.e. for constant displacement),
- the bent axis angle $\beta = \beta(t)$ obtained from the system dynamic equilibrium in dynamic analysis (i.e. for variable displacement).

Figure 2.80 shows the views of interest for the variable displacement valve plate, where we have highlighted the component parametrization.

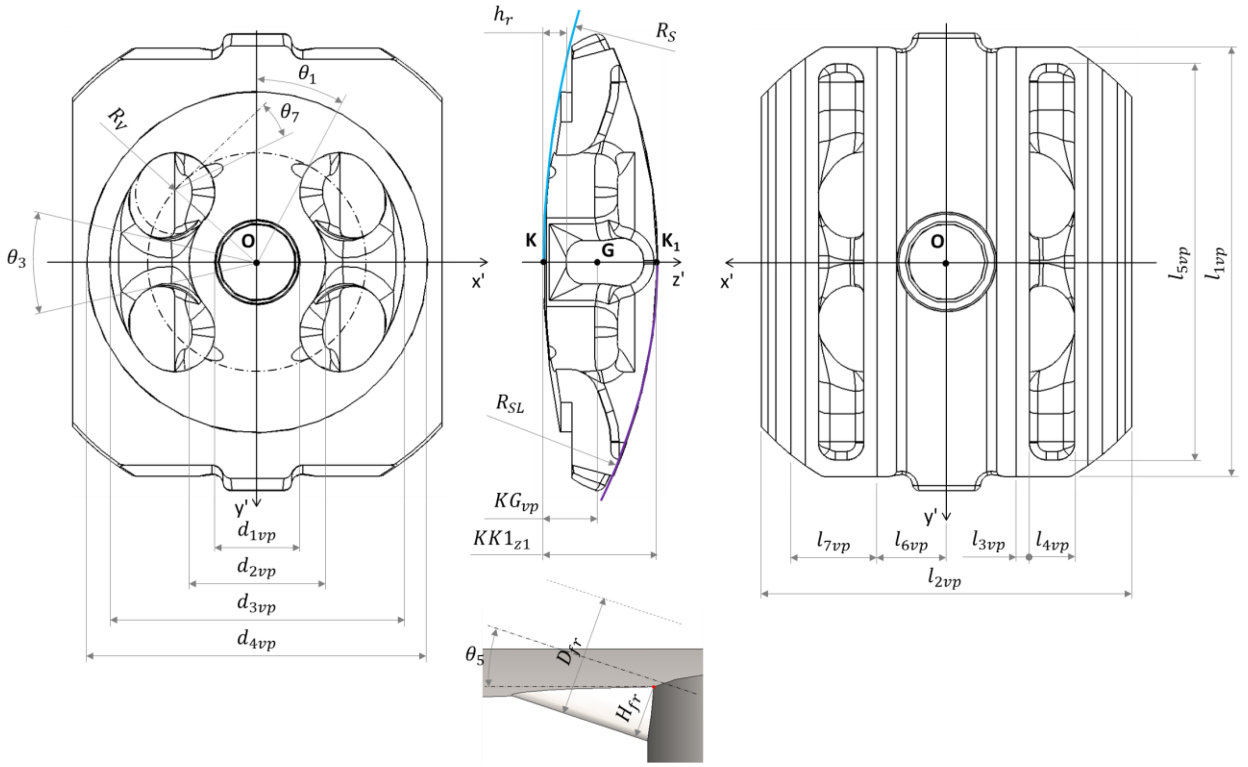

Figure 2.80: Parametrization for the variable displacement valve plate

Table 2.23 lists and describes the geometrical and non-geometrical quantities used for the variable valve plate parameterization and modelling.

Table 2.23: Parameters required for the variable valve plate model

Symbol	Description
α_E	Euler angle α
β_E	Euler angle β
γ_E	Euler angle γ
R_v	Kidney mean radius
s_{asola}	Kidney width

R_{SL}	Radius of curvature of valve plate rear surface
R_S	Radius of curvature of valve plate front surface
L_{OK}	Distance between O (reference frame centre) and K (valve plate front surface centre)
$L_{KK'}$	Distance between K (valve plate front surface centre) and K' (valve plate rear surface centre)
$L_{KG_{vp}}$	Distance between K (valve plate front surface centre) and G_{vp} (valve plate centre of mass)
m_{vp}	Valve plate mass
$I_{vp_{xx}}$	Valve plate $x'x'$ moment of inertia
$d_{1_{vp}}$	Sealing diameter 1 between cylinder block and valve plate
$d_{2_{vp}}$	Sealing diameter 2 between cylinder block and valve plate
$d_{3_{vp}}$	Sealing diameter 3 between cylinder block and valve plate
$d_{4_{vp}}$	Sealing diameter 4 between cylinder block and valve plate
$l_{1_{vp}}$	Characteristic 208ength 1 of the valve plate
$l_{2_{vp}}$	Characteristic 208ength 2 of the valve plate
$l_{3_{vp}}$	Characteristic 208ength 3 of the valve plate
$l_{4_{vp}}$	Characteristic 208ength 4 of the valve plate
$l_{5_{vp}}$	Characteristic 208ength 5 of the valve plate
$l_{6_{vp}}$	Characteristic 208ength 6 of the valve plate
$l_{7_{vp}}$	Characteristic 208ength 7 of the valve plate
h_r	Valve plate-rib distance
D_{fr}	Diameter of the groove milling cutter (parabolic grooves)
H_{fr}	Groove height (parabolic grooves)
β_{max}	Maximum angle for bent axis inclination
β_{min}	Minimum angle for bent axis inclination
θ_1	Kidney starting angular position
θ_2	Kidney angular extension
θ_3	Rib angular extension
θ_4	Groove angular extension (triangular grooves)
θ_5	Groove angular inclination with respect to the horizontal plane (triangular/parabolic grooves)
θ_6	Milling inclination angle for opening/closing grooves (triangular grooves)
θ_7	Groove angular inclination with respect to R_v (triangular/parabolic grooves)
$f_{fr_{case}}$	Valve plate-cover kinetic friction coefficient
b	Viscous friction coefficient

Kinematic analysis

Regarding the kinematic analysis of the valve plate for variable displacement, we analysed the relationships linking the linear displacement of the servo piston with the variation of the displacement angle β of characterizing the valve plate and cylinder block inclination.

Figure 2.81 shows the servo piston and valve plate detail in the machine section.

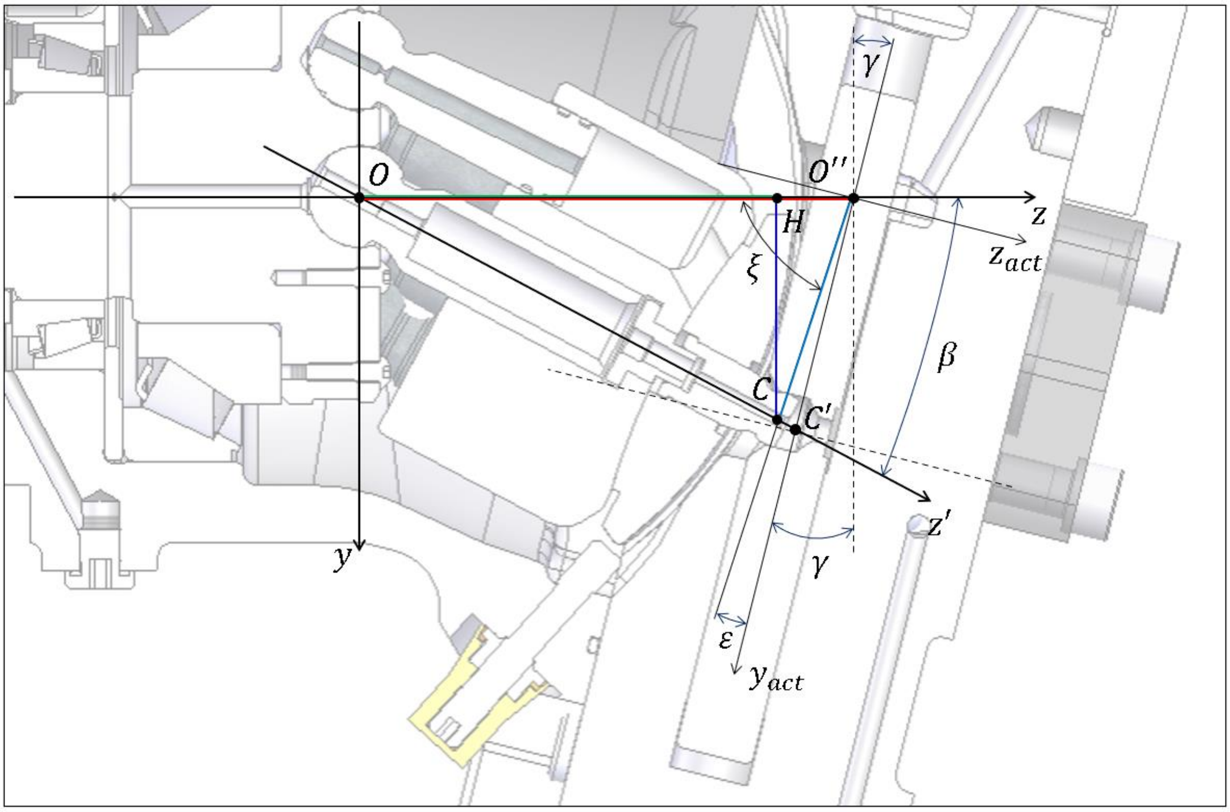

Figure 2.81: Servo piston and valve plate detail for the displacement variation

Table 2.24 lists the parameters necessary for the kinematic analysis in addition to **Table 2.23**.

Table 2.24: Parameters required for the kinematic analysis of the valve plate

Symbol	Description
$\overline{OC}$	Distance between O (reference frame centre) and C (centre of the guide pin ball joint)
$\overline{OO''}$	Distance between O (reference frame centre) and O'' (point of intersection between z axis and y_{act} axis of the servo piston)
γ	Inclination angle of the servo piston axis (y_{act} axis)

We can obtain **Eq. (2.338)** referring to **Figure 2.81** and applying the Pythagorean theorem to $HO''C$ triangle.

$$\overline{O''C} = \sqrt{\left(\overline{OO''} - \overline{OC}\cos\beta\right)^2 + (-\overline{OC}\sin\beta)^2} \tag{2.338}$$

Applying instead Carnot's theorem to $OO''C$ triangle, we can derive the expression of ξ angle as given in **Eq. (2.339)**.

$$\xi = \cos^{-1}\left(\frac{\overline{OO''}^2 + \overline{O''C}^2 - \overline{OC}^2}{2 \cdot \overline{OO''} \cdot \overline{O''C}}\right) \tag{2.339}$$

Eq. (2.340) expresses the distance $\overline{O''C'}$, where $\overline{O''C}$ and ξ are those defined by **Eq. (2.338)-(2.339)**.

$$\overline{O''C'} = \overline{O''C} \cdot \cos\left(\frac{\pi}{2} - \gamma - \xi\right) \tag{2.340}$$

The distance $\overline{O''C'}$ define the position of the servo piston as a function of the bent axis angle β and vice versa.

We can then obtain the expression of the servo piston speed by deriving $\overline{O''C'}$. It is possible to simply this derivative considering $\overline{O''C'}$ as product of two functions $\overline{O''C'} = \overline{O''C'}\ (\beta) = f(\beta) \cdot g(\beta)$, where **Eq. (2.341)- (2.342)** define $f(\beta)$ and $g(\beta)$.

$$f(\beta) = \sqrt{\left(\overline{OO''} - \overline{OC}\cos\beta\right)^2 + (-\overline{OC}\sin\beta)^2} \tag{2.341}$$

$$g(\beta) = \cos\left(\frac{\pi}{2} - \gamma - \left(\cos^{-1}\left(\frac{\overline{OO''}^2 + \left(\left(\overline{OO''} - \overline{OC}\cos\beta\right)^2 + (-\overline{OC}\sin\beta)^2\right) - \overline{OC}^2}{2\cdot\overline{OO'}\cdot\sqrt{(\overline{OO''} - \overline{OC}\cos\beta)^2 + (-\overline{OC}\sin\beta)^2}}\right)\right)\right) \tag{2.342}$$

Eq. (2.340) can then be derived exploiting the product rule to obtain the speed of the servo piston as function of $\beta(t)$.

Dynamic analysis

Similarly to what we have done with the previous components, we can now move on with the introduction of all the known and unknown forces/moments acting on the valve plate for variable displacement.

Weight force. The weight force expressed in the $Ox'y'z'$ reference frame can be obtained by rotating the components of the weight force vector expressed in the fixed reference frame of the machine (assumed known) using the rotation matrix $R_{O\to O'}$ (**Eq. 2.44**). The point of application of this force is the centre of mass G_{vp} of the valve plate.

$$[F_{vp_{g_{Ox'y'z'}}}] = R_{O\to O'}[F_{vp_{g_{BAU}}}] \tag{2.343}$$

which translates into **Eq. (2.344)-(2.345)-(2.346)**.

$$F_{vp_{g_{x'}}} = F_{vp_{g_x}} \tag{2.344}$$

$$F_{vp_{g_{y'}}} = F_{vp_{g_y}} \cdot \cos\beta - F_{vp_{g_z}} \cdot \sin\beta \tag{2.345}$$

$$F_{vp_{g_{z'}}} = F_{vp_{g_y}} \cdot \sin\beta + F_{vp_{g_z}} \cdot \cos\beta \tag{2.346}$$

Pressure forces. As done for the fixed valve plate, it is first necessary to identify the different areas of interest on which a certain pressure acts to assess the different contributions of hydrostatic forces. **Figure 2.82** shows the front and rear views of the valve plate, highlighting the areas on which different pressures act.

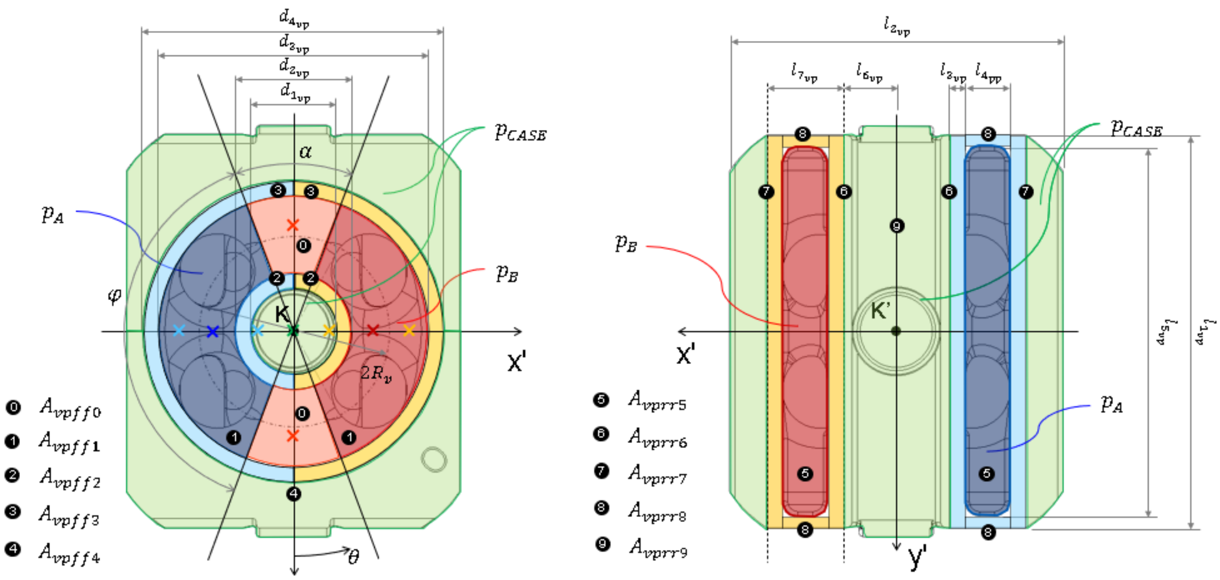

Figure 2.82: Areas of interest for the pressure forces calculation on variable valve plate

The following relationships express the various areas of interest for the variable valve plate exploiting some known expressions for geometric area calculations.

$$A_{vpff0} = \frac{\pi}{180}\frac{\left(2\pi - \theta_{fbc_S} + \theta_{iba}\right)}{2}\frac{1}{4}\left(d_{3_{vp}}^{\ 2} - d_{2_{vp}}^{\ 2}\right) \tag{2.347}$$

$$A_{vpff0_S} = \frac{\pi}{180}\frac{\left(\theta_{iba_S} - \theta_{fbc}\right)}{2}\frac{1}{4}\left(d_{3_{vp}}^{\ 2} - d_{2_{vp}}^{\ 2}\right) \tag{2.348}$$

$$A_{vpff1} = \frac{\pi}{180}\frac{\left(\theta_{fbc} - \theta_{iba}\right)}{2}\frac{1}{4}\left(d_{3_{vp}}^{\ 2} - d_{2_{vp}}^{\ 2}\right) \tag{2.349}$$

$$A_{vpff1_S} = \frac{\pi}{180}\frac{\left(\theta_{fbc_S} - \theta_{iba_S}\right)}{2}\frac{1}{4}\left(d_{3_{vp}}^{\ 2} - d_{2_{vp}}^{\ 2}\right) \tag{2.350}$$

$$A_{vpff2} = \frac{1}{2}\cdot\frac{\pi}{4}\left(d_{2_{vp}}^2 - d_{1_{vp}}^2\right) \tag{2.351}$$

$$A_{vpff3} = \frac{1}{2}\cdot\frac{\pi}{4}\left(d_{4_{vp}}^2 - d_{3_{vp}}^2\right) \tag{2.352}$$

$$A_{vpff4} = \frac{\pi}{4}\cdot d_{7_{vp}}^2 - 2\left(A_{vpff2} + A_{vpff3}\right) - A_{vpff0} - A_{vpff0_S} - A_{vpff1} - A_{vpff1_S} \tag{2.353}$$

$$A_{vprr5} = l_{5_{vp}}\cdot l_{4_{vp}} \tag{2.354}$$

$$A_{vprr6} = l_{3_{vp}}\cdot l_{1_{vp}} \tag{2.355}$$

$$A_{vprr7} = \left(l_{7_{vp}} - l_{3_{vp}} - l_{4_{vp}}\right)\cdot l_{1_{vp}} \tag{2.356}$$

$$A_{vprr8} = l_{4_{vp}}\cdot\frac{l_{1_{vp}} - l_{5_{vp}}}{2} \tag{2.357}$$

$$A_{vprr9} = l_{1_{vp}} \cdot l_{2_{vp}} - 2 \cdot \left(A_{vprr5} + A_{vprr6} + A_{vprr7} + 2 \cdot A_{vprr8}\right) \tag{2.358}$$

Once again, it is also necessary to identify the barycentres of these areas of interest to know the points of application of the pressure forces acting on these areas.

As done in fixed valve plate model, we have considered the two A_{vpff0} areas ('upper' and 'lower' in **Figure 2.82**) together so that their barycentre is positioned at the point K (since the pressure is the same on both A_{vpff0} areas). We have exploited the component symmetry and some geometric analytic expression to derive the following positions reported in **Eq. (2.359)-(3.90)**.

$$x_{ff0} = 0 \tag{2.359}$$

$$y_{ff0} = 0 \tag{2.360}$$

$$x_{ff1B} = \frac{2}{3} \cdot \frac{\sin\left(\theta_{fbc} - \theta_{iba}\right)}{\left(\theta_{fbc} - \theta_{iba}\right)} \cdot \frac{180}{\pi} \cdot \frac{\left(\frac{d_{3_{vp}}}{2}\right)^2 + \left(\frac{d_{2_{vp}}}{2}\right)^2 + \frac{d_{3_{vp}}}{2} \cdot \frac{d_{2_{vp}}}{2}}{\frac{d_{3_{vp}}}{2} + \frac{d_{2_{vp}}}{2}} \tag{2.361}$$

$$y_{ff1B} = 0 \tag{2.362}$$

$$x_{ff1A} = -\frac{2}{3} \cdot \frac{\sin\left(\theta_{fbc_S} - \theta_{iba_S}\right)}{\left(\theta_{fbc_S} - \theta_{iba_S}\right)} \cdot \frac{180}{\pi} \cdot \frac{\left(\frac{d_{3_{vp}}}{2}\right)^2 + \left(\frac{d_{2_{vp}}}{2}\right)^2 + \frac{d_{3_{vp}}}{2} \cdot \frac{d_{2_{vp}}}{2}}{\frac{d_{3_{vp}}}{2} + \frac{d_{2_{vp}}}{2}} \tag{2.363}$$

$$y_{ff1A} = 0 \tag{2.364}$$

$$x_{ff2B} = \frac{4}{3\pi} \frac{\left(\frac{d_{2_{vp}}}{2}\right)^2 + \left(\frac{d_{1_{vp}}}{2}\right)^2 + \frac{d_{2_{vp}}}{2} \cdot \frac{d_{1_{vp}}}{2}}{\frac{d_{2_{vp}}}{2} + \frac{d_{1_{vp}}}{2}} \tag{2.365}$$

$$y_{ff2B} = 0 \tag{2.366}$$

$$x_{ff2A} = -x_{A_{vpff2B}} \tag{2.367}$$

$$y_{ff2A} = 0 \tag{2.368}$$

$$x_{ff3B} = \frac{4}{3\pi} \frac{\left(\frac{d_{4_{vp}}}{2}\right)^2 + \left(\frac{d_{3_{vp}}}{2}\right)^2 + \frac{d_{4_{vp}}}{2} \cdot \frac{d_{3_{vp}}}{2}}{\frac{d_{4_{vp}}}{2} + \frac{d_{3_{vp}}}{2}} \tag{2.369}$$

$$y_{ff3B} = 0 \tag{2.370}$$

$$x_{ff3A} = -x_{A_{vpff3B}} \tag{2.371}$$

$$y_{ff3A} = 0 \tag{2.372}$$

$$x_{ff4} = 0 \tag{2.373}$$

$$y_{ff4} = 0 \tag{2.374}$$

$$x_{rr5B} = \left(l_{6_{vp}} + \frac{l_{7_{vp}}}{2}\right) \tag{2.375}$$

$$y_{rr5B} = 0 \tag{2.376}$$

$$x_{rr5A} = -x_{rr5B} \tag{2.377}$$

$$y_{rr5A} = 0 \tag{2.378}$$

$$x_{rr6B} = \left(l_{6_{vp}} + \frac{l_{3_{vp}}}{2}\right) \tag{2.379}$$

$$y_{rr6B} = 0 \tag{2.380}$$

$$x_{rr6A} = -x_{rr6B} \tag{2.381}$$

$$y_{rr6A} = 0 \tag{2.382}$$

$$x_{rr7A} = \left(l_{6_{vp}} + l_{7_{vp}} - \frac{\left(l_{7_{vp}} - l_{3_{vp}} - l_{4_{vp}}\right)}{2}\right) \tag{2.383}$$

$$y_{rr7A} = 0 \tag{2.384}$$

$$x_{rr8A} = \left(l_{6_{vp}} + l_{3_{vp}} + \frac{l_{4_{vp}}}{2}\right) \tag{2.385}$$

$$y_{rr8A} = 0 \tag{2.386}$$

$$x_{rr8B} = -x_{rr8A} \tag{2.387}$$

$$y_{rr8B} = 0 \tag{2.388}$$

$$x_{rr9} = 0 \tag{2.389}$$

$$y_{rr9} = 0 \tag{2.390}$$

Eq. (2.391)-(2.399) report the hydrostatic force acting on these areas of interest considering a pressure linear trend withing the gap. We could then consider the average pressure value for each area based on its boundary conditions.

$$F_{ff0_A} = \frac{p_A + p_B}{2} \cdot A_{vpff0} \tag{2.391}$$

$$F_{ff0_B} = \frac{p_A + p_B}{2} \cdot A_{vpff0} \tag{2.392}$$

$$F_{ff1_A} = p_A \cdot A_{vpff1} \tag{2.393}$$

$$F_{ff1_B} = p_B \cdot A_{vpff1} \tag{2.394}$$

$$F_{ff2_A} = \frac{p_A + p_{case}}{2} \cdot A_{vpff2} \tag{2.395}$$

$$F_{ff2_B} = \frac{p_B + p_{case}}{2} \cdot A_{vpff2} \tag{2.396}$$

$$F_{ff3_A} = \frac{p_A + p_{case}}{2} \cdot A_{vpff3} \tag{2.397}$$

$$F_{ff3_B} = \frac{p_B + p_{case}}{2} \cdot A_{vpff3} \tag{2.398}$$

$$F_{ff4} = p_{case} \cdot A_{vpff4} \tag{2.399}$$

Once again, we decided to group these forces together in order to make the writing of the subsequent equations more compact. As done for the fixed valve plate, we considered the hydrostatic force $F_{hydro_{ff_{z'}}}$ acting on the valve plate front surface and its point of application, which can be evaluated exploiting the Varignon's theorem. The y' coordinate of the point of application of the resultant force is zero for symmetry reasons.

$$F_{hydro_{ff_{z'}}} = F_{ff0_A} + F_{ff0_B} + F_{ff1_A} + F_{ff1_B} + F_{ff2_A} + F_{ff2_B} + F_{ff3_A} + F_{ff3_B} + F_{ff4} \tag{2.400}$$

$$x_{F_{vp_{hydro-ff}}} = \frac{F_{ff0_A} \cdot x_{ff0_A} + F_{ff0_B} \cdot x_{ff0_B} + F_{ff1_A} \cdot x_{ff1_A} + \ \dots \ + F_{ff4} \cdot x_{ff4}}{F_{ff0_A} + F_{ff0_B} + F_{ff1_A} + F_{ff1_B} + F_{ff2_A} + \ \dots + F_{ff3_B} + F_{ff4}} \tag{2.401}$$

The point of application of $F_{hydro_{ff_{z'}}}$, always called H_3, has the following coordinates.

$$\overline{OH_3}|_{x'} = x_{F_{vp_{hydro-ff}}} \tag{2.402}$$

$$\overline{OH_3}|_{y'} = 0 \tag{2.403}$$

$$\overline{OH_3}|_{z'} = \overline{OK}|_{z'} \tag{2.404}$$

Similarly, the expressions of the pressure forces for the rear section of the plate are given below in **Eq. (2.405)-(2.413)**.

$$F_{rr5_A} = p_A \cdot A_{vpff5} \tag{2.405}$$

$$F_{rr5_B} = p_B \cdot A_{vpff5} \tag{2.406}$$

$$F_{rr6_A} = \frac{p_A + p_{case}}{2} \cdot A_{vprr6} \tag{2.407}$$

$$F_{rr6_B} = \frac{p_B + p_{case}}{2} \cdot A_{vprr6} \tag{2.408}$$

$$F_{rr7_A} = \frac{p_A + p_{case}}{2} \cdot A_{vprr7} \tag{2.409}$$

$$F_{rr7_B} = \frac{p_B + p_{case}}{2} \cdot A_{vprr7} \tag{2.410}$$

$$F_{rr8_A} = \frac{p_A + p_{case}}{2} \cdot A_{vprr8} \tag{2.411}$$

$$F_{rr8_B} = \frac{p_B + p_{case}}{2} \cdot A_{vprr8} \tag{2.412}$$

$$F_{rr9} = p_{case} \cdot A_{vprr9} \tag{2.413}$$

The total hydrostatic pressure force acting on the valve plate rear surface and its point of application can be derived in a similar way.

$$F_{hydro_{rr_{z'}}} = F_{rr5_A} + F_{rr5_B} + F_{rr6_A} + F_{rr6_B} + F_{rr7_A} + F_{rr7_B} + F_{rr8_A} + F_{rr8_B} + F_{rr9} \tag{2.414}$$

$$x_{F_{vp_{hydro-rr}}} = \frac{F_{rr5_A} \cdot x_{rr5_A} + F_{rr5_B} \cdot x_{rr5_B} + \cdots + F_{rr8_B} \cdot x_{rr8_B} + F_{rr9} \cdot x_{rr9}}{F_{rr5_A} + F_{rr5_B} + \cdots + F_{rr8_B} + F_{rr9}} \tag{2.415}$$

The point of application of $F_{hydro_{ff_{z'}}}$, always called H_4, has the following coordinates.

$$\overline{OH_4}|_{x'} = x_{F_{vp_{hydro-rr}}} \tag{2.416}$$

$$\overline{OH_4}|_{y'} = 0 \tag{2.417}$$

$$\overline{OH_4}|_{z'} = \overline{OK}|_{z'} + \overline{KK'}\Big|_{z'} \tag{2.418}$$

<u>**Cylinder block reaction forces**</u>. These are the contact/hydrodynamic forces generated at the spherical cap interface between cylinder block and valve plate, which are known from the cylinder block analysis.

$$\begin{gathered} F_{cb_{contact_{x'}}} \\ F_{cb_{contact_{y'}}} \\ F_{cb_{contact_{z'}}} \end{gathered} \tag{2.327}$$

The point of application of this force (H_2) has position ($x_{H_2}, y_{H_2}, z_{H_2}$) known from the cylinder block analysis.

Cover reaction forces/moments. The reaction forces generated by the mixed contact (mediated through oil film and metal to metal contact) between valve plate and unit cover are unknowns of the equilibrium system.

We have considered a force applied at point C along x' to ensure the valve plate translational balance along this axis.

$$F_{case_{contact_{C,x'}}} \tag{2.420}$$

Similarly, we have also considered two force components along the y' and z' axes.

$$\begin{gathered} F_{case_{contact_{y'}}} \\ F_{case_{contact_{z'}}} \end{gathered} \tag{2.421}$$

The unit cover supports the variable valve plate with two cylindrical slides, which allow the valve plate rotation around the x' axis varying β angle. However, we have concentrated in a single contribution these two slide contact forces for simplicity. This simplification (among others) is necessary to reduce the number of unknown terms and thus obtain a determined system of equilibrium equations.

This single contact force has its own equivalent point of application. However, we have considered this force located at the point K' and introduced two transport moments around y' and z', for the sake of convenient. These two moments are unknows too.

$$
\begin{gathered}
M_{case_{y'}} \\
M_{case_{z'}}
\end{gathered}
\tag{2.422}
$$

Servo piston forces. The servo piston that manages the displacement variation exerts these forces on the guide pin ball joint along y' and z' axes. We are not considering the x' component as it can be included within the cover reaction force $F_{case_{contact_{C,x'}}}$.

$$
\begin{gathered}
F_{(act-vp),C_{y'}} \\
F_{(act-vp),C_{z'}}
\end{gathered}
\tag{2.423}
$$

We are presenting the evaluation of these contributions in the following pages dividing the cases of steady-state ($\beta = \text{constant}$) and dynamic analysis ($\beta = \text{variable}$).

Friction forces/moments between valve plate and unit cover. This contribution represents the friction force that arises between the valve plate and unit cover relating to their relative motion. It is a mixed friction as there is usually both metal to metal friction and friction mediated through oil film. Having reported the contact forces at point K', we assumed to evaluate this contribution using the force normal to the spherical contact interface $F_{case_{contact_{z'}}}$ to calculate the friction force along y', as reported in **Eq. (2.424)**.

$$
F_{vp_{fr_{y'}}} = f_a \cdot F_{case_{contact_{z'}}}
\tag{2.424}
$$

Since the valve plate can rotate around the x' axis for the displacement variation, we have also considered stiction and kinetic friction moment calculated as follows within the C++ code.

$$
M_{coul} = \left| F_{vp_{fr_{y'}}} \right| \cdot \left(\overline{OK}|_{z'} + \overline{KK'}|_{z'} \right) \cdot k_{coul}
\tag{2.425}
$$

$$
M_{stict} = M_{coul} \cdot k_{stict}
\tag{2.426}
$$

Note that we are not including these contributions in the equilibrium equations but only in the dynamic analysis part of the code for the calculation of β, $\dot{\beta}$ and $\ddot{\beta}$.

Friction moment between cylinder block and valve plate. This contribution is already known from the cylinder block analysis.

$$
M_{cb-vp}
\tag{2.427}
$$

Free body diagrams

Figure 2.83-2.84 show the free body diagrams for the resolution of the variable valve plate equilibrium, where we have highlighted the unknown terms in red.

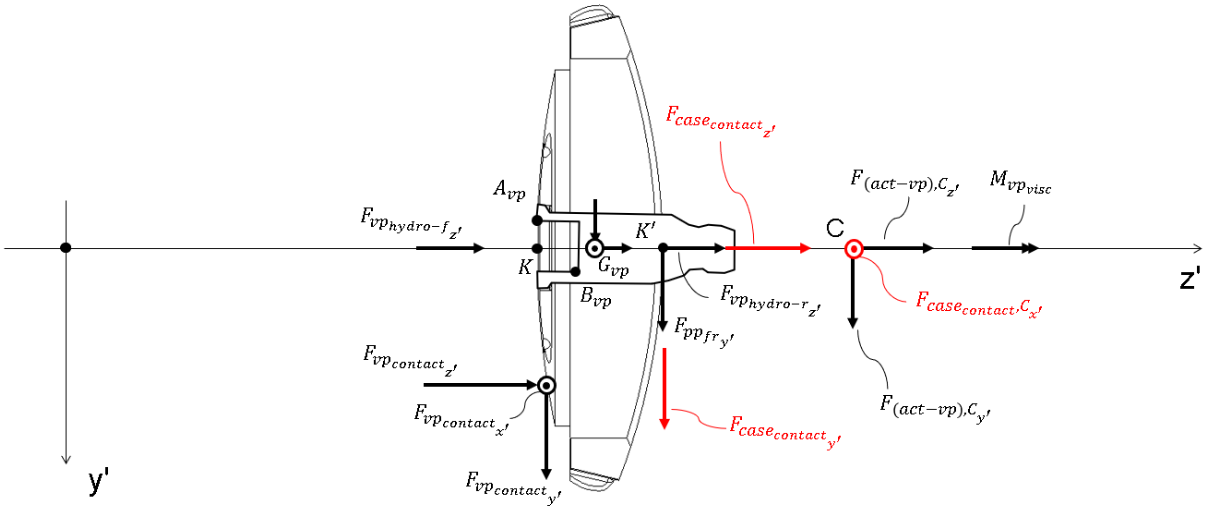

Figure 2.83: Free body diagram for the variable valve plate ($y'z'$ plate)

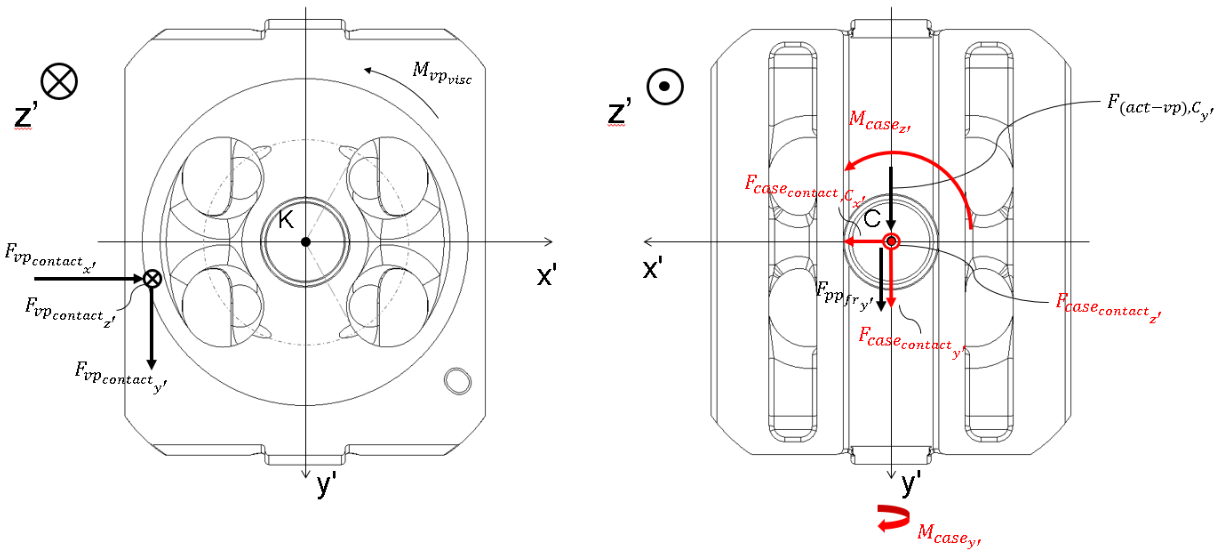

Figure 2.84: Free body diagram for the variable valve plate ($x'y'$plate)

We are first considering the five equations of static equilibrium (translation along x', y', z' and rotation around y' and z'). The sixth equation (rotation around x') will be consider as static equilibrium for steady-state analysis ($\beta = \text{constant}$) or dynamic equilibrium for dynamic analysis ($\beta = \text{variable}$). The latter will consider the dynamic (inertial and damping terms) terms $I_{xx} \cdot \ddot{\beta} + b \cdot \dot{\beta}$ to assess the unknown concerning the bent axis angle $\beta = \beta(t)$.

Table 2.25 shows the equilibrium equations for the variable valve plate.

Table 2.25: Equilibrium equations for variable valve plate

Translational equilibrium – x' axis	
$F_{vp_{contact_{x'}}} + F_{vp_{g_{x'}}} + F_{case_{contact},C_{x'}} = 0$	(2.428)
Translational equilibrium – y' axis	
$F_{vp_{contact_{y'}}} + F_{vp_{g_{y'}}} + F_{pp_{fr_{y'}}} + F_{(act-vp),C_{y'}} + F_{case_{contact_{y'}}} = 0$	(2.429)
Translational equilibrium – z' axis	
$F_{vp_{contact_{z'}}} + F_{(act-vp),C_{z'}} + F_{vp_{hydro-f_{z'}}} + F_{vp_{hydro-r_{z'}}} + F_{case_{contact_{z'}}} + F_{vp_{g_{z'}}} = 0$	(2.430)
Rotational equilibrium about $O - y'$ axis	
$M_{vp_{contact_{y'}}} - F_{vp_{hydro-ff_{z'}}} \cdot \overline{OH_3}\vert_{x'} - F_{vp_{hydro-rr_{z'}}} \cdot \overline{OH_4}\vert_{x'} + M_{case_{y'}} + F_{case_{contact},C_{x'}} \cdot \overline{OC}\vert_{z'} + F_{vp_{g_{x'}}} \cdot \overline{OG_{vp}}\vert_{z'} = 0$	(2.431)

Rotational equilibrium about $O - z'$ axis	
$M_{pp_{visc}} + M_{vp_{contact_{z'}}} + M_{case_{z'}} = 0$	(2.432)

This is a system with 5 equations in the following 5 unknowns:

- $F_{case_{contact},C_{x'}}$
- $F_{case_{contact_{y'}}}$
- $F_{case_{contact_{z'}}}$
- $M_{case_{y'}}$
- $M_{case_{z'}}$

As mentioned, $F_{(act-vp),C_{y'}}$ and $F_{(act-vp),C_{z'}}$ depend on the valve plate analysis. It is thus necessary to separate the two following cases.

- **Steady-state analysis**

The the ball joint connecting the guide pin with the servo piston absorbs any moments that tend to rotate the plate around x'. The servo piston forces (and subsequent moment) are assumed to be zero since the tilting angle β of the valve plate remains constant.

$$F_{(act-vp),C_{y'}} = 0 \tag{2.433}$$

$$F_{(act-vp),C_{y'}} = 0 \tag{2.434}$$

$$M_{(act-vp)_{x'}} = 0 \tag{2.435}$$

We can thus evaluate the tilting moment $M_{tilting}$ that tends to rotate the valve plate around the x' axis considering the static equilibrium of the rotation ($\sum M = 0$).

$$M_{tilting} = M_{(act-vp)_{x'}} + M_{vp_{contact_{x'}}} - F_{vp_{fr_{y'}}} \cdot (\overline{OK}|_{z'} + \overline{KK'}|_{z'}) - F_{vp_{g_{y'}}} \cdot \overline{OG_{vp}}\Big|_{z'} \tag{2.436}$$

It is then possible to evaluate the ideal force (acting on the ball joint centre C) that the servo piston must exert to balance this $M_{tilting}$ and maintain a constant displacement of the unit.

$$F_{act_{ideal_{y'}}} = -\frac{M_{tilting}}{\overline{OC}|_{z'}} \tag{2.437}$$

It will be then possible to obtain the differential pressure in the servo piston chambers to achieve this force in **Eq. (2.437)**.

Dynamic Analysis

We are deriving the servo piston forces along y' and z' by decomposing the force exerted by the piston along its axis (y_{act}), which is function of the pressure difference within the servo piston chambers.

$$F_{(act-vp),C_{y'}} = \left(F_{1_{y_{act}}} - F_{2_{y_{act}}}\right) \cdot \cos(-(\beta + \gamma)) \tag{2.438}$$

$$F_{(act-vp),C_{y'}} = \left(F_{1_{y_{act}}} - F_{2_{y_{act}}}\right) \cdot \sin(-(\beta+\gamma)) \tag{2.439}$$

The servo piston also provides a moment around x'.

$$M_{(act-vp)_{x'}} = -F_{(act-vp),C_{y'}} \cdot \overline{OC}|_{z'} \tag{2.440}$$

Figure 2.85 highlights these contributions.

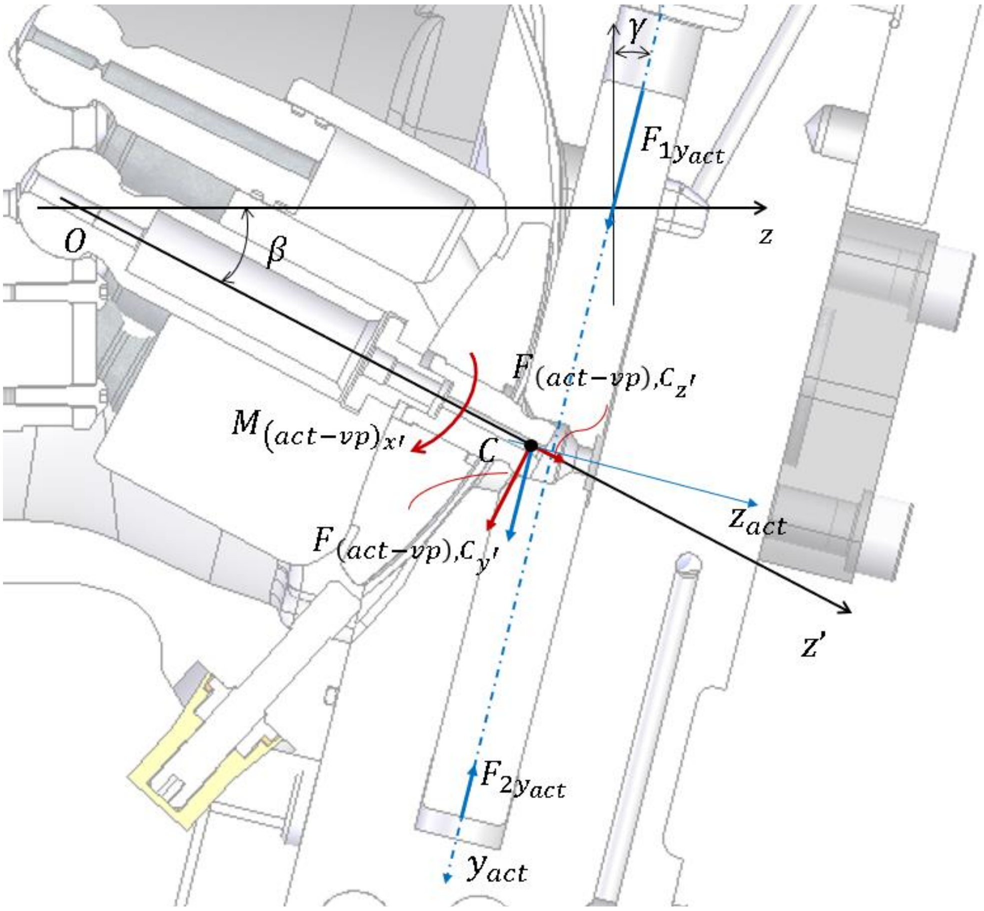

Figure 2.85: Servo actuator forces and moment acting on the variable valve plate in dynamic analysis

Eq. (2.441) express the dynamic equilibrium equation ($\sum M = I \cdot \ddot{\alpha} + b \cdot \dot{\alpha}$) concerning the rotation around x'.

$$\begin{aligned} M_{(act-vp)_{x'}} + M_{vp_{contact_{x'}}} - F_{vp_{fr_{y'}}} \cdot (\overline{OK}|_{z'} + \overline{KK'}|_{z'}) - F_{vp_{g_{y'}}} \cdot \overline{OG_{vp}}\big|_{z'} \\ = I_{vp_{xx}} \cdot \ddot{\beta} + b \cdot \dot{\beta} \end{aligned} \tag{2.441}$$

It is then possible to derive the sixth unknown $\beta(t)$ of the dynamic analysis by isolating the term $\ddot{\beta}$ and then integrating twice.

$$\ddot{\beta} = \frac{M_{(act-vp)_{x'}} + M_{vp_{contact_{x'}}} - F_{vp_{fr_{y'}}} \cdot (\overline{OK}|_{z'} + \overline{KK'}|_{z'}) - F_{vp_{g_{y'}}} \cdot \overline{OG_{vp}}\big|_{z'} - b \cdot \dot{\beta}}{I_{vp_{xx}}} \tag{2.442}$$

$$\dot{\beta} = \int \ddot{\beta} \tag{2.443}$$

$$\beta = \int \dot{\beta} = \text{variabile} \tag{2.444}$$

Table 2.26 shows the resolution for the first five equilibrium equations.

Table 2.26: Resolution of the equilibrium equation for the variable valve plate

Translational equilibrium – x' axis	
$F_{case_{contact},C_{x'}} = -\left(F_{vp_{contact_{x'}}} + F_{vpg_{x'}}\right)$	(2.445)
Translational equilibrium – y' axis	
$F_{case_{contact_{z'}}} = -\left(F_{vp_{contact_{z'}}} + F_{(act-vp),C_{z'}} + F_{vp_{hydro-f_{z'}}} + F_{vp_{hydro-r_{z'}}} + F_{vpg_{z'}}\right)$	(2.446)
Translational equilibrium – z' axis	
$F_{case_{contact_{y'}}} = -\left(F_{vp_{contact_{y'}}} + F_{vpg_{y'}} + F_{pp_{fr_{y'}}} + F_{(act-vp),C_{y'}}\right)$	(2.447)
Rotational equilibrium about $O - y'$ axis	
$M_{case_{y'}} = -\left(M_{vp_{contact_{y'}}} - F_{vp_{hydro-ff_{z'}}} \cdot \overline{OH_3}\|_{x'} - F_{vp_{hydro-rr_{z'}}} \cdot \overline{OH_4}\|_{x'} + F_{case_{contact},C_{x'}} \cdot \overline{OC}\|_{z'} + F_{vpg_{x'}} \cdot \overline{OG_{vp}}\|_{z'}\right)$	(2.448)
Rotational equilibrium about $O - z'$ axis	
$M_{case_{z'}} = -\left(M_{pp_{visc}} + M_{vp_{contact_{z'}}}\right)$	(2.449)

The sixth equation (rotation around the x' axis) resolution requires to proceed, as seen, differentiating between the cases of steady-state or dynamic analysis.

Simcenter Amesim Submodel Editor® model

It was then possible to realize the Simcenter Amesim® submodel concerning the valve plate for variable displacement units, from the definition of the connection ports with adjacent elements to the implementation of the C++ code.

Figure 2.86 shows the representation of the Simcenter Amesim® icon of the variable valve plate submodel BAUVVSP000, while **Table 2.27** describes the variables associated to the submodel ports.

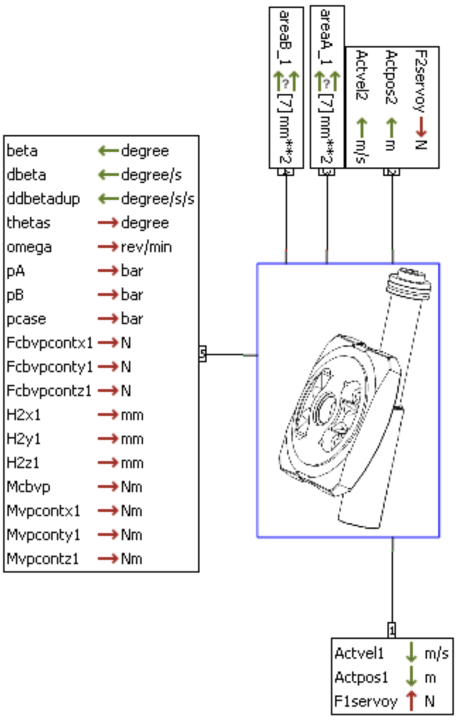

Figure 2.86: Icon of the submodel concerning the variable displacement valve plate developed in Simcenter Amesim®

Table 2.27: Inputs/outputs at each port of the submodel concerning the variable displacement valve plate developed in Simcenter Amesim®

PORT	VARIABLE	DESCRIPTION	SYMBOL	TYPE
1	Input	Servo piston force (port 1)	$F_{1_{servo_y}}$	Scalar
	Output	Linear position of servo piston (port 1)	Act_{pos1}	
		Linear velocity of servo piston (porta 1)	Act_{vel1}	
2	Input	Servo piston force (port 2)	$F_{2_{servo_y}}$	Scalar
	Output	Linear position of servo piston (port 2)	Act_{pos2}	
		Linear velocity of servo piston (porta 2)	Act_{vel2}	
3	Output	Flow areas between chambers and port A	$Area_A$	Vector
4	Output	Flow areas between chambers and port B	$Area_B$	Vector
5	Input	Cylinder block angular position	θ_S	Scalar
		Cylinder block angular velocity	ω	
		Port A pressure	p_A	
		Port B pressure	p_B	
		Casing pressure	p_{case}	
		Cylinder block-valve plate mixed contact force – x' axis	$F_{cbvp_{contact_{x'}}}$	
		Cylinder block-valve plate mixed contact force – y' axis	$F_{cbvp_{contact_{y'}}}$	
		Cylinder block-valve plate mixed contact force – z' axis	$F_{cbvp_{contact_{z'}}}$	
		H_2 position – x' axis	$H_{2_{x'}}$	
		H_2 position – y' axis	$H_{2_{y'}}$	
		H_2 position – z' axis	$H_{2_{z'}}$	
		Cylinder block-valve plate friction moment	M_{cbvp}	
		Cylinder block-valve plate mixed contact moment – x' axis	$M_{vp_{contact_{x'}}}$	
		Cylinder block-valve plate mixed contact moment – y' axis	$M_{vp_{contact_{y'}}}$	
		Cylinder block-valve plate mixed contact moment – z' axis	$M_{vp_{contact_{z'}}}$	
	Output	Cylinder block inclination angle	β	Scalar
		Derivative of cylinder block inclination angle	$\dot{\beta}$	
		Second derivative of cylinder block inclination angle	$\ddot{\beta}$	

2.3.5 Shaft model

The last component of interest for the mechanical modelling is the machine shaft, which is mounted with two tapered roller bearings to balance the loads acting on it. The magnitudes of the axial and radial loads determine the life of the bearings and (in ideal conditions) the life of the motor itself.

Figure 2.87 shows the machine section where we have highlighted the shaft and its centre of mass G_{sh}.

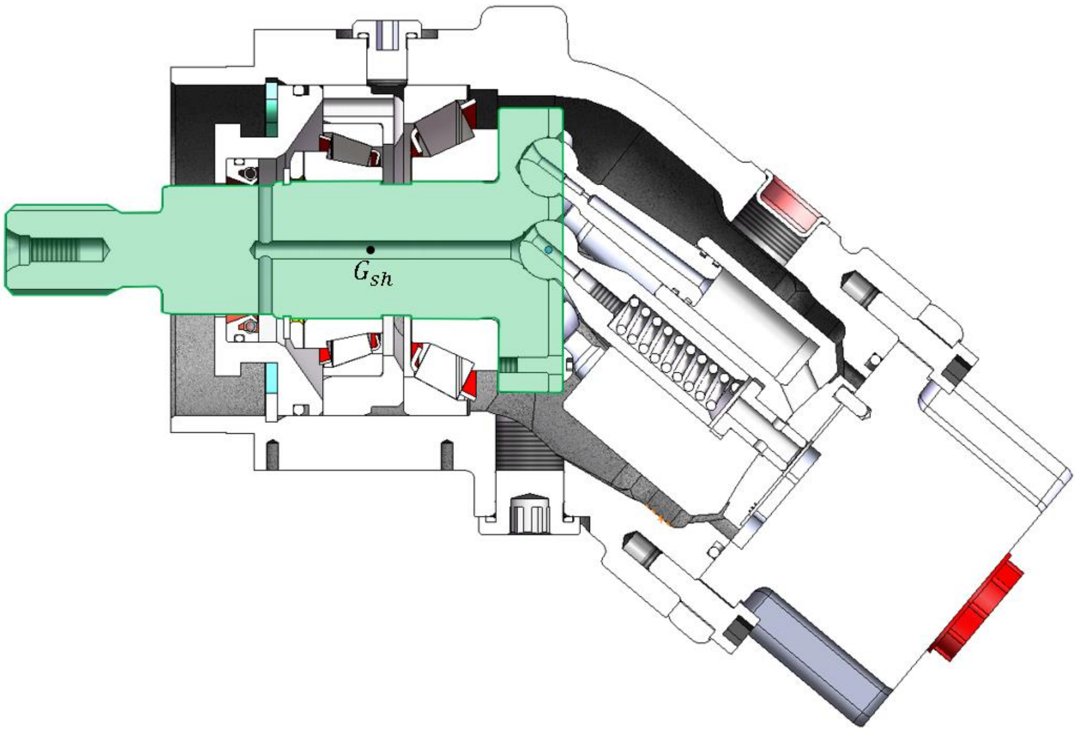

Figure 2.87: Unit shaft in the bent axis unit section

Before proceeding with the analysis and the free body diagram of the shaft, we are reporting the assumptions we have considered:

- the shaft and bearings stiffness are considered infinite, i.e. no shaft and bearings deformations,
- the contact between shaft and the *i*-th piston is considered centred in the *i*-th ball joint centre A_i,
- the contact between shaft and central pivot is considered centred in the central ball joint centre O.

The main outputs of the shaft modelling are:

- torque absorbed or delivered to the shaft, depending on whether the machine is used as pump or motor,
- radial and axial loads discharged by the shaft on tapered roller bearings.

We have considered two different arrangements for the tapered roller bearings to keep the analysis as general as possible:

- O arrangement (**Figure 2.88**),
- X arrangement (**Figure 2.89**).

The loads exerted on the bearings differ depending on the arrangement.

Figure 2.88-2.89 shows the shaft parametrization dividing the O-arrangement case and X-arrangement case. This parametrization considers l_{C_1} and l_{C_2} as negative values, and a_1 and a_2 as positives values regardless of the bearing arrangement.

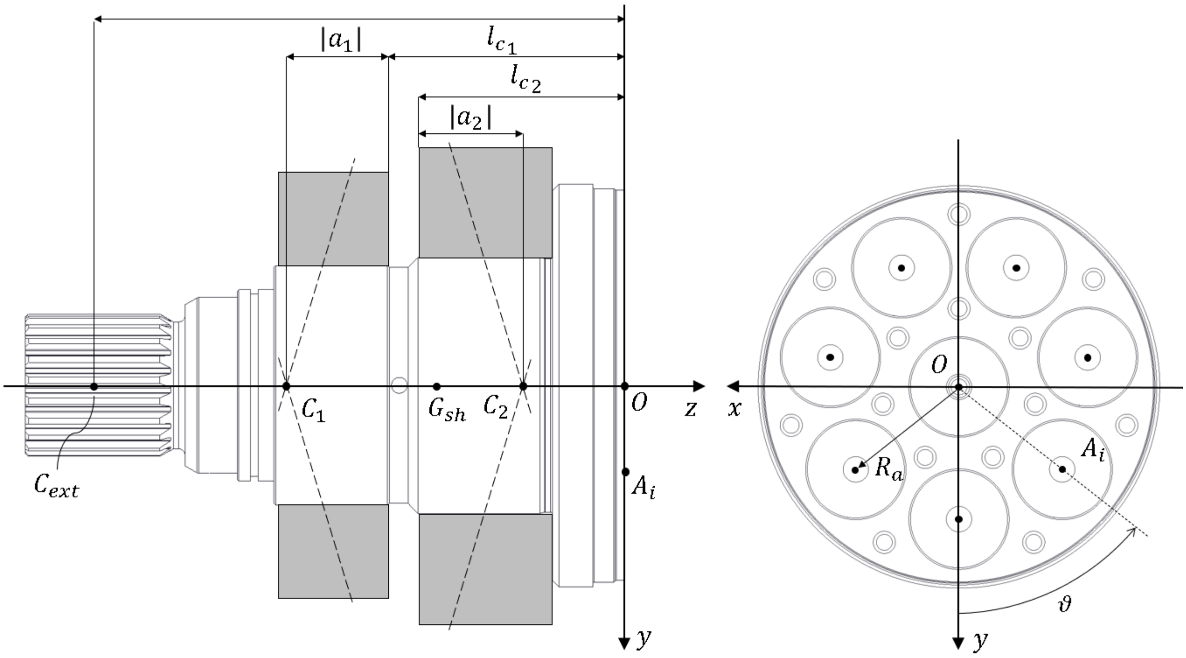

Figure 2.88: Shaft parametrization with O arrangement of the bearings

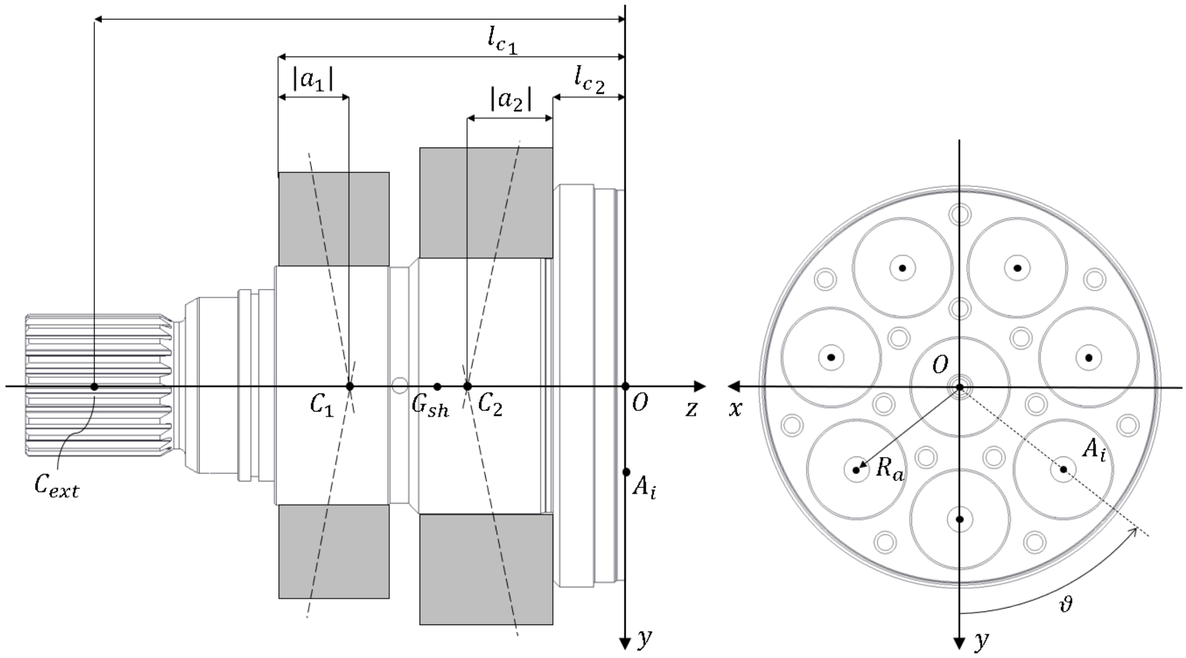

Figure 2.89: Shaft parametrization with X arrangement of the bearings

Eq. (2.450) defines the distances b_1 and b_2 of points C_1 and C_2 from O with O arrangement, while **Eq. (2.450)** reports the evaluation of these distances for X arrangement.

$$O \text{ arrangement:} \quad \begin{aligned} b_1 &= (l_{c1} - |a_1|) \\ b_2 &= (l_{c2} + |a_2|) \end{aligned} \tag{2.450}$$

$$X \text{ arrangement:} \quad \begin{aligned} b_1 &= (l_{c1} + |a_1|) \\ b_2 &= (l_{c2} - |a_2|) \end{aligned} \tag{2.451}$$

Figure 2.90 depicts the generic parameterization of the tapered roller bearing.

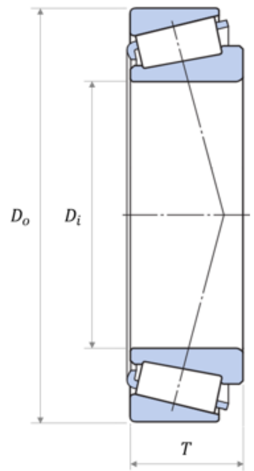

Figure 2.90: Tapered roller bearing parametrization

As usual, **Table 2.28** lists and describes the geometric and non-geometric quantities used in the shaft parameterization and modelling.

Table 2.28: Parameters required for the variable valve plate model

Symbol	Description
α_E	Euler angle α
β_E	Euler angle β
γ_E	Euler angle γ
l_{C_1}	Distance of the outer bearing contact surface from O (reference frame centre) (< 0)
l_{C_2}	Distance of the inner bearing contact surface from O (reference frame centre) (< 0)
l_e	Distance of C_{ext} (point of application of shaft external forces) from O (reference frame centre) (< 0)
a_1	Distance between the outer bearing contact surface and C_1 (point of application of outer bearing loads) (> 0 or < 0)
a_2	Distance between the inner bearing contact surface and C_1 (point of application of inner bearing loads) (> 0 or < 0)
OG_{sh}	Distance between O (reference frame centre) and G_{sh} (shaft centre of mass)
m_{sh}	Shaft mass
F_{rext_x}	External force in C_{ext} along x axis
F_{rext_y}	External force in C_{ext} along y axis
F_{rext_z}	External force in C_{ext} along z axis
D_{o1}	Outside diameter of outer bearing (bearing 1)
D_{o2}	Outside diameter of inner bearing (bearing 2)
D_{i1}	Bore diameter of outer bearing (bearing 1)
D_{i2}	Bore diameter of inner bearing (bearing 2)
T_1	Outer bearing width (bearing 1)
T_2	Inner bearing width (bearing 2)
Y_1	Y parameter of outer bearing (bearing 1)
Y_2	Y parameter of inner bearing (bearing 2)
D_s	Seal diameter
R_{roll_1}	Mean radius of outer bearing rolling elements (bearing 1)
R_{roll_2}	Mean radius of inner bearing rolling elements (bearing 2)
f_{roll}	Bearing rolling friction coefficient

We are directly proceeding with the shaft dynamic analysis as we have assumed it to rotate with constant angular velocity ω.

Dynamic analysis

We can now move on with the introduction of all the known and unknown forces/moments acting on the unit shaft in the same way as we have done for the other components. We are considering the fixed reference frame $Oxyz$ to express all the forces/moments and report the equilibrium equations.

Weight force. We have carried out the shaft weight analysis considering the fixed reference frame $Oxyz$ as it is more convenient for this component. The weight force components are therefore simply equal to the machine frame ones.

$$[F_{sh_{g_{Oxyz}}}] = [F_{sh_{g_{BAU}}}] \tag{2.452}$$

$$\begin{matrix} F_{sh_{gx}} \\ F_{sh_{gy}} \\ F_{sh_{gz}} \end{matrix} \tag{2.453}$$

Piston reaction forces/moments. The mutual forces and moments exchanged between the shaft and pistons are known since they have been already calculated in the piston equilibrium. We have thus reported these contributions to the $Oxyz$ reference system using the inverse rotation matrix $R_{O\prime \to O}$ of **Eq. (2.45)**. Note that we have considered both the contact forces between the *i*-th piston and shaft, and the pressure forces generated ball joint leakage gap. Obviously, it is necessary to reverse the sign of these contributions to consider the reaction forces exerted by the pistons on the shaft (**Eq. 2.454**).

$$F_{pi-sh} = -F_{sh-pi} \tag{2.454}$$

We can obtain more compact expression using summations to consider all the pistons.

$$F_{cont_{pi-sh_{tot,x}}} = \sum_{i=1}^{n} F_{pi-sh_{x_i}} \tag{2.455}$$

$$F_{cont_{pi-sh_{tot,y}}} = \sum_{i=1}^{n} F_{pi-sh_{y_i}} \tag{2.456}$$

$$F_{cont_{pi-sh_{tot,z}}} = \sum_{i=1}^{n} F_{pi-sh_{z_i}} \tag{2.457}$$

$$F_{p,shere_{tot,x}} = \sum_{i=1}^{n} F_{sh_{p,ball_{x_i}}} \tag{2.458}$$

$$F_{p,shere_{tot,y}} = \sum_{i=1}^{n} F_{sh_{p,ball_{y_i}}} \tag{2.459}$$

$$F_{p,shere_{tot,z}} = \sum_{i=1}^{n} F_{sh_{p,ball_{z_i}}} \tag{2.460}$$

It is also possible to combine the contributions along the same axis.

$$F_{(pi-sh)_{tot_x}} = F_{cont_{pi-sh_{tot,x}}} + F_{p,shere_{tot,x}} \tag{2.461}$$

$$F_{(pi-sh)_{tot_y}} = F_{cont_{pi-sh_{tot,y}}} + F_{p,shere_{tot,y}} \tag{2.462}$$

$$F_{(pi-sh)_{tot_z}} = F_{cont_{pi-sh_{tot,z}}} + F_{p,shere_{tot,z}} \tag{2.463}$$

We have also considered the moments (**Eq. (2.464)-(2.465)-(2-466)**) generated by these forces on the shaft. In fact, each of these forces has its own point of application centred in A_i (*i*-th ball joint centre). Note that $M_{(pi-sh)_{tot,z}}$ is the moment that rotates the shaft.

$$M_{(pi-sh)_{tot,x}} = \sum_{i=1}^{n} \left(F_{(pi-sh)_{z_i}} + F_{sh_{p,ball_{z_i}}}\right) \cdot y_{Ai} \tag{2.464}$$

$$M_{(pi-sh)_{tot,y}} = \sum_{i=1}^{n} -\left(F_{(pi-sh)_{z_i}} + F_{sh_{p,ball_{z_i}}}\right) \cdot x_{Ai} \tag{2.465}$$

$$M_{(pi-sh)_{tot,z}} = \sum_{i=1}^{n} \left[-\left(F_{(pi-sh)_{x_i}} + F_{sh_{p,ball_{z_i}}}\right) \cdot y_{Ai} + (F_{(pi-sh)_{y_i}} + F_{sh_{p,ball_{y_i}}}) \cdot x_{Ai}\right] \tag{2.466}$$

We have also considered the friction moments between the shaft and pistons generated by the relative rotation of the latter within the ball joints (δ_i and λ_i). These contributions (with reverse sign) are known from the piston analysis.

$$M_{(pi-sh)_{fr,tot,x}} = \sum_{i=1}^{n} M_{(pi-sh)_{fr,x_i}} \tag{2.467}$$

$$M_{(pi-sh)_{fr,tot,y}} = \sum_{i=1}^{n} M_{(pi-sh)_{fr,y_i}} \tag{2.468}$$

$$M_{(pi-sh)_{fr,tot,z}} = \sum_{i=1}^{n} M_{(pi-sh)_{fr,z_i}} \tag{2.469}$$

<u>Central pivot reaction forces</u>. These forces are known from the resolution of the equilibrium of the cylinder block-central pivot system. As done before, the forces exerted by the central pivot on the shaft have reverse sign with respect to those that the shaft exerts on the pivot. We have also exploited the $R_{O'\rightarrow O}$ matrix to report these contributions on $Oxyz$.

$$\begin{matrix} F_{(cb-sh)_x} \\ F_{(cb-sh)_y} \\ F_{(cb-sh)_z} \end{matrix} \tag{2.470}$$

<u>Shaft external forces</u>. These terms are known external forces applied on C_{ext}. This is thus the shaft external load, which can have three non-zero components.

$$
\begin{array}{c}
F_{r_{ext_x}} \\
F_{r_{ext_y}} \\
F_{r_{ext_z}}
\end{array}
\tag{2.471}
$$

Bearing reaction forces. Each tapered roller bearing performs both radial reactions F_r (which can be divided in the x and y components) and axial (along z axis) reactions F_a. However, it is convenient to consider the total axial reaction K_a instead of the single contributions.

These forces are unknowns of the system and must be obtain from the equilibrium resolution.

$$
\begin{array}{c}
F_{r_{C1_x}} \\
F_{r_{C1_y}} \\
F_{r_{C2_x}} \\
F_{r_{C2_y}} \\
K_a = F_{a_{C1_z}} + F_{a_{C2_z}}
\end{array}
\tag{2.472}
$$

Free body diagrams

Once we have introduced all the forces/moments acting on the unit shaft, it is possible to proceed to the realization of the free body diagrams.

Figure 2.91 shows the known and unknown forces/moments just defined for solving shaft equilibrium, where we have considered an O arrangement of the bearings. As anticipated, however, the analysis remains the same for a X arrangement, where the only difference is the definition of b_1 and b_2 (**Eq. (2.450)-(2.451)**).

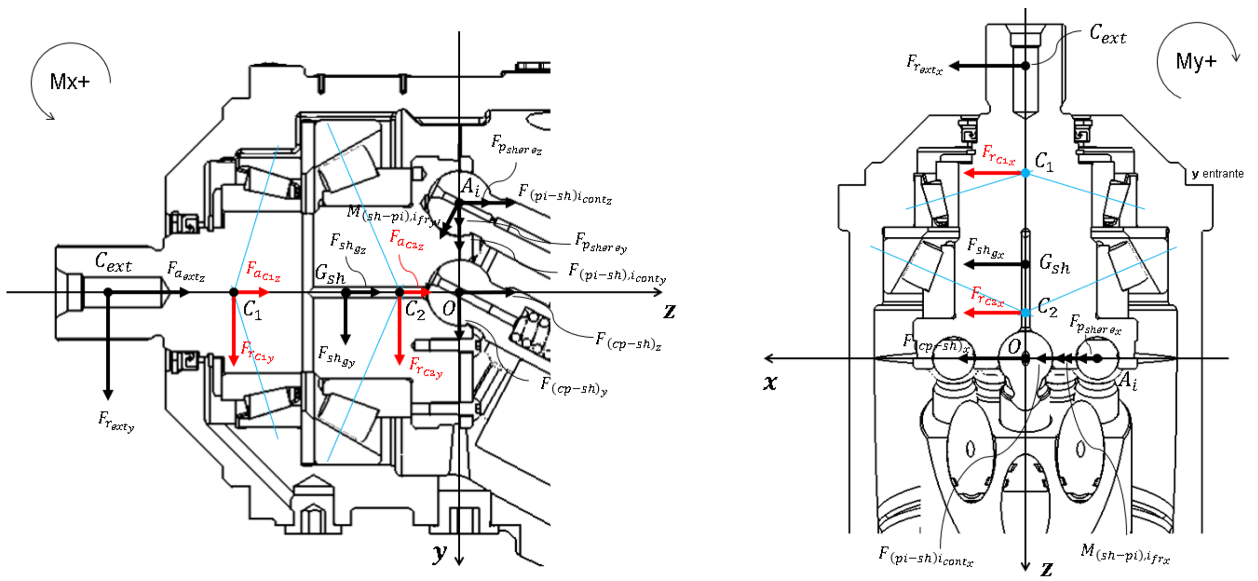

Figure 2.91: Free body diagrams for the unit shaft with the unknown terms highlighted in red

Table 2.29 shows the equation of equilibrium for the unit shaft. Note that the equilibrium equation concerning the rotation around z is missing since we have not yet evaluated the rolling friction moments exerted by the bearings, which are function of the unknown bearing reactions.

Table 2.29: Equilibrium equation for the shaft

Translational equilibrium – x axis	
$F_{r_{ext_x}} + F_{r_{C1_x}} + F_{r_{C2_x}} + F_{sh_{g_x}} + F_{(cp-sh)_x} + F_{(pi-sh)_{tot_x}} = 0$	(2.473)
Translational equilibrium – y axis	

$F_{r_{ext_y}} + F_{r_{C1_y}} + F_{r_{C2_y}} + F_{sh_{g_y}} + F_{(cp-sh)_y} + F_{(pi-sh)_{tot_y}} = 0$	(2.474)
Translational equilibrium – z axis	
$F_{a_{ext_z}} + \left(F_{a_{C1_z}} + F_{a_{C2_z}}\right) + F_{sh_{g_z}} + F_{(cp-sh)_z} + F_{(pi-sh)_{tot_z}} = 0$	(2.475)
Rotational equilibrium about $O-x$ axis	
$-F_{r_{ext_y}} \cdot l_e - F_{r_{C1_y}} \cdot b_1 - F_{sh_{g_y}} \cdot \overline{OG_{sh}} - F_{r_{C2_y}} \cdot b_2 + M_{(pi-sh)_{tot,x}} + M_{(pi-sh)_{fr,tot,x}} = 0$	(2.476)
Rotational equilibrium about $O-y$ axis	
$F_{r_{ext_x}} \cdot l_e + F_{r_{C1_x}} \cdot b_1 + F_{sh_{g_x}} \cdot \overline{OG_{sh}} + F_{r_{C2_x}} \cdot b_2 + M_{(pi-sh)_{tot,y}} + M_{(pi-sh)_{fr,tot,x}} = 0$	(2.477)

This is a system with 5 equations in the following 5 unknowns:

- $F_{r_{C1_x}}$
- $F_{r_{C2_x}}$
- $F_{r_{C1_y}}$
- $F_{r_{C2_y}}$
- $F_{a_{C1_z}} + F_{a_{C2_z}}$

The system can be easily solved by known methods, e.g. by substitution.

Table 2.30 reports the resolution of the equilibrium equations highlighting the unknow expressions.

Table 2.30: Resolution of the equilibrium equation for the shaft

Rotational equilibrium about $O-x$ axis	
$F_{r_{C2_y}} = \dfrac{M_{(pi-sh)_{tot,x}} + F_{sh_{g_y}} \cdot (b_1 - \overline{OG_{sh}}) - F_{r_{ext_y}} \cdot (b_1 - l_e) + \left(F_{(cp-sh)_y} + F_{(pi-sh)_{tot_y}}\right) \cdot b_1 + M_{(pi-sh)_{fr,tot,x}}}{(b_2 - b_1)}$	(2.478)
Rotational equilibrium about $O-y$ axis	
$F_{r_{C2_x}} = \dfrac{M_{(pi-sh)_{tot,y}} + F_{sh_{g_x}} \cdot (\overline{OG_{sh}} - b_1) + F_{r_{ext_x}} \cdot (l_e - b_1) - \left(F_{(cp-sh)_x} + F_{(pi-sh)_{tot_x}}\right) \cdot b_1 + M_{(pi-sh)_{fr,tot,y}}}{(b_1 - b_2)}$	(2.479)
Translational equilibrium – x axis	
$F_{r_{C1_x}} = -\left(F_{r_{ext_x}} + F_{r_{C2_x}} + F_{sh_{g_x}} + F_{(cp-sh)_x} + F_{(pi-sh)_{tot_x}}\right)$	(2.480)
Translational equilibrium – y axis	
$F_{r_{C1_y}} = -\left(F_{r_{ext_y}} + F_{r_{C2_y}} + F_{sh_{g_y}} + F_{(cp-sh)_y} + F_{(pi-sh)_{tot_y}}\right)$	(2.481)
Translational equilibrium – z axis	
$K_a = \left(F_{a_{C1_z}} + F_{a_{C2_z}}\right) = -\left(F_{a_{ext_z}} + F_{sh_{g_z}} + F_{(cp-sh)_z} + F_{(pi-sh)_{tot_z}}\right)$	(2.482)

Once we have evaluated the single components of radial bearing forces, it is possible to calculate the total radial loads with **Eq. (2.483)-(2.484)**.

$$F_{r_{C1}} = \sqrt{F_{r_{C1_x}}^2 + F_{r_{C1_y}}^2} \tag{2.483}$$

$$F_{r_{C2}} = \sqrt{F_{r_{C2x}}^2 + F_{r_{C2y}}^2} \tag{2.484}$$

Before going on to calculate the friction torques and thus the machine torque transmitted to (motor) or absorb by (pump) the shaft, we are proceeding to the evaluation of the bearing reactions.

Eq. (2.485)-(2-491) reports the forces exerted by the shaft on the bearing, where we have reversed the sign of the reaction exerted by the bearings on the shaft and introduced a b subscript.

$$F_{r_{C1x_b}} = -F_{r_{C1x}} \tag{2.485}$$

$$F_{r_{C1y_b}} = -F_{r_{C1y}} \tag{2.486}$$

$$F_{r_{C2x_b}} = -F_{r_{C2x}} \tag{2.487}$$

$$F_{r_{C2y_b}} = -F_{r_{C2y}} \tag{2.488}$$

$$F_{r_{C1_b}} = -F_{r_{C1}} \tag{2.489}$$

$$F_{r_{C2_b}} = -F_{r_{C2}} \tag{2.490}$$

$$K_{a_b} = -K_a \tag{2.491}$$

We then evaluated the single bearing axial forces from the sign and magnitudes of both the radial forces and the total axial force K_{a_b} exploiting a standard approach proposed by SKF [69]. **Figure 2.92** shows this approach, which has been adapted to the present case.

- CASE 1 (K_{a_b} considered positive with direction→; $K_{a_b} > 0$ in the reference frame $Oxyz$)

a. $\begin{cases} \left|\frac{F_{r_{C2_b}}}{Y_2}\right| \geq \left|\frac{F_{r_{C1_b}}}{Y_1}\right| \\ (K_{a_b} \geq 0) \end{cases}$

$F_{a_{C2_b}} = (-)0.5 \cdot \left|\frac{F_{r_{C2_b}}}{Y_2}\right|$

$F_{a_{C1_b}} = -F_{a_{C2_b}} + K_{a_b}$

b. $\begin{cases} \left|\frac{F_{r_{C2_b}}}{Y_2}\right| < \left|\frac{F_{r_{C1_b}}}{Y_1}\right| \\ K_{a_b} \geq 0.5 \cdot \left(\frac{F_{r_{C1_b}}}{Y_1} - \frac{F_{r_{C2_b}}}{Y_2}\right) \end{cases}$

$F_{a_{C2_b}} = (-)0.5 \cdot \left|\frac{F_{r_{C2_b}}}{Y_2}\right|$

$F_{a_{C1_b}} = -F_{a_{C2_b}} + K_{a_b}$

c. $\begin{cases} \left|\frac{F_{r_{C2_b}}}{Y_2}\right| < \left|\frac{F_{r_{C1_b}}}{Y_1}\right| \\ K_{a_b} < 0.5 \cdot \left(\frac{F_{r_{C1_b}}}{Y_1} - \frac{F_{r_{C2_b}}}{Y_2}\right) \end{cases}$

$F_{a_{C1_b}} = (+)0.5 \cdot \left|\frac{F_{r_{C1_b}}}{Y_1}\right|$

$F_{a_{C1_b}} = -\left(F_{a_{C2_b}} - K_{a_b}\right)$

- CASE 2 (K_{a_b} considered positive with direction ←; $K_{a_b} < 0$ in the reference frame $Oxyz$)

a. $\begin{cases} \left|\frac{F_{r_{C2_b}}}{Y_2}\right| \leq \left|\frac{F_{r_{C1_b}}}{Y_1}\right| \\ (|K_{a_b}| \geq 0) \end{cases}$

$F_{a_{C1_b}} = (+)0.5 \cdot \left|\frac{F_{r_{C1_b}}}{Y_1}\right|$

$F_{a_{C2_b}} = -\left(F_{a_{C1_b}} + |K_{a_b}|\right)$

b. $\begin{cases} \left|\frac{F_{r_{C2_b}}}{Y_2}\right| > \left|\frac{F_{r_{C1_b}}}{Y_1}\right| \\ |K_{a_b}| \geq 0.5 \cdot \left(\frac{F_{r_{C2_b}}}{Y_2} - \frac{F_{r_{C1_b}}}{Y_1}\right) \end{cases}$

$F_{a_{C1_b}} = (+)0.5 \cdot \left|\frac{F_{r_{C1_b}}}{Y_1}\right|$

$F_{a_{C2_b}} = -\left(F_{a_{C1_b}} + |K_{a_b}|\right)$

c. $\begin{cases} \left|\frac{F_{r_{C2_b}}}{Y_2}\right| > \left|\frac{F_{r_{C1_b}}}{Y_1}\right| \\ |K_{a_b}| < 0.5 \cdot \left(\frac{F_{r_{C2_b}}}{Y_2} - \frac{F_{r_{C1_b}}}{Y_1}\right) \end{cases}$

$F_{a_{C2_b}} = (-)0.5 \cdot \left|\frac{F_{r_{C2_b}}}{Y_2}\right|$

$F_{a_{C1_b}} = -\left(F_{a_{C1_b}} - |K_{a_b}|\right)$

Figure 2.92: SKF approach for the definition of bearing axial loads [69]

As mentioned, we have then exploited this approach to evaluate $F_{a_{C1_b}}$ and $F_{a_{C2_b}}$ depending on the shaft working conditions.

Once we have obtained the axial loads acting on the single bearings, it is then possible to evaluate the equivalent dynamic load, which will then be used to estimate the bearing life. We considered the approach reported in the "Ball and Roller Bearings" catalogue produced by Koyo [70] for this calculation.

Figure 2.93 shows the calculation of the equivalent dynamic loads P_{C1} and P_{C2} for the inner and outer shaft bearings.

- CASE 1 (K_{a_b} considered positive with direction→; $K_{a_b} > 0$ in the reference frame $Oxyz$)

  a. $\left|\frac{F_{rC2_b}}{2Y_2}\right| + |K_{a_b}| \geq \left|\frac{F_{rC1_b}}{2Y_1}\right|$

  $$P_{C2} = |F_{rC2_b}|$$
  $$P_{C1} = X|F_{rC1_b}| + Y_1\left(\left|\frac{F_{rC2_b}}{2Y_2}\right| + |K_{a_b}|\right) \quad \text{se} \quad P_{C1} > |F_{rC1_b}|$$
  $$P_{C1} = |F_{rC1_b}| \quad \text{se} \quad P_{C1} \leq |F_{rC1_b}|$$

  b. $\left|\frac{F_{rC2_b}}{2Y_2}\right| + |K_{a_b}| < \left|\frac{F_{rC1_b}}{2Y_1}\right|$

  $$P_{C1} = |F_{rC1_b}|$$
  $$P_{C2} = X|F_{rC2_b}| + Y_2\left(\left|\frac{F_{rC1_b}}{2Y_1}\right| - |K_{a_b}|\right) \quad \text{se} \quad P_{C2} > |F_{rC2_b}|$$
  $$P_{C2} = |F_{rC2_b}| \quad \text{se} \quad P_{C2} \leq |F_{rC2_b}|$$

- CASE 2 (K_{a_b} considered positive with direction ←; $K_{a_b} < 0$ in the reference frame $Oxyz$)

  a. $\left|\frac{F_{rC2_b}}{2Y_2}\right| \leq \left|\frac{F_{rC1_b}}{2Y_1}\right| + |K_{a_b}|$

  $$P_{C1} = |F_{rC1_b}|$$
  $$P_{C2} = X|F_{rC2_b}| + Y_2\left(\left|\frac{F_{rC1_b}}{2Y_1}\right| + |K_{a_b}|\right) \quad \text{se} \quad P_{C2} > |F_{rC2_b}|$$
  $$P_{C2} = |F_{rC2_b}| \quad \text{se} \quad P_{C2} \leq |F_{rC2_b}|$$

  b. $\left|\frac{F_{rC2_b}}{2Y_2}\right| > \left|\frac{F_{rC1_b}}{2Y_1}\right| + |K_{a_b}|$

  $$P_{C2} = |F_{rC2_b}|$$
  $$P_{C1} = X|F_{rC1_b}| + Y_1\left(\left|\frac{F_{rC2_b}}{2Y_2}\right| - |K_{a_b}|\right) \quad \text{se} \quad P_{C1} > |F_{rC1_b}|$$
  $$P_{C1} = |F_{rC1_b}| \quad \text{se} \quad P_{C1} \leq |F_{rC1_b}|$$

Figure 2.93: Koyo approach for the calculation of the equivalent dynamic loads of the bearings [70]

As anticipated, it is possible to estimate the bearing life knowing these dynamic loads.

Finally, it is necessary to consider all the system internal losses for the calculation of the shaft torque. Note that all these losses reduce the torque available at the shaft if we are considering a motor, while increase the torque absorbed by the shaft considering a pump.

Eq. (2.492) reports the expression of the total torque at the shaft considering the sum of all contributions characterized by its own direction defined by the sign. Note that this expression has been aligned with the Simcenter Amesim® sign convention between ports.

$$M_{torque} = -(M_{(pi-sh)_{tot,z}} + M_{cb_{fr,z}} + M_{pi_{fr,z}} + M_{(pi-sh)_{fr,tot,z}} + M_{roll_{ss}} + M_{rr} + M_{sl} + M_{drag}) \tag{2.492}$$

where

- $M_{cb_{fr,z}}$ is the sum of cylinder block losses (friction and churning losses),
- $M_{pi_{fr,z}}$ is the sum of pistons losses (friction and churning losses),
- $M_{roll_{ss}}$ is the resistant moment generated by the shaft seal,
- M_{rr} is the shaft rolling friction moment,
- M_{sl} is the shaft sliding friction moment,
- M_{drag} are the shaft churning losses.

Please refer to SKF standard [71] for the evaluation of $M_{roll_{ss}}$, M_{rr}, M_{sl} e M_{drag} depending on the working condition.

Simcenter Amesim Submodel Editor® model

As it was done for the previous components, it was then possible to realize the Simcenter Amesim® submodel concerning the unit shaft, from the definition of the connection ports with adjacent elements to the implementation of the C++ code.

Figure 2.94 shows the representation of the Simcenter Amesim® icon of the shaft submodel BAUSHE000, while **Table 2.31** describes the variables associated to the submodel ports.

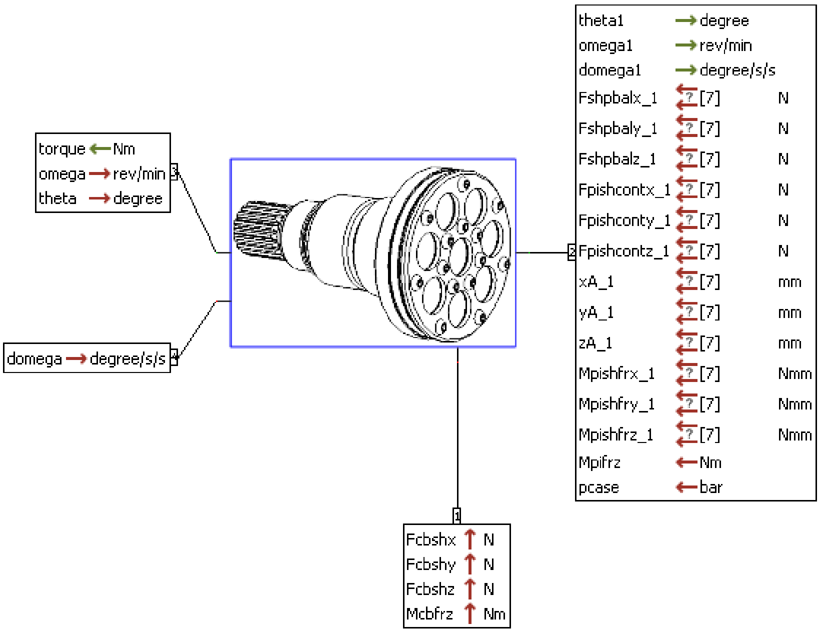

Figure 2.94: Icon of the shaft submodel developed in Simcenter Amesim®

Table 2.31: Inputs/outputs at each port of the shaft submodel developed in Simcenter Amesim®

PORT	VARIABLE	DESCRIPTION	SYMBOL	TYPE
1	Input	Cylinder block-shaft contact force – x axis	$F_{(cb-sh)_x}$	Scalar
		Cylinder block-shaft contact force – y axis	$F_{(cb-sh)_x}$	
		Cylinder block-shaft contact force – z axis	$F_{(cb-sh)_x}$	
		Cylinder block churning losses moment – z' axis	$M_{cb_{fr_z}}$	
2	Input	Ball joint pressure force on shaft – x' axis	$F_{shp,ball_{i_x}}$	Vector
		Ball joint pressure force on shaft – y' axis	$F_{shp,ball_{i_y}}$	
		Ball joint pressure force on shaft – z' axis	$F_{shp,ball_{i_z}}$	
		Piston-shaft contact force – x' axis	$F_{(pi-sh)_{i_x}}$	
		Piston-shaft contact force – y' axis	$F_{(pi-sh)_{i_y}}$	
		Piston-shaft contact force – z' axis	$F_{(pi-sh)_{i_z}}$	
		A_i position – x axis	x_{Ai}	
		A_i position – y axis	y_{Ai}	
		A_i position – z axis	z_{Ai}	
		Piston-shaft friction moment – x axis	$M_{(pi-sh)_{fr_{i_x}}}$	
		Piston-shaft friction moment – x axis	$M_{(pi-sh)_{fr_{i_y}}}$	
		Piston-shaft friction moment – x axis	$M_{(pi-sh)_{fr_{i_z}}}$	
		Piston churning losses moment – z' axis	$M_{pi_{fr_z}}$	Scalar
		Casing pressure	p_{case}	
	Output	Shaft angular position	θ	
		Shaft angular velocity	ω	

		Shaft angular acceleration	$\dot{\omega}$	
3	Input	Shaft angular position	θ	Scalar
		Shaft angular velocity	ω	
	Output	Shaft torque	M_{torque}	
4	Output	Shaft angular acceleration	$\dot{\omega}$	

2.4 Complete model

Once we had completed the entire Simcenter Amesim® custom library for the fluid-dynamic and mechanical modelling of bent axis piston machines, it was possible to link the various element together to create the complete model of the unit.

We performed the elements connection following the schematics of **Figure 2.15** for the fluid-dynamic part and **Figure 2.34** for the mechanical part. In addition to these, it was also necessary to connect the "mixed" ports thanks to which mechanical elements exchange information with fluid-dynamic ones and vice versa.

Figure 2.95 shows the diagram of the complete model of the bent axis unit, where we have highlighted the fluid-dynamic part in blue (upper part) and the mechanical part in green (lower part).

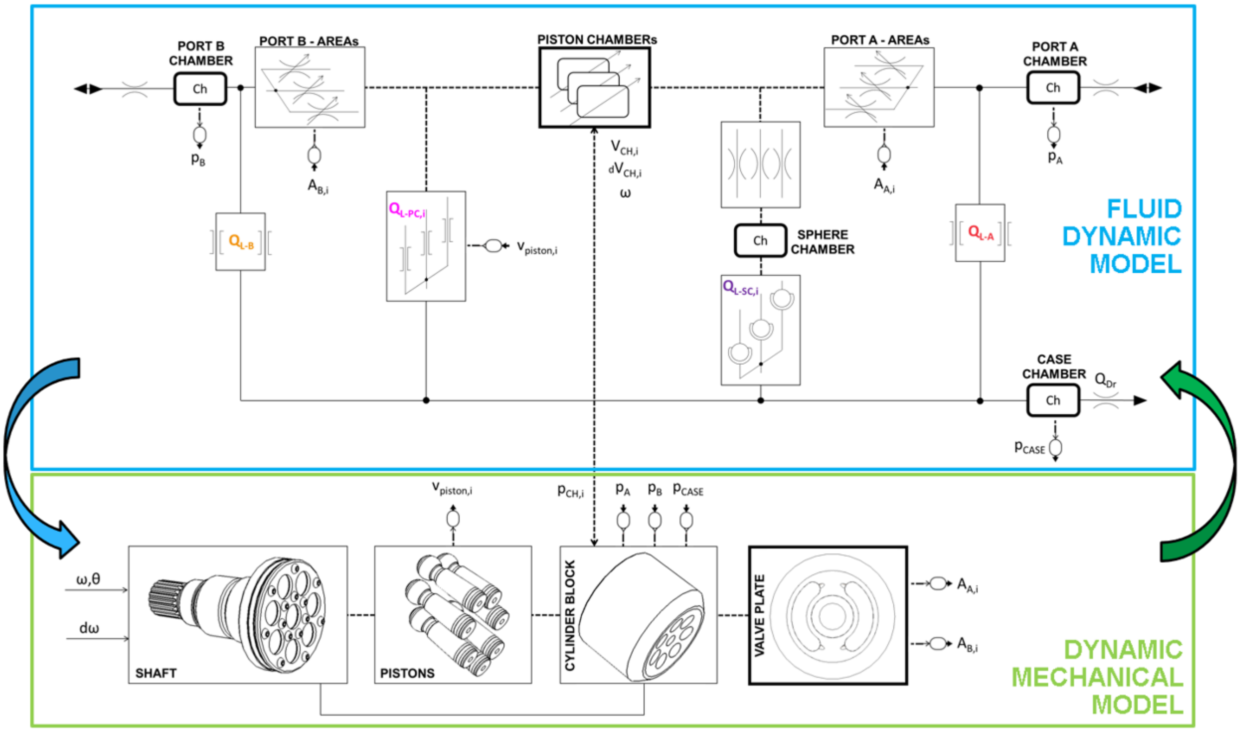

Figure 2.95: Schematic diagram of the complete ben taxis unit with fluid-dynamic (blue) and mechanical part (green)

Figure 2.96 shows the complete Simcenter Amesim® lumped parameter model realized starting from the scheme in **Figure 2.95** concerning a bent axis unit with fixed displacement. Note how we used both the custom elements presented in the previous sections and standard Amesim® elements.

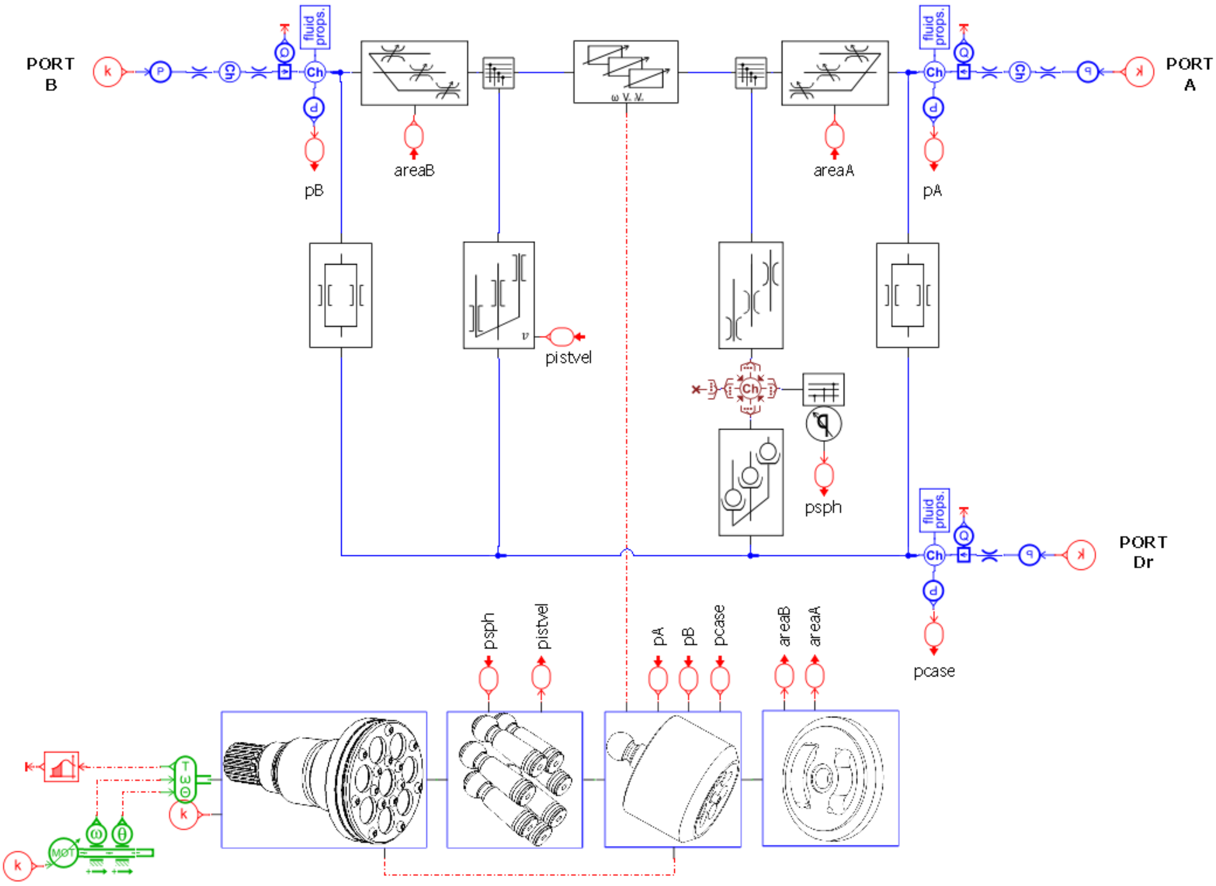

Figure 2.96: Simcenter Amesim® complete model of a bent axis piston unit (with fixed displacement)

The red elements identified by specific labels are receivers/transmitters of the *Signal, Control* standard library. We decided to exploit these elements to connect input and output ports of 'distant' elements to keep the model comprehensible without connecting these ports via many orthogonal lines.

As said, we also introduced other standard Amesim® elements to complete the model, such as orifices, hydraulic chambers and flow/pressure sensors from the *Hydraulic* and *Hydraulis Component Design* libraries, or as an electric motor and sensors connected to the machine shaft from the *1D Mechanical* library.

For the sake of completeness, we are reporting the complete Simcenter Amesim® model for bent axis unit with variable displacement in **Figure 2.97**.

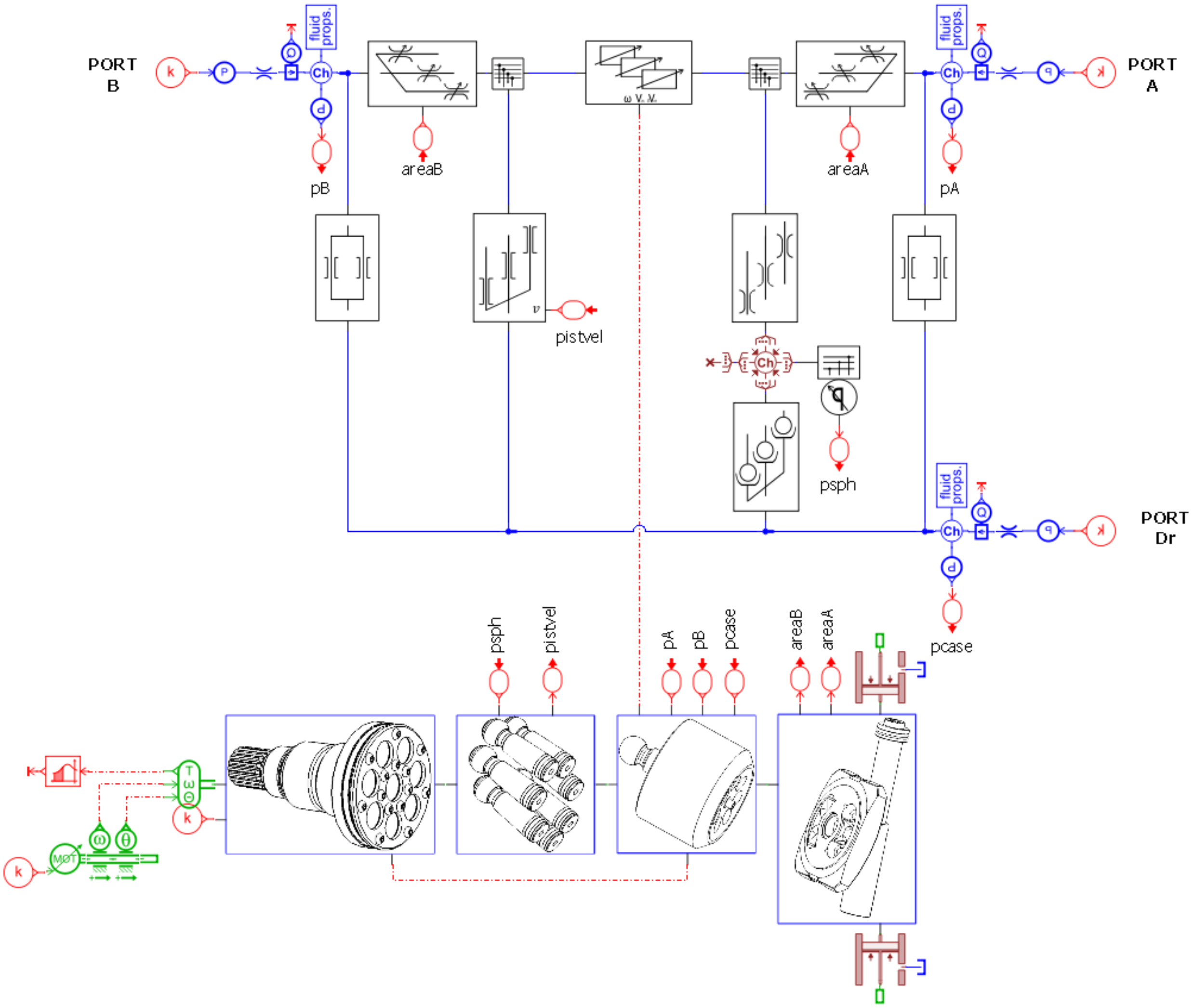

Figure 2.97: Simcenter Amesim® complete model of a bent axis piston unit (with variable displacement)

Note that the only difference between the two complete models is the use of a different valve plate element, while everything else is entirely congruent.

It is also necessary to add the elements for modelling the servo actuator that controls the displacement variation in the model for variable displacement units. Two hydraulic pistons connected to two different pressure sources of pressure define the force acting on the valve plate to vary the unit displacement.

Once the machine model sketching phase has been completed, it is necessary to continue (as seen in **Section 1.3.1**) with the selection of the submodels to use in the simulation. Note that we have created just one submodel for each custom element, so the choice is rather simple.

The Parameter Mode follows the submodel selection, i.e. the model characterization by introducing all the geometric and non-geometric parameters to unambiguously define the bent axis unit under examination.

Finally, it is possible to define the simulation parameters, such as the simulation time, the print interval, or the integration method (variable step, fixed step, numerical method, etc.). The simulation and post processing phase can be easily managed as a standard Simcenter Amesim® model, analysing the results and plotting graphs.

The complete model of the bent axis piston machine presented in this chapter can be exploited to support the design of new machines. Once calibrated, in fact, it is possible to use this model to assess the impact of the variation of one or more characteristic parameters on the machine performances (e.g. looking for a better components balancing, or even an improvement in volumetric and mechanical efficiency). All this, of course, without needing to realize and test a different prototype for each modification.

The following section shows some results obtained from simulations carried out with the complete model presented.

2.5 Results

This section shows some results obtained by exploiting the complete model of bent axis units.

This complete model can be used to analyse several variables, such forces and moments exchanged between the components or balancing coefficients of pistons and cylinder block. However, these results depend on certain parameters entered by the user, which are generally unknown (unless considering standard values from literature).

As anticipated in the activity introduction, one of the goals was exactly the characterization and calibration of these unknown model parameters using the experimental results, such as the leakage gap heights or the mixed (metal to metal and through oil film) friction coefficients between components.

First, together with the Dana engineering department, we decided to consider the SH7V55 bent axis unit with variable displacement, manufactured by the company and already introduced in **Section 2.1**.

We then decided to "optimize" the unknown parameters for this reference machine to minimize the error made on mechanical and volumetric efficiency between simulation and experimental data. We considered different points (Δp [bar], n [rpm]) within the unit range of use and thus minimized the summation of errors to look for an optimal combination of unknown parameters.

In particular, we considered the 'optimization' of the following parameters:

- leakage gap height between cylinder block and valve plate h_{CV},
- leakage gap height between piston side and cylinder block chamber h_{PC},
- leakage gap height between piston spherical end and ball joint seat in the shaft flange h_{SJ},
- friction coefficient between cylinder block and valve plate f_{cb-vp},
- friction coefficient between piston and cylinder block chamber f_{pi-cb},
- friction coefficient between piston spherical end and ball joint seat in the shaft flange f_{pi-sh},
- viscous friction coefficient for churning losses C_d,
- rolling friction coefficient for bearings f_{roll}.

As already mentioned, this approach defined by the company may not lead to the actual combination of gap heights and friction coefficients, but it ensures to identify a parameter combination that minimizes the error regarding the complete machine behaviour. Anyway, note that we have considered realistic ranges of variation for these parameters during the optimization to guarantee a realistic solution.

We have thus accepted to commit possible (small) errors on the individual internal characteristics of the machine to obtain an optimum model alignment concerning the overall unit behaviour.

Moreover, note that it would be difficult to realize a complete validation of all the internal contributions without using the unit efficiencies, as it would be almost impossible to acquire experimental data relating to mutual reaction forces and moments.

We then realize a dedicated test rig to acquire the experimental data of bent axis units. **Figure 2.98** depicts the ISO diagram of the bent axis test rig.

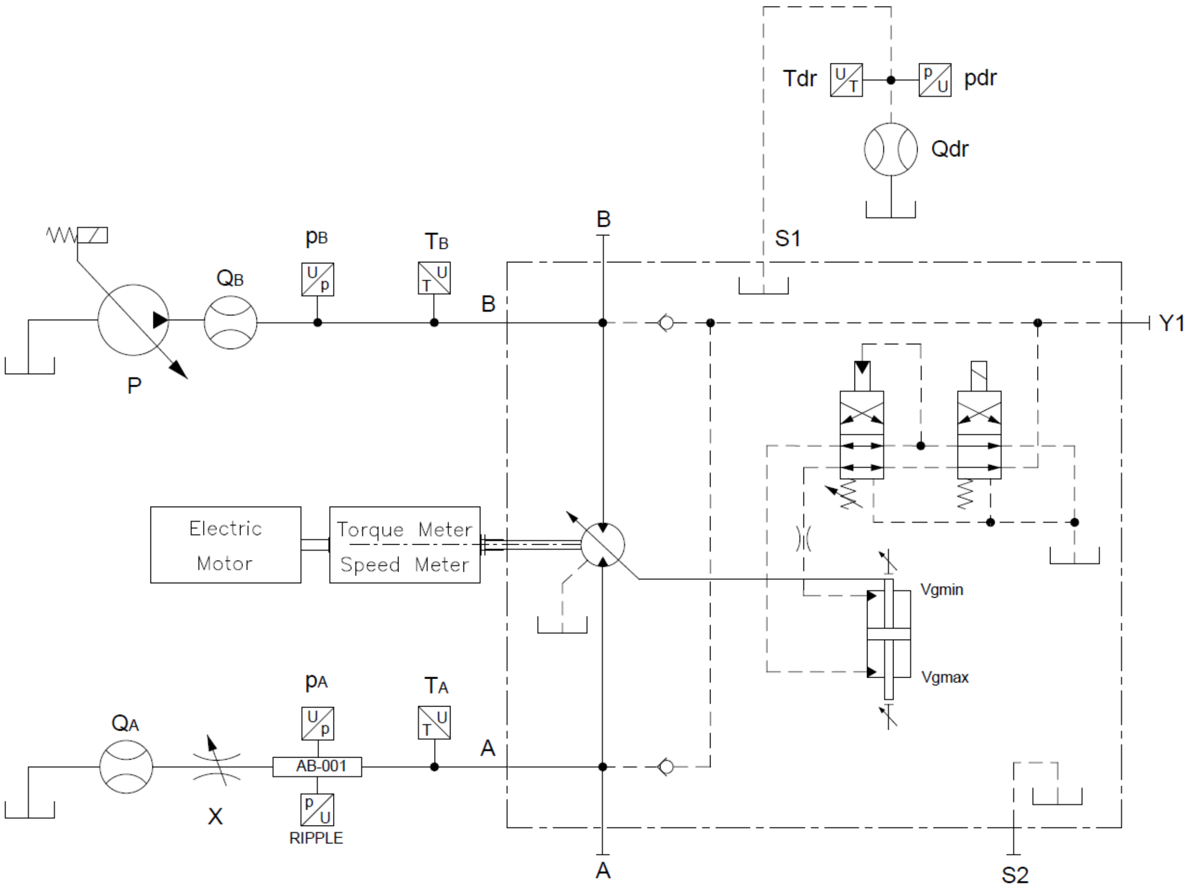

Figure 2.98: ISO scheme diagram of the bent axis test rig

Note that **Figure 2.98** refers to experimental tests carried out on a bent axis unit used as hydraulic motor, where $p_A - p_B < 0$, port B is the high-pressure port of the unit. The considered operating condition for the unit can be highlighted in the four quadrants diagram as reported in **Figure 2.99**.

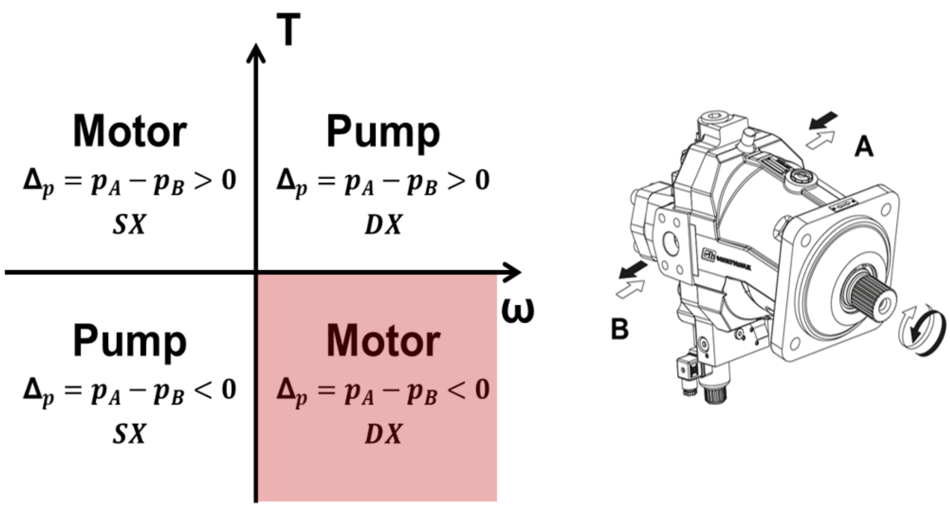

Figure 2.99: Unit working condition quadrant refereed to the results shown

Obviously, we tested the unit in the other working configurations too, simply by reversing the unit installation on the test rig and/or switching the high-pressure port from B to A. However, the results obtained are totally similar to those reported for the fourth quadrant.

We acquired the following experimental data from the test rig:

- unit angular speed (n)
- torque at unit shaft (T)
- tank oil temperature (T_{OIL})
- port B pressure (p_B)
- port B temperature (T_B)
- port B flow rate (Q_B)
- port A pressure (p_A)
- port A temperature (T_A)
- port A flow rate (Q_A)
- drain pressure (p_{Dr})
- drain temperature (T_{Dr})
- drainage flow rate (Q_{Dr})

As mentioned above, it is necessary to considered different points (Δp [bar], n [rpm]) within the unit range of use in order to carry out a general calibration of the unknown parameters. These are steady-state points defined by an angular speed of the unit and a differential pressure across it (with p_A=0).

Figure 2.100 shows a dimensionless graph $\Delta p - n$, where we have highlighted the grid formed by these points examined on the test rig.

This steady-state point grid was then replicated for different displacements to consider the entire range of use of the unit. In particular, we repeated the experimental tests and data acquisitions at 25%, 50%, 75% and 100% of the maximum displacement of the reference bent axis unit.

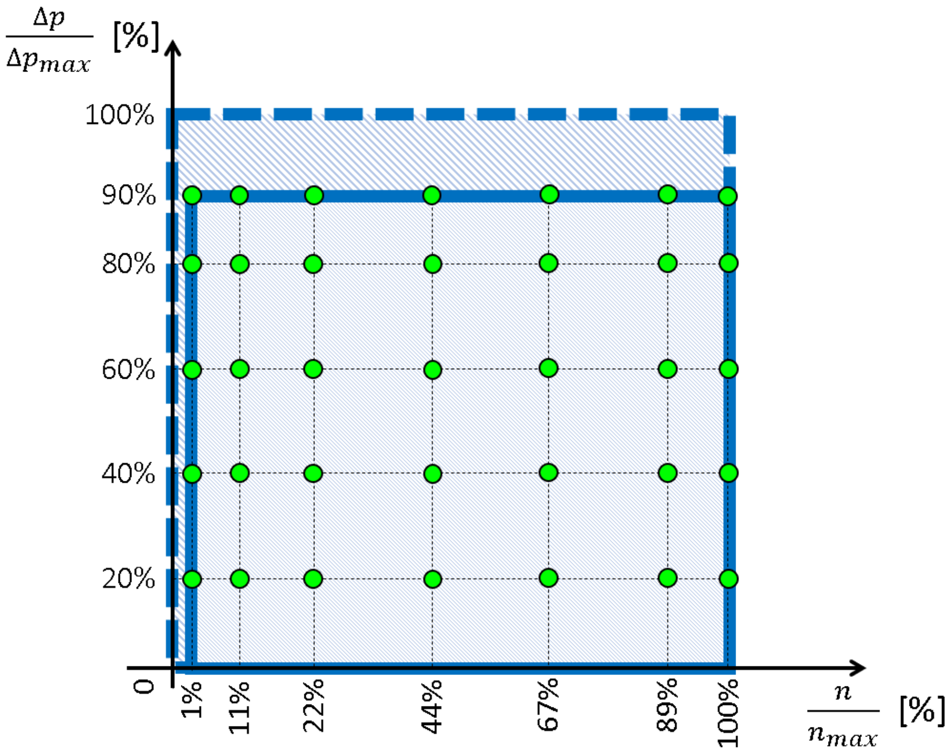

Figure 2.100: Grid of the tested steady state points ($n, \Delta p$)

We could estimate the volumetric and hydro-mechanical efficiency for each working point from the experimental data.

It was then possible to carry out the "optimization" of the unknown parameters considered starting from these experimental efficiency values. The objective functions of the optimization were, as mentioned, the minimization of the error on volumetric (**Eq. (2.493)**) and hydro-mechanical efficiency (**Eq. (2.494)**) concerning the entire range of use of the unit.

$$F_{obj-\eta_V} = \sum \sqrt{\left[\left(\frac{\eta_V^{exp} - \eta_V^{sim}}{\eta_V^{exp}}\right)\right]^2} \tag{2.493}$$

$$F_{obj-\eta_{HM}} = \sum \sqrt{\left[\left(\frac{\eta_{HM}^{exp} - \eta_{HM}^{sim}}{\eta_{HM}^{exp}}\right)\right]^2} \tag{2.494}$$

Note that we have used the summations in **Eq. (2.493)-(2.494)** precisely to consider the error over all the operating points.

This process was the basis of an activity carried out by Dana Incorporated to ‘optimize’ the unknown parameters presented before. Despite this was not an activity performed during the PhD years, we have decided to report some results of interest as they have been obtained exploiting the complete bent axis model.

Figure 2.101-2.102-2.103-2.104 show the comparison between experimental and numerical volumetric/hydro-mechanical efficiencies over the entire range of use of the machine, carried out for various displacements. In particular, we are reporting in this section the results obtained for displacements equal to 75% and 100% of the maximum unit displacement.

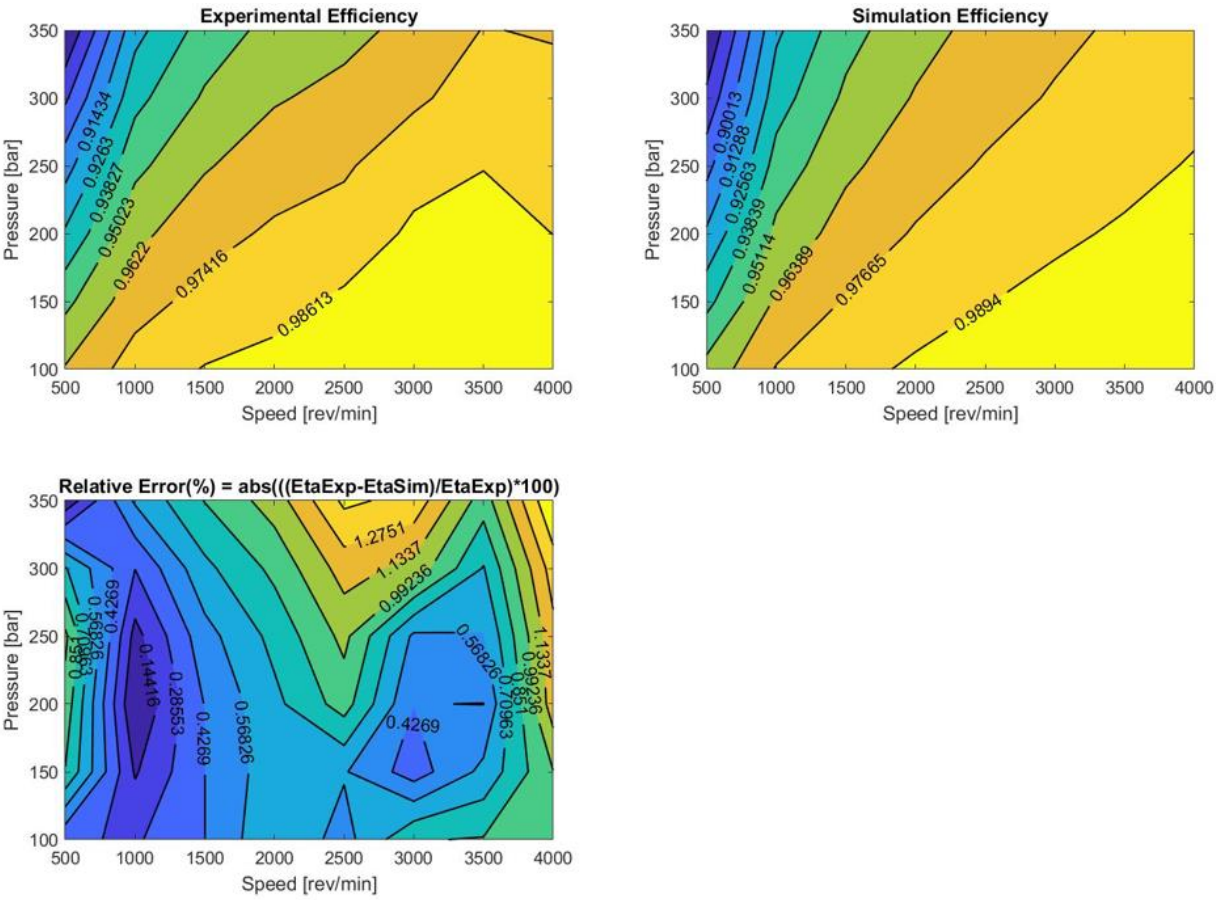

Figure 2.101: Comparison between experimental and numerical volumetric efficiency after the unknown parameter ‘optimization’ with displacement at 75%

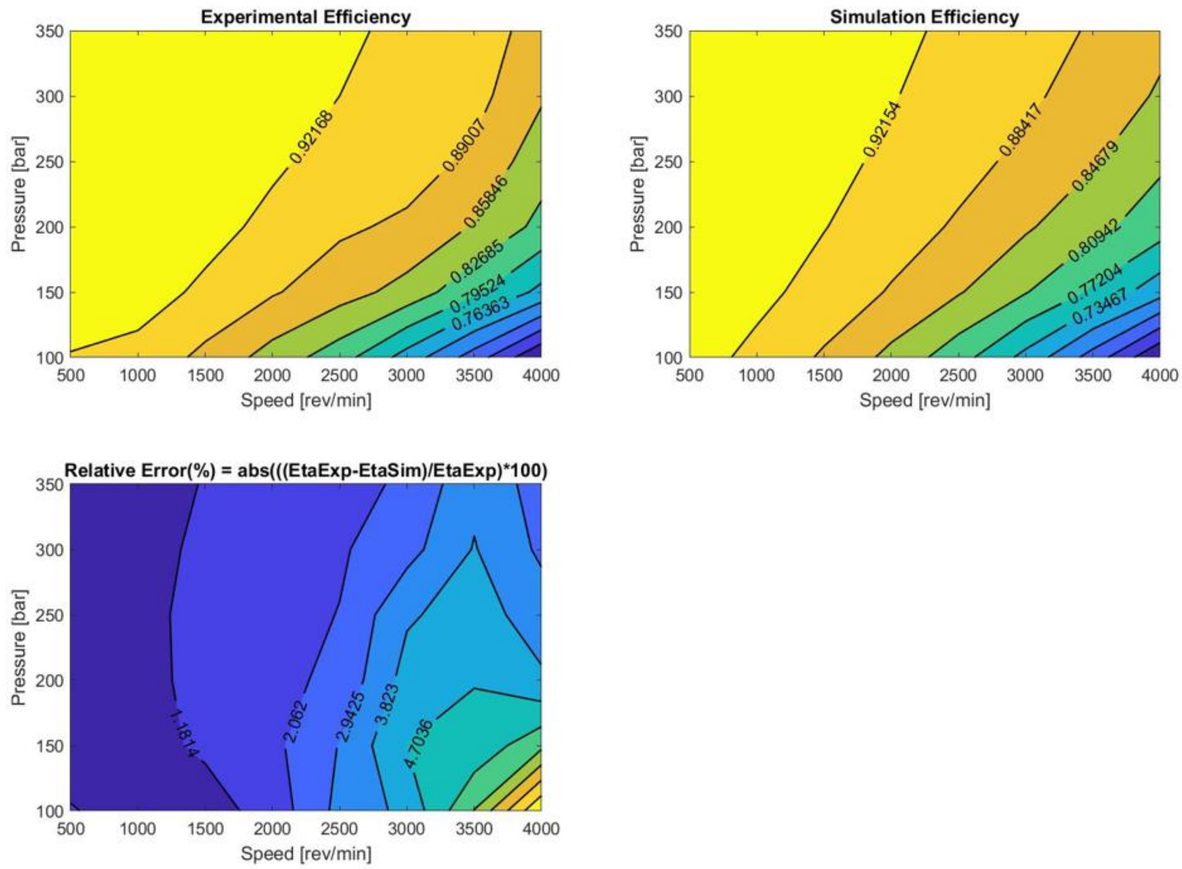

Figure 2.102: Comparison between experimental and numerical hydro-mechanical efficiency after the unknown parameter 'optimization' with displacement at 75%

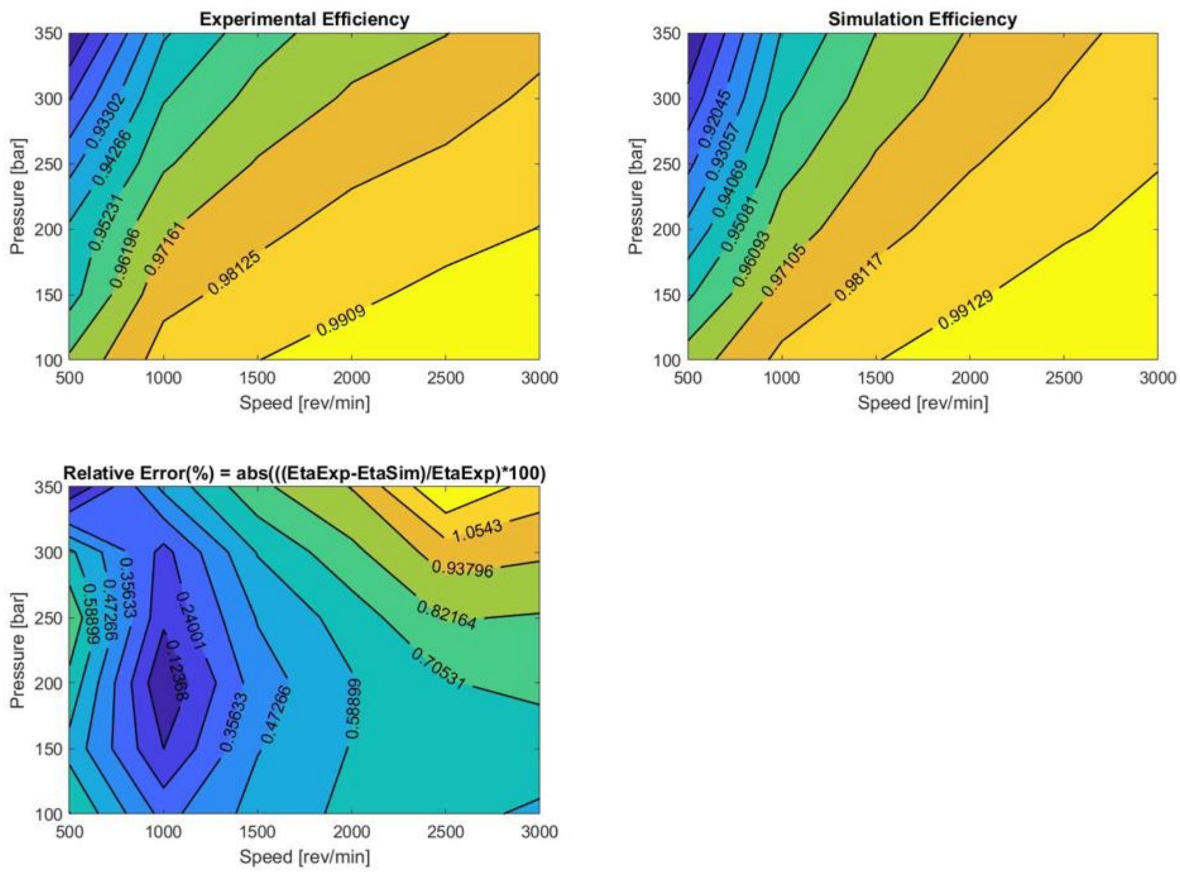

Figure 2.103: Comparison between experimental and numerical volumetric efficiency after the unknown parameter 'optimization' with displacement at 100%

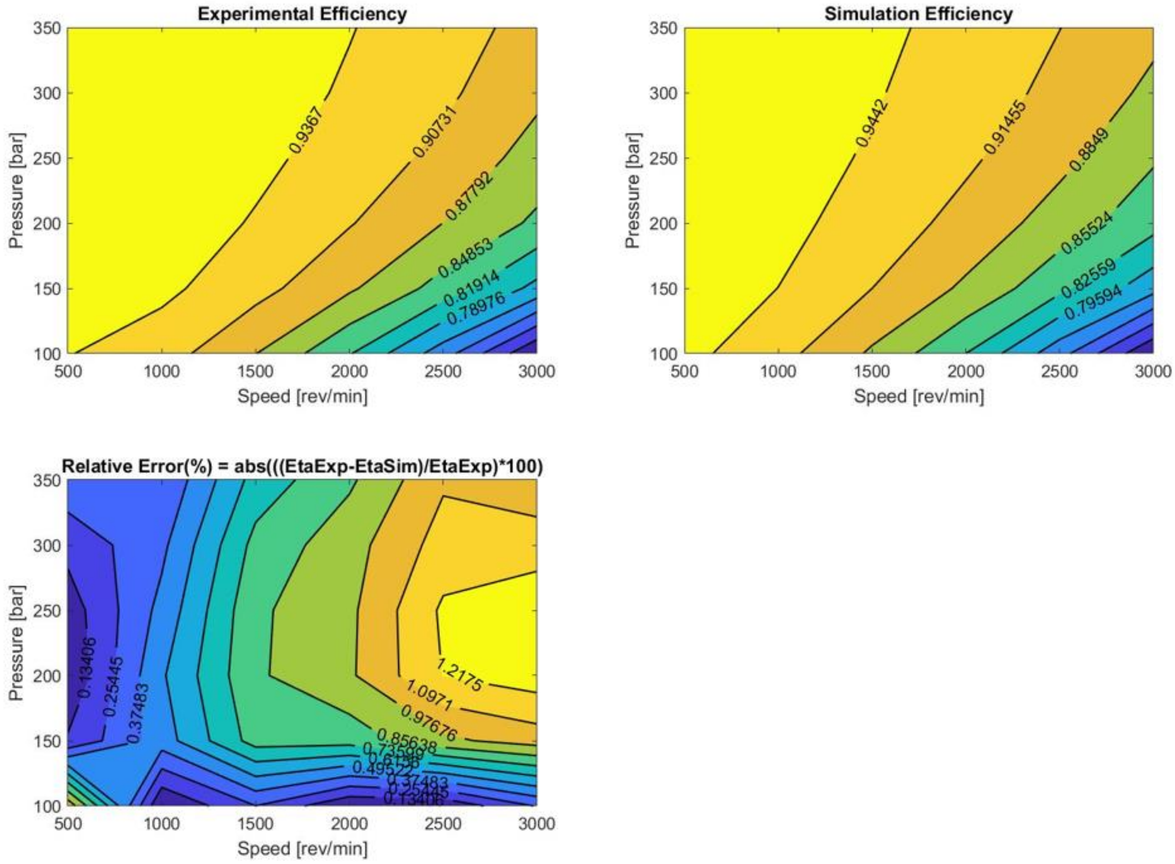

Figure 2.104: Comparison between experimental and numerical hydro-mechanical efficiency after the unknown parameter 'optimization' with displacement at 100%

The graphs show how the set of 'optimized' unknown parameter allows a considerable result alignment concerning both volumetric and hydro-mechanical efficiency, i.e. the general behaviour of the machine. The relative errors obtained by comparing the 'optimized' model efficiencies with their experimental counterparts are decidedly small, in the order of a few percentage units at most, but generally close to the 1% threshold.

The results obtained for displacement at 25% and 50% do not differ much from those presented in the figures above.

We can thus conclude that this "optimization" allowed to calibrate certain unknown parameters which are otherwise impossible to define without more in-depth analyses (CFD, multibody, etc.). This unknown parameter 'optimization' guaranteed an excellent alignment in the machine general behaviour of the complete model with respect to the experimental data.

Once we had completed this optimization, the model can be considered experimentally validated and can therefore be used for further simulations.

Obviously, if we wanted to simulate the behaviour of a different bent axis unit, a new "optimisation" of the unknown parameters would be necessary to calibrate the model. However, the parameter set found for the reference machine can also be used for different machines accepting a few small errors in the first instance.

2.6 Conclusions

The activity presented in this chapter allowed the detailed analysis of bent axis piston units (acting as pump and/or motor). We carried out the modelling of the machine under consideration in a parametric, vectorial, and modular manner to ensure model validity not only for the reference unit, but also for a huge number of machine with similar geometry and characteristics.

We divided the unit model into its fluid-dynamic and mechanical parts, focusing on the latter since the former had already been started by the Dana Incorporated engineering department.

The mechanical (kinematic and dynamic) analysis required the identification of the main components of the bent axis machine. This allowed to perform the mechanical analysis on the individual components, considering the interconnection (inputs/outputs exchanged) with adjacent elements. However, the analysis required the introduction of certain simplifying assumptions to obtain a system that could be solved without the use of further CFD or multibody analysis, which require long time for accuracy and reliability, in terms of both development and experimental validation.

It was then possible to obtain the machine complete model by combining the models of the individual components with the fluid-dynamic part.

It was then possible to create a Simcenter Amesim® library of custom elements suitable for the numerical simulation of this type of hydraulic machine starting from the modelling presented and exploiting the potential of the Submodel Editor tool. This tool, as mentioned, allows the creation from scratch of Submodel Amesim® elements and submodels, from the definition of the parametrization and connection ports to the implementation of the equations of interest in C++ code.

The main output of this activity was therefore the realization of a numerical lumped parameter tool, suitable for the simulation of bent axis piston unit. Once calibrated, this tool can replace experimental tests to characterize the machines under examination or assess the impact of the variation of one or more parameters of interest on the overall behaviour of the unit during the design phase.

Some characteristic parameters affecting the performance of these machines are generally unknow or difficult to evaluate, such as the gap heights or the friction coefficients between the components. We then implemented an optimization to minimize the relative error between the numerical results and the reference experimental results to achieve a calibration of these unknown parameters and then allow the model calibration. A calibrated model can thus be exploited to reliably simulate the behaviour of the machine over the entire range of use.

General conclusions

As anticipated in the introduction, this paragraph only reports some final considerations on the activities carried out during the three years of the PhD course in Industrial and Environmental Engineering at the University of Modena and Reggio Emilia, since the specific conclusions on the individual activities have already been reported at the end of the dedicated chapters.

The activity carried out in these years mainly focused on the numerical modelling of both hydraulic components (bent axis piston machine) and systems (independent hydro-pneumatic suspension). The realization of numerical models capable of both replicating the detailed behaviour of these components/systems and ensuring short simulation times is (and will still be) an important challenge in engineering research for years to come.

Numerical modelling of hydraulics components and systems, however, must co-exist with experimental tests on test rig, which are necessary for the validation of the models themselves. It is precisely for this reason that we decided (in agreement with Dana Incorporated) to carry out the PhD research period abroad by focusing more on the experimental aspects of this field, as briefly described in the Appendix.

In this way, I was able to encounter all the various aspects concerning the fluid power research during my PhD, from the design to component/system modelling, to experimental testing. This has allowed me to get a general overview of the main research activities in fluid power, both academic and company-driven.

Appendix

This appendix provides a brief description of the research activity carried out abroad at Maha Fluid Power Research Center at Purdue University in West Lafayette, Indiana, USA, from 21/02/2022 to 18/09/2022.

Maha Fluid Power Research Center hosts cutting-edge research in hydraulics and fluid power. Every aspect of fluid power and motion control is explored at Maha, from computer modelling of pumps and motors to experimental verification on real-world equipment. This research centre has always been confirmed as one of the leading global centres in the field of hydraulics, both under the previous management of Prof. Monika Ivantysynova (founder) and the current management of Prof. Andrea Vacca. Maha Fluid Power Research Centre is also a founding member of the Global Fluid Power Society, an international community of institutes for networking in the area of fluid power and fluid techniques.

The research activity carried out during these months involved the analysis and initial experimental activities on a prototype of a hybrid hydraulic power-split transmission installed on a Ford F150 pick-up truck.

Power-split transmissions are CVT transmission capable of continuously varying the transmission ratio, like common hydraulic transmissions. However, power-split transmissions possess a planetary gear to manage the division of the power flows from the prime mover to the wheels in addition to a simple hydraulic transmission composed by two hydraulic units (pump/motor). The addition of hydraulic accumulators also allows the possibility of storing and regenerating energy, for example during vehicle braking. This type of system therefore has considerable potential, but obviously requires advanced control logic to manage all these aspects correctly.

This prototype had been developed in collaboration between Folsom Technologies International, the University of Minnesota and Ford to replace the standard transmission of Crown Victoria taxis of the state of New York. It was subsequently accepted at Maha Fluid Power Research Centre to investigate the possibilities of a hybrid power-split transmission, also because there is little research or publication activity on this topic.

The first step of my activity therefore involved the study and analysis of the system under investigation, with the identification of the main components and the deduction of the general operations. The detailed analysis of both the hydraulic part and the mechanical planetary gear is also fundamental to develop a correct numerical model of the system. Once we had understood the general functioning of the transmission, we could identify its possible working modes, from 'standard' power-split transmissions to hybrid transmissions exploiting the capability of regenerating energy during braking and using it to support propulsion.
First, we decided to remove the controller and acquisition system already installed on the vehicle, as they were not working at all. We then upgraded these with a CompactRIO produced and distributed by National Instruments, which is the controller usually used at Maha. This is a controller used both in academic and, above all, industrial applications, capable of managing inputs and outputs of different natures simultaneously thanks to its modular nature. The controller is based on a LabView code.
The following step was the identification of all the inputs (position and pressure sensor signals, vehicle CAN signals, etc.) and outputs (power supply signals for the on/off and proportional valves, supply signals for the displacement variation system of the two hydraulic units, etc.) exchanged between the system and the controller. It was then possible to implement the code concerning the acquisition system for the transmission under examination in Labview, which was tested on the system.
Once we had positively tested the acquisition system, we could define of the first experimental tests to be performed on the power-split transmission. In particular, we decided to use some simple shift maps designed to replicate the behaviour of a manual transmission to vary the displacement of the two hydraulic units depending on the position of the throttle pedal. We realised how the angular speed of the vehicle engine (prime mover) was very sensitive to changes in the throttle pedal position while we were testing this simple control logic. This aspect can be explained also due to the absence of wheel load. The research centre, in fact, does not have a dedicated test rig for carrying out these types of tests on automotive vehicles.
However, it was possible to connect the electrical cables of interest directly to the CompactRIO to manage the throttle valve position ‘manually’ through the controller itself thanks to the presence of throttle by wire. We could thus keep the prime mover's angular speed almost constant regardless of the throttle pedal position, which was used only to define the displacement of the hydraulic units.

We were then able to successfully test these first shift maps, although we encountered some problems always due to the absence of wheel load. This aspect, in fact, affected the ‘high pressure’ of the hydrostatic transmission, which turned out to be very low (a few bars above that of the low-pressure branch) leading to system instability and inconsistent behaviour in the tests.
We also proposed a second and more complex version of shift maps, which were more similar to manual transmissions. This second version involved the use of two maps: a first map (1) used to define the upshifting and downshifting depending on the throttle pedal position and the wheel speed, and a second map (2) used to define the displacement of the two hydraulic units depending on the gear defined by map 1.
A possible third version of the shift maps may involve the use of variable displacements of the units ‘within’ the same gear depending on the engine status.
Parallel to the activity concerning the definition of the transmission control logic, we develop the lumped parameter numerical model of the system exploiting Simcenter Amesim®. However, it was not possible to complete the model calibration and subsequent experimental validation of this virtual tool due again to the lack of test on loaded system.

During this research period abroad, therefore, I laid the foundations for the implementation of advanced control logic for the hybrid hydraulic power-split under examination. At the same time, I exploited this period to gain experience with control logics and experimental tests for hydraulic systems, which were the aspects least analysed during my PhD course.

This experience therefore has allowed to complete my overview of fluid power and hydraulic research.

Bibliography

[1] Bauer, W., *Hydropneumatic suspension systems*, Springer, Berlin, Heidelberg, 2011.

[2] Panetta, G., Mancarella, F., Borghi, M., Zardin, B., Pintore, F., *Dynamic modelling of an off-road vehicle for the design of a semi-active, hydropneumatic spring-damper system*, Proceedings of the ASME 2015 International Mechanical Engineering Congress and Exposition. Volume 4B: Dynamics, Vibration, and Control. Houston, Texas, USA. November 13–19, 2015.

[3] Cole, D. J., *Fundamental Issues in Suspension Design for Heavy Road Vehicles*, Vehicle System Dynamics, 35:4-5, 319-360, 2001.

[4] Previati, G., Gobbi, M., Mastinu, G., *Farm tractor models for research and development purposes*, Vehicle System Dynamics: International Journal of Vehicle Mechanics and Mobility, Volume 45, Issue 1, pp. 37-60, 2007.

[5] Gobbi, M., Mastinu, G., Previati, G., *Farm tractors with suspended front axle: anti-dive and anti-lift characteristics*, Journal of Terramechanics, Volume 56, Pages 157-172, December 2014.

[6] Biral, F., Grott, M., Oboe, R., Maffei, C., Vincenti, E., *Modelling, control and design of heavy duty suspension systems,* AMC'08 The 10th IEEE International Workshop on Advanced Motion Control, 2008.

[7] Grott, M., Biral, F., Oboe, R., Cis, A., Vincenti, E., *Semi-active suspension systems for heavy-duty vehicles: multibody model development, identification and control algorithm evaluation*, Proceedings of the ASME 2009 International Mechanical Engineering Congress and Exposition, Lake Buena Vista, Florida, USA, November 13–19, 2009.

[8] Grott, M., Biral, F., Sorniotti, A., Oboe, R., et al., *Vehicle simulation for the development of an active suspension system for an agricultural tractor*, SAE International Journal of Commercial Vehicles, 2010.

[9] Tey, J.Y., Ramli, R., Kheng, C.W., Chong, S.Y., Abidin, M.A.Z., *Identification of vehicle suspension parameters by design optimization*, Engineering Optimization, 46(5), 669–686, 2014.

[10] Imine, H., Madani, T., *Heavy vehicle suspension parameters identification and estimation of vertical forces: experimental results*, International Journal of Control, 88(2), 324–334, 2015.

[11] Choi, B.L., Choi, J.H. and Choi, D.H., *Reliability-based design optimization of an automotive suspension system for enhancing kinematics and compliance characteristics*, Int. J. Automotive Technology 6, 5, 235– 242, 2004.

[12] Chun, H.H., Kwon, S.J. and Tak, T., *Reliability-based design optimization of automotive suspension systems*, Int. J. Automotive Technology 8, 6, 713−722, 2007.

[13] Yuen, T.J., Rahizar, R., Mohd Azman, Z.A., Anuar, A., Afandi, D., *Design optimization of full vehicle suspension based on ride and handling performance*, Proceedings of the FISITA 2012 World Automotive Congress, Lecture Notes in Electrical Engineering, vol. 195, 2013.

[14] Nishimura, K., Perkins, N.C., Zhang, W., S*uspension dynamics and design optimization of a high speed railway vehicle*, ASME ASME/IEEE 2004 Joint Rail Conference, 129–139, 2004.

[15] Verros, G., Natsiavas, S., Papadimitriou, C., *Design optimization of quarter-car models with passive and semi-active suspensions under random road excitation*, Journal of Vibration and Control, 11(5), 581–606, 2005.

[16] Guo, S., Chen, L., Pan, Y., Wang, X., Tan, G., *Hydraulic integrated interconnected regenerative suspension: sensitivity analysis and parameter optimization*, Electronics 12, 891, 2023.

[17] Suh, K., Yoon, H., D*esign optimization of a rear independent suspension for the Korean light tactical vehicle*, Int.J Automot. Technol. 19, 245–252, 2018.

[18] Kang, D.O., Heo, S.J., Kim, M.S*., Robust design optimization of the McPherson suspension system with consideration of a bush compliance uncertainty*, Proceedings of the Institution of Mechanical Engineers, Part D: Journal of Automobile Engineering, 224(6), 2010.

[19] Su, Z., Xu, F., Hua, L., Chen, H., Wu, K., Zhang, S., *Design optimization of minivan MacPherson-strut suspension system based on weighting combination method and neighborhood cultivation genetic algorithm*, Proceedings of the Institution of Mechanical Engineers, Part D: Journal of Automobile Engineering, 095440701878930–, 2018.

[20] Esfahani, M., Mosayebi, M., Pourshams, M., Keshavarzi, A., *Optimization of double wishbone suspension system with variable camber angle by hydraulic mechanism*, Digital Open Science Index, Mechanical and Mechatronics Engineering Vol:4, No:1, 2010.

[21] Yi, Y., Park, J., and Hong, K., *Design optimization of suspension kinematic and compliance characteristics*, SAE Technical Paper 2014-01-0394, 2014.

[22] Gubitosa, M., Anthonis, J., Albarello, N., Desmet, W., *A system engineering approach for the design optimization of a hydraulic active suspension*, IEEE Vehicle Power and Propulsion Conference, 1122–1130, 2009.

[23] Smith, W.A., Zhang, N., *Hydraulically interconnected vehicle suspension: optimization and sensitivity analysis*, Proceedings of the Institution of Mechanical Engineers, Part D: Journal of Automobile Engineering, 224(11), 1335–1355, 2010.

[24] Baumal, A.E., McPhee, J.J., Calamai, P.H., *Application of genetic algorithms to the design optimization of an active vehicle suspension system*, Computer Methods in Applied Mechanics and Engineering, 163(1-4), 87–94, 1998.

[25] Kang, D.O., Heo, S.J., Kim, M.S. et al., *Robust design optimization of suspension system by using target cascading method*, International Journal of Automotive Technology, 13, 109–122, 2012.

[26] Cui, T., Zhao, W., Wang, C. et al., *Design optimization of a steering and suspension integrated system based on dynamic constraint analytical target cascading method*, Structural and Multidisciplinary Optimization, 62, 419–437 (2020).

[27] ISO 2631-1:2014, Mechanical vibration and shock – Evaluation of human esposure to whole-body vibration.

[28] ISO 5008:2002, Agricultural wheeled tractors and field machinery – Measurement of whole-body vibration of the operator.

[29] Cutini, M., Brambilla, M., Bisaglia, C., *Assessment of a ride comfort number for agricultural tractors: a simplified approach*, Biosistems engineering, 185, 35-44. 2019.

[30] Kim, P., *Rigid body dynamics for beginners: Euler angles and quaternions*, Createspace, 2013.

[31] Simcenter Amesim Help Manual.

[32] Pacejka, H., *Tire and vehicle dynamics*, SAE, 2002.

[33] ISO 8855:2011, Road vehicles – Vehicles dynamics and road-holding ability – Vocabulary.

[34] Nussbaumer, H. J., *Fast Fourier transform and convolution algorithms*, Springer Series in Information Sciences, vol 2, Springer, Berlin, Heidelberg, 1981.

[35] Guiggiani, M., *The science of vehicle dynamics*, Springer, Pisa, 2018.

[36] Kochenderfer, M. J., Wheeler, T. A. *Algorithms for optimization*, The MIT Press, 2019.

[37] Mazzoldi, P., Nigro, M., Voci, C., *Meccanica e Termodinamica*, EdiSES Edizioni, 2000.

[38] ISO 3888-2:2011, Passenger cars – Test track for a severe lane-change manoeuvre – Part 2: Obstacle avoidance.

[39] Manco', S., Nervegna, N., *Simulation of an external gear pump and experimental verification*, Proceedings of the JFPS International Symposium on Fluid Power, 1989(1), 147–160, 1989.

[40] Casoli, P., Vacca, A., Franzoni, G., *A numerical model for the simulation of external gear pumps*, Proceedings of the JFPS International Symposium on Fluid Power, 2005(6), 705–710, 2005.

[41] Vacca, A., Guidetti, M., *Modelling and experimental validation of external spur gear machines for fluid power applications*, Simulation Modelling Practice and Theory, 19, 2007–2031, 2011.

[42] Shah, Y., Vacca, A., Dabiri, S., *Air release and cavitation modeling with a lumped parameter approach based on the Rayleigh–Plesset equation: the case of an external gear pump*, Energies, 11(12), 3472–, 2018.

[43] Battarra, M., Mucchi, E., *On the assessment of lumped parameter models for gear pump performance prediction*, Simulation Modelling Practice and Theory, 99(), 102008–, 2020.

[44] Mancò, S., Nervegna, N., Rundo, M., Armenio, G., Pachetti, C., Trichilo, R., *Gerotor Lubricating Oil Pump for IC Engines*, SAE Technical Paper Series [SAE International International Fall Fuels and Lubricants Meeting and Exposition - (Oct. 19, 1998)], 1998.

[45] Fabiani, M., Mancò, S., Nervegna, N., Rundo, M., Armenio, G., Pachetti, C., Trichilo, R., *Modelling and simulation of gerotor gearing in lubricating oil pumps*, SAE Technical Paper Series [SAE International International Congress & Exposition - (Mar. 01, 1999)], 1999.

[46] Mancò, S., Nervegna, N., Rundo, M., A *contribution to the design of hydraulic lube pumps*, International Journal of Fluid Power, 3(1), 21–32, 2002.

[47] Rundo, M., *Models for flow rate simulation in gear pumps: a review*, Energies, 10(9), 1261–, 2017.

[48] Altare, G., Rundo, M., *Advances in simulation of gerotor pumps: an integrated approach*, Proceedings of the Institution of Mechanical Engineers, Part C: Journal of Mechanical Engineering Science, 231(7), 1221–1236, 2017.

[49] Ivantysyn, J., Ivantysynova, M., *Hydrostatic pumps and motors: principles, design, performance, modelling, analysis, control and testing*, Tech Books International, 2003.

[50] Nervegna, N., Rundo, M., *Fluid Power*, Epics, 2018.

[51] Zeiger, G., Akers, A., *Dynamic analysis of an axial piston pump swashplate control*, Proceedings of the Institution of Mechanical Engineers, Part C: Journal of Mechanical Engineering Science, 1986.

[52] Milestone, W. D., Solomon, A., Olsen, G., *The kinematic analysis odf axial-piston pumps*, Mechanism and Machine Theory Vol. 18, No. 6, pp. 475-479, Pergamon Press. Ltd., 1983.

[53] Zhiru, S., Parker, G., Granstrom, J., *Kinematic Analysis of a Swash-Plate Controlled Variable Displacement Axial-Piston Pump With a Conical Barrel Assembly*, Journal of Dynamic Systems, Measurement, and Control, 132(1), 2010.

[54] Bing, X., Junhui, Z., Ying, L., Qun, C., *Modeling and analysis of the churning losses characteristics of swash plate axial piston pump*, International Conference on Fluid Power and Mechatronic, 2015.

[55] Mancò, S., Nervegna, N., Lettini, A., Gilardino, L., *Advances in the simulation of axial piston pumps*, Fifth JFPS International Symposium, 2002.

[56] Casoli, P., Vacca, A., Franzoni, G., Berta, G.L., *Modelling of fluid properties in hydraulic positive displacement machines*, Simulation Modelling Practice and Theory 14, 1059–1072, 2006.

[57] Roccatello, A., Mancò, S., Nervegna, N., *Modelling a variable displacement axial piston pump in a multibody simulation environment*, Journal of Dynamic Systems, Measurement, and Control, 129(4), 456–, 2007.

[58] Rundo, M., Altare, G., *Lumped parameter and three-dimensional CFD simulation of a variable displacement vane pump for engine lubrication*, Journal of Fluids Engineering, 2017.

[59] Caretto, R., Mancò, S., Nervegna, N., Rundo, M., *Modelling, simulation and experimental studies on a variable displacement radial piston pump prototype for automotive applications*, The ASME International Mechanical Engineering Congress and Exposition, Fluid Power Systems and Technology, Vol. 3, 1-9, 1996.

[60] Abuhaiba, M., Olson, W. W., *Geometric and kinematic modeling of a variable displacement hydraulic bent-axis piston pump*, Journal of Computational and Nonlinear Dynamics, Vol.5, 2010.

[61] Stolarski, T., *Tribology in machine design*, Elsevier, 1999.

[62] Bassani, R., Picciogallo, B., *Hydrostatic Lubrication*, Elsevier, 1992.

[63] Hong, Y. S., Doh, Y. H., *Analysis on the friction losses of a bent-axis type hydraulic piston pump*, KSME International Journal 18, 1668–1679, 2004.

[64] Kumar, N., Dasgupta, K., Ahmad, F., *Analysis of Leakage Flow characteristics in Bent Axis Motors*, Proceedings of the 1st International and 16th National Conference on Machines and Mechanisms, India, 2013.

[65] Roccatello, A., Nervegna, N., *Mechanical modelling of a bent axis pump*, International Journal of Fluid Power, 10:2, 57-72, 2009.

[66] ISO 1219-1:2012, Fluid power systems and components – Graphical symbols and circuit diagrams – Part 1: Graphical symbols for conventional use and data-processing applications.

[67] Vacca, A., Franzoni, G., *Hydraulic Fluid Power: fundamentals, applications and circuits*, John Wiley and Sons Inc., 2021.

[68] Bergada, J. M., Kumar, S., Davies, D. Ll., Watton, J., *A complete analysis of axial piston pump leakage and output flow ripples*, Applied Mathematical Modelling, 36, 1731-1751, 2011.

[69] SKF, *Rolling bearings* catalogue.

[70] Koyo, *Ball & Roller Bearings* catalogue.

[71] SKF, *The SKF model for calculating the frictional moment*.